Universitat de Barcelona

Rare Earth-Doped Silicon-Based Light Emitting Devices: Towards new Integrated Photonic Building Blocks

Joan Manel Ramírez

ADVERTIMENT. La consulta d'aquesta tesi queda condicionada a l'acceptació de les següents condicions d'ús: La difusió d'aquesta tesi per mitjà del servei TDX (**www.tdx.cat**) i a través del Dipòsit Digital de la UB (**diposit.ub.edu**) ha estat autoritzada pels titulars dels drets de propietat intel·lectual únicament per a usos privats emmarcats en activitats d'investigació i docència. No s'autoritza la seva reproducció amb finalitats de lucre ni la seva difusió i posada a disposició des d'un lloc aliè al servei TDX ni al Dipòsit Digital de la UB. No s'autoritza la presentació del seu contingut en una finestra o marc aliè a TDX o al Dipòsit Digital de la UB (framing). Aquesta reserva de drets afecta tant al resum de presentació de la tesi com als seus continguts. En la utilització o cita de parts de la tesi és obligat indicar el nom de la persona autora.

ADVERTENCIA. La consulta de esta tesis queda condicionada a la aceptación de las siguientes condiciones de uso: La difusión de esta tesis por medio del servicio TDR (**www.tdx.cat**) y a través del Repositorio Digital de la UB (**diposit.ub.edu**) ha sido autorizada por los titulares de los derechos de propiedad intelectual únicamente para usos privados enmarcados en actividades de investigación y docencia. No se autoriza su reproducción con finalidades de lucro ni su difusión y puesta a disposición desde un sitio ajeno al servicio TDR o al Repositorio Digital de la UB. No se autoriza la presentación de su contenido en una ventana o marco ajeno a TDR o al Repositorio Digital de la UB (framing). Esta reserva de derechos afecta tanto al resumen de presentación de la tesis como a sus contenidos. En la utilización o cita de partes de la tesis es obligado indicar el nombre de la persona autora.

WARNING. On having consulted this thesis you're accepting the following use conditions: Spreading this thesis by the TDX (**www.tdx.cat**) service and by the UB Digital Repository (**diposit.ub.edu**) has been authorized by the titular of the intellectual property rights only for private uses placed in investigation and teaching activities. Reproduction with lucrative aims is not authorized nor its spreading and availability from a site foreign to the TDX service or to the UB Digital Repository. Introducing its content in a window or frame foreign to the TDX service or to the UB Digital Repository is not authorized (framing). Those rights affect to the presentation summary of the thesis as well as to its contents. In the using or citation of parts of the thesis it's obliged to indicate the name of the author.

Rare Earth-Doped Silicon-Based Light Emitting Devices: Towards new Integrated Photonic Building Blocks

A dissertation by

JOAN MANEL RAMÍREZ

In Partial Fulfilment of the

Requirements for the Degree of Doctor of Philosophy in Physics

at the

UNIVERSITAT DE BARCELONA

July 2015

Director

BLAS GARRIDO FERNÁNDEZ

To my parents, my sister and my wonderful partner Alícia, with my gratitude for their unconditional support, patience and love

Author:

Joan Manel Ramírez

B Garrido

Director:

Prof. Dr. Blas Garrido Fernández

Abstract

Rare earth (RE) doped Si-based light emitting devices are meant to provide solutions to the monolithic integration of photonic and electronic functions in a single chip. Being Si the ultimate material for microelectronics, intense research is being conducted towards the implementation of Si-based photonic devices using the mainstream CMOS technology. Such milestone, if successfully accomplished, would address the interconnect bottleneck of microelectronics while offering competent performance in other arenas such as the datacom, sensing, optical metrology or lighting technologies. Also, from the environmental viewpoint, the convergence of photonics and microelectronics in a single process is expected to impact on the global energy demand, providing high energy saving due to a more efficient device operation.

In that framework, the incorporation of tiny luminescent centres such as silicon nanocrystals (Si-ncs)[1] or RE ions into the gate oxide of a Metal-Insulator-Semiconductor (MIS) device was proposed as an effective tool to fulfil such requirement. Although Si is an indirect bandgap material and thus displays poor luminescence properties, a considerable enhancement of its optical properties is obtained by an effective de-localization of the electron-hole wavefunction through quantum confinement in nanostructured Si. As a consequence, intense light emission from the visible region of the electromagnetic spectrum up to the near infrared (NIR) has been reported by several authors. Moreover, Si-ncs have demonstrated to be excellent sensitizers for RE ions, providing a continuous absorption spectra in the UV range and enhanced RE luminescence governed by an energy transfer exchange between Si-ncs and RE ions. Concerning the optical activity of RE ions, they yield intense and narrow emission lines originated as a consequence of a radiative de-excitation of RE excited states. Similarly than for Si-ncs, Si-based light emitting devices operating at different wavelengths can be developed by choosing one RE ion or another.

Therefore, in view of the fascinating milestones and challenges mentioned above, this dissertation presents the work carried out towards the implementation of RE-doped Si-based light emitting devices as integrated optoelectronic building blocks for silicon photonics. This work spans from the fundamentals such as the structure, the morphology of active layers containing Si-ncs and/or RE ions or the origin of the electroluminescence (EL) emission under different voltage excitations, to the development of advanced Si-based light emitting devices, providing insights on the device design, mask layout, device fabrication and the optoelectronic characterization. Also, novel layer architectures are proposed to overcome some of the inherent limitations of studied devices, paving the way towards efficient and reliable Si-based

---

[1] *The word silicon nanocrystals will be used from now on to refer to tiny Si agglomerations, regardless of their degree of crystallinity (also for amorphous Si clusters).*

light emitting devices. This dissertation is divided in two main blocks: one dedicated to the study of Er-doped Si-based light emitting devices emitting

at 1.54 μm for on-chip optical data routing, and another one focussed on the structural and luminescence properties of Tb^{3+} and Ce^{3+} doped silicon oxide and oxynitride thin films with different layer compositions as enabling materials for sensing and RGB micro display applications. Also, different multilayer architectures containing alternated RE-doped single layers are explored.

In the first part of this dissertation, the optoelectronic properties of MIS devices containing optically active Er^{3+} ions embedded in either a silicon oxide (SiO_2) or a silicon nitride (Si_3N_4) host with variable Si excess are presented. The dependence of the host matrix morphology, the annealing treatments or the Si excess on the main charge transport phenomena taking place in Er-doped MIS devices is studied. A bulk-limited conduction is disclosed when the annealing treatment does not fully passivate intraband defect sites located in the host matrix. On the contrary, well-passivated layers with low defect density show an electrode-limited mechanism. In that line, a second order dependence is also reported for the Si excess, obtaining a switching of the transport mechanism from electrode-limited (low Si excess) to bulk-limited conduction (high Si excess) in off-stoichiometric silicon oxides (SiO_x, being $x < 2$) when the Si excess percentage is increased above a certain limit (~16%). Also, the origin of the Er^{3+} excitation under different pulsed driving polarizations is investigated. Direct impact excitation of hot conduction band electrons is thought to dominate Er^{3+} excitation under DC polarization and also for high pulsed voltages and low driving frequencies, whereas an energy transfer process from Si-ncs to Er^{3+} ions is triggered upon low voltage and high frequency bipolar pulsed excitation. Non-linear phenomena such as excited state absorption are identified under high current injection, before the device breakdown. Also, a thorough study on the EL efficiency is assessed, demonstrating that those active layers displaying electrode-limited conduction mechanisms such as Fowler-Nordheim Tunnelling (FNT) or Trap-Assisted Tunnelling (TAT) are the most suitable hosts to excite Er^{3+} ions under electrical pumping. Such fact is in close agreement with the theory of hot electron injection, since electrode-limited mechanisms show remarkably higher hot electron injection ratio compared to silicon sub-oxides with a high Si excess or to silicon nitrides (SiN_x), where bulk-limited conduction is more prone to dominate. Moreover, a trade-off between Er^{3+} EL efficiency and device operation lifetime is pointed out, caused by the low selectivity of injected hot electrons to impact with luminescent centres and not with other impurities such as hydrogen, which are in part responsible for the early device breakdown. In order to boost the overall optoelectronic performance of Er-doped MIS devices, alternative layer morphologies are proposed to merge the good electrical properties displayed by SiN_x with the outstanding EL efficiency of Er^{3+} ions in the SiO_2 layer. It consists in a bilayer structure composed by a SiO_2 and an Er-doped SiN_x layer especially designed to maximize the hot electron injection while retaining large device operation lifetime. In basis of the promising results displayed by this structure, an Er-doped superlattice approach is also studied, with the aim of providing a sequential restoring of the average energy of injected electrons in their pathway towards the cathode. Instead, bulk-limited conduction has proven to dominate through defect sites located at the interfaces of the superlattice. Additionally, the role of the injector layer in the EL properties of and Er-implanted SiO_2 active layers are tested, demonstrating enhanced EL efficiency under low charge injection.

By other side, a novel Er-doped MIS device is presented. Since the on-chip optical routing necessitates from efficient coupling with other passive components of the photonic chip, a new approach that merges the Er-doped MIS cross-section and a slot waveguide configuration is performed to allow for efficient charge injection and light confinement at once. Therefore, these Si-based devices are able to generate light by means of electrical injection and transmit it to the rest of the photonic circuit with no need of external coupling from a bulky laser source. The mask layout of an integrated photonic circuit composed by an electroluminescent Er-doped Si slot waveguide coupled to a passive bus waveguide with an output grating coupler is presented, along with the process flow and the most challenging steps that had to be tackled for the device fabrication. Two different hosts are tested: a SiO_2 and a SiO_x containing Si-ncs, both with the same Er dose. A detailed analysis of the most important optoelectronic features is also displayed, obtaining good transversal magnetic (TM) mode confinement of about 42% with propagation and coupling losses of about 40 dB/cm and 20 dB/cm, respectively. The study of the main transport mechanism inside the Er-doped slot waveguide has depicted a lowering of the injection barrier height modulated by the preceding charge transport in the undoped polysilicon electrode of waveguides. A transmitted EL signal of tens of $\mu W/cm^2$ is measured at the output grating coupler. This value, although still low, marks the first step towards the integration of a Si-based electroluminescent device in waveguide configuration with its passive optical circuitry in a single process flow. Moreover, an electrical pump-and-probe scheme is performed to further insight on the optoelectronic properties of Er-doped slot waveguides. A maximum probe transmittance of -60 dB/cm is measured under high voltage excitation, with a modulation depth of the probe signal as high as 75%. Moreover, optical amplification of the probe signal is discarded in these devices. Finally, a coupled system of two concatenated slot waveguides is proposed to obtain light generation and modulation simultaneously.

In the second block of this dissertation, the structural and luminescence properties of Ce^{3+} and Tb^{3+} doped SiO_x (with $x \sim 2$)and oxynitride (SiO_xN_y) thin films fabricated by Electron Cyclotron Resonance Plasma Enhanced Chemical Vapour Deposition (ECR-PECVD) are explored. The effect of the layer composition on the luminescence properties of both RE ions is presented. For that, a series of samples was fabricated by performing

a gradual substitution of oxygen by nitrogen in the host matrix. A complete description of the fabrication process carried out to obtain such gradual variation of the layer composition is detailed. Also, each sample has undergone to different annealing temperatures to investigate its influence on the morphology and luminescence of samples. Variable Angle Spectroscopic Ellipsometry (VASE) measurements combined with Rutherford Backscattering Spectrometry (RBS) and Transmission Electron Microscopy (TEM) characterization allowed us to obtain a general picture of the most relevant structural properties. Enhanced light emission and absorption due to the formation of tiny RE silicates is observed in samples annealed at the highest temperature studied, i.e. 1180°C.

Additionally, photoluminescence (PL) measurements suggest that SiO_xN_y is a better host than SiO_x to allocate RE ions, since almost temperature independent PL emission is observed. Moreover, higher PL intensity is generally measured for RE-doped SiO_xN_y thin films compared to SiO_x films with the same annealing temperature. Strong PL easily observable by the naked eye is demonstrated regardless of the annealing treatment or the matrix composition, even in as-deposited samples. Layer co-doping of two different RE ions embedded in a single layer and the multilayer approach of RE-doped single layers stacked in a single luminescence structure are also described in this dissertation. Several layer architectures are proposed, departing from a Ce^{3+} and Tb^{3+} doped single SiO_xN_y thin film, through a multilayer stack composed by alternating layers of either Ce^{3+} or Tb^{3+} doped SiO_xN_y separated by thin SiO_2 spacers, to a sub-nanometre Tb-doped SiO_xN_y / SiO_2 superlattice structure for optoelectronic applications. TEM images show a well-defined superlattice with sharp interfaces, hence validating the deposition process. Remarkably, the multilayer structure is preserved after the annealing treatment up to an annealing temperature as high as 1000°C. Wide colour tunability is reported from one design to another, hence covering the spectral region that spans from the cobalt blue to the emerald green. Such fact is corroborated by the representation of the xyz colour coordinates of different spectra in the CIE chromaticity diagram.

A preliminary optoelectronic characterization on selected samples is also described. For that, electroluminescent test devices were developed over representative luminescent samples by patterning transparent electrodes using a shadow mask approach in an Electron Beam Physical Vapour Deposition system (EB-PVD). The inspection of charge transport allowed devising an electrode-limited conduction governed by Trap-Assisted Tunnelling (TAT) in RE-doped SiO_x thin films, whereas Poole-Frenkel (PF) conduction is identified as the dominant mechanism for RE-doped SiO_xN_y. EL spectra with characteristic narrow emission lines are displayed, validating the excitation of RE ions under voltage excitation. Moreover, an early device breakdown is identified for single layers due to the high voltage needed to produce the EL emission. On the contrary much more stable emission is reported for the sub-nanometre Tb-doped

superlattice, since an EL onset voltage as low as 7V is required to excite Tb^{3+} ions. Finally, a route map proposal to continue and expand the work here presented is provided at the end of this dissertation.

Acknowledgements

The first lines of this section must be dedicated, with no doubt to Alícia. I will always be in debt with her for the unconditional support, comprehension and tolerance shown during these years. Her emotional intelligence and common sense have always been essential for me. Also, I am deeply grateful to my family, but especially to my parents and my sister for their love and encouragement in critical moments. Most importantly, they taught me to believe in myself, and to never give up and tackle every single challenge in life. All the goals I have reached in my life would have never been possible without them.

I am deeply grateful to my supervisor Prof. Blas Garrido Fernández for giving me the opportunity to work in his research group. His knowledge, expertise and leadership skills have been indispensable for the development of this dissertation. As an advisor, he gave me independence and encouraged me to develop my own ideas.

Also, I would like to acknowledge the rest of the members of the research group for their moral support and advice, but especially for the countless fun times we have spent together. I should give a special mention to Yonder Berencén, my office mate and my 'scientific partner'. I have the impression that our scientific battles will not be forgotten by many... Joking apart, he has always been highly motivated and ready to discuss about physics at any time. Julià López also deserves a special mention, since our friendship goes back to our student days (not so long ago!). We share the passion for football (we are both Barça fans), and he has been a valuable ally against Yonder when discussing about football (despite my esteem to Yonder, he has a downside as he is a Madrid fan). Oriol Blázquez (the evaporator man), Adrià Huguet (his accent from Empordà gives him away, although he still claims he was born in Barcelona), Martí Busquets (best santfeliuenc I have ever met) and Dr. Sergi Hernández (the Glasgow lad) are also acknowledged for their help, support and funny jokes during all these years.

I appreciate the help of former members of the group, especially Dr. Olivier Jambois who supervised my work and help me with several lab issues during the first year of my PhD. I will always be grateful to Dr. Daniel Navarro-Urrios for transmitting me his enthusiasm and energy, and also for his help, guidance and valuable teaching in many occasions. I owe him most of the acquired knowledge in optical characterization. He has always been a reference for me. Also, I would like to thank Dr. Federico Ferrarese Lupi for his valuable help in the lab at some points of my PhD and for fruitful discussions, but especially for showing me the magic of ‘quilombo’. Special thanks to Dr. Javier Rubio, my favourite Asturian.

I would like to express my gratitude to Prof. Albert Cornet, head of the Departament d’Electrònica, for his support, his good spirit and his permanent positivism.

Special thanks to the Lens group led by Dr. Francesca Peiró for the fruitful collaboration and for their valuable assistance in the interpretation of the TEM characterization. Sònia Estradé, Lluís López, Josep Manel Rebled, Alberto Eljarrat and Alícia Ruiz should be mentioned.

Prof. Peter Mascher and Dr. Jacek Wojcik deserve special thanks, since they welcomed me at McMaster University, in Canada, and supervised my work during my stage in 2013. The rest of the personnel from CEDT are also acknowledged for their help and assistance during this period.

My gratitude to Dr. Rosalía Serna for receiving me at Instituto de Óptica in Madrid. Although it was a short experience, I had a great time learning the basics of pulsed laser deposition. Thanks to Ivan Camps and Javier Hernández for their hospitality, sympathy and friendship. Other members that interacted with me by that time are also acknowledged.

I appreciate the help of the faculty staff who helped me in crucial moments. Among others, I may cite Roser Marzo, Conchita Pachuelo, Montse Farré, Trini Patús, Sílvia and Sílvia, Blai (the master of burocracy), Josep Maria Herrero (qué pasa neeeeeng?), Antonio Cruz (the master of SAP), Andrés Romero and Francisco López.

Many thanks to Dr. Albert Cirera, Dr. Albert Romano, Dr. Paolo Pellegrino, Dr. Anna Vilà, Dr. Javier Sieiro, Dr. Ángel Diéguez, Dr. Òscar Alonso, Dr. Frank Güell, Dr. Daniel Prades, Dr. Òscar Ruiz, Dr. Mauricio Moreno, Pau Torruella, Gemma Martín, Lluís Yedra, Oriol Monereo, Giovani Vescio, Jordi Samà, Bea Medina, Fran Tarzán, Sergio Illera, Xavi Arrese, Elena Xuriguera, Javi (eldelbar), and the rest of the people from the departament d’Electrònica.

Thanks to my student colleagues Pau Flores, Marc Torres, Marc Chamorro, Sara Teller, Ione Verdeny, Raquel Ballarín, David Frigola, Daniel Pacheco, Marc Jesús, Jesús Gómez, Miquel Vila, Carlos Camacho, Javi Muñoz, Juan Bertrand, Albert Carrillo and Marc Gargallo, among others.

Aside from the academic environment, there are a lot of people to whom I should express my gratitude. My colleagues from my native town in La Bisbal d’Empordà (and surroundings) are acknowledged, especially Pau Vilà, Jack McGee, Ferran Miàs, Albert and Dúnia Riera, Franki Pereira, Mireia Villacampa, Sergi Guasch, Àlex Iglesias, Natalia Borrego, María Díaz, Esther Pujol, Neus Frigola, Sílvia Artigas, Laura Hidalgo, Marc

Romero, Laia Muntaner, Jessica Ramírez and my colleagues from my hometown football team.

My gratitude to the people from Mas Pou, especially to Josep María Frigola and Paco Velasco for the good time I spent with them and for making me feel at home whenever I go.

My most sincere gratitude to the members of my football teams Black sheep and Ten Vets. I had such a great time playing football with you, and I really enjoyed the post-match get-together.

I am deeply grateful to all the people who has actively contributed, in one way or another to make possible my PhD.

This work was supported by the financial support of Secretariat for Universities and Research of Generalitat de Catalunya through the program FI-DGR 2013, by the European projects HELIOS (FP7-ICT 224312) and NASCEnT (FP7-245977), and also by the Spanish Ministry of Science and Innovation (TEC2012-38540-C02-01).

Joan Manel Ramírez,

July 2015, Barcelona

List of publications

List of appended papers

I. **Effect of the annealing treatments on the electroluminescence efficiency of SiO_2 layers doped with Si and Er**
O. Jambois, J. M. Ramírez, Y. Berencén, D. Navarro-Urrios, A. Anopchenko, A. Marconi, N. Prtljaga, A. Tengattini, P. Pellegrino, N. Daldosso, L. Pavesi, J. P. Colonna, J. M. Fedeli, B. Garrido. *J. Phys. D: Appl. Phys.* 45, 045103-5pp (2012). doi: 10.1088/0022-3727/45/4/045103

Author's contribution: I performed the electro-optical characterization of devices, analyzed the data jointly with O. Jambois and took part in the discussion.

II. **Copropagating pump and probe experiments on Si-nc in siO_2 rib waveguides doped with Er: The optical role of non-emitting ions**
D. Navarro-Urrios, F. Ferrarese Lupi, N. Prtljaga, A. Pitanti, O. Jambois, J. M. Ramírez, Y. Berencén, N. Daldosso, B. Garrido, L. Pavesi. *Appl. Phys. Lett.* 99, 231114-3pp (2011). doi: 10.1063/1.3665950

Author's contribution: I helped in the interpretation of analyzed data and took part in the discussion.

III. **Limit to the erbium ions emission in silicon-rich oxide films by erbium ion clustering**
N. Prtljaga, D. Navarro-Urrios, A. Tengattini, A. Anopchenko, J. M. Ramírez, J. M. Rebled, S. Estradé, J. P. Colonna, J. M. Fedeli, B. Garrido, L. Pavesi. *Optical Materials Express*, 2, 1278-8pp (2012). doi: 10.1364/OME.2.001278

Author's contribution: I analyzed the TEM data jointly with D. Navarro-Urrios, J. M. Rebled, S. Estradé and F. Peiró and took part in the discussion.

IV. **Erbium emission in MOS light emitting devices: from energy transfer to direct impact excitation**
J. M. Ramírez, F. Ferrarese Lupi, O. Jambois, Y. Berencén, D. Navarro-Urrios, A. anopchenko, A. Marconi, N. Prtljaga, A. Tengattini, L. Pavesi, J. P. Colonna, J. M. Fedeli, B. Garrido. *Nanotechnology*, 23, 125203-8pp (2012). doi: 10.1088/0957-4484/23/12/125203

Author's contribution: I performed the optoelectronic characterization of devices, performed the PL measurements jointly with D. Navarro-Urrios and F. Ferrarese Lupi, conducted the data analysis, lead the discussion and wrote the paper.

V. **Bipolar pulsed excitation of erbium-doped nanosilicon light emitting diodes**
A. Anopchenko, A. Tengattini, A. Marconi, N. Prtljaga, J. M. Ramírez, O. Jambois, Y. Berencén, D. Navarro-Urrios, B. Garrido, F. Milesi, J. P. Colonna, J. M. Fedeli, L. Pavesi. *J. Appl. Phys.* 111, 063102-5pp (2012). doi: 10.1063/1.3694680

Author's contribution: I performed part of the optoelectronic characterization of devices, helped on the interpretation of collected data and took part in the discussion.

VI. **Polarization strategies to improve the emission of Si-based light sources emitting at 1.55 μm**
J. M. Ramírez, O. Jambois, Y. Berencén, D. Navarro-Urrios, A. Anopchenko, A. Marconi, N. Prtljaga, N.Daldosso, L. Pavesi, J. P. Colonna, J. M. Fedeli, B. Garrido. *Mat. Sci. Eng. B.* 177, 734-5pp (2012). doi: 10.1016/j.mseb.2011.12.023

Author's contribution: I performed the optoelectronic characterization of devices, conducted the data analysis, lead the discussion and wrote the paper.

VII. **Role of silicon excess in Er-doped silicon-rich nitride light emitting devices at 1.54 μm**
J. M. Ramírez, S. Cueff, Y. Berencén, C. Labbé, B. Garrido. *J. Appl. Phys.* 116, 083103-4pp (2014). doi: 10.1063/1.4893706

Author's contribution: I performed the optoelectronic characterization of devices, conducted the data analysis, lead the discussion and wrote the paper.

VIII. **Electroluminescence efficiencies of erbium in silicon-based hosts**
S. Cueff, J. M. Ramírez, J. A. Kurvits, Y. Berencén, R. Zia, B. Garrido, R. Rizk, C. Labbé. *Appl. Phys. Lett.* 103, 191109-5pp (2013). doi: 10.1063/1.4829142

Author's contribution: This a jointly work with S. Cueff. We performed the electro-optical characterization of devices, conducted the data analysis, lead the discussion and wrote the paper.

IX. Carrier transport and electroluminescence efficiency of erbium-doped silicon nanocrystals superlattices
J. M. Ramírez, Y. Berencén, L. López-Conesa, J. M. Rebled, F. Peiró, B. Garrido. *Appl. Phys. Lett.* 103, 081102-5pp. (2013). doi: 10.1063/1.4818758

Author's contribution: I performed the optoelectronic characterization of devices, conducted the data analysis, lead the discussion and wrote the paper.

X. Toward a 1.54 μm Electrically Driven Erbium-Doped Silicon Slot Waveguide and Optical Amplifier
A. Tengattini, D. Gandolfi, N. Prtljaga, A. Anopchenko, J. M. Ramírez, F. Ferrarese Lupi, Y. Berencén, D. Navarro-Urrios, R. Rivallin, K. Surana, B. Garrido, J. M. Fedeli, L. Pavesi. *J. Lightwave Technol.* 31, 391-6pp. (2013). doi: 10.1109/JLT.2012.2231050

Author's contribution: I performed the optoelectronic characterization of devices jointly with A. Tengattini, helped on the interpretation of analyzed data, performed SEM measurements and took part in the discussion.

XI. Er-doped light emitting slot waveguides monolithically integrated in a silicon photonic chip
J. M. Ramírez, F. Ferrarese Lupi, Y. Berencén, A. Anopchenko, J. P. Colonna, O. Jambois, J. M. Fedeli, L. Pavesi, N. Prtljaga, R. Rivallin, A. Tengattini, D. Navarro-Urrios, B. Garrido. *Nanotechnology*, 24, 115202-8pp (2013). doi: 10.1088/0957-4484/24/11/115202

Author's contribution: I mounted a new optoelectronic setup configuration jointly with F. Ferrarese Lupi, Y. Berencén and D. Navarro-Urrios, performed the electro-optical characterization of devices, conducted the data analysis, lead the discussion and wrote the paper.

XII. Electrical pump & probe and injected carrier losses quantification in Er doped Si slot waveguides
J. M. Ramírez, Y. Berencén, F. Ferrarese Lupi, D. Navarro-Urrios, A. Anopchenko, A. Tengattini, N. Prtljaga, L. Pavesi, R. Rivallin, J. M. Fedeli, B. Garrido. *Optics Express*, 20, 28808-11pp (2012). doi: 10.1364/OE.20.028808

Author's contribution: I mounted a new optoelectronic setup configuration jointly with F. Ferrarese Lupi, Y. Berencén and D. Navarro-Urrios, performed the electro-optical characterization of devices, conducted the data analysis, lead the discussion and wrote the paper.

XIII. **Electrically pumped Er-doped light emitting slot waveguides for on-chip optical routing at 1.54 μm**
J. M. Ramírez, Y. Berencén, D. Navarro-Urrios, F. Ferrarese Lupi, A. Anopchenko, N. Prtljaga, P. Rivallin, A. Tengattini, J. P. Colonna, J. M. Fedeli, L. Pavesi, B. Garrido. *Proc. SPIE 8767, Integrated Photonics: Materials, Devices, and Applications II*, 87670I-7pp. doi: 10.1117/12.2017250

Author's contribution: I performed the optoelectronic characterization of devices, conducted the data analysis, lead the discussion and wrote the paper.

XIV. **On the photoluminescence of as-deposited Tb-doped silicon oxides and oxynitrides fabricated by ECR-PECVD**
J. M. Ramírez, J. Wojcik, Y. Berencén, P. Mascher, B. Garrido. *Proc. SPIE 9133, Silicon Photonics and Photonic Integrated Circuits IV*, 913309-8pp (2014). doi: 10.1117/12.2052571

Author's contribution: I fabricated the samples, conducted VASE and RBS measurements, performed the optical characterization, conducted the data analysis, lead the discussion and wrote the paper.

XV. **Amorphous sub-nanometre Tb-doped SiO_xN_y/SiO_2 superlattices for optoelectronics**
J. M. Ramírez, J. Wojcik, Y. Berencén, A. Ruiz-Caridad, S. Estradé, F. Peiró, P. Mascher, B. Garrido, *Nanotechnology*, 26, 085203-7pp (2015). doi: 10.1088/0957-4484/26/8/085203

Author's contribution: I fabricated the samples, conducted VASE and RBS measurements, performed the optical characterization, fabricated the electroluminescent devices, performed the SEM and the optoelectronic characterization, conducted the data analysis, lead the discussion and wrote the paper.

Throughout this dissertation, these publications are referred to by their Roman numerals.

List of publications not included in this dissertation

1. **Far-field characterization of the thermal dynamics in lasing microspheres**
   J. M. Ramírez, D. Navarro-Urrios, N. E. Capuj, Y. Berencén, A. Pitanti, B. Garrido, A. Tredicucci, *Submitted to Sci. Rep.*

2. **Optical performance of thin films produced by the pulsed laser deposition of SiAlON and Er targets**
   I. Camps, J. M. Ramírez, A. Mariscal, R. Serna, B. Garrido, M. Perálvarez, J. Carreras, N. P. Barradas, L. C. Alves, E. Alves, *Accepted in Applied Surface Science.* doi: 10.1016/j.apsusc.2014.12.013

3. **The electroluminescence mechanism of Er^{3+} in different silicon oxide and silicon nitride environments**
   L. Rebohle, Y. Berencén, R. Wutzler, M. Braun, D. Hiller, J. M. Ramírez, B. Garrido, M. Helm, W. Skorupa, *J. Appl. Phys*. 116, 123104-7pp (2014). doi: 10.1063/1.4896588

4. **Charge trapping and physical parameters of Er^{3+} doped light-emitting field-effect transistors**
   J. M. Ramírez, Y. Berencén, B. Garrido, *Phys. Status Solidi A*, 211(2), 467-4pp (2014). doi: 10.1002/pssa.201300343

5. **Intense green-yellow electroluminescence from Tb^{+}-implanted silicon-rich silicon nitride/oxide light emitting devices**
   Y. Berencén, R. Wutzler, L. Rebohle, D. Hiller, J. M. Ramírez, J. A. Rodríguez, W. Skorupa, B. Garrido, *Appl. Phys. Lett.* 103, 111102-3pp (2013). doi: 10.1063/1.4820836

6. **Structural and compositional properties of Er-doped silicon nanoclusters/oxides for multi-layered photonic devices studied by STEM-EELS**
   A. Eljarrat, L. López-Conesa, J. M. Rebled, Y. Berencén, J. M. Ramírez, B. Garrido, C. Magén, S. Estradé, F. Peiró, *Nanoscale*, 5, 9963-8pp (2013). doi: 10.1039/c3nr02754f

7. **Correlation between charge transport and electroluminescence properties of Si-rich oxide/nitride/oxide-based light emitting capacitors**
   Y. Berencén, J. M. Ramírez, O. Jambois, C. Domínguez, J. A. Rodríguez, B. Garrido, *J. Appl. Phys.* 112, 033114-5pp (2012). doi: 10.1063/1.4742054

8. **Blue-green to near-IR switching electroluminescence from Si-rich silicon oxide/nitride bilayer structures**

Y. Berencén, O. Jambois, J. M. Ramírez, J. M. Rebled, S. Estradé, F. Peiró, C. Domínguez, J. A. Rodríguez, B. Garrido, *Opt. Lett.* 36, 2617-3pp (2011). doi: 10.1364/OL.36.002617

9. **Metal-nitride-oxide-semiconductor light-emitting devices for general lighting**
Y. Berencén, J. Carreras, O. Jambois, J. M. Ramírez, J. A. Rodríguez, C. Domínguez, C. E. Hunt, B. Garrido, *Opt. Express* 19, A234-11pp (2011). doi: 10.1364/OE.19.00A234

List of conference proceedings not included in this dissertation

10. **(Invited) Transport and Electroluminescence Properties of Size-Controlled Silicon Nanocrystals Embedded in SiO_2 Matrix Following the Superlattice Approach**
J. López-Vidrier, Y. Berencén, L. López-Conesa, O. Blázquez, J. M. Ramírez, S. Estradé, F. Peiró, S. Hernández, B. Garrido, *ECS Trans.* 61(5), 133-7pp (2014). doi: 10.1149/06105.0133ecst

11. **(Invited) Rare Earth Doped Metal-Oxide-Semiconductor Structures: A Promising Material System or a Dead End of Optoelectronic Evolution?**
L. Rebohle, Y. Berencén, M. Braun, B. Garrido, D. Hiller, B. Liu, J. M. Ramírez, J. Sun, R. Wutzler, M. Helm, W. Skorupa, *ECS Trans.* 61(5), 175-11pp (2014). doi: 10.1149/06105.0175ecst

12. **Electroluminescence from Si-based light emitting devices**
Y. Berencén, J. M. Ramírez, J. Montserrat, C. Domínguez, B. Garrido, *Óptica pura y aplicada*, 46(4), 315-5pp (2013). doi: 10.7149/OPA.46.4.315

13. **(Invited) Optimizing Er-Doped Layer Stacks for Integrated Light Emitting Devices**
J. M. Ramírez, Y. Berencén, L. López-Conesa, J. M. Rebled, A. Eljarrat, S. Estradé, F. Peiró, J. M. Fedeli, B. Garrido, *ECS Trans.* 53(4), 81-4pp (2013). doi: 10.1149/05304.0081ecst

14. **Role of electron and hole transport processes in conductivity and light emission of silicon nanocrystals field-effect transistors**
L. Cattoni, A. Tengattini, A. Anopchenko, J. M. Ramírez, F. Ferrarese Lupi, Y. Berencén, B. Garrido, J. M. Fedeli, L. Pavesi, *Proc. SPIE 8629, Silicon Photonics VIII,* 862914-10pp (2013). doi: 10.1117/12.2003084

15. **Er-doped Si-based electroluminescent capacitors: Role of different host matrices on the electrical and luminescence properties**

Y. Berencén, J. M. Ramírez, B. Garrido, *in Proceedings of the 2013 Spanish Conference on Electron Devices*, 245-4pp (2013). doi: 10.1109/CDE.2013.6481388

16. **Opto-Electrical Characterization of Erbium Doped Slot Waveguides**
A. Tengattini, D. Gandolfi, A. Marconi, A. Anopchenko, N. Prtljaga, J. M. Ramírez, F. Ferrarese Lupi, Y. Berencén, D. Navarro-Urrios, B. Garrido, J. M. Fedeli, P. Rivallin, K. Surana, L. Pavesi, *Proc. SPIE 8431, Silicon Photonics and Photonic Integrated Circuits III* 843118-8pp (2012). doi: 10.1117/12.922695

17. **1.54 µm Er-doped light emitting devices: Role of Silicon content**
A. Tengattini, A. Marconi, A. Anopchenko, N. Prtljaga, L. Pavesi, J. M. Ramírez, O. Jambois, Y. Berencén, D. Navarro-Urrios, B. Garrido, F. Milesi, J. P. Colonna, J. M. Fedeli, *The 8th IEEE International Conference on Group IV Photonics*, 77-3pp (2011). doi: 10.1109/GROUP4.2011.6053721

18. **Effect of the annealing treatments on the transport and electroluminescence properties of SiO_2 layers doped with Er and Si nanoclusters**
O. Jambois, J. M. Ramírez, Y. Berencén, D. Navarro-Urrios, S. Hernández, A. Anopchenko, A. Marconi, N. Prtljaga, N. Daldosso, L. Pavesi, J. P. Colonna, J. M. Fedeli, B. Garrido, *Material Research Society (MRS) proceeding* 1289 (2010). doi: 10.1557/opl.2011.1409

Book chapters

1. **Authors:** B. Garrido, S. Hernández, Y. Berencén, J. López-Vidrier, J. M. Ramírez, O. Blázquez, B. Mundet
Chapter Title: Electrical transport in Si-based nanostructured superlattices
Book Title: Nanotechnology and Photovoltaic Devices: Light Energy Harvesting with Group IV Nanostructures
Publisher: CRC Press 2014 (Pan Stanford)
Number of authors: 7
Year: 2015
ISBN: ISBN 9789814463638

Table of Contents

CHAPTER 1

1. Introduction

Silicon has become, with no doubt, the most important material for electronics of the second half of the 20th century. Since the introduction of the first silicon integrated circuit in 1958 by Texas Instruments [1], a race towards more complex and functional silicon chips has been triggered, something that was forecasted by the Moore's law [2]. Among the large number of elements listed in the periodic table, silicon was the preferred choice to integrate circuits due to the wide range of advantages displayed, such as: (i) silicon is the second most abundant material on Earth, after oxygen; (ii) silicon has an ideal bandgap of 1.1 eV that allows for efficient device operation at room temperature; (iii) the diamond phase of crystalline silicon provides strong bonding that easies the handing of silicon crystals, displaying excellent mechanical properties; (iv) silicon has good response to light radiation and a high dielectric strength that makes it suitable for solar cells and power devices; (v) impurity doping is easily performed on silicon, with a high solubility of dopants of about 10^{21} at/cm^3 and (vi) high quality silicon oxide can be obtained from silicon.

Such unique properties motivated the appearance of a standardized technological process to develop large scale compact electronic circuits: the Complementary-Metal-Oxide Semiconductor (CMOS) technology. Since then, downscaling of silicon microelectronics has evolved at an unprecedented speed if compared with other areas of research, providing more complex designs with superior performance and a vast knowledge of silicon. In fact, the outstanding know-how acquired during the last 50 years makes silicon one of the most well-known semiconductor materials existing so far. Till date, the downscaling of microelectronic components such as CMOS transistors has become of utmost importance to cope with the incremental market demands, providing silicon chips with superior functionality while lowering the cost-per-chip. Nevertheless, miniaturization of transistors is known to reach a physical limit in the short term that threatens the further development of microelectronics as it does at present. Even with the recent implementation of low-power multigate devices like FinFETs that provides higher design flexibility and low-power consumption to silicon chips, [3] the impossibility of downscaling interconnects to the same extend is causing a strong bottleneck that limits the overall performance of microelectronic chips. Moreover, other associated drawbacks such as information latency, cross talk noise, increased skew rate or the need for a more efficient power dissipation design arise when the number of integrated components is increased in a single chip [4].

Thus, it is interesting to inspect alternative technological approaches that could shed light to the current limitations of the microelectronics industry. Integrated Photonics is one of the most promising emerging platforms and is expected to provide effective solutions to most of the weak points of microelectronics and adding new functionalities in other fields such as sensing, lighting, photovoltaics or data handling, among others. In that line, Photonic Integrated Circuits (PICs) are becoming valuable assets in next generation datacom, complementing the standalone electronics to provide optical interconnects and advanced photonic components with superior performance. Such approach is expected to yield large operation bandwidths at low power expense. To an extent, this integrated photonic platform could be considered as a natural step forward of long-haul optical communications. Owing to a low propagation loss well below 1 dB/Km in the range between 1.3 and 1.6 μm, long-haul photonics has monopolized telecommunications up to date, providing high data transfer rates. Similarly, the development of integrated photonic components is expected to offer low-cost on-chip optical solutions with efficient data management.

Nevertheless, an important restriction must be accomplished for this new platform to succeed: the compatibility with the CMOS technology. It is to be expected that such new photonic platform would preserve the cost-per-chip as low as possible to be competitive, in direct analogy with microelectronics. Hence, such requirement can only be tackled if using the already available standalone CMOS tools employed for electronics production. As a consequence, over the last few years an increasing number of researchers have concerned about developing silicon microphotonic devices. An impressive outcome of devices has been reported since then. To better illustrate the expansion of the silicon photonics field, figure 1.1 shows the evolution of the number of published papers during the last 25 years in which a silicon photonics topic has been discussed (left side in figure 1.1), as well as the total silicon photonics application revenue from 2010 to 2017 (right side in figure 1.1). As seen, the interest of the scientific community and the funding organizations has increased year after year. More importantly, a positive progression is expected for the near future, especially for datacom applications.

Within such a scenario one could speculate on a higher impact of silicon photonics on the day-to-day of forthcoming generations. Still, silicon photonics technology platforms are in an early stage of development, far from the advanced logistic network already available with CMOS technology. As a consequence, intense research is being conducted to make progress towards silicon photonics marketable products. Several distinguished scientific works deserve special mention due to their relevant contribution to the field, providing important breakthroughs that have allowed for a better understanding of particularly striking issues in silicon photonics. I shall introduce some of them in the following, the ones which under my humble viewpoint are of major relevance.

Nevertheless, there is a considerable number of excellent reviews to which the reader may refer for a more extended knowledge of the history of silicon photonics [5-12].

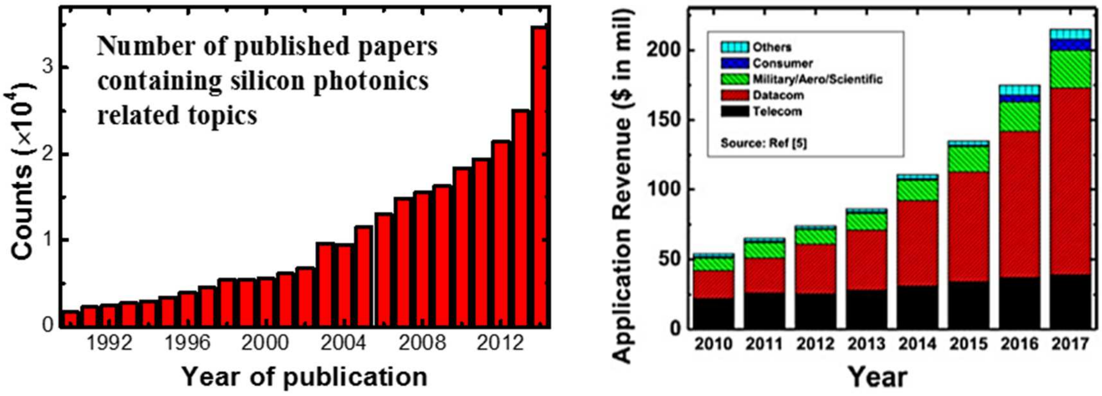

Figure 1.1. (Left) Number of silicon photonics related papers as a function of the year of publication from 1990 to 2014. Extracted from Google Scholar dataset. (Right) Silicon photonics application revenue from 2010 to 2017. Extracted from [11].

1.1. Silicon Photonics: State-of-the-art

Despite not displaying the statistics of the late 80's in the histogram of figure 1.1, the work carried out by R. A. Soref at that time deserves consideration because of the importance of his research. His study on optical switching devices, especially the ones that take advantage from the free-carrier absorption in a p-n crystalline silicon junction [13], opened an entire world of possibilities for forthcoming development of silicon optical modulators. Up to that time, light modulation was typically employed by making use of linear electro-optical effects (the so called Pockels effect), that relied on non-centro-symmetric crystals from which silicon was excluded. Nevertheless, R. A. Soref and co-workers managed to modulate light in silicon waveguides by modifying the number of free carriers in the area of light confinement, which changes real and imaginary parts of the silicon dielectric constant [14].

Still, up to date the most efficient modulation of silicon-based devices relies on this concept, providing light switching at tens of GHz [15]. Also in that paper, Soref. *et al.* introduced the Si waveguide for the first time taking advantage from the refractive index difference between a heavily-doped monocrystalline silicon substrate and a deposited Si rib waveguide. Nevertheless, the low refractive index step between the guiding rib waveguide and the silicon substrate yielded low mode confinement and therefore high mode overlapping with the Si substrate, obtaining propagation losses as large as 15 dB/cm. It was not until the development of silicon-on-insulator substrates that low propagation losses were achieved [16]. Optical waveguiding in a Ge layer deposited onto silicon substrate was also demonstrated [17]. Shortly after, an N x N integrated optical multiplexer on silicon was presented [18]. Also in 1991, silicon Mach-Zehnder waveguide interferometers (MZI) based on the plasma dispersion effect were reported

[19], as well as the first Micro OptoElectronic Mechanical switch [20]. The latter one consisted of an electrically driven suspended waveguide on a Si substrate. Upon an external bias voltage, the waveguide was deflected towards the substrate by electrostatic force, resulting in a loss enhancement of tens of dB due to the coupling of guided light into the substrate. Later on, Soref. *et al.* presented the monolithically integrated silicon 'superchip' proposed by Abstreiter [21, 22]. The system consisted of silicon waveguides, bipolar BiCMOS, hetero-bipolar transistors, electro-optic modulators, directional couplers, optical amplifiers, photodetectors and a novel fiber-to-waveguide butt-coupling system that consisted of V-like trenches to provide high-precision positioning of optical fibers. Somehow, such microphotonic chip could be considered as the first proposal including multiple photonic elements.

In 1992, the first all-silicon photodetector working at telecom wavelengths was experimentally demonstrated [23]. A heavily doped silicon was used to narrow the silicon bandgap, obtaining measurable signals under 1.3 μm light emission. A fairly good time resolution of 20 ps was reported. Nevertheless, the low efficiency displayed, of about 10^{-7}, pushed researchers back to the earlier works in which SiGe hybrid integration schemes were proposed [24]. A good example is the work of Colace *et al.*, in which Ge-on-Si photodetectors with high speed and sensitivity were demonstrated [25]. Still up to date, Ge photodetectors on silicon show superior performance, with optical bandwidth of 120 GHz, detection speeds of 40 Gb/s and responsivity of 0.8 A/W at 1.54 μm [26]. In 1995, Z. H. Lu, D. J. Lockwood and J.-M. Baribeau reported on quantum confinement and visible light emission from Si/SiO_2 superlattices [27]. Also, rare-earth doped thin films had been used by that time to produce light at different wavelength ranges [28-31]. Especially interesting was the light emission at 1.54 μm exhibited by Er-doped silicon-rich silicon oxide [32], proposing a good scenario to develop integrated telecom light sources for on-chip routing.

In 2000, optical gain of randomly dispersed Si-ncs in a silicon dioxide (SiO_2) matrix was reported [33]. An astonishing net modal gain of 100 cm^{-1} was obtained, with a photon absorption cross-section of $\sigma = 3\times10^{-16}$ cm^2. Such results encouraged the silicon photonics community to push towards the implementation of an all-silicon laser using Si-ncs. Unfortunately, such challenge still remains a utopia in spite of the fact that later work also reported on stimulated emission from Si-ncs [34, 35]. However, instead of giving up, many research groups addressed their efforts into the luminescent properties of silicon-based materials. For instance, Shin's group reported on optical gain at 1.54 μm in Er-doped Si-ncs waveguides taking advantage of the efficient energy transfer from Si-ncs to Er^{3+} ions [36, 37]. Shortly after, an Er-doped electroluminescent device containing Si-ncs was published [38]. An Er excitation cross-section of 1×10^{-14} cm^2 was found under electrical pumping, two orders of magnitude higher than the one obtained from the same system under optical pumping [39].

In 2003, Almeida. *et al.* successfully demonstrated compact mode conversion between an optical fibre and a sub-micrometre waveguide [40]. The efficient fibre-to-wavelength coupling was paid by additional insertion losses of 3.3 and 6 for the TM and TE modes, respectively. In that very same year, and despite silicon-based photonic crystal structures had already been reported by that time [41, 42], the first high-Q photonic nanocavity in a two-dimensional photonic crystal was described, being the quality factor Q = 45000, and the modal volume V = 7×10^{-14} cm^3 [43]. In 2004, the Photonics Research Group at Ghent reported on a compact efficient broadband grating coupler with coupling loss below 1 dB for the TE mode [44]. These structures presented a series of advantages compared to inverted tapers because they could be implemented not only at the edges of the chip (like inverted tapers), but as well within the chip to perform wafer-scale testing of optical devices. Moreover, polishing of facets was not required and large bandwidth was provided.

In 2004, the first Silicon Raman laser was proposed. Pulsed Raman laser emission was reported by O. Boyraz and B. Jalali at a wavelength of 1675 nm and a repetition rate of 25 MHz [45]. A year later, in 2005, Paniccia's group obtained a continuous-wave RAMAN silicon laser with a side mode suppression of > 55 dB [46]. Also in the same year, a resonant silicon modulator was demonstrated, with a total device footprint as small as 12 μm and a modulation speed of 1.5 Gb/s. The device working principle consisted in the insertion of additional free-carrier transmission losses by electrically driving a p-i-n ring resonator-like structure with a voltage as low as 1 V [47]. Such devices presented a smaller footprint than Mach-Zehnder Interferometer (MZI), hence becoming good candidates for silicon on-chip integration. Unfortunately, the good efficiency of modulation displayed by this kind of injection devices was paid by a strong limitation of speed modulation, which was around of 12.5 Gbit/s in the best case scenario [48]. With the demonstration of the first depletion device however, higher modulation speeds were achieved [49]. The operation concept was very similar to injection-based modulators, but this time a reverse bias was applied to sweep out carriers from a p-n junction. Modulation speeds as high as 40 Gbit/s were achieved, still being one of the fastest modulators reported so far.

In 2006, taking advantage from the amplification provided by the third-order susceptibility trough four-wave mixing (FWM), Gaeta's group at Cornell reported on optical parametric gain at third telecom wavelengths (around of 1.54 μm) in silicon-on-insulator (SOI) waveguides [50]. Later on, Razzari, *et al.* made use of such hyper-parametric gain to develop an integrated multiple-wavelength laser source at 1.54 μm using a high-Q microring resonator. A broadband parametric oscillation of > 200 nm was reported. [51]. Also, it is worth to mention the work done at MIT about silicon nitride (Si_3N_4) waveguide-based add-drop filters with an extinction ratio of 50 dB. Interesting features such as a low drop loss of 2 dB, a free spectral range of 20 nm and a 30 dB adjacent channel rejection in the drop port were reported by the first time in that paper [52]. Also in the same year, Luxtera launched the first silicon photonics technology node using silicon-on-insulator technology [53].

At that time, with several silicon photonic devices already demonstrated, the race towards the implementation of silicon-based photonic integrated circuits motivated the investigation of different strategies to obtain silicon light sources. Despite the efforts devoted to the development of fully CMOS compatible light sources, the low efficiency displayed promoted the investigation of alternative approaches based on hybrid integration of III-V materials onto silicon. As a representative example, I may note the work of J. E. Bowers and co-workers, in which electrically pumped hybrid AlGaInAs-silicon evanescent lasers were reported [54]. Later on, microdisks-based lasing devices were demonstrated, providing continuous multi-wavelength laser operation of compact devices with small feature size [55].

In 2007, Liu, *et al.* opened a new interesting route towards the implementation of a new generation of hybrid group IV semiconductor lasing devices using bandgap engineered germanium thin films by increasing the direct bandgap radiative transition ratio of Ge. In order to do that, both tensile strain and heavy n-type doping were applied onto Ge to provide a theoretical net gain of 400 cm^{-1} [56]. These results were experimentally proven few years later with the demonstration of the first germanium laser electrically pumped with output multimode lasing power of 1 mW [57].

In 2010, R. Won and M. Paniccia presented the first integrated silicon photonics link operating at 50 Gb/s with a bit error rate as low as 10^{-12} [58]. In 2011, a polarization splitting and rotating device was demonstrated [59]. The device was built on a silicon-on-insulator platform, with low insertion losses (0.6 dB) and extinction ratio of 12 dB. Shortly after, second-harmonic generation in strained silicon waveguides was reported for the first time [60]. Remarkable second-order nonlinear signal of 40 pmV^{-1} was observed at 2.3 μm. Another striking breakthrough in silicon photonics was the discovery of a continuous-wave Raman silicon laser with micrometer dimensions [61]. The system consisted of a photonic crystal nanocavity emitting at 1.54 μm with a high quality factor and a threshold lasing power as low as 1 μW.

Recently, new functionalities were derived from the observation of soliton-effect pulse compression in slow-light silicon photonic crystal waveguides [62]. Also, other related fields such as plasmonics, photovoltaics or cavity optomechanics often rely on silicon-based systems to carry out their research [63-65]. As a representative example of the progress conducted in such fields, of particular interest is the work published by Gomis-Bresco *et al.*, in which a *phoXonic crystal* with a full phononic bandgap for acoustic modes at 4 GHz is demonstrated [66]. In the same line, Atwater's group has recently proved coherent quantum interference in plasmonic waveguides, opening an interesting pathway towards plasmonic integrated circuits [67].

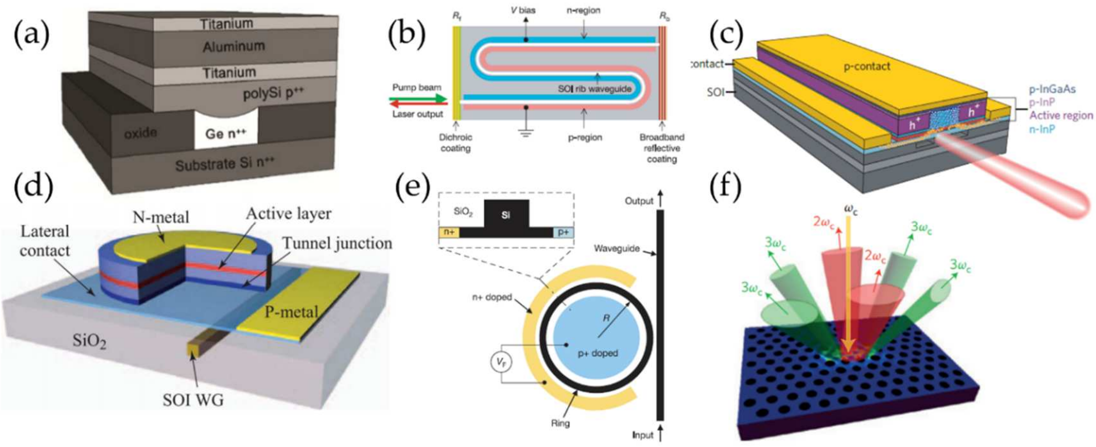

Figure 1.2. Some examples of advanced photonic devices with outstanding performance: (a) Device cross-section of the first Ge laser [57]; (b) schematic of the continuous-wave Raman silicon laser [46]; (c); a hybrid Si Fabry-Pérot Laser [9]; (d) an integrated laser source based on cascaded InP microdisks [55]; (e) a slot waveguide ring-resonator based modulator [47]; (f) PhC cavity showing simultaneous second-harmonic generation [64].

Therefore, the impressive staging of silicon photonics during the last 25 years has increased the awareness for a standardized silicon photonics process line, leading to a new technological framework whereby important companies join efforts to offer outstanding facilities to customers. As a case in point, I shall mention the collaboration between Luxtera and ST microelectronics to develop a 300 mm silicon photonics line, or the one established by the Institute of Microelectronics (IME), Bell Labs, GlobalFoundries (GF) and Alcatel-Lucent (ALU) to establish solid bonds between silicon photonics and industry. Also Kotura, recently acquired by Mellanox Technologies, has launched in 2012 Ultra Variable Optical Attenuators (VOA) fabricated at his in-house 150 nm foundry. Moreover, the fact that a leading supplier of interconnect solutions such as Mellanox Technologies has purchased an innovative silicon photonics company leads to foresee an encouraging future for silicon photonics products. In that line, other important technological corporations such as Intel or IBM are getting in on the act as well [68, 69].

Nevertheless, there is one particular issue that prevents these companies from large investment of monetary resources in silicon photonics: the low customer demand. Till date, the number of requests for silicon photonic components is still orders of magnitude below the outcome of silicon microelectronics. To some extent, it could be considered as a vicious circle since low customer demand is sometimes motivated by a limited supply offer due to an inadequate infrastructure. In order to palliate this circumstance, a Multi Project Wafer (MPW) platform has been launched recently. It consists in a new technological service that offers cost-sharing among customers that do not need an extended wafer surface to fabricate their designs. Then, each customer would receive a diced wafer containing the requested design uniquely. Apart from the evident cost savings in comparison with the standard procedure, such approach becomes a very attractive alternative for research groups or companies that do not have access to in-house fabrication facilities. An appropriate example may be OPtoelectronics Systems Integration in Silicon (OpSIS), an organization launched to provide MPW solutions for silicon photonics in United States mainly [68]. As for the European counterpart, ePIXfab is leading the silicon photonics MPW shuttle run philosophy by means of the technological partners IMEC and CEA-LETI [70].

1.2. Silicon-based Light emitting Devices

This section is devoted to review important development accomplished in the search for an efficient silicon light emitting device (Si-LED). Since the discovery of visible light emission from a reversed-biased p-n junction in 1955 [71], many researchers strived to enhance the light emission properties of silicon. Being silicon an indirect bandgap semiconductor, the inter-band radiative transition is mediated by the emission or absorption of a phonon that changes the k-space accordingly and provides the electron-hole pair with the same k-momentum. As a consequence, the electrical-to-optical conversion in bulk silicon systems drops to values as low as 1% in the best case scenario [72]. In other words, the non-radiative processes are much faster than the radiative ones. Therefore, several strategies have been tackled to improve the efficiency of bulk silicon. Among them, there are mainly two approaches that are directly correlated with this dissertation and thus deserve special attention: the use of quantum confinement in silicon nanocrystals (Si-ncs) to enhance light emission and the narrow emission provided by rare-earth (RE) ions when embedded in optically favourable host matrices. The following two sub-sections are devoted to briefly review some outstanding works that utilize such light emitters to realize Si-based light emitting devices. Also, other interesting applications using either Si-ncs or RE-ions will be reviewed.

Nevertheless, prior to that, it is worth mentioning that other strategies have also been inspected to boost silicon light emission. In fact, the first experimental observation of visible light emission from a p-n junction did not rely on any of the above mentioned strategies. It was intraband radiative relaxation from high-energy carriers that produced visible light in p-n junctions when working in avalanche breakdown regime [73]. Shortly after, an interesting work performed at Bell Labs spatially correlated the light emission produced by avalanche breakdown current (named avalanche breakdown microplasmas ever since) with crystal dislocations at the p-n junction [74]. However, the notorious device degradation and fast aging of devices as a consequence of defect generation by hot electrons prevented these devices from practical applications [75]. Porous silicon has also been used to obtain silicon-based electroluminescent devices [76]. At that time, several works focussed on the implementation of porous Si as a luminescent layer for Si-LEDs. However, in spite of the progress done in that direction [77, 78], the poor thermal and chemical stability made impractical the development of reliable Si-LEDs with competitive characteristics. Meanwhile, other luminescent layers emerged with promising features. Remarkable is the work undertaken by that time at Cavendish Laboratory, in UK, where a polymer optoelectronic system consisting of an LED driven by a P3HT field-effect-transistor was demonstrated [79]. Apart from the luminescent layer, novel device designs were investigated to optimize the out-coupling efficiency. Green *et al.* [80] combined three different strategies to boost the light extraction by a factor of one hundred: (i) Inverted pyramids on top of the LED surface, (ii) rear metal reflector, and (iii) an antireflecting coating. Another popular technique to improve silicon emission is the introduction of dislocation loops in a p-n junction. These loops are meant to spatially confine charge carriers, hence improving the band-edge emission of silicon. Still, low external quantum efficiency values of about 10^{-3} were measured at room temperature [81].

Within the literature, we may also find examples of hybrid approaches, some of them integrating organic compounds, III-V or II-VI materials with functional silicon chips to provide fast driving performance and efficient light emission at once [82]. Nevertheless, such approach does not meet all the requirements of an all-silicon LED, as it introduces additional technological challenges and a considerable increase of the cost-per-chip. Alternatively, other group IV materials have also shown good luminescent properties when embedded in silicon-based hosts. Ge in particular, has attracted much attention due to the good control of composition provided by the alloy $Si_{1-x}Ge_x$ that makes it a good candidate for telecom applications in the range of 1.3-1.54 μm [83]. SiGe p-i-n light emitting diodes with internal quantum efficiency of 0.1% at room temperature were reported [84]. Even recently, as previously remarked, an electrically pumped Ge laser was demonstrated in highly doped and strained Ge layers [57]. In the visible range, carbon is a good candidate to produce blue light when embedded in SiO_2 layers. Rebohle *et al.* implemented Si/C-rich SiO_2 layers by co-implantation of C^+ and Si^+ to synthesize luminescent $Si_yC_{1-y}O_x$ complexes [83]. Moreover, the bluish emission from carbon-doped SiO_2 can be combined with the reddish one from Si-ncs to obtain white Si-LEDs. There is a considerable number of reports that study the optical and structural properties of carbon-doped SiO_2 layers [84-87]. At this point, I shall mention the notable work of the Electro-Photonics Laboratory in Barcelona in C-rich SiO_2 luminescent materials. Publications on charge transport phenomena [88], microstructure [89] or electroluminescence (EL) tunability of white C- and Si-rich oxide light emitting devices [90] have been reported by our research group in the last few years. More recently, Franzò *et al.* introduced Eu^{2+} ions in SiOC thin films to provide intense white emission [91].

1.2.1. Silicon nanocrystals

Si-ncs have been object of intense research during the last 20 years due to the good luminescent properties displayed. Probably, they are amongst the most promising systems to obtain an all-Si LED since they show enhanced red-NIR luminescence and can be entirely fabricated in a standard CMOS line along with their electronic drivers.

Somehow, they may be considered as worthy successors of porous silicon, as they show similar optical features with superior chemical and thermal stability. Being only few nanometers in diameter, Si-ncs offer new physics phenomena not observed in bulk Si such as quantum confinement (QC). QC occurs when at least one of the dimensions is comparable to the Bohr radius. Such small dimensionality provides a strong spatial localization of carriers, which in turn causes a strong de-localization in the reciprocal space that breaks the momentum conservation rules. This phenomenon is described by Heisenberg's uncertainty principle:

$$\Delta x \cdot \Delta p \geq \frac{\hbar}{2} \tag{1.1}$$

Where Δx is the spatial uncertainty, Δp is the momentum uncertainty, and $\hbar$ is the reduced Planck's constant. Therefore, an electron-hole pair respectively located in the conduction and valence band of a single Si-nc (an exciton) will become strongly bounded by the effect of the strong confinement potential, providing a considerable wavefunction overlap. Bulk Si, on the contrary, does not benefit from QC effects and therefore the exciton is only preserved by the coulombic interaction between the electron-hole pair, which is known to be weaker than the confinement potential [92]. Consequently, limited wavefunction overlap takes place, which ultimately diminishes the probability of radiative recombination in bulk Si with regard to Si-ncs. Another point in favour of Si-ncs is that non-radiative defect states due to crystal impurities are thermodynamically unfavourable inside Si-nc, hence obtaining superior crystal purity that further enhances the radiative emission.

In that context, the term 'degree of freedom' is normally used in literature to describe a particular dimension in which QC phenomena do not apply. Hence, Si-ncs are often described as zero dimensional systems or quantum dots (QD) since all the dimensions are ruled by QC effects. Similarly, quantum wires or nanowires (NWs) and quantum wells (QW) are commonly described as 1D and 2D systems, respectively. In the framework of the effective mass approximation (EMA), and departing from the number of states per unit volume per unit energy, the density of states (DOS) can be defined as:

$$\rho(E) = \frac{\partial N}{\partial E} \tag{1.2}$$

Being E the energy of a particular state and N the total number of states per unit volume in a single quantum dot. For a single Si-nc, N becomes discretized, and the DOS reads:

$$\rho_{QD}(E) = 2 \sum_{n_x, n_y, n_z} \delta\left(E - E_{n_x, n_y, n_z}\right) \frac{\partial N}{\partial E} \tag{1.3}$$

Where n_x, n_y, and n_z refer to each confinement direction. The expression for the allowed energy levels can be obtained solving the Schrödinger equation assuming an infinite square potential well for the three directions of confinement:

$$E_{n_x,n_y,n_z} = \frac{n^2 \cdot \pi^2 \cdot h^2}{2 \cdot m^* \cdot D^2_{n_x,n_y,n_z}} \tag{1.4}$$

With m^* being the effective mass of electrons and D the confinement diameter. In addition, an energy offset that takes into account the bandgap energy of the material (E_0) should be added when calculating the DOS in the conduction band.

Consequently, the bandgap energy of Si-ncs becomes consistently enlarged with respect to bulk Si, enabling light emission in the visible range. Such emission can be effectively tuned by controlling the mean Si-nc size, from a value of 1.12 eV (Bulk Si emission energy), up to 1.6 eV for tiny Si-ncs of 2.5 nm [93, 94]. For even smaller Si-ncs, light emission is believed to be ruled not only by QC, but also by radiative defective states located at the surroundings of Si-ncs [95]. In fact, some works have suggested the co-existence of both mechanisms, and have provided accurate modelling depending on the structural environment of Si-ncs [96, 97]. It is also known that only a small fraction of Si-ncs contributes to the PL emission due to the interaction of surrounding non-radiative defects with bounded electron-hole pairs [98]. This issue could be solved if high quality Si-ncs with a defect-free shell structure are synthesized.

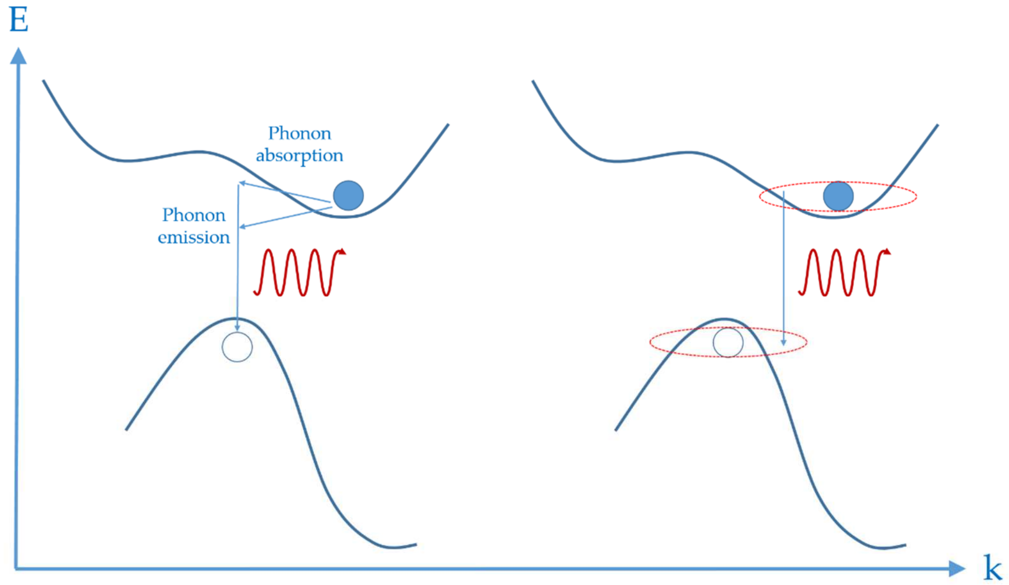

Figure 1.3. Comparison between the phonon-mediated e-h recombination in bulk Si (left) and the phonon-free recombination in Si-ncs caused by the strong wavefunction delocalization.

Currently, Si-ncs have been obtained over a wide variety of techniques, each one offering a series of advantages and disadvantages. One of the most popular approaches is the off-stoichiometric deposition of silicon oxides (or nitrides). Then, off-stoichiometric Er-Si_3N_4 and Er-SiO_2 layers with Si excess are often fabricated on purpose to allow Si-nc formation during the annealing process (named Er-SiO_x and Er-SiN_x from now on, being $x < 2$ in the first case and $x < 4/3$ in the second one). There is a countless number of publications and review papers to which readers can refer for a more extended knowledge of the synthesis and properties of Si-ncs [99-104]. In the following, I will review the most popular fabrication approaches used so far:

Plasma Enhanced Chemical Vapour Deposition (PECVD). This method has long been used to deposit SiO_x films containing Si-ncs. Some representative works can be found in the literature [105]. It consists in the mixing of reactive precursor gases that undergone a chemical breakdown process prior to film deposition. A radio-frequency (RF) signal between two electrodes accelerates the chemical breakdown of species. The system works as following: The substrate is placed in a deposition stage that works as both a hot plate and anode of the RF signal. Then, precursor gases are released into the chamber. In SiO_x deposition for instance, silane (SiH_4) and either nitrous oxide (N_2O) or oxygen (O_2) are needed. Afterwards, the RF signal is switched on, and free electrons contained in the delivered plasma accelerate in the chamber, colliding with gas molecules and causing the dissociation into radicals and ionized particles. The formation of the solid film takes place by adsorption and eventual chemical reaction at the surface of ionized molecules. The process is controlled by a number of factors: (i) precursor gas flow ratio, (ii) RF signal, (iii) substrate temperature, and (iv) run pressure in the chamber. Interesting advantages of this technique are a high deposition rate, the relatively low temperature of the process (typically between 100°C-400°C) and the homogeneity of the film. On the contrary, there are also drawbacks to consider, such as the deposition of undesired radicals and other residual atoms or the substrate damaging due to plasma bombardment. One of the most common contaminants when depositing SiO_x is hydrogen, which is known to detrimentally affect the reliability of devices based on these layers [106]. Also nitrogen is typically found. Concerning the substrate damaging, there are however some modifications of the PECVD system that implement remote plasma generation chambers to minimize substrate bombardment by highly energetic ions and/or radicals. The electron-cyclotron-resonance (ECR) PECVD system is a representative example. During my PhD, I had the opportunity to successfully operate this system at McMaster University, in Canada, under the supervision of Prof. Peter Mascher. Further details of the work carried out by that time can be found in the fourth chapter of this dissertation.

Another alternative is to use **Low Pressure Chemical Vapour Deposition (LPCVD)** [107]. This technique is widely used for the fabrication of oxide and nitride-based thin films and polycrystalline silicon, among others, and provides thin layers with good conformity and uniformity. In this case, wafers are placed in a quartz tube surrounded by heating coils. Then, precursor gases are introduced into the chamber. The reaction takes place at the heated substrate surface, forming the solid films by thermal decomposition. This process is driven at low pressure (between $10\text{-}10^3$ Pa), with substrate temperatures between 600°C to 800°C. Main advantages of this process is the high density of deposited layers and the fact that multiple wafers can be loaded simultaneously (up to hundreds in some cases), strongly reducing the fabrication costs. On the contrary, the high temperature required for deposition makes this technique not suitable when pre-patterned wafers with metallic junction contacts are introduced in the chamber, as undesired doping diffusion drift into the substrate may occur. Also, in-situ sample pre-cleaning is not generally available in LPCVD.

Sputtering of targets is usually done by means of Ar^+ ion bombardment [108]. In that case, material is physically sputtered from a target and directed towards the substrate. The targets to be deposited are placed in a chamber filled with an inert gas (Ar in most cases), also called sputtering gas. The sputtering process occurs when upon application of a DC or RF electric field, free electrons accelerate and impact with the gas, creating ions. These ions are then directed towards the targets under the action of the electric field, removing atoms that ultimately will be deposited in the substrate. The difference between using a DC or an RF voltage source (the last one usually at 13.56 MHz) relies on the conductivity of chosen targets. Conductive targets can be sputtered by a DC voltage source, whereas RF is used for insulating targets. The deposition is controlled with the substrate heating, the DC or RF power, the chamber pressure and the sputtered targets. The sputtering yield, which accounts for the ratio between the number of sputtered atoms and the total number of incident ions, is often used to identify a particular deposition. SiO_x layers are typically deposited by co-sputtering of SiO_2 and Si targets. Noteworthy, O atoms are preferentially sputtered over Si and consequently an additional Si target is needed to adjust the Si excess of the layer. A point in favor is the versatility of the system, as the complexity of the deposited film can be increased just by adding several targets into the deposition chamber. Furthermore, materials with very high melting points can be easily sputtered, in contrast with other techniques in which the film growth takes place by evaporation of targets (thermal evaporation, electron beam evaporation). Moreover, hazardous precursor gases such as silane or ammonia (NH_3) are no longer required to obtain SiO_x or SiN_x thin films since chemically stable Si, SiO_2 and Si_3N_4 targets can be used instead. On the other hand, the quality of deposited layers is not as good as in CVD systems. Also, the diffusivity of deposited agents makes difficult to target a specific region of the substrate. Being a high energy deposition (~ 1 eV), layer intermixing is prominent and consequently multilayer morphologies are not successful. Nowadays, there are several types of sputtering deposition techniques that respond to different needs and demands such as ion-beam sputtering, ion-assisted deposition, reactive sputtering or gas flow sputtering. Among them, reactive sputtering is particularly interesting as it is often used to deposit SiO_x and SiN_x films. This time a reactive gas is also introduced in the chamber apart from the sputtering gas. By doing this, the sputtered material chemically reacts with the gas before being deposited in the substrate. A better control of layer composition can be obtained by modifying the amount of reactive gas in the chamber.

Ion implantation of Si^+ into SiO_2 or Si_3N_4 thin films [109]. Si^+ ions are generated and accelerated at high energies prior to impact over a substrate or a thin film. Ion implantation has been largely used in silicon microelectronics to dope silicon either with boron or phosphorous. Nevertheless, a large variety of ions such as arsenic, lanthanides or germanium can also be implanted. A sputter source generates the ions, which enter into an injector magnet (mass selector) that selects the ionized species to be implanted. Then, another magnet accelerates the ion beam up to the targeted energy of implantation. Finally, the beam enters the implantation chamber where the substrate is allocated, and the ion implantation is performed. The implantation penetration of ions into the substrate (or film) depends basically on four factors: (i) the ions to be implanted, (ii) the substrate, (iii) the kinetic energy of implanted ions, and (iv) the implantation angle. Fortunately, there is a number of implantation simulators and software packages that accurately predict the implantation profile of doping species. I may note the one developed by J. F. Ziegler and co-workers: The Stopping and Range of Ions in Matter (SRIM) [110].

Molecular Beam Epitaxy (MBE) [111]. This approach provides epitaxial layers with high control of layer stoichiometry. This technique is typically characterized by low growth rates (1 monolayer per second) that allows nearly atomically abrupt interfaces. It is widely used to grow high quality II-VI or III-V materials for optoelectronic purposes, such as solid state lasers or photodetectors. MBE operates under Ultra High Vacuum environment (UHV) to minimize the defect creation by contaminants. A nearly ballistic transport of evaporated material takes place in the chamber, with large mean free paths of species. In order to maintain these conditions, the system is usually equipped with several vacuum chambers, each one with an autonomous pumping system. For example, a separated chamber is normally used to introduce the substrate. The same chamber also outgases the substrate by heating the holder. Then, the substrate is ready to enter the growth chamber. Depending on the materials used and the desired morphology, multiple growth chambers can be implemented in the system to avoid crossed contamination. For instance, multilayer approaches of alternating III-V semiconductors necessitate from two different chambers since the components of one are dopants in the other. Growth material is evaporated from effusion cells situated in the chamber (source ovens). A chilled jacket (liquid N_2 circuit) surrounds the source ovens to minimize heat radiation into other parts of the system. Also, a special shape is designed (normally conical) to improve growth homogeneity up to a larger area. Directional flux beams of material are highly undesired. A rotating substrate is used to further improve the homogeneity of growth. Similarly, oxidation of source material detrimentally affects the final morphology of layers, introducing defects and dislocations. Layer morphology is controlled by different parameters, including: (i) deposition rate, (ii) surface material, (iii) crystallographic orientation and (iv) substrate temperature. The latter one is of critical importance. The substrate temperature should remain high to provide atoms with sufficient diffusivity to efficiently allocate into the lattice sites, but also low enough to avoid layer-to-substrate inter-diffusion. Therefore, there is an ideal heating window for sample growth.

Another interesting feature of MBE is the in-situ monitoring of layer morphology during sample growth. The implementation of analysis tools in the deposition chamber yields an efficient control of components at any time during material deposition. Typically, Reflection High-Energy Electron Diffraction (RHEED) is used for that purpose, although other techniques such as Auger Electron Spectroscopy (AES), X-ray Photoelectron Spectroscopy (XPS) or mass spectroscopy have been also incorporated at will in MBE systems. Si-ncs are normally grown by deposition of tiny Si islands with subsequent capping with an oxide. MBE has the advantage of providing high quality interfaces and nearly perfect stoichiometry of grown materials. Also, substrate damaging does not occur since the deposition is performed at low energy (~ 0.1 eV). On the other hand, the low deposition rates displayed and the need for a nearly atomically clean substrate are the main drawbacks of this technique. Generally, three different growth modes can be identified depending on the growth parameters: (i) Franck-van der Merwe growth mode, (ii) Vollmer-Weber growth mode and (iii) Stranski-Krastanov growth mode.

Laser ablation of Si targets [112]. An excimer laser beam (typically a UV laser) with a pulse width of nanoseconds (or picoseconds), a repetition rate of few Hz (between 5-20 Hz typically) and laser fluences of about few J/cm^2 is directed at a certain angle towards a material target placed in a vacuum chamber, removing material from its surface. As a consequence, a plume of material is formed. The substrate is placed in front of the target so that material can be condensed at its surface. Rotating and heating of substrate holder can be implemented to improve deposition homogeneity and adsorption of components, respectively. The layer stoichiometry and deposition rate can be modified upon changing the laser parameters or the distance between the substrate and the target. Also, the chamber can be filled with a reactive gas (such as oxygen) to further modify the deposition stoichiometry. Film thickness is monitored by an in-situ ellipsometer operating at a single wavelength of 632.8 nm.

This technique presents several advantages, such as: (i) it is a flexible system, as many targets can be placed at the vacuum chamber simultaneously by using a rotational carroussel assembly, (ii) films can be grown in any environment, (iii) complicated sample stoichiometry with multiple components can be easily deposited, (iv) low temperatures are required for deposition and (v) good control of growth, upon variation of laser parameters. Concerning the main disadvantages, I should mention the high defect concentration in deposited layers or the impossibility of PLD implementation for large-scale film growth. SiO$_x$ layers can be produced by direct ablation from a Si target in an oxygen filled deposition chamber. Besides, PLD technique is attractive since allows fabricating a wide range of nanoparticles made of, for instance, Ge [113], Cu [114] or Ag [115]. RE luminescent layers such as Er- or Bi-doped oxides have also been developed [116]. In that case, PLD becomes particularly interesting since allows studying the interaction between ions in the growth direction just by alternating RE deposition with a set of different buffer layer thicknesses.

With regard to PLD technique, I should add some words about my experience with the system. Despite it is not included in this dissertation, I had the opportunity to run a PLD system for a few weeks at the *Instituto de Óptica, Consejo Superior de Investigaciones Científicas (CSIC), Madrid*, under the supervision of Dr. Rosalía Serna. Our main goal was to develop Eu-doped SiAlON thin films fabricated by PLD using commercial SiAlON targets and metallic Eu tablets. Some results obtained from that particular investigation can be found elsewhere [117].

Electron Beam Physical Vapor Deposition (EB-PVD) of Si and SiO_2 targets [118]. This technique lies in the same group as MBE, except for the fact that an electron beam is used to heat up the targets, instead of an effusion cell. Also, EB-PVD does not normally utilizes in-situ analysis tools to control growth process. Only a quartz-crystalline microbalance (QCM) is used to monitor deposition rate. The system is driven under UHV conditions, with base pressure values around of 10^{-7} Torr. Material target is placed in a crucible stage, and heated up to evaporation temperature (some materials sublimate directly) by means of a highly energetic electron beam. A tungsten filament serves as electron supplier. A variable voltage is selected in the filament (between 6 to 10 kV, typically). The current is modulated in order to control the evaporation rate of each target (from few milliamperes up to hundreds of milliamperes). Evaporated material condenses on the substrate, which is placed in a rotating holder that sometimes includes a quartz lamp with radiation shield to allow heating of the substrate. Sometimes, EB-PVD systems include a gas flow system income to provide higher versatility in layer composition. The system is equipped with a cooled water circuit that maintains the QCM, the electron gun, the crucibles and the vacuum chamber at low temperature. Among the advantages of this technique over others, it is remarkable the extremely large range of deposition rates available. Film deposition rate can be tuned from few nanometers per minute to as high as few micrometers per minute. Because of this, fairly good layer stoichiometry can be obtained when needed, but also 'bulky' layers can be deposited in few minutes when the layer stoichiometry is not a critical parameter. Another point in favor is the fact that only the target is heated and not the container (crucible), minimizing contamination. This is in high contrast with conventional thermal evaporation by incandescent filament, as in this case both the target and the crucible are evenly heated. On the other hand, there is a number of materials (refractory materials or high temperature dielectrics, for instance) that have low vapor pressures and therefore are difficult to evaporate. Film adhesion may also be an issue in some cases. Moreover, in-situ pre-cleaning of substrates is not generally available in EB-PVD systems. SiO_x can be obtained by EB-PVD by means of mixed Si and SiO_2 solid powders. The components are weighted to obtain the desired Si/SiO_2 ratio. Afterwards, they are evenly mixed and compressed to form a tablet of source material that will be loaded into the crucible for evaporation.

During the last year of my PhD, I run an EB-PVD system (Pfeiffer classic 500) to develop luminescent oxides, transparent conductive oxides and nanowires. The equipment was installed at the clean-room facility of University of Barcelona. Being myself designated as one of the authorized technical operators to run the system, we rapidly noticed the wide range of possibilities offered by the EB-PVD system. In fact, few months later (at the time of this writing), several nice results were already obtained with the equipment. A representative example of the work carried out with the EB-PVD can be found at the end of chapter 4 and in chapter 5 (future perspectives).

As seen, a large number of fabrication processes are available to fabricate SiO_x layers. However, they all require from a common final step to grow Si-ncs: the annealing treatment. After layer deposition, samples are introduced into a furnace and are annealed at high temperature to promote phase separation of Si and SiO_2. Performing an adequate furnace treatment is crucial since the optical and electrical properties of deposited layers can be completely modified. Several gas environments are normally used to assist passivation, being the most commonly used nitrogen (N_2), oxygen (O_2), air (N_2 and O_2 mainly) or forming gas (a variable mixture of N_2 and H_2). With regard to the annealing treatment, in spite of the fact that different techniques are also available in this case, a temperature around of 1000°C (or superior) is normally required to form Si-ncs at ambient pressure. Typical annealing treatments stand for: (i) conventional annealing (CA), (ii) rapid thermal annealing (RTA), and (iii) flash lamp annealing (FLA). The main differences between them reside on the heating ramps, being CA the slower one (typical rate of 15° per minute), followed by the RTA which can reach the targeted temperature within few seconds, and finally the FLA that exposes layers to delta-like heating peaks.

The insights provided during the last 25 years on Si-nc structural and optical properties are notable. These works were not limited only to provide a greater theoretical knowledge, but also paved the way towards the implementation of all-silicon solutions to overcome inherent limitations of certain applied fields such as energy storage or photovoltaics. To give a general overview and a better understanding of the subject, some interesting results on Si-ncs are briefly summarized below.

In spite of the fact that the boom of Si-ncs and Si-based quantum structures is generally attributed to L. Canham after his work on porous silicon [119], there are some previous studies that already used Si-ncs to boost current injection and light emission, as well as to demonstrate quantum confinement in 0D structures. Among them, it is highly remarkable the work performed by DiMaria and co-workers at IBM, since they made important contributions towards the understanding of charge transport in off-stoichiometric SiO_x and SiN_x layers. Their notorious research about Metal-Insulator-Semiconductor (MIS) structures allowed implementing more accurate modelling of charge transport in silicon oxides and nitrides. Even nowadays some of his former designs on hot electron injection are of current interest. In fact, some of them have recently been successfully implemented by the Electro-Photonics Laboratory in Barcelona to further boost the EL efficiency of Si-based light emitting devices. Further details of this ongoing investigation can be found at the end of chapter 2.

Back to the eighties, DiMaria *et al.* reported on high current injection in MIS structures containing Si nanostructures [120]. In his work, he attributed the enhanced current injection to a reduction of the energy barrier of injected electrons when Si-ncs are embedded in the oxide control layer. Moreover, he proposed two different applications for these devices: an Electrically Programmable Read-Only Memory (EPROM) with low programming voltage, and multilayer structures alternating sub-layers of Si-ncs and SiO_2. Later on, he demonstrated EL emission from a MIS structure containing Si-ncs [121]. Quantum size effects in tiny Si islands was proposed to explain the emission. This hypothesis was corroborated few years later by Takagi *et al.*, providing experimental evidences of quantum confinement in hydrogen passivated Si-ncs [122]. The PL peak energy was found to follow an inverse quadratic relationship with particle size for Si-nc diameters ranging from 2.5 nm to 5 nm. Rapidly, several works reported on quantum confinement in Si nanostructures. Size-selective precipitation (SSP) with controlled pore diameter was implemented to fabricate Si-ncs with quantum yields as high as 50% at low temperature [123]. Also, RF co-sputtering was used to obtain luminescent Si clusters with various Si excess [124]. An increase in size diameter was detected upon annealing, correlating the red-shift of the photoluminescence (PL) peak with the decrease in bandgap energy between the highest-occupied molecular orbital (HOMO) and the lowest-unoccupied molecular orbital (LUMO) for larger Si clusters. Later on, synthesis of Si-ncs was carried out at Massachussets Institute of Technology (MIT) by pulsed laser ablation [125]. A mean particle diameter of about 3 nm was produced. Structural analysis confirmed the crystal structure and the quantum confinement was experimentally evidenced upon UV excitation, displaying intense visible emission. Few years later, in 1996, Tiwari *et al.* presented volatile and non-volatile memories with nano-crystal storage [126]. Single electron storage in individual Si-ncs was demonstrated using a single transistor memory structure with Si-ncs floating gates operating at voltages < 3 V. These devices showed efficient charge storage over time and fast programming cycles [127]. Noteworthy, the investigation of Si-nc memory cells has experienced great progress ever since, obtaining superior features in Si-nc flash memory cells [128, 129].

Wang *et al.* reported an interesting size-dependent blue shifted EL emission in devices operating at room temperature by controlling the thickness of hydrogenated amorphous Si layers in a Si/amorphous-SiN_x superlattice [130]. This result somehow resembles the one obtained in 1995 by Lu *et al.* in which quantum confinement in Si/SiO_2 superlattices was reported [27]. In this case however, the SiO_2 barrier layers were substituted by SiN_x, and the amorphous Si layer was crystallized by KrF excimer laser annealing to form Si nanocrystallites. Still, despite the large number of papers reporting QCE in Si-ncs, a convincing theoretical model able to correlate the PL peak shifting with Si-nc size had not been developed yet. Most of them lack of a consistent explanation of the fact that luminescence energy was lower than expected from a QC model, plus it was limited to green-red emission even for smaller Si-ncs. Wolkin *et al.* shed some light to this issue, providing detailed theoretical modelling and correlating electronic states and luminescence in porous Si-ncs with a new Si=O bond [131]. They stated that electronic states in Si-ncs were defined not only by the QC model, but also by surface passivation. This effect was found to be negligible for large Si-ncs (> 3 nm). On the other hand, for smaller Si-ncs, the surface-to-volume ratio is more pronounced and therefore surface passivation significantly modifies the available electronic states of Si-ncs.

In 2000, optical gain in Si-ncs was reported [33]. Si-ncs were formed by means of Si implantation into ultra-pure quartz substrate. A Variable Stripe Length method (VSL) was used to test the amplified spontaneous emission of samples. A pulsed laser operating at 1 $KW \cdot cm^{-2}$ was used to pump Si-ncs. A maximum net gain mode of $g = 100$ cm^{-1} was recorded. The authors used a quasi-two level model based on population inversion of radiative states in Si-ncs to explain their findings. This work represented a turning point in silicon photonics since the missing key device, the silicon laser, seemed to be within reach in the short term. This work was endorsed by Khriatchtchev *et al.* a year later, as they reported optical gain in Si/SiO_2 lattices upon excitation with nanosecond pulses [132]. Several papers were published over the following years, detailing all sorts of experiments to further insight into the amplification properties of Si-ncs [133-135]. Nevertheless, in spite of the promising results reported by that time, these samples seemed to lack of reproducibility since optical gain in Si-ncs was not further obtained in the upcoming years.

Going one step further, researchers started to worry not only about the optical properties of Si-ncs, but also on the optoelectronic features when embedded in MOS structures. Remarkable is the work of Priolo's group, in Catania, about Si-ncs based light emitting devices [136, 137]. The EL efficiency, that accounts for the ratio between number of emitted photons by number of incident electrons, was found to be of about 10^2 times higher than the PL efficiency (number of emitted photons divided by number of incident photons). An excitation cross-section of $4.7\ 10^{-14}$ cm^2 was measured. Also, direct impact was proposed as the main excitation mechanism for Si-ncs. Nevertheless, the use of systems based in Si-ncs embedded into SiO_2 started to be questioned by that time, especially for those applications in which charge injection was required. Si-nc MOS light emitting devices for instance, despite showing promising optical properties, required impractical large voltages to inject carriers due to the wide bandgap of SiO_2. As a consequence, new host matrices with reduced bandgap were implemented to accommodate Si-ncs. Si_3N_4 seemed to be the ideal candidate for this purpose, since has a smaller bandgap compared to SiO_2, larger dielectric constant and is compatible with the CMOS technology. The first work reporting on experimental evidence of quantum confinement in amorphous Si quantum dots embedded in a Si_3N_4 matrix dates back to 2001 [138]. Notice that Si agglomeration was observed in the amorphous form, not crystalline. In this paper, authors proposed a new equation for the dependence between the energy gap and the mean size diameter for an amorphous Si QD in a silicon nitride matrix. Their findings were compared with the analogous case of a Si-nc in a SiO_2 matrix, where:

$$E(eV) = 1.6 + 0.72/d^2 \quad \textit{for the system Si QD/SiO}_2 \quad [139] \tag{1.5}$$

$$E(eV) = 1.56 + 2.40/d^2 \quad \textit{for the system Si QD/Si}_3\textit{N}_4 \tag{1.6}$$

With the independent variable corresponding to the bulk energy, d is the mean diameter of the Si QD and the multiplying factor is a fitting constant. In their work, N.-M. Park and co-workers justified the new formula by assuring higher quantum confinement of amorphous Si QD of a factor of 3 when embedded in Si_3N_4 with respect to SiO_2. The QC in silicon nitride was further corroborated by other authors [140, 141]. However, there has been controversy around Si QD embedded in silicon nitride matrices, as other authors have also suggested that the origin of energy shift might come from defect states rather than from QC in Si QD indeed [142]. At the Electro-Photonics Lab in Barcelona, after working with Si QD/Si_3N_4 systems for a long time, we are of the opinion that no quantum confinement takes place neither, and that luminescence and absorption energy shifts are mainly due to intraband defective states or 'tail states' rather than due to quantum confinement in Si QD [143]. In this work, silicon-rich nitride (SiN_x) layers were alternated with stoichiometric silicon nitride buffer layers to provide good control of the mean Si-nc size. A protocol for critical examination of QC evidences in Si QD embedded in silicon nitride is proposed.

Apart from the early works on Si-ncs superlattices, a remarkable paper was published in 2002 by Zacharias *et al.* [144]. Good ordering and size control of Si-ncs was demonstrated, as well as QC effects in the PL of samples. Later on, similar Si-nc superlattices were used to provide a general overview of the properties of Si-ncs and their potential applications in different areas [145]. Particularly interesting is the work published in 2009 by Marconi *et al.* on Si-nc superlattices as effective EL emission with low turn-on voltage and high power efficiency was reported [146]. Such interesting properties have been recently revisited by our research group to fabricate Er-doped Si-ncs superlattices and Tb-doped SiO_xN_y/SiO_2 superlattices with improved functionality. Further insight on the optoelectronic properties of our RE-doped superlattices will be reviewed in chapters 2 and 4.

In 2005, field-effect EL emission in Si-ncs was demonstrated [147]. A CMOS transistor with a SiO_x control layer was fabricated. The large charge retention time of Si-ncs was used to sequentially inject electrons and holes into Si-ncs to form electron-hole pairs. Bipolar programming cycles were defined at the transistor gate to allow sequential injection. The EL signal raised up to a maximum driving gate frequency of 10 KHz, hence experiencing a fast decay due to several effects: (i) incomplete electron (hole) charging of Si-ncs, (ii) auger effects in Si-ncs, and (iii) limitation of the gate capacitive charging time constant. The main arguments in favor of field-effect light emitting devices (FELEDs) with respect to LED-based Si-ncs light sources are a better control of carrier-injection processes and the fact that hot carriers do not play any significant role in the excitation of luminescent centres. This latter fact avoids excessive heating due to hot carrier thermalization and also improves reliability of devices.

Alternative device designs to enhance light extraction were also implemented. A good example is the work published by Presti *et al.* in which a photonic crystal is implemented on top of a SiO_x film containing Si-ncs to improve the outcoupling efficiency [148]. The photonic crystal is directly patterned on top of the polycrystalline silicon electrode using conventional optical lithography, enhancing the light extraction up to a factor of 4 with no need of buried reflector or antireflecting coating. Other approaches have obtained an EL enhancement of about 25 times with external quantum efficiency twice as efficient as that of the reference sample [149]. Such considerable improvement was accomplished embedding a Si-ncs/SiO_2 superlattice in a distributed Bragg reflector (DBR) cavity. It consisted of a 4-period DBR of alternated 200 nm thick SiO_2 layers and 45 nm thick amorphous Si (a-Si) at the bottom of the luminescent layer and a 2-period DBR with identical parameters situated on top. Spectral narrowing of the emission was measured, with full width at half maximum narrowing from 200 nm for the reference sample down to 20 nm in the cavity.

Si-ncs have not only been used as light emitters or charge storage sites for memory applications. They have also been suggested as efficient absorbers for photovoltaics applications. Conibeer *et al.* reported on the convenience of using Si-ncs to engineer a multi-bandgap tandem solar cell to increase the efficiency of solar cells [150]. This work aimed to respond to the need of developing a third photovoltaic generation that embraces higher efficiency, low cost and thin film deposition processing at once. New routes for Si-ncs were established, widening the range of applications from charge storage and integrated light emitting devices to all-Si photovoltaics. A considerable research activity on Si-nc photovoltaics took place in following years. To cite some representative works with applications in photovoltaics, Timmerman *et al.* demonstrated space-separated quantum cutting in Si-ncs [151], Yuan *et al.* used Si-ncs as efficient PL down shifters [152] and Govoni *et al.* studied the carrier multiplication effect between interacting Si-ncs to increase solar cell efficiency [153].

Also in our group, at the Electro-Photonics Laboratory in Barcelona, intense research on Si-ncs tandem solar cells was carried out by means of the European project Nascent (acronym for Silicon **Na**nodots for **S**olar **Ce**ll **nT**andem) [154]. Our main role was the optoelectronic characterization of Si-ncs solar cells. Standard parameters such as voltage open circuit, fill factor, or the optical-to-electrical power conversion were examined in three different matrices: SiO_2, Si_3N_4 and SiC [155]. Poor efficiency was found in Si-ncs embedded in SiO_2 matrices, mainly because of the large band-offset difference that makes difficult charge extraction just by using the work function difference between p and n regions. Si_3N_4 matrices also showed low performance due to the large number of defects or trapping sites within the material. Only SiC matrices containing Si-ncs displayed promising characteristics for solar cells. The reduced band offset between SiC and Si-ncs (0.5 eV and 0.9 eV for the conduction and valence band, respectively) allowed charge extraction with a voltage open circuit value of 518 mV. P-i-n solar cells with free-standing SiC membranes were also fabricated to study the generated current and voltage open circuit in the SiC layer uniquely. Despite the encouraging voltage-open-circuit value obtained in the membrane (370 mV) [156], a remarkably low short circuit current of 6.8% with respect to the total generated current was extracted. The large number of recombination defects in the depletion region was believed to be the origin of such low value [157].

Moreover, Si-ncs have been successfully tested as biological markers for bio-imaging purposes. An interesting work was published in 2008, in which Si QDs were used instead of conventional organic fluorescent dyes [158]. Their cytotoxicity was found to be ten times lower compared to CdSe-QD. In addition, oxygen radical generation was identified as the main membrane damage mechanism when using Si QD in living cells. Later works further confirmed these findings [159, 160].

During the last five years, interesting new non-linear phenomena has been identified in Si-ncs. As a case in point, I shall mention the former work performed by our group in collaboration with the Nanophotonics Technology Center (NTC) in Valencia, the CEA-LETI in Grenoble and the Nanoscience Laboratory in Trento, in which all-optical switching in Si-nc-based slot waveguides was observed at telecom wavelengths. A modulation depth of 50% with output pulse duration of 10 ps was achieved upon excitation of a Si-nc/SiO_2 slot ring resonator with optical power of about 100 mW [161]. Also in the same year, Tom Gregorkiewicz's Group at the University of Amsterdam demonstrated increased quantum efficiency in small Si-ncs in a phonon-free radiative transition [162]. Time-resolved and spectral measurements were combined to verify their hypothesis. An ultrafast visible PL band (in the range of picoseconds) and a spectral red-shift were identified as experimental evidences of a no-phonon hot carrier radiative recombination in Si-ncs. Few years later, the same group demonstrated increased quantum yield in Si-ncs embedded in a SiO_2 matrix as a consequence of carrier multiplication upon excitation with high energy photons [163].

In 2012, stimulated Raman scattering in Si-ncs was demonstrated under non-resonant excitation at infrared wavelengths [164]. A signal four times greater than in bulk silicon was obtained, opening the way towards an all-Si laser with extremely small footprint (a few micrometers).

Also remarkable is the work carried out by Maier-Flaig and co-workers on organic Si LEDs. Multicolor Si-LEDs were developed with external quantum efficiencies up to 1.1% and low turn-on voltages [165]. Furthermore, in-situ analysis was performed in Si-LEDs to elucidate the main mechanisms that lead to the early device breakdown, identifying three main modes of failure in polydisperse Si QDs: (i) short circuits due to larger particles inside the SiQD layer, (ii) interlayer diffusion of very small particles, and (iii) inhomogeneities of the overall Si QD layer [166]. However, these breakdown mechanisms were not identified in size-separated QDs, providing an evident reliability enhancement and no observable morphological or compositional changes.

Another interesting characteristic of SiO_x layers is their resistive switching behavior. Unipolar and bipolar switching at room temperature have recently been demonstrated by Kenyon's group at the University College of London [167]. In their work, they attribute the bipolar switching to reversible conductive paths formed by oxygen vacancies that dissociate due to the oxygen vacancy drift during the reset cycle, whereas unipolar switching would be dominated by silicon conductive filaments through Si-ncs. In that case however, the dissolution of conductive paths during reset function is triggered by thermally activated radial diffusion. Quantum conductance was also identified in these layers, and attributed to the SiO_x layer itself and not due to the drift of metallic ions from adjacent electrodes [168]. These findings suggested the implementation of all-Si memristors with a switching functionality fully driven by SiO_x layers.

1.2.2. Rare earth doping

Another well-known strategy to obtain Si-based light emitting devices is by means of RE doping. Optically active RE ions are able to absorb and emit light when located in a suitable local environment. Most of them (except for Ce^{3+} ions) require a non-centro-symmetric bonding between the RE ion and the host matrix to break the parity forbidden intra 4-f wavefunctions. Under this condition, the dipole transition becomes weakly allowed and radiative de-excitation from the RE ion excited states occurs, with a typical lifetime of few milliseconds. This method is commonly referred as optical doping, since dopants are introduced to provide and optical functionality instead of an electrical one, as is the case for B and P in extrinsic semiconductors. Similarly, RE doping yields an extrinsic emission that varies depending on the distribution of discrete energy levels of each RE ion, spanning from the UV in Gd-doped materials to the NIR range in Er-doped thin films. It is worth noting that the latter group of materials has played an important role in the evolution of RE-doped Si-based hosts due to the foreseen applications in integrated telecom systems. As already underlined at the beginning of this chapter, an efficient Si-based optical link operating at 1.54 μm would overcome some of the current limitations and issues of the microelectronics industry, and will suppose an enormous step forward for the development of the silicon photonics platform. On the other hand, visible light emitting RE-doped devices are expected to provide low-cost solutions for biosensing applications and full colour micro-displays. In fact, RE-doped oxynitrides have already been widely used to develop down-converting phosphors for solid state lighting with a conversion efficiency over 90% [169, 170]. Nevertheless, such phosphors are based on sintered powders that must be processed at very high temperatures which are incompatible with the CMOS technology (typically between 1600°C-1800°C). Moreover, the fabrication of smooth thin films with good conformity and high planarity is out of reach if departing from sintered luminescent phosphors. As a consequence, commercial RE-doped luminescent powders can only be implemented as functional down-converting coatings in high brightness LEDs, but not as electroluminescent layers directly. Therefore, the implementation of much simpler pixel cells formed by a color-tunable electroluminescent thin films embedded in CMOS compatible MIS structures for integrated lighting applications faces fascinating challenges and breakthroughs that deserve attention.

Several fabrication processes can be used to tackle the development of RE-doped luminescent thin films. Among the previously described fabrication techniques, ion implantation and simultaneous co-sputtering of RE oxides and Si-based hosts are commonly used [171, 172], although others such as PLD [173], EB-PVD [174] or sol-gel synthesis [175] have also been reported as efficient methods to obtain luminescent RE-doped materials. In any case, the atomic concentration of RE dopants in the host should be maintained low (a few percentage) to avoid ion-ion interaction (when the ion inter-distance is very small) and RE clustering (for values above the solubility limit of the host material). Also, the annealing treatment is of high importance, especially the temperature of the process, since an optimum thermal budget would yield a high number of emitting RE ions while avoiding RE clustering.

With regard to the interest of the scientific community on RE-doped Si-based luminescent materials, I may note that although the number of publications is notorious (especially for Er-doped Si-based materials), it is not comparable to the work conducted on the electrical and optical properties of Si-ncs. Among other reasons, a plausible explanation for that would be the limited access that many research groups have to the specific fabrication facilities required to perform RE doping in Si-based materials. As already mentioned, ion implantation and co-sputtering are the most popular approaches. Also, RE sublimation of targets located in thermal effusion cells has been used to obtain such luminescent materials [176]. However, such systems generally necessitate from an exclusive use to avoid cross-contamination with other CMOS processes and consequently are more restricted than usual. In the following, a summary of the most remarkable works on luminescent RE-doped Si-based hosts is detailed. Readers may find a more extended review of these materials elsewhere [171, 177-181].

Er-doped Si-based materials deserve a special focus due to the large number of publications available in the literature. The search for an efficient Er-doped Si light emitting device dates back to 1985, where an electrically pumped Er-doped Silicon LED was demonstrated [182]. In that work, H. Ennen and co-workers reported a sharp EL emission at 1.54 μm assigned to 4f-4f transitions when biasing devices in the forward direction at 77 K. Despite this promising result, devices had to operate at unpractical cryogenic temperatures, strongly limiting the optoelectronic performance. It was not until 1994, when an Er-doped Silicon light-emitting diode emitting at 1.54 μm and operating at room temperature was demonstrated that Er-doped microphotonic systems became genuine candidates for the implementation of efficient Si-based sources [183]. Sharp spectral emission was reported, with a saturation of the EL intensity at 5 A/cm^2 and an inverse dependence of the EL emission with the temperature. Nevertheless, in spite of such breakthroughs, a major constraint was identified in Er-doped Si: the energy back transfer. Such effect accounts for a non-radiative energy migration from excited Er^{3+} ions back to the Si host as a consequence of a resonant intraband process. A comprehensive study of this detrimental effect was presented in 1996 [184]. From this point on, although additional research on Er-doped Si was regularly published over the following years, many authors focused on other Si-based hosts with larger energy bandgap to avoid undesired back transfer phenomena. SiO$_2$ hosts for instance, were good candidates to allocate Er^{3+} ions. Similarly than Erbium Doped Fiber Amplifiers (EDFA) for the long-haul communications [185], CMOS compatible integrated photonic amplifiers operating in the third telecom window were envisaged. Nevertheless, the low excitation cross-section and a limited solubility of the RE dopant in SiO$_2$ provided an insufficient optical outcome to carry out this task. Interestingly, a sensitization method to boost the optical properties of Er^{3+} ions was published in 1994 by Kenyon *et al.* and later on corroborated by M. Fujii and co-workers [186, 187]. These works are considered by many as a turning point in the quest for an efficient integration of Er-doped light sources, as it contributed in a decisive manner to forthcoming research on the field. A continuous absorption spectrum was measured at 1.54 μm in presence of Si-ncs, and an enhanced absorption cross-section of about 4 orders of magnitude higher than the one previously obtained in Er-doped SiO$_2$ layers (i.e. ~ 10^{-17} cm^2 instead of ~ 10^{-21} cm^2). Noticeably, Si-ncs demonstrated to be efficient sensitizers not only for Er, but also for other luminescent RE ions such as Nd^{3+}, Tm^{3+} or Yb^{3+}, as reported in ref. 188. Main evidences supporting this fact were: (i) SiO$_2$ hosts containing RE ions and Si-ncs show much higher PL emission than the one observed in RE:SiO$_2$ materials free of Si-ncs; (ii) the increase of the RE concentration implies a consistent decrease of the PL emission associated to Si-ncs at 0.85 μm; (iii) the excitation wavelength dependence of RE-related luminescence is very similar to the one observed for Si-ncs in samples without RE ions, pointing out that the sharp luminescence at 1.54 μm is governed by Si-ncs in the form of an efficient energy transfer. From this point on, further insight into the physical phenomena of the Si-ncs-Er interaction was provided in forthcoming years, with several works fully devoted to the study and understanding of this system [189-193].

Later on, optical gain at 1.5 μm in Er-doped silica waveguides containing Si-ncs was reported [194]. A maximum gain value of 3 dB/cm was presented upon excitation with a commercial blue LED emitting at 470 nm in top pumping configuration. Also in 2005, high Q sol-gel lasing microresonators were fabricated on silicon substrates [195]. Quality factors of $Q \sim 2\times10^7$ at 1561 nm with a laser threshold as low as 660 nW were reported. Shortly after, the same research group demonstrated lasing action in Er-doped silica microdisk resonators fabricated on a silicon chip under 1450 nm pumping excitation. A pump threshold of 43 μW was measured, with a coupling factor of $\beta \sim 1\times10^{-3}$ [196]. Similarly, an Er-implanted silica microsphere laser with a quality factor of $Q \sim 2\times10^7$ and lasing threshold of 150-250 μW was reported in the same year [197]. As seen, several lasing devices were demonstrated by that time. However, further investigation on Er-doped thin films was required to assess the suitability of these layers to function as active parts in electrically driven electroluminescent devices, hence getting rid of the external and bulky laser source responsible for the excitation of Er^{3+} ions. Remarkable is the work done by the Electro-Photonics Lab in Barcelona, where a thorough discussion on the main limiting factors affecting Er^{3+} emission was inspected [198]. Modelling of the experimental curves was carried out by means of rate equations, obtaining a maximum fraction of excited Er of about 2% of the total Er content. An Auger-type short-range energy transfer from Si-ncs to Er^{3+} ions with a characteristic interaction distance of ~ 0.4 nm was reported. Later publications from our research group and collaborators on this issue provided additional knowledge of the role of emitting (and non-emitting) Er^{3+} ions in the optical performance of Er-doped SiO_2 thin films [199-203]. In 2009, a 20% of Er inversion was estimated in electrically pumped Er-doped SiO_2 thin films sensitized with Si-ncs [204]. This value is amongst the highest ever reported for an Er-doped Si-based light emitting device. Only recently, in a joint work with the Ion Beam Physics and Materials Research in Dresden, a higher population inversion has been reported, of about the 50% of the total Er content [205]. Notice that this percentage matches with the minimum condition required to obtain Amplified Spontaneous Emission (ASE). An ongoing investigation is being performed to embed these layers in resonant cavities for laser testing.

Apart from SiO_2 other CMOS compatible hosts have also been explored. Among them, I shall mention Si_3N_4 as one of the most promising hosts for Er^{3+} ions. In spite of having lower bandgap than SiO_2, it is still high enough to avoid Er^{3+} energy back transfer. Furthermore, charge injection in Si_3N_4 is easier than in SiO_2 as it presents a lower potential barrier height with the injecting electrode, and also a higher refractive index that makes it suitable for the fabrication of electrically pumped resonant devices. Moreover, and similarly to SiO_2, Si-ncs can be formed inside the Si_3N_4 host to enhance the Er^{3+} emission [206]. Room temperature EL emission in Er-doped SiN_x layers was demonstrated in 2010 by Yerci *et al.* [207]. An EL turn-on voltage as low as 5 V was measured, with an Er excitation cross-section at 1.54 μm of $\sigma \sim 1.2\times10^{-15}$ cm^2. In view of such promising performance, other groups investigated on the optoelectronic properties of similar layers [208, 209]. Er-doped SiN_x microdisk resonators were also demonstrated [210, 211]. Several works on these luminescent materials were also published by the Electro-Photonics group in Barcelona [212-214].

In 2011, a novel device design was proposed to accomplish efficient EL emission at 1.54 μm and light confinement at once [215]. The integrated system consisted of a Si rib waveguide coupled with a MIS device containing the Er-doped active layer. Promising optical performance was foreseen by the simulated structure, obtaining that the 75% of the light emitted from the active layer was transmitted through the rib waveguide (only the TM was supported). This work somehow reminds a previous attempt to merge the electrical and optical functions of Si-based devices containing Er-doped SiO_2 active layers published by the Cornell Nanophotonics Group [216]. Noteworthy, these works are only supported by simulations, hence lacking of an experimental data outcome from real devices. To the best of my knowledge, only the Electro-Photonics Lab in Barcelona (in collaboration with the University of Trento and the CEA Leti) has studied the optoelectronic performance of electrically pumped Er-doped Si slot waveguides based on experimental data [217-219]. Although interesting new phenomena was identified in these structures, the optoelectronic performance is still lower than expected, and a lot more work is needed in that direction.

Recently, other luminescent layers made of different materials are being explored as active elements in microphotonics. As a representative example, the well-known amplifying properties of Er-doped Al_2O_3 films have been used to build integrated lasing systems [220, 221]. Furthermore, organic light emitting materials containing optically active Er^{3+} ions are gaining importance lately [222, 223].

As seen, Er-doped thin films have garnered the attention of many research groups as potential candidates for the development of integrated light emitting devices at 1.54 μm. Nevertheless, there are other RE ions with different spectral emission lines that may be used for other applications. For instance, Nd^{3+} ions have also been used to fabricate micro-laser systems [224-226], Yb^{3+} and Ce^{3+} ions as efficient sensitizers of Er^{3+} and Tb^{3+} respectively [227, 228], or Eu-doped SiO_2 as two-colour switchable EL device [229]. At this point, it is worth to remark the pioneering work of the Institute of Ion Beam Physics in Dresden on the development of RE-doped electroluminescent MIS devices. Among others, they were the first to demonstrate EL emission from a MIS capacitor containing either Gd^{3+} ions or Tb^{3+} ions emitting at 316 nm and 550 nm, respectively [230, 231]. Also, they reported an increase of the blue EL emission in Ce-doped SiO_2 layers through sensitization by Gd^{3+} ions [232]. Nd-doped MOS devices were also explored by Rebohle *et al.* [233]. More recently, in a joint collaboration with the Electro-Photonics group in Barcelona, Tb-doped SiN_x layers were investigated, obtaining a promising optoelectronic performance [234]. In that regard, probably the most encouraging outcome reported to date is the one provided by SiO_2-Tb_2O_3-Al_2O_3 mixed layers fabricated by atomic layer deposition [235]. Intense green EL observable by the naked eye (see figure 1.4) and a power efficiency of 0.15% was obtained.

Other groups have also dedicated efforts to develop luminescent Si-based thin films by means of RE doping. For instance, the silicon photonics group at McMaster University lead by Prof. Peter Mascher has been working on Ce- and Tb-doped SiO_x and SiN_x thin films for several years [176, 236-238]. Similarly, Eu-doped SiOC thin films have been proposed by researchers in Catania and Zhejiang for white light emitting devices [239-241]. The EL emission of Yb-doped SiO_2 layers emitting at 980 nm were also studied, showing a power efficiency of 0.01% [242].

As seen, the search for efficient RE-doped Si-based light emitting devices has motivated intense research by many research groups, each one contributing to the knowledge of this exciting topic. However, there is still a lot more work to do as there are many open questions not yet solved. Thus, this dissertation aims at providing further insight into some of these issues by means of a thorough study of the electrical and optical properties of RE-doped Si-based light emitting devices for integrated photonics.

Figure 1.4. Top view of a MIS light emitting device containing an active layer of SiO_2-Tb_2O_3-Al_2O_3 in forward polarization under an injection current density of 0.16 mA/cm^2 (left), 1.6 mA/cm^2 (centre) and 16 mA/cm^2 (right). Images have been extracted from [235].

1.3. Thesis goal and outline

The aim of this dissertation is to investigate the optical and electrical properties of metal-insulator-semiconductor light emitting devices containing Si-ncs and/or RE ions. It is intended to provide a detailed and comprehensive route map towards efficient and CMOS integrated light emitting sources emitting in the visible and in the near-infrared range using RE ions. This work extends from the fundamental physics that lead to thin-film luminescence generation to the implementation of new device architectures to boost the optoelectronic features of devices. This work has been divided in two main blocks.

Block 1. This part is devoted to the study of the optoelectronic properties of Er-doped and undoped SiO_x and SiN_x thin films embedded in a MIS structure. The main points to be covered are:

- ***Charge transport in Er-doped (undoped) Si-rich oxide and nitride layers.*** Current flow in SiO_x and SiN_x layers takes place upon excitation with an external field in d. c. operation. The main transport mechanism that governs conduction and the role of Si-ncs and Er^{3+} ions in the electrical conduction of oxide layers will be studied.

- ***Identification of the main excitation mechanism for Er^{3+} ions under electrical excitation.*** The main excitation mechanisms that lead to Er^{3+} emission will be discussed, correlating the electrical properties with the EL emission.

- ***Dependence of fabrication parameters on the transport mechanisms and the EL emission.*** Optoelectronic properties of films are strongly affected by fabrication parameters. A detailed description of the influence of fabrication parameters on the overall performance of luminescence films will be provided.

- ***Number of excited Er^{3+} ions under electrical pumping.*** A first order calculation of the percentage of excited Er^{3+} will be performed.

- ***Investigation of the best Si-based host matrix to allocate Er^{3+} ions.*** Investigation on the advantages and disadvantages of different Si-based host matrices such as SiO_2, SiO_x, Si_3N_4 or SiN_x will be carried out. Optimum Si excess that balances electrical and optical functionality will be provided.

- ***Exploration of alternative device designs and layer morphologies to increase EL efficiency of Er^{3+} ions.*** Different layer architectures will be studied with the aim of providing enhanced EL emission of Er^{3+} ions at telecom wavelengths. The injector layer, the accelerator layer and the superlattice approach will be tested in Er-doped MIS devices.

- ***Development of an electrically pumped Er-doped slot waveguide: the horizontal optoelectronic approach.*** The MIS structure will be re-designed to allow for mode confinement and efficient transmission at 1.54 μm in the horizontal direction. An active all-Si optical link electrically pumped will be demonstrated.

- ***Assessing signal enhancement in Er-doped slot waveguides.*** The optoelectronic properties of active slot waveguides will be characterized by means of time-resolved electrical pump-and-probe measurements.

The work detailed in the first block has been conducted under the coverage of the European project *HELIOS* (ICT-FP7-224312) and the *ICTS access program* ICTS-NGG-235.

Further details of HELIOS project can be found elsewhere [243]. Sample fabrication was accomplished in three different technological centres:

- Laboratorie d'Électronique des Technologies de l'Information (CEA-LETI) in Grenoble, France.
- Centre de Recherche sur les Ions, les Matériaux et la Photonique (CIMAP) in Ensicaen, France.
- Integrated Nano and Microelectronics Clean Room at Instituto de Microelectrónica de Barcelona del Centro Nacional de Microelectrónica (IMB-CNM) in Barcelona, Spain.

Block 2. This second part focuses on the development of light emitting devices emitting in the visible range. Ce^{3+} and Tb^{3+} ions will be incorporated in a SiO_x (or SiO_xN_y) matrix to obtain intense blue and green emission, respectively. The fabrication process will be detailed, and also the experiments conducted to uncover the morphology and composition of thin films. Also, sample co-doping will be tackled and compared to the multilayer approach in which different single doped layers are stacked sequentially. Finally, amorphous sub-nanometre RE-doped SiO_xN_y/SiO_2 superlattices fabricated by ECR-PECVD will be demonstrated, and their main applications detailed. The major key points to study are:

- ***Identification of the best host for Ce^{3+} and Tb^{3+} ions.*** Similarly to the Er case, an optimization of the luminescence yield as a function of the host matrix will be performed.

- ***Evolution of morphology, composition and luminescence of Ce^{3+}- and Tb^{3+}-doped silicon oxides and oxynitrides as a function of fabrication parameters.*** The best fabrication parameters will be identified for each rare earth in terms of luminescence, sample density or refractive index.

- ***Multilayer approach and co-doping.*** Influence of optical properties when co-doping single layers with Ce^{3+} and Tb^{3+} ions, and its comparison with the multilayer approach in which each layer is doped with a single RE uniquely.

- ***Colour tunability***. A smart combination of Ce^{3+} and Tb^{3+} doped samples will result in a wide colour tunability.

- ***Investigation on the optoelectronic properties of Ce^{3+}- and Tb^{3+}-doped oxynitrides.*** Electroluminescence test devices will be fabricated and characterized upon electrical excitation.

- ***Sub-nanometer RE-doped superlattices.*** Development of sub-nanometre RE-doped superlattice structures to improve the overall performance of devices. An optoelectronic characterization will be carried out.

The second block is supported by the coordinated project LEOMIS (Light emitting and electro-optical integrated devices in silicon photonics CMOS technology. Towards disruptive and smart silicon solid state lighting and functional optical interconnects). Sample fabrication was accomplished in:

- Valencia Nanophotonics Technology Center (NTC) at the Polytechnic University of Valencia, in Spain.
- Centre for Emerging Device Technologies (CEDT) at McMaster University, Canada.
- Laboratory of Micro/Nanotechnologies (cleanroom facility) at the University of Barcelona, Spain.

1.4. List of references

[1] Instruments, T. (2011). "The chip that jack built." *Online: http://www. ti. com/corp/docs/kilbyctr/jackbuilt. shtml (07.07. 2009).*

[2] Moore, G. E. (1965). "Cramming more components onto integrated circuits", Electronics, Volume 38, Number 8, April 19, 1965.

[3] Hisamoto, D., Kaga, T., & Takeda, E. (1991). "Impact of the vertical SOIDELTA'structure on planar device technology." *Electron Devices, IEEE Transactions on*, *38*(6), 1419-1424.

[4] Pavesi, L., & Guillot, G. (2006). "Optical interconnects." *Springer Series in Optical Sciences*, *119*.

[5] Reed, G. T., Headley, W. R., & Png, C. J. (2005, March). "Silicon photonics: The early years." In *Integrated Optoelectronic Devices 2005* (pp. 1-18). International Society for Optics and Photonics.

[6] Soref, R. (2006). "The past, present, and future of silicon photonics." *Selected Topics in Quantum Electronics, IEEE Journal of*, *12*(6), 1678-1687.

[7] Soref, R. (2010). "Silicon photonics: a review of recent literature." *Silicon*, *2*(1), 1-6.

[8] Reed, G. T., Mashanovich, G., Gardes, F. Y., & Thomson, D. J. (2010). "Silicon optical modulators." *Nature photonics*, *4*(8), 518-526.

[9] Liang, D., & Bowers, J. E. (2010). "Recent progress in lasers on silicon." *Nature Photonics*, *4*(8), 511-517.

[10] Vahala, K. J. (2003). "Optical microcavities." *Nature*, *424*(6950), 839-846.

[11] Lim, A. J., Song, J., Fang, Q., Li, C., Tu, X., Duan, N., ... & Liow, T. Y. (2014). "Review of silicon photonics foundry efforts." *Selected Topics in Quantum Electronics, IEEE Journal of*, *20*(4), 405-416.

[12] Vivien, L., & Pavesi, L. (Eds.). (2013). *Handbook of silicon photonics*. CRC Press.

[13] Soref, R. A., & Bennett, B. R. (1987). "Electrooptical effects in silicon." *Quantum Electronics, IEEE Journal of*, *23*(1), 123-129.

[14] Soref, R. A., & Lorenzo, J. P. (1986). "All-silicon active and passive guided-wave components for lambda = 1.3 and 1.6 microns." *IEEE Journal of Quantum Electronics*, *22*, 873-879.

[15] Baba, T., Akiyama, S., Imai, M., Hirayama, N., Takahashi, H., Noguchi, Y., ... & Usuki, T. (2013). "50-Gb/s ring-resonator-based silicon modulator." *Optics express*, *21*(10), 11869-11876.

[16] Soref, R. A., Cortesi, E., Namavar, F., & Friedman, L. (1991). "Vertically integrated silicon-on-insulator waveguides." *Photonics Technology Letters, IEEE*, *3*(1), 22-24.

[17] Soref, R. A., Namavar, F., & Lorenzo, J. P. (1990). "Optical waveguiding in a single-crystal layer of germanium silicon grown on silicon." *Optics letters*, *15*(5), 270-272.

[18] Dragone, C., Edwards, C. A., & Kistler, R. C. (1991). "Integrated optics N* N multiplexer on silicon." *Photonics Technology Letters, IEEE*, *3*(10), 896-899.

[19] Treyz, G. V., May, P. G., & Halbout, J. M. (1991). "Silicon Mach–Zehnder waveguide interferometers based on the plasma dispersion effect." *Applied physics letters*, *59*(7), 771-773.

[20] Watts, R., Robinson, A. L., & Soref, R. A. (1991, October). "Electromechanical optical switching and modulation in micromachined silicon-on-insulator waveguides." In *SOI Conference, 1991. Proceedings, 1991., IEEE International*(pp. 62-63). IEEE.

[21] Soref, R. A. (1993). "Silicon-based optoelectronics." *Proceedings of the IEEE*,*81*(12), 1687-1706.

[22] Abstreiter, G. (1992). "Engineering the future of electronics." *Physics World*, *5*(3), 36-39.

[23] Ghioni, M., Lacaita, A., Ripamonti, G., & Cova, S. (1992). "All-silicon avalanche photodiode sensitive at 1.3 μm with picosecond time resolution." *Quantum Electronics, IEEE Journal of*, *28*(12), 2678-2681.

[24] Luryi, S., Pearsall, T. P., Temkin, H., & Bean, J. C. (1986). "Waveguide infrared photodetectors on a silicon chip." *Electron Device Letters, IEEE*, *7*(2), 104-107.

[25] Colace, L., Masini, G., & Assanto, G. (1999). "Ge-on-Si approaches to the detection of near-infrared light." *Quantum Electronics, IEEE Journal of*, *35*(12), 1843-1852.

[26] Vivien, L., Polzer, A., Marris-Morini, D., Osmond, J., Hartmann, J. M., Crozat, P., ... & Fédéli, J. M. (2012). "Zero-bias 40Gbit/s germanium waveguide photodetector on silicon." *Optics express*, *20*(2), 1096-1101.

[27] Lu, Z. H., Lockwood, D. J., & Baribeau, J. M. (1995). "Quantum confinement and light emission in SiO_2/Si superlattices." *Nature*, 378, 258-260.

[28] Yoshihara, M., Sekiya, A., Morita, T., Ishii, K., Shimoto, S., Sakai, S., & Ohki, Y. (1997). "Rare-earth-doped films prepared by plasma-enhanced chemical vapour deposition." *Journal of Physics D: Applied Physics*, *30*(13), 1908.

[29] Kido, J., Hayase, H., Hongawa, K., Nagai, K., & Okuyama, K. (1994). "Bright red light-emitting organic electroluminescent devices having a europium complex as an emitter." *Applied physics letters*, *65*(17), 2124-2126.

[30] Carlos, L. D., Ferreira, R. S., Bermudez, V. D. Z., Molina, C., Bueno, L. A., & Ribeiro, S. J. (1999). "White light emission of Eu^{3+}-based hybrid xerogels." *Physical Review B*, *60*(14), 10042.

[31] Kawamura, Y., Wada, Y., Hasegawa, Y., Iwamuro, M., Kitamura, T., & Yanagida, S. (1999). "Observation of neodymium electroluminescence." *Applied physics letters*, *74*(22), 3245-3247.

[32] Tsybeskov, L., Duttagupta, S. P., Hirschman, K. D., Fauchet, P. M., Moore, K. L., & Hall, D. G. (1997). "Room-temperature photoluminescence and electroluminescence from Er-doped silicon-rich silicon oxide." *Applied physics letters*, *70*(14), 1790-1792.

[33] Pavesi, L., Dal Negro, L., Mazzoleni, C., Franzo, G., & Priolo, F. (2000). "Optical gain in silicon nanocrystals." *Nature*, *408*(6811), 440-444.

[34] Dal Negro, L., Cazzanelli, M., Pavesi, L., Ossicini, S., Pacifici, D., Franzo, G., ... & Iacona, F. (2003). "Dynamics of stimulated emission in silicon nanocrystals." *Applied Physics Letters*, *82*(26), 4636-4638.

[35] Dohnalová, K., Žídek, K., Ondič, L., Kůsová, K., Cibulka, O., & Pelant, I. (2009). "Optical gain at the F-band of oxidized silicon nanocrystals." *Journal of Physics D: Applied Physics*, *42*(13), 135102.

[36] Han, H. S., Seo, S. Y., & Shin, J. H. (2001). "Optical gain at 1.54 μm in erbium-doped silicon nanocluster sensitized waveguide." *Applied physics letters*, *79*(27), 4568-4570.

[37] Kik, P. G., Brongersma, M. L., & Polman, A. (2000). "Strong exciton-erbium coupling in Si nanocrystal-doped SiO_2." *Applied Physics Letters*, *76*(17), 2325-2327.

[38] Iacona, F., Pacifici, D., Irrera, A., Miritello, M., Franzò, G., Priolo, F., ... & Fallica, P. G. (2002). "Electroluminescence at 1.54 μm in Er-doped Si nanocluster-based devices." *Applied Physics Letters*, *81*(17), 3242-3244.

[39] Priolo, F., Franzò, G., Pacifici, D., Vinciguerra, V., Iacona, F., & Irrera, A. (2001). "Role of the energy transfer in the optical properties of undoped and Er-doped interacting Si nanocrystals." *Journal of Applied Physics*, *89*(1), 264-272.

[40] Almeida, V. R., Panepucci, R. R., & Lipson, M. (2003). "Nanotaper for compact mode conversion." *Optics Letters*, *28*(15), 1302-1304.

[41] Lin, S. Y., Fleming, J. G., Hetherington, D. L., Smith, B. K., Biswas, R., Ho, K. M., ... & Bur, J. (1998). "A three-dimensional photonic crystal operating at infrared wavelengths." *Nature*, *394*(6690), 251-253.

[42] Blanco, A., Chomski, E., Grabtchak, S., Ibisate, M., John, S., Leonard, S. W., ... & van Driel, H. M. (2000). "Large-scale synthesis of a silicon photonic crystal with a complete three-dimensional bandgap near 1.5 micrometres." *Nature*, *405*(6785), 437-440.

[43] Taillaert, D., Bienstman, P., & Baets, R. (2004). "Compact efficient broadband grating coupler for silicon-on-insulator waveguides." *Optics letters*, *29*(23), 2749-2751.

[44] Akahane, Y., Asano, T., Song, B. S., & Noda, S. (2003). "High-Q photonic nanocavity in a two-dimensional photonic crystal." *Nature*, *425*(6961), 944-947.

[45] Boyraz, O., & Jalali, B. (2004). "Demonstration of a silicon Raman laser." *Optics express*, *12*(21), 5269-5273.

[46] Rong, H., Jones, R., Liu, A., Cohen, O., Hak, D., Fang, A., & Paniccia, M. (2005). "A continuous-wave Raman silicon laser." *Nature*, *433*(7027), 725-728.

[47] Xu, Q., Schmidt, B., Pradhan, S., & Lipson, M. (2005). "Micrometre-scale silicon electro-optic modulator." *Nature*, *435*(7040), 325-327.

[48] Xu, Q., Manipatruni, S., Schmidt, B., Shakya, J., & Lipson, M. (2007). "12.5 Gbit/s carrier-injection-based silicon micro-ring silicon modulators." *Optics express*, *15*(2), 430-436.

[49] Liu, A., Liao, L., Rubin, D., Nguyen, H., Ciftcioglu, B., Chetrit, Y., ... & Paniccia, M. (2007). "High-speed optical modulation based on carrier depletion in a silicon waveguide." *Optics Express*, *15*(2), 660-668.

[50] Foster, M. A., Turner, A. C., Sharping, J. E., Schmidt, B. S., Lipson, M., & Gaeta, A. L. (2006). "Broad-band optical parametric gain on a silicon photonic chip." *Nature*, *441*(7096), 960-963.

[51] Razzari, L., Duchesne, D., Ferrera, M., Morandotti, R., Chu, S., Little, B. E., & Moss, D. J. (2010). "CMOS-compatible integrated optical hyper-parametric oscillator." *Nature Photonics*, *4*(1), 41-45.

[52] Popovic, M. A., Barwicz, T., Watts, M. R., Rakich, P. T., Socci, L., Ippen, E. P., ... & Smith, H. I. (2006). "Multistage high-order microring-resonator add-drop filters." *Optics letters*, *31*(17), 2571-2573.

[53] Gunn, C. (2006). "CMOS photonics for high-speed interconnects." *Micro, IEEE,26*(2), 58-66.

[54] Fang, A. W., Park, H., Cohen, O., Jones, R., Paniccia, M. J., & Bowers, J. E. (2006). "Electrically pumped hybrid AlGaInAs-silicon evanescent laser." *Optics express*, *14*(20), 9203-9210.

[55] Van Campenhout, J., Liu, L., Romeo, P. R., Van Thourhout, D., Seassal, C., Regreny, P., ... & Baets, R. (2008). "A compact SOI-integrated multiwavelength laser source based on cascaded InP microdisks." *Photonics Technology Letters, IEEE*, *20*(16), 1345-1347.

[56] Liu, J., Sun, X., Pan, D., Wang, X., Kimerling, L. C., Koch, T. L., & Michel, J. (2007). "Tensile-strained, n-type Ge as a gain medium for monolithic laser integration on Si." *Optics Express*, *15*(18), 11272-11277.

[57] Camacho-Aguilera, R. E., Cai, Y., Patel, N., Bessette, J. T., Romagnoli, M., Kimerling, L. C., & Michel, J. (2012). "An electrically pumped germanium laser." *Optics express*, *20*(10), 11316-11320.

[58] Won, R., & Paniccia, M. (2010). "Integrating silicon photonics." *Nat. Photonics*, 4(8), 498-499.

[59] Liu, L., Ding, Y., Yvind, K., & Hvam, J. M. (2011). "Silicon-on-insulator polarization splitting and rotating device for polarization diversity circuits." *Optics express*, *19*(13), 12646-12651.

[60] Cazzanelli, M., Bianco, F., Borga, E., Pucker, G., Ghulinyan, M., Degoli, E., ... & Pavesi, L. (2012). "Second-harmonic generation in silicon waveguides strained by silicon nitride." *Nature materials*, *11*(2), 148-154.

[61] Takahashi, Y., Inui, Y., Chihara, M., Asano, T., Terawaki, R., & Noda, S. (2013). "A micrometre-scale Raman silicon laser with a microwatt threshold." *Nature*, *498*(7455), 470-474.

[62] Blanco-Redondo, A., Husko, C., Eades, D., Zhang, Y., Li, J., Krauss, T. F., & Eggleton, B. J. (2014). "Observation of soliton compression in silicon photonic crystals." *Nature communications*, *5*.

[63] Atwater, H. A., & Polman, A. (2010). "Plasmonics for improved photovoltaic devices." *Nature materials*, *9*(3), 205-213.

[64] Priolo, F., Gregorkiewicz, T., Galli, M., & Krauss, T. F. (2014). "Silicon nanostructures for photonics and photovoltaics." *Nature nanotechnology*, *9*(1), 19-32.

[65] Kippenberg, T. J., & Vahala, K. J. (2008). "Cavity optomechanics: back-action at the mesoscale." *science*, *321*(5893), 1172-1176.

[66] Gomis-Bresco, J., Navarro-Urrios, D., Oudich, M., El-Jallal, S., Griol, A., Puerto, D., ... & Torres, C. S. (2014). "A one-dimensional optomechanical crystal with a complete phononic band gap." *Nature communications*, *5*.

[67] Fakonas, J. S., Lee, H., Kelaita, Y. A., & Atwater, H. A. (2014). Two-plasmon quantum interference. *Nature Photonics*, *8*(4), 317-320.

[68] OpSIS. [Online]. Available: http://opsisfoundry.org/

[69] Yang, X., & Babakhani, A. (2013, March). "Optical Waveguides and Photodiodes in 0.18 μm CMOS SOI with No Post-processing." In *Optical Fiber Communication Conference* (pp. OTu2C-6). Optical Society of America.

[70] ePIXfab.[Online]. Available: http://www.epixfab.eu/

[71] Newman, R. (1955). "Visible Light from a Silicon p-n Junction." *Physical Review*,*100*(2), 700.

[72] Green, M. A., Zhao, J., Wang, A., Reece, P. J., & Gal, M. (2001). "Efficient silicon light-emitting diodes." *Nature*, *412*(6849), 805-808.

[73] Chynoweth, A. G., & Pearson, G. L. (1958). "Effect of Dislocations on Breakdown in Silicon p-n Junctions." *Journal of Applied Physics*, *29*(7), 1103-1110.

[74] de La Bardonnie, M., Jiang, D., Kerns, S. E., Kerns Jr, D. V., Mialhe, P., Charles, J. P., & Hoffman, A. (1999). "On the aging of avalanche light emission from silicon junctions." *Electron Devices, IEEE Transactions on*, *46*(6), 1234-1239.

[75] Richter, A., Steiner, P., Kozlowski, F., & Lang, W. (1991). "Current-induced light emission from a porous silicon device." *Electron Device Letters, IEEE*, *12*(12), 691-692.

[76] Hirschman, K. D., Tsybeskov, L., Duttagupta, S. P., & Fauchet, P. M. (1996). "Silicon-based visible light-emitting devices integrated into microelectronic circuits." *Nature*, 384, 338-341.

[77] Cullis, A. G., Canham, L. T., & Calcott, P. D. J. (1997). "The structural and luminescence properties of porous silicon." *Journal of Applied Physics*, *82*(3), 909-965.

[78] Sirringhaus, H., Tessler, N., & Friend, R. H. (1998). "Integrated optoelectronic devices based on conjugated polymers." *Science*, *280*(5370), 1741-1744.

[79] Ng, W. L., Lourenco, M. A., Gwilliam, R. M., Ledain, S., Shao, G., & Homewood, K. P. (2001). "An efficient room-temperature silicon-based light-emitting diode." *Nature*, *410*(6825), 192-194.

[80] Huang, Y., Duan, X., & Lieber, C. M. (2005). "Nanowires for integrated multicolor nanophotonics." *Small*, *1*(1), 142-147.

[81] Lockwood, D. J., Baribeau, J. M., Kamenev, B. V., Lee, E. K., & Tsybeskov, L. (2008). "Structural and optical properties of three-dimensional $Si1{-}_xGe_x/Si$ nanostructures." *Semiconductor science and technology*, *23*(6), 064003.

[82] Stoica, T., & Vescan, L. (2003). "Quantum efficiency of SiGe LEDs." *Semiconductor science and technology*, *18*(6), 409.

[83] Rebohle, L., Gebel, T., Fröb, H., Reuther, H., & Skorupa, W. (2001). "Ion beam processing for Si/C-rich thermally grown SiO_2 layers: photoluminescence and microstructure." *Applied surface science*, *184*(1), 156-160.

[84] Tetelbaum, D. I., Mikhaylov, A. N., Vasiliev, V. K., Belov, A. I., Kovalev, A. I., Wainstein, D. L., ... & Osherov, A. (2009). "Effect of carbon implantation on visible luminescence and composition of Si-implanted SiO_2 layers. "*Surface and Coatings Technology*, *203*(17), 2658-2663.

[85] Chen, D., Liao, Z. M., Wang, L., Wang, H. Z., Zhao, F., Cheung, W. Y., & Wong, S. P. (2003). "Photoluminescence from β-SiC nanocrystals embedded in SiO_2 films prepared by ion implantation." *Optical Materials*, *23*(1), 65-69.

[86] Guo, Y. P., Zheng, J. C., Wee, A. T. S., Huan, C. H. A., Li, K., Pan, J. S., ... & Chua, S. J. (2001). "Photoluminescence studies of SiC nanocrystals embedded in a SiO_2 matrix." *Chemical physics letters*, *339*(5), 319-322.

[87] Fan, J. Y., Wu, X. L., & Chu, P. K. (2006). "Low-dimensional SiC nanostructures: fabrication, luminescence, and electrical properties." *Progress in Materials Science*, *51*(8), 983-1031.

[88] Jambois, O., Vilà, A., Pellegrino, P., Carreras, J., Pérez-Rodríguez, A., Garrido, B., ... & BenAssayag, G. (2006). "Charge transport along luminescent oxide layers containing Si and SiC nanoparticles." *Journal of luminescence*, *121*(2), 356-360.

[89] Pérez-Rodrıguez, A., Gonzalez-Varona, O., Garrido, B., Pellegrino, P., Morante, J. R., Bonafos, C., ... & Claverie, A. (2003). "White luminescence from Si^+ and C^+ ion-implanted SiO_2 films." *Journal of applied physics*, *94*(1), 254-262.

[90] Jambois, O., Carreras, J., Pérez-Rodríguez, A., Garrido, B., Bonafos, C., Schamm, S., & Assayag, G. B. (2007). "Field effect white and tunable electroluminescence from ion beam synthesized Si-and C-rich SiO_2 layers." *Applied Physics Letters*, *91*(21), 211105-211105.

[91] Bellocchi, G., Franzò, G., Iacona, F., Boninelli, S., Miritello, M., Cesca, T., & Priolo, F. (2012). "Eu^{3+} reduction and efficient light emission in Eu_2O_3 films deposited on Si substrates." *Optics express*, *20*(5), 5501-5507.

[92] Hill, N. A., & Whaley, K. B. (1995). "Size dependence of excitons in silicon nanocrystals." *Physical review letters*, *75*(6), 1130.

[93] Takeoka, S., Fujii, M., & Hayashi, S. (2000). "Size-dependent photoluminescence from surface-oxidized Si nanocrystals in a weak confinement regime." *Physical Review B*, *62*(24), 16820.

[94] Sykora, M., Mangolini, L., Schaller, R. D., Kortshagen, U., Jurbergs, D., & Klimov, V. I. (2008). Size-dependent intrinsic radiative decay rates of silicon nanocrystals at large confinement energies. *Physical review letters*, *100*(6), 067401.

[95] Koponen, L., Tunturivuori, L. O., Puska, M. J., & Nieminen, R. M. (2009). "Effect of the surrounding oxide on the photoabsorption spectra of Si nanocrystals." *Physical Review B*, *79*(23), 235332.

[96] Guerra, R., Degoli, E., & Ossicini, S. (2009). "Size, oxidation, and strain in small Si/SiO_2 nanocrystals." *Physical Review B*, *80*(15), 155332.

[97] Guerra, R., & Ossicini, S. (2010). "High luminescence in small Si/SiO_2 nanocrystals: A theoretical study." *Physical Review B*, *81*(24), 245307.

[98] Valenta, J., Juhasz, R., & Linnros, J. (2002). "Photoluminescence from single silicon quantum dots at room temperature." *Journal of luminescence*, *98*(1), 15-22.

[99] Barbagiovanni, E. G., Lockwood, D. J., Simpson, P. J., & Goncharova, L. V. (2014). "Quantum confinement in Si and Ge nanostructures: Theory and experiment." *Applied Physics Reviews*, *1*(1), 011302.

[100] Mangolini, L. (2013). "Synthesis, properties, and applications of silicon nanocrystals." *Journal of Vacuum Science & Technology B*, *31*(2), 020801.

[101] Ray, S. K., Maikap, S., Banerjee, W., & Das, S. (2013). "Nanocrystals for silicon-based light-emitting and memory devices." *Journal of Physics D: Applied Physics*, *46*(15), 153001.

[102] Rodríguez, J. A., Vásquez-Agustín, M. A., Morales-Sánchez, A., & Aceves-Mijares, M. (2014). "Emission Mechanisms of Si Nanocrystals and Defects in SiO_2 Materials." *Journal of Nanomaterials, 2014*.

[103] Khriachtchev, L., Ossicini, S., Iacona, F., & Gourbilleau, F. (2012). "Silicon Nanoscale Materials: From Theoretical Simulations to Photonic Applications." *International Journal of Photoenergy, 2012*.

[104] Priolo, F., Gregorkiewicz, T., Galli, M., & Krauss, T. F. (2014). "Silicon nanostructures for photonics and photovoltaics." *Nature nanotechnology*, *9*(1), 19-32.

[105] Iacona, F., Franzò, G., & Spinella, C. (2000). Correlation between luminescence and structural properties of Si nanocrystals. *Journal of Applied Physics*, *87*(3), 1295-1303.

[106] Fleetwood, D. M. (2002). "Effects of hydrogen transport and reactions on microelectronics radiation response and reliability." *Microelectronics Reliability*, *42*(4), 523-541.

[107] Donahue, T. J., & Reif, R. (1985). "Silicon epitaxy at 650–800° C using low-pressure chemical vapor deposition both with and without plasma enhancement." *Journal of applied physics*, *57*(8), 2757-2765.

[108] Charvet, S., Madelon, R., Gourbilleau, F., & Rizk, R. (1999). "Spectroscopic ellipsometry analyses of sputtered Si/SiO_2 nanostructures." *Journal of applied physics*, *85*(8), 4032-4039.

[109] Kanemitsu, Y., Shimizu, N., Komoda, T., Hemment, P. L., & Sealy, B. J. (1996). "Photoluminescent spectrum and dynamics of Si+-ion-implanted and thermally annealed SiO_2 glasses." *Physical Review B*, *54*(20), R14329.

[110] http://srim.org

[111] Arthur, J. R. (2002). "Molecular beam epitaxy." *Surface science*, *500*(1), 189-217.

[112] Movtchan, I. A., Dreyfus, R. W., Marine, W., Sentis, M., Autric, M., Le Lay, G., & Merk, N. (1995). "Luminescence from a Si-SiO_2 nanocluster-like structure prepared by laser ablation." *Thin Solid Films*, *255*(1), 286-289.

[113] De Sande, J. C. G., Afonso, C. N., Escudero, J. L., Serna, R., Catalina, F., & Bernabeu, E. (1992). "Optical properties of laser-deposited a-Ge films: a comparison with sputtered and e-beam-deposited films." *Applied optics*, *31*(28), 6133-6138.

[114] Ballesteros, J. M., Serna, R., Afonso, C. N., Petford-Long, A. K., Osborne, D. H., & Haglund, R. F. (1997). "Pulsed laser deposition of Cu: Al 2 O 3 nanocrystal thin films with high third-order optical susceptibility." *Applied physics letters*, *71*(17), 2445-2447.

[115] Barnes, J. P., Petford-Long, A. K., Doole, R. C., Serna, R., Gonzalo, J., Suarez-Garcia, A., ... & Hole, D. (2002). "Structural studies of Ag nanocrystals embedded in amorphous Al_2O_3 grown by pulsed laser deposition." *Nanotechnology*, *13*(4), 465.

[116] Serna, R., de Castro, M. J., Chaos, J. A., Afonso, C. N., & Vickridge, I. (1999). "The role of Er^{3+}–Er^{3+} separation on the luminescence of Er–doped Al_2O_3 films prepared by pulsed laser deposition." *Applied Physics Letters*, *75*(26), 4073-4075.

[117] Camps, I., Ramírez, J. M., Mariscal, A., Serna, R., Garrido, B., Perálvarez, M., ... & Alves, E. (2014). "Optical performance of thin films produced by the pulsed laser deposition of SiAlON and Er targets." *Applied Surface Science*.

[118] Rinnert, H., Jambois, O., & Vergnat, M. (2009). "Photoluminescence properties of size-controlled silicon nanocrystals at low temperatures." *Journal of Applied Physics*, *106*(2), 023501.

[119] Canham, L. T. (1990). "Silicon quantum wire array fabrication by electrochemical and chemical dissolution of wafers." *Applied Physics Letters*, *57*(10), 1046-1048.

[120] DiMaria, D. J., & Dong, D. W. (1980). "High current injection into SiO_2 from Si rich SiO_2 films and experimental applications." *Journal of applied physics*, *51*(5), 2722-2735.

[121] DiMaria, D. J., Kirtley, J. R., Pakulis, E. J., Dong, D. W., Kuan, T. S., Pesavento, F. L., ... & Brorson, S. D. (1984). "Electroluminescence studies in silicon dioxide films containing tiny silicon islands." *Journal of Applied Physics*,*56*(2), 401-416.

[122] Takagi, H., Ogawa, H., Yamazaki, Y., Ishizaki, A., & Nakagiri, T. (1990). "Quantum size effects on photoluminescence in ultrafine Si particles." *Applied Physics Letters*, *56*(24), 2379-2380.

[123] "Wilson, W. L., Szajowski, P. F., & Brus, L. E. (1993). "Quantum confinement in size-selected, surface-oxidized silicon nanocrystals." *SCIENCE-NEW YORK THEN WASHINGTON-*, *262*, 1242-1242.

[124] Hayashi, S., Nagareda, T., Kanzawa, Y., & Yamamoto, K. (1993). "Photoluminescence of Si-rich SiO_2 films: Si clusters as luminescent centers." *Japanese journal of applied physics*, *32*(9R), 3840.

[125] Werwa, E., Seraphin, A. A., Chiu, L. A., Zhou, C., & Kolenbrander, K. D. (1994). "Synthesis and processing of silicon nanocrystallites using a pulsed laser ablation supersonic expansion method." *Applied physics letters*, *64*(14), 1821-1823.

[126] Tiwari, S., Rana, F., Hanafi, H., Hartstein, A., Crabbe, E. F., & Chan, K. (1996). "A silicon nanocrystals based memory." *Applied Physics Letters*, *68*(10), 1377-1379.

[127] Gerardi, C., Molas, G., Albini, G., Tripiciano, E., Gely, M., Emmi, A., ... & Maurelli, A. (2008, December). "Performance and reliability of a 4Mb Si nanocrystal NOR Flash memory with optimized 1T memory cells." In *Electron Devices Meeting, 2008. IEDM 2008. IEEE International* (pp. 1-4). IEEE.

[128] Chen, H. B., Wu, Y. C., Chen, L. C., Chiang, J. H., Yang, C. K., & Chang, C. Y. (2012). "High-reliability trigate poly-Si channel flash memory cell with Si-nanocrystal embedded charge-trapping layer." *Electron Device Letters, IEEE*,*33*(4), 537-539.

[129] Gay, G., Molas, G., Bocquet, M., Jalaguier, E., Gely, M., Masarotto, L., ... & De Salvo, B. (2012). "Performance and Modeling of Si-Nanocrystal Double-Layer Memory Devices With High-Control Dielectrics." *Electron Devices, IEEE Transactions on*, *59*(4), 933-940.

[130] Wang, M., Huang, X., Xu, J., Li, W., Liu, Z., & Chen, K. (1998). "Observation of the size-dependent blueshifted electroluminescence from nanocrystalline Si

fabricated by KrF excimer laser annealing of hydrogenated amorphous silicon/amorphous-SiN_x: H superlattices." *Applied physics letters*, *72*(6), 722-724.

[131] Wolkin, M. V., Jorne, J., Fauchet, P. M., Allan, G., & Delerue, C. (1999). "Electronic states and luminescence in porous silicon quantum dots: the role of oxygen." *Physical Review Letters*, *82*(1), 197.

[132] Khriachtchev, L., Rasanen, M., Novikov, S., & Sinkkonen, J. (2001). "Optical gain in Si/SiO 2 lattice: experimental evidence with nanosecond pulses." *Applied Physics Letters*, *79*(9), 1249-1251.

[133] Ruan, J., Fauchet, P. M., Dal Negro, L., Cazzanelli, M., & Pavesi, L. (2003). "Stimulated emission in nanocrystalline silicon superlattices." *Applied Physics Letters*, *83*(26), 5479-5481.

[134] Dal Negro, L., Cazzanelli, M., Daldosso, N., Gaburro, Z., Pavesi, L., Priolo, F., ... & Iacona, F. (2003). "Stimulated emission in plasma-enhanced chemical vapour deposited silicon nanocrystals." *Physica E: Low-dimensional Systems and Nanostructures*, *16*(3), 297-308.

[135] Dal Negro, L., Cazzanelli, M., Danese, B., Pavesi, L., Iacona, F., Franzo, G., & Priolo, F. (2004). "Light amplification in silicon nanocrystals by pump and probe transmission measurements." *Journal of applied physics*, *96*(10), 5747-5755.

[136] Irrera, A., Pacifici, D., Miritello, M., Franzo, G., Priolo, F., Iacona, F., ... & Fallica, P. G. (2002). "Excitation and de-excitation properties of silicon quantum dots under electrical pumping." *Applied physics letters*, *81*(10), 1866-1868.

[137] Franzo, G., Irrera, A., Moreira, E. C., Miritello, M., Iacona, F., Sanfilippo, D., ... & Priolo, F. (2002). "Electroluminescence of silicon nanocrystals in MOS structures." *Applied Physics A*, *74*(1), 1-5.

[138] Park, N. M., Choi, C. J., Seong, T. Y., & Park, S. J. (2001). "Quantum confinement in amorphous silicon quantum dots embedded in silicon nitride." *Physical Review Letters*, *86*(7), 1355.

[139] Lu, Z. H., Lockwood, D. J., & Baribeau, J. M. (1996). "Visible light emitting $SiSiO_2$ superlattices." *Solid-State Electronics*, *40*(1), 197-201.

[140] Kim, T. W., Cho, C. H., Kim, B. H., & Park, S. J. (2006). "Quantum confinement effect in crystalline silicon quantum dots in silicon nitride grown using SiH_4 and NH_3." *Applied Physics Letters*, *88*(12), 123102-123102.

[141] Chen, L. Y., Chen, W. H., & Hong, F. C. N. (2005). "Visible electroluminescence from silicon nanocrystals embedded in amorphous silicon nitride matrix." *Applied Physics Letters*, *86*(19), 193506-193506.

[142] Dal Negro, L., Yi, J. H., Michel, J., Kimerling, L. C., Chang, T. W., Sukhovatkin, V., & Sargent, E. H. (2006). "Light emission efficiency and dynamics in silicon-rich silicon nitride films." *Applied physics letters*, *88*(23), 233109.

[143] Hiller, D., Zelenina, A., Gutsch, S., Dyakov, S. A., López-Conesa, L., López-Vidrier, J., ... & Zacharias, M. (2014). "Absence of quantum confinement effects

in the photoluminescence of Si_3N_4–embedded Si nanocrystals." *Journal of Applied Physics*, *115*(20), 204301.

[144] Zacharias, M., Heitmann, J., Scholz, R., Kahler, U., Schmidt, M., & Bläsing, J. (2002). "Size-controlled highly luminescent silicon nanocrystals: A SiO/SiO_2 superlattice approach." *Applied Physics Letters*, *80*(4), 661-663.

[145] Heitmann, J., Müller, F., Zacharias, M., & Gösele, U. (2005). "Silicon nanocrystals: size matters." *Advanced Materials*, *17*(7), 795-803.

[146] Marconi, A., Anopchenko, A., Wang, M., Pucker, G., Bellutti, P., & Pavesi, L. (2009). "High power efficiency in Si-nc/SiO_2 multilayer light emitting devices by bipolar direct tunneling." *Applied Physics Letters*, *94*(22), 221110.

[147] Walters, R. J., Bourianoff, G. I., & Atwater, H. A. (2005). "Field-effect electroluminescence in silicon nanocrystals." *Nature materials*, *4*(2), 143-146.

[148] Presti, C. D., Irrera, A., Franzò, G., Crupi, I., Priolo, F., Iacona, F., ... & Fallica, P. G. (2006). "Photonic-crystal silicon-nanocluster light-emitting device." *Applied physics letters*, *88*(3), 033501.

[149] Creazzo, T., Redding, B., Marchena, E., Hao, R., Murakowski, J., Shi, S., & Prather, D. W. (2010). "Distributed Bragg reflector enhancement of electroluminescence from a silicon nanocrystal light emitting device." *Thin Solid Films*, *518*(15), 4394-4398.

[150] Conibeer, G., Green, M., Cho, E. C., König, D., Cho, Y. H., Fangsuwannarak, T., ... & Mansfield, D. (2008). "Silicon quantum dot nanostructures for tandem photovoltaic cells." *Thin Solid Films*, *516*(20), 6748-6756.

[151] Timmerman, D., Izeddin, I., Stallinga, P., Yassievich, I. N., & Gregorkiewicz, T. (2008). "Space-separated quantum cutting with silicon nanocrystals for photovoltaic applications." *Nature Photonics*, *2*(2), 105-109.

[152] Yuan, Z., Pucker, G., Marconi, A., Sgrignuoli, F., Anopchenko, A., Jestin, Y., ... & Pavesi, L. (2011). "Silicon nanocrystals as a photoluminescence down shifter for solar cells." *Solar Energy Materials and solar cells*, *95*(4), 1224-1227.

[153] Govoni, M., Marri, I., & Ossicini, S. (2012). Carrier multiplication between interacting nanocrystals for fostering silicon-based photovoltaics. *Nature Photonics*, *6*(10), 672-679.

[154] Janz, S., Löper, P., Schnabel, M., Zacharias, M., Hiller, D., Gutsch, S., ... & Canino, M. (2011). "The Nascent Project." In *Proceedings of the 26th European Photovoltaic Solar Energy Conference* (pp. 22-27).

[155] Janz, S., Löper, P., & Schnabel, M. (2013). "Silicon nanocrystals produced by solid phase crystallisation of superlattices for photovoltaic applications." *Materials Science and Engineering: B*, *178*(9), 542-550.

[156] Löper, P., Stüwe, D., Künle, M., Bivour, M., Reichel, C., Neubauer, R., ... & Glunz, S. W. (2012). "A Membrane Device for Substrate-Free Photovoltaic Characterization of Quantum Dot Based p-i-n Solar Cells." *Advanced materials*,*24*(23), 3124-3129.

[157] Löper, P., Canino, M., Qazzazie, D., Schnabel, M., Allegrezza, M., Summonte, C., ... & Zacharias, M. (2013). "Silicon nanocrystals embedded in silicon carbide: investigation of charge carrier transport and recombination." *Applied Physics Letters*, *102*(3), 033507.

[158] Fujioka, K., Hiruoka, M., Sato, K., Manabe, N., Miyasaka, R., Hanada, S., ... & Yamamoto, K. (2008). "Luminescent passive-oxidized silicon quantum dots as biological staining labels and their cytotoxicity effects at high concentration." *Nanotechnology*, *19*(41), 415102.

[159] Stan, M. S., Memet, I., Sima, C., Popescu, T., Teodorescu, V. S., Hermenean, A., & Dinischiotu, A. (2014). "Si/SiO$_2$ quantum dots cause cytotoxicity in lung cells through redox homeostasis imbalance." *Chemico-biological interactions*,*220*, 102-115.

[160] Shubenkov, A. N., Korovin, S. B., Andreeva, E. R., Buravkova, L. B., & Pustovoy, V. I. (2014). "In vitro evaluation of crystalline silicon nanoparticles cytotoxicity." *Biophysics*, *59*(1), 105-109.

[161] Martínez, A., Blasco, J., Sanchis, P., Galán, J. V., García-Rupérez, J., Jordana, E., ... & Martí, J. (2010). "Ultrafast all-optical switching in a silicon-nanocrystal-based silicon slot waveguide at telecom wavelengths." *Nano letters*,*10*(4), 1506-1511.

[162] De Boer, W. D. A. M., Timmerman, D., Dohnalova, K., Yassievich, I. N., Zhang, H., Buma, W. J., & Gregorkiewicz, T. (2010). "Red spectral shift and enhanced quantum efficiency in phonon-free photoluminescence from silicon nanocrystals." *Nature nanotechnology*, *5*(12), 878-884.

[163] Timmerman, D., Valenta, J., Dohnalová, K., De Boer, W. D. A. M., & Gregorkiewicz, T. (2011). "Step-like enhancement of luminescence quantum yield of silicon nanocrystals." *Nature nanotechnology*, *6*(11), 710-713.

[164] Sirleto, L., Ferrara, M. A., Nikitin, T., Novikov, S., & Khriachtchev, L. (2012). "Giant Raman gain in silicon nanocrystals." *Nature communications*, *3*, 1220.

[165] Maier-Flaig, F., Rinck, J., Stephan, M., Bocksrocker, T., Bruns, M., Kübel, C., ... & Lemmer, U. (2013). "Multicolor silicon light-emitting diodes (SiLEDs)." *Nano letters*, *13*(2), 475-480.

[166] Maier-Flaig, F., Kübel, C., Rinck, J., Bocksrocker, T., Scherer, T., Prang, R., ... & Lemmer, U. (2013). "Looking Inside a Working SiLED." *Nano letters*, *13*(8), 3539-3545.

[167] Mehonic, A., Cueff, S., Wojdak, M., Hudziak, S., Labbé, C., Rizk, R., & Kenyon, A. J. (2012). "Electrically tailored resistance switching in silicon oxide." *Nanotechnology*, *23*(45), 455201.

[168] Mehonic, A., Vrajitoarea, A., Cueff, S., Hudziak, S., Howe, H., Labbé, C., ... & Kenyon, A. J. (2013). "Quantum conductance in silicon oxide resistive memory devices." *Scientific reports*, *3*.

[169] Xia, Z., & Liu, R. S. (2012). "Tunable blue-green color emission and energy transfer of Ca2Al3O6F: Ce^{3+}, Tb^{3+} phosphors for near-UV white LEDs." *The Journal of Physical Chemistry C, 116*(29), 15604-15609.

[170] Xie, R. J., & Hirosaki, N. (2007). "Silicon-based oxynitride and nitride phosphors for white LEDs—A review." Science and Technology of Advanced Materials, 8(7), 588-600.

[171] L. Rebohle, W. Skorupa, *Rare-Earth Implanted MOS Devices for Silicon Photonics*, (Springer Series Materials Science, Germany, 2010).

[172] Garrido, B., García, C., Seo, S. Y., Pellegrino, P., Navarro-Urrios, D., Daldosso, N., ... & Rizk, R. (2007). "Excitable Er fraction and quenching phenomena in Er-doped Si O 2 layers containing Si nanoclusters." *Physical Review B, 76*(24), 245308.

[173] Serna, R., Ballesteros, J. M., de Castro, M. J., Solis, J., & Afonso, C. N. (1998). "Optically active Er–Yb doped glass films prepared by pulsed laser deposition." *Journal of applied physics, 84*(4), 2352-2354.

[174] Steveler, E., Rinnert, H., & Vergnat, M. (2014). "Photoluminescence properties of Nd-doped silicon oxide thin films containing silicon nanoparticles." *Journal of Luminescence, 150*, 35-39.

[175] Yu, M., Lin, J., Fu, J., Zhang, H. J., & Han, Y. C. (2003). "Sol–gel synthesis and photoluminescent properties of LaPO 4: A (A= Eu^{3+}, Ce^{3+}, Tb^{3+}) nanocrystalline thin films." *Journal of Materials Chemistry, 13*(6), 1413-1419.

[176] Wilson, P. R. (2013). *Study of Luminescent Silicon-Rich Silicon Nitride and Cerium and Terbium Doped Silicon Oxide Thin Films.*

[177] Kenyon, A. J. (2005). "Erbium in silicon." *Semiconductor Science and Technology, 20*(12), R65.

[178] Lockwood, D. J., & Pavesi, L. (2004). *Silicon photonics*. Berlin: Springer.

[179] Bünzli, J. C. G., & Eliseeva, S. V. (2010). "Lanthanide NIR luminescence for telecommunications, bioanalyses and solar energy conversion." *Journal of Rare Earths, 28*(6), 824-842.

[180] Polman, A. (1997). "Erbium implanted thin film photonic materials." *Journal of Applied Physics, 82*(1), 1-39.

[181] Polman, A., & van Veggel, F. C. (2004). "Broadband sensitizers for erbium-doped planar optical amplifiers: review." *JOSA B, 21*(5), 871-892.

[182] Ennen, H., Pomrenke, G., Axmann, A., Eisele, K., Haydl, W., & Schneider, J. (1985). "1.54-μm electroluminescence of erbium-doped silicon grown by molecular beam epitaxy." *Applied Physics Letters, 46*(4), 381-383.

[183] Zheng, B., Michel, J., Ren, F. Y. G., Kimerling, L. C., Jacobson, D. C., & Poate, J. M. (1994). "Room-temperature sharp line electroluminescence at λ= 1.54 μm from an erbium-doped, silicon light-emitting diode." *Applied physics letters, 64*(21), 2842-2844.

[184] Palm, J., Gan, F., Zheng, B., Michel, J., & Kimerling, L. C. (1996). "Electroluminescence of erbium-doped silicon." *Physical Review B, 54*(24), 17603.

[185] Desurvire, E. (2002). *Erbium-doped fiber amplifiers: principles and applications*. Wiley-Interscience.

[186] Kenyon, A. J., Trwoga, P. F., Federighi, M., & Pitt, C. W. (1994). "Optical properties of PECVD erbium-doped silicon-rich silica: evidence for energy transfer between silicon microclusters and erbium ions." *Journal of Physics: Condensed Matter*, *6*(21), L319.

[187] Fujii, M., Yoshida, M., Kanzawa, Y., Hayashi, S., & Yamamoto, K. (1997). "1.54 μm photoluminescence of Er^{3+} doped into SiO_2 films containing Si nanocrystals: evidence for energy transfer from Si nanocrystals to Er^{3+}." *Applied Physics Letters, 71*(9), 1198-1200.

[188] Franzo, G., Vinciguerra, V., & Priolo, F. (1999). "The excitation mechanism of rare-earth ions in silicon nanocrystals." *Applied Physics A, 69*(1), 3-12.

[189] Pacifici, D., Franzo, G., Priolo, F., Iacona, F., & Dal Negro, L. (2003). "Modeling and perspectives of the Si nanocrystals–Er interaction for optical amplification." *Physical Review B, 67*(24), 245301.

[190] Wojdak, M., Klik, M., Forcales, M., Gusev, O. B., Gregorkiewicz, T., Pacifici, D., ... & Iacona, F. (2004). "Sensitization of Er luminescence by Si nanoclusters." *Physical Review B, 69*(23), 233315.

[191] Izeddin, I., Moskalenko, A. S., Yassievich, I. N., Fujii, M., & Gregorkiewicz, T. (2006). "Nanosecond dynamics of the near-infrared photoluminescence of Er-doped SiO_2 sensitized with Si nanocrystals." *Physical review letters, 97*(20), 207401.

[192] Kenyon, A. J., Chryssou, C. E., Pitt, C. W., Shimizu-Iwayama, T., Hole, D. E., Sharma, N., & Humphreys, C. J. (2002). "Luminescence from erbium-doped silicon nanocrystals in silica: Excitation mechanisms." *Journal of Applied Physics, 91*(1), 367-374.

[193] Polman, A. (2002). "Photonic materials: Teaching silicon new tricks." *Nature Materials, 1*(1), 10-12.

[194] Lee, J., Shin, J. H., & Park, N. (2005). "Optical gain at 1.5 μm in nanocrystal Si-sensitized Er-doped silica waveguide using top-pumping 470 nm LEDs." *Journal of lightwave technology, 23*(1), 19.

[195] Yang, L., Carmon, T., Min, B., Spillane, S. M., & Vahala, K. J. (2005). "Erbium-doped and Raman microlasers on a silicon chip fabricated by the sol–gel process." *Applied Physics Letters, 86*(9), 091114-091114.

[196] Kippenberg, T. J., Kalkman, J., Polman, A., & Vahala, K. J. (2006). "Demonstration of an erbium-doped microdisk laser on a silicon chip." *Physical Review A, 74*(5), 051802.

[197] Kalkman, J., Polman, A., Kippenberg, T. J., Vahala, K. J., & Brongersma, M. L. (2006). "Erbium-implanted silica microsphere laser." *Nuclear Instruments and*

Methods in Physics Research Section B: Beam Interactions with Materials and Atoms, *242*(1), 182-185.

[198] Garrido, B., García, C., Seo, S. Y., Pellegrino, P., Navarro-Urrios, D., Daldosso, N., ... & Rizk, R. (2007). "Excitable Er fraction and quenching phenomena in Er-doped Si O_2 layers containing Si nanoclusters." *Physical Review B, 76*(24), 245308.

[199] Navarro-Urrios, D., Pitanti, A., Daldosso, N., Gourbilleau, F., Rizk, R., Garrido, B., & Pavesi, L. (2009). "Energy transfer between amorphous Si nanoclusters and Er^{3+} ions in a SiO_2 matrix." *Physical Review B, 79*(19), 193312.

[200] Hijazi, K., Rizk, R., Cardin, J., Khomenkova, L., & Gourbilleau, F. (2009). "Towards an optimum coupling between Er ions and Si-based sensitizers for integrated active photonics." *Journal of Applied Physics, 106*(2), 024311.

[201] Yuan, Z., Anopchenko, A., Daldosso, N., Guider, R., Navarro-Urrios, D., Pitanti, A., ... & Pavesi, L. (2009). "Silicon nanocrystals as an enabling material for silicon photonics." *Proceedings of the IEEE, 97*(7), 1250-1268.

[202] Prtljaga, N., Navarro-Urrios, D., Tengattini, A., Anopchenko, A., Ramírez, J. M., Rebled, J. M., ... & Pavesi, L. (2012). "Limit to the erbium ions emission in silicon-rich oxide films by erbium ion clustering." *Optical Materials Express, 2*(9), 1278-1285.

[203] Navarro-Urrios, D., Lupi, F. F., Prtljaga, N., Pitanti, A., Jambois, O., Ramírez, J. M., ... & Pavesi, L. (2011). "Copropagating pump and probe experiments on Si-nc in SiO2 rib waveguides doped with Er: The optical role of non-emitting ions." *Applied Physics Letters, 99*(23), 231114.

[204] Jambois, O., Gourbilleau, F., Kenyon, A. J., Montserrat, J., Rizk, R., & Garrido, B. (2010). "Towards population inversion of electrically pumped Er ions sensitized by Si nanoclusters." *Optics express, 18*(3), 2230-2235.

[205] Rebohle, L., Berencén, Y., Wutzler, R., Braun, M., Hiller, D., Ramírez, J. M., ... & Skorupa, W. (2014). "The electroluminescence mechanism of Er^{3+} in different silicon oxide and silicon nitride environments." *Journal of Applied Physics,116*(12), 123104.

[206] Dal Negro, L., Li, R., Warga, J., & Basu, S. N. (2008). "Sensitized erbium emission from silicon-rich nitride/silicon superlattice structures." *Applied Physics Letters, 92*(18), 181105.

[207] Yerci, S., Li, R., & Dal Negro, L. (2010). "Electroluminescence from Er-doped Si-rich silicon nitride light emitting diodes." *Applied Physics Letters, 97*(8), 081109.

[208] Xu, L., Jin, L., Li, D., & Yang, D. (2013). "Effects of excess silicon on the 1540 nm Er^{3+} luminescence in silicon rich oxynitride films." *Applied Physics Letters,103*(7), 071101.

[209] Yin, Y., Xu, W., Ran, G., Qin, G., & Zhang, B. (2011). "Er^{3+} infrared photo-and electro-luminescence from Er-doped Si-rich silicon nitride films with varying Si and Er contents." *Functional Materials Letters, 4*(03), 255-259.

[210] Chang, J. S., Eom, S. C., Sung, G. Y., & Shin, J. H. (2009). "On-chip, planar integration of Er doped silicon-rich silicon nitride microdisk with SU-8 waveguide with sub-micron gap control." *Optics express, 17*(25), 22918-22924.

[211] Hryciw, A. C., Kekatpure, R. D., Yerci, S., Dal Negro, L., & Brongersma, M. L. (2011). "Thermo-optic tuning of erbium-doped amorphous silicon nitride microdisk resonators." *Applied Physics Letters, 98*(4), 041102.

[212] Ramírez, J. M., Cueff, S., Berencén, Y., Labbé, C., & Garrido, B. (2014). "Role of silicon excess in Er-doped silicon-rich nitride light emitting devices at 1.54 µm." *Journal of Applied Physics, 116*(8), 083103.

[213] Cueff, S., Ramírez, J. M., Kurvits, J. A., Berencén, Y., Zia, R., Garrido, B., ... & Labbé, C. (2013). "Electroluminescence efficiencies of erbium in silicon-based hosts." *Applied Physics Letters, 103*(19), 191109.

[214] Berencén, Y., Ramírez, J. M., & Garrido, B. (2013, February). "Er-doped Si-based electroluminescent capacitors: Role of different host matrices on the electrical and luminescence properties." *In Electron Devices (CDE), 2013 Spanish Conference on* (pp. 245-248). IEEE.

[215] Jayatilleka, H., Nasrollahy-Shiraz, A., & Kenyon, A. J. (2011). "Electrically pumped silicon waveguide light sources." *Optics express, 19*(24), 24569-24576.

[216] Barrios, C. A., & Lipson, M. (2005). "Electrically driven silicon resonant light emitting device based on slot-waveguide." *Optics express, 13*(25), 10092-10101.

[217] Ramírez, J. M., Lupi, F. F., Berencén, Y., Anopchenko, A., Colonna, J. P., Jambois, O., ... & Garrido, B. (2013). "Er-doped light emitting slot waveguides monolithically integrated in a silicon photonic chip." *Nanotechnology, 24*(11), 115202.

[218] Ramírez, J. M., Berencén, Y., Lupi, F. F., Navarro-Urrios, D., Anopchenko, A., Tengattini, A., ... & Garrido, B. (2012). "Electrical pump & probe and injected carrier losses quantification in Er doped Si slot waveguides." *Optics express,20*(27), 28808-28818.

[219] Tengattini, A., Gandolfi, D., Prtljaga, N., Anopchenko, A., Ramírez, J. M., Lupi, F. F., ... & Pavesi, L. (2013). "Toward a 1.54 µm Electrically Driven Erbium-Doped Silicon Slot Waveguide and Optical Amplifier." *Lightwave Technology, Journal of, 31*(3), 391-397.

[220] Sun, J., Adam, T. N., Leake, G., Coolbaugh, D., Bradley, J. D., Hosseini, E. S., & Watts, M. R. (2013). "C-and L-band erbium-doped waveguide lasers with wafer-scale silicon nitride cavities." *Optics letters, 38*(11), 1760-1762.

[221] Bradley, J. D., & Pollnau, M. (2011). "Erbium-doped integrated waveguide amplifiers and lasers." *Laser & Photonics Reviews, 5*(3), 368-403.

[222] Ye, H. Q., Li, Z., Peng, Y., Wang, C. C., Li, T. Y., Zheng, Y. X., ... & Gillin, W. P. (2014). "Organo-erbium systems for optical amplification at telecommunications wavelengths." *Nature materials, 13*(4), 382-386.

[223] Martín-Ramos, P., Silva, M. R., Lahoz, F., Martín, I. R., Chamorro-Posada, P., Eusebio, M. E. S., ... & Martín-Gil, J. (2014). "Highly fluorinated erbium (III) complexes for emission in the C-band." *Journal of Photochemistry and Photobiology A: Chemistry,* 292, 16-25.

[224] Kitagawa, T., Hattori, K., Hibino, Y., & Ohmori, Y. (1994). "Neodymium-doped silica-based planar waveguide lasers." *Lightwave Technology, Journal of, 12*(3), 436-442.

[225] Lefèvre-Seguin, V. (1999). "Whispering-gallery mode lasers with doped silica microspheres." *Optical Materials, 11*(2), 153-165.

[226] Mwarania, E. K., Reekie, L., Wang, J., & Wilkinson, J. S. (1990). "Low-threshold monomode ion-exchanged waveguide lasers in neodymium-doped BK-7 glass." *Electronics Letters, 26*(16), 1317-1318.

[227] Hehlen, M. P., Cockroft, N. J., Gosnell, T. R., & Bruce, A. J. (1997). "Spectroscopic properties of Er^{3+}-and Yb^{3+}-doped soda-lime silicate and aluminosilicate glasses." *Physical Review B, 56*(15), 9302.

[228] Jia, D., Wang, X. J., Jia, W., & Yen, W. M. (2003). "Persistent energy transfer in $CaAl_2O_4$: Tb^{3+}, Ce^{3+}." *Journal of applied physics, 93*(1), 148-152.

[229] Prucnal, S., Sun, J. M., Skorupa, W., & Helm, M. (2007). "Switchable two-color electroluminescence based on a Si metal-oxide-semiconductor structure doped with Eu." *Applied physics letters, 90*(18), 181121-181121.

[230] Sun, J. M., Skorupa, W., Dekorsy, T., Helm, M., Rebohle, L., & Gebel, T. (2004). "Efficient ultraviolet electroluminescence from a Gd-implanted silicon metal–oxide–semiconductor device." *Applied physics letters, 85*(16), 3387-3389.

[231] Sun, J. M., Skorupa, W., Dekorsy, T., Helm, M., Rebohle, L., & Gebel, T. (2005). "Bright green electroluminescence from Tb^{3+} in silicon metal-oxide-semiconductor devices." *Journal of applied physics, 97*(12), 123513-123513.

[232] Sun, J. M., Prucnal, S., Skorupa, W., Helm, M., Rebohle, L., & Gebel, T. (2006). "Increase of blue electroluminescence from Ce-doped SiO_2 layers through sensitization by Gd^{3+} ions." *Applied physics letters, 89*(9), 091908-091908.

[233] Rebohle, L., Wutzler, R., Germer, S., Lehmann, J., Helm, M., & Skorupa, W. (2012, June). "Er-and Nd-implanted MOS light emitting devices and their use for integrated photonic applications." *In SPIE Photonics Europe* (pp. 843116-843116). International Society for Optics and Photonics.

[234] Berencén, Y., Wutzler, R., Rebohle, L., Hiller, D., Ramírez, J. M., Rodríguez, J. A., ... & Garrido, B. (2013). "Intense green-yellow electroluminescence from Tb^{+}-implanted silicon-rich silicon nitride/oxide light emitting devices." *Applied Physics Letters, 103*(11), 111102.

[235] Rebohle, L., Braun, M., Wutzler, R., Liu, B., Sun, J. M., Helm, M., & Skorupa, W. (2014). "Strong electroluminescence from SiO2-Tb2O3-Al2O3 mixed layers fabricated by atomic layer deposition." *Applied Physics Letters*, *104*(25), 251113.

[236] Podhorodecki, A., Zatryb, G., Misiewicz, J., Wojcik, J., Wilson, P. R. J., & Mascher, P. (2012). "Green light emission from terbium doped silicon rich silicon oxide films obtained by plasma enhanced chemical vapor deposition." *Nanotechnology, 23*(47), 475707.

[237] Li, J., Zalloum, O. H. Y., Roschuk, T., Heng, C. L., Wojcik, J., & Mascher, P. (2008). "Light emission from rare-earth doped silicon nanostructures." *Advances in Optical Technologies, 2008*.

[238] Li, J., Zalloum, O., Roschuk, T., Heng, C., Wojcik, J., & Mascher, P. (2009). "The formation of light emitting cerium silicates in cerium-doped silicon oxides." *Applied Physics Letters, 94*(1), 011112.

[239] Bellocchi, G., Franzò, G., Miritello, M., & Iacona, F. (2014). "White light emission from Eu-doped SiOC films." *Applied Physics Express, 7*(1), 012601.

[240] Bellocchi, G., Iacona, F., Miritello, M., Cesca, T., & Franzò, G. (2013). "SiOC thin films: an efficient light source and an ideal host matrix for Eu^{2+} ions." *Optics express, 21*(17), 20280-20290.

[241] Li, D., Zhang, X., Jin, L., & Yang, D. (2010). "Structure and luminescence evolution of annealed Europium-doped silicon oxides films." *Optics express,18*(26), 27191-27196.

[242] Castagna, M. E., Coffa, S., Monaco, M., Caristia, L., Messina, A., Mangano, R., & Bongiorno, C. (2003). "Si-based materials and devices for light emission in silicon." *Physica E: Low-dimensional Systems and Nanostructures, 16*(3), 547-553.

[243] http://www.helios-project.eu

CHAPTER **2**

---

2. Er-Doped Metal-Insulator-Semiconductor Light Emitting Devices Containing Silicon Nanocrystals

As explained in the previous chapter, the search for efficient integrated light sources has triggered the attention of several research groups who seek for the implementation of PICs with outstanding performance. One of the major challenges in that line is the development of near infrared Si-based light sources emitting at 1.54 μm. These devices are expected to open a new technological framework for competitive on-chip photonics and telecommunications. In that context, Er-doped MIS light emitting devices are promising candidates to carry out this task, and consequently much effort has been made. Several breakthroughs were accomplished as a consequence of the intense research in this area, some of them described in the previous chapter. However, there are still many uncertainties and not-well understood phenomena that sometimes yield to a vague interpretation of results. Consequently, it is not uncommon to find controversial works in the literature that defend opposed considerations. This chapter aims to put forward in a comprehensive way our research work carried out in Er-doped electroluminescent MIS devices while contributing to solve some aspects still under debate.

This chapter is divided in several parts. First, a general overview of the main charge transport mechanisms that take place in MIS structures is described, followed by a brief explanation on the atomic structure and the optical activity of Er^{3+} ions. Then, an extended discussion about the main excitation mechanism of Er^{3+} ions under electrical pumping is introduced. This is followed by a first order quantification of the output optical power of devices and the fraction of excited Er^{3+} ions in Er-doped MIS light emitting devices. Also, the best Si-based host for Er^{3+} ions is debated, providing experimental evidences to support our statements. Finally, I will end this chapter comparing different device architectures especially designed to enhance the Er^{3+} excitation efficiency, based on the main conclusions drawn from previous sections. A summary of the most important points and findings on Er-doped MIS light emitting devices are attached at the end of this chapter.

2.1. Charge transport in dielectric media: An overview

Understanding charge transport in dielectric matrices has been a matter of concern since the beginning of the microelectronic industry. Key issues such as leakage gate current, reliability and charge trapping in MOS devices have been largely studied by many authors, providing an extended knowledge of the transport phenomena in dielectrics [1]. Far from being an outdated topic, nowadays charge transport still triggers the attention of many researchers who want to provide further insight into their novel materials. Moreover, the study and understanding of charge flow into matter yields devising intrinsic physical properties that can often be correlated with layer morphology, energy conversion efficiency or premature aging of devices. Therefore, it is useful to obtain a general picture of the main transport mechanisms occurring in our layers.

Ideal MIS structures show no conductivity. Real insulators however, they do show significant conductivity depending on the applied voltage or the temperature. Normally, charge transport in dielectrics is investigated upon application of an external electric field in a MIS (or MIM) structure. Figure 2.1 shows the polarization scheme of a typical device cross-section composed by a highly n-type doped polysilicon electrode 100 nm thick, an Er-doped SiO_2 layer 50 nm thick, a p-type Si substrate and an aluminum back electrode 200 nm thick.

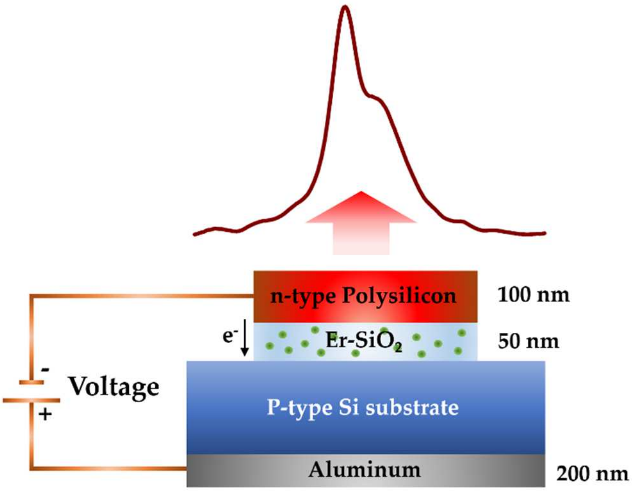

Figure 2.1. Device cross-section and polarization scheme of a light emitting capacitor.

Charge carriers are injected into the active layer (mainly electrons for the structure of figure 2.1), and transported either by assistance of intraband defect sites (defect-assisted transport) or tunnel over the conduction and/or valence bands. In most cases, the total current flow is composed by several transport mechanisms that take place simultaneously, hence making the identification process a laborious task. Therefore, first order approximations are often carried out when there is a predominant candidate, depicting an idealized compact model in which a single transport mechanism governs the charge transport uniquely. Effective-mass approximation (EMA), parabolic bands and conservation of parallel momentum are assumed to derive charge transport equations. In addition, there is a number of perturbations such as charge trapping, band bending or flat-band voltage that are overlooked in these equations. Thus, if not otherwise stated, the applied electric field will be calculated as the ratio between the applied voltage and the dielectric thickness directly. Despite this, fairly good modeling of experimental measurements can be obtained for medium-high external electric fields. For low electric fields (below 1 MV/cm), however, these perturbations may be of importance and therefore a more accurate analysis is required sometimes. In the following, I will review the most relevant transport mechanisms in dielectrics departing from phenomenological compact equations, since a complete theoretical development of charge transport lies out of the scope of this section. Nevertheless, there are several excellent books and review papers on transport phenomena if a more fundamental description of charge transport equations wants to be revisited [1- 3].

Charge transport in a MIS structure does not only depend on the nature of the insulator, but also on the applied voltage, the temperature, contact quality or the electrode-dielectric potential barrier height. Precisely, we can divide charge transport mechanisms in two main groups: electrode-limited current injection and bulk-limited current injection. In electrode-limited current injection, injected carriers are strongly modulated by the electrode-dielectric potential barrier height. It is typical from low-defective dielectrics with a large band offset with the injecting electrode (such as silicon dioxide), and mostly occurs under medium-high electric field regime, when the applied voltage is larger than the electrode-dielectric potential barrier height. On the contrary, bulk-limited conduction occurs when the injected current is limited by the intrinsic dielectric properties and not by the electrode-dielectric barrier height. A typical case is silicon nitride, which presents high number of defects and charge trapping sites that strongly limit the injected current. In this case, the range of voltages in which each transport mechanism arises can strongly vary depending on the studied dielectric layer.

2.1.1. Electrode-limited conduction mechanisms

As already stated, in this case the number of injected carriers is mainly governed by the electrode-dielectric potential barrier height instead of by the number of free sites (or defects) in the dielectric layer. Eventually, they can be split in either Richardson-Schottky (thermionic) emission or tunnel injection.

- **Richardson-Schottky emission**

Charge transport takes place only by thermionic emission of electrons over a reduced potential barrier height. This process is commonly observed at high temperatures or when the potential barrier height is low. Thick insulators, in which the tunnel transparency is low, are also suitable candidates for thermionic emission if defect density is low. The action of an external electric field effectively lowers the potential barrier height by image-force effect and easies the thermionic emission. The Schottky barrier height lowering is expressed as:

$$\Delta\varphi_b = q\sqrt{\frac{qE}{4\pi\varepsilon_0\varepsilon_r}} = \beta\sqrt{E} \tag{2.1}$$

Being φ_b the potential barrier height (in eV), q the elementary charge, E the applied electric field, ε_0 and ε_r the absolute and relative permittivity respectively. Hence, the general expression of the Richardson-Schottky emission using a one-dimensional and time-independent Wentzel-Kramers-Brillouin (WKB) approximation is [2]:

$$J_{Schottky} = \frac{4\pi m^* q}{h^3} k_B^2 T^2 \, exp\left(-\frac{\varphi_b}{k_B T}\right) exp\left(\frac{\beta}{k_B T} E^{1/2}\right) \tag{2.2}$$

Where $\frac{4\pi m^* q}{h^3} k_B^2$ is the Richardson constant (sometimes named A^*), m^* is the effective mass of electrons, h the Planck's constant and $K_B T$ is the thermal energy.

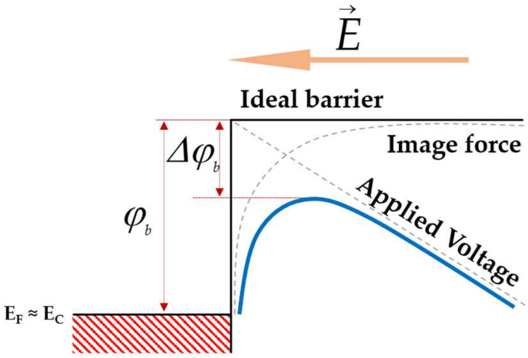

Figure 2.2. Energy band diagram depicting the barrier height lowering effect upon application of an external electric field.

A clear case of Richardson-Schottky emission would be the metal-polysilicon system, especially when the polysilicon is lightly doped [4]. In that case, electrons are injected over a potential barrier height at the grain boundaries of polysilicon. Further details of this interface and experimental measurements are found in chapter 3.

- **Tunnel injection**

Charge tunneling takes place when an electron with energy below the electrode-dielectric potential barrier height and situated at the electrode quasi-Fermi level penetrates directly into the dielectric (or substrate) conduction band with no need of being transported by intermediate defective states located in the dielectric bandgap. This effect can only be understood under the coverage of quantum theory, which predicts a non-zero probability of transmission of a particle when faces a finite potential barrier. The transmission probability rises exponentially with the inverse of barrier thickness.

This process normally takes place at medium-high electric fields or for very thin dielectrics. If we only consider the shape of the potential barrier height that carriers have to tunnel, we may distinguish between direct tunneling (DT) and Fowler-Nordheim tunneling (FNT). Both processes are considered band-to-band mechanisms, since injected carriers tunnel directly from the electrode Fermi level to either the dielectric or the substrate conduction band. Also, there is a particular case in which the tunneling is assisted by an intermediate defect site located in the dielectric bandgap (TAT, trap-assisted tunneling).

A finer distinction may be made depending on the tunneling event, distinguishing between ECB tunneling (electrons tunneling from the conduction band), EVB tunneling (electrons tunneling from the valence band) or HVB (holes tunneling from the valence band). For the present work however, being silicon oxide the only dielectric that has shown electrode-limited tunneling currents among all the studied dielectric materials, I have mainly considered ECB tunneling since in silicon dioxide the valence band potential barrier height is considerably higher than the one measured at the conduction band (4.8 eV and 3.1 eV, respectively). Thus, EVB and HVB tunneling is highly improbable in these systems.

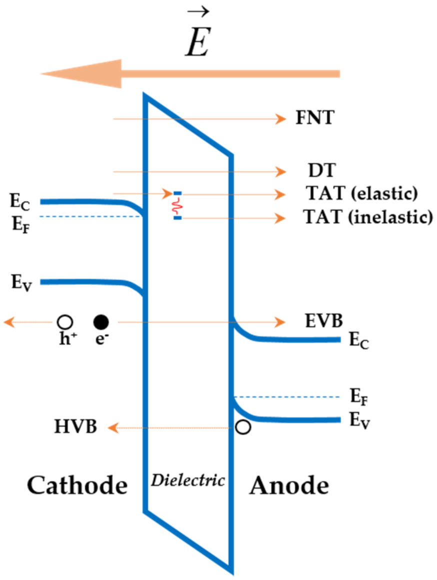

Figure 2.3. Schematic description of different tunneling transport events in a dielectric film: Fowler-Nordheim tunneling (FNT), elastic/inelastic trap-assisted tunneling (TAT), electron valence band (EVB) and hole valence band tunneling (HVB).

- **Direct tunneling (DT)**

DT occurs when carriers tunnel through a trapezoidal barrier height with no further interaction with the dielectric. In this case, the tunneling distance coincides with the dielectric thickness. It is normally observed in thin dielectrics (below 5 nm) with low permittivity (for instance, SiO_2). For this process to take place, the applied voltage should be lower than the potential barrier height at the electrode-dielectric interface. The compact equation for the DT mechanism can be derived from the Tsu-Esaki formulation [5]:

$$j_{DT} = \frac{q^3}{8\pi h\left(\varphi_b^{1/2} - (\varphi_b - qE\cdot d)^{1/2}\right)^2} E^2 \exp\left(-\left(\frac{8\pi\sqrt{2m^*}}{3hqE}\left(\varphi_b^{3/2} - (\varphi_b - qE\cdot d)^{3/2}\right)\right)\right) \tag{2.3}$$

- **Fowler-Nordheim tunneling (FNT)**

This transport phenomenon is observed when electrons tunnel through a triangular potential barrier height. In this case, the applied voltage is larger than the electrode-dielectric barrier height. As a consequence, the dielectric conduction band suffers a strong bending downwards that modifies the tunneling transparency of the potential barrier height. In particular, the distance that electrons have to tunnel becomes effectively reduced, enhancing the tunneling probability of electrons. Contrary to DT, FNT is typically observed in thicker dielectrics with low number of trap sites (thickness between 10-50 nm). The FNT current density reads as follows [6]:

$$J_{FN} = \frac{q^3}{16\pi^2 \hbar m_{ox}\varphi_b} E^2 \exp\left(-\frac{4\sqrt{2m^*}}{3\hbar q}\frac{\varphi_b^{3/2}}{E}\right) \tag{2.4}$$

- **Trap-assisted tunneling (TAT)**

This tunneling mechanism occurs when charge tunneling from the electrode to the dielectric conduction band is mediated by an intermediate intraband defect state. It is a multi-step process, with a sequence of concatenated tunneling events. In fact, this phenomenon has been largely used in memory devices in which writing/erasing cycles are addressed by injecting/removing charges from floating gates by TAT [7]. In addition, it is also responsible for the increased leakage current in gate oxides that leads to the premature failure of electronic MOS devices [8]. Upon prolonged electric field stress, defect sites or trap centres are continuously created in the dielectric layer, resulting in an increase of the TAT injection and the eventual device breakdown. This phenomenon is called Stress-Induced Leakage Current (SILC).

Depending on the overall energy balance, TAT can be elastic (no energy loss) or inelastic (energy loss). Figure 2.3 describes both situations. The generalized TAT current injection calculated on the basis of simple one-dimensional model can be written as:

$$J_{TAT} = \frac{qn_t}{2\tau} \exp\left(-\frac{4\sqrt{2m^*}}{3\hbar q}\frac{\phi_t^{3/2}}{E}\right) \tag{2.5}$$

Where n_t is the trap area density, τ is the relaxation time between subsequent tunneling events (capture + emission times) and ϕ_t is the energy value at which the trap is situated with respect to the conduction band.

TAT is normally observed under medium-high electric fields in low-defective matrices. Most times TAT emerges before the FNT mechanism, especially in these situations in which external voltage is not high enough to induce tunneling along the entire effective dielectric thickness, although sufficient to procure effective tunneling to a nearby defect site located within the vicinity of the electrode-dielectric interface. This process has been observed in Si-nc/SiO_2 superlattice structures (see the end of this chapter).

2.1.2. Bulk-limited conduction mechanisms

Contrary to the above explained transport mechanisms, bulk-limited conduction occurs when at steady state conduction the dielectric cannot evacuate all the carriers supplied by the electrode. In few words, the rate at which carriers are transported within the dielectric is lower than the supplying rate provided by injecting electrodes. For this case, the transport will be strongly affected by the intrinsic characteristics of the dielectric (electron mobility, permittivity, stoichiometry, trap defect density …). We can differentiate between two different regimes that strongly depend on the applied voltage. In the low voltage regime, and if Mott-Gurney contacts are defined at the electrode-dielectric interface, the transport will be governed by ohmic-like conduction. For this conduction to take place however, the electrode work function ($\psi_{electrode}$) should necessarily be smaller than the dielectric work function (ψ_{diel}). From an experimental viewpoint, ohmic conduction is normally identified if a linear dependence between current density and applied electric field is measured. The effective dielectric conductance value should be close to 1 under this condition:

$$G = \frac{VdI}{IdV} \approx 1 \tag{2.6}$$

Moreover, an Arrhenius plot is often performed to evaluate the thermal activation energy. Nevertheless, if the J-V curve does not satisfy the above characteristics at low voltage, then the contact is more likely to behave as a Schottky barrier. Then, no ohmic behavior is obtained, being the charge transport limited by the potential barrier height. At medium-high voltages however, the charge transport is dominated by the dielectric layer.

Under this condition, several bulk-limited mechanisms may take place, depending on the layer morphology.

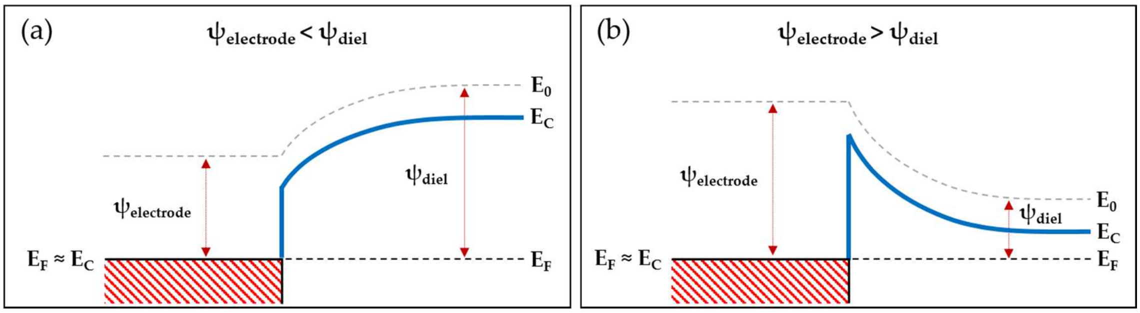

Figure 2.4. Energy band diagram of a Mott-Gurney contact (a) and a Schottky contact (b) at the electrode-dielectric interface.

- **Poole-Frenkel conduction (PF)**

PF conduction can be considered as the analogue of the Schottky emission for intrinsic electrons inside a dielectric layer. Charge transport is governed by trapping and de-trapping carrier dynamics inside the dielectric bandgap. Trap charges are released to the conduction band and rapidly trapped again by a new intraband centre. This process is repeated over and over until charges reach the other electrode. Therefore, the effective free path of electrons in the conduction band is very small compared to dielectrics governed by tunnel injection currents, where only phonon scattering is remarkable. Charge de-trapping is modulated by the applied voltage that reduces the trap ionization energy required for an electron to escape the Coulomb potential energy. Equally than in Schottky emission, such barrier diminution easies the carrier ionization by thermal emission. The diminution of the potential energy can also be calculated with equation 2.1. In these dielectrics in which PF effect clearly dominates over other mechanisms, the current density can be modeled as [9]:

$$J_{PF} = q\mu N_C E\, exp\left(-\frac{\left(\phi_t - \sqrt{q^3 E/(\pi\varepsilon_0\varepsilon_r)}\right)}{k_B T}\right) \tag{2.7}$$

Being μ the electronic drift mobility (which is temperature dependent) and N_C the density of states. Despite the evident similarities between Schottky emission and PF conduction, the origin of the energy barrier lowering is different, as Schottky emission is assisted by the image force barrier lowering whereas PF conduction is activated by the reduction of the Coulomb potential energy. Therefore, PF conduction normally governs in dielectrics with high defect density, high voltages and high temperature conditions.

In some cases however, a more detailed analysis of PF conduction is required. For instance, when the number of emitted electrons from donor states is reduced by the action of trapping centres, hence decreasing the overall PF current. For this particular case, the PF equation should be re-written depending on the ratio between the density of traps (N_T) and the density of donor centres (N_D) [10]:

$$J_{PF} = q\mu N_C \frac{N_D - N_T}{N_T} E \exp\left(- \frac{\left(\phi_D - \sqrt{q^3 E/(\pi\varepsilon_0\varepsilon_r)}\right)}{k_B T} \right) \qquad \text{if } N_T < N_D \tag{2.8}$$

$$J_{PF} = q\mu N_C \left(\frac{N_D}{N_T}\right)^{1/2} E\,exp\left(- \frac{\left(\phi_D - \phi_t - \sqrt{q^3 E/(\pi\varepsilon_0\varepsilon_r)}\right)}{2k_B T} \right) \qquad \text{if } N_T \approx N_D \tag{2.9}$$

Where ϕ_D represents the donor energy value. When the above equations apply, the transport mechanism is called anomalous PF conduction.

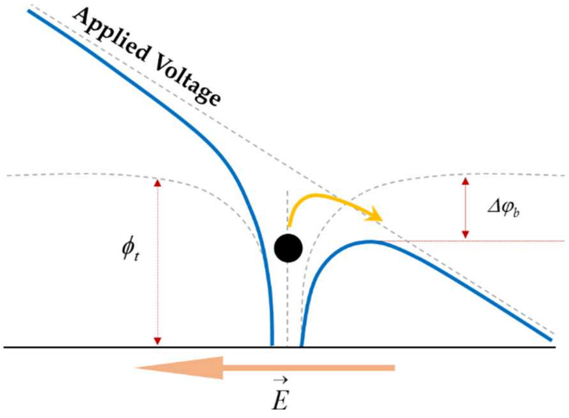

Figure 2.5. Poole-Frenkel ionization of a single trapping site assisted by the applied voltage.

- **Space-charge-limited current (SCLC)**

SCLC takes place when the dielectric layer can no longer compensate injected charge. As a result, charges spatially accumulate along the dielectric layer creating a charge distribution that screens upcoming charges. This process is responsible for the spatial deformation of the potential barrier height under high injection regime. In few words, SCLC occurs when trapping sites are completely filled up and new injected charge moves 'freely' in the dielectric. At this point, the Fermi level moves up above the electron trapping energy level (ϕ_t). This condition is commonly known as trap-filled limit (TFL). This transport mechanism is normally preceded by a low voltage ohmic behavior and an intermediate regime where the carrier transit time (τ_c) starts to dominate over the dielectric relaxation time for charge redistribution (τ_d). The voltage at which this transport switching takes place is called transition voltage (V_{tr}). Hence, the equations that fully describe the entire process:

$$J_{Ohm} = qn_0\mu\frac{V}{d} \qquad \text{for } V < V_{tr} \tag{2.10}$$

$$J_{TFL} = \frac{9}{8}\mu\varepsilon_0\varepsilon_r\theta\frac{V^2}{d^3} \quad , \quad \text{being } \theta = \frac{N_C}{g_n N_t}\exp\left(\frac{-E_A}{K_B T}\right) \qquad \text{for } V_{tr} < V < V_{TFL} \tag{2.11}$$

$$J_{SCLC} = \frac{9}{8}\mu\varepsilon_0\varepsilon_r\frac{V^2}{d^3} \qquad \text{for } V > V_{TFL} \tag{2.12}$$

Where E_A is the activation energy, i. e. the value from the trap states energy level to the conduction band edge (E_c), and d is the layer thickness. Figure 2.6 depicts the three regimes of SCLC conduction:

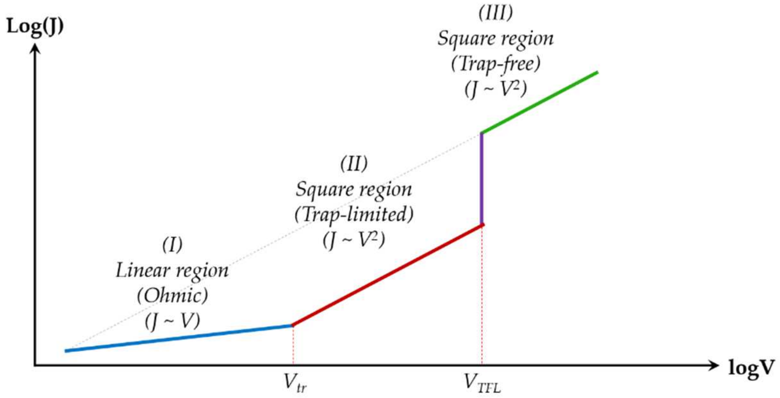

Figure 2.6. J-E characteristic displaying the three regimes of SCLC conduction.

In addition V_{tr}, V_{TFL}, τ_c and τ_d can be calculated as:

$$V_{tr} = \frac{8}{9}\frac{qn_0d^2}{\varepsilon_0\varepsilon_r\theta} \tag{2.13}$$,

$$V_{TFL} = \frac{qN_td^2}{2\varepsilon_0\varepsilon_r} \tag{2.14}$$

$$\tau_c = \frac{d^2}{\mu\theta V_{tr}} \tag{2.15}$$,

$$\tau_d = \frac{\varepsilon_0\varepsilon_r}{qn\mu\theta} \tag{2.16}$$

Being n the concentration of free carriers in the insulator. SCLC normally governs charge transport in silicon nitrides and oxynitrides at high level of injection and when deep levels for trapping are considered [2]. Nevertheless, the above described transport equations are sometimes not enough accurate to model bulk-limited charge transport in dielectrics, since SCLC is often assisted by a barrier height lowering effect due to the external electric field (as in the PF case). As a consequence, modeled current by SCLC is lower than the one measured experimentally. Murgatroyd solved this inaccuracy by introducing the PF barrier lowering effect in the SCLC equation [11]:

$$J = \frac{9}{8}\mu\varepsilon_0\varepsilon_r\frac{V^2}{d^3}\theta exp\left(\frac{0.891}{k_BT}\left(\frac{q^3E}{\pi\varepsilon_0\varepsilon_r}\right)^{1/2}\right) \tag{2.17}$$

This equation is known as Space Charge-Limited Current enhanced by Poole-Frenkel effect (SPCLC-PF).

- **Hopping conduction**

Hopping conduction occurs when trapped electrons in a dielectric tunnel from one trap site to another directly. It is considered a purely intraband mechanism, without any interaction with the conduction band. This inter-trap tunneling mechanism is observed when charges do not have enough energy to overcome the potential barrier height by thermionic emission. In this case, charges can tunnel to a nearby trapping site if the tunneling distance is sufficiently low. The expression reads:

$$J_{hopping} = qan\upsilon \exp\left(\frac{qaE - E_A}{k_B T}\right) \tag{2.18}$$

Where *a* is the mean hopping distance, *n* the electron concentration in the conduction band of the dielectric and *v* the frequency of thermal vibration of electrons at trap sites. This equation describes the trend of a trap electron to hop to the lowest activation energy and the shortest hopping distance. Nevertheless, in most cases both conditions cannot be satisfied simultaneously, thus finding a compromise solution that maximizes hopping probability via optimum hopping distance of the most favorable intraband defect states. This process is called Variable Range Hopping (VRH) conduction, and the dielectric resistivity is described by Mott's law [12, 13]:

$$\rho_{VRH} = \rho_0 \exp\left(\left(\frac{21.2}{k_B a^3 T N_F}\right)^{1/4}\right) \tag{2.19}$$

Being N_F the density of states at the Fermi level. Hopping normally manifests at low temperatures and low applied voltages (typically < 1 V) and consequently it is not generally taken under consideration in experiments carried out at room temperature. Nevertheless, there are some exceptions in which VRH can be observed at room temperature, as in Oxide-Nitride-Oxide (ONO) structures, where experimental evidences of VRH were provided at low voltages [14].

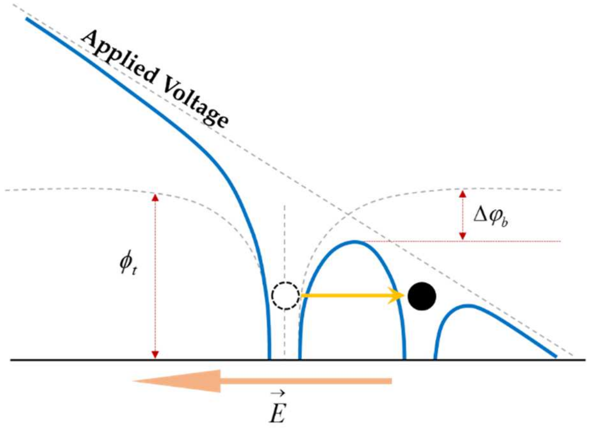

Figure 2.7. Hopping conduction between two spatially close intraband trapping sites.

The above presented equations constitute a general overview of the most probable transport mechanisms in dielectric thin films. In the next section I will apply some of these conduction models to experimental curves obtained in Er-doped SiO_2 and Si_3N_4. Also, some published works in which the role of the annealing temperature or the silicon excess in Er-doped SiO_x and SiN_x layers is highlighted. Finally, a numerical procedure based on the power exponent method is provided to easily identify the dominant transport mechanism in a dielectric layer.

2.2. Charge transport of Er-doped silicon-rich oxide (nitride) light emitting capacitors

In this section, a comprehensive discussion about charge transport phenomena in different Er-doped matrices is provided. A series of examples are shown to illustrate the most common emerging features during the modeling of experimental J-E curves.[2] The simpler case of study is presented in figure 2.8 (a), where the J-E characteristic of an Er-doped SiO_2 MIS device is compared with the one of an Er-doped Si_3N_4. Er-doped SiO_2 layer is 50 nm thick, with a total Er concentration of 5×10^{20} at./cm^3 embedded in a thermally grown SiO_2 (High Thermal Oxidation, HTO). A post-annealing treatment at 800°C for 6h was carried out. On the contrary, the Er-doped Si_3N_4 layer was fabricated by co-sputtering technique, with same thickness and Er-concentration. Devices were biased under direct current (DC) polarization from 0 V until the device breakdown, with a voltage step of 50 mV/s that allows a quasi-static analysis of curves. A brief inspection on the main features of both curves denotes the peculiarities of each layer. Whereas the Er-SiO_2 layer shows a high resistivity region in which an almost constant current density value is obtained for a range of electric fields from 0 to 4.5 MV/cm, a more accentuated conduction is observed in the Er-doped Si_3N_4 layer since the beginning of the curve. The flat plateau observed in the Er-doped SiO_2 can be understood as the displacement current of an ideal capacitor. Hence, an approximate value of layer capacity can be obtained with the following formula:

$$J = C_0 \frac{\Delta V}{\Delta t} \tag{2.20}$$

Where C_0 is the layer capacity and $\Delta V / \Delta t$ is the polarization voltage step. In this case, a value of $C_0 = 0.2 \, \mu F / cm^2$ is obtained for the Er-SiO_2. On the other hand, the Er-Si_3N_4

---

[2] *Notice that the conclusions drawn in this section are based on the experimental results obtained from Er-implanted (and Er-free) SiO_x and SiN_x layers fabricated by HTO, LPCVD, PECVD and co-sputtering with a specific thermal budget (it will be detailed when needed). Consequently, different trends on charge transport cannot be discarded when characterizing other devices fabricated by a different technique (as EB-PVD or MOCVD) or with a different annealing treatment (as flash lamp annealing).*

layer showed an ohmic-like conduction in the low voltage regime as a consequence of the large number of defects located within the bandgap. Such effect impedes the observation of the displacement current since it becomes completely screened by the ohmic conduction. Instead, the nitride layer shows a fairly homogeneous conduction along the entire range of electric fields. In particular, PF conduction has shown the best fitting parameters (red line in figure 2.8 (a)).

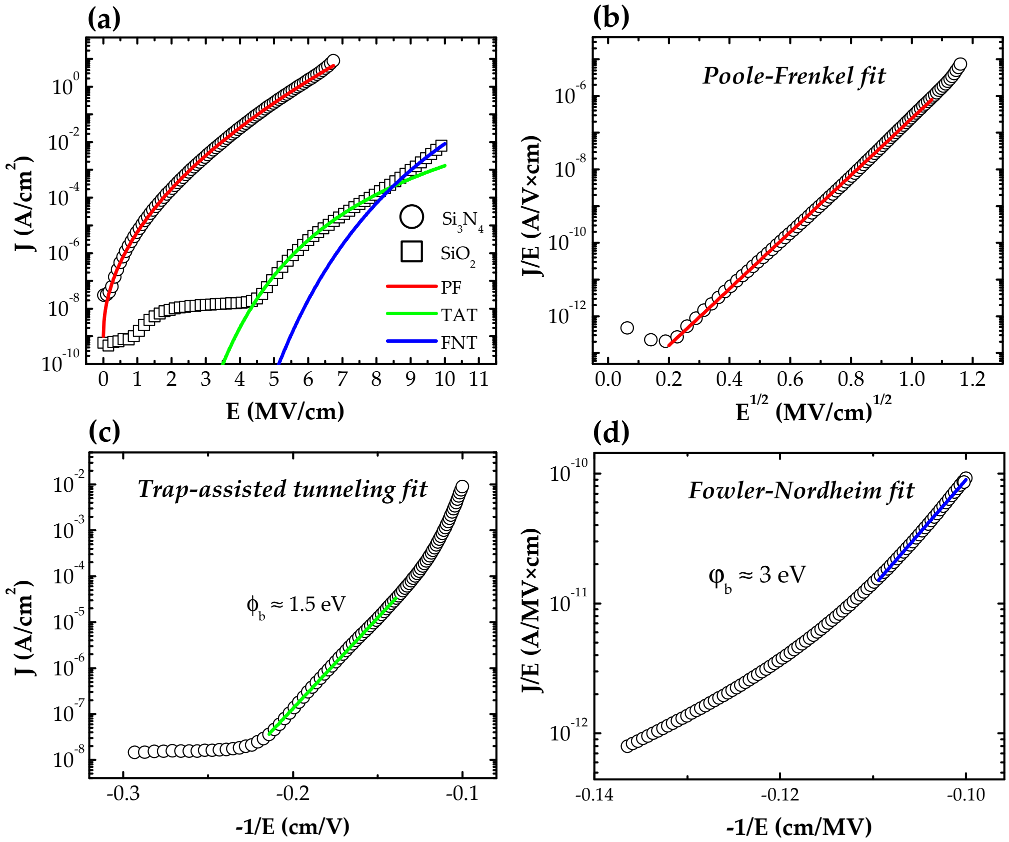

Figure 2.8. (a) J-E characteristic of an Er-doped Si_3N_4 layer (empty circles) and an Er-doped SiO_2 (empty squares). (b), (c) and (d) show J-E curves modified according to PF conduction, TAT and FNT, respectively. A linear fit is performed to evaluate the accuracy of the chosen transport mechanism.

An alternative method to validate the transport mechanism can be performed by means of a different J-E configuration. This time, experimental J-E values are modified accordingly to the desired expression to yield a straight line of points. Then, a linear fit is performed, obtaining the physical parameters of the equation. An example is shown in figure 2.8 (b). Y-axis consists in the ratio between *J* and *E*, whereas x-axis accounts for the square root of *E*. By doing this, and according to PF expression (equation 2.7), the value of the relative permittivity can be directly extracted from the slope of the fit. A highly bended figure of merit with a poor fit correlation rate or a meaningless value is recovered when the wrong transport mechanism is modeled most of the times. For the current example however, a good fit correlation rate (0.9999) and a value of $\varepsilon_r \sim 8$ is estimated, in agreement with the Si_3N_4 relative permittivity ($\varepsilon_r \sim 7.5$) [15].

Concerning the Er-SiO_2, a remarkable knee of conduction is observed from 4.5 MV/cm on. This abrupt change in conduction marks the beginning of a conduction mechanism. In particular, a TAT conduction has been modeled in a range from 4.5 MV/cm to 8 MV/cm (green line in figure 2.8 (a)). Equally than for the Er-Si_3N_4, the TAT configuration has been accomplished (figure 2.8 (c)), obtaining a mean energy value of ϕ_t ~ 1.5 eV for TAT intraband sites. Finally, FNT has been modeled at high field regime (blue line in figure 2.8 (a)), obtaining a mean barrier height in agreement with the electrode-SiO_2 barrier height, i.e. φ_b ~ 3.1 eV.

Remarkably, large differences in charge transport phenomena between identical samples fabricated by different methods (as PECVD and co-sputtering, for example) have not been observed in the course of this dissertation. On the contrary, the layer stoichiometry and the annealing treatment have proved to be crucial parameters with a strong influence on the charge transport of dielectric media. Thus, two samples with same stoichiometry and annealing treatment but fabricated at different systems should yield similar charge transport mechanisms. A representative example can be provided comparing the results shown in figure 2.8 with the ones reported in *paper VIII* (figure 3). In this work, charge transport evaluation of an Er-doped SiO_2 sample fabricated by co-sputtering is performed, obtaining similar results than figure 2.8 with a sequential combination of TAT and FNT. Also prominent is the fact that Er implantation does not change the transport mechanism significantly. Nevertheless, a noticeably diminution of the injected current density has been observed in comparison with undoped samples. This fact is discussed in *paper V*, where the I-V curves of Er-doped/undoped Si-nc LEDs are compared. Charge trapping at deep energy levels due to Er implantation was suggested to explain such differences. Both papers will be revisited in upcoming sections.

Nevertheless, the above considerations are sometimes not sufficient to properly study conduction phenomena in dielectrics, and therefore a more accurate evaluation of the whole picture should be carried out. The reader should take into account that it is not unusual to obtain reasonable fitting parameters with physical meaning when using the wrong charge transport mechanism. In this case, a proper reasoning and additional measurements are needed to validate the chosen transport mechanism. For instance, FNT is only allowed from 5 MV/cm and beyond in silicon oxide hosts. Thus, it is senseless to fit such transport mechanism at lower electric fields, even if an extremely good fitting is obtained. Similarly, it is not plausible a system in which DT dominates if the oxide layer is much thicker than 5 nm. A simple but powerful tool to evaluate if the studied layer shows an electrode-limited or a bulk-limited conduction consists in the direct observation of the J-E symmetry under positive and negative polarization. Bulk-limited conduction provides a symmetric J-E curve, whereas an asymmetric trend is expected for electrode-limited conduction since different barrier height values are typically obtained in a MIS device.[3]

- **Variable-temperature charge transport analysis**

An often used complementary measurement to validate charge transport mechanisms is the variable-temperature J-E characterization. This approach is very useful since allows devising the dependence of charge transport with the temperature. Moreover, this method permits discarding nearly temperature-independent transport mechanisms such as FNT. On the contrary, temperature-dependent mechanisms (for instance PF conduction) show a characteristic trend with temperature that is often modeled in an Arrhenius plot. The mean activation energy from which intraband traps release an electron in the conduction band can be obtained from this figure of merit. An example is shown below. J-E curves of an Er-doped Si_3N_4 are displayed in figure 2.9 at different temperatures, ranging from room temperature (297 K) up to 575 K). As observed, the current density is increased with the temperature accordingly (see figure 2.9 (a)). The Arrhenius plot is shown in figure 2.9 (b). Four different point datasets are displayed, each one corresponding to the layer conductivity (*J*/*E*) of a particular electric field when increasing the temperature. The activation energy of the Er-Si_3N_4 layer extracted from the linear fit displays a maximum value of E_A = 0.294 eV at 1 MV/cm and a minimum of E_A = 0.173 eV. These values are consistent with previous reported works with similar layers [14], and are physically reasonable since lower E_A is expected for higher electric fields as a consequence of the Coulombic barrier lowering (see section 2.1.1). Finally, figure 2.9 (c) shows a semi logarithmic plot of the E_A as a function of the applied electric field.

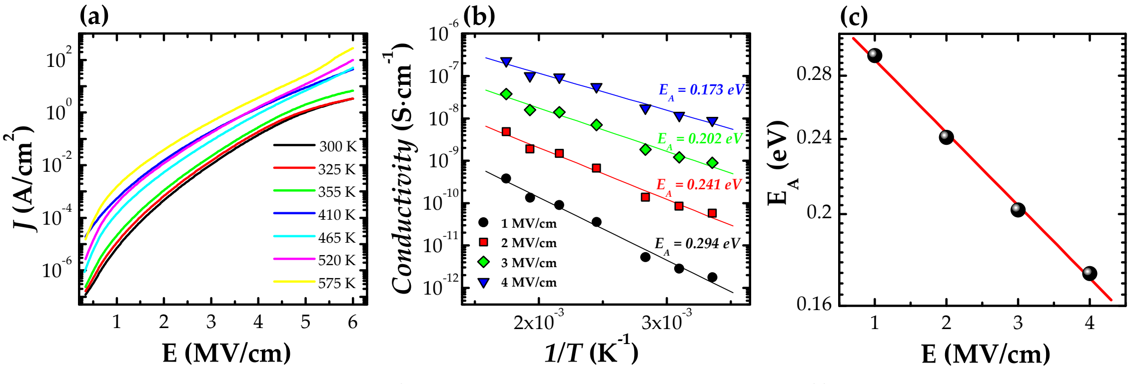

Figure 2.9. (a) J-E characteristic of an Er-doped Si_3N_4 layer under different temperature values. (b) Arrhenius plot of J-E curves. A value of E_A is obtained from each fit at a given *E* value. (c) Dependence of E_A values extracted from (b) as a function of *E*.

---

[3] *This reasoning does not apply for MIM devices with twin electrodes.*

As seen, accurate linear fitting can be performed, suggesting that E_A presents an exponential dependence with the electric field in the form:

$$E_A \propto \alpha e^{-\beta E} \tag{2.21}$$

Being α and β fitting constants. Thus, Er-Si_3N_4 layers show bulk-limited conduction governed by PF, whereas Er-SiO_2 layers display an electrode-limited mechanism mainly composed by either TAT or FNT depending on the electric field range. Apart from these systems, another interesting case of study is the one that incorporates Si excess in these matrices. As explained in the previous chapter, Si-ncs are efficient optical sensitizers for RE ions when embedded in a dielectric media. Under optical pumping, Si-ncs are beneficial since dramatically increase the absorption cross-section of Er^{3+} ions and provide a continuous PL excitation spectra [16, 17]. Similarly, Si-ncs are expected to increase the absorption cross-section of Er^{3+} ions under electrical pumping. Although the effect of Si-ncs on the EL of Si_3N_4 and SiO_2 thin films will be discussed in the next section, it is also interesting to overview their electrical properties first.

Starting from the J-E characteristic, figures 2.10 (a) and 2.10 (b) show a coherent increase of current density with the Si excess in both Er-SiO_x and Er-SiN_x layers, as previously reported [18]. Er-SiO_x samples were fabricated by LPCVD and annealed at 900°C for 1 h in N_2 ambient. An Er implantation dose of 1×10^{15} cm^{-2} at 20 keV was performed, followed by a post-annealing treatment at 800°C for 6 h. On the contrary, Er-SiN_x layers were fabricated by magnetron co-sputtering, with a similar Er concentration. Although the Si excess range is different in oxide-based and nitrogen-based layers, the nature of the transport mechanism remains constant for each one, being the conduction of Er-SiO_x layers limited by the electrode and the one of Er-SiN_x by the bulk. For instance, Er-SiN_x layers all show PF conduction with $\varepsilon_r \sim 8$, similar E_A, and inverse dependence between Si excess and the trapped charge density, i.e. the higher the Si excess is, the lower the charge trapped density becomes. This latter effect, although it may seem controversial, it has been ascribed to efficient charge de-trapping via localized intraband defects (charge migration). Further details about the role of Si excess in Er-doped SiN_x layers can be found in *paper VII*.

On the other hand, Er-SiO_x layers do show some differences upon modification of Si excess. In particular, substantial lowering of the mean barrier height for tunneling is obtained. Figure 2.10 (c) shows the dependence between the tunneling barrier height and the Si excess for the studied range of values. It is worth noting that a Si excess of 16% lowers the barrier height by a factor of two with respect to the stoichiometric Er-SiO_2 layer (from 3.1 eV to 1.5 eV). Hence, from a conceptual viewpoint, an Er-SiO_2 layer with 16% of Si excess will show a very similar conductivity than an electrode-limited system with an electrode-layer barrier height of ~ 1.5 eV.

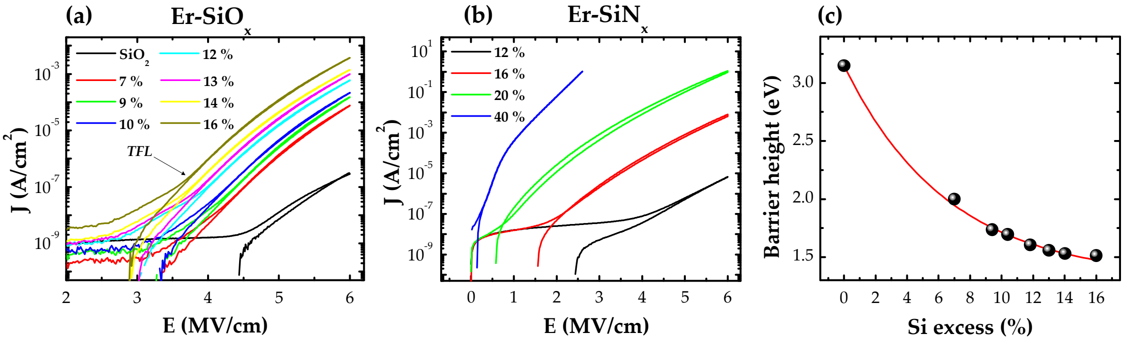

Figure 2.10. J-E characteristic of Er-SiO_x (a) and Er-SiN_x (b) layers with different Si excess. (c) Barrier height obtained from the FNT fit of J-E curves in (a) as a function of the Si excess. Red line is a guide to the eye.

Then, it seems clear that for this particular set of fabrication parameters, the dominant charge transport mechanism is not modified during the entire voltage sweep in both Er-SiO_x (display TAT conduction) and Er-SiN_x (PF conduction) layers regardless of the Si excess. Being Si_3N_4 a highly defective matrix per se, the incorporation of Si excess is only expected to provide a trapped filled voltage shift towards higher values, since a larger number of intraband traps is created. Nevertheless, the main charge transport mechanism is expected to be bulk-limited at all times. On the contrary, SiO_2 shows a more interesting scenario when Si excess is introduced since two dominant transport mechanisms of different origin could arise during polarization, depending on the applied electric field. A representative example is provided in *paper I*. In this work, four different SiO_x layers are studied, two with 9% and two with 16% of Si excess respectively, each sample containing a different Si excess annealed by means of rapid thermal annealing (RTA) at 1100°C for 5 minutes or by conventional annealing (CA) at 1100°C for 1 h. The Si excess has been introduced by ion implantation in this case. The nomenclature used for the paper is:

9% RTA 1100°C 5 min. → L1 *16% RTA 1100°C 5 min. → H1*

9% CA 1100°C 1 h → L2 *16% CA 1100°C 1 h → H2*

This set of samples allows studying the influence of two different fabrication parameters on the charge transport mechanism of samples: the Si excess (comparing L1-H1 and L2-H2) and the annealing treatment (L1-L2 and H1-H2 should be compared in this case). Interestingly, same charge transport phenomena was identified in samples with different Si excess but identical thermal budget, denoting the relatively weak influence of the Si excess on the charge transport. In particular, PF conduction dominates the conduction of the entire polarization range in samples that have undergone an RTA treatment (L1 and H1). On the contrary, two different transport mechanisms seem to arise in L2 and H2 samples, i.e. PF at low voltages and FNT under high voltages. A plausible explanation of the strong dependence of charge transport with annealing conditions is also provided. Whereas both annealing treatments have demonstrated to be efficient in the formation of Si-ncs for the established annealing temperature (1100°C) [19, 20], the relatively low annealing time in the RTA treatment (5 minutes) may not be enough to remove defects produced by the Si implantation. As a consequence, samples L1 and H1 show a high defect density in the active layer that limits conduction, hence being limited by bulk. On the contrary, L2 and H2 samples have undergone an annealing treatment for 1 h, which may be sufficient to induce substantial reduction of the layer defect density. Within this scenario, electrode-limited conduction is allowed under high field polarization.

As seen, several transport mechanisms may arise over the course of a single polarization sweep. Because of this, the interpretation of experimental curves and the correct fitting choice may be complicated. There is, however, an interesting method to ease this process. It is often called the power exponent method, and was first introduced by Mikhaelashvili, *et al.* [21]. This method relies on numerical analysis of the J-E characteristic to identify the main transport mechanism. It is especially powerful when multiple transport mechanisms are concatenated in a single J-E curve, as in *paper I*. Moreover, power exponent is equally sensitive to all the studied transport mechanisms, contrary to the temperature-dependent J-E characterization where only transport mechanisms with high temperature dependence can be evaluated. The power exponent ($a_{Mikh.}$) is defined by:

$$a_{Mikh.} = \frac{d[ln(J)]/dV}{d[ln(V)]/dV} \tag{2.22}$$

In their paper, Mikhaelashvili and co-workers used the $a-\sqrt{V}$ plot to distinguish between Schottky emission and PF conduction. In view of the above equation, the power exponent applied to these transport mechanisms is:

$$a_{Sch} = \frac{1}{4}\beta\sqrt{V} \tag{2.23}$$

$$a_{PF} = 1+\frac{1}{2}\beta\sqrt{V} \tag{2.24}$$

Where β has been previously defined in equation 2.1. As seen, both expressions have different slope values (1/4 and 1/2) and independent variables (0 and 1) when plotted in $a-\sqrt{V}$ configuration. In basis of this methodology, we have developed a similar approach based in a compact and precise numerical method to evaluate the main charge transport mechanism of studied samples. Firstly, assume that the current density in a dielectric can be generalized to an expression of the following type:

$$J = \delta \cdot E^{r+1} \cdot \exp\left(\gamma \cdot E^{s}\right) \tag{2.25}$$

Where δ and γ are constants and r and s parametric values. Now, let us perform a small perturbation on the power exponent in the form:

$$a = \frac{d[ln(\sigma)]/dE}{d[ln(E)]/dE} \tag{2.26}$$

Where $\sigma = J/E$ is the layer conductivity, i.e:

$$\sigma = \delta \cdot E^r \cdot exp\left(\gamma \cdot E^s\right) \tag{2.27}$$

Then, substituting equation 2.27 in 2.26, the following relation is obtained:

$$a = r + \gamma \cdot E^s \tag{2.28}$$

Now, bearing in mind the expressions for each charge transport mechanism, a table with representative parametric values can be performed according to the power exponent of equation 2.28:

Transport mechanism	**r**	**s**
Ohmic	0	0
Hopping	0	1
Poole-Frenkel	0	$1/2$
Diode[4]	-1	1
Schottky	-1	$1/2$
Space charge limited current	1	0
Trap-assisted tunneling	-1	-1
Fowler-Nordheim tunneling	1	-1

Table 2.1. Power exponent parametric values for each transport mechanism.

Thus, each transport mechanism can be unambiguously identified by means of a unique set of parametric values. An illustrative example is shown in figure 2.11. Experimental data corresponds to sample L2. In *paper I*, I-V curve shows two different transport mechanisms that depend on the applied voltage. From 0 V to 25-30 V approximately, PF conduction is predominant. From this value on, FNT with a mean barrier height of 2 eV governs charge transport. In figure 2.11, the power exponent method clearly evidences two dominant transport mechanisms that exchange around 5-

---

[4] *It has been added for completeness.*

6 MV/cm. Red line corresponds to PF conduction with parametric values r = 0 and s = ½, whereas FNT is predominant under high *E* values with r = 1 and s = -1.

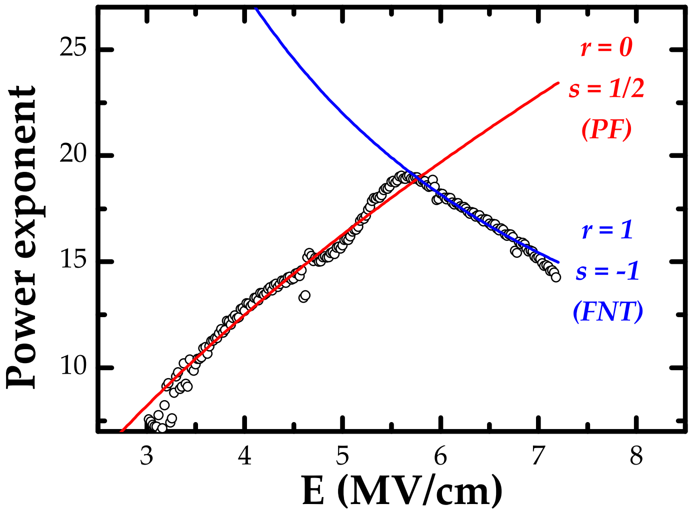

Figure 2.11. Power exponent representation of the J-E characteristic of sample L2 of *paper I*. Red and blue lines depict the modeling of PF conduction and FNT respectively, with parametric values according to table 2.1.

Therefore, a comprehensive overview of the most important factors to consider when analyzing charge transport phenomena in silicon oxides and nitrides has been carried out in this section. Representative examples of charge transport modeling have been presented and discussed. The influence of fabrication parameters on transport mechanisms has been discussed, with especial emphasis on the Si excess and the thermal budget of samples. Finally, a systematic analytical procedure to distinguish concatenated transport mechanisms in a single J-E characteristic has been developed departing from the power exponent method.

2.3. Erbium in its trivalent state: atomic structure and optical activity

Erbium is a rare earth element with an atomic number of Z = 68 and an electronic configuration of Er = [Kr] $4d^{10} 5s^2 5p^6 4f^{12} 6s^2$. It belongs to the group of lanthanides in the periodic table, and therefore shares many chemical properties with other elements such as terbium, europium or neodymium. A peculiarity of these elements is that s and p orbitals are located at the outer shells of the atomic structure, shielding 4f levels from the environment. Such isolation is high enough to provide a strong wavefunction localization in the atomic structure. This condition induces lanthanides embedded in dielectric matrices to preserve their narrow absorption and emission bands. For Er atoms in particular, their outer orbitals behave as a metallic shield for the rest of transitions, giving up the two $6s^2$ electrons and one electron from the $4f^N$ states to the dielectric, although preserving inner electronic states. Thus, the Er atom becomes ionized in its trivalent state. Still, and despite this shielding, Er^{3+} transition levels are weakly perturbed by the surrounding matrix, breaking the degeneracy of levels by means of the Stark splitting effect and turning the former forbidden dipole-dipole optical transitions of free Er^{3+} ions in weakly allowed transitions. This effect is experimentally observed by the widening of the narrow emission lines and also by very long transition lifetimes, in the order of milliseconds.

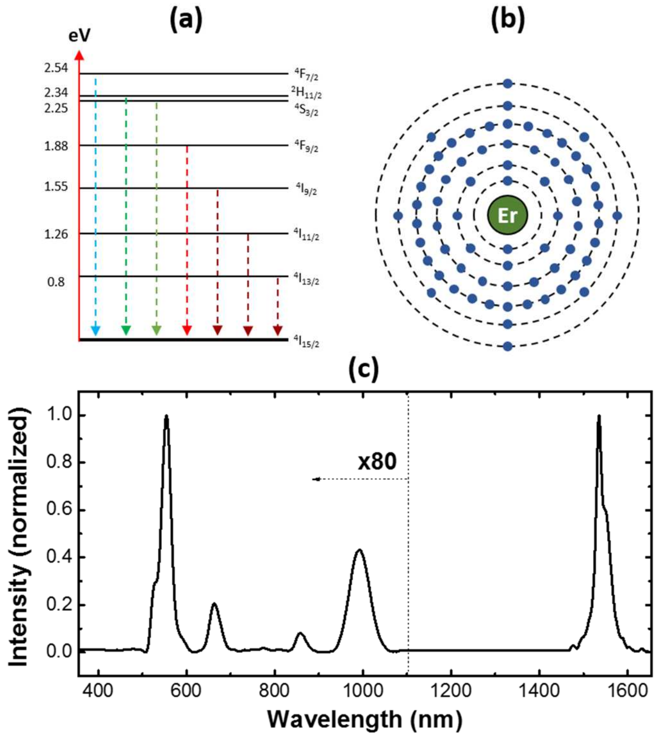

Figure 2.12. (a) Erbium transition levels with radiative decay energy levels. (b) Erbium electronic structure. (c) Spectral emission lines of Er^{3+} when embedded in a SiO_2 matrix, displaying the emission of the first excited state around of 1540 nm and the emission of upper levels (between 530-988 nm), multiplied by a factor of 80.

As can be observed in figure 2.12, the relaxation of the first excited transition level provides an intense and narrow light emission around of 1540 nm. This wavelength is of particular interest in telecommunications since coincides with a minimum of absorption of silicon oxides (used in optical fibres). As a consequence, a light emitting device working at this wavelength and coupled to an optical fiber would be able to transmit light through large distances without being absorbed. Moreover, being the emission lifetime of about few ms, stimulated emission (SE) can be obtained provided that population inversion condition is accomplished. In fact, Erbium Doped Fiber Amplifiers (EDFA) already carry out this task, amplifying light at 1.54 μm in long-haul optical networks. In this case, EDFA is optically pumped by a laser wavelength which is resonant with Er^{3+} ions (normally at either 1480 nm or 980 nm), stimulating the inversion population and the subsequent SE signal in which excited Er^{3+} ions are de-excited by emitting coherent photons with same phase and energy. This process can be explained with the following scheme:

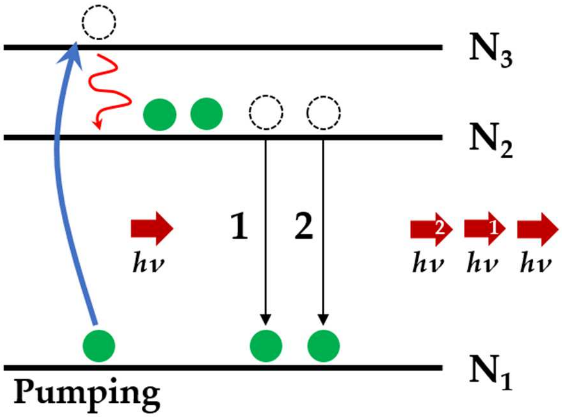

Figure 2.13. Er^{3+} energy diagram describing the stimulation emission process.

The pumping source excites Er^{3+} ions from the ground state to an excited state called N_3. Then, and because such state is not metastable, Er^{3+} ions rapidly de-excite to N_2 level, that corresponds to the first excited state. At this point, if the population in N_2 state is higher than in N_1, i.e. $N_2 > N_1$, optical gain may occur upon stimulation of a photon, generating new photons with an energy value equal to the energy difference between level N_2 and N_1 and with the same phase than the incoming photon. The population inversion can be modeled by means of the rate equation, in which a quasi-two level system is considered:

$$\frac{dN_{Er,2}}{dt} = \sigma_{abs}\phi_{exc}N_{Er,1} - \frac{N_{Er,2}}{\tau_{lifetime}} \tag{2.29}$$

Where $N_{Er,2}$ is the number of excited Er^{3+} ions in N_2 level (in at./cm^3), σ_{abs} stands for the effective absorption cross-section, ϕ_{exc} is the excitation pumping flux, $N_{Er,1}$ is the number of Er^{3+} ions in the ground state (in at./cm^3), i.e. N_{total}-$N_{Er,2}$, and $\tau_{lifetime}$ is the mean lifetime of Er^{3+} ions in the first excited state N_2. Considering the simplest case and steady state conditions, the absorption and excitation cross-sections match, i.e. $\sigma_{abs} = \sigma_{exc}$, and the total lifetime is de-convoluted in radiative (τ_{rad}) and non-radiative ($\tau_{non-rad}$) lifetimes as:

$$\frac{1}{\tau_{lifetime}} = \frac{1}{\tau_{rad}} + \frac{1}{\tau_{non-rad}} \tag{2.30}$$

Also, the total number of excited Er^{3+} ions can be obtained by solving equation 2.29:

$$N_{Er,2} = \frac{\sigma_{abs}\phi_{exc}\tau_{lifetime}N_{Er,1}}{\sigma_{abs}\phi_{exc}\tau_{lifetime} + 1} \tag{2.31}$$

Nevertheless, I shall remark that these equations are trustworthy when applied under certain conditions only, as other side effects such as cooperative up-conversion, auger quenching of excited Er^{3+} ions or the dependence of the absorption cross-section with the incident flux are overlooked in the above described set of equations (linear, time-independent and first order rate equations). Despite this, the accuracy of the model is fairly good in the low flux regime, where the effective absorption cross-section can be considered flux independent and up-conversion processes are not activated yet. For this latter case however, an additional quadratic coefficient (C_{up}) is sometimes added in equation 2.29 in order to include cooperative up-conversion phenomena:

$$\frac{dN_{Er,2}}{dt} = \sigma_{abs}\phi_{exc}N_{Er,1} - \frac{N_{Er,2}}{\tau_{lifetime}} - C_{up}N_{Er,2}^{2} \qquad (2.32)$$

Apart from the number of excited Er^{3+} ions, another remarkable parameter to consider is the ratio between the number of emitting Er^{3+} ions and the ones that only absorb energy from the pumping source. Although, in theory, all the embedded Er^{3+} ions in the solid host are suitable to absorb and emit light, several experimental evidences often point out to a completely different situation in which only a few percentage of the absorbing ions emit photons. In particular, *paper II* provides further insights into the role of non-emitting Er^{3+} ions in SiO_2 rib waveguides containing Si-ncs. The work is divided in two main parts: in a first stage, infrared spectral absorption losses are evaluated in waveguides to determine the number of absorbing Er^{3+} ions. A maximum absorption loss of 3.5 dB/cm is measured at 1535 nm. Being this value below the maximum internal gain reported so far in Er-doped silicon nanocluster sensitized waveguides, i.e. 4 dB/cm [22], a maximum net optical gain of 0.5 dB/cm is expected. Moreover, a similar number of Er^{3+} ions in the matrix was obtained from absorption losses when compared with the number of Er^{3+} ions measured by Secondary Ion Mass Sepctrometry (SIMS), hence validating that the totality of embedded Er^{3+} ions contribute to absorption ($\sim 5\times10^{20}$ at./cm^3).

In the second part of the work, efforts to accurately determine the net internal gain of waveguides are performed. For that, a pump-and-probe experiment is carried out, determining a maximum net internal gain of 0.55 dB/cm, far below the minimum required to compensate absorption losses (3.5 dB/cm). Finally, the number of emitting Er^{3+} ions is calculated, obtaining that only the 16% of the total population is able to emit light whereas the remaining 84%, although absorbing, does not contribute to emission.

A second work (*paper III*) further confirmed the above considerations, providing comprehensive reasoning of the most plausible causes for the low percentage of emitting Er^{3+} ions. This time however, Er-doped SiO_x layers 50 nm thick are characterized instead of rib waveguides. The up-conversion constant (C_{up}) and the intrinsic lifetime at 1535 nm (τ_0) are first calculated according to ref. [23], obtaining a value of $2.1 \pm 0.3\times10^{-15}$ cm^3/s and 2.13 ± 0.05 ms, respectively. Then, time-resolved measurements are carried out, obtaining a maximum number of emitting Er^{3+} ions of ~ 2×10^{18} at./cm^3, that corresponds to the ~ 0.7% of the totality of Er^{3+} ions in the matrix. Also, energy filtered and bright field scanning transmission electron microscopy (EFTEM and BF-STEM) was performed to support PL measurements, showing large Er clustering in samples, of about the 55% of the total number of Er. Although this number does not justify the high percentage of non-emitting Er^{3+} ions encountered in these layers (> 99%), a plausible explanation was derived from the fact that under TEM characterization, small Er clusters of few atoms cannot be resolved and therefore may be overlooked. Under this hypothesis, there would be a 55% of evident Er clustering, a 44% that is agglomerated in tiny clusters not observable by TEM, and finally around of 1% that is actually contributing to the emission.

Thus, it seems clear that the low fraction of emitting Er^{3+} ions under optical pumping is due to a massive agglomeration of Er in the matrix. The morphology of Er clusters has been previously studied [24], denoting an oxidized compound in the form of Er_2O_3. Three different strategies can be tackled to overcome this issue: (i) to reduce the number of Er^{3+} ions in the solid host; (ii) to accomplish a better Er distribution in the solid host, or (iii) to investigate alternative solid hosts with higher Er solubility. The first point is straightforward from a technological viewpoint since a lower implantation dose or a diminution of the RE content in the active layer can be easily defined. Nevertheless, this strategy presents an important drawback with respect to the total emitted optical power. Having integrated devices smaller footprints compared to EDFAs, the total number of Er^{3+} ions should increase accordingly to obtain optical power values with practical applications. In fact, taking into account the above equations for a two-level system, the total optical power generated in the active layer can be estimated with the following formula:

$$W_{opt}^{100\%} = \frac{N_{Er} \cdot t \cdot h\nu \cdot A}{\tau_{rad}} \tag{2.33}$$

Where t is the layer thickness, $h\nu$ is the energy of the emitted photon, and A is the area of the device. For instance, assuming an Er concentration of 5×10^{20} at./cm^3 in a 50 nm thick active layer embedded in a device with an area of 10^{-4} cm^2 (typical footprint of Er-doped MIS devices studied in this dissertation) and a radiative lifetime of 10 ms as in ref. 25, a maximum optical power of 3 μW would be obtained. This value, although far below the one obtained from an EDFA (few Watts), it would be sufficient for on-chip optical routing in integrated optical networks of few centimeters. However, a strong reduction of the number of Er^{3+} ions would imply a diminution of the optical power accordingly, hence becoming impractical in real applications. Thus, although slight modifications of the total concentration will be performed, profound diminution of the number of embedded Er in the matrix will be discarded by now (a concentration of

1.6×10^{20} at./cm^3 will be normally taken as the lower limit, as it would deliver 1 μW of optical power for a 100% of emitting ions in the host).

The second option is to obtain a better distribution of Er in the host matrix. In *paper III*, an ion implantation is carried out on samples. As a consequence, a non-homogeneous Er distribution is obtained, with a maximum concentration peak situated in the middle of the active layer. Ion implantation has the advantage of being a very precise technique that provides high control of the number of embedded ions in the system and good positioning of the implantation peak just by readjusting the dose and the implantation energy. However, several ion implantation steps are often needed to obtain a flat in-depth profile, causing damage and modifying the morphology and composition of layers sometimes. As a consequence, only a single ion implantation has been considered, producing a non-flat profile of Er that stimulates Er clustering around the maximum of the concentration in some cases. Figure 2.14 depicts this situation. The Er clustering is evaluated in two samples in which a different Er doping technique has been performed. For that, High Resolution Transmission Electron Microscopy (HRTEM) is used, as seen in figures 2.14 (a) and 2.14 (d).[5] In presence of clusters, Energy Filtered TEM (EFTEM) imaging is carried out to identify the element that agglomerates in the layer. In that case, transmitted electrons are filtered either by the Si plasmon peak at 17 eV (figures 2.14 (b) and (e)) or by the SiO_2 plasmon peak at 23 eV (figures 2.14 (c) and (f)). Figures 2.14 (a), (b) and (c) correspond to an Er implanted thermal SiO_2 layer with an implantation dose of 2.5×10^{15} at./cm^2 ($N_{Er,total} \sim 5\times10^{20}$ at./cm^3) and a post-annealing treatment at 800°C for 6 h. Figures 2.14 (d), (e) and (f) belong to a sputtered Er-doped SiO_2 with same Er concentration than the ion-implanted sample, but fabricated using two different targets (SiO_2 and Er_2O_3) in a magnetron sputtering system. An annealing treatment at 950°C for 30 minutes was performed this time. Notice that both samples were treated with a different thermal budget. In particular, the sputtered sample underwent to higher annealing temperature than the implanted one (950°C versus 800°C). Bearing in mind that a higher annealing temperature normally implies larger RE clustering in silicon [26], higher Er clustering could be expected in the sputtered sample. However, TEM images show the opposite, as larger Er clustering is observed in the ion implanted sample. In particular, an average Er cluster size of 4-6 nm is observed for the Er-implanted sample, whereas a smaller mean size of about 2-3 nm is shown in the sputtered layer. Moreover, the implanted layer presents large Er clustering along a well-defined line that corresponds with the ion stopping depth of the Er implantation. On the contrary, Er clustering is randomly distributed in the sputtered sample, with no preferential direction.

---

[5] *All TEM images shown in this dissertation have been provided by the Lens group at the University of Barcelona, led by Dr. Francesca Peiró.*

Therefore, figure 2.14 further confirms the importance of defining a flat Er doping profile in the active layer to avoid clustering. For this particular example, in spite of the fact that Er clustering was observed in both samples, a homogeneous Er distribution within the layer has provided smaller Er clustering compared to the ion implanted sample (mean Er cluster size is reduced by a factor of two). Hence, larger Er emitting fraction is expected in the sputtered layer. Experimental confirmation of this hypothesis will be provided in following sections, where a more detailed analysis on the optoelectronic properties of these layers will be carried out. Despite the evident improvement on Er clustering when performing a homogeneous Er-doping of the active layer, alternative strategies should be inspected to completely avoid Er agglomeration in the active layer.

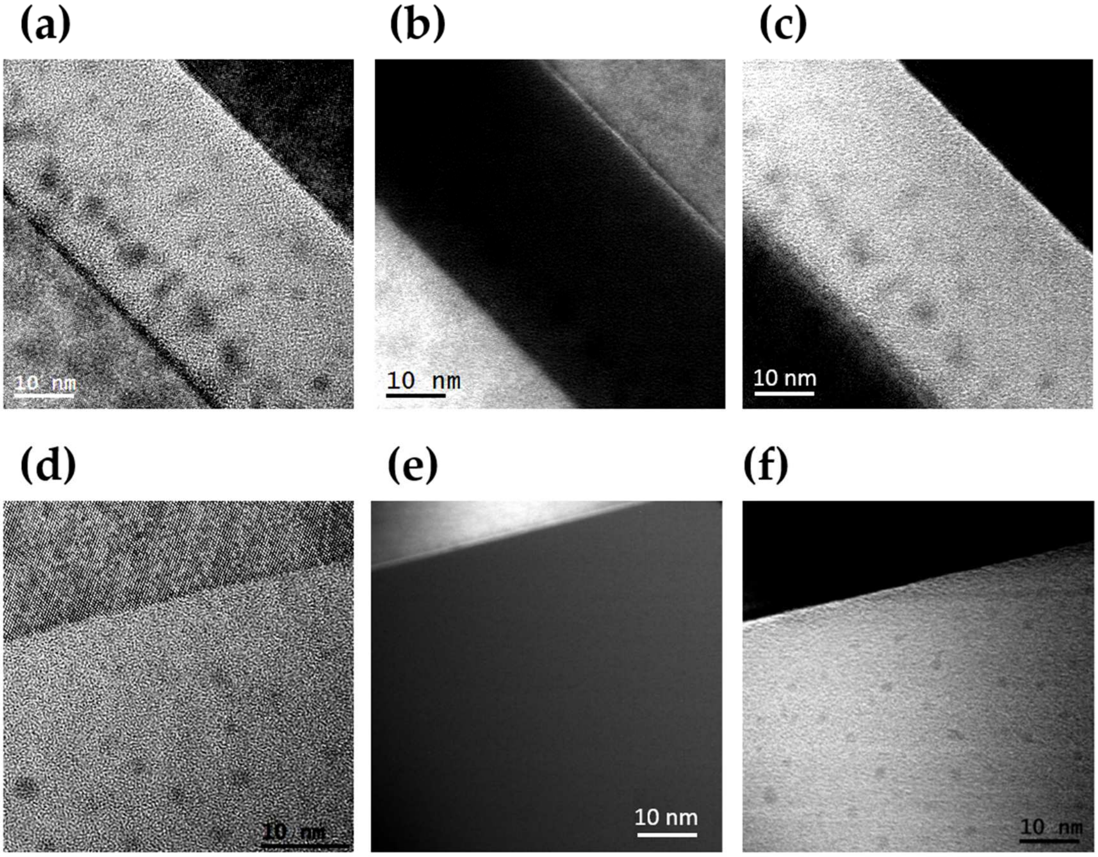

Figure 2.14. TEM characterization of the Er-implanted SiO_2 layer (upper panels, i.e. (a), (b) and (c)) and the Er-doped SiO_2 layer fabricated by cosputtering (lower panels, i.e. (d), (e) and (f)). (a) - (d) panels are HRTEM images of the Er-implanted and sputtered samples, respectively. (b) - (e) correspond to EFTEM images of both samples filtering by the Si plasmon peak (17 eV), and (c) - (f) panels to EFTEM images when filtering by the SiO_2 plasmon peak (23 eV).

Another strategy to improve the fraction of emitting Er^{3+} ions is to modify the host matrix. As it has been shown above, the maximum number of Er^{3+} ions able to allocate in an optically favorable environment is limited by the solubility of the host. Thus, a concentration of 5×10^{20} at./cm^3 seems to be above the solubility limit of Er in a silicon oxide host, stimulating Er clustering. Therefore, it is interesting to investigate other matrices with higher solubility in which Er optical activity is optimized. A plausible solution is to include nitrogen in the host. SiN_x and SiO_xN_y compounds are very interesting since are CMOS compatible materials, have a reduced bandgap with respect to silicon oxides, higher refractive index and are very robust under electrical injection. From the morphological viewpoint, silicon nitrides have higher Er solubility with respect to silicon oxide, and consequently no Er clustering is observed in HRTEM images. In order to illustrate this, figure 2.15 displays an HRTEM image (left) and an EFTEM image (right) filtered by the Si plasmon peak (17 eV) of a uniformly doped Er-Si_3N_4 layer fabricated by co-sputtering, with same fabrication parameters than the above mentioned co-sputtered Er-doped SiO_2. Also, same annealing treatment was performed over the sample, i.e. at 950°C for 30 minutes. As seen, there is no evident Er clustering in the sample in spite of the fact that same Er concentration was measured by SIMS (~ 5×10^{20} at./cm^3).

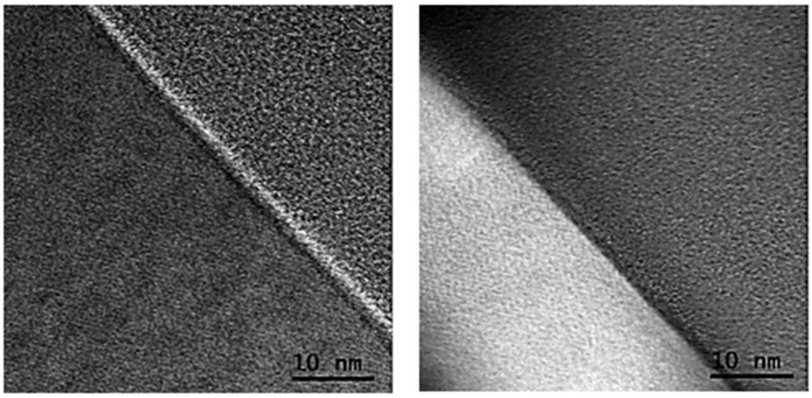

Figure 2.15. HRTEM (left) and EFTEM (right) images of an Er-Si_3N_4 layer fabricated by sputtering.

Thus, it seems that, based on these samples, a nitrogen-based host may be a better candidate to allocate Er^{3+} ions, as higher Er concentration can be implemented in the matrix without evident Er clustering. Nevertheless, it should be stressed that the suitability of these materials as efficient hosts for Er^{3+} ions does not only depend on the observed clustered fraction of Er. Other key points such as the luminescence yield or the electron excitation efficiency must be evaluated. Er^{3+} ions should be allocated on a suitable local environment to yield luminescence. Some works have suggested that Er emission is enhanced via Si=O states [27]. Concerning the excitation efficiency, Si-ncs have been typically used to increase the Er absorption cross-section. It is then interesting to observe the morphological properties of Er-doped SiN_x and SiO_x layers. Figure 2.16 depicts an HRTEM image of an Er-doped SiO_x layer (figure 2.16 (a)) along with an EFTEM image filtered by the crystalline Si plasmon peak at 17 eV of an Er-doped SiO_x

(figure 2.16 (b)) and an Er-doped SiN_x[6] (figure 2.16 (c)) for comparison. Bright spots are observed in EFTEM images, denoting the presence of Si-ncs in both layers. This fact is of relevance since Si-ncs are not always observed in SiN_x samples [28]. In this case however, visible Si-ncs are clearly observed, with a mean diameter of 3-5 nm.

An interesting effect on the Si excess was reported in ref. 29 when studying Tb-doped SiO_x layers. In this work, Tb agglomeration in the form Tb_2O_3 was apparently suppressed in matrices with high Si excess. On the contrary, evident Tb clustering (mean size > 10 nm) occurred in nearly stoichiometric samples. A tentative explanation was proposed based on a lower probability of finding oxygen atoms located in the vicinity of Tb ions in films with high Si excess. Thus, Si-ncs may change the morphology of layers remarkably. Nevertheless, such effect was never observed in our samples. Despite the origin of this divergence remains unclear at the time of this writing, a suitable explanation may be the remarkable differences on the thermal budget used in each case. Forthcoming sections will provide a more detailed discussion on the best host for Er^{3+} ions to maximize luminescence at 1.54 μm.

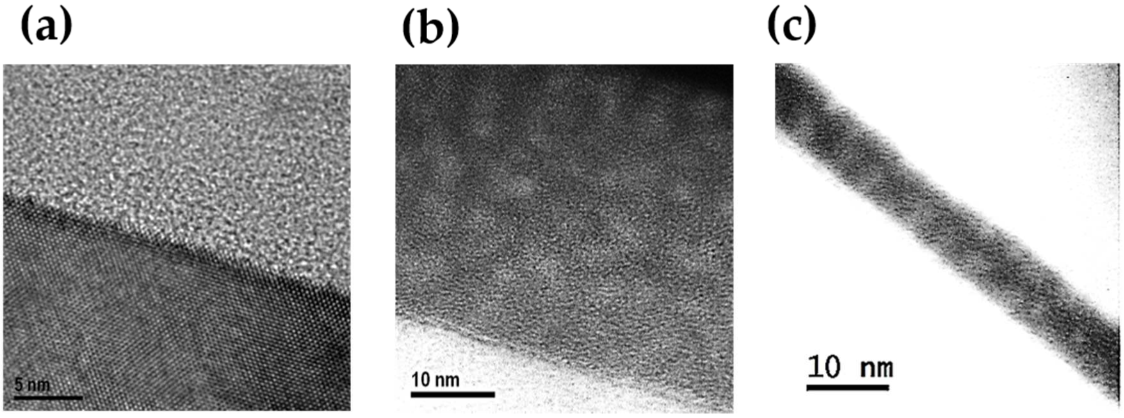

Figure 2.16. TEM characterization showing (a) an HRTEM image and (b) an EFTEM image of an Er-SiO_x layer filtering by the Si plasmon peak. (c) EFTEM image of the Er-SiN_x layer filtered by the Si plasmon peak.

2.4. The Er^{3+} excitation controversy: Energy transfer or direct impact excitation?

This section intends to provide a comprehensive analysis of the main excitation mechanisms of Er^{3+} ions under electrical pumping. There is a large number of published works that ascribe the Er^{3+} excitation in SiO_x (SiN_x) layers to an energy transfer process from Si-ncs to Er^{3+} ions regardless of the excitation source, i.e. a laser beam or an electric field. Being the Er^{3+} excitation mainly governed by energy transfer under optical pumping in Er-SiO_x (SiN_x) layers, it is often assumed that the same process would dominate when electrons replace photons in the excitation process. Nevertheless, there

---

[6] *This image was taken on an Er-doped SiN_x layer with an unexpected thickness of ~ 8 nm.*

are several experimental evidences that point to a completely different scenario. In fact, in the following I will provide consistent reasoning that suggests that Er^{3+} ions are excited by direct impact of hot electrons in most cases, with independence of the host matrix, i.e. SiO_x, SiN_x, SiO_2 or Si_3N_4. Only under limited applied voltage conditions the energy transfer mechanism prevails over direct impact excitation.

First of all, let me recall the most important mechanisms that explain energy migration in a solid host prior to deepen onto the physics of Er-doped Si-based hosts. They can be divided in three main categories:

- **Dipole-dipole interaction (Förster transfer)**

Energy transfer is performed via dipole-dipole interaction. The following formula governs the process [30]:

$$\omega_{Tr}^{Förster} = \omega_{PL}\left(\frac{R_0}{r}\right)^6 \tag{2.34}$$

Where ω_{PL} is the PL rate, R_0 is the distance at which $\omega_{Tr} = \omega_{PL}$, and r is the distance between the two interacting species.

- **Electronic exchange (Dexter transfer)**

This process takes place only when there is an effective wavefunction overlap between the donor and acceptor species. The probability of the event is dominated by a distance-dependent exponential decay function [31]:

$$\omega_{Tr}^{Dexter} = A_0 e^{-\frac{r}{R_D}} \tag{2.35}$$

Being A_0 the transfer probability at the surface of the donor specimen, and R_D the mean interaction distance between donor and acceptor elements.

- **Emission-reabsorption excitation**

This process takes place when the acceptor re-absorbs a photon emitted by the donor element.

As highlighted in the previous chapter, the first consistent evidence of energy transfer between Si-ncs and Er^{3+} ions was reported in 1994 by Kenyon *et al.* [16], and corroborated few years later by researchers in Kobe (Japan) [17]. In their work, they reported an inverse dependence between the PL emission of Si-ncs (centred at 810 nm) and the one of Er^{3+} ions (at 1.54 μm) when the Er concentration is increased. In particular, a gradual decrease of Si-nc PL was observed as a function of the Er concentration, whereas an evident PL enhancement was detected for the Er signal at 1.54 μm. However, probably the most stunning result from this work was the fact that a completely different Er absorption feature was measured in presence of Si-ncs. In particular, a continuous PL excitation spectra was observed in Er:Si-ncs samples, in contrast with the discrete characteristic displayed in Er-SiO_2 layers.

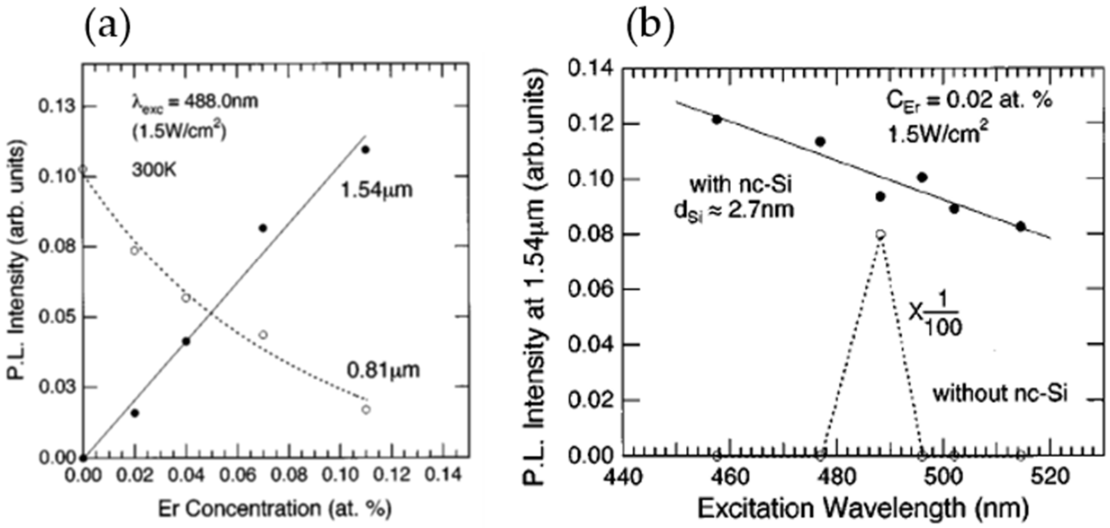

Figure 2.17. Dependence of PL emission from Si-ncs (at 810 nm) and from Er^{3+} ions (1.54 μm) as a function of the Er concentration. (b) Evolution of the PL intensity at 1.54 μm with the laser excitation wavelength. Extracted from [17].

Under electrical pumping however, the excitation mechanism of Er^{3+} ions is quite different and therefore deserves further attention. This time, a continuous electron energy distribution is used to excite Er^{3+} ions and/or Si-ncs instead of a laser beam with discrete and well-controlled photon energies. Therefore, a precise Er^{3+} excitation spectral feature like the one observed in figure 2.17 (b) cannot be obtained under electrical injection. As a consequence, an alternative experiment was set up to provide evidences of the main excitation mechanism of Er^{3+} ions under electrical pumping. Such evidences are based on three main points: (i) the comparison of the Er excitation cross-section between an Er-doped SiO_2 layer and an Er-doped SiO_x layer with same Er concentration, (ii) the study of the time-response EL signal at 1.54 μm upon excitation with different polarization conditions and (iii) the evolution of the EL spectra of higher Er^{3+} energy transitions in the visible range as a function of the applied voltage excitation.

Paper IV summarizes the most relevant results obtained from this study. Two different Er-doped layers were embedded in a MIS structure to investigate the main optoelectronic characteristic: an Er-doped SiO_2 layer grown by dry thermal oxidation and an Er-doped SiO_x layer with 12% of Si excess fabricated by LPCVD. Er^{3+} ions were embedded by ion implantation, with a mean value of 3×10^{20} at./cm^3 measured by Time-Of-Flight Secondary Ion Mass Spectrometry (TOF-SIMS). The first evidence was provided from the direct comparison of the excitation cross-section of Er^{3+} ions in both samples. In order to do that, a unipolar pulsed voltage was applied in samples, switching the device polarization from 0 V to high voltages (V_{input}) above the direct current EL threshold voltage while collecting the EL signal simultaneously.

Figure 2.18 shows the temporal response of the EL signal at 1.54 μm under unipolar pulsed excitation:

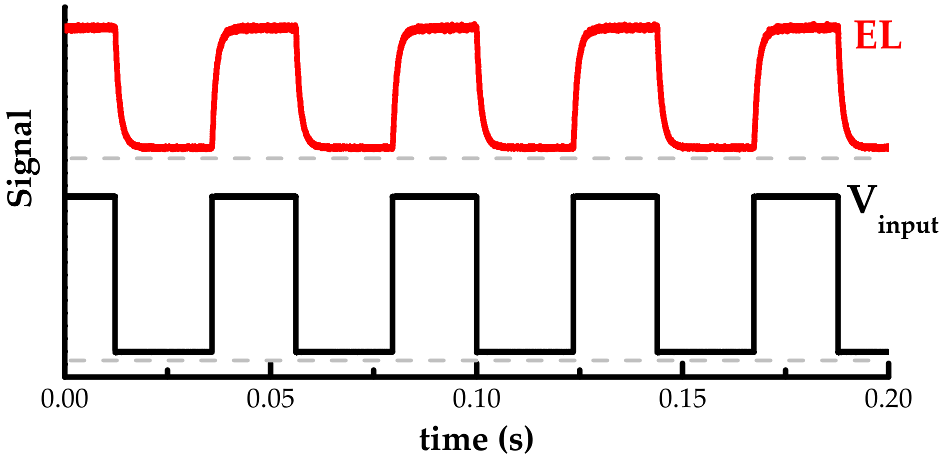

Figure 2.18. EL time-resolved characteristic of an Er-doped SiO$_x$ layer under a unipolar pulsed voltage.

Hence, the rise and decay times of EL signal can be fitted accordingly. The Er^{3+} excitation cross-section was extracted from equation 2.29 when biasing devices at different injected carrier flux values. Surprisingly, a value of ~ 6×10^{-14} cm^2 was obtained in both the Er-SiO$_2$ and the Er-SiO$_x$ layers, suggesting that Si-ncs were not involved in Er^{3+} excitation. Our reported value is in accordance with a previous work from Iacona *et al.* where an Er excitation cross-section of ~1×10^{-14} cm^2 was reported [32]. Therefore, this result suggests that Er^{3+} excitation is governed by direct impact of hot carriers over the conduction band in both samples, regardless of Si-ncs. Also, it is worth to mention that for the calculation of the excitation cross-section, carrier fluxes were maintained as low as possible to avoid non-linear effects in Er excitation such as excited state absorption (ESA). *Paper VI* relates on this effect in similar Er-doped devices. Further details of this study will be provided later on.

To further corroborate the above considerations, a second evidence was provided by comparing the EL signal of the Er-doped SiO$_x$ layer under very specific polarization conditions, i.e. under unipolar and bipolar pulsed polarization. The idea was to discern between two different regimes under electrical pumping: the energy transfer and the direct impact excitation. Other authors have previously demonstrated that it is possible to excite Si-ncs under low voltage conditions via sequential injection of electrons and holes under bipolar pulsed polarization [33]. A very characteristic time-response EL signal is obtained in this case, with two EL overshoots located at the edge of each pulse. Moreover, the overshoot intensity varies depending on the switch due to different tunneling back times for holes and electrons. Therefore, if energy transfer from Si-ncs to Er^{3+} ions takes place in our devices, a very similar EL time-response at 1.54 μm would be expected upon bipolar pulsed excitation. For this new experiment to succeed however, a careful evaluation of the Er^{3+} EL threshold voltage (V_{th}^{EL}) for direct impact excitation was needed. A value of $V_{th}^{EL} = 25$ V was obtained under direct current and unipolar pulsed polarization, respectively. Thus, hot carrier direct impact excitation of Er^{3+} ions provided a measurable EL signal from 25 V on. As a consequence, lower bipolar pulsed voltage values were defined (for instance, ±20 V).

Interestingly, our hypothesis was confirmed, obtaining an Er^{3+} EL time-response at 1.54 μm that strongly resembled the one of Si-ncs at 800 nm when polarizing under bipolar pulsed excitation at ±20 V. Figure 2.19 shows a comprehensive comparison between them:

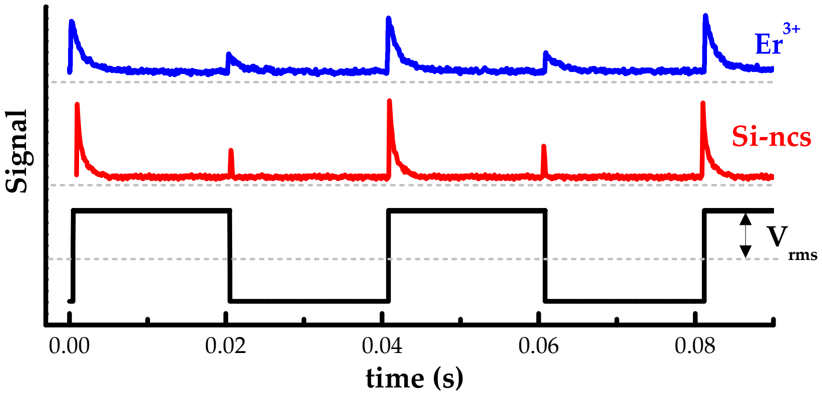

Figure 2.19. EL time-resolved measurements of the Er-SiO$_x$ layer under bipolar pulsed excitation. Black line represents the driving polarization. Red line is EL taken at 800 nm and blue line is the EL taken at 1.54 μm.

The EL phenomena inside Si-ncs under sequential injection is as follows: Starting from positive polarization, electrons are injected from the inversion layer of a MIS structure (with a p-type substrate) into Si-ncs, hence becoming negatively charged. Then, pulsed polarization is switched towards negative voltages, promoting the opposite trend: Substrate majority carriers (holes) injected into Si-ncs. Therefore, electron-hole pairs will be formed in those Si-ncs that still remain negatively charged from the previous cycle. Moreover, quantum confinement will enhance charge retention time, hence boosting the luminescence. Precisely, charge retention times (also called tunneling back times) are the origin of the observed differences in the overshoot intensity when the polarization is switched. Electron retention times inside Si-ncs are known to be shorter than for holes, and therefore injected holes into Si-ncs will find lower number of negatively charged Si-ncs with regard to its counterpart, i.e. electrons being injected into positively charged Si-ncs.

Finally, the third evidence provided in *paper IV* comes from the observation of the visible Er^{3+} spectra under both direct current and bipolar pulsed polarization. Whereas higher radiative energy transitions were observed under DC polarization for $V > V_{th}^{EL}$

(for instance, at -40 V), none of them was measured under bipolar pulsed polarization for $V < V_{th}^{EL}$ (at ±22 V). Only the broad emission typical from Si-ncs and centred at 800 nm was observed in this case. Concerning the infrared emission, both polarization strategies showed the characteristic Er^{3+} emission at 1.54 μm, although the DC emission was more intense by more than two orders of magnitude. Again, such differences can be correlated with two main excitation mechanisms: energy transfer under low voltage bipolar pulsed polarization and direct impact excitation under DC polarization when $V > V_{th}^{EL}$.

A last experiment further corroborated our interpretation. For that, time-resolved measurements under bipolar pulsed polarization were performed around V_{th}^{EL}. Thus, four different square pulses were defined: ±24 V, ±25 V, ±26 V and ±27 V. Noticeably, EL-t characteristic at 1.54 μm shifted from the one shown in figure 2.19 with a sharp overshoot at each voltage switch, to the one of figure 2.18 with an EL feature triggered by the DC value of V_{input}. A clear difference in the Er^{3+} EL rise time is observed, being the one at $V < V_{th}^{EL}$ much shorter than for $V > V_{th}^{EL}$. These results demonstrated the coexistence of two competing excitation mechanisms under bipolar pulsed excitation governed by V_{rms}. These mechanisms would be separated by V_{th}^{EL}, hence being energy transfer dominant for lower voltages, and direct impact excitation from this value and beyond.

It is worth to mention that the same experiment was performed in an Er-doped SiO_2 layer free of Si-ncs. In that case, in spite of the fact that a sharp EL overshoot at 1.54 μm was observed under bipolar pulsed polarization regime below V_{th}^{EL}, it was not correlated with the Er^{3+} emission since a very fast decay time was measured (in the order of few microseconds). Moreover, same EL overshoot was observed at 1300 nm, which is well away from any Er^{3+} related emission. Radiative emission from intraband defects at SiO_2 was ascribed to be the origin of such fast overshoot.

Moreover, an additional study was carried out in order to further insight into the dynamical processes that govern the EL emission by direct hot impact excitation. The aim of this experiment was to determine the effective time that Er^{3+} ions need to be excited by the driving voltage. For that, a unipolar square voltage was defined, with $V_{input} >> V_{th}^{EL}$ (for instance, 40 V). Under these particular conditions, Er^{3+} ions are mainly excited by direct impact of hot carriers, as in figure 2.18. Then, a progressive shortening of T_{on} was carried out while maintaining T_{off} at 3 ms, and the EL-t characteristic was monitored at all time. A summary of results is shown in figure 2.20.

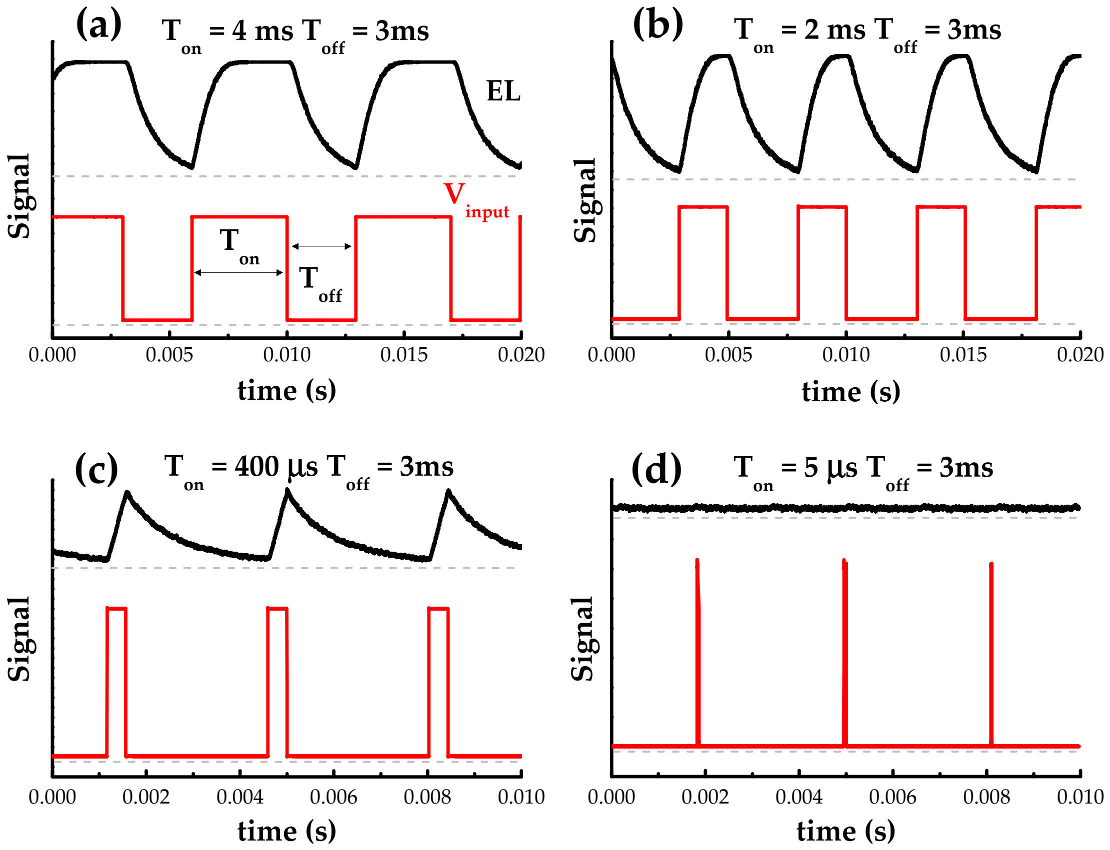

Figure 2.20. EL-t characteristic at 1.54 µm under variable unipolar pulsed voltages with progressive shortening of T_{on}, being T_{off} = 3ms. In particular, with T_{on} = 4 ms (panel a), T_{on} = 2 ms (panel b), T_{on} = 400 µs (c) and finally T_{on} = 5 µs (d). Gray dashed lines mark the zero signal condition.

Figure 2.20 (a) shows the EL-t feature at 1.54 µm upon excitation of a unipolar square voltage with T_{on} = 4 ms and T_{off} = 3 ms. As can be observed, EL rises and reaches saturation for a period of time before it decays again when the voltage is switched off. Typical Er^{3+} rise and decay times in the order of 1 ms were identified. EL saturation shortens in figure 2.20 (b), where T_{on} has been reduced by a half (2 ms). Even in figure 2.20 (c) some EL emission is observed for T_{on} = 400 µs. However, Er^{3+} emission is completely suppressed for a T_{on} = 5 µs and T_{off} = 3 ms (figure 2.20 (d)), which suggests the lack of evident hot electron injection in the active layer. Therefore, the above example demonstrates that hot electrons need of a certain period of time to excite Er^{3+} ions.

A second paper published on this topic provided further insight on the energy transfer dynamics between Si-ncs and Er^{3+} ions (*paper V*). This time, the Er-doped SiO_x layer was compared with an Er-free SiO_x layer. Fabrication parameters are similar to the previous paper, except that for a much longer annealing time for the present devices (~ 14 h instead of 1 h). The paper is divided in two main sections: a first part, in which the optoelectronic properties are tested and compared in DC polarization, and a second section where a frequency sweep is performed under bipolar pulsed excitation. The first part served to evaluate the similarities between both devices under DC polarization. Er-doped SiO_x devices showed higher resistivity than the ones free of Er. The reason relies on the fact that Er implantation also introduces deep defect sites positively charged that are susceptible to trap electrons, producing a 'screening effect' for incoming carriers. In addition, visible spectra further confirmed the appearance of Er^{3+} high energy peaks as described previously. It is worth noting that device emission was observable at the naked eye under daylight conditions, displaying a reddish luminescence for Er-free Si-ncs devices and green luminescence for Er-doped SiO_x devices.

An interesting figure of merit is the one that displays the external quantum efficiency (EQE)[7] as a function of injected current. A maximum value of 0.5% is obtained under low injection regime (the highest value reported by then), which decreases down to 0.05% for the highest injected current (100 μA). Such deterioration of EQE can be correlated with an enhanced charge trapping phenomena due to the rapid aging of devices when current injection is raised. Bearing in mind that direct impact excitation governs the EL signal under DC polarization, new defects will be created upon hot carrier injection. Such defects will trap charges in the vicinity of luminescent centres (i.e. Si-ncs or Er^{3+} ions), screening incoming hot carriers and hence diminishing the number of excitation events per second. Nevertheless, the keystone of this paper lies in the dynamic study performed on the Er-Si-nc coupled system. Bipolar pulsed excitation was swept from low frequency values (10 Hz) up to 100 kHz in both devices, showing efficient switching of the Er^{3+} excitation mechanism for the Er-doped SiO_x device. Moreover, two different bipolar pulsed voltages were defined: ± 25 V, which was below V_{th}^{EL}, and a moderate voltage above this value, i.e. ± 35 V.

First evidence came up from direct comparison of EL frequency evolution of Er-doped SiO_x devices between two different bipolar pulsed voltages, at ± 25 V and at ± 35 V. Whereas energy transfer was observed in the entire range of frequency values under low voltage excitation (± 25 V), the moderate voltage polarization (± 35 V) showed two well defined behaviors: direct impact excitation under low frequency regime (up to 800 Hz), and energy transfer from this point on. Notice that this value roughly coincides with the inverse of Er^{3+} emission lifetime (~ 1 ms), which explains the switching mechanism since Si-ncs have faster decay times (few μs). For low driving frequencies (below 800 Hz), both Si-ncs and Er^{3+} can excite and de-excite in consecutive excitation pulses. On the contrary, only Si-ncs are able to follow the driving frequency in a range from 800 Hz to 100 kHz, hence being the energy transfer from Si-ncs to Er^{3+} ions mainly limited by the non-radiative dynamics of excited Er^{3+} ions. This interpretation was further supported by inspecting the line-shape of visible EL spectra. Whereas high Er^{3+} radiative transitions were clearly observed in the low frequency domain, a broad feature typical from Si-ncs arised at high driving frequency values. Moreover, the evolution of the EL at 1.54 μm as a function of the root mean square voltage for two different

---

[7] *This parameter will be defined in the following section.*

frequency values (10 Hz Vs 10 kHz) denoted a different EL-V dependence which was associated to either energy transfer or direct impact excitation.

Table 2.2 summarizes the main Er excitation mechanisms observed depending on polarization conditions:

	DC polarization	**Bipolar pulsed excitation**	
	-	**f < 1 kHz**	**100 kHz > f > 1 kHz**
$V_{th}^{EL} > V$	None	Transfer	Transfer
$V_{th}^{EL} < V$ (moderate voltages)	Direct impact	Direct impact	Transfer
$V_{th}^{EL} <<< V$ (high voltages)	Direct impact	Direct impact	Direct impact

Table 2.2. Summary of dominant excitation mechanisms as a function of the driving frequency and the applied voltage.

Finally, the second-order EL properties of Er-doped SiO_x layers were tested under high pumping regime. For that, DC polarization was applied over devices at different current density values until device breakdown, while collecting visible EL spectra. *Paper VI* illustrates the main results extracted from this experiment. A linear trend in the EL-J characteristic of each Er^{3+} radiative transition was observed for low-moderate injected current density values. On the contrary, super-linear behavior of the $^4S_{3/2} \rightarrow {}^4I_{15/2}$ radiative transition at 550 nm (2.25 eV) emerged under high injection regime, revealing the onset of up-conversion processes in our devices. In particular, excited state absorption (ESA) was unambiguously identified. In our case, ESA occurs when two excited Er^{3+} ions in the $^4I_{11/2}$ level (~ 1.26 eV) interact with each other, resulting in a non-radiative relaxation of one of them to the ground state ($^4I_{15/2}$), followed by the promotion of the other one to an energy level that doubles the former excited state, i.e. from $^4I_{11/2}$ transition (~ 1.26 eV) to $^4F_{7/2}$ transition (~ 2.54 eV). Then, the excited Er^{3+} ion is relaxed to the metastable transition $^4S_{3/2}$ from which radiative emission at 550 nm (~ 2.25 eV) takes place. Such non-linear effect can be easily identified in a log-log graph in which the EL intensity at 550 nm (~ 2.25 eV) is plotted as a function of the EL at 984 nm (~ 1.26 eV), as shown below. It is worth to mention that this mechanism effectively limits the radiative emission at 1.54 µm since excited Er^{3+} ions, which may potentially decay to the first excited level ($^4I_{13/2}$) an emit a photon at 1.54 µm, are sent towards higher excited states with the subsequent radiative emission at undesired wavelengths (550 nm instead of 1.54 µm in our case).

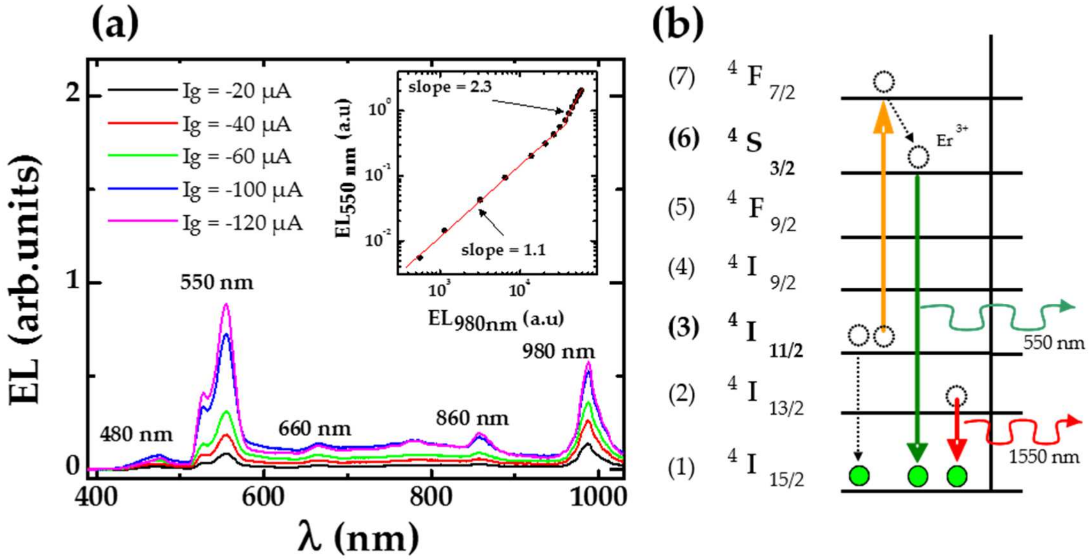

Figure 2.21. (a) Visible Er^{3+} EL transitions at different current values. The inset shows the EL emission at 550 nm (2.25 eV) as a function of the EL at 984 nm (1.26 eV). (b) Er^{3+} energy diagram displaying the ESA process, from left to right: An excited Er^{3+} ion at $^4I_{11/2}$ de-excites non-radiatively, transferring its energy E_1 to a neighbor ion in the same excited state, hence being promoted to $^4F_{7/2}$ state with energy $E_2 = 2 \cdot E_1$. Then, the ion de-excites non-radiatively to the metastable transition $^4S_{3/2}$, and finally relaxes to ground state ($^4I_{15/2}$) emitting a photon at 550 nm. Red arrow at the right symbolizes the radiative relaxation of an excited Er^{3+} ion in the first excited state ($^4I_{13/2}$) when no ESA processes are involved.

Consequently, an exhaustive evaluation of second-order optical effects in Er-doped dielectric matrices is also required to determine the suitability of a particular Er-doped medium to develop efficient light emitting devices working at telecom wavelengths. Despite this drawback, such perturbation of linearity only dominates under high current injection regime where our Er-doped devices are unstable and close to the device breakdown.

Apart from ESA, another non-linear effect was identified in our devices when pumped under electrical excitation. Concretely, auger processes were observed under DC polarization. Visible EL emission at 800 nm from Er-free devices containing well passivated Si-ncs (SiO_x layers) seemed to be far more vulnerable to auger quenching than SiO_x layers passivated at lower temperatures. Similarly, Er^{3+} EL emission at 1.54 μm from Er-doped SiO_x devices proved to be also insensitive to auger phenomena. Three devices containing different active layers were compared in this case: two Er-free SiO_x layers, annealed for 1 h at 1100°C and at 900°C respectively, and an Er-doped SiO_x layer annealed for 1 h at 900°C (see *paper VI* for further details on the fabrication process). Time-resolved measurements were performed in all devices, applying a unipolar pulsed voltage with $V_{input} >> V_{th}^{EL}$.

Remarkable differences in the EL-t characteristic of Er-free SiO_x layers was observed. A comparison between these two samples is provided in Figure 2.22:

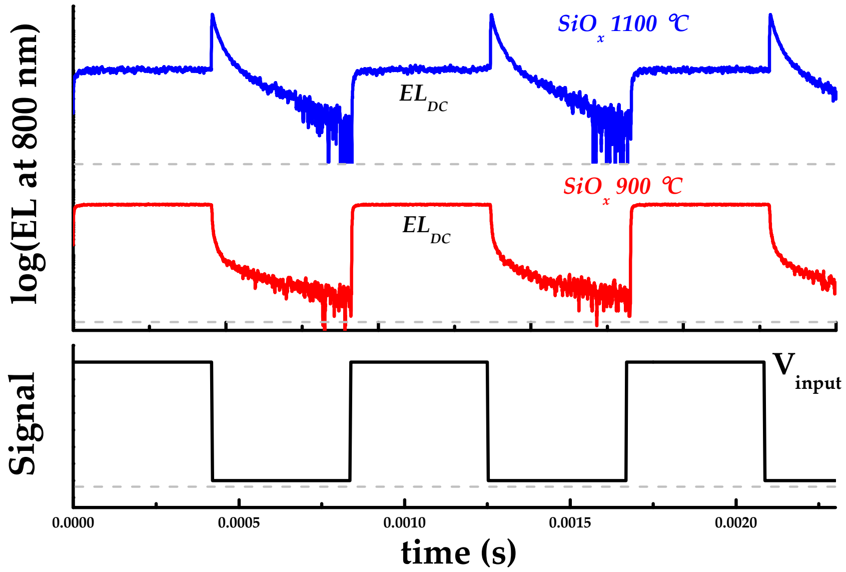

Figure 2.22. EL-t signal of two Er-free SiO$_x$ layers annealed at 900°C (red line) and at 1100°C (blue line). Bottom signal depicts the driving voltage of both layers.

As seen, sharp EL overshoots are observed when V_{input} is switched off in the SiO$_x$ layer annealed at 1100°C, but not in the sample annealed at 900°C. It is worth to remark that under these polarization conditions, EL is produced by direct impact excitation of hot injected carriers over the conduction band since $V_{input} >> V_{th}^{EL}$. Consequently, the observed EL overshoot cannot be attributed to sequential carrier injection unlike in figure 2.19, where the electrical pumping was driven by a bipolar pulsed injection with $V_{input} < V_{th}^{EL}$. Moreover, if sequential carrier injection would take place, another EL overshoot should be observed at the V_{input} switch on, which is not the case in figure 2.22. Consequently, it seems logical to attribute the EL overshoot observed in the SiO$_x$ layer annealed at 1100°C either to auger quenching or to impact excitation of confined e-h pairs in Si-ncs. Both processes occur when additional carriers (mostly electrons in our case) interfere with an exciton confined in a Si-nc either via energy absorption or by impact ionization of the confined e-h pair.

Thus, SiO$_x$ layers polarized under hot injection regime (as in figure 2.22) would present a DC EL signal governed by two competing mechanisms: from one side, hot electron injection would excite Si-ncs by direct impact excitation, creating a large number of e-h pairs. On the other hand however, the fact that hot electrons are continuously injected in the SiO$_x$ motivates auger quenching (or impact ionization) of previously excited Si-ncs that still contain excitons suitable to recombine radiatively. Therefore, the only moment at which none of these quenching processes takes place is at the voltage switch off. At this precise moment, hot electron injection is suppressed and consequently all generated excitons in Si-ncs can recombine radiatively with no external perturbation by incoming hot electrons. It is worth noting that this effect is remarkable in the SiO$_x$

layer annealed at 1100°C since there is a difference of more than one order of magnitude between the DC EL signal and the EL overshoot (see figure 2.22).

On the contrary, no EL overshoot is observed in the SiO_x layer annealed at 900°C. The reason relies on the fact that a much shorter excitonic radiative recombination lifetime is expected for this particular annealing temperature. In fact, the absence of EL overshoot in this sample suggests that such radiative lifetime is even shorter than the time needed to remove hot injected electrons from the layer when the voltage is switched off. As a consequence, almost all the excited Si-ncs are able to recombine before hot carriers are removed from the SiO_x layer and therefore no EL overshoot is displayed in the EL-t feature. In order to validate this assertion, the mean radiative lifetime was measured in both Er-free SiO_x layers.

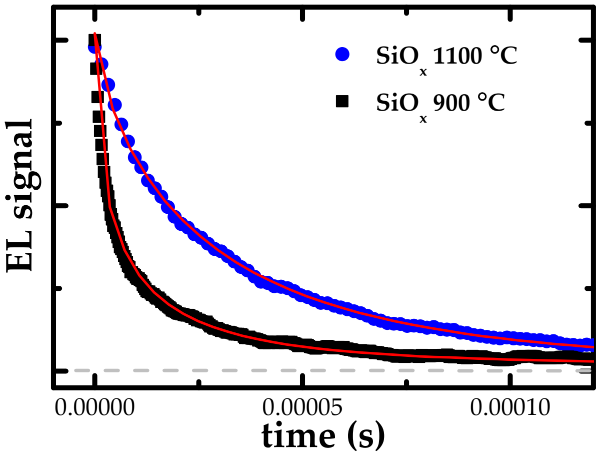

Figure 2.23. Normalized EL-t characteristic for devices containing SiO_x layers annealed at 900°C (black squares) and at 1100°C (blue dots). EL decay of sample SiO_x 1100°C has been taken from the maximum of the EL overshoot.

Figure 2.23 depicts the fitting of normalized EL decay times of both Er-free layers using a stretched exponential function, which reads [34]:

$$EL(t) = EL_{DC} \cdot exp\left(-\left(\frac{t}{\tau} \right)^{\beta} \right) \tag{2.36}$$

Where EL_{DC} is the EL intensity under DC polarization, τ is the effective emission lifetime of Si-ncs and β is a fitting parameter between 0 and 1. Whereas β is comprised between 0.5 and 1 in most cases, τ may display a wide range of values from few microseconds to hundreds of microseconds for well passivated Si-ncs. In our case, a value of $\tau \sim 3\ \mu s$ was obtained for the SiO_x layer annealed at 900°C, and $\tau \sim 30\ \mu s$ for the one annealed 1100°C. It is worth to mention that our setup characteristic response time is about few microseconds (between 1-5 μs). Therefore, we cannot discard the lifetime of the SiO_x layer annealed at 900°C to be much faster than τ ~ 3 μs. Precisely, such experimental limitation impedes us to measure the lifetime of hot injection in the SiO_x

layer annealed at 1100°C after the voltage switch off, i.e. the time needed to sweep out injected charge (in absence of setup limitations, it would correspond to the rise time of the EL overshoot). In any case, these values differ by one order of magnitude at least, which is in close agreement with our previous interpretation.

On the other hand, no EL overshoot was observed in the Er-doped SiO_x layer, suggesting that quenching phenomena by hot electron injection does not considerably affect the emission of Er^{3+} ions in a wide range of values. Only under high current injection regime the EL becomes modulated by second order effects (see figure 2.21). Moreover, on the basis of these results, we could speculate on the fact that quenching phenomena does only affect EL emission of well-passivated Si-ncs but not Er^{3+} ions. A plausible explanation would be a much larger excitation cross-section in Si-ncs compared to Er^{3+} ions. A value of $\sigma_{exc}^{Si\text{-}ncs} \sim 4\times10^{-13}$ cm² and $\sigma_{exc}^{Er} \sim 5\times10^{-14}$ cm² was reported in *paper VI* for Si-ncs and Er^{3+} ions, respectively.

The above argumentation also explains the evolution of integrated EL intensity as a function of frequency. *Paper VI* compares the EL-f characteristic for both Er-free layers (figure 3). The sample annealed at 1100°C shows a remarkable EL signal improvement of about one order of magnitude when driven with a unipolar pulsed voltage at 20 kHz with respect to the EL_{DC} value (30 V in this case). From this frequency on, the integrated EL signal slightly decays with the frequency. On the other hand, the sample annealed at 900°C does not improve with regard to EL_{DC} due to the fact that no EL overshoot arises at the voltage switch off. In order to better understand the evolution of the EL-f feature in the SiO_x layer annealed at 1100°C, time-resolved measurements were performed at three different representative frequency values: 1 kHz, 20 kHz and 50 kHz. Figure 2.24 shows the measured EL-t response:

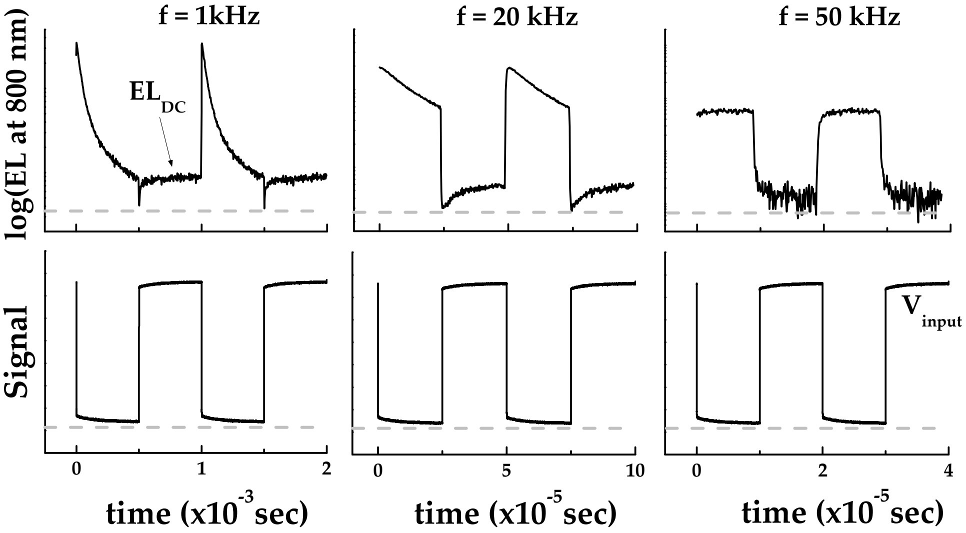

Figure 2.24. Time-resolved EL at 800 nm (top panels) and driving voltage (bottom panels) for an Er-free SiO_x sample annealed at 1100°C polarized at three different frequencies. From left to right: at 1 kHz, at 20 kHz and at 50 kHz.

As can be observed, the EL-t signal driven at 1 kHz (left panels) shows well defined EL overshoots at the voltage switch off. Interestingly, the EL signal rapidly drops to zero when the voltage is switched on, hence displaying the typical rise time of Si-ncs until the EL_{DC} saturation level. Then, the cycle is repeated and the EL overshoot emerges again. A similar sequence is shown when the driving frequency is increased up to 20 kHz (centre panels). This time however, a more evident auger quenching phenomena is displayed, as the EL intrinsic decay trend of Si-ncs becomes abruptly interrupted at the voltage switch on. Finally, EL-t at 50 kHz is shown (right panels). At this point, two linked processes diminish the EL signal. Firstly, V_{input} is only triggered by a short period of time (10 μs) which is lower than the effective EL rise time (~ 20 μs) of Si-ncs. As a consequence, a smaller number of Si-ncs will be excited compared to previous driving frequency values, where EL_{DC} was achieved. Secondly, the T_{off} semi-cycle is small enough to impede the EL overshoot to intrinsically decay, hence rapidly quenching the signal shortly after its maximum intensity. As a consequence, a square-like line shape is observed in the EL-t characteristic. This latter figure unambiguously correlates the hot electron injection with the quenching phenomena that take place in the EL emission of well-passivated Si-ncs.

Thus, the main Er^{3+} excitation mechanisms under electrical pumping have been discussed. A series of experiments were designed to identify the origin of Er^{3+} excitation, displaying two complementary mechanisms that depend on the driving polarization. In addition, other non-linear phenomena occurring in our devices have been revisited, providing consistent evidences that support our interpretations. The most relevant conclusions derived from this section have been taken into account in following designs of light emitting device architectures later explained in this dissertation.

2.5. Quantifying Er^{3+} excitation under electrical pumping: A first order calculation

Similarly to the optical case, it is very interesting to quantify the number of Er^{3+} ions that contribute to luminescence under electrical excitation. This time however, a different procedure will be used. For the optical case, the number of emitting Er^{3+} ions was obtained combining time-resolved measurements with rate equations. Another suitable approach consists in the direct comparison of the optical power generated by the external excitation with the emitted optical power of the ideal case scenario in which the 100% of Er^{3+} ions is emitting. Such calculation method was intentionally avoided when exciting Er^{3+} ions under optical pumping due to the expected inaccuracy of several fundamental parameters such as: (i) the collected fraction of the internally generated emission, (ii) the absorption depth of the excitation laser source, and (iii) the area of the excitation laser beam. On the contrary, this methodology becomes more 'doable' under electrical excitation, since only the first point should be tackled. Hence, this section will describe a comprehensive procedure to calculate the total number of emitting Er^{3+} ions in a planar MIS device under electrical pumping.

First of all however, it is necessary to introduce some important definitions commonly used in planar LEDs:

- **Internal quantum efficiency (IQE)**

This term correlates the number of photons generated in the active layer per second and the number of injected electrons in the active layer per second. It is an intrinsic parameter that only depends on the active layer itself and not on the device design. To some extent, it could be considered as the analogous of the quantum yield in PL measurements. The number of generated photons is calculated by dividing the internally generated optical power in the active layer ($P_{opt\ int}$) by the energy of a single photon ($h\nu$). Similarly, the number of injected electrons is obtained by dividing the current (I) by the elementary charge (e):

$$\eta_{IQE} = \frac{P_{opt\,\mathrm{int}}/(h\nu)}{I/e} \tag{2.37}$$

It is worth to mention that a careful evaluation of the layer morphology should be performed if a direct comparison of IQE values between two different luminescent layers wants to be realized. In order to establish a fair comparison, the total number of potential luminescent centres ($N_{LC,total}$) should be the same in both layers. In ion-implanted samples, this number is provided by $N_{LC,total} = D \cdot A$, where D is the implantation dose and A the area of the device [26]. Thus, IQE of samples with different implantation doses and/or different areas could be compared provided that $N_{LC,total}$ (sample 1) = $N_{LC,total}$ (sample 2). This number also applies to homogenously doped samples, although this time the implantation dose should be replaced by the product of atomic concentration and layer thickness.

- **Outcoupling efficiency (Outc)**

This parameter is very important in light emitting devices. It denotes the ratio between the number of photons emitted into free space per second and the number of photons generated in the active layer per second. Contrary to IQE, outcoupling efficiency is considered an extrinsic parameter as it strongly depends on the device design. The formula reads:

$$\eta_{outc} = \frac{P_{opt}/(h\nu)}{P_{opt\,\mathrm{int}}/(h\nu)} \tag{2.38}$$

Where P_{opt} is the externally emitted optical power into free space. In spite of the fact that Outc can be directly derived from the ratio between P_{opt} and $P_{opt\ int}$ in all the studied devices in this dissertation, such relation is not always preserved in commercial light emitting devices where down-converting phosphor coatings are usually designed. A typical example are white light emitting devices based on GaN, in which the yellow emission from a phosphor coating is combined with the intrinsic blue light provided by the GaN layer to produce white light emission. In this case, P_{opt} and $P_{opt\ int}$ have to be divided by different photon energy values.

- **External quantum efficiency (EQE)**

This term evaluates the efficiency of light extraction of a given light emitting device. From a conceptual viewpoint, is very similar to the IQE, but replacing the internally generated optical power in the active layer by the externally emitted optical power into free space (P_{opt}). Also, it could be directly calculated by multiplying the above described factors, i.e. the IQE and the Outc:

$$\eta_{EQE} = \frac{P_{opt}/(h\nu)}{I/e} = \eta_{IQE} \cdot \eta_{Outc} \tag{2.39}$$

Equally than the IQE, the same consideration have to be assumed if two devices with different morphology are to be compared.

- **Power efficiency or wallplug efficiency (PE)**

This value performs a direct evaluation of the electrical-to-optical power conversion efficiency. It correlates the emitted optical power into free space with the electrical power provided:

$$\eta_{PE} = \frac{P_{opt}}{I \cdot V} \tag{2.40}$$

In order to obtain the number of excited Er^{3+} ions under electrical excitation, the internally generated optical power should be calculated first. For that, the following expression will be used:

$$f_{\text{Opt. Power}} = \frac{P_{Opt}}{P_{Opt\,\text{int}}} \cdot \frac{P_{collected}}{P_{Opt}} = \frac{P_{collected}}{P_{Opt\,\text{int}}} \quad \Rightarrow \quad P_{Opt\,\text{int}} = \frac{P_{collected}}{f_{\text{Opt. Power}}} \tag{2.41}$$

Where $f_{Opt.Power}$ is the fraction between the collected optical power by the objective ($P_{collected}$) and the internally generated optical power in the active layer ($P_{Opt\ int}$). Whereas a calibrated experimental setup provides $P_{collected}$ directly, $f_{Opt.Power}$ should be carefully calculated assuming two conditions: (i) the maximum solid angle collected by the objective ($\theta_{collected}$), and (ii) the optical transmittance of the top electrode. Figure 2.25 depicts a sketch of the collection setup for a planar Er-doped light emitting device composed by a polysilicon electrode, an Er-doped SiO_2 layer, and an aluminum back electrode.

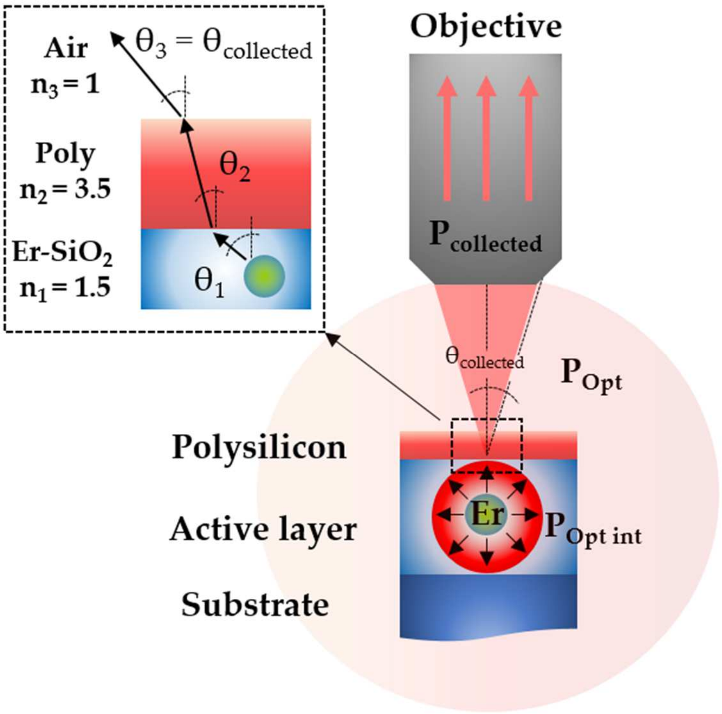

Figure 2.25. Collection scheme of a planar device containing luminescent Er3+ ions. The magnified region shows the pathway of an escaping photon emitted from the active layer. Dimensions are not scaled.

Assuming an isotropic emission pattern of Er^{3+} ions, the $f_{Opt.Power}$ of a punctual light source will be given by [35]:

$$f_{Opt.Power} = \frac{P_{collected}}{P_{opt\,int}} = T(\lambda) \cdot \frac{2\pi r^2 (1-\cos(\theta_1))}{4\pi r^2} \tag{2.42}$$

Where *T(λ)* is the transmittance of the top electrode (polysilicon) at the emission wavelength, i.e. 154 μm and *r* is the radius of the emitting sphere. The collection angle can be obtained from the numerical aperture (*NA*) of the objective:

$$NA = n \cdot \sin(\theta_{collected}) \tag{2.43}$$

Where *n* is the refractive index of the collection medium (air in this case). Bearing in mind that NA = 0.4, a value of $\theta_{collected} = 23.6°$ is obtained. According to Snell's law and the nomenclature of figure 2.25, θ_1 can be calculated:

$$\frac{\sin(\theta_2)}{\sin(\theta_3)} = \frac{n_3}{n_2} \quad \Rightarrow \quad \sin(\theta_2) = \frac{1}{3.5} \cdot \sin(23.6^\circ) \Rightarrow \theta_2 = 6.6^\circ \tag{2.44}$$

$$\frac{\sin(\theta_1)}{\sin(\theta_2)} = \frac{n_2}{n_1} \quad \Rightarrow \quad \sin(\theta_1) = \frac{3.5}{1.5} \cdot \sin(6.6^\circ) \Rightarrow \theta_1 = 15.6^\circ \tag{2.45}$$

Thus, the second term of equation 2.42 is:

$$\frac{2\pi \cdot \left(1-\cos\left(15.6^\circ\right)\right)}{4\pi} = 0.037 \tag{2.46}$$

The transmittance of the polysilicon at 1.54 μm has been calculated assuming a single interference model, non-polarized light, normal light beam incidence ($\theta = 0°$) and a non-absorbing material:

$$T = T_{polysilicon-air} \cdot T_{activelayer-polysilicon} = \frac{4n_2n_3}{\left(n_2+n_3\right)^2}\frac{4n_1n_2}{\left(n_1+n_2\right)^2} = 0.58 \tag{2.47}$$

Being $n_1 = 1.5$, $n_2 = 3.5$ and $n_3 = 1$. Hence, according to above calculation, the 58% of light is transmitted through the polysilicon top electrode. In order to validate this number, the experimental transmittance of a 100 nm thick polysilicon layer deposited on a fused silica substrate has been measured. Results are shown in figure 2.26:

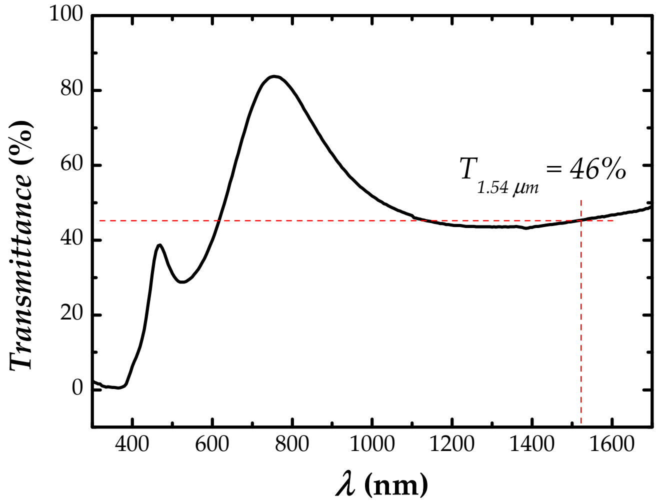

Figure 2.26. Transmittance spectrum of a 100 nm thick polysilicon layer. Dashed lines mark the transmittance at 1.54 μm.

As can be observed, the experimental transmittance is lower than the above calculated value (46% instead of 58%), denoting that multiple interference and absorption effects may not be negligible for this particular case. Taking into account that the energy of Er^{3+} emission is lower than silicon bandgap (0.8 eV versus 1.1 eV), a small absorption coefficient is expected for polysilicon. Therefore, the discrepancy between the calculated transmittance and the measured one is expected to originate from the fact that multiple interference modeling has not been assumed in equation 2.47.

Finally, the ratio between the collected optical power and the internally generated optical power can be obtained by multiplying the two factors of equation 2.42:

$$f_{Opt.Power} = \frac{P_{collected}}{P_{opt\,\mathrm{int}}} = 0.46 \cdot 0.037 = 0.017 \approx 0.02 \tag{2.48}$$

Therefore, of about the 2% of the internally generated optical power is collected by the experimental setup. Finally, the internally generated optical power is:

$$P_{opt\,\mathrm{int}} = \frac{P_{collected}}{0.02} \tag{2.49}$$

It is worth to remark that escaping light that has previously been emitted downwards and then reflected by the back aluminum electrode has not been taken into account. A more precise calculation could be accomplished including this back reflection term.

Once the internal optical power is calculated, the percentage of excited Er^{3+} ions is extracted by dividing $P_{opt\,int}$ by the total optical power obtained from equation 2.33:

$$Excited\ Er^{3+}\ ions\,(\%) = \frac{P_{Opt\ int}}{W_{opt}^{100\%}} \cdot 100 \tag{2.50}$$

This value will automatically deliver the number of excited Er^{3+} ions with respect to the total number of luminescent ions in the matrix.

Apart from the total optical power generated in the active layer, another interesting calculation commonly used to evaluate the suitability of a particular design is the abovementioned outcoupling efficiency, Outc. In fact, there are several works which are entirely devoted to this subject [36-38]. Among them, probably the most popular approaches are the ones that include either antireflecting coatings [35], electrode patterning or coupled photonic crystals to enhance light extraction [39]. In this dissertation, the first option has been adopted to improve light extraction of devices when required. Let's first consider the simplest case depicted in figure 2.1, where not one of the above mentioned strategies has been performed to enhance light extraction. Whereas the first term of equation 2.42 will not vary, i.e. the polysilicon transmittance, the second term should be redefined to account for the critical angle from which light generated in the active layer gets trapped in the device, i.e. $\theta_3 = 90°$:

$$\frac{sin\left(\theta_2^{critic}\right)}{sin\left(\theta_3^{critic}\right)} = \frac{n_3}{n_2} \quad \Rightarrow sin\left(\theta_2^{critic}\right) = \frac{1}{3.5}\,sin\left(90^\circ\right) \Rightarrow \quad \theta_2^{critic} = 16.6^\circ \tag{2.51}$$

Similarly, θ_1^{critic} will be given by:

$$\frac{sin\left(\theta_1^{critic}\right)}{sin\left(\theta_2^{critic}\right)} = \frac{n_2}{n_1} \quad \Rightarrow \quad sin\left(\theta_1^{critic}\right) = \frac{3.5}{1.5} \cdot sin(16.6^\circ) \Rightarrow \theta_1^{critic} = 41.8^\circ \tag{2.52}$$

Therefore, a light beam emitted at an angle higher than 41.8° by a punctual light emitter in the active layer will not be transmitted into free space, hence becoming totally reflected by the top polysilicon electrode. Finally, the outcoupling efficiency will be given by:

$$\eta_{\mathrm{Outc}} = \frac{P_{Opt}}{P_{opt\,\mathrm{int}}} = 0.46 \cdot \frac{2\pi \cdot \left(1 - \cos\left(41.8^\circ\right)\right)}{4\pi} \qquad \Rightarrow \quad \eta_{\mathrm{Outc}} = 0.058 \approx 0.06 \tag{2.53}$$

Thus, only the ~ 6% of the generated light in the active layer is able to escape into free space. Therefore, a direct correlation between the collected optical power and the emitted optical power can be obtained:

$$P_{opt\,\mathrm{int}} = \frac{P_{collected}}{0.02} = \frac{P_{Opt}}{0.06} \Rightarrow \frac{P_{collected}}{P_{Opt}} = \frac{1}{3} \tag{2.54}$$

Only one third of the total emitted optical power is collected by our particular experimental setup.

Now, consider a new device design in which an antireflecting coating (ARC) has been fabricated to improve light extraction. In particular, a bilayer composed by a Si_3N_4 and a SiO_2 has been deposited on top of the polysilicon layer. Being the refractive index values of Si_3N_4 and SiO_2 n = 2 and n = 1.5 respectively, such design is expected to enhance light extraction as it will diminish the high refractive index contrast between polysilicon (n = 3.5) and air (n = 1). Figure 2.27 shows a TEM cross-section image of the multilayered system. Starting from the bottom, a 50 nm thick Er-doped SiO_2 layer is observed. Then, a polysilicon electrode is deposited, with a mean thickness of 86 nm. Although this number slightly differs from the expected nominal value (100 nm), remarkable differences in the transmittance spectrum are not expected. Finally, a 45 nm thick Si_3N_4 and a 35 nm SiO_2 are deposited to function as ARC.

In order to calculate the Outc of the new device design, the new light escape cone is calculated. Then, starting from the SiO_2-air interface, we can define the critical angle from which generated light will not escape into free space:

$$\sin\left(\theta_4^{critic}\right) = \frac{n_{air}}{n_{SiO2}} \Rightarrow \theta_4^{critic} = 41.8^\circ \tag{2.55}$$

Similarly, at the SiO_2-Si_3N_4 interface:

$$\sin\left(\theta_3^{critic}\right) = \sin\left(\theta_4^{critic}\right)\frac{n_{SiO2}}{n_{Si3N4}} \Rightarrow \theta_3^{critic} = 30^\circ \tag{2.56}$$

And at the Si_3N_4-polysilicon interface:

$$\sin\left(\theta_2^{critic}\right) = \sin\left(\theta_3^{critic}\right)\frac{n_{Si3N4}}{n_{poly}} \Rightarrow \theta_2^{critic} = 16.6^\circ \tag{2.57}$$

And finally, at the polysilicon-active layer interface:

$$\sin\left(\theta_1^{critic}\right) = \sin\left(\theta_2^{critic}\right)\frac{n_{poly}}{n_{active\ layer}} \Rightarrow \theta_1^{critic} = 41.8^\circ \tag{2.58}$$

As seen, the ARC does not modify the critical light escape angle with respect to the uncoated device (see equation 2.52).

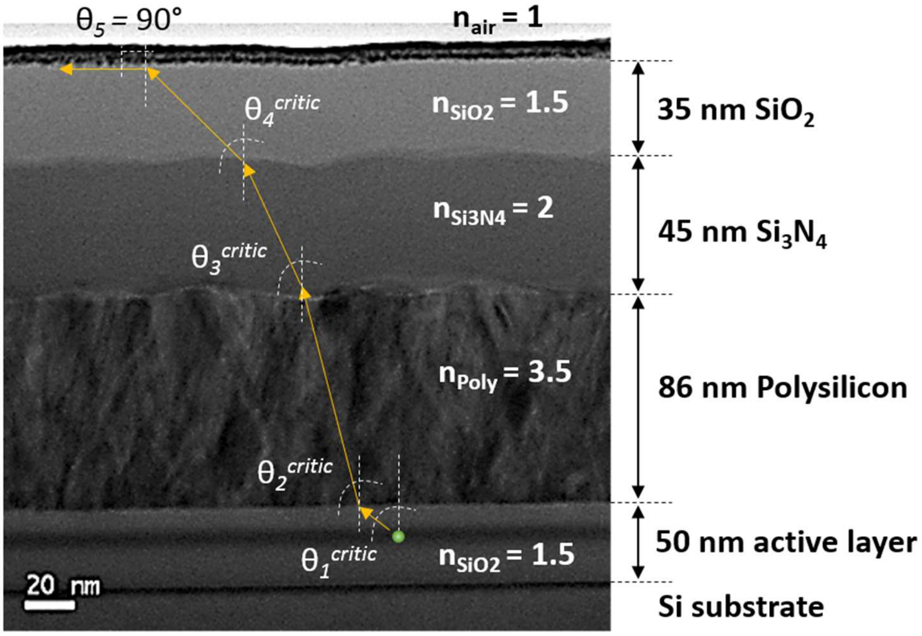

Figure 2.27. TEM image of an Er-SiO$_2$ device containing an ARC. In a top-to-down cross-section exploration: the SiO$_2$ and Si$_3$N$_4$ layers (ARC), the polysilicon layer (top electrode), the Er-SiO$_2$ layer (Notice the horizontal dark line corresponding to Er clustering) and finally the Si substrate (p-type). The critical light pathway from which photons will not escape from the device is symbolized with dark yellow arrows.

Accordingly, the transmittance of the polysilicon-ARC system has to be also obtained. This time however, experimental measurements are not available. In view of the significant divergence between the measured transmittance and the calculated one when using single interference equations (see figure 2.26), a more realistic modelling has been performed assuming multiple interference phenomena. In this framework, the ratio between transmitted and incident intensity is defined by:

$$\frac{I_t}{I_i} = \frac{1}{1+F\sin\left(\frac{\delta}{2}\right)^2} \quad , \quad \text{Where} \quad F = \frac{4R}{(1-R)^2} \quad \text{and} \quad R = \left|\frac{n_1 - n_2}{n_1 + n_2}\right|^2 \tag{2.59}$$

Applying the above equations to each interface, the following values are provided:

- At the active layer-polysilicon interface: $\frac{I_t}{I_i} = 0.93$ (2.60)
- At the polysilicon-Si$_3$N$_4$ interface: $\frac{I_t}{I_i} = 0.76$ (2.61)
- At the Si$_3$N$_4$-SiO$_2$ interface: $\frac{I_t}{I_i} = 0.99$ (2.62)
- At the SiO$_2$-air interface: $\frac{I_t}{I_i} = 0.99$ (2.63)

The transmittance of the whole system reads: $T = 0.93 \cdot 0.76 \cdot 0.99 \cdot 0.99 = 0.69$ (2.64)

Therefore, the outcoupling efficiency of the ARC device is:

$$\eta_{Outc}^{ARC}=\frac{P_{Opt}^{ARC}}{P_{opt\,\mathrm{int}}}=0.69\cdot\frac{2\pi\left(1-\cos\left(41.8^\circ\right)\right)}{4\pi}\quad\Rightarrow\quad\eta_{Outc}^{ARC}=0.088\approx0.09\tag{2.65}$$

Hence, the ~ 9% of the internally generated optical power in the active layer is extracted into free space. This value corresponds to a light extraction enhancement of about 50% with respect to the uncoated device, which was 6%.

Therefore, in spite of the fact that the critical angle of emission remains unchanged when including the ARC in our Si-based MIS devices, the transmittance is enhanced remarkably (from 46% to 69%). This fact has to be taken into account when the generated optical power in ARC devices is calculated in our experimental setup. Back to equation 2.48 where the fraction of collected optical power is obtained, the new fraction of collected optical power will be given by:

$$f_{Opt.Power}^{ARC}=\frac{P_{collected}^{ARC}}{P_{opt\,\mathrm{int}}}=T^{ARC}(\lambda)\cdot\frac{2\pi r^2\left(1-\cos\theta_{collected}\right)}{4\pi r^2}=0.69\cdot0.042=0.029\approx0.03\tag{2.66}$$

And subsequently:

$$P_{opt\,\mathrm{int}}=\frac{P_{collected}^{ARC}}{0.03}\tag{2.67}$$

As a consequence, the collected optical power of the ARC device is about the ~ 3% of the internally generated optical power. The following table compares the main parameters obtained in both devices (uncoated and with ARC):

	Uncoated device (figure 2.25)	**Device with ARC (figure 2.27)**
Escaping light cone, θ_{critic} (°)	41.8	41.8
Transmittance, T (%)	46	69
Fraction of collected optical power, $f_{opt.Power}$ (%) [8]	2	3
Fraction of emitted optical power into free space, P_{opt} (%)	6	9

Table 2.3. Summary of important parameters to quantify light emission in Er-doped MIS devices. These values correspond to an active layer with n = 1.5.

In order to illustrate the above theoretical considerations with a practical example, the number of excited Er^{3+} ions and layer efficiency will be calculated in three different devices, each one containing one of the above shown active layers: (i) an Er-implanted

---

[8] *This parameter, unlike the other ones shown in table 2.3, depends on the collection system used.*

SiO_2 (figures 2.14 (a), (b) and (c)), (ii) a sputtered layer of Er-doped SiO_2 (figures 2.14 (d), (e) and (f), and (iii) a sputtered layer of Er-doped Si_3N_4 (figure 2.15). The active layer is 50 nm thick in all devices. Nevertheless, only the device containing the Er-implanted SiO_2 layer has been coated with an antireflecting coating to improve outcoupling efficiency.

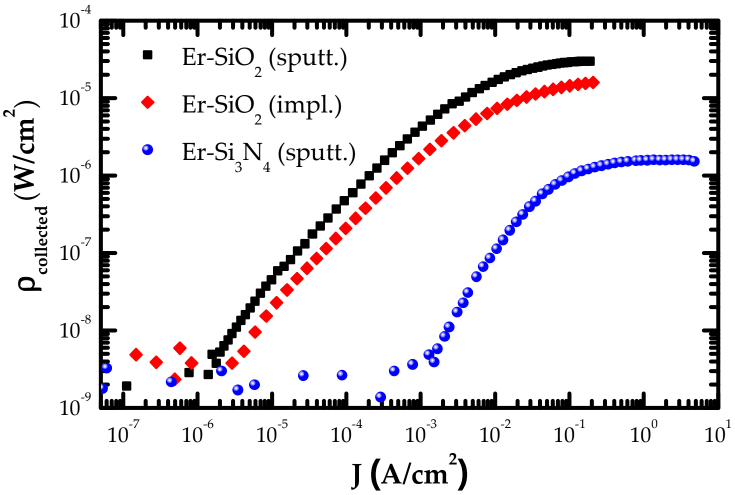

Figure 2.28. Collected optical power density as a function of the injected current density for three layers under study. A sputtered Er-SiO_2, an ion-implanted Er-SiO_2 and finally a sputtered Er-Si_3N_4.

Figure 2.28 shows the collected optical power density-current density curve for each device from the EL threshold until the device breakdown. Thus, assuming the previous mathematical development, the internally generated optical power will be given by equation 2.49:

$$P_{Opt\ \mathrm{int}}^{\mathrm{Er\text{-}SiO_2}}\ (\mathrm{sputt.}) = \frac{3\cdot 10^{-5}\ \mathrm{W}/\mathrm{cm}^2}{0.02} = 15\cdot 10^{-4}\ \mathrm{W}/\mathrm{cm}^2 \tag{2.68}$$

$$P_{Opt\ \mathrm{int}}^{\mathrm{Er\text{-}SiO_2}}\ (\mathrm{impl.}) = \frac{1.6\cdot 10^{-5}\ \mathrm{W}/\mathrm{cm}^2}{0.03} = 5.2\cdot 10^{-4}\ \mathrm{W}/\mathrm{cm}^2 \tag{2.69}$$

For the Er-Si_3N_4 layer, we have to recalculate the critical angle from the light escape cone. Applying equation 2.52, a value of $\theta_{critic} = 30°$ was obtained. As this number is still higher than the maximum collection angle by the objective ($\theta_{collected} = 23.6°$), the same correction will be used to obtain the internally generated optical power:

$$P_{Opt\ \mathrm{int}}^{\mathrm{Er\text{-}Si_3N_4}}\ (\mathrm{sputt.}) = \frac{1.6\cdot 10^{-6}\ \mathrm{W}/\mathrm{cm}^2}{0.02} = 8\cdot 10^{-5}\ \mathrm{W}/\mathrm{cm}^2 \tag{2.70}$$

And the maximum total optical power generated in the active layer, according to equation 2.33:[9]

$$W_{opt}^{100\%} \big/ cm^2 = \frac{5\cdot 10^{20}\cdot 50\cdot 10^{-7}\cdot 6.626\cdot 10^{-34}\cdot 3\cdot 10^{10}}{1.54\cdot 10^{-4}\cdot 10^{-2}} = 32\,\mathrm{mW}\big/\mathrm{cm}^2 \tag{2.71}$$

Thus, the fraction of excited Er^{3+} ions in each device is (equation 2.50):

$$P_{Opt\,\mathrm{int}}^{\mathrm{Er\text{-}SiO_2}}\,(\mathrm{sputt.}) = \frac{15\cdot 10^{-4}}{32\cdot 10^{-3}}\cdot 100 = 4.5\,\% \tag{2.72}$$

$$P_{Opt\,\mathrm{int}}^{\mathrm{Er\text{-}SiO_2}}\,(\mathrm{impl.}) = \frac{5.2\cdot 10^{-4}}{32\cdot 10^{-3}}\cdot 100 = 1.6\,\% \tag{2.73}$$

$$P_{Opt\,\mathrm{int}}^{\mathrm{Er\text{-}Si_3N_4}}\,(\mathrm{sputt.}) = \frac{8\cdot 10^{-5}}{32\cdot 10^{-3}}\cdot 100 = 0.25\,\% \tag{2.74}$$

Therefore, the Er-SiO_2 layer fabricated by sputtering is the one that shows higher number of excited Er^{3+} ions, of about 4.5%. This number is three times higher than in the implanted Er-SiO_2 layer, and exceeds the excited Er^{3+} fraction in Si_3N_4 by a factor of 18. These numbers suggests that sputtered Er-SiO_2 layers with homogeneous distribution of Er^{3+} ions are the best candidates to provide bright EL devices, rather than ion implanted samples. This conclusion is in agreement with the previous section in which smaller Er clustering was observed in the sputtered layer (see figure 2.14). Concerning the Er-Si_3N_4 layer, remarkable lower percentage is obtained compared to SiO_2. This time, such poor Er^{3+} excitation fraction cannot be attributed to Er clustering since it was not observed in TEM images (see figure 2.15). Instead, the low fraction of excited Er^{3+} ions in Si_3N_4 is ascribed to a higher trapping de-trapping rate in silicon nitride due to intra-band defect states. Being Si_3N_4 a highly defective matrix, injected electrons into the conduction band are rapidly trapped by intra-band defect sites, strongly decreasing the electron free path in the conduction band and consequently the probability of impact excitation of Er^{3+} ions.

It is worth to recall that one of the unnegotiable conditions required to succeed on the realization of an injected Er-doped Si laser is the population inversion, i.e. at least 50% of excited Er^{3+} ions. Despite the fact that the calculated values obtained in the current example are far from this milestone, I may note that several approximations have been performed and consequently these numbers should be taken as a first order approximation uniquely. A systematic error of about 20% is expected in the fraction of excited Er^{3+} ions. Therefore, only the relative comparison between samples in which a similar estimation has been carried out provides reliable conclusions. In basis of this consideration, subsequent optimized samples fabricated over the course of this work have shown considerable improvement of the Er^{3+} excited fraction. For instance, a

---

[9] *A radiative time of 10 ms has been considered, similarly than in ref. 25.*

fraction of 15% is reported in *paper VIII*, where a second run of sputtered Er-SiO_2 devices have been fabricated with a homogeneous Er concentration of 1×10^{20} at./cm^3 instead of 5×10^{20} at./cm^3. Also in ref. 40, a value of 50% is estimated. This value is, to the best of my knowledge, the higher fraction of excited Er^{3+} ions ever reported in silicon-based light emitting devices under electrical pumping. In this case, the device active layer is formed by a bilayer structure composed by a SiO_xN_y layer and an Er-implanted SiO_2 layer with an expected Er percentage of 1.5%. Moreover, a higher fraction of excited Er^{3+} ions in SiO_2 compared to Si_3N_4 is also provided, in agreement with the results derived from figure 2.28.

An important figure of merit of Si-based light emitting devices is the one that correlates the emitted optical power density ($\rho_{emitted}$) with the injected current density (J). In fact, this new figure has been obtained multiplying the curves presented in figure 2.28 by a factor of 3 for Er-SiO_2 devices, which is the ratio between the emitted optical power into free space (6% of $P_{opt\ int}$) and the collected optical power (2% of $P_{opt\ int}$). Similarly, the optoelectronic feature of the Er-Si_3N_4 layer in figure 2.28 should be multiplied by a factor of 3/2. After these considerations, a direct evaluation of the EQE value can be carried out at a first glance:

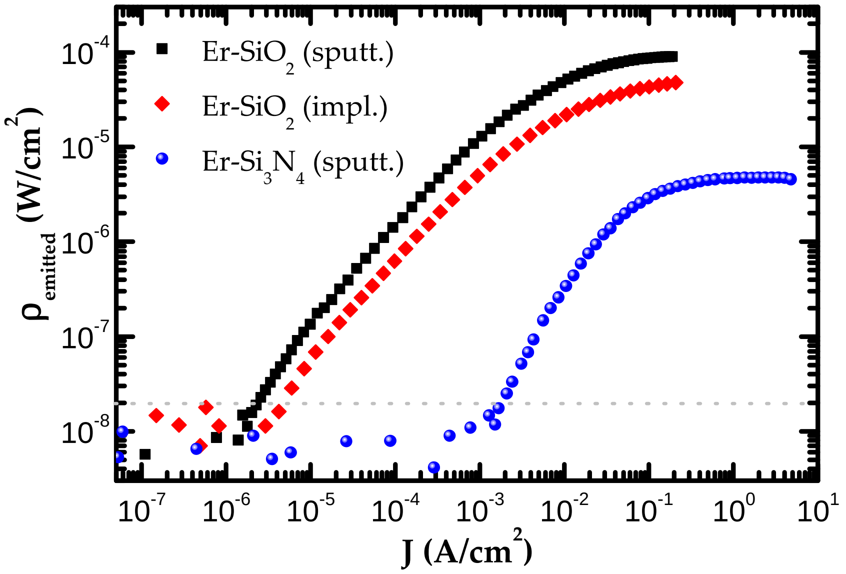

Figure 2.29. Emitted optical power density as a function of injected current density for the three layers under study: A sputtered Er-SiO_2, an ion-implanted Er-SiO_2 and finally a sputtered Er-Si_3N_4.

Notice that all devices show two different regimes, depending on the injected current: (i) under low-medium current injection, the EL raises monotonically according to a power law, and (ii) under high current injection, the optical power density saturates, leading to a maximum emitted optical value before the device breakdown. In the power law regime, the dependence between the optical power density and current density is governed by:

$$\rho_{Opt} = J_0^{dark} \cdot J^n \tag{2.75}$$

Where J_0^{dark} stands for the 'dark' current density range in which no EL signal is detected, and n corresponds to the power exponent. In Er-doped SiO_2 devices, J_0^{dark} lies in the range of 1-10 μA/cm^2, and n ~ 1. Whereas, Er-doped Si_3N_4 devices show remarkably higher dark current values, in the order of mA/cm^2, with a power factor of n ~ 1.3. Noticeably, such values already evidence remarkable differences in the excitation dynamics of Er^{3+} ions between SiO_2 and Si_3N_4 hosts. There is more than two orders of magnitude difference in the EQE values. Bearing in mind that EQE is often taken at the EL threshold value:

$$EQE = \frac{\rho_{Opt}^{th} \big/ h\upsilon}{J_0^{dark} \big/ e} \tag{2.76}$$

A maximum value of ~ 1% is delivered by the Er-sputtered SiO_2 device, ~ 0.6% for the Er-implanted SiO_2 device and ~ 0.001% for the Er-sputtered Si_3N_4 device. These numbers evidence that Er^{3+} ions are excited more efficiently in SiO_2 than in Si_3N_4. Similarly, the power exponent reveals that EQE is maintained for a wide range of current injection in Er-SiO_2 hosts until saturation onset, whereas an EQE enhancement is observed in Er-Si_3N_4 hosts. In particular, EQE raises from 0.001% at the EL threshold up to 0.005% at J = 0.024 A/cm^2. The physical interpretation of this effect is the following: Under low current injection regime, most of the Si_3N_4 intraband defect states are empty and consequently a considerable percentage of injected charge is subsequently trapped by them. In this scenario, the mean electron free path in the conduction band becomes highly reduced, hence diminishing the probability of excitation of Er^{3+} ions. As the charge injection is increased, a gradual fulfillment of trapping sites takes place (trap-filled limit), reducing the trapping probability and stimulating incoming charge to flow over the conduction band for a longer distance and therefore exciting Er^{3+} ions more efficiently. As seen in figure 2.29, this effect is less relevant in SiO_2 hosts since they contain considerable lower number of defects compared to Si_3N_4.

A closer look into the high current injection regime of devices, i.e. when the saturation of ρ_{Opt} becomes evident, suggests that either all the electrically excitable Er^{3+} ions are emitting or that new non-radiative conductive paths are being created as a consequence of the high electric field applied. As already explained, this latter fact can diminish the power factor consistently. In fact, after analyzing hundreds of devices under different polarization conditions, we are almost certain that such saturation is mostly due to a degradation of the excitation efficiency. Figure 2.29 also outlines a higher current injection tolerance in the Er-Si_3N_4 device with respect to Er-SiO_2, and also a lower fraction of excited Er^{3+} ions. This effect is reproducible and has been observed in a large variety of samples fabricated by different deposition techniques, suggesting that SiO_2 is a better host that Si_3N_4 to excite Er^{3+} ions under electrical pumping. This last remark is directly connected with the next section, which provides a comprehensive discussion about the most suitable host for Er^{3+} excitation.

2.6. Debating the best Si-based host for Er^{3+} ions

In view of the previous discussion, it has been clearly demonstrated that the Er^{3+} EL emission in MIS devices presents many subtle nuances that strongly depend not only on the device design and the layer morphology, but also on the driving polarization. Among them however, and from the humblest author's viewpoint, probably the most important factor that must be considered to develop an Er-doped Si-based light emitting device stands for the correct chose of the Er^{3+} host. To some extent, one could identify similarities with the trade and production philosophy, in which the prospects for success are most times conditioned to a proper development of raw materials. In our case, finding an optimum Er host raw material from both the optical and the electrical viewpoint will maximize the chances of success in the race to develop Er-doped Si-based light emitting devices.

From the electrical viewpoint, it has been previously shown in section 2.2 that the inclusion of Si-ncs in either Er-SiO_x or Er-SiN_x layers increases layer conductivity by several orders of magnitude (figure 2.10). Consequently, a silicon-rich layer aiming at a specific current density value can be driven at considerably lower DC voltages compared to its stoichiometric analogous layer. Thus, the inclusion of Si excess in the Er host seems advantageous from the electrical viewpoint. Moreover, Si excess helps to drain trapped charge from the active layer, which enhances the device operation lifetime [41]. Inspecting at the optoelectronic feature however, a trade-off is observed since a gradual deterioration of efficiency takes place when a larger amount of Si excess is incorporated.

Figure 2.30 shows the EQE values at 1.54 μm of the Er-SiO_x samples presented in figure 2.10 as a function of either the applied electric field (figure 2.30 (a)) or the Si excess (figure 2.30 (b)). The most efficient device is the one containing an Er-doped stoichiometric SiO_2 layer, displaying a value of ~ 1%. On the other hand, the device containing 16% of Si excess showed the worst EQE (~ 0.01%), two orders of magnitude lower than the one of Er-doped SiO_2. Remarkably, the semi-log plot of figure 2.30 (b) displayed a linear trend between EQE and Si excess. Other authors have already reported on the detrimental effect of Si-ncs on the Er^{3+} EL emission, and attributed this effect to an efficient scattering of hot injected electrons by negatively charged Si-ncs [42].

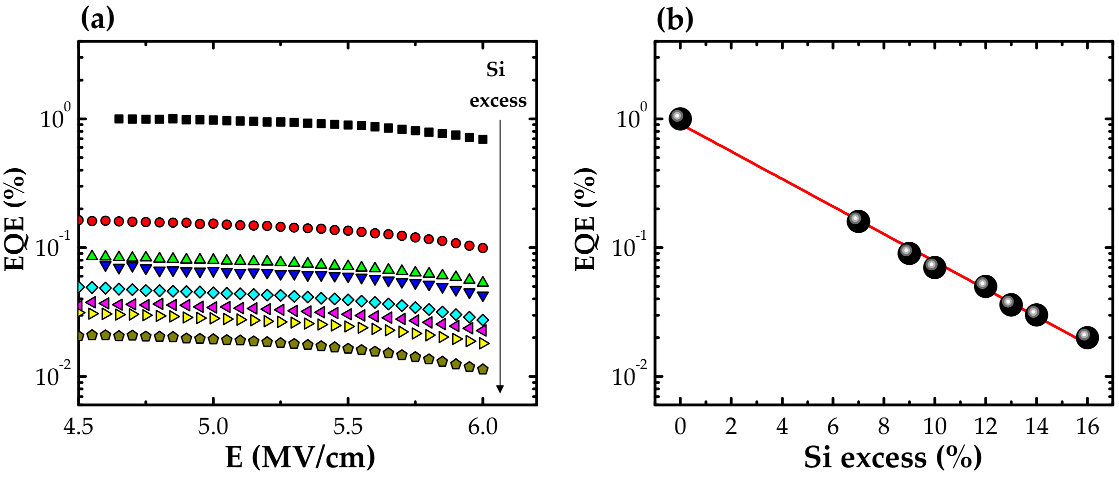

Figure 2.30. EQE at 1.54 µm of various Er-SiO$_x$ layers containing different Si excess as a function of *E* (a) and the Si excess (b). A straight line in (b) has been drawn to guide the eye. Further insight on the electrical properties of these layers has been provided in figure 2.10.

Thus, despite reducing V_{th}^{EL} and improving device operation lifetime due to a better charge release in the active layer, Si-ncs also impede efficient excitation of Er^{3+} ions by direct impact excitation. A similar characteristic is observed in Er-doped SiN$_x$ devices. *Paper VII* further inspects on this issue. It is worth to mention that although there are several works in literature that focus on the role of Si excess in the electrical and optoelectronic properties of SiO$_x$ films [18, 43], not many of them perform a comprehensive study in SiN$_x$ layers. Therefore, four different co-sputtered Er-doped SiN$_x$ films were investigated, each one with a different Si excess of 12%, 16%, 20% and 40% (see *paper VII* for more details on the fabrication process). Firstly, the electrical properties were uncovered, whose details have been already discussed in section 2.2 (see figure 2.10). In few words, considerable increase of layer conductivity for higher Si excess was observed. Also, the main charge transport mechanism (P-F conduction) was preserved regardless of the Si excess. Nevertheless, the most important message of *paper VII* comes from the correlation between the electrical and optoelectronic phenomena, depicting a singular scenario in which a multi-variable relation between layer conductivity, power efficiency, trapped charge density and Si excess is suggested. An optimum Si excess of 16% that balances both electrical and optical properties of Er-SiN$_x$ layers is reported. In addition, *paper VII* also points to direct impact of hot electrons as the main excitation mechanism of Er^{3+} ions, similarly than in Er-SiO$_x$ and Er-SiO$_2$ layers. Arguments in favor are: (i) a diminution of the EQE with the Si excess, (ii) a direct correlation between E and power efficiency, providing higher efficiency for larger E values, and (iii) the fact that Er-SiN$_x$ light emitting devices show lower efficiency values compared to their Er-SiO$_x$ counterpart, since lower number of hot electrons are present in nitride-based hosts showing a bulk-limited conduction [44].

A second work on this topic (*paper VIII*) was performed to provide a quantitative analysis of the EL efficiency of Er^{3+} ions in different Si-based hosts. The direct comparison between three Er-doped devices containing different hosts (namely a SiO_2, a Si_3N_4 and a SiN_x) allowed us to draw conclusions on the most suitable active layer. The I-V characteristic was inspected, revealing the expected charge transport trend for SiO_2 and Si_3N_4 hosts, i.e. TAT+FNT in the first case and PF conduction in the other (see figure 2.8). However, SiN_x showed a deviation in charge transport phenomena from previously studied off-stoichiometric layers, since the fitting of PF conduction model provided a meaningless relative permittivity with values well above the Si relative permittivity, i.e. $\varepsilon_r > 12$.[10] Thus, alternative models were inspected. Among them, the one that better adjusted our experimental curve with reasonable fitting parameters was optimum channel field emission. In this process, charge transport takes place through preferential conduction pathways created by intraband localized states [3]. On the other hand, Er-doped SiO_2 layers displayed higher EQE values than nitride-based hosts of at least three orders of magnitude, in concordance with figure 2.29. Moreover, the excitation cross-section of Er^{3+} ions in different hosts was extracted. A value of $\sigma_{exc} = 3\times10^{-14}$ cm^2 was calculated for the Er-SiO_2, $\sigma_{exc} = 3\times10^{-16}$ cm^2 for Er-Si_3N_4 and finally $\sigma_{exc} = 1\times10^{-15}$ cm^2 for the Er-SiN_x layer.[11]

Moreover, important conclusions were drawn from this study. For instance, the fact that nitride-based hosts enhance layer conductivity and reduce V_{th}^{EL} compared to silicon oxide hosts. This is remarkable for device applications, especially in integrated photonics were low voltages are mandatory in CMOS technology. On the other hand, the low V_{th}^{EL} value is paid by lower Er^{3+} excitation efficiency also, which showed its maximum value in the Er-SiO_2 host. A last figure is presented to better illustrate the excitation efficiency in a set of devices with various Si-based hosts and fabricated by different techniques. In particular, figure 2.32 shows the EL-J characteristic of three oxide-based layers and three nitride-based layers, all of them doped with Er^{3+} ions and fabricated either by sputtering or by ion implantation. As seen, Er-SiO_2 shows the best efficiency, followed by the Er-SiO_x, the Er-Si_3N_4 and finally the Er-SiN_x layer. Concerning the device lifetime, a reversed order was observed, being the device containing the Er-SiN_x layer the most reliable and the device with the Er-SiO_2 layer the one that displayed lower device operation times.

---

[10] *The reader may note that this layer belongs to a second batch of samples that were fabricated with exactly the same parameters than the previous run from which paper VII was published. Therefore, there is not a well-funded explanation of the origin of such discrepancies on the electronic transport with regard to previously studied layers. Anomalous processing errors during device fabrication in run 2 lies out of the scope of the author.*

[11] *Notice that higher EQE and σ_{exc} values were obtained in the Er-SiN_x layer compared to Er-Si_3N_4. This result was unique for this sample, as the inclusion of Si excess normally deteriorates the optoelectronic performance of devices. The origin of such unexpected performance is still under investigation.*

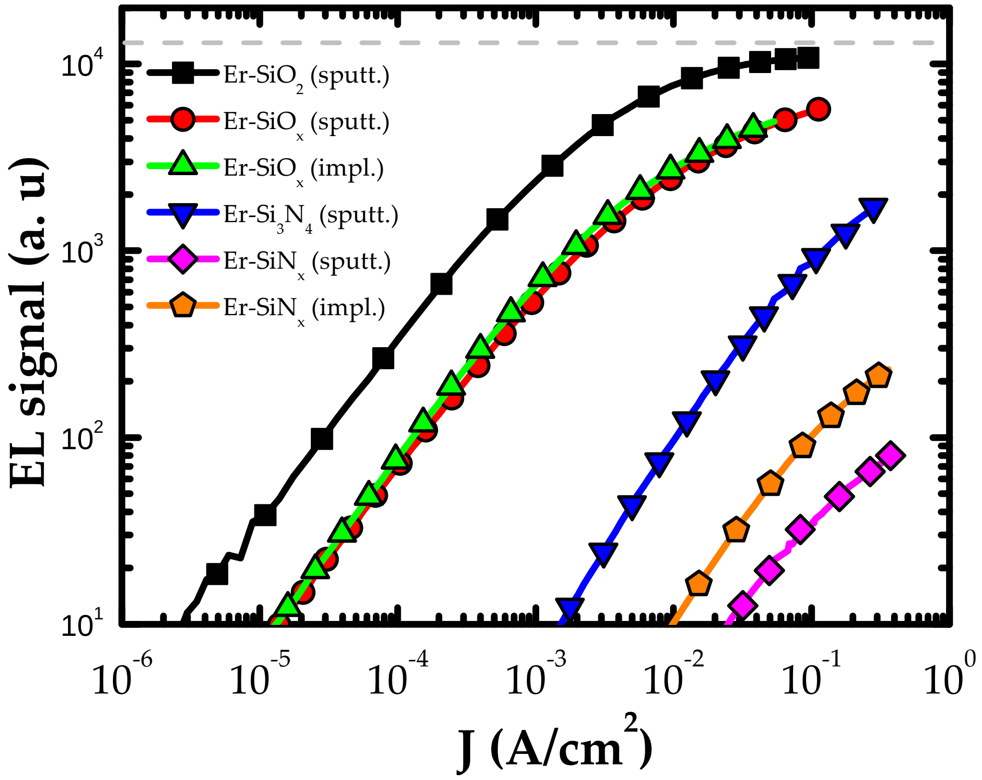

Figure 2.32. Comparison of the EL-J characteristic at 1.54 μm of various light emitting devices containing different Er-doped hosts: a SiO_2, a SiO_x, a SiN_x or a Si_3N_4.The EL signal has been normalized by the device area and the total number of Er^{3+} ions measured by TOF-SIMS. The Si excess in layers is expected to be around 12% in all samples.

Therefore, nitride-based host display interesting electrical characteristics, whereas oxide-based devices clearly outperform nitrides on the excitation efficiency. Such dichotomy could be used to our advantage if both layers are properly combined. Therefore, we can use an oxide-based layer to generate a large number of hot carriers with energies well-above the conduction band, and attach it to an Er-doped SiN_x layer to boost the efficiency of the impact excitation. This bilayer design, although conceptually simple, it has rarely been reported in the literature of Si-based LEDs [26, 45]. On the contrary, the combination of several layers, each one with a different functionality, is fairly common in other areas of research such as the one devoted to the development of Organic LEDS [46]. Thus, the next section will explore different layer morphologies and architectures with the aim of providing an improved optoelectronic performance in Er-doped Si-based devices by means of the efficient separation between the electronic and optical phenomena.

2.7. Exploring alternative device designs to improve the EL efficiency of Er-doped MIS devices: accelerator layer, superlattices and injector layer

As already introduced at the end of the previous section, the main purpose of this block is to inspect other layer morphologies to boost the optoelectronic properties of Er-doped Si-based devices. Then, we will depart explaining the study carried out on bilayer structures composed by an accelerator layer and an active layer containing the luminescent species (Er^{3+} ions in this case). This bilayer structure is expected to flood the active layer with a large number of hot electrons, hence maximizing the probability to excite Er^{3+} ions by by hot impact excitation. It could be considered, to some extent, as the integrated successor of the cathode ray tube display, where a source of electrons is directed towards a fluorescent screen. In our case, a thin SiO_2 layer is used to accelerate electrons instead of an electron gun disposed in a vacuum tube. Similarly, an Er-doped SiN_x layer is attached to the SiO_2 layer to work as an emitting phosphor layer.

In order to facilitate the understanding of the pathway of injected electrons into the active layer, figure 2.33 compares the energy band diagram of a single Er-doped SiN_x layer (figure 2.33 (a)) with the one of the proposed bilayer structure (figure 2.33 (b)). The most relevant optoelectronic phenomena are also numbered in figure 2.33 (a), depicting the thermally-assisted PF conduction (1), the direct impact excitation of Er^{3+} ions by hot CB electrons (2), the radiative recombination of intraband defect sites (3), the electron-hole radiative recombination in the Si substrate (4) and the anode hole injection (5). As discussed before, the Er-SiN_x layer has a low percentage of hot electrons and consequently a modest EQE is normally obtained in these systems. On the contrary, figure 2.33 (b) describes the electron injection process through a thin SiO_2 layer. In this case, injected electrons into the Er-doped SiN_x layer benefit from two factors: the energy provided to CB electrons in the SiO_2, with an average value of 3 eV [44], and the potential energy step at the SiO_2-SiN_x interface, that results in an additional energy gain from injected electrons of 1.2 eV. Therefore, an electron facing the Er:SiN_x layer will have an average energy of $\sim 3+1.2 = 4.2$ eV above the conduction band. Such high energy together with the enhanced hot electron injection ratio obtained in the bilayer structure is responsible for the increase of the EQE in the Er:SiN_x layer by more than one order of magnitude, up to values comparable to the Er:SiO_2 system.

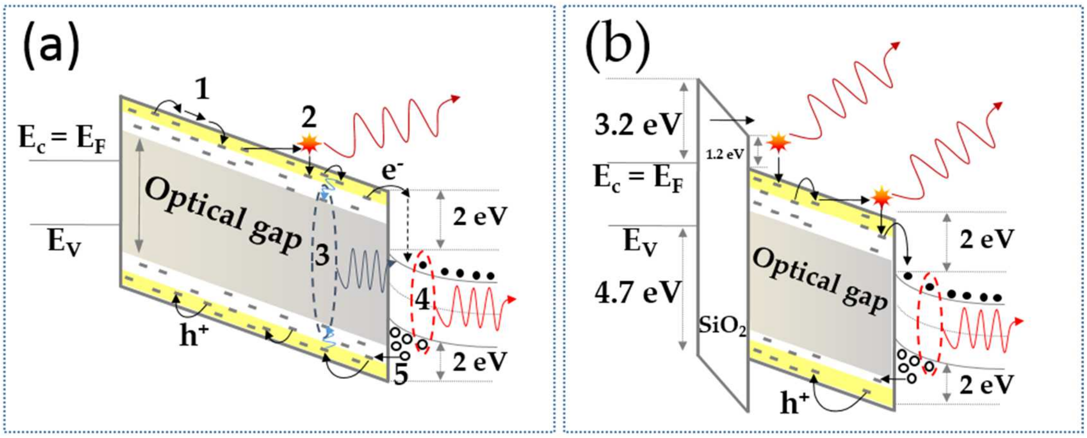

Figure 2.33. Energy band diagram of (a) a single SiN_x layer and (b) a SiO_2-SiN_x bilayer system, both embedded between a highly n-type polysilicon electrode and a Si substrate and polarized under a negative voltage.

This new strategy to boost the EL efficiency of RE-doped SiN_x layers was tested in a light emitting device containing a Tb:SiN_x/SiO_2 bilayer. A 40 nm thick Tb:SiN_x layer was deposited over a 30 nm SiO_2, and polarized accordingly so that hot electrons were injected from the SiO_2 into the Tb:SiN_x layer. Good optoelectronic properties were obtained, with an optical power density as high as 0.5 mW/cm^2 and an EQE of 0.1%, the largest ever reported in RE-doped silicon nitrides. Further details of this study can be found in ref. 45. Concerning the optimum SiO_2 thickness for electron acceleration, layer thicknesses between 10-40 nm are typically reported [26, 45]. Ongoing work is currently being made on Er-doped SiN_x/SiO_2 bilayer devices of different thicknesses to further proof these values.

Despite the good results displayed with the accelerator layer, I shall note that this design is optimum for luminescent layers with a thickness comparable to the electron thermalization distance. Therefore, we are limited to a few tens of nanometers at most. Thus, a further increase of the RE-doped layer thickness will not enhance the EL efficiency accordingly since hot electron injection would have previously thermalized in a region close to the SiO_2-active layer band edge. In that regard, one may think of a periodic structure in which the electron is sequentially accelerated while passing through the active layer. Thus, in view of the nice results obtained in the bilayer structure, it is reasonable to believe that a straightforward design to obtain even better optoelectronic performance could be done by stacking several bilayers to form a multilayered system. Enhanced EL efficiency and higher emitted optical power are foreseen upon careful chose of the layer thickness of each sub-layer conforming the multilayer approach. Ideally, injected hot electrons would impact with luminescent centres, lose its energy, and be re-launched again by another SiO_2 accelerator to face the next luminescent sub-layer with an average energy of 3 eV over the CB. In practice however, other issues that do not have a remarkable effect in single layers or bilayer structures may arise in this case. Indeed, *paper IX* further insights on this fact. In this work, the carrier transport and EL efficiency of Er-doped Si-ncs superlattices is discussed. The superlattice structure is composed by a sequential deposition (in a PECVD system) of 2 nm thick SiO_2 and 3 nm thick SiO_x layers with a nominal Si excess of 20%. Then, a single Er implantation is performed over the superlattice, followed by an annealing treatment at 900°C for 1h to form Si-ncs and induce the optical activation of Er^{3+} ions. A well-ordered Si-ncs superlattice resulted, with alternated monolayers of Si-ncs. Noteworthy, very thin SiO_2 sub-layers were intentionally deposited in an attempt to preserve a reasonable value for the driving voltage. The band diagram of the superlattice is presented in figure 2.34. As seen, several quantum wells are shown, with a discrete density of states as a consequence of the quantum confinement inside Si-ncs. Also, the band diagram of the superlattice presents several similarities with the one typically reported for Multiple Quantum Well (MQW) lasers [47]. However, in our case the EL emission is not generated by electron-hole recombination at the quantum well, but rather by direct impact excitation of hot electrons.

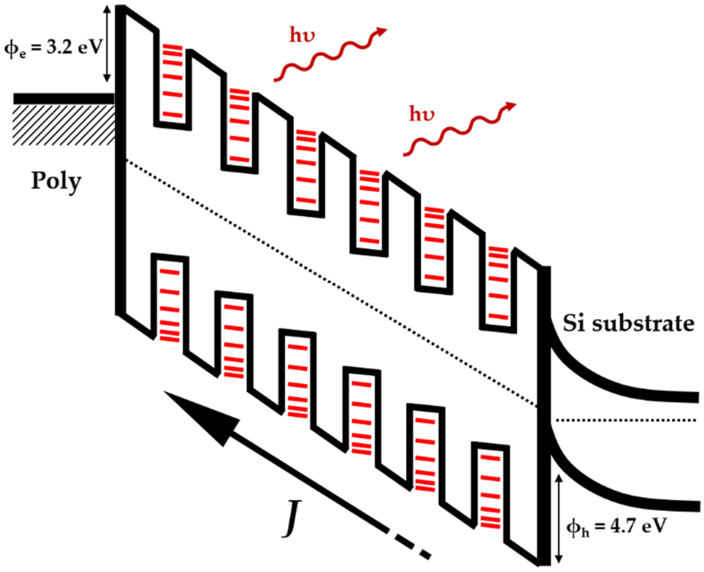

Figure 2.34. Energy band diagram of the Er-doped Si-nc superlattice structure upon negative voltage polarization.

The optoelectronic performance of the Er-doped Si-nc superlattice was compared with that of an Er-doped SiO_2 and with an Er-doped SiO_x single layer containing the same overall Si percentage than the superlattice, i.e. 12%. As expected, the Er-doped SiO_x layer showed a TAT conduction with reduced barrier height almost since the beginning of the charge injection (E ~ 3 MV/cm) up to the device breakdown (E ~ 8.5 MV/cm). In the same line, the Er-doped SiO_2 layer displayed a TAT conduction at the beginning, followed by a FNT from 7 MV/cm on. Thereby, by simple logics one could anticipate a mix of the above mentioned mechanisms for the superlattice structure, since it has been built alternating SiO_x and SiO_2 layers. Nevertheless, the J-E curve displayed a charge transport mechanism governed by PF conduction, followed by a TAT mechanism at high fields. Such bulk-limited conduction encountered in the low-medium field regime was ascribed to the superlattice structure, since injected electrons have to pass through several interfaces that are known to have an enhanced density of dislocations. This fact proofs that charge transport in dielectric media does not only depend on the chosen raw material, but also on the layer stack design. Moreover, the comparison of the EQE feature between the superlattice and both single layers denoted a decrease of performance for the superlattice, obtaining a photon electron ratio of $1/(3\times10^2)$ for the Er:SiO_2 layer, $1/(3\times10^3)$ for the Er:SiO_x layer and $1/(1\times10^5)$ for the Er:SiO_2/Si-nc superlattice. The origin of such modest operation was revealed after further inspection of the visible EL spectra of devices, attributing the low EQE of the Er-doped superlattice structure to a low hot electron injection rate compared to single layers (bulk-limited conduction) and also to the fact that injected electrons have remarkably lower energy values in the superlattice structure (< 1.26 eV) than in the SiO_2 or SiO_x single layers (~ 3 eV). Such fact, although it is detrimental from the efficiency point of view, it could be used to our advantage to design multilayered devices with high control of the average energy of injected electrons. In fact, an average energy of ~ 3 eV is not desired in most cases since decreases the device reliability by means of defect creation by direct impact excitation. As discussed before, the selectivity of hot electrons inside the active layer is poor, hence impacting with luminescent centres but also with other impurities (such as hydrogen) and weak chemical bonds in their pathway towards the cathode. As a consequence, the active layer is gradually damaged and the device operation lifetime dramatically reduced. Therefore, superlattices may be considered as efficient structures to modulate such electron energy when required.

Finally, a different approach that could lead to a better performance of Si-based light emitting devices is the efficient increase of the number of injected electrons into the active layer. Such strategy could be accomplished with an injector layer, which could be combined with the accelerator layer to enable good injection ratio and high electron acceleration at once. For the case of Si-based light emitting devices, we are strongly restricted since only certain materials can serve as injectors. One of them is a SiO_x layer with a fairly high Si content (16% will be used in this case). In order to further investigate on this issue, we have designed another bilayer structure especially suited to study the effect of the injector layer in Er-doped SiO_2. A new device was developed to accomplish this purpose. In particular light emitting field-effect transistors (LEFETs) containing an Er-doped SiO_2/SiO_x bilayer were fabricated. Such devices are halfway between previously studied light emitting MIS devices and the standard MOSFETs used in microelectronics. A sketch is illustrated in Figure 2.34.

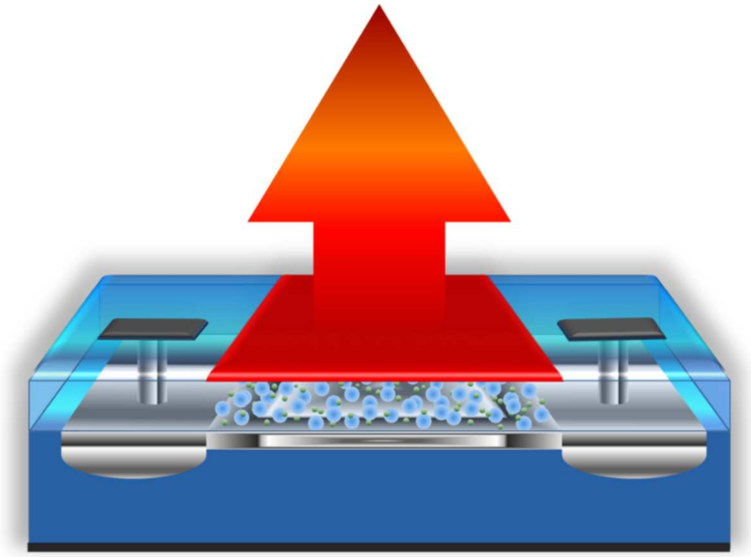

Figure 2.34. Sketch of a LEFET device containing Si-ncs and Er^{3+} ions embedded in the control oxide. A highly n-type doped polysilicon is used as gate electrode, being the source and drain placed at both sides. The arrow symbolizes the escaping EL emission.

It is worth noting that this new device presents an additional characterization complexity with respect to previously studied MIS capacitors since it is driven by four different terminals instead of two. Nevertheless, it also provides interesting benefits, as yields charge injection in a bilayer structure from two different sides. Therefore, the idea is to compare the EQE of the device when injecting electrons from the top polysilicon electrode directly into the Er-doped SiO_2 layer with the one obtained when electron injection takes place from the SiO_x injector placed underneath. For that however, an appropriated polarization scheme should be implemented to provide an infinite electron reservoir from both the top and bottom of the Er-doped SiO_2 layer. Whereas a highly n-type doped top polysilicon electrode will surely accomplish this purpose for the top injection, the bottom electron injection necessitates from a well-formed channel to provide the desired injection level. Therefore, source and drain terminals were grounded as displayed in figure 2.35. In that configuration, an inexhaustible source of electrons is guaranteed for the bottom injection.

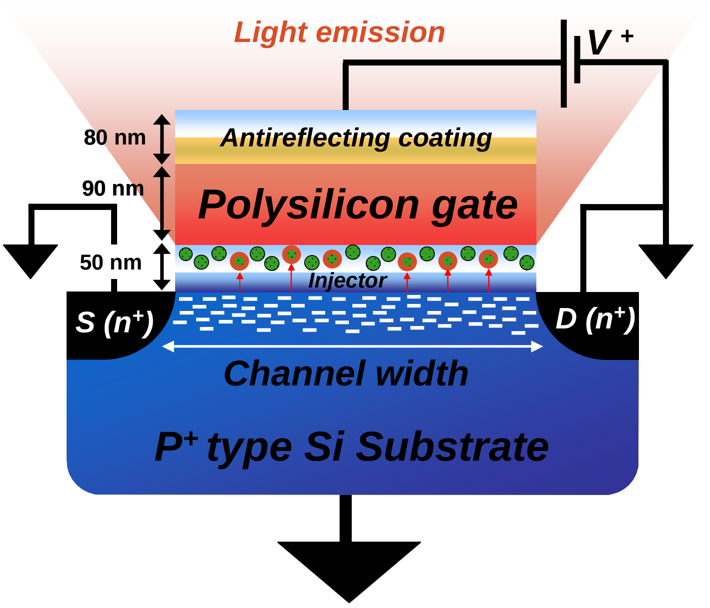

Figure 2.35. Studied device cross-section and polarization scheme used for the positive injection regime, with the source and drain grounded. A bilayer structure composed by an Er-doped SiO_2 and a SiO_x is placed under the gate electrode, replacing the gate oxide. The polysilicon gate is covered by an antireflecting coating like the one described in section 2.5. The EL layer ($Er:SiO_2$) is expected to be flooded by a large number of electrons injected from the transistor channel and assisted by the SiO_x layer.

Main results of this study are shown in the following. First of all, a structural characterization was performed to guarantee the existence of a well-defined bilayer structure. For that, a TEM characterization was accomplished. A summary of the most relevant results is shown in figure 2.36. A 20 nm thick SiO_x and a 30 nm thick Er-doped SiO_2 compose the bilayer structure, both deposited by PECVD and annealed at 900°C for 1 h. Since the Er doping was carried out by means of ion implantation, a line of Er clusters around the stopping depth formed after the annealing treatment, as observed in figure 2.36 (a). Remarkably, Si-ncs were only observed at the bottom of the bilayer, as seen in figure 2.36 (b). Finally, TRIM simulations done using the same dose and implantation energy displayed a maximum Er concentration of 5×10^{20} at./cm^3 and a doping profile completely introduced into the SiO_2 layer, as expected.

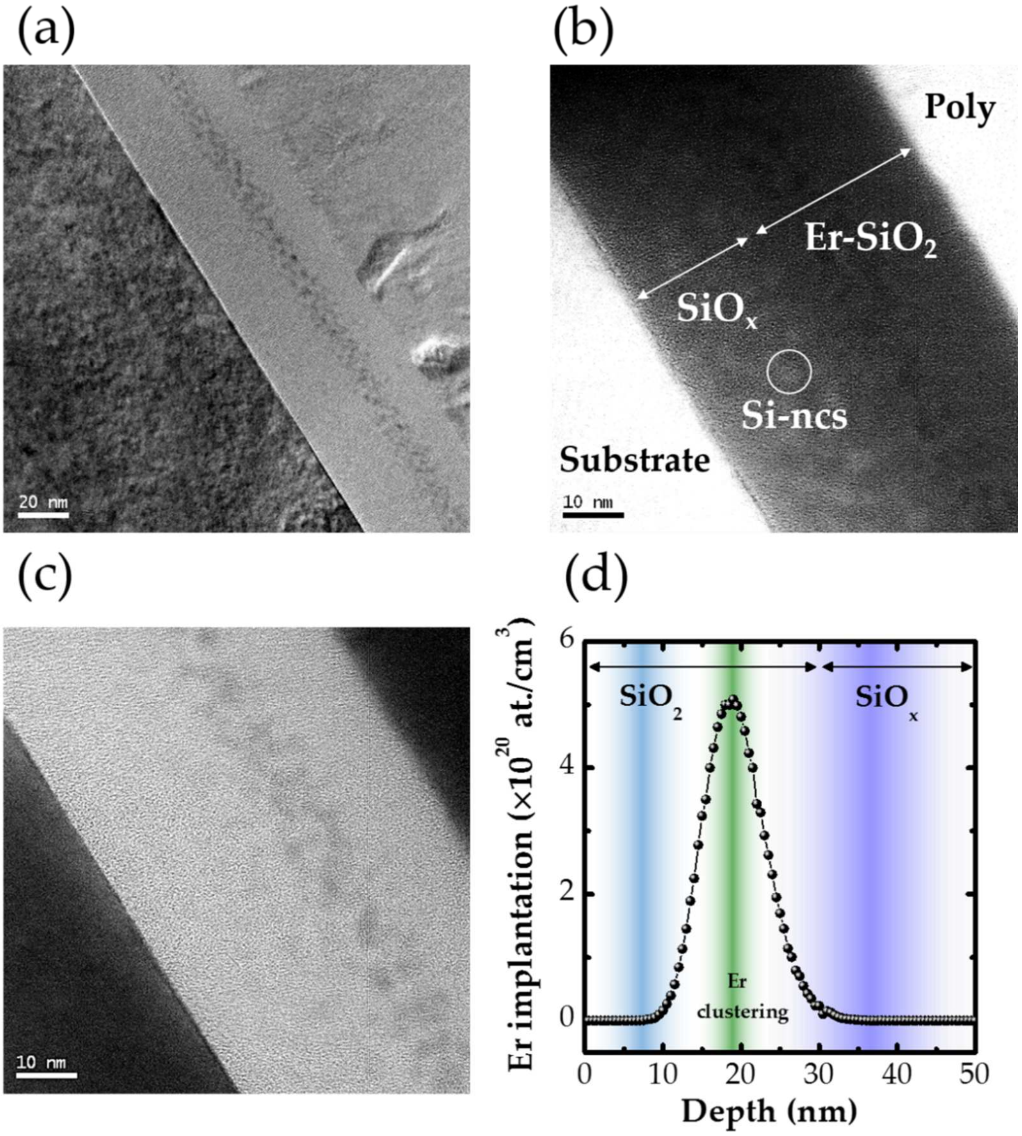

Figure 2.36. (a) Low magnification TEM image of the bilayer structure, depicting a well-defined line of Er clusters. (b) and (c) correspond to EFTEM images (medium magnification) filtering by the Si (17 eV) and the SiO_2 (23 eV) plasmon peak, respectively. Si-ncs are seen within a thickness of 20 nm from the Si substrate, corroborating the formation of the SiO_x layer (in (b)). Similarly, the line of Er clusters is well-resolved in (c). The simulated Er profile is shown in (d), denoting a peak concentration of 5×10^{20} at./cm^3. The line of Er clusters observed by TEM is also highlighted, demonstrating a good agreement with the simulated profile.

Once the bilayer structure was validated, the electron injection yield of the injector layer was inspected. Thus, the visible and infrared EL signal from emitting Er^{3+} ions was recorded as a function of the injected current density from both the top and the bottom of the bilayer. Figure 2.37 (a) illustrates the visible EL spectra of devices under different current injection regimes. The applied current density value over the polysilicon gate electrode is detailed in each case. As can be observed, a broad EL emission centred at 800 nm is observed under positive bias regardless of the current injection rate, associated with the EL of Si-ncs (see black filled squares in figure 2.37 (a)). On the contrary, a less relevant Si-ncs emission can be observed upon negative polarization (electrons injected from the polysilicon gate). This fact evidences a better Si-nc excitation when exciting from the transistor channel. Also, it is worth noting that Er^{3+}-related emission peaks are also observed, although in this case very similar EL intensity is recorded in both polarizations. The infrared EL-J curve of both configurations is depicted in figure 2.37 (b). Interestingly, at low flux, slightly higher EL signal is measured under bottom injection regime compared to the top injection. Such direct comparison puts forward the impact of the injector layer on the EL efficiency of the device under low current injection, since higher EQE is obtained when charges are injected into the Er:SiO_2 from the SiO_x. Remarkably, both EL-J curves converge at higher current densities, suggesting that the injector layer is only efficient up to a certain injection ratio. In our particular case, such transition would take place around of 0.1 mA/cm^2. Therefore, we can conclude by saying that the implementation of a SiO_x injector layer in Er-doped SiO_2 MIS devices is only effective at low current densities, with a modest EL enhancement of a factor of 3. Under high current injection however, the implementation of a layer injector is pointless since it does not provide any remarkable improvement on the optoelectronic efficiency. Further investigation is needed to assess the effect of the injector layer on the device operation lifetime and reliability.

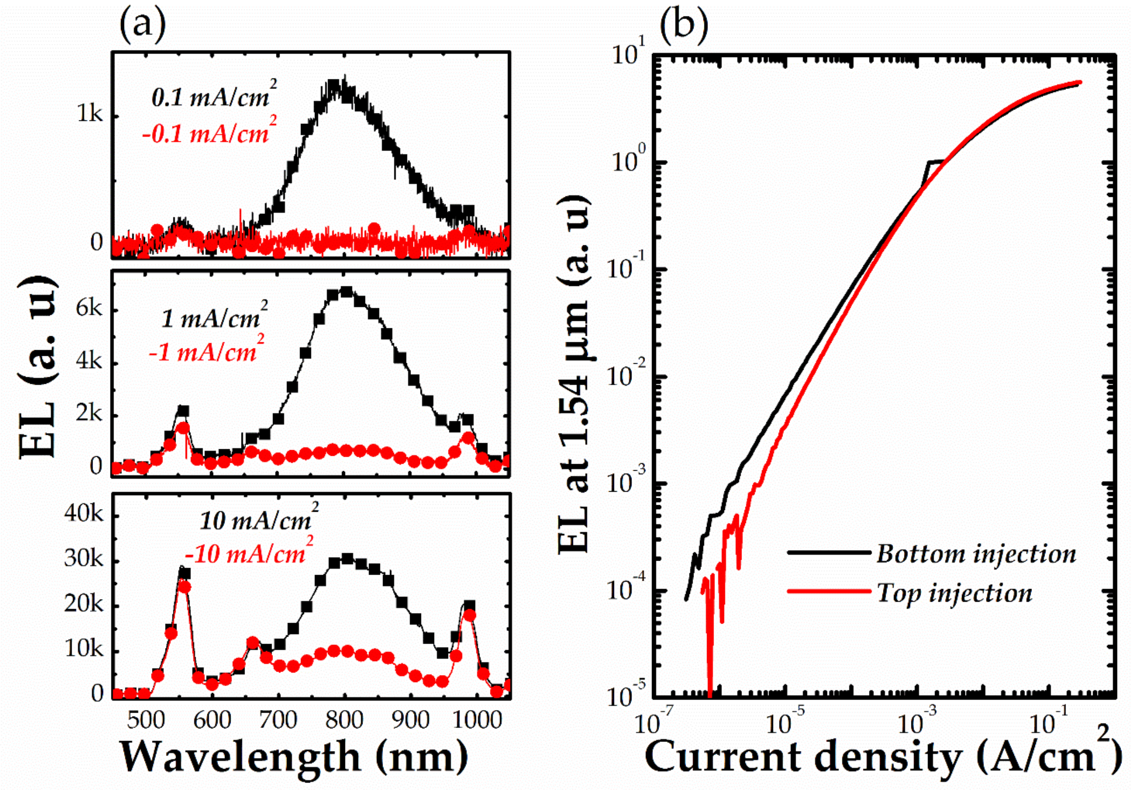

Figure 2.37. (a) Comparison of the visible EL spectra of the Er:SiO_2/SiO_x LEFET device taken under different polarizations and current densities. Black squares correspond to positive polarization, with electrons injected from the SiO_x layer (injector), whereas the red dot spectra belong to a negative polarization with electrons injected from the polysilicon gate into the Er:SiO_2 directly.

2.8. Summary and outlook

The structural, morphological and optoelectronic properties of Er-doped MIS devices with various Si-based hosts have been studied. A comprehensive investigation on the charge transport mechanisms, Er-clustering or the total optical power delivered into free space as a function of the device architecture and layer composition have been carried out. Also, particular emphasis has been placed on the main excitation mechanism of Er^{3+} ions under electrical pumping. A set of experiments has been designed to unambiguously identify the origin of such excitation, providing an extended and reasoned argumentation. Finally, alternative layer architectures have been explored, departing from the assumption that the most efficient Er^{3+} excitation is yield upon hot electron injection into the conduction band. The main points covered in this chapter are highlighted here after:

- ✓ SiO_2 layer or sub-oxides with low Si excess (SiO_x) present an electrode limited charge transport mechanism (TAT at low-medium fields, FNT at high fields), whereas silicon nitrides and silicon sub-oxides with high Si excess show a carrier injection regime that is dominated by bulk (PF conduction).
- ✓ The increase of Si excess in the host matrix boosts the injected current via additional defective sites in samples with bulk-limited conduction and by a diminution of the injection barrier height in layers with an electrode-limited charge injection.
- ✓ The annealing treatment has been identified as one of the most important fabrication parameters that govern charge transport in SiO_x samples.
- ✓ An adapted model from the one presented by Mikhaelashvili *et al.* has been implemented and tested in the experimental J-E curves of Er-doped SiO_x layers. The model has proved to be especially suited when samples present two concatenated charge transport mechanisms of different origin.
- ✓ The morphological properties of Er-implanted samples have been compared to Er-sputtered layers, revealing an enhanced Er clustering along the ion stopping depth in ion implanted samples. On the contrary, smaller Er clusters homogeneously distributed have been identified in sputtered samples.
- ✓ Three different evidences that elucidate a well-defined transition between the Si-ncs-to-Er^{3+} energy transfer regime and the direct impact of Er^{3+} ions by hot electron injection have been described.
- ✓ In addition, a bipolar pulsed excitation has been used to govern the nature of Er^{3+} excitation, providing efficient switching between energy transfer and direct impact excitation.
- ✓ Non-linear effects of Er^{3+} excitation under electrical pumping have been identified. Particularly, ESA has been identified as one of the main limiting phenomena under high current injection.

- ✓ The fraction of collected and emitted optical power into free space as well as the approximate percentage of emitting Er^{3+} ions has been calculated for MIS devices and compared to the ones with an antireflecting coating, obtaining a wide range of values from a few percent (4.5%) for the first run of devices up to 15% for the optimized layers. Later on, values as high as 50% of inverted Er^{3+} ions were reported in a jointly work with the Institute of Ion Beam Physics and Materials Research in Desden [40].

- ✓ The role of Si excess in various Si-based hosts has been debated, suggesting that there is an optimum Si excess that balances power efficiency, conductivity and charge trapping density.

- ✓ The direct comparison of the EL-J characteristic on various Si-based hosts has proven that the most suitable host for Er^{3+} ions is SiO_2, which yields an EQE enhancement of at least one order of magnitude with respect to silicon nitride.

- ✓ Alternative device designs and layer morphologies have been explored, denoting that the injector layer is only functional in the low-medium injection regime whereas considerable efficiency improvement is obtained using a bilayer system composed by a SiO_2 accelerator layer and a silicon nitride EL layer.

- ✓ In view of previous results, Er-doped Si-ncs superlattices have been designed, fabricated and characterized, obtaining a modest efficiency at 1.54 μm due to a low number of injected hot electrons in the structure compared to single layers. The origin of such low efficiency has been attributed to the large number of interfaces that electrons have to go through in their way towards the anode. The mean electron energy over the conduction band has been roughly estimated, obtaining average energy values of ~ 1.3 eV in the best case scenario.

2.9. List of references

[1] Kao, K. C. (2004). *Dielectric phenomena in solids*. Academic press.

[2] Sze, S. M., & Ng, K. K. (2006). *Physics of semiconductor devices*. John Wiley & Sons.

[3] Nardone, M., Simon, M., Karpov, I. V., & Karpov, V. G. (2012). "Electrical conduction in chalcogenide glasses of phase change memory." *Journal of Applied Physics*, *112*(7), 071101.

[4] Lee, J. Y. M., & Cheng, I. C. (1982). "Electrical properties of lightly doped polycrystalline silicon." *Journal of Applied Physics*, *53*(1), 490-495.

[5] Gehring, A. (2003) "Simulation of Tunneling in Semiconductor Devices." Ph.D. Thesis.

[6] Fowler, R. H., & Nordheim, L. (1928, May). "Electron emission in intense electric fields." In *Proceedings of the Royal Society of London A: Mathematical, Physical and Engineering Sciences* (Vol. 119, No. 781, pp. 173-181). The Royal Society.

[7] Yu, S., Guan, X., & Wong, H. S. P. (2011). "Conduction mechanism of TiN/HfO_x/Pt resistive switching memory: a trap-assisted-tunneling model." *Applied Physics Letters*, *99*(6), 063507.

[8] Gehring, A., & Selberherr, S. (2004). "Modeling of tunneling current and gate dielectric reliability for nonvolatile memory devices." *Device and Materials Reliability, IEEE Transactions on*, *4*(3), 306-319.

[9] Pai, D. M. (1975). "Electric-field-enhanced conductivity in solids." *Journal of Applied Physics*, *46*(12), 5122-5126.

[10] Angle, R. L., & Talley, H. E. (1978). "Electrical and charge storage characteristics of the tantalum oxide-silicon dioxide device." *Electron Devices, IEEE Transactions on*, *25*(11), 1277-1283.

[11] Murgatroyd, P. N. (1970). "Theory of space-charge-limited current enhanced by Frenkel effect." *Journal of Physics D: Applied Physics*, *3*(2), 151.

[12] Mott, N. F., & Davis, E. A. (2012). *Electronic processes in non-crystalline materials*. Oxford University Press.

[13] Jenderka, M., Barzola-Quiquia, J., Zhang, Z., Frenzel, H., Grundmann, M., & Lorenz, M. (2013). "Mott variable-range hopping and weak antilocalization effect in heteroepitaxial Na_2 IrO_3 thin films." *Physical Review B*, *88*(4), 045111.

[14] Berencén, Y., Ramírez, J. M., Jambois, O., Domínguez, C., Rodríguez, J. A., & Garrido, B. (2012). "Correlation between charge transport and electroluminescence properties of Si-rich oxide/nitride/oxide-based light emitting capacitors." *Journal of Applied Physics*, *112*(3), 033114.

[15] L. Dothanh and P. Balk, *Insulating Films on Semiconductors* (Elsevier Science Publishers B. V., North-Holland, 1983.

[16] Kenyon, A. J., Trwoga, P. F., Federighi, M., & Pitt, C. W. (1994). "Optical properties of PECVD erbium-doped silicon-rich silica: evidence for energy transfer between silicon microclusters and erbium ions." *Journal of Physics: Condensed Matter*, *6*(21), L319.

[17] Fujii, M., Yoshida, M., Kanzawa, Y., Hayashi, S., & Yamamoto, K. (1997). "1.54 μm photoluminescence of Er3+ doped into SiO_2 films containing Si nanocrystals: evidence for energy transfer from Si nanocrystals to Er^{3+}." *Applied Physics Letters*, *71*(9), 1198-1200.

[18] DiMaria, D. J., Dong, D. W., Pesavento, F. L., Lam, C., & Brorson, S. D. (1984). "Enhanced conduction and minimized charge trapping in electrically alterable read-only memories using off-stoichiometric silicon dioxide films." *journal of applied physics*, *55*(8), 3000-3019.

[19] Mutti, P., Ghislotti, G., Bertoni, S., Bonoldi, L., Cerofolini, G. F., Meda, L., ... & Guzzi, M. (1995). "Room-temperature visible luminescence from silicon nanocrystals in silicon implanted SiO_2 layers." *Applied physics letters*, *66*(7), 851-853.

[20] Daldosso, N., Das, G., Larcheri, S., Mariotto, G., Dalba, G., Pavesi, L., ... & Rocca, F. (2007). "Silicon nanocrystal formation in annealed silicon-rich silicon oxide films prepared by plasma enhanced chemical vapor deposition." *Journal of applied physics*, *101*(11), 113510.

[21] Mikhaelashvili, V., Betzer, Y., Prudnikov, I., Orenstein, M., Ritter, D., & Eisenstein, G. (1998). "Electrical characteristics of metal-dielectric-metal and metal-dielectric-semiconductor structures based on electron beam evaporated Y_2O_3, Ta_2O_5 and Al_2O_3 thin film." *Journal of applied physics*, *84*(12), 6747-6752.

[22] Han, H. S., Seo, S. Y., & Shin, J. H. (2001). "Optical gain at 1.54 μm in erbium-doped silicon nanocluster sensitized waveguide." *Applied physics letters*, *79*(27), 4568-4570.

[23] Garrido, B., García, C., Seo, S. Y., Pellegrino, P., Navarro-Urrios, D., Daldosso, N., ... & Rizk, R. (2007). "Excitable Er fraction and quenching phenomena in Er-doped SiO_2 layers containing Si nanoclusters." *Physical Review B*, *76*(24), 245308.

[24] Kanjilal, A., Rebohle, L., Skorupa, W., & Helm, M. (2009). "Correlation between the microstructure and electroluminescence properties of Er-doped metal-oxide semiconductor structures." *Applied Physics Letters*, *94*(10), 101916.

[25] Jambois, O., Gourbilleau, F., Kenyon, A. J., Montserrat, J., Rizk, R., & Garrido, B. (2010). "Towards population inversion of electrically pumped Er ions sensitized by Si nanoclusters." *Optics express*, *18*(3), 2230-2235.

[26] Rebohle, L., & Skorupa, W. (2010). *Rare-earth implanted MOS devices for silicon photonics: microstructural, electrical and optoelectronic properties* (Vol. 142). Springer Science & Business Media.

[27] Jin, L., Li, D., Xiang, L., Wang, F., Yang, D., & Que, D. (2013). "Energy transfer from luminescent centers to Er^{3+} in erbium-doped silicon-rich oxide films." *Nanoscale research letters*, *8*(1), 1-6.

[28] Berencén, Y., Jambois, O., Ramírez, J. M., Rebled, J. M., Estradé, S., Peiró, F., ... & Garrido, B. (2011). "Blue–green to near-IR switching electroluminescence from Si-rich silicon oxide/nitride bilayer structures." *Optics letters*, *36*(14), 2617-2619.

[29] Podhorodecki, A., Zatryb, G., Misiewicz, J., Wojcik, J., Wilson, P. R. J., & Mascher, P. (2012). "Green light emission from terbium doped silicon rich silicon oxide films obtained by plasma enhanced chemical vapor deposition." *Nanotechnology*, *23*(47), 475707.

[30] Choy, K., Lenz, F., Liang, X. X., Marsiglio, F., & Meldrum, A. (2008). "Geometrical effects in the energy transfer mechanism for silicon nanocrystals and Er^{3+}." *Applied Physics Letters*, *93*(26), 261109.

[31] Miyakawa, T., & Dexter, D. L. (1970). "Phonon sidebands, multiphonon relaxation of excited states, and phonon-assisted energy transfer between ions in solids." *Physical Review B*, *1*(7), 2961.

[32] Iacona, F., Pacifici, D., Irrera, A., Miritello, M., Franzò, G., Priolo, F., ... & Fallica, P. G. (2002). "Electroluminescence at 1.54 μm in Er-doped Si nanocluster-based devices." *Applied Physics Letters*, *81*(17), 3242-3244.

[33] Walters, R. J., Bourianoff, G. I., & Atwater, H. A. (2005). "Field-effect electroluminescence in silicon nanocrystals." *Nature materials*, *4*(2), 143-146.

[34] Zatryb, G., Podhorodecki, A., Misiewicz, J., Cardin, J., & Gourbilleau, F. (2011). "On the nature of the stretched exponential photoluminescence decay for silicon nanocrystals." *Nanoscale Res Lett*, *6*, 106.

[35] Schubert, E. F., Gessmann, T., & Kim, J. K. (2005). *Light emitting diodes*. John Wiley & Sons, Inc.

[36] Möller, S., & Forrest, S. R. (2002). "Improved light out-coupling in organic light emitting diodes employing ordered microlens arrays." *Journal of Applied Physics*, *91*(5), 3324-3327.

[37] Sun, Y., & Forrest, S. R. (2008). "Enhanced light out-coupling of organic light-emitting devices using embedded low-index grids." *Nature Photonics*, *2*(8), 483-487.

[38] Savio, R. L., Portalupi, S. L., Gerace, D., Shakoor, A., Krauss, T. F., O'Faolain, L., ... & Galli, M. (2011). "Room-temperature emission at telecom wavelengths from silicon photonic crystal nanocavities." *Applied Physics Letters*, *98*(20), 201106.

[39] Wierer, J. J., David, A., & Megens, M. M. (2009). "III-nitride photonic-crystal light-emitting diodes with high extraction efficiency." *Nature Photonics*, *3*(3), 163-169.

[40] Rebohle, L., Berencén, Y., Wutzler, R., Braun, M., Hiller, D., Ramírez, J. M., ... & Skorupa, W. (2014). "The electroluminescence mechanism of Er^{3+} in different silicon oxide and silicon nitride environments." *Journal of Applied Physics,116*(12), 123104.

[41] Berencén, Y., Ramírez, J. M., & Garrido, B. (2013, February). "Er-doped Si-based electroluminescent capacitors: Role of different host matrices on the electrical and luminescence properties." In *Electron Devices (CDE), 2013 Spanish Conference on* (pp. 245-248). IEEE.

[42] Nazarov, A., Sun, J. M., Skorupa, W., Yankov, R. A., Osiyuk, I. N., Tjagulskii, I. P., ... & Gebel, T. (2005). "Light emission and charge trapping in Er-doped silicon dioxide films containing silicon nanocrystals." *Applied Physics Letters,86*(15), 151914-151914.

[43] Gutsch, S., Laube, J., Hartel, A. M., Hiller, D., Zakharov, N., Werner, P., & Zacharias, M. (2013). "Charge transport in Si nanocrystal/SiO_2 superlattices." *Journal of Applied Physics*, *113*(13), 133703.

[44] DiMaria, D. J., & Abernathey, J. R. (1986). "Electron heating in silicon nitride and silicon oxynitride films." *Journal of applied physics*, *60*(5), 1727-1729.

[45] Berencén, Y., Wutzler, R., Rebohle, L., Hiller, D., Ramírez, J. M., Rodríguez, J. A., ... & Garrido, B. (2013). "Intense green-yellow electroluminescence from Tb^{+}-implanted silicon-rich silicon nitride/oxide light emitting devices." *Applied Physics Letters*, *103*(11), 111102.

[46] Müller, C. D., Falcou, A., Reckefuss, N., Rojahn, M., Wiederhirn, V., Rudati, P., ... & Meerholz, K. (2003). "Multi-colour organic light-emitting displays by solution processing." *Nature*, *421*(6925), 829-833

[47] Kuo, Y. K., Chang, J. Y., Tsai, M. C., & Yen, S. H. (2009). "Advantages of blue InGaN multiple-quantum well light-emitting diodes with InGaN barriers." *Applied Physics Letters*, *95*(1), 011116.

IOP PUBLISHING JOURNAL OF PHYSICS D: APPLIED PHYSICS

J. Phys. D: Appl. Phys. **45** (2012) 045103 (5pp) doi:10.1088/0022-3727/45/4/045103

Effect of the annealing treatments on the electroluminescence efficiency of SiO_2 layers doped with Si and Er

O Jambois[1], J M Ramírez[1], Y Berencén[1], D Navarro-Urrios[1], A Anopchenko[2], A Marconi[2], N Prtljaga[2], A Tengattini[2], P Pellegrino[1], N Daldosso[2,3], L Pavesi[2], J-P Colonna[4], J-M Fedeli[4] and B Garrido[1]

[1] Departament d'Electrònica, Universitat de Barcelona, Carrer Martì i Franquès 1, Barcelona 08028, Spain
[2] Nanoscience Laboratory, Department of Physics, University of Trento, Via Sommarive 14, Povo (Trento) 38123, Italy
[3] Dipartimento di Informatica, Università di Verona, Strada Le Grazie 15, 37134 Verona, Italy
[4] CEA,LETI, Minatec 17 rue des Martyrs, 38054 Grenoble cedex 9, France

E-mail: ojambois@el.ub.es

Received 4 July 2011, in final form 7 November 2011
Published 13 January 2012
Online at stacks.iop.org/JPhysD/45/045103

Abstract
We studied the effect of rapid thermal processing and furnace annealing on the transport properties and electroluminescence (EL) of SiO_2 layers doped with Si and Er ions. The results show that for the same annealing temperature, furnace annealing decreases the electrical conductivity and increases the probability of impact excitation, which leads to an improved external quantum efficiency. Correlations between predictions from phenomenological transport models, annealing regimes and erbium EL are observed and discussed.

(Some figures may appear in colour only in the online journal)

1. Introduction

For several years, silicon-based photonic devices have been widely considered in order to develop integrated circuits allowing to overcome the microelectronic bottlenecks. The challenge for silicon photonics is to manufacture high performance and low-cost information processing components using standard and mature CMOS technology. Numerous photonic devices have already been developed in the last years for light propagation, modulation or detection on silicon substrates. The ultimate challenge for the photonic and electronic convergence would be to monolithically integrate powerful Si-based light sources into the CMOS photonic integrated circuits [1, 2].

Among various Si-based materials demonstrated as promising for the fabrication of an electrically driven source, the Er doped silicon-rich silicon oxide (SRSO) system has been studied with great interest in recent years [3–6], mainly to achieve an injection Si-based laser emitting at 1.54 μm. But some efforts have still to be dedicated to understand the underlying physics of injection, transport and Er excitation mechanisms in those layers under electrical pumping. Although some issues on the active material properties have still to be solved [7], getting a more efficient excitation of Er ions at low electrical fluxes is a key to obtain population inversion [8].

In this work we report the study of charge injection and transport in SiO_2 layers doped with Si and Er ions. First, Er-free layers are studied in order to understand the role of the annealing on the charge transport and on the electroluminescence (EL) excitation mechanisms. Then, a layer in which Er has been incorporated is studied. The origin of the Er EL, by direct excitation or by transfer from Si-nc, is addressed.

2. Experiment

The starting materials are 50 nm thick SRSO layers obtained by Si implantation in a SiO_2 layer grown by LPCVD onto a p-type Si substrate. Two different Si excesses have been

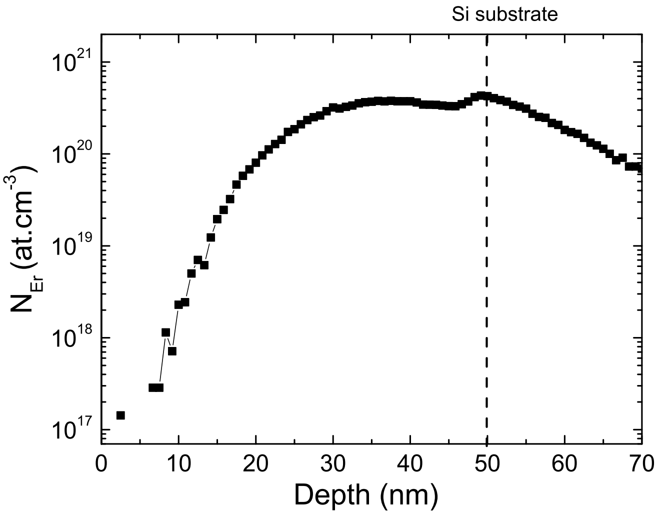

Figure 1. SIMS profile of the Er concentration in our devices.

introduced by varying the dose of implantation. Measurements made by x-ray photon spectroscopy (XPS) show that the Si excess in the layers can be around 9 or 16 at%. To form the Si nanocrystals (Si-nc), the layers were submitted to a thermal treatment. Two annealing processes at 1100 °C in nitrogen ambient are compared, one during 1 h in a conventional furnace and another one by rapid thermal processing (RTP) for 5 min. In the following, the samples with low/high Si excess are labelled L/H, and followed by 1 or 2 if the annealing has been made by RTP or by conventional annealing, respectively. In addition to those four layers, a fifth layer identical to layer L1 has been fabricated, and then implanted with Er ions. The Er concentration in this layer has been measured by means of secondary ion mass spectroscopy (SIMS) to be about 4×10^{20} at cm^{-3} at the peak concentration (see figure 1). After this implantation step, the layer has been annealed at 800 °C for 6 h to activate the Er ions. In the text, this fifth layer is labelled L1Er. To contact the layers a gate electrode has been formed by deposition of an n-type semitransparent polycrystalline silicon layer over an area of 300 μm by 300 μm. In this study the device has been forward polarized (negative voltage on the gate). Current–voltage (I–V) measurements have been carried out with a semiconductor analyser. EL spectra were measured using a spectrometer coupled to a charge-coupled device (CCD) for the visible range, and to a photomultiplier tube (PMT) for the infrared domain.

3. Results and discussion

The current–voltage (I–V) characteristics at room temperature of the four layers are shown in figure 2. An almost exponential growth of the current versus voltage is observed for all layers. Two main trends can be observed. The first one is that larger Si excess results in a larger conductivity, irrespective of the annealing procedure. The second point is that the layers annealed by RTP are much more conductive. This suggests that by means of the annealing one can modulate the transport properties.

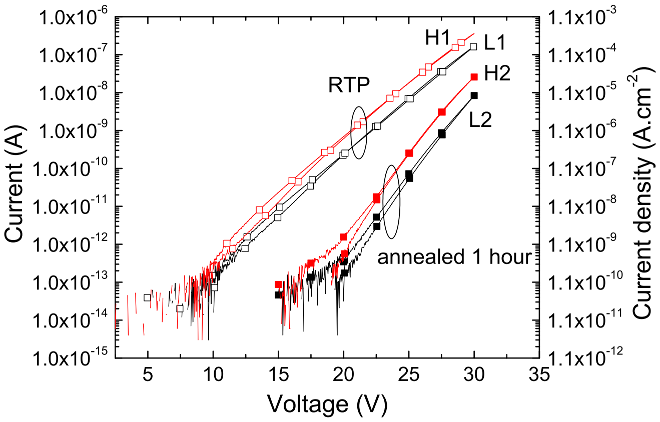

Figure 2. Current–Voltage (I–V) and current density–voltage (j–V) characteristics of the layers L1, L2, H1 and H2.

In order to understand the differences observed in the conductivity in depth, we have applied two models commonly used in the literature to analyse the I–V characteristics in silica and/or SRSOs. Those models are (i) the Poole–Frenkel (P–F) model that corresponds to thermally activated conduction between localized states in the gap assisted by the electric field [9] and (ii) the Fowler–Nordheim (F–N) model that describes the tunnelling of charges through a triangular barrier, from the electrode into the dielectric [10], or between localized states. Note that the localized state may refer to defects in the oxide matrix, or Si nanoclusters. Although those two models are too approximative [9, 10] to describe such a complex system, we will see that they will provide us some insight into the results of EL. The P–F model is described by the relation $I \propto V\exp(e/kT\sqrt{eV/\pi\varepsilon_0\varepsilon_r d})$, where ε_0 is the vacuum permittivity, ε_r the relative permittivity and d the thickness of the layer. For the F–N model, the following relation can be found between I and V: $I \propto V^2\exp(-(4\sqrt{2m_{ox}\phi_b^3})/3e\hbar V)$, with m_{ox} the effective mass of the electrons in the dielectric, taken such as $m_{ox} = 0.5m_e$ the mass of the electron in vacuum, ϕ_b the potential barrier between Si and SiO$_2$ and $\hbar$ the Planck constant. Each of the experimental I–V curves has been fitted with the help of those relations (see figure 3).

The fitting with both models of the curves provides an interesting evolution of the transport properties with respect to the annealing treatment, which is believed to affect the material microstructure. Indeed, at low voltage the layers annealed by RTP show a current that is too large to be originated from F–N injection. A better agreement with the P–F law is found on a wide range of voltages. However, in layers annealed in the conventional furnace, the overall current is lower, and a better agreement with the F–N law is found. This suggests that for the same annealing temperature (1100 °C), the injection is more difficult when the annealing time is longer, leading to the requirement of larger voltages to promote charge transport. As a consequence, the probability of having hot carrier injection in those layers is higher than in RTP layers. The influence of the annealing treatment on the material properties can have several origins. On the one hand, it is well known that a thermal treatment is required to cure the layer from the defects introduced by the implantation. An annealing of 5 min may

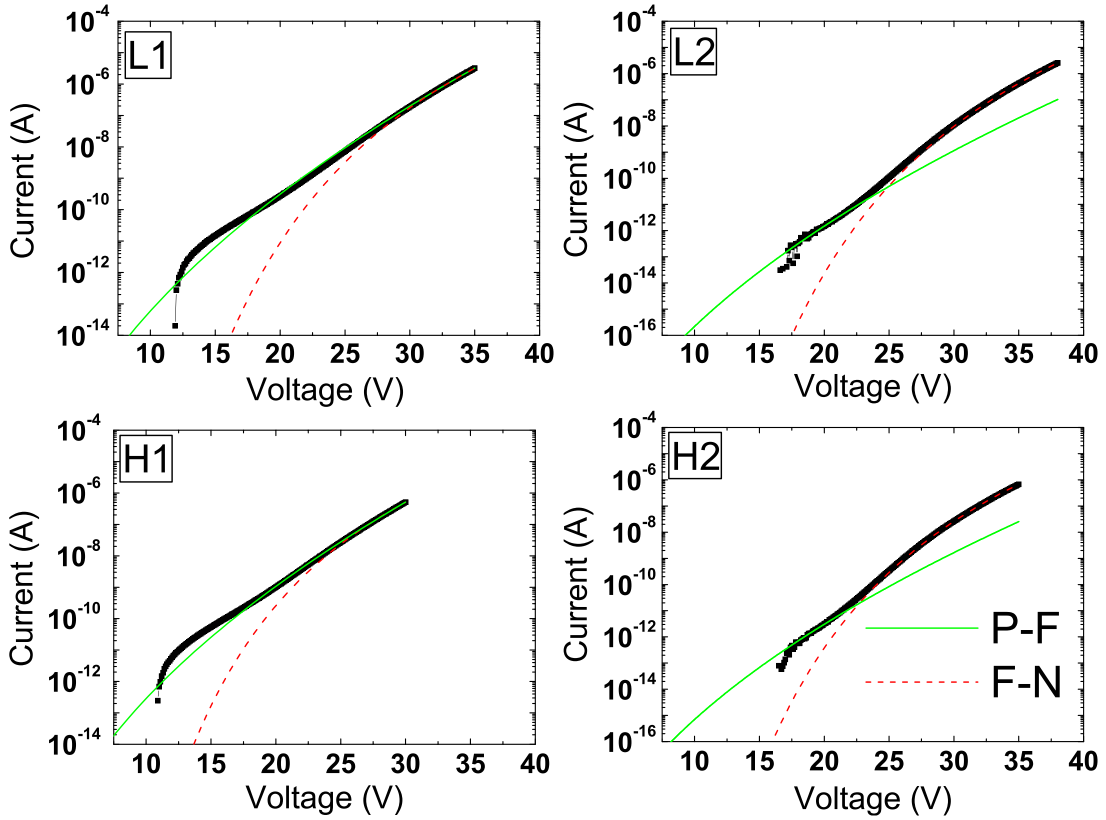

Figure 3. Fits of the I–V curves by the models P–F (green continuous line) and F–N (red dashed line). For layers L2 and H2, the fit with the P–F model is shown by keeping the permittivity found for layers L1 and H1 (see text for details).

Table 1. Injection barrier and permittivity extracted by fitting the I–V by the model F–N and P–F, respectively, on the whole voltage range.

	Barrier height (eV) (F–N)	Relative permittivity (P–F)
L1	1.61	4.52
L2	2.00	2.42
H1	1.32	5.06
H2	1.84	2.49

not be enough for that purpose [11]. On the other hand, at this temperature the formation of Si nanoclusters is expected, as confirmed by the measured large EL band in the visible-near infrared range centered at around 800 nm (see inset of figure 4), that is attributed to quantum confinement or to Si-nc surface states [12, 13]. We suggest that a different nanocluster size and spatial distribution are obtained by each of the annealing processes. However, the Si excess does not seem to have any significant influence on the transport mechanism for the range of Si excesses studied here. We can just observe larger currents when a larger Si excess is introduced. To go further we have looked at the relative permittivity we can extract by fitting the I–V curves with the P–F law, or the injection barrier height that we can extract from the F–N fit. These values are reported in table 1, when fitting the whole voltage range of the I–V of figure 3.

When the P–F model is used to fit the I–V curves at high voltages (larger than 30 V), a permittivity of about 4.5–5 is found for the RTP layers, and less than 2.5 for the layers treated in the conventional furnace. This latter value is too low to be acceptable, while 4.5–5 is an expected value for a Si-rich silicon oxide [14]. In figure 3, the fit by the P–F law has been repeated, this time fixing a permittivity of about 4.5–5, as found for samples L1 and H1, and just adjusting the exponential prefactor. This leads to an agreement with the P–F model at lower voltage, on a reduced range of voltages. Above a threshold voltage, the F–N law is found to reproduce well the I–V curves. Concerning the barrier heights found from the F–N fit, larger values have been found for the layers annealed for 1 h. Those values corroborate that (i) injection is more difficult for those layers than for the RTP ones, and (ii) the transport involves mainly electrons, because hole contribution would have implied a larger barrier height, as holes see a much larger potential barrier than electrons. Note, however, that hole injection in a region close to the Si substrate cannot be discarded [15]. To summarize, in the layers annealed for 1 h in the furnace, the F–N regime is the dominant conduction mechanism at high voltages. In the RTP layers, even if F–N may be activated at high voltages, the current is essentially limited by a P–F-type conduction. Moreover, as the effective barrier in those layers is lower due to a larger amount of defects, injection is favoured and conduction occurs at a lower voltage. This explains why the I–V curves in figure 2 of the RTP layers are shifted towards lower voltages. It is interesting now to observe how the difference in injection and transport affects the EL behaviour. To investigate this point, in figure 4 we have plotted the evolution of the EL intensity versus the electrical current.

A linear dependence is observed between EL and current intensities, implying that saturation of the luminescent centers

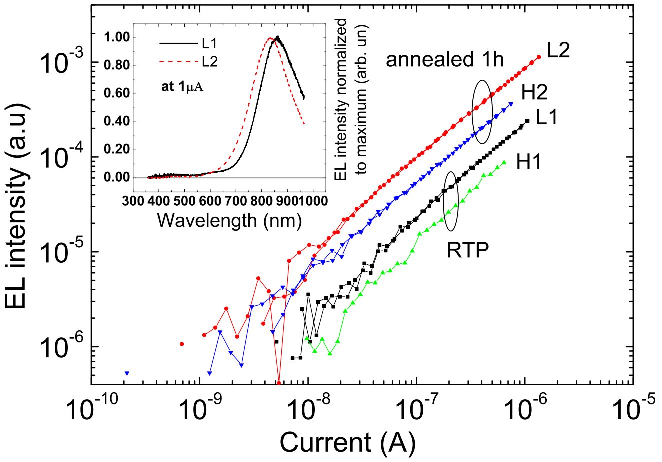

Figure 4. Evolution of the EL intensity versus current. The inset shows the normalized EL spectra of wafers L1 and L2 for a constant current of 1 μA.

still has not been reached. The corresponding EL spectra of devices L1 and L2 under a current of 1 μA are shown in the inset. By comparing the behaviour of the layers treated under the same conditions at a fixed current, one can observe that a lower Si excess results in a brighter emission. This means a larger external efficiency, defined as the ratio between the EL and the current intensities, is obtained for the layers with the lowest Si excess, irrespective of the applied annealing. Regarding the annealing, if we compare the curves at the same current, one can clearly observe that the layers annealed for 1 h are brighter than their counterpart RTP layers. As a consequence, the layers annealed for 1 h present a higher external quantum efficiency than the RTP layers. Looking at the normalized EL spectrum in the inset, we can see that layer L2 is emitting at a higher energy than layer L1. This is in contrast to what can be expected from the quantum confinement theory, as a longer thermal budget should lead to larger Si-nc and thus to a lower energy of emission. This disagreement can, however, be explained by the larger voltage that has to be applied to the L2 layer to obtain the same current, which in turn allows the excitation of smaller Si-nc. Or, as suggested by the I–V curve, this could be due to the larger number of defects present in the matrix of the L1 layer. Indeed, those defects around the Si-nc induce a weaker quantum confinement effect and thus a smaller blueshift of the light emission [12].

Finally, we have studied the possibility of getting EL at 1.54 μm by implanting Er ions in a layer similar to the L1 layer (lower Si excess and with RTP). There are several possible mechanisms of Er excitation, such as (i) direct impact excitation, (ii) impact of Si-nc that transfer their energy to Er ions, and/or (iii) electron-hole injection inside the Si-nc and subsequent energy transfer to the Er ions. In order to observe Er EL due to energy transfer from the Si-nc, we have chosen a layer identical to layer L1 (lower Si excess and RTP), to reduce direct impact excitation of Er that is favoured when the F–N regime is dominant. Figure 5(*a*) shows the EL obtained in the visible range and at 1.54 μm in the inset. An intense EL is observed at 1.54 μm. If we look at the visible range, we see that the Si-nc broad emission is superimposed to various peaks, whose energy coincides with Er transitions at higher levels [16]. Although a second order mechanism of high level excitation like cooperative up-conversion cannot be discarded [17], the fact that in figure 5(*a*) we observe at low injection fluxes all the visible emission spectra of Er ions suggests that in those devices, the Er is excited preferentially by direct impact excitation, rather than through indirect excitation of the coupled Si-nc. The excitation of the energy levels of Er in the visible is in agreement with the average energy acquired by the electrons injected by F–N mechanism, of about 2.5–3 eV in those kind of layers, as calculated in [18]. For the layer L1Er, a power efficiency of 10^{-3}% at 1.54 μm has been estimated, a value that is one order of magnitude lower than that already reported for other devices and layers [6, 8]. Note that although the experiment has not been carried out on a L2 type layer (annealed for 1 h) implanted with Er, we expect that, as the F–N regime would be more dominant because of a lower density of traps, the intensity of the Er peaks in the visible and at 1.54 μm should be more intense. As the current would also be lower, this should allow an increase in efficiency, in the same way as described for the EL in the visible range.

As an illustration, we show in figure 5(*b*) the spectrum, in the visible region, of a layer where the SRSO is grown by LPCVD, annealed at 1100 °C for 1 h as for layer L2 and then implanted with Er with the same implantation parameters as the layer L1Er. The validity of such a comparison can be checked in the inset of figure 5(*b*), where the I–V curve of this layer is superimposed on the one of layer L2. Both layers have been submitted to the same furnace annealing at 1100 °C for 1 h, and show very similar I–V characteristics, and quite good agreement with the F–N injection model.

The optical transitions of Er ions in the visible range are clearly much more intense. For this layer, a stronger EL intensity at 1.54 μm is found, typically 20 times stronger for the same current, attributed to a larger amount of impact excitation than in layer L1Er. As a consequence, when only one kind of charge—here the electrons—are involved in the charge transport, one has to optimize the hot electrons injection to enhance impact excitation, in order to get higher EL intensity and external quantum efficiency. Nazarov *et al* suggest that a very large Si excess is detrimental for direct impact excitation of Er, as the Si-nc act as scattering centres [3]. Sun *et al* observe that in their LEDs the direct impact of Er for low Si excesses is not efficient [19]. They get a current density of 1.5 A cm^{-2} at 25 V for a 90 nm thick layer. This is several orders of magnitude larger than the density current we have measured (see figure 3). This suggests that the defects that assist transport through a P–F type conduction mechanism in the present case, or a space charge limited current in the case of [19] are responsible for the thermalization of the injected hot electrons, an undesired effect that prevents direct impact excitation. In the case of the layers annealed for 1 h at 1100 °C, the results suggest that most of the electrons are flowing through the SiO$_2$ conduction band at high voltage. An appropriate low Si excess will favour injection at lower voltages, as the effective F–N barrier decreases (see table 1), enhancing the reliability of the layers. Another approach to increase the reliability can be working in the pulsed excitation regime.

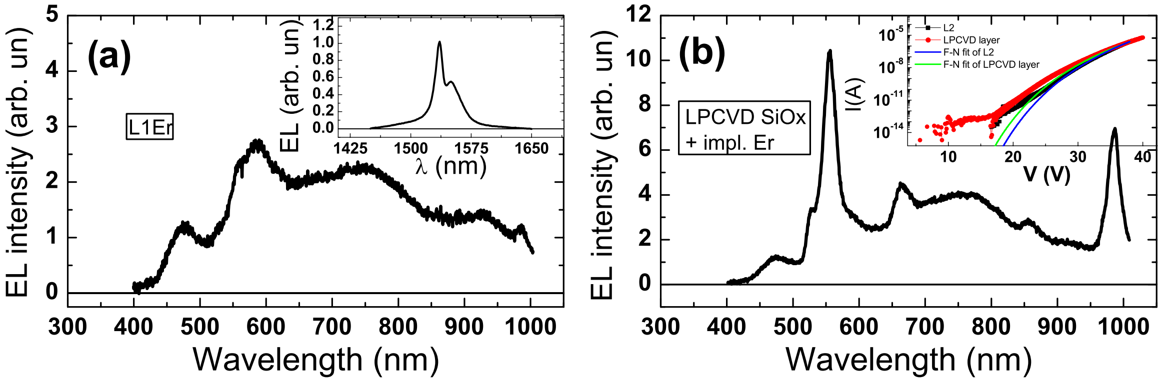

Figure 5. (*a*) EL Spectra in the visible range and at 1.54 μm in the inset, of the layer L1Er, at a forced current of 10 μA. (*b*) EL spectra of an SiO_x layer made by LPCVD annealed at 1100 °C during 1 h and then implanted with Er at the same current for comparison.

Note finally that apart from the Er excited by direct impact, some of the Er may be excited by energy transfer. This fraction could be increased by controlling the hole injection in the active layers. It remains interesting to increase this fraction, as the onset voltage of EL could be reduced, and thus efficiency and reliability would increase. One possibility to do this could be by working in a sequential regime, in the SiO_x system [20] or SiO_x : Er system [21], as no transport inside the layer is required. The other possibility could be to work with a multilayer system SiO_x/SiO_2, in order to control the bipolar current injection, and be able to balance their injection rate by means of a careful engineering of the Si-nc sizes [22]. By introducing Er in the system, one can expect a larger fraction of excited Er by indirect excitation.

4. Conclusion

The effect of RTP and furnace annealing on the transport properties and electroluminescence of Si-nc embedded in SiO_2 layers doped or not with Er ions has been investigated. By changing the thermal treatment, an evolution of the external quantum efficiency is shown, and is correlated with the different transport mechanisms activated. The main excitation mechanism is attributed to impact excitation. The observation of sharp EL peaks of Er in the visible suggests that Er is also excited directly by impact. In this case, the results suggest that the matrix defects promote charge conduction but are detrimental to the electroluminescence, as they lead to an undesired thermalization of the hot electrons injected at high field.

Acknowledgments

This work was supported by the European Community through the HELIOS Project (ICT-FP7-224312). OJ thanks the Spanish Ministry of Science for financial support (Juan de la Cierva program).

References

[1] Khriachtchev L (ed) *Silicon Nanophotonics: Basic Principles, Present Status and Perspectives*

[2] Liang D and Bowers J E 2010 *Nature Photon.* **4** 511

[3] Nazarov A, Sun J M, Skorupa W, Yankov R A, Osiyuk I N, Tjagulskii I P, Lysenko V S and Gebel T 2005 *Appl. Phys. Lett.* **86** 151914

[4] Irrera A, Iacona F, Franzò G, Miritello M, Lo Savio R, Castagna M E, Coffa S and Priolo F 2010 *J. Appl. Phys.* **107** 054302

[5] Yin Y, Xu W J, Wei F, Ran G Z, Qin G G, Shi Y F, Yao Q G and Yao S D 2010 *J. Phys. D: Appl. Phys.* **43** 335102

[6] Jambois O, Berencen Y, Hijazi K, Wojdak M, Kenyon A J, Gourbilleau F, Rizk R and Garrido B 2009 *J. Appl. Phys.* **106** 063526

[7] Cueff S, Labbé C, Cardin J, Doualan J L, Khomenkova L, Hijazi K, Jambois O, Garrido B and Rizk R 2010 *J. Appl. Phys.* **108** 064302

[8] Jambois O, Gourbilleau F, Kenyon A J, Montserrat J, Rizk R and Garrido B 2010 *Opt. Express* **18** 2230

[9] Pai D M 1975 *J. Appl. Phys.* **46** 5122

[10] Pananakakis G, Ghibaudo G, Kies R and Papadas C 1995 *J. Appl. Phys.* **78** 2635

[11] López M, Garrido B, García C, Pellegrino P, Pérez-Rodrìguez A, Morante J R, Bonafos C, Carrada M and Claverie A 2002 *Appl. Phys. Lett.* **80** 1637

[12] Jambois O, Rinnert H, Devaux X and Vergnat M 2005 *J. Appl. Phys.* **98** 046105

[13] Godefroo S, Hayne M, Jivanescu M, Stesmans A, Zacharias M, Lebedev O I, Van Tendeloo G and Moshchalkov V V 2008 *Nature Nanotechnol.* **3** 174

[14] Prezioso S, Anopchenko A, Gaburro Z, Pavesi L, Pucker G, Vanzetti L and Bellutti P 2008 *J. Appl. Phys.* **104** 063103

[15] Berencén Y, Carreras Josep, Jambois O, Ramírez J M, Rodríguez J A, Domínguez C, Hunt C E and Garrido B 2011 *Opt. Express* **19** A234

[16] van den Hoven G N, Snoeks E, Polman A, van Dam C, van Uffelen J W M and Smit M K 1996 *J. Appl. Phys.* **79** 1258

[17] Yerci S, Li R and Dal Negro L 2010 *Appl. Phys. Lett.* **97** 081109

[18] Placencia I, Martin F, SuAet J and Aymerich X 1990 *J. Phys. D: Appl. Phys.* **23** 1576

[19] Sun K, Xu W J, Zhang B, You L P, Ran G Z and Qin G G 2008 *Nanotechnology* **19** 105708

[20] Walters R J, Bourianoff G I and Atwater H A 2005 *Nature Mater.* **4** 143

[21] Priolo F, Presti C D, Franzò G, Irrera A, Crupi I, Iacona F, Di Stefano G, Piana A, Sanfilippo D and Fallica P G 2006 *Phys. Rev.* B **73** 113302

[22] Marconi A, Anopchenko A, Wang M, Pucker G, Bellutti P and Pavesi L 2009 *Appl. Phys. Lett.* **94** 221110

APPLIED PHYSICS LETTERS **99**, 231114 (2011)

Copropagating pump and probe experiments on Si-nc in SiO_2 rib waveguides doped with Er: The optical role of non-emitting ions

D. Navarro-Urrios,[1,a)] F. Ferrarese Lupi,[1] N. Prtljaga,[2] A. Pitanti,[2,3] O. Jambois,[1]
J. M. Ramírez,[1] Y. Berencén,[1] N. Daldosso,[2,4] B. Garrido,[1] and L. Pavesi[2]
[1]*MIND-IN2UB, Dept. Electrònica, Universitat de Barcelona, C/Martí i Franquès 1, 08028 Barcelona, Spain*
[2]*Laboratorio di Nanoscienze, Dipartimento di Fisica, Università di Trento, Via Sommarive 14, I-38100 Povo (Trento), Italy*
[3]*NEST, Scuola Normale Superiore, Istituto di Nanoscienze-CNR, Piazza San Silvestro 12, 56127 Pisa, Italy*
[4]*Dipartimento di Informatica, Università di Verona, Strada Le Grazie 15, 37134 Verona, Italy*

(Received 22 June 2011; accepted 14 November 2011; published online 9 December 2011)

We present a study that demonstrates the limits for achieving net optical gain in an optimized waveguide where Si nanoclusters in SiO_2 codoped with Er^{3+} are the active material. By cross correlating absorption losses measurements with copropagant pump ($\lambda_{pump} = 1.48\,\mu m$) and probe ($\lambda_{probe} = 1.54\,\mu m$) experiments we reveal that the role of more than 80% of the total Er^{3+} population present on the material (intended for optical amplification purposes) is to absorb the propagating light, since it is unfeasible to invert it. © *2011 American Institute of Physics.* [doi:10.1063/1.3665950]

Within the last decade, lots of efforts have been dedicated towards the realization of the "holy grail" of silicon photonics, i.e., a monolithic silicon optical amplifier or laser. As an active medium for achieving this goal, Si nanoclusters (Si-nc) in dielectric matrices coupled to Er^{3+} ions have been one of the most promising alternatives.[1] Initial reports of internal optical gain on strip waveguides contributed to raise further the expectations.[2–4] Most of the works present in the literature are focused on the understanding of the physical characteristics of the Si-nc to Er^{3+} transfer and the optimization of the coupled content, where a maximum of just few tens percents was achieved.[5–9] But even though those are certainly key issues towards the optimization of the material, yet a more disturbing feature is the existence of a sizeable Er^{3+} population (up to more than 80% of the total content) that is not emitting light efficiently, even under direct pumping.[10–12] The few reports present in the literature focused on this Er^{3+} content did not study the optical role that those dark ions may play from the point of view of an optical amplification application, i.e., if they are just transparent or they absorb light. The present letter addresses this issue in a conclusive way by comparing the absorption with maximum amplification values measured on a rib loaded waveguide, whose active layer is composed of an optimized material.

The sample under analysis has been produced by using standard deposition processes. Initially, 5 μm of SiO_2 have been deposited above a crystalline Si substrate, becoming the optical bottom cladding of the waveguides. The active layer has afterwards been fabricated by means of a RF reactive magnetron co-sputtering method of 2-in. confocal pure SiO_2 and Er_2O_3 targets under Argon-Hydrogen gas mixture.[13] As a result, 1.2 μm of substoichiometric silicon-rich silicon oxide (SRSO) doped with Er^{3+} ions have been deposited. A further top cladding layer of 1 μm of SiO_2 has been finally grown. This was followed by an annealing treatment under a pure nitrogen flow to promote phase separation between silicon and its oxide in the active layer. The various deposition parameters (H_2 partial pressure, substrate temperature during active layer deposition and annealing temperature) have been varied for optimising two main figures of merit: the PL intensity under non-resonant pumping ($\lambda = 476$ nm) and the lifetime of the $^4I_{13/2} \rightarrow {}^4I_{15/2}$ Er^{3+} transition.[13,14] This manuscript deals with the best layer obtained following this optimisation. Its composition was measured by x-ray photoelectron spectroscopy and secondary ions mass spectroscopy, presenting a Si excess of about 5% and an Er^{3+} content of $3.4 \pm 0.2 \times 10^{20}\,cm^{-3}$. The layer has been annealed at 910 °C during 60 min, so it likely contains Si in an amorphous nanocluster form. The active material has the same nominal composition of sample A from Refs. 6 and 15 and sample B from Ref. 12.

In order to produce monomodal rib-loaded waveguides with high confinement factor, a dry etching of the top SiO_2 cladding has been performed down to 200 nm over the active layer. We will report on 5 μm wide waveguides (see Fig. 2 for a waveguide profile).

The optical losses of the waveguides have been determined by means of the cut-back technique along the spectral range provided by a tunable laser (from 1460 to 1580 nm). A tapered fiber was used to butt-couple the input light, leading to coupling losses of about 4 dB.

The evaluation of the cross section at 1480 nm from time resolved μ-PL measurements has been performed following the procedure described in a previous work.[12]

Pump and probe experiments were carried out to evaluate the signal enhancement (SE) of a probe signal coupled to the waveguides, when a pump signal is also present.[4] We have used as a probe signal a tunable laser and as a pump signal a high power diode laser emitting at 1.48 μm (far away from the absorption spectrum of Si-nc). Both lasers have been combined in a wavelength-division-multiplexer (WDM) fiber, connected to a tapered fiber and finally butt-coupled into the active waveguide. In order to filter out the contribution of the amplified spontaneous emission (ASE)

[a)]Electronic mail: dnavarro@el.ub.es. Present address: Catalan Institute of Nanotechnology (CIN2-CSIC), Campus UAB, Edifici CM3, 08193 Bellaterra, Spain.

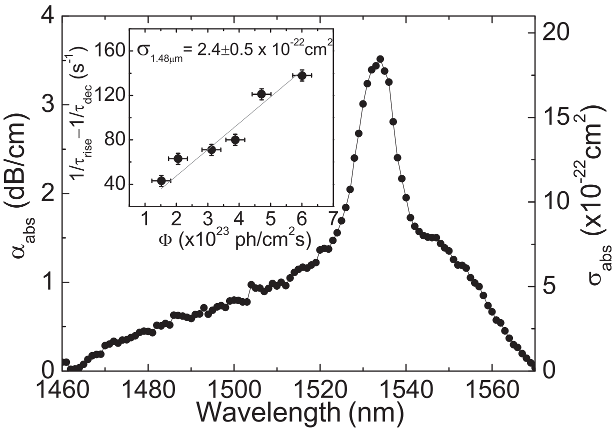

FIG. 1. Spectral dependence of the absorption losses (left axis) and of the absorption cross section (right axis). Inset: difference of the inverses of the rise and decay lifetimes as a function of Φ. The gray curve corresponds to the linear fit used to extract σ_{abs}.

signal related to the pump we have modulated the probe signal and used a lock-in at the detection stage.

As an initial step we have quantified the spectral losses of the waveguide. The raw insertion loss spectrum showed the Er^{3+} related absorption peak superimposed to a background that decreases by increasing the wavelength. Those background losses values were about (3.0 ± 0.5) dB/cm at 1535 nm and (4.0 ± 0.5) dB/cm at 1480 nm and are associated to passive scattering losses from the Si nanostructures present in the matrix and the matrix itself.[16] On Fig. 1 we show the result of subtracting those passive losses from the propagation losses, the remaining contribution being that associated to the direct absorption losses (α_{abs}) of Er^{3+}. It is worth to mention that α_{abs} is related to the total Er^{3+} absorbing content (N_{abs}) by the following relation:

$$\alpha_{abs}(\mathrm{dB/cm}) = 4.34\sigma_{abs}\mathrm{N}_{abs}\Gamma, \tag{1}$$

where Γ is the confinement factor of the waveguides ($\Gamma = 0.8$ as extracted from beam propagation method (BPM) simulations) and σ_{abs} is the absorption cross section at the tested wavelength. It is important to note that the maximum of absorption losses is about (3.5 ± 0.2) dB/cm at 1534 nm. Therefore, if full population inversion is achieved, the internal gain values would compensate for the passive losses and net optical gain of about 0.5 dB/cm would be possible.

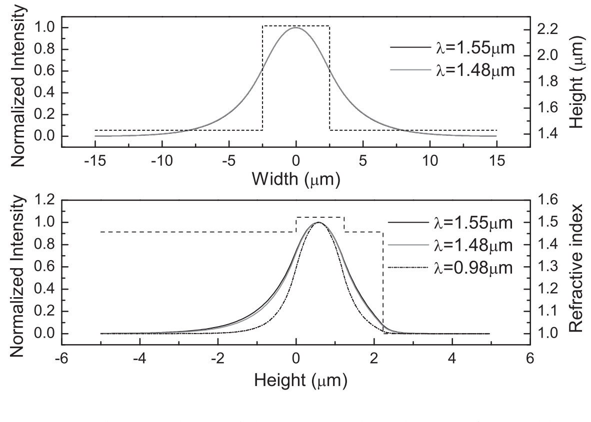

FIG. 2. (a) Horizontal shape of the supported modes at 1.54 μm (black) and 1.48 μm (gray). The horizontal profile of the waveguide is also shown (dashed line). (b) Vertical shape of the supported modes at 1.54 μm (solid black), at 1.48 μm (gray) and at 0.98 μm (dash dotted black). The vertical profile of the refractive index of the waveguide is also shown (dashed line).

It is possible to extract the spectral shape of σ_{abs} by estimating it at a certain wavelength and then using the spectral shape of the absorption losses. We have done this procedure at $\lambda = 1.48\,\mu$m with high photon flux (Φ) time resolved PL measurements.[12] The difference of the inverses of the lifetimes as a function of Φ is a linear curve whose slope is proportional to σ_{abs} at the pumping wavelength. In the inset of Fig. 1 these data are presented, providing a value of σ_{abs} $(1.48\,\mu\mathrm{m}) = (2.4 \pm 0.5) \times 10^{-22}\,\mathrm{cm}^2$. If we apply the McCumber relationship for extracting the emission cross section ($\sigma_{em}(\upsilon) = \sigma_{abs}(\upsilon)e^{\frac{\varepsilon-h\upsilon}{kT}}$, where ε is the average energy of the transition, k the Boltzmann constant, and T the temperature), it is possible to calculate that $\sigma_{em}(\lambda = 1.48\,\mu\mathrm{m})$ is about 4 times lower than $\sigma_{abs}(\lambda = 1.48\,\mu\mathrm{m})$.

Moreover, from σ_{abs} and Eq. (1) the concentration of absorbing Er^{3+} can be calculated to be $N_{abs} = (4.9 \pm 1.0) \times 10^{20}\,\mathrm{cm}^{-3}$. N_{abs} is slightly higher than the total content measured by SIMS, but compatible with this value. Even though there is a sizeable error bar derived from the entire experimental procedure, we can state that most of Er^{3+} absorbs.

To determine the concentration of emitting Er^{3+} (N_{em}), we have performed pump and probe measurements. Since excitation is performed at 1.48 μm, we can assume an effective two level system to describe the population of the $^4\mathrm{I}_{13/2}$ level (N_2) and of the $^4\mathrm{I}_{15/2}$ level (N_1), being $N_1 + N_2 = N_{em}$.

In Fig. 2, we show the profile of the TE mode in the horizontal (top panel) and vertical (bottom panel) directions for $\lambda = 1.48\,\mu$m (pump) and $\lambda = 1.54\,\mu$m (probe) wavelengths as extracted from beam propagation method (BPM) simulations. The overlap between the pump and the probe optical modes is higher than 98%.

The ratio between the probe signal with the pump on ($I_{pump\&probe}$) and the probe signal with the pump off (I_{probe}) is defined as the SE measured at the output of the waveguide. We will assume the emission and absorption cross sections (σ_{em} and σ_{abs} respectively) to be equal, which are reasonable around the maximum of the emission-absorption spectrum and take into account the stimulated emission contribution at the pump wavelength. Under those circumstances, SE and the internal gain (g_{int}) are

$$SE = \frac{e^{(N_2\sigma_{em}-N_1\sigma_{abs})\Gamma L}}{e^{-N_{Em}\sigma_{abs}\Gamma L}} \approx e^{2\sigma_{abs}\frac{\sigma_{exc}N_{Em}\Phi}{\frac{1}{\tau_d}+1.25\sigma_{exc}\Phi}\Gamma L} = e^{2g_{\mathrm{int}}L}, \tag{2}$$

$$g_{\mathrm{int}}(\mathrm{dB/cm}) = 4.34\sigma_{abs}\frac{\Phi\sigma_{exc}\mathrm{N}_{em}}{\frac{1}{\tau_{\mathrm{d}}} + 1.25\Phi\sigma_{exc}}\Gamma = \frac{G_{\mathrm{int}}}{L}, \tag{3}$$

where G_{int} is the total internal gain, τ_d is the decay lifetime of the $^4\mathrm{I}_{13/2} \rightarrow {}^4\mathrm{I}_{15/2}$ transition, $\sigma_{exc} = \sigma_{abs}(1.48\,\mu\mathrm{m})$, and L is the length of the waveguide. Note that Φ is reported at the input waveguide facet and decays along the waveguide with approximately 4 dB/cm loss. For low Φ, $\tau_d^{-1} \gg \Phi\sigma_{exc}$ and $g_{\mathrm{int}} = \tau_d\sigma_{abs}N_{em}\sigma_{exc}\Gamma\Phi$, linear in Φ.

In Fig. 3(a), the spectral dependences of SE for low and high Φ are reported for a 6 mm long waveguide (black squares and red dots respectively). By comparing these two measurements it is clear how SE increases with Φ. For a 14 mm long waveguide (green triangles in Fig. 3(a)) it is possible to enhance further SE in an almost exponential way, revealing

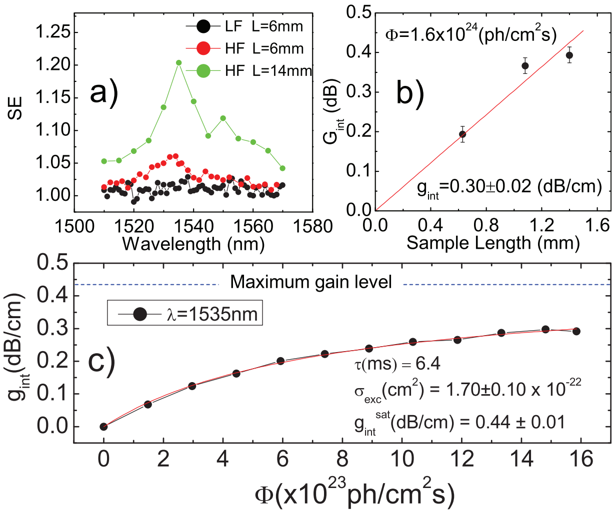

FIG. 3. (Color online) (a) SE of a 6 mm long waveguide at low and high Φ (black squares and red dots, respectively) and of 14 mm long waveguide at high Φ (green triangles). (b) G_{int} for different waveguide lengths at high Φ. A linear fit to the data is also shown. (c) g_{int} as a function of Φ for a waveguide length of 6 mm. A fit using Eq. (3) is also shown.

very clearly the Er^{3+} signature. Fig. 3(b) shows G_{int} as a function of the waveguide length for the high Φ. From the linear fit of the data, a g_{int} of about 0.3 dB/cm can be extracted. The deviation from the linear behavior is due to a pump depletion. Finally, in Fig. 3(c) we show g_{int} at $\lambda = 1535$ nm as a function of Φ for the shortest waveguide. The experimental data present a sublinear behavior, which is a clear indication that saturation is close to be achieved although not yet reached due to pump power limitations. We report a maximum value of $g_{\text{int}} = 0.3$ dB/cm at $\Phi = 1.6 \times 10^{24}$ (ph/cm^2 s), with an error of less than 5%. The experimental points are fit by Eq. (3), where $\tau_d = 6.4$ ms as extracted from the pure exponential behavior of the ${}^4I_{13/2} \rightarrow {}^4I_{15/2}$ PL decay. The fit yields two parameters: σ_{exc} and g_{int} at saturation, $g_{\text{int}}^{\text{sat}}$. The best fit is shown in Fig. 3(c) as a line. The first best fit parameter results $\sigma_{exc} = (1.7 \pm 0.1) \times 10^{-22}\,\text{cm}^{-2}$, which is similar to the one derived by the analysis of Fig. 1. The second best fit parameter is $g_{\text{int}}^{\text{sat}} = (0.44 \pm 0.01)$ dB/cm, which could be 0.55 dB/cm in the absence of pump induced stimulated emission. The latter value is just (16 ± 2)% of the absorption at the same wavelength (Fig. 1). From this result it is straightforward to conclude that most of the Er^{3+} within the matrix is able to absorb but cannot emit light efficiently. Even more, within the approximation of equal absorption and emission cross sections, we could conclude that 84% of the Er^{3+} population cannot be inverted. In a previous work, we have reported that the maximum Er^{3+} content able to emit light efficiently under direct optical pumping was $N_{em} = 0.64 \times 10^{20}\,\text{cm}^{-3}$.[12] This value is 19% of the total Er^{3+} content present in the sample, which is compatible with the 16% reported here.

Moreover, the emitting Er^{3+} population does not suffer from strong cooperative up-conversion mechanisms.[15] Therefore, based on all the previous observations, we postulate the existence of two Er^{3+} ions: (i) one able to recombine radiatively with roughly the same probability and (ii) another surrounded by quenching centers where the radiative recombination probability is extremely small. Although it is not the intention of the paper to provide a thorough insight of the microscopic physical properties of the non-emitting Er^{3+} ions, we are of the opinion that they may be placed within the Si-nc or that they clusterize and suffer from quenching effects. Indeed, it has already been reported in bulk glasses that the concentration of Er^{3+} is not homogeneous and clusters of ions can locally form whereas elsewhere they are isolated.[17,18] In all cases, the fact that more than 80% of the Er^{3+} acts as absorber is the first indispensible step of knowledge towards a clear understanding of those ions, which may allow optimizing the emitting and coupled content beyond the threshold of transparency.

In conclusion, we have reported on the absorption and amplification properties of an optimized waveguide with Si-nc coupled to Er^{3+} in a SiO_2 matrix as an active layer. By comparing the absorption losses and the maximum achievable internal gain we have determined that only 16% of the Er^{3+} ions can be inverted, even under resonant copropagant pumping, the rest 84% contributing only to absorption. The extracted internal gain values are conclusive since: (i) the spatial distribution of the waveguide modes for the pump and probe wavelengths is practically equivalent, (ii) the internal gain values are almost driven to saturation, (iii) the pump light suffers low losses, so it can pump effectively the whole length of the waveguide. On the basis of these results we conclude that net optical gain under optical pumping is still far to be accomplished.

We acknowledge R. Rizk and F. Gourbilleau from CIMAP, UMR CEA/CNRS/ENSICAEN/Univ. CAEN (France) for the sample growth and the financial support of the HELIOS Project (FP7 224312). D.N.-U. thanks A. Trifonova for fruitful discussions.

[1] D. Liang and J. E. Bowers, Nat. Photon. **4**, 511 (2010).
[2] J. H. Shin, H. S. Han, and S. Y. Seo, *Towards the First Silicon Laser*, edited by L. Pavesi, S. V. Gaponenko, and L. Dal Negro (Kluwer, Dordrecht, 2003), NATO Science Series II, Vol. 93, p. 401.
[3] J. Lee, J. H. Shin, and N. Park, J. Lightwave Technol. **23**, 19 (2005).
[4] N. Daldosso, D. Navarro-Urrios, M. Melchiorri, L. Pavesi, F. Gourbilleau, M. Carrada, R. Rizk, C. Garcia, P. Pellegrino, B. Garrido, and L. Cognolato, Appl. Phys. Lett. **86**, 261103 (2005).
[5] B. Garrido, C. García, S.-Y. Seo, P. Pellegrino, D. Navarro-Urrios, N. Daldosso, L. Pavesi, F. Gourbilleau, and R. Rizk, Phys. Rev. B **76**, 245308 (2007).
[6] A. Pitanti, D. Navarro-Urrios, N. Prtljaga, N. Daldosso, F. Gourbilleau, R. Rizk, B. Garrido, and L. Pavesi, J. Appl. Phys. **108**, 053518 (2010).
[7] M. Wojdak, M. Klik, M. Forcales, O. B. Gusev, T. Gregorkiewicz, D. Pacifici, G. Franzò, F. Priolo, and F. Iacona, Phys. Rev. B **69**, 233315 (2004).
[8] P. G. Kik and A. Polman, J. Appl. Phys. **88**, 1992 (2000).
[9] I. Izeddin, A. S. Moskalenko, I. N. Yassievich, M. Fujii, and T. Gregorkiewicz, Phys. Rev. Lett. **97**, 207401 (2006).
[10] S. Minissale, T. Gregorkiewicz, M. Forcales, and R. G. Elliman, Appl. Phys. Lett. **89**, 171908 (2006).
[11] P. Pellegrino, B. Garrido, J. Arbiol, C. Garcia, Y. Lebour, and J. R. Morante, Appl. Phys. Lett. **88**, 121915 (2006).
[12] D. Navarro-Urrios, Y. Lebour, O. Jambois, B. Garrido, A. Pitanti, N. Daldosso, L. Pavesi, J. Cardin, K. Hijazi, L. Khomenkova, F. Gourbilleau, and R. Rizk, J. Appl. Phys. **106**, 093107 (2009).
[13] F. Gourbilleau, C. Dufour, M. Levalois, J. Vicens, R. Rizk, C. Sada, F. Enrichi, and G. Battaglin, J. Appl. Phys. **94**, 3869 (2003).
[14] F. Gourbilleau, M. Levalois, C. Dufour, J. Vicens, and R. Rizk, J. Appl. Phys. **95**, 3717 (2004).
[15] D. Navarro-Urrios, A. Pitanti, N. Daldosso, F. Gourbilleau, L. Khomenkova, R. Rizk, and L. Pavesi, Physica E **41**, 1029 (2009).
[16] N. Daldosso, D. Navarro-Urrios, M. Melchiorri, C. García, P. Pellegrino, B. Garrido, C. Sada, G. Battaglin, F. Gourbilleau, R. Rizk, and L. Pavesi, IEEE J. Sel. Top. Quantum Electron. **12**, 1607 (2006).
[17] B. J. Ainslie, S. P. Craig-Ryan, S. T. Davey, J. R. Armitage, C. G. Atkins, J. F. Massicott, and R. Wyatt, IEE Proc.-J: Optoelectron. **137**, 205 (1990).
[18] B. J. Ainslie, J. Lightwave Technol. **9**, 220 (1991).

Limit to the erbium ions emission in silicon-rich oxide films by erbium ion clustering

Nikola Prtljaga,[1,*] Daniel Navarro-Urrios,[2] Andrea Tengattini,[1] Aleksei Anopchenko,[1] Joan Manel Ramírez,[3] José Manuel Rebled,[3,4] Sònia Estradé,[3,5] Jean-Philippe Colonna,[6] Jean-Marc Fedeli,[6] Blas Garrido,[3] and Lorenzo Pavesi[1]

[1]*NanoScience Lab, Department of Physics, University of Trento, Via Sommarive 14, 38123 Povo, Trento, Italy*
[2]*Catalan Institute of Nanotechnology (CIN2-CSIC), Campus UAB, Edifici CM3, 08193 Bellaterra, Spain*
[3]*MIND–IN2UB, Departament D'Electrònica, Universitat de Barcelona, Carrer Martí i Franquès, 08 028 Barcelona, Spain*
[4]*Barcelona Materials Science Institute (ICMAB), CSIC, Campus UAB, Bellaterra 08193, Spain*
[5]*TEM-MAT, Scientific and Technological Centers, (CCiT), Universitat de Barcelona, Carrer Martí i Franquès, 08 028 Barcelona, Spain*
[6]*CEA/Léti, Minatec 17 rue des Martyrs, 38054 Grenoble cedex 9, France*
**nikolap@science.unitn.it*

Abstract: We have fabricated a series of thin (~50 nm) erbium-doped (by ion implantation) silicon-rich oxide films in the configuration that mitigates previously proposed mechanisms for loss of light emission capability of erbium ions. By combining the methods of optical, structural and electrical analysis, we identify the erbium ion clustering as a driving mechanism to low optical performance of this material. Experimental findings in this work clearly evidence inadequacy of the commonly employed optimization procedure when optical amplification is considered. We reveal that the significantly lower erbium ion concentrations are to be used in order to fully exploit the potential of this approach and achieve net optical gain.

OCIS codes: (130.3130) Integrated optics materials; (160.5690) Rare-earth-doped materials; (250.5230) Photoluminescence; (310.6860) Thin films, optical properties.

References and links

1. D. Liang and J. E. Bowers, "Recent progress in lasers on silicon," Nat. Photonics **4**(8), 511–517 (2010).
2. A. Polman and F. C. J. M. van Veggel, "Broadband sensitizers for erbium-doped planar optical amplifiers: review," J. Opt. Soc. Am. B **21**(5), 871–895 (2004).
3. M. Fujii, M. Yoshida, Y. Kanzawa, S. Hayashi, and K. Yamamoto, "1.54 μm photoluminescence of Er^{3+} doped into SiO_2 films containing Si nanocrystals: evidence for energy transfer from Si nanocrystals to Er^{3+}," Appl. Phys. Lett. **71**(9), 1198–1200 (1997).
4. G. Franzò, S. Boninelli, D. Pacifici, F. Priolo, F. Iacona, and C. Bongiorno, "Sensitizing properties of amorphous Si clusters on the 1.54-μm luminescence of Er in Si-rich SiO_2," Appl. Phys. Lett. **82**(22), 3871–3873 (2003).
5. I. Izeddin, D. Timmerman, T. Gregorkiewicz, A. Moskalenko, A. Prokofiev, I. Yassievich, and M. Fujii, "Energy transfer in Er-doped SiO_2 sensitized with Si nanocrystals," Phys. Rev. B **78**(3), 035327 (2008).
6. O. Jambois, F. Gourbilleau, A. J. Kenyon, J. Montserrat, R. Rizk, and B. Garrido, "Towards population inversion of electrically pumped Er ions sensitized by Si nanoclusters," Opt. Express **18**(3), 2230–2235 (2010).
7. I. Izeddin, A. S. Moskalenko, I. N. Yassievich, M. Fujii, and T. Gregorkiewicz, "Nanosecond dynamics of the near-infrared photoluminescence of Er-doped SiO_2 sensitized with Si nanocrystals," Phys. Rev. Lett. **97**(20), 207401 (2006).
8. C. J. Oton, W. H. Loh, and A. J. Kenyon, "Er^{3+} excited state absorption and the low fraction of nanocluster-excitable Er^{3+} in SiO_x," Appl. Phys. Lett. **89**(3), 031116 (2006).
9. B. Garrido, C. García, P. Pellegrino, D. Navarro-Urrios, N. Daldosso, L. Pavesi, F. Gourbilleau, and R. Rizk, "Distance dependent interaction as the limiting factor for Si nanocluster to Er energy transfer in silica," Appl. Phys. Lett. **89**(16), 163103 (2006).
10. O. Savchyn, F. Ruhge, P. Kik, R. Todi, K. Coffey, H. Nukala, and H. Heinrich, "Luminescence-center-mediated excitation as the dominant Er sensitization mechanism in Er-doped silicon-rich SiO_2 films," Phys. Rev. B **76**(19), 195419 (2007).
11. D. Navarro-Urrios, Y. Lebour, O. Jambois, B. Garrido, A. Pitanti, N. Daldosso, L. Pavesi, J. Cardin, K. Hijazi, L. Khomenkova, F. Gourbilleau, and R. Rizk, "Optically active Er^{3+} ions in SiO_2 codoped with Si nanoclusters," J. Appl. Phys. **106**(9), 093107 (2009).

#170884 - $15.00 USD Received 21 Jun 2012; revised 8 Aug 2012; accepted 8 Aug 2012; published 21 Aug 2012

12. D. Navarro-Urrios, F. Ferrarese Lupi, N. Prtljaga, A. Pitanti, O. Jambois, J. M. Ramírez, Y. Berencén, N. Daldosso, B. Garrido, and L. Pavesi, "Copropagating pump and probe experiments on Si-nc in SiO_2 rib waveguides doped with Er: the optical role of non-emitting ions," Appl. Phys. Lett. **99**(23), 231114 (2011).
13. S. Cueff, C. Labbé, O. Jambois, B. Garrido, X. Portier, and R. Rizk, "Thickness-dependent optimization of Er^{3+} light emission from silicon-rich silicon oxide thin films," Nanoscale Res. Lett. **6**(1), 395 (2011).
14. C. A. Barrios and M. Lipson, "Electrically driven silicon resonant light emitting device based on slot-waveguide," Opt. Express **13**(25), 10092–10101 (2005).
15. J. T. Robinson, K. Preston, O. Painter, and M. Lipson, "First-principle derivation of gain in high-index-contrast waveguides," Opt. Express **16**(21), 16659–16669 (2008).
16. B. Garrido, C. García, S.-Y. Seo, P. Pellegrino, D. Navarro-Urrios, N. Daldosso, L. Pavesi, F. Gourbilleau, and R. Rizk, "Excitable Er fraction and quenching phenomena in Er-doped SiO_2 layers containing Si nanoclusters," Phys. Rev. B **76**(24), 245308 (2007).
17. F. Iacona, C. Bongiorno, C. Spinella, S. Boninelli, and F. Priolo, "Formation and evolution of luminescent Si nanoclusters produced by thermal annealing of SiO_x films," J. Appl. Phys. **95**(7), 3723–3732 (2004).
18. F. Priolo, G. Franzò, D. Pacifici, V. Vinciguerra, F. Iacona, and A. Irrera, "Role of the energy transfer in the optical properties of undoped and Er-doped interacting Si nanocrystals," J. Appl. Phys. **89**(1), 264–272 (2001).
19. R. S. Quimby, W. J. Miniscalco, and B. Thompson, "Clustering in erbium-doped silica glass fibers analyzed using 980 nm excited-state absorption," J. Appl. Phys. **76**(8), 4472–4478 (1994).
20. P. Pellegrino, B. Garrido, J. Arbiol, C. Garcia, Y. Lebour, and J. R. Morante, "Site of Er ions in silica layers codoped with Si nanoclusters and Er," Appl. Phys. Lett. **88**(12), 121915 (2006).
21. I. F. Crowe, R. J. Kashtiban, B. Sherliker, U. Bangert, M. P. Halsall, A. P. Knights, and R. M. Gwilliam, "Spatially correlated erbium and Si nanocrystals in coimplanted SiO_2 after a single high temperature anneal," J. Appl. Phys. **107**(4), 044316 (2010).
22. X. Wang, P. Li, M. Malac, R. Lockwood, and A. Meldrum, "The spatial distribution of silicon NCs and erbium ion clusters by simultaneous high-resolution energy filtered and Z-contrast STEM and transmission electron tomography," Phys. Status Solidi., C Curr. Top. Solid State Phys. **8**(3), 1038–1043 (2011).
23. D. A. Stanley, H. Alizadeh, A. Helmy, N. P. Kherani, L. Qian, and S. Zukotynski, "SEM-mapped micro-photoluminescence studies of highly luminescent micro-clusters in erbium-doped silicon-rich silicon oxide," J. Lumin. **131**(1), 72–77 (2011).
24. M. Shah, M. Wojdak, A. J. Kenyon, M. P. Halsall, H. Li, and I. F. Crowe, "Rate equation modelling of erbium luminescence dynamics in erbium-doped silicon-rich-silicon-oxide," J. Lumin. (to be published).
25. A. Anopchenko, A. Tengattini, A. Marconi, N. Prtljaga, J. M. Ramírez, O. Jambois, Y. Berencén, D. Navarro-Urrios, B. Garrido, F. Milesi, J.-P. Colonna, J.-M. Fedeli, and L. Pavesi, "Bipolar pulsed excitation of erbium-doped nanosilicon light emitting diodes," J. Appl. Phys. **111**(6), 063102 (2012).
26. S. Minissale, T. Gregorkiewicz, M. Forcales, and R. G. Elliman, "On optical activity of Er^{3+} ions in Si-rich SiO_2 waveguides," Appl. Phys. Lett. **89**(17), 171908 (2006).
27. M. Wojdak, M. Klik, M. Forcales, O. Gusev, T. Gregorkiewicz, D. Pacifici, G. Franzò, F. Priolo, and F. Iacona, "Sensitization of Er luminescence by Si nanoclusters," Phys. Rev. B **69**(23), 233315 (2004).
28. G. Franzò, M. Miritello, S. Boninelli, R. Lo Savio, M. G. Grimaldi, F. Priolo, F. Iacona, G. Nicotra, C. Spinella, and S. Coffa, "Microstructural evolution of SiO_x films and its effect on the luminescence of Si nanoclusters," J. Appl. Phys. **104**(9), 094306 (2008).
29. C. Maurizio, F. Iacona, F. D'Acapito, G. Franzò, and F. Priolo, "Er site in Er-implanted Si nanoclusters embedded in SiO_2," Phys. Rev. B **74**(20), 205428 (2006).
30. G. Franzò, E. Pecora, F. Priolo, and F. Iacona, "Role of the Si excess on the excitation of Er doped SiO_x," Appl. Phys. Lett. **90**(18), 183102 (2007).
31. M. de Dood, L. Slooff, A. Polman, A. Moroz, and A. van Blaaderen, "Local optical density of states in SiO_2 spherical microcavities: theory and experiment," Phys. Rev. A **64**(3), 033807 (2001).
32. N. Daldosso, D. Navarro-Urrios, M. Melchiorri, L. Pavesi, C. Sada, F. Gourbilleau, and R. Rizk, "Refractive index dependence of the absorption and emission cross sections at 1.54 μm of Er^{3+} coupled to Si nanoclusters," Appl. Phys. Lett. **88**(16), 161901 (2006).
33. N. Daldosso, D. Navarro-Urrios, M. Melchiorri, L. Pavesi, F. Gourbilleau, M. Carrada, R. Rizk, C. García, P. Pellegrino, B. Garrido, and L. Cognolato, "Absorption cross section and signal enhancement in Er-doped Si nanocluster rib-loaded waveguides," Appl. Phys. Lett. **86**(26), 261103 (2005).
34. P. Horak, W. H. Loh, and A. J. Kenyon, "Modification of the Er^{3+} radiative lifetime from proximity to silicon nanoclusters in silicon-rich silicon oxide," Opt. Express **17**(2), 906–911 (2009).
35. L. Borowska, S. Fritzsche, P. G. Kik, and A. E. Masunov, "Near-field enhancement of infrared intensities for f-f transitions in Er^{3+} ions close to the surface of silicon nanoparticles," J. Mol. Model. **17**(3), 423–428 (2011).
36. E. M. Purcell, "Spontaneous emission probabilities at radio frequencies," Phys. Rev. **69**, 681 (1946).
37. E. Snoeks, A. Lagendijk, and A. Polman, "Measuring and modifying the spontaneous emission rate of erbium near an interface," Phys. Rev. Lett. **74**(13), 2459–2462 (1995).
38. H. Urbach and G. Rikken, "Spontaneous emission from a dielectric slab," Phys. Rev. A **57**(5), 3913–3930 (1998).
39. C. Creatore, L. C. Andreani, M. Miritello, R. Lo Savio, and F. Priolo, "Modification of erbium radiative lifetime in planar silicon slot waveguides," Appl. Phys. Lett. **94**(10), 103112 (2009).

#170884 - $15.00 USD Received 21 Jun 2012; revised 8 Aug 2012; accepted 8 Aug 2012; published 21 Aug 2012

1. Introduction

Erbium (Er^{3+})-doped silicon-rich oxide (SRO) films are studied as active material to a silicon-integrated optical amplifier or laser [1,2]. By using the sensitization action of silicon nanoclusters (Si-ncl) [3], limitations of the Er^{3+} excitation process are avoided (small absorption cross-section, spectrally narrow absorption lines [2]), and the overall material emission performance is improved [3–5]. At the same time, complementary-metal-oxide-semiconductor (CMOS) process compatibility is maintained, and emission in the third telecom window (1.53 μm) is achieved [1]. This allows for direct compatibility with the mainstream semiconductor technology, which yields mass manufacturing and heavy integration density of photonic devices [1]. Additional attractiveness is given by the possibility of electrical injection through electrical transport in the Si-ncl [6].

Despite these premises, optical gain achievement is still eluding. There is consensus in the literature that the principal reason obstructing the optical gain achievement in this material is a low fraction of sensitized erbium ions [7–10]. Recently, we have demonstrated that this is followed by the loss of light emission capability of Er^{3+} when embedded in SRO material [11]. While the main fraction of embedded erbium ions does not participate in the process of light emission, absorption properties of non-emitting ions remain unaltered [12]. Evidently, this becomes a major obstacle toward population inversion in this material. At this point, elucidating the origin of this phenomenon becomes of paramount significance for further material optimization and device development. In this work, we address this issue in a conclusive way and report on the mechanism responsible for it, i.e., erbium ion clustering.

2. Experiment

The samples used in this work are thin Er^{3+}-doped (by ion implantation) films of alternating SRO and SiO_2 layers deposited on a crystalline silicon wafer by low-pressure chemical vapor deposition (LPCVD) in a standard CMOS line. Thin films (d ~50 nm) have the advantage that can be studied by electrical [6], optical [13] and optoelectronic means [14]. Deposition starts with a d = 2 nm thin SiO_2 layer deposited on p-type crystalline silicon wafer on top of which is deposited a d = 3 nm thick SRO layer with nominal silicon excess of 20 at. %. The procedure is repeated 10 times in order to reach the desired thickness of d ~50 nm for optimum performance in slot waveguide amplifier [15]. Finally, a d = 2 nm thin layer of SiO_2 is deposited on top. After deposition, samples are thermally treated in order to induce phase separation and amorphous silicon nanoparticles growth and formation ($T_{annealing} = 900°C$ for t = 1 h) [16,17]. Subsequently, the samples were implanted with erbium ions (dose: 1×10^{15} at./cm^2 and energy: 20 keV) and thermally treated for a second time ($T_{post\text{-}annealing} = 800°C$ for t = 6 h) to recover implantation damage.

Photoluminescence (PL) measurements were done by employing the three different lines of an argon ion laser: λ_{exc} = 488 nm (resonant, excitation wavelength coincides with absorption line of Er^{3+}), λ_{exc} = 476 nm (non-resonant, Er^{3+} are excited by energy transfer from Si-ncl) and an additional line in UV λ_{exc} = 361 nm for the continuous wave (CW) visible PL measurements. In addition, a laser diode (λ_{exc} = 974 nm, resonant) was used as well. Time-resolved (TR) PL measurements in the infrared were performed by modulating the laser beam with a mechanical chopper in the case of excitation with the argon ion laser, or by modulating the diode driving current by an external function generator in the case of excitation with the laser diode. For detection in the visible, a GaAs photomultiplier tube (PMT) for CW PL is used, and an InGaAs PMT is used for the IR (both CW and TR PL measurements). In the case of TR PL measurements in IR, the InGaAs PMT was interfaced with a multichannel scalar averager. In all cases before detection, the optical signal was spectrally filtered with a monochromator.

Electroluminescence (EL) spectra are collected using a fiber bundle and analyzed with a Spectra-Pro 2300i monochromator coupled with a nitrogen-cooled charge-coupled device (CCD) cameras (one in visible and one in IR). Emitted optical power and external quantum

#170884 - $15.00 USD Received 21 Jun 2012; revised 8 Aug 2012; accepted 8 Aug 2012; published 21 Aug 2012

efficiency (EQE) are measured using either a calibrated LED or a Ge photodiode. The acceptance angle of the photodiode is taken into account.

For transmission electron microscopy (TEM), a JEOL 2010-FEG (200kV) scanning transmission electron microscope was used, equipped with a GIF spectrometer for STEM-EELS and EFTEM imaging mode. Samples for TEM observations were prepared through conventional mechanical polishing with a final Ar^+ bombardment using a PIPS Gatan system. Erbium concentrations were determined by secondary ion mass spectrometry (SIMS) calibrated with a sample of known erbium concentration. The silicon excess was calculated with the formula $(1 - x/2)/(1 + x)$, with $x = [O]/[Si]$ as measured by x-ray photon spectroscopy (XPS).

3. Results and discussion

The erbium concentration profile in our thin films has been determined by SIMS, and it is reported in Fig. 1(a). The peak concentration $n_{peak} = 5.2 \times 10^{20}$ at./cm^3 is located in the center of the active layer, at approximately d ~20 nm below the sample surface. The average erbium concentration is $n_{average} = 2.9 \times 10^{20}$ at./cm^3. A silicon excess of 9 at. % was determined by XPS. The thickness of the active material d ~44 nm was found by TEM (see Appendix A). Note that this Er^{3+} concentration was chosen based on previous reports that indicate long lifetimes and high emission intensities, i.e., no cooperative photoluminescence quenching effects [18].

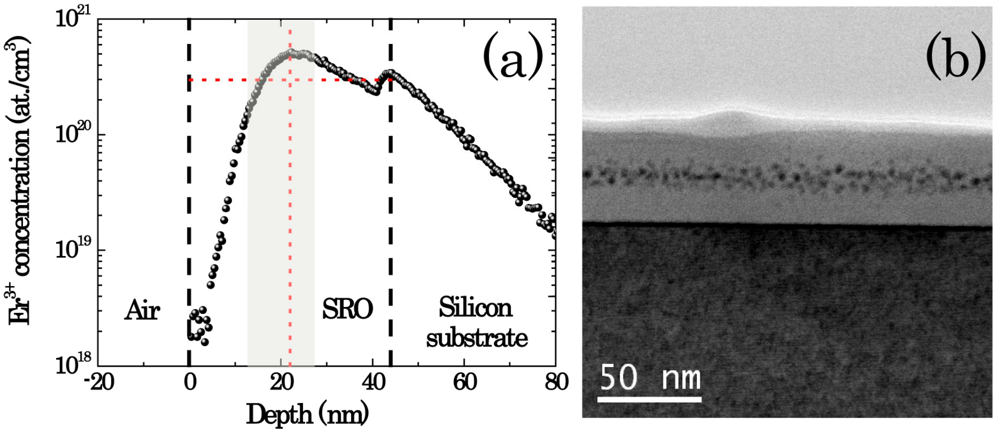

Fig. 1. (a) Semi-log plot of erbium concentration profile in the studied samples obtained by SIMS. Thick vertical dashed lines indicate interfaces between air/SRO and SRO/silicon substrate. Vertical red dotted line corresponds to the peak Er^{3+} concentration, and the horizontal red dotted line to an average Er^{3+} concentration in the active layer. The shaded area corresponds to the layer where erbium clusters are visible in TEM images. (b) Bright field scanning TEM (STEM) image of the sample.

Surprisingly, erbium clusters are visible as a dark spotted layer in TEM image (Fig. 1(b)). This erbium cluster layer is located at d ~20 nm below the sample surface, and it is approximately 15 nm wide (see Fig. 1(b)). It contains 55 ± 5% of the total number of erbium ions (shaded area in Fig. 1(a)). This is a first insight on what could limit the Er^{3+} emission capability as the clustered erbium ions emit light very inefficiently [19]. However, not all of the Er^{3+} in this layer may be clustered and, on the other hand, owing to the finite resolution of TEM, the erbium clustered region could be wider, as small erbium clusters (formed by a few atoms only) may escape detection. Thus, we correlate these findings with the results of a spectroscopic analysis.

It is worth mentioning that similar local inhomogeneity in erbium ions spatial distribution and the tendency to clusterize in silicon rich oxide films have been reported previously in thin films prepared with very different deposition techniques [20–24]. Thus, this type of behavior

#170884 - $15.00 USD Received 21 Jun 2012; revised 8 Aug 2012; accepted 8 Aug 2012; published 21 Aug 2012

is not inherent to LPCVD but is quite general for Er^{3+} concentrations larger than 10^{20} at./cm^3 [20–24].

Er^{3+} emission can be observed in our samples both by non-resonant (Fig. 2(a) - $\lambda_{exc} = 476$ nm with an excitation photon flux $\Phi_{exc} = 3 \times 10^{20}$ ph./cm^2) and resonant optical excitation, as well as by electrical excitation (see Appendix B). In Fig. 2(b), a visible PL spectrum under CW UV optical excitation ($\lambda_{exc} = 364$ nm, $\Phi_{exc} = 3 \times 10^{18}$ ph./cm^2) is also reported. The broad PL band in Fig. 2(b) situated at $\lambda = 750$ nm is attributed to residual Si-ncl PL. The additional peak at 550 nm, which is observable only under UV optical excitation or electrical bias, could be associated with direct excited state emission ($^4S_{3/2}$ – $^4I_{15/2}$ radiative Er^{3+} transition) visible owing to its high emission cross section. Moreover, the presence of cooperative upconversion (CUC) processes are observed by the shortening of the lifetimes of the 1.535 μm Er^{3+} emission with increased excitation photon flux (Fig. 3(a) - $\lambda_{exc} = 476$ nm, excitation photon flux varies from $\Phi_{exc} = 2.8 \times 10^{18}$ ph./cm^2 to 2.7×10^{20} ph./cm^2).

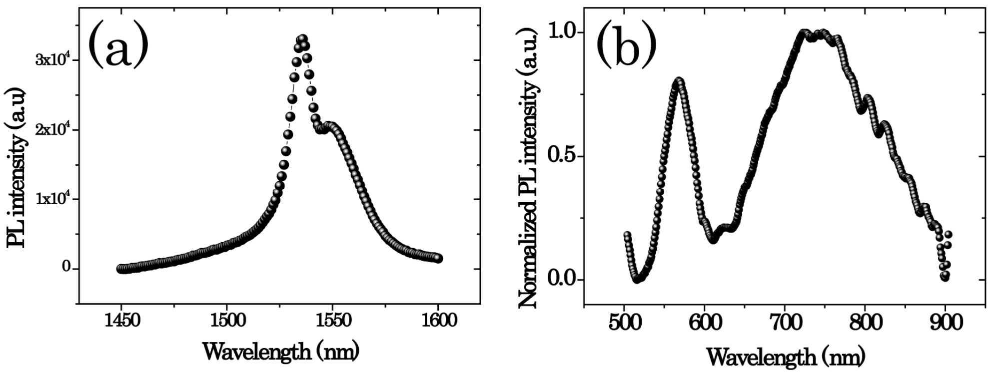

Fig. 2. (a) PL spectrum of the $^4I_{13/2}$ – $^4I_{15/2}$ radiative erbium transition in the studied sample under non-resonant optical excitation. (b) Normalized visible PL spectrum under CW UV optical excitation.

In order to evaluate the fraction of Er^{3+} that emits light efficiently, n_{active}, CUC has been quantified with the method of [16]. The PL measurements were carried out by resonant (λ_{exc} = 974 nm) and non-resonant (λ_{exc} = 476 nm) optical excitation. The experimental data were fitted by Eq. (1) [16]:

$$\frac{1}{\tau_{PL}(\Phi_{exc})} = \frac{n_2 * C_{up}}{\ln(1+\tau_0 * n_2 * C_{up})} \tag{1}$$

where n_2 is the excited state population of erbium ions at $t_0 = 0$, and C_{up} is the CUC's coefficient; τ_0 is the Er^{3+} decay time in the absence of CUC, τ_{PL} is the measured Er^{3+} emission decay time and Φ_{exc} is the excitation photon flux. In both cases (resonant and non-resonant optical excitation), the same results (within experimental error) were found.

An example of the fit of experimental data by Eq. (1) is reported in Fig. 3(a) (λ_{exc} = 476 nm). The fit yields $C_{up} = 2.1 \pm 0.3 \times 10^{-15}$ cm^3/s, and $\tau_0 = 2.13 \pm 0.05$ ms. This is a long lifetime considering the estimated radiative lifetimes in these samples (7 ms, see Appendix C). It is worth noticing that this same material shows a very high EQE under electrical bias (~0.4%) [25].

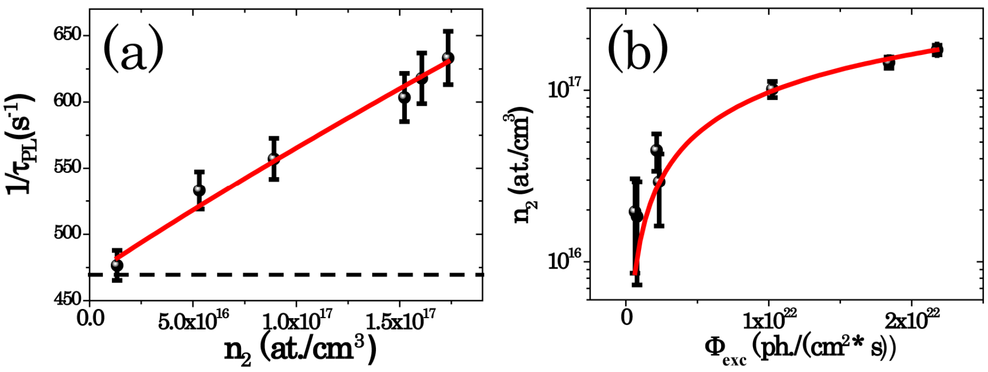

Fig. 3. (a) The best fit (red line) of experimental data (black spheres) obtained using non-resonant optical excitation by Eq. (1). Dashed horizontal line represents the time decay in absence of cooperative upconversion. (b) The best fit (red line) of experimental data (black spheres) obtained using resonant optical excitation by Eq. (2).

C_{up} is significantly higher than the previously reported value for similar Er^{3+} concentrations [9], although it is in agreement with the large erbium clustering observed in TEM images. Note that C_{up} represents an average value, and the local C_{up} can vary significantly across the active layer owing to the Er^{3+} concentration profile (see Fig. 1(a)).

Knowing C_{up} and σ_{abs}, the direct Er^{3+} absorption cross-section (measured value agrees with those reported in [11] within the experimental errors), n_{active} can be estimated by fitting the experimental data obtained using resonant optical excitation (λ_{exc} = 974 nm) with the following Eq. (2) (Fig. 3(b)) [11]:

$$n_2 = \frac{[(\sigma_{abs}(974nm)*\Phi_{exc}+\frac{1}{\tau_0})^2+4*\sigma_{abs}(974nm)*C_{up}*n_{active}*\Phi_{exc}]^{1/2}}{2*C_{up}} - \frac{(\sigma_{abs}(974nm)*\Phi_{exc}+\frac{1}{\tau_0})}{2*C_{up}}. \tag{2}$$

It is found $n_{active} = 2.1 \pm 0.2 \times 10^{18}$ at./cm^3. This accounts for approximately 0.72 ± 0.11% of the total Er^{3+} content measured by SIMS.

This number is significantly lower than the non-clustered fraction estimated from TEM (~45%). However, in the TEM images only clusters of certain size can be seen (few nm of size). Thus, if erbium clusters consist of only few erbium ions they will not be observed by TEM, although they will heavily influence the optical properties of the active material. This explains the observations of previous reports, even though higher fractions of active erbium ions were reported [11,26,27]. Therefore, Er^{3+} clustering is the main phenomenon that limits n_{active}.

While different fabrication protocols could lead to different matrix quality [28] and consequently, a different local Er^{3+} environment [29], loss of emission capability of erbium ions is a frequently reported issue [11,20,21], indicating a similar quenching mechanism. This is here studied on samples made by LPCVD. Furthermore, variations in silicon excess (0 at.% - 10 at.%) and thermal treatment do confirm the data presented here. We studied variation in annealing temperatures (900°C – 1100°C), duration (5 – 60 min.) and methods (furnace or rapid thermal processing)

Although we observe a certain variations in n_{active} and CUC's coefficient among different samples, the degree of these variations (n_{active} being always ≤ 1% of total Er^{3+} content) is not sufficient to provide an amplifier material (which requires $n_{active} > 50\%$) or to change the overall picture. For sake of completeness, we have not found appreciable difference in SIMS profiles and TEM images between different samples.

It is important to emphasize that in these samples, a significant fraction of erbium ions is situated in the silica layers that prevent the suggested silicon excess induced Er^{3+} ion de-excitation [30]. Moreover, n_{active} is determined by using a sub-bandgap (for Si-ncl) resonant (for Er^{3+}) optical excitation, avoiding the possibility of energy back-transfer toward the Si-ncl [7]. Furthermore, we would like to stress the fact that no optical gain was reported in this material (silicon-rich oxide) with high Er^{3+} concentration ($> 1 \times 10^{20}$ at./cm^3) regardless of the particular deposition technique used. Thus, we conclude that the erbium ion clustering is the main mechanism responsible for the low optical activity of Er^{3+} ions in this material at the used erbium concentration ($\sim 10^{20}$ at./cm^3).

Therefore, to achieve full Er^{3+} inversion (i.e. net optical gain), the Er^{3+} concentration should be decreased significantly with respect to the usually considered optimum value of $n_{Er3+} \sim 10^{20}$ at./cm^3 [18]. This will reduce the maximum gain value achievable.

4. Conclusions

In summary, thin erbium-doped films of alternating layers of SRO and silica were fabricated and characterized in a configuration that mitigates previously proposed mechanisms for loss of light emission capability of erbium ions [7,8,30]. Even though promising results in terms of erbium PL lifetime (~2 ms) and EQE under electrical bias have been obtained, the main fraction of erbium ions does not contribute efficiently to the light emission owing to erbium ion clustering. The only possibility left to achieve net gain in this material system is to decrease the Er^{3+} concentration to level where clustering no longer occurs.

Appendix A: Structural analysis of the samples

Energy filtered (EFTEM) TEM image of the sample obtained by filtering at 15 eV (c-Si plasmon peak) is reported in Fig. 4(a). An active layer, approximately 44 nm thin, can be clearly seen, with the SRO (bright lines) and oxide layer (darker lines) visible. Erbium clusters can be seen close to the center of the active layer (dark spots in Fig. 4(a)) their chemical nature confirmed by HAADF (Fig. 4(b) - bright line in the center of the layer corresponds to a high concentration of erbium (Z = 68) clusters), EFTEM and EELS (not shown). These clusters lay at $d \approx 20$ nm and extend in a region 15 nm thick.

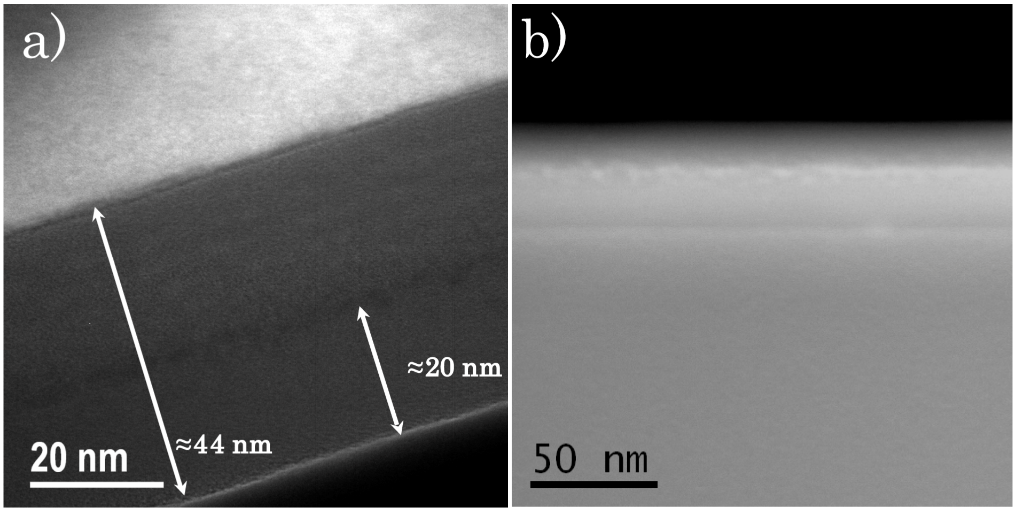

Fig. 4. (a) EFTEM image of the sample. (b) High angle annular dark field STEM image of the sample.

#170884 - $15.00 USD Received 21 Jun 2012; revised 8 Aug 2012; accepted 8 Aug 2012; published 21 Aug 2012

Appendix B: Electroluminescence (EL) spectrum of the samples

EL spectrum of the samples in the IR obtained with an injected current of I = 100 μA and a forward bias of U = 45.1 V is reported in Fig. 5. This spectrum, owing to the $^4I_{13/2} - ^4I_{15/2}$ erbium radiative transition, resembles the one obtained under optical excitation (Fig. 2(a)).

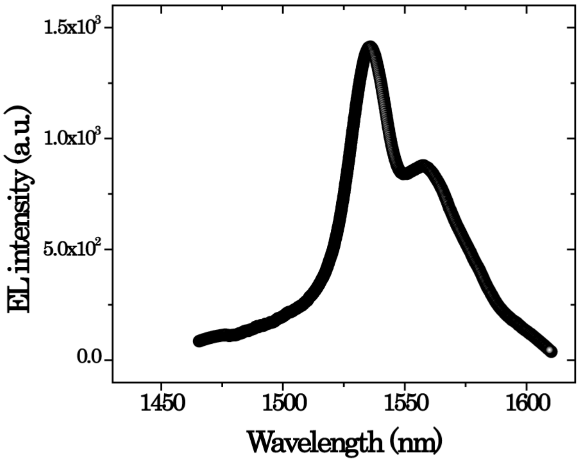

Fig. 5. EL spectrum of the $^4I_{13/2} - ^4I_{15/2}$ radiative erbium transition in the studied samples.

Appendix C: Erbium radiative lifetime estimate

To estimate the CUC's coefficient [16] and the fraction of Er^{3+}, which can emit efficiently [11], we estimate the Er^{3+} radiative lifetime. In the literature, it is reported that Er^{3+} in a bulk silica has a radiative lifetime τ_{rad} = 18 ms [31]. However, since in SRO films refractive index is different than in SiO_2 [32], the radiative lifetime of Er^{3+} changes. Considering the silicon excess (9 at.%) and literature reports [6,16,27,32,33], a radiative lifetime of τ_{rad} ~ 10 ms can be estimated in our films.

This value is also what is expected for bulk samples when accounting for the near-field enhancement of radiative rate in vicinity of silicon nanoparticles (τ_{rad} = 10 ms [34] - τ_{rad} = 7 ms [35]). Finally, since we are using thin films deposited on a high refractive index material (silicon substrate), a certain enhancement of the radiative rate is expected [36–39], and therefore we assumed a value of τ_{rad} = 7 ms.

Acknowledgments

This work was supported by EC through the project ICT-FP7-224312 HELIOS and by Italy-Spain integrated actions. D. N.-U. thanks the financial support of AGAUR through the Beatriu de Pino`s program and J.-M. R. thanks the CSIC for a JAE predoc grant. Authors would like to acknowledge the Laboratory of Electron NanoScopy, MIND-IN2UB, Dept. Electrònica, and the Scientific and Technological Centers (Universitat de Barcelona). A. Ruiz-Caridad, F. Peiró, Y. Berencén and O. Jambois are acknowledged for electron microscopy analysis and fruitful discussion. We acknowledge the contributions from N. Daldosso and A. Marconi at an early stage of the work.

#170884 - $15.00 USD Received 21 Jun 2012; revised 8 Aug 2012; accepted 8 Aug 2012; published 21 Aug 2012

IOP PUBLISHING NANOTECHNOLOGY

Nanotechnology **23** (2012) 125203 (8pp) doi:10.1088/0957-4484/23/12/125203

Erbium emission in MOS light emitting devices: from energy transfer to direct impact excitation

J M Ramírez[1], **F Ferrarese Lupi**[1], **O Jambois**[1], **Y Berencén**[1], **D Navarro-Urrios**[1,2], **A Anopchenko**[3], **A Marconi**[3], **N Prtljaga**[3], **A Tengattini**[3], **L Pavesi**[3], **J P Colonna**[4], **J M Fedeli**[4] **and B Garrido**[1]

[1] Departament d'Electrònica, Universitat de Barcelona, Carrer Martí i Franquès 1, Barcelona 08028, Spain
[2] Catalan Institute of Nanotechnology (CIN2-CSIC), Campus UAB, edifice CM3, 08193 Bellaterra, Spain
[3] Nanoscience Laboratory, Department of Physics, University of Trento, Via Sommarive 14, Povo (Trento) 38123, Italy
[4] CEA, Léti, Minatec Campus, 17 Rue des Martyrs, 38054 Grenoble Cedex 9, France

E-mail: jmramirez@el.ub.es

Received 24 October 2011, in final form 23 January 2012
Published 13 March 2012
Online at stacks.iop.org/Nano/23/125203

Abstract

The electroluminescence (EL) at 1.54 μm of metal–oxide–semiconductor (MOS) devices with Er^{3+} ions embedded in the silicon-rich silicon oxide (SRSO) layer has been investigated under different polarization conditions and compared with that of erbium doped SiO_2 layers. EL time-resolved measurements allowed us to distinguish between two different excitation mechanisms responsible for the Er^{3+} emission under an alternate pulsed voltage signal (APV). Energy transfer from silicon nanoclusters (Si-ncs) to Er^{3+} is clearly observed at low-field APV excitation. We demonstrate that sequential electron and hole injection at the edges of the pulses creates excited states in Si-ncs which upon recombination transfer their energy to Er^{3+} ions. On the contrary, direct impact excitation of Er^{3+} by hot injected carriers starts at the Fowler–Nordheim injection threshold (above 5 MV cm^{-1}) and dominates for high-field APV excitation.

(Some figures may appear in colour only in the online journal)

1. Introduction

The realization of an efficient and integrated silicon based light emitter is considered as one of the key points if silicon photonics are to achieve monolithic electronic and photonic functional integration in the same chip. In particular, Er^{3+} doped materials have been thoroughly studied, as the radiative 4f shell intraband transition provides efficient emission at telecom wavelengths (1.54 μm) [1–3].

Several works have cited the silicon-rich silicon oxide (SRSO) system as the most promising host for Er^{3+} ions [4–6]. When an as-deposited SRSO undergoes annealing at high temperature, the excess silicon segregates into a nanophase composed of nanoclusters and/or nanocrystals depending on the annealing conditions. The optimized environment of the erbium ions inside the silicon oxide matrix and the contribution of silicon nanostructures to Er^{3+} emission results in an enhancement and a spectral broadening of the effective excitation cross-section at 1.54 μm under optical pumping [6–8].

Nonetheless, under electrical pumping the coupling between silicon nanoclusters or nanocrystals (Si-ncs) and Er^{3+} ions is still controversial. Some authors have reported an enhancement of the Er^{3+} electroluminescence (EL) in SRSO

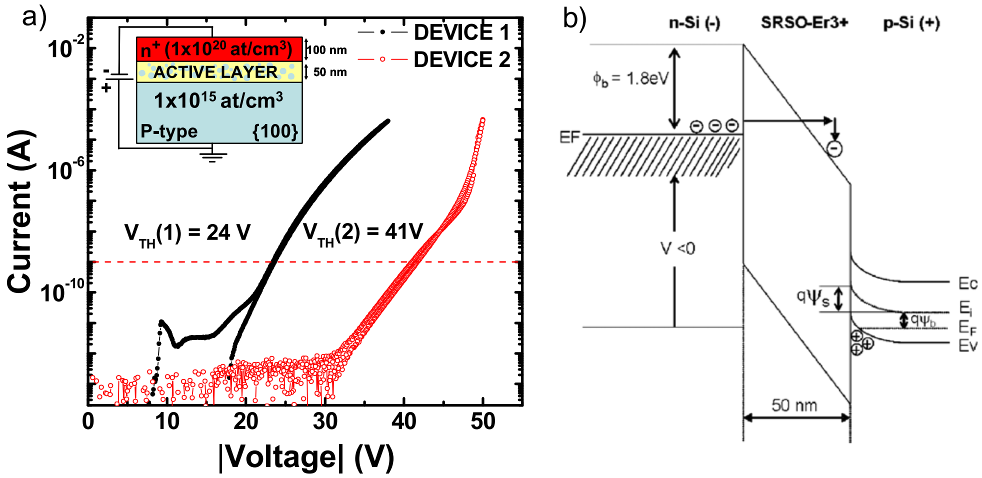

Figure 1. (a) Quasi-static $I(V)$ characteristics of devices. (b) Energy band diagram of the structure under high-field conditions for device 1.

at low voltages [9, 10]. Others reported a diminution of the EL signal for increasing Si excess and postulated leakage of currents through Si-ncs paths and/or less energetic injected carriers—in comparison with pure SiO_2—as the main reason for decreasing efficiency [11].

The visible/near infrared emission of Si-ncs under different polarization conditions, i.e. a direct current (DC) or alternate pulsed voltage (APV) regime, has been widely studied. In APV conditions, EL at low voltages is greatly enhanced due to the sequential injection of electron and holes into Si-ncs at the edges of the pulses and the following radiative recombination [12, 13]. However, the behavior of Er^{3+} emission under APV excitation has not been studied in detail. If indirect excitation of Er^{3+} ions (through Si-ncs) were to occur efficiently for electrical excitation, APV polarization could bring about significant improvement in the performance of Er^{3+} MOSLEDs (MOS capacitor or transistors acting as light emitting devices).

In this work, we have fabricated Si based MOSLEDs containing Er^{3+} ions embedded in either stoichiometric SiO_2 or SRSO layers. We have characterized the electrical and optical response when polarizing MOSLEDs under DC or APV signals. Results show two different EL excitation mechanisms for the coupled system with Si-ncs and Er^{3+}: (i) indirect excitation—cold carriers excite Si-ncs by sequential injection and the energy is transferred to Er^{3+}; and (ii) direct excitation—Er^{3+} is directly energized by hot energetic carriers through impact excitation. Moreover, we demonstrate the existence of a narrow voltage window, where the Er^{3+} excitation mechanism changes from energy transfer to direct impact excitation. Finally, a fast EL overshoot has been observed at high APV signals, attributed to the emission of highly stressed defects in the host matrix.

2. Sample fabrication and experimental setup

Two series of MOS devices were fabricated using standard complementary metal–oxide–semiconductor (CMOS) techniques, where the oxide layer has been replaced either by a SRSO or by a dry thermal silicon oxide with the same Er^{3+} implantation. In the following, all the devices with a SRSO layer will be labeled as 'device 1', while those containing a thermal silicon oxide will be labeled as 'device 2'.

Concerning device 1 a 50 nm thick substoichiometric SiO_x ($x < 2$) film was deposited on a low resistivity p-type Si substrate by low pressure chemical vapor deposition (LPCVD). The nominal value of silicon excess in the matrix was 12%, allowing Si-nc formation after annealing at 900 °C for 1 h. The same annealing treatment was applied to grow the thermal oxide in device 2.

After the annealing treatment, both films were implanted with Er^{3+} ions with a dose of 10^{15} at cm^{-2} at 20 keV of energy. Finally, post-implantation annealing was performed in order to activate Er^{3+} ions and cure the matrix from the implantation. Further details concerning Er^{3+} implantation profiles, photoluminescence (PL), x-ray photoelectron spectroscopy (XPS) and surface ion mass spectrometry (SIMS) measurements can be found in [14].

In addition, 100 nm thick poly-crystalline silicon with an n-type doped layer (1×10^{20} at cm^{-3}) was deposited on top and used as an optically semi-transparent gate electrode. 100×100 μm^2 aluminum pads were photolithographically defined on the devices to facilitate electrical polarization and light extraction. The emission area is composed of a square of area 0.09 mm^2. The cross-section of the devices can be observed in the inset of figure 1(a).

A semiconductor device analyzer (Agilent B1500A) and a probe station (Cascade Microtech Summit 1100) were used for current–voltage (I–V) measurements. APV excitation under a square voltage signal at low frequencies was performed replacing the semiconductor device analyzer by a pulse generator (Agilent 8114A).

EL signals were analyzed by an Acton 2300i grating spectrometer and detected by a cryogenically cooled PI spec-10-100B/LN charge-coupled device or a photomultiplier tube (H10330-25). A digital oscilloscope was finally used for data collection with a temporal resolution of 1 μs.

The micro-photoluminescence (μPL) measurements were performed in a standard μPL setup in a 45° configuration. The PL signal of the samples was studied by using two different lines of an argon laser (488 and 476 nm) as a pump source. The 488 nm line is resonant with the $^4I_{15/2} \rightarrow ^4F_{7/2}$ transition of the Er^{3+} ions, while the 476 nm line is non-resonant with an Er^{3+} transition and only excites the Si-ncs, which have slightly higher excitation cross-section at this wavelength than at 488 nm.

The shape of the pumping spot on the sample is ellipsoidal, with an area of 6×10^{-5} mm^2, which is small enough to ensure the excitation of a single device.

A short working distance objective was used to collect the PL emission and to focus it in a monochromator with focal length of 750 mm and a spectral resolution of 0.03 nm, coupled to the same photomultiplier tube described above.

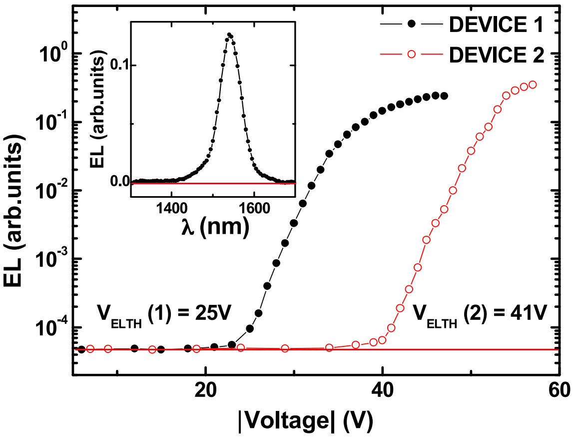

Figure 2. EL(V) characteristics for devices. The inset shows a typical measured spectrum ($V_g = -40$ V for device 1).

3. Results and discussion

3.1. Electro-optical characterization

The electrical excitation in DC was done under accumulation conditions, i.e. applying negative voltages over the gate electrode with the substrate grounded (see figure 1(b)). This configuration is more convenient as it provides the majority of carriers from both the gate electrode (electrons) and from the substrate (holes). Quasi-static $I(V)$ characteristics of devices at room temperature are shown in figure 1 (20 mV s^{-1}). A difference of 17 V between the SRSO layer (device 1) and the pure SiO_2 (device 2) is observed in the threshold voltage for conduction (V_{TH}), defined arbitrarily as the voltage required to obtain 1 nA of gate current. It is worth noting that a homogeneity study was performed on each wafer obtaining around 95% of reproducibility in the electro-optical characteristics.

It is thus clear that Si-ncs are responsible for an increased conductivity in the SRSO with respect to pure SiO_2. By a detailed fitting procedure, it has been determined that the dominant conduction is injection limited and proceeds for both SRSO and SiO_2 (after a threshold voltage) by Fowler–Nordheim (FN) tunnel injection of hot electrons coming from the gate electrode [15]:

$$J = \frac{q^3 E^2}{8\pi h \phi_b} \exp\left(-\frac{4\sqrt{2m^*_{ox}(q\phi_b)^3}}{3\hbar q E}\right) \qquad (1)$$

where m^*_{ox} is the effective mass of electrons in the conduction band, E is the electric field applied, ϕ_b is the potential barrier height, q is the single electron charge and $h(\hbar)$ is the (reduced) Planck's constant.

The agreement with the FN conduction law suggests that neither Si-ncs nor Er^{3+} create a large number of trapping defects in the oxide—if this was the case, conduction would proceed by a Poole–Frenkel type mechanism [16].

Then, assuming that the erbium implantation does not lower the Si–SiO_2 barrier height, the effective mass for the Er^{3+} doped SiO_2 can be extracted from the experimental $I(V)$ curves. Using equation (1) and the accepted value for the Si–SiO_2 barrier height at the interface, i.e. 3.15 eV [17, 18], an effective mass of $m^*_{ox} = 0.4m_0$ (m_0 the electron mass) was found, in agreement with the ones previously reported in Si–SiO_2 systems [19]. On the other hand, doing the same study for the Er^{3+} doped SRSO layer, we obtained a barrier height of 1.6 eV using an effective mass of $0.4m_0$, or 1.8 eV using $m^*_{ox} = 0.5m_0$ as taken by various authors [18, 20]. In both cases, a reduction of the injection barrier height is obtained when Si-ncs are introduced.

A thorough study of the evolution of the EL at 1.54 μm as a function of the applied DC voltage is reported in figure 2. The voltages were swept from low to just below the breakdown voltage, integrating the whole EL spectrum at each voltage value (see inset of figure 2). However, care should be taken with the highest electric fields applied (above 7 MV cm^{-1} for device 1 and 10 MV cm^{-1} for device 2), as Si bulk emission at 1.1 μm has been observed in the spectra leading to a tail until the 1.5 μm region. In this regime, the active layer is not thick enough to cool down the highly energetic electrons from the gate, which pass through the layer and impact the silicon bulk directly. Furthermore, at these high electric fields the devices are partially broken due to the high electric stress, providing (i) higher leakage currents for a given voltage, (ii) lower EL values for a given current, and (iii) poor device reliability. As a consequence, the depletion of the EL(V) characteristic at high voltages cannot be considered as a complete saturation of the optically active Er^{3+} ions, but as a diminution of the electro-optical properties of the devices.

Therefore, the optimum working conditions were established below these maximum fields. Additionally, the threshold voltage for the EL (V_{EL-TH}) can be extracted from figure 2, determining a minimum voltage for light emission of 25 V in device 1 (5 MV cm^{-1}) and 41 V (8 MV cm^{-1}) for device 2. These values are very similar to the threshold voltage for conduction and allow extracting a minimum gate current to observe EL of around 1 nA. From those results, the power efficiency was found to be very similar in both devices with values around 0.01%, pointing out that the emission properties at 1.54 μm are not enhanced by the presence of Si-ncs, although the conductivity across the active layer is improved.

In order to study the dynamics of our system in the infrared region, time-resolved EL measurements centered at

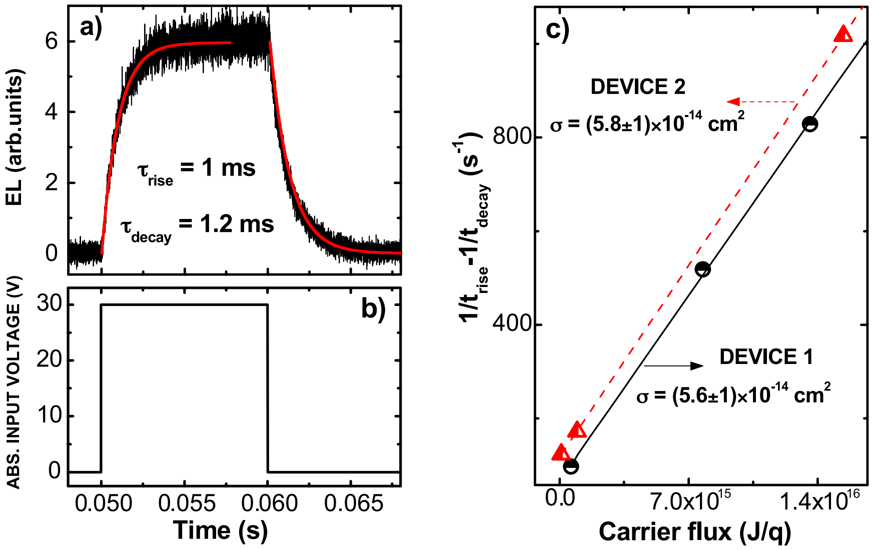

Figure 3. (a) EL(t) at 1.54 μm of device 1 with the exponential fits of the decay and rise times. (b) A negative square voltage (from 0 to −30 V) was used for the excitation. (c) Effective excitation cross-section fit at 1.54 μm for the Er^{3+}:SRSO device (solid line, black circles) and for the Er^{3+}:SiO_2 system (dashed line, red triangles). Error bars are smaller than the experimental points shown.

1.54 μm were carried out. The time evolution of the EL signal at negative square voltages is reported in figure 3(a) for the Er^{3+}:SRSO sample. The signal can be modeled by using the rate equations for a nearly two-level system [21, 22]:

$$\frac{\mathrm{d}N_2}{\mathrm{d}t} = \sigma\frac{j}{e}(N_{\text{total}} - N_2) - \frac{N_2}{\tau_{\text{decay}}}, \tag{2}$$

with

$$\frac{1}{\tau_{\text{decay}}} = \frac{1}{\tau_{\text{rad}}} + \frac{1}{\tau_{\text{non-rad}}} \tag{3}$$

where σ is the effective excitation cross-section, j is the incident current density, e is the single electron charge, τ_{decay} is the total lifetime [radiative (τ_{rad}) and non-radiative ($\tau_{\text{non-rad}}$)] and N_{total} and N_2 are the total implanted and the excited Er^{3+} ions in the first energy level, respectively. When the electric excitation is turned on, the EL intensity behaves as:

$$\text{EL}_{\text{on}}(t) = \text{EL}_0\left\{1 - \exp\left[-\left(\sigma\frac{j}{e} + \frac{1}{\tau_{\text{decay}}}\right)t\right]\right\}. \tag{4}$$

With EL_0 the electroluminescence in the steady state, the rise time will hence follow the equation:

$$\frac{1}{\tau_{\text{rise}}} = \frac{1}{\tau_{\text{decay}}} + \frac{j}{e}\sigma \tag{5}$$

and the expression for the turn-off of EL:

$$\text{EL}_{\text{off}}(t) = \text{EL}_0 \exp\left(-\frac{t}{\tau_{\text{decay}}}\right). \tag{6}$$

Therefore, using equations (4) and (6) to determine the time constants (τ_{rise} and τ_{decay}), the effective excitation cross-section at 1.54 μm was extracted. Figure 3(a) shows the fits of the EL signal under a square APV signal from 0 to −30 V at 50 Hz (figure 3(b)) with a rise time of 1 ms and a decay time of 1.2 ms [22]. An effective excitation cross-section value of $\sigma = (5.6 \pm 1) \times 10^{-14}$ cm^2 was determined for the Er^{3+}:SRSO sample, and $\sigma = (5.8 \pm 1) \times 10^{-14}$ cm^2 for the Er^{3+} doped SiO_2 layer, with a given current density ranging from 1 μA cm^{-2} to 5 mA cm^{-2} (figure 3(c)). Then, the resemblance between both values becomes conclusive proof of the direct excitation of Er^{3+} ions under DC polarization at high voltages, even when Si-ncs are present in the matrix. Notice that the effective excitation cross-sections presented in the present work are the highest ever reported [23, 24]. The understanding of these values needs further investigation.

3.2. Symmetric alternate pulsed polarization for energy transfer activation

The transient EL signal was also studied in our devices when polarizing under symmetric square voltage signals (i.e. equal negative and positive voltages relative to zero) at frequencies ranging from 25 Hz up to 1 kHz, which corresponds with the typical lifetime of Er^{3+}ions (1 ms). Figure 4 shows the EL at 1.54 μm for a square voltage switched from −20 to 20 V at 25 Hz, below the EL threshold voltage in DC. The first thing to point out is that, contrary to the DC case, EL is observed at 1.54 μm at this low applied voltage, as shown by the EL transients that appear at each voltage switch (by fixing the monochromator at 1.54 μm; see figure 4(c)). Decay times were fitted for both peaks, obtaining values of 1.5 ms (figure 4(a)) and 1.8 ms, respectively (figure 4(b)). Those values are very close to the decay lifetimes measured in figures 3(a) and (b) under a negative APV excitation. Moreover, very fast rise times were observed in the EL when the voltage is switched, showing up the characteristic time ($\tau = RC$) of the setup (about 1 μs).

The presence of these two peaks has already been reported in the visible region by other authors when working

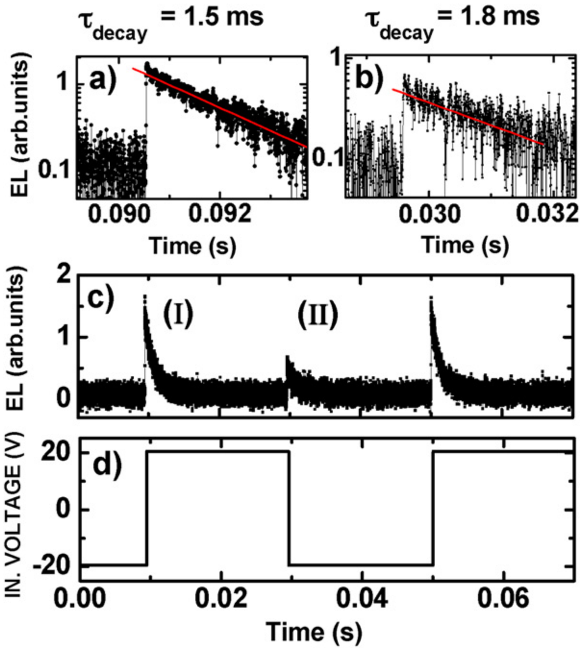

Figure 4. Time-resolved EL measurements (c) performed in device 1 under a square voltage signal (d), with time decay fits for the first (I) and the second (II) EL overshoots (figures (a) and (b), respectively).

in APV excitation conditions with undoped Si-ncs based devices [25], and was ascribed to the sequential injection of holes and electrons into Si-ncs. Also, the difference in intensity between these two peaks can be explained considering that holes have tunneling back times longer than electrons, increasing the probability of creating an exciton at the positive semi-cycle (electrons tunneling towards Si-ncs). Therefore, the observed temporal behavior of the infrared EL (smaller rise time) suggests the influence of Si-ncs on the emission under this polarization, and more concretely their function as sensitizers for Er^{3+} ions. Moreover, time-resolved measurements were also performed in the visible range under the same polarization conditions, showing two EL peaks similar to the ones reported in figure 4(c) (not shown).

More in-depth evidence of the indirect excitation of the Er^{3+} ions for this excitation scheme comes from the comparison, in device 1, of the EL rise time under both negative (empty squares) and symmetrical (empty circles) square pulse voltage signals (see figure 5). Starting from the assumption that the energy transfer from Si-ncs to Er^{3+} ions is known to be a very fast process [26], we report a difference of at least 200 μs in the temporal EL response depending on the polarization scheme (see the inset to figure 5). In addition, looking at the rise times, we observe a factor of ~1000 between them (lower than 1 μs in front of 1 ms) which suggest very different excitation cross-sections (also a factor of 1000) if equation (5) is assumed. Consequently a correlation between the slower rise time (empty squares) and the direct excitation of Er^{3+} ions, and the faster rise time (empty circles) with the energy transfer between Si-ncs to Er^{3+} ions was inferred.

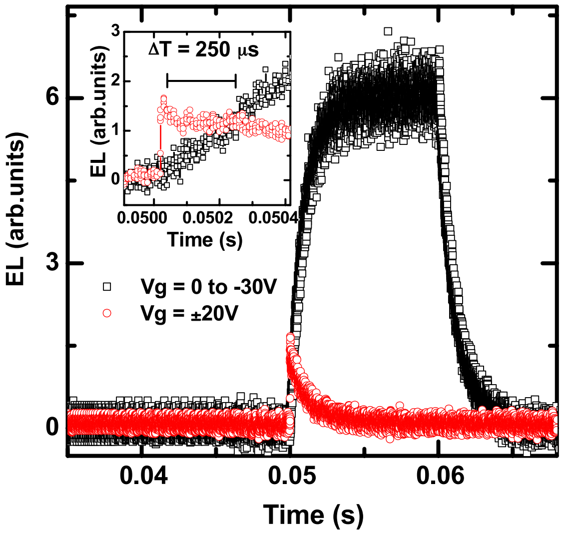

Figure 5. Rise time comparison between the EL obtained under a symmetric AC signal (empty circles) and a negative square signal (empty squares). The inset is a zoom of the increasing EL.

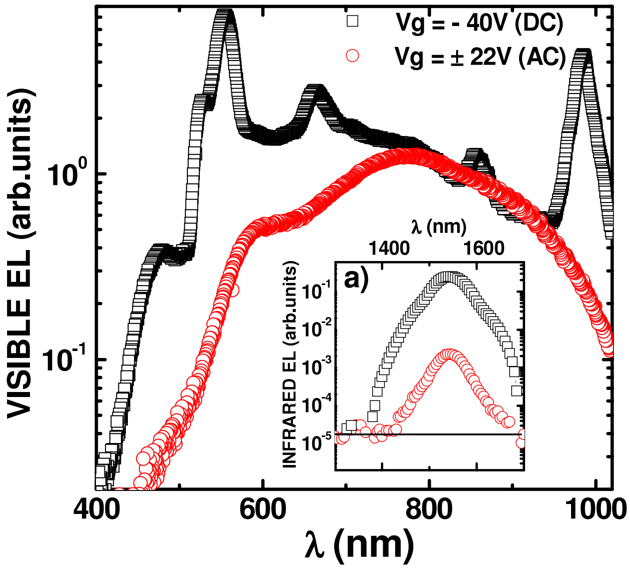

Figure 6. EL spectrum in the visible region for device 1 under DC (empty squares) or symmetric AC (empty circles) polarization scheme. Infrared EL emission is shown in the inset.

Visible and infrared spectra were acquired under different electric polarization conditions in order to correlate the emission of Si-ncs and Er^{3+} ions. Figure 6 shows the visible spectra of the EL under both DC and APV excitation on device 1. As can be observed, different radiative transitions belonging to the excited state levels of Er^{3+} ions are detected when a DC voltage is applied. Note that the same line shape was always observed whatever the voltage (from −25 to −45 V). In particular, even the most energetic peaks appear at low voltages, preserving a linear ratio between the EL of each peak and the current applied, evincing a direct excitation of Er^{3+} by means of hot carriers injected into the active layer [27].

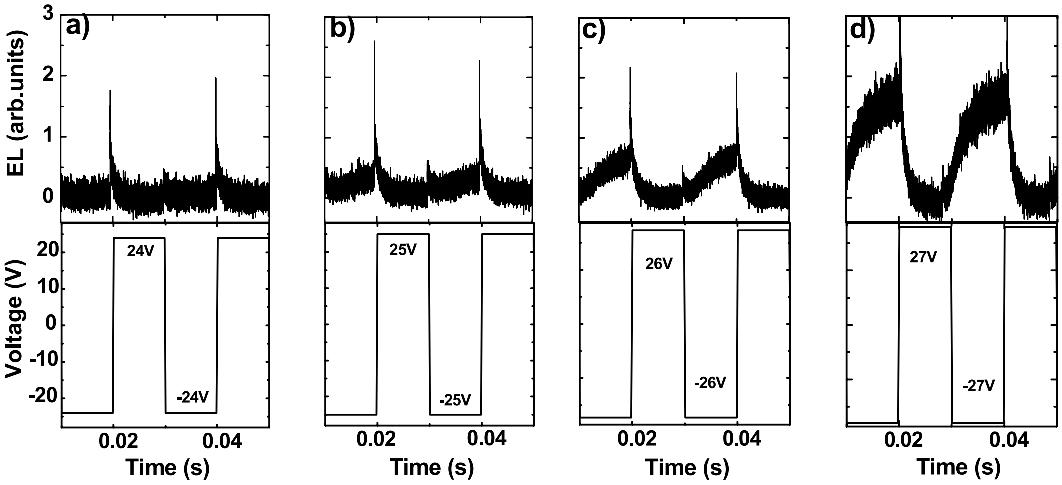

Figure 7. EL(t) at 1.54 μm for different square symmetric voltage signals around the DC voltage threshold for device 1.

On the contrary, under a symmetrical square wave voltage excitation (empty circles of figure 6), no Er^{3+} related peaks appear in the studied frequency range (25 Hz–1 kHz) and only a broad emission attributed to Si-ncs is observed. Furthermore, lower voltages are required to obtain luminescence in this regime, with a threshold voltage of ±15 V. Such a value lies 10 V below the minimum DC threshold voltage observed in figure 2.

The latest results provide evidence of different excitation mechanisms depending on the polarization applied in a single device. In particular, we are able to observe: (i) direct impact excitation of Er^{3+} ions under a DC regime and (ii) energy transfer from Si-ncs to Er^{3+} ions under symmetric square excitation. At this point it is important to state that the applied APV excitation plays a principal role in the energy transfer: for values below the DC threshold (<25 V), carriers do not have enough energy to excite Si-ncs or Er^{3+} ions directly, although exciton formation is allowed inside nanocrystals by sequential injection, resulting in the energy transfer to Er^{3+} ions. On the contrary, when the symmetric APV regime reaches higher values than the threshold voltage in DC (>25 V), a large number of carriers are able to excite Er^{3+} (and also Si-ncs) by direct impact, screening almost completely the contribution of the energy transfer to the EL at 1.54 μm.

In order to further support our interpretation, we did time-resolved measurements under APV excitation around the EL threshold voltage on device 1 (figure 2). Figure 7 shows the transition between the two different EL excitation mechanisms at 1.54 μm, depending on the APV signal applied. As observed, a small shoulder starts to appear on the EL(t) signal at ±25 V and it is reinforced as the voltage values become larger, suggesting the appearance of a contribution to the excitation due to direct impact. Such a shoulder completely screens the contribution of the indirect excitation at higher voltages, because (i) the Er^{3+} ions excited by transfer are located in a region close to the Si substrate only and (ii) the amount of Er^{3+} ions coupled to Si-ncs is only a fraction of those which can be excited directly. Note finally that the transition voltage range (i.e. from energy transfer to impact ionization) is very narrow, about 2 V after the first signs of the EL shoulder.

3.3. Fast EL component

In addition to the Er^{3+} ions' EL dynamics at 1.54 μm discussed above, at larger voltages sharp EL overshoots have been observed, characterized with much smaller decay time (in the order of few μs). They could be observed either in samples with or without Si-ncs, as shown in figures 7(b)–(d) for device 1 and figure 8 for device 2. In order to discard the influence of Si-nc, we have studied this feature on device 2. As the device requires larger voltages, we had to reduce duty cycle to 10% in order to overcome the power limitation of our setup. This allowed us to observe just one EL transient of typically 4 μs of decay time, as can be seen in figure 8. Moreover, the same behavior was observed at 1300 nm, which is well away from any Er^{3+} related contribution, and also in the visible part of the spectrum (not shown). This fast component has already been observed by other authors [26, 28] when carrying out PL measurements in SRSO layers with and without Er^{3+} ions, obtaining very fast decay times (typically of nanoseconds). Nevertheless, the nature of this emission is not clear yet. Some authors [28, 29] suggest an effect of recombination of defective centers either in the silica matrix or at the interface with the Si-nc, or an intraband recombination mechanism [26]. Others attribute this fast emission to Auger processes related to transitions of confined electrons or holes between the space-quantized levels of Si-ncs [30]. In our case, it is clear that it is not provided by any Er^{3+} related transitions since it does not show its characteristic spectral features. Furthermore, this fast contribution is also appreciable in pure silica layers with Er^{3+} ions, suggesting that it may not be related to Si-ncs but to defects on the silica matrix.

In order to better understand the origin of the fast component, μPL measurements were carried out. Active device area was pumped at two different wavelengths, one resonant with an Er^{3+} transition (488 nm), and the other

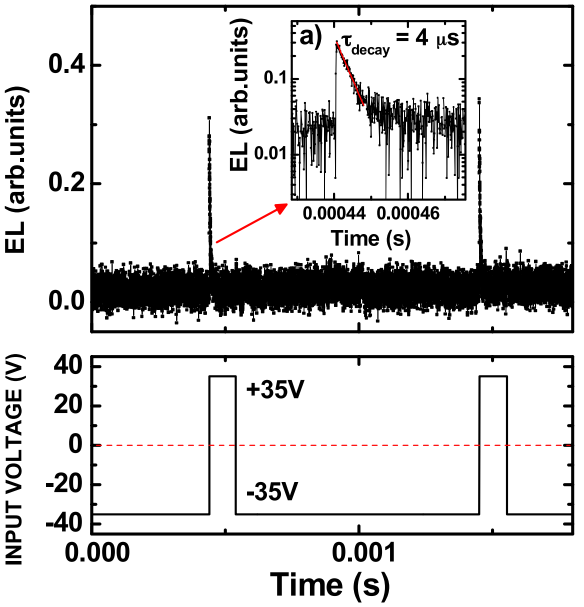

Figure 8. EL(t) at 1.54 μm under a square symmetric voltage signal for device 2. The inset (a) shows the EL decay fit of the sharp EL overshoot.

non-resonant (476 nm). The resultant IR emission was collected and integrated as a function of the photon flux in both devices, as observed in figure 9. The highest PL intensity in device 1 (inset of figure 9(a)) is obtained at 476 nm (red circles), which is in strong agreement with an energy transfer mechanism from Si-ncs to Er^{3+} ions [31]. Indeed, the absorption cross-section of Si-ncs under 476 nm pumping wavelength is slightly higher than at 488 nm. On the contrary, in the sample free of Si-ncs (device 2), it is the 488 nm pumping which gives higher PL intensity values (inset of figure 9(b), black squares). Weak PL was observed under 476 nm pumping. Nonetheless, there is a small PL emission at 1.54 μm from the non-resonant pumping in device 2 (see inset to figure 9(b)). This is quite a surprising result, since it seems that there is a small contribution from sensitized Er^{3+}, the origin of which is currently under study. Furthermore, a background emission was detected along a spectral range much broader than that covered by the Er^{3+} emission in both devices (insets of figures 9(a) and (b)). This emission might be correlated with the fast EL peak observed under EL measurements (see inset of figure 8), which also showed an extremely broad spectral contribution.

4. Conclusions

In summary, we have studied the electroluminescence properties in near infrared of silicon based LEDs containing silicon-rich silicon oxide layers doped with Er^{3+} ions under different polarization schemes. Time-resolved EL measurements allowed us to show the presence of two different mechanisms of Er^{3+} excitation under electrical pumping. Under DC excitation, Fowler–Nordheim injection and visible transition on the Er^{3+} spectra suggest that direct impact of Er^{3+} is the main mechanism. Under an alternative pulsed excitation, there is a window of voltages where transfer to Er^{3+} ions is clearly demonstrated, through the creation of exciton in the Si-nc by sequential injection of electrons and holes. Under this regime, a much smaller rise time is observed. This is a promising result, as this lead to a much larger absorption cross-section which can be used in an optimized material to obtain a much larger efficiency of pumping.

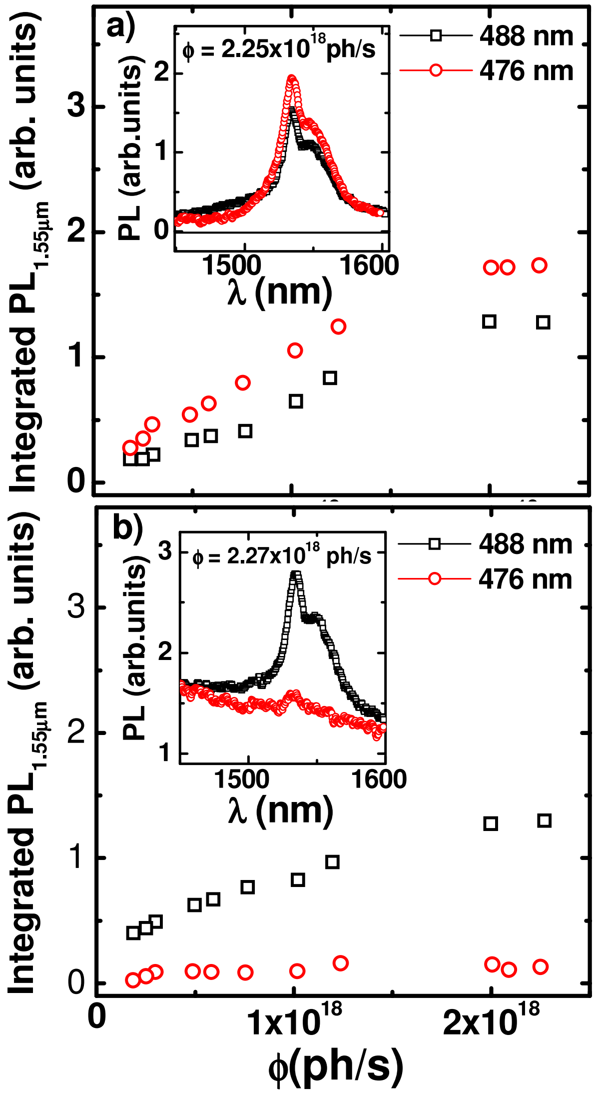

Figure 9. μPL intensity dependence with ϕ in device 1 (a) and device 2 (b). The insets show the obtained spectrum for a given ϕ. The y-axis scales are comparable in both graphs.

Finally, a fast EL overshoot observed in Er^{3+}:SRSO and Er^{3+}:SiO_2 devices at high alternately pulsed voltages was ascribed to the emission of defects in the host silica matrix, and correlated with the background emission in μPL measurements.

Acknowledgments

This work was supported by EC through the project ICT-FP7-224312 HELIOS and by Italy–Spain integrated actions.

References

[1] Jambois O, Gourbilleau F, Kenyon A J, Montserrat J, Rizk R and Garrido B 2010 *Opt. Express* **18** 2230

[2] Yerci S, Li R, Kucheyev S O, Van Buuren T, Basu S N and Dal Negro L 2009 *Appl. Phys. Lett.* **95** 031107

[3] Gallis S, Huang M, Efstathiadis H, Eisenbraun E, Kaloyeros A E, Nyein E E and Hommerich U 2005 *Appl. Phys. Lett.* **87** 091901

[4] Wodjak M, Klik M, Forcales M, Gusev O B, Gregorkiewicz T, Pacifici D, Franzò G, Priolo F and Iacona F 2004 *Phys. Rev.* B **69** 233315

[5] Izeddin I, Moskalenko A S, Yassievich I N, Fujii M and Gregorkiewicz T 2006 *Phys. Rev. Lett.* **97** 207401

[6] Miller G M, Briggs R M and Atwater H 2010 *J. Appl. Phys.* **108** 063109

[7] Kik P G, Brongersma M L and Polman A 2000 *Appl. Phys. Lett.* **76** 2325

[8] Navarro-Urrios D, Jambois O, Ferrarese Lupi F, Pellegrino P, Garrido B, Pitanti A, Prtljaga N, Daldosso N and Pavesi L 2011 *Opt. Mater.* **33** 1086

[9] Ran G Z, Chen Y, Qin W C, Fu J S, Ma Z C, Zong W H, Lu H, Qin J and Qin G G 2001 *J. Appl. Phys.* **90** 5835

[10] Sun K, Xu W J, Zhang B, You L P, Ran G Z and Qin G G 2008 *Nanotechnology* **19** 105708

[11] Sun J M, Skorupa W, Dekorsky T, Helm M and Nazarov A N 2005 *Opt. Mater.* **27** 1050

[12] Perálvarez M, Barreto J, Carreras J, Morales A, Navarro-Urrios D, Lebour Y, Domínguez C and Garrido B 2009 *Nanotechnology* **20** 405201

[13] Carreras J, Arbiol J, Garrido B, Bonafos C and Montserrat J 2008 *J. Appl. Phys. Lett.* **92** 091103

[14] Prtljaga N *et al* 2011 *Opt. Mater.* **33** 1083

[15] DiMaria D J, Dong D W, Falcony C, Theis T N, Kirtley J R, Tsang J C, Young D R and Pesavento F L 1983 *J. Appl. Phys.* **54** 10

[16] Jambois O, Berencén Y, Hijazi K, Wodjak M, Kenyon A J, Gourbilleau F, Rizk R and Garrido B 2009 *J. Appl. Phys.* **106** 63526

[17] Konig D, Rennau M and Henker M 2007 *Solid-State Electron.* **51** 650

[18] Hadjadj A, Simonetti O, Maurel T, Salace G and Petit C 2002 *Appl. Phys. Lett.* **80** 18

[19] Lenzlinger M and Snow E H 1969 *J. Appl. Phys.* **40** 1

[20] DiMaria D J, Kirtley J R, Pakulis E J, Dong D W, Kuan T S, Pesavento F L, Theis T N and Cutro J A 1984 *J. Appl. Phys.* **56** 2

[21] Coffa S, Franzò G and Priolo F 1996 *Appl. Phys. Lett.* **69** 2077

[22] Wang S, Eckau A, Neufeld E, Carius R and Buchal Ch 1997 *Appl. Phys. Lett.* **71** 2824

[23] Lombardo S, Campisano S U, Van den Hoven G N and Polman A 1995 *J. Appl. Phys.* **77** 6504

[24] Iacona F, Pacifici D, Irrera A, Miritello M, Franzò G and Priolo F 2002 *Appl. Phys. Lett.* **81** 3242

[25] Walters R J, Bourianoff G I and Atwater H A 2005 *Nature Mater.* **4** 143

[26] Navarro-Urrios D, Pitanti A, Daldosso N, Gourbilleau F, Rizk R, Garrido B and Pavesi L 2009 *Phys. Rev.* B **79** 193312

[27] Kanjilal A, Rebohle L, Skorupa W and Helm M 2009 *Appl. Phys. Lett.* **94** 101916

[28] Izeddin I, Timmerman D, Gregorkiewicz T, Moskalenko A S, Prokofiev A A and Yassievich I N 2008 *Phys. Rev.* B **78** 0.35327

[29] Savchyn O, Ruhge F R, Kik P G, Todi R M, Coffey K R, Nukala H and Heinrich H 2007 *Phys. Rev.* B **76** 195419

[30] Prokofiev A A, Moskalenko A S and Yassievich I N 2008 *Mater. Sci. Eng.* B **146** 121

[31] Fujii M, Yoshida M, Kanzawa Y, Hayashi S and Yamamoto K 1997 *Appl. Phys. Lett.* **71** 1198

JOURNAL OF APPLIED PHYSICS **111**, 063102 (2012)

Bipolar pulsed excitation of erbium-doped nanosilicon light emitting diodes

A. Anopchenko,[1,a)] A. Tengattini,[1] A. Marconi,[1] N. Prtljaga,[1] J. M. Ramírez,[2] O. Jambois,[2] Y. Berencén,[2] D. Navarro-Urrios,[2,b)] B. Garrido,[2] F. Milesi,[3] J.-P. Colonna,[3] J.-M. Fedeli,[3] and L. Pavesi[1]
[1]*Nanoscience Laboratory, Department of Physics, University of Trento, Via Sommarive 14, Povo 38123, Italy*
[2]*Department of Electronics, University of Barcelona, Carrer Martì i Franquès 1, Barcelona 08028, Spain*
[3]*CEA/Léti, Minatec, 17 rue des Martyrs, 38054 Grenoble cedex 9, France*

(Received 13 October 2011; accepted 17 February 2012; published online 21 March 2012)

High quantum efficiency erbium doped silicon nanocluster (Si-NC:Er) light emitting diodes (LEDs) were grown by low-pressure chemical vapor deposition (LPCVD) in a complementary metal-oxide-semiconductor (CMOS) line. Erbium (Er) excitation mechanisms under direct current (DC) and bipolar pulsed electrical injection were studied in a broad range of excitation voltages and frequencies. Under DC excitation, Fowler-Nordheim tunneling of electrons is mediated by Er-related trap states and electroluminescence originates from impact excitation of Er ions. When the bipolar pulsed electrical injection is used, the electron transport and Er excitation mechanism change. Sequential injection of electrons and holes into silicon nanoclusters takes place and nonradiative energy transfer to Er ions is observed. This mechanism occurs in a range of lower driving voltages than those observed in DC and injection frequencies higher than the Er emission rate. © *2012 American Institute of Physics*. [http://dx.doi.org/10.1063/1.3694680]

I. INTRODUCTION

The Er-doped silicon nanocluster (Si-NC:Er) system is studied as a gain medium in silicon photonics since it could potentially allow for efficient and integrable light sources.[1,2] Room temperature Si-NC:Er light emitting diodes (LEDs) with an external quantum efficiency (EQE) at 1.54 μm larger than 0.1% have been demonstrated.[1,3–5] Er excitation in the Si-NC:Er system is either due to a direct impact of hot electrons or via an indirect energy transfer from nonradiative recombination of electron-hole pairs/excitons confined in silicon nanoclusters. The energy transfer is well documented and several mechanisms of the energy transfer under optical excitation have been suggested in recent publications.[6–8]

Pulsed electrical excitation of the Si-NC:Er system has not been studied in as much detail as optical excitation or direct current electroluminescence. Walters *et al.*[9] and Peralvarez *et al.*[10] demonstrated sequential injection of electrons and holes into Si nanocrystals under a bipolar pulsed excitation of a field-effect LED. Priolo *et al.* suggested this excitation scheme as a solution to overcome nonradiative Auger deexcitation of Er in Si-NC:Er LEDs.[11] Miller *et al.* calculated a modal gain of 2 dB/cm in a slot waveguide confined Si-NC:Er under the pulsed excitation which mitigates excited carrier absorption.[12]

In this work, we will evaluate erbium excitation mechanisms and emission in Si-NC:Er LED under electrical pumping using both direct current and bipolar pulsed excitation schemes, i.e., when the polarity of the applied voltage pulse is periodically changed.

II. EXPERIMENTAL

The silicon nanoclusters (Si-NCs) are formed during 14(1/2)-h-long high temperature anneal at 900 °C of a silicon-rich silicon oxide layer with a nominal 12% of silicon excess (9% measured by x-ray photoelectron spectroscopy) grown by low-pressure chemical vapor deposition process (LPCVD).[13] As measured by secondary ion mass spectrometry, peak Er-ion concentration of $\sim 4 \times 10^{20}$ cm^{-3} is obtained by Er implantation with a fluence of 10^{15} ions/cm^2 and energy of 25 keV. Post-implantation anneal is performed at 800 °C for 6 h. A schematic layout of the *n*-type complementary metal-oxide-semiconductor (CMOS) Si-NC:Er LED is shown in Fig. 1. The thickness of the active layer is 50 nm. A semitransparent window is formed by a conductive 150-nm-thick polycrystalline silicon layer and an antireflection coating of 93 nm of Si_3N_4 and 136 nm of SiO_2. The device studied in this work has a square gate area with a size of 500 μm × 500 μm and an *n*-type polysilicon gate. The direct current (DC) bias polarity convention is shown in Fig. 1.

Electrical and optical measurements are performed at room temperature. Current-voltage (*I-V*) characteristics are recorded with an Agilent B1500 A semiconductor device analyzer. High frequency, 100 kHz, capacitance-voltage (*C-V*) measurements are performed with HP 4284 A precision LCR meter. A 2-m-long extension cable is used. The open circuit corrections are performed according to the operation manual. The alternating current (AC) signal voltage level is 50 mV. A function generator, Tektronix AFG 3252, coupled with a high-voltage amplifier, Falco Systems WMA-300, is used to drive the device in time-resolved electroluminescence (EL) measurements.

Time-resolved EL signal is collected with a single-photon detector module, id-Quantique 201, and recorded with a multichannel scaler, SRS 430. EL spectra are collected

---

[a)] Electronic mail: anopchenko@science.unitn.it.

[b)] Present address: Catalan Institute of Nanotechnology (CIN2-CSIC), Campus UAB, Edifici CM3, 08193 Bellaterra, Spain.

0021-8979/2012/111(6)/063102/5/$30.00

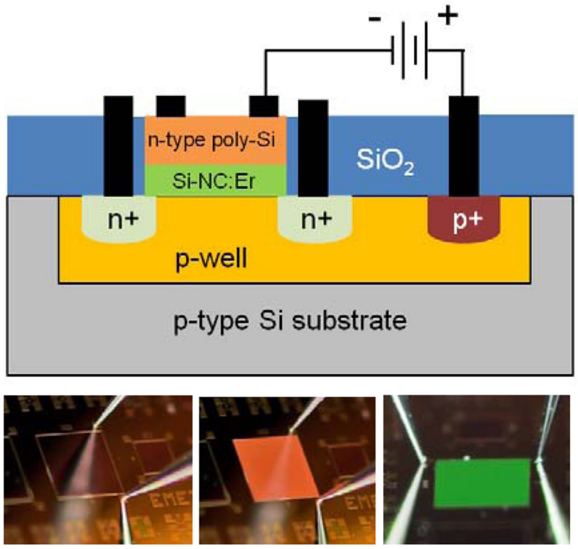

FIG. 1. (top) A schematic cross section of the *n*-type CMOS Si-NC:Er LED layout. Green color stands for the Er-doped Si-NC layer, blue – oxide, and black – titanium-aluminum-copper metal contact sandwich. (bottom, left to right) Photographs of the unbiased Si-NC LED, an orange emitting Si-NC LED under forward bias (a red square at the probe tips) and green emitting Si-NC:Er LED.

using a fiber bundle and analyzed with a Spectra-Pro 2300i monochromator coupled with nitrogen cooled charge-coupled device (CCD) cameras (one in visible and one in infrared, IR). Emitted optical power and EQE of the Si-NC:Er LED are measured using either a calibrated LED or a Ge photodiode. The acceptance angle of the photodiode is taken into account. The photodiode is placed within a few millimeters above the LED. The optical power emitted by the LED is estimated as $P = P_m / \sin^2\varphi$, where φ is the acceptance angle of the photodiode and P_m is a measured fraction of the total optical power emitted into air.

III. RESULTS AND DISCUSSION

A. Direct current excitation

Electrical charge transport in our Si-NC LEDs is due to electric field-enhanced tunneling of electrons with the involvement of either defects[14–16] or confined energy states of Si-NCs.[17,18] Erbium implantation produces deep energy trapping levels which change the transport properties of the Si-NC LED.[11,19] This is supported by the DC *I-V* and *C-V* characteristics shown in Fig. 2. The *I-V* curves of both Si-NC and Er-doped Si-NC LEDs are shown in a voltage range where EL signal is observed under forward bias (Si substrate is in accumulation, see Fig. 1). EL emission is also observed under reverse bias in both undoped and doped Si-NC LEDs, but at higher voltages and with lower quantum efficiency. The *I-V* curves are well described by the Fowler-Nordheim field-enhanced tunneling law[17] with effective energy barrier heights of 1.4 and 1.9 eV for Si-NC and Si-NC:Er LED, respectively (assuming an effective electron mass of 0.3 m_0).[20] The Er-doped device is less conductive than the undoped device, which we ascribe to charge trapping at deep energy levels due to Er ion implantation.[21] This is also supported by the *C-V* measurements (Fig. 2). A hysteresis loop is observed in the *C-V* curves, which is due to charge trapping. The hysteresis is wider for the Er-doped Si-NC LED than for the undoped Si-NC LED. Trapped charge density estimated from *C-V* hysteresis width of the Si-NC LED is 4.3×10^{12} cm^{-2}. Assuming one trapped electron per Si-NC, this value serves as a good estimate of the Si-NC density.[22]

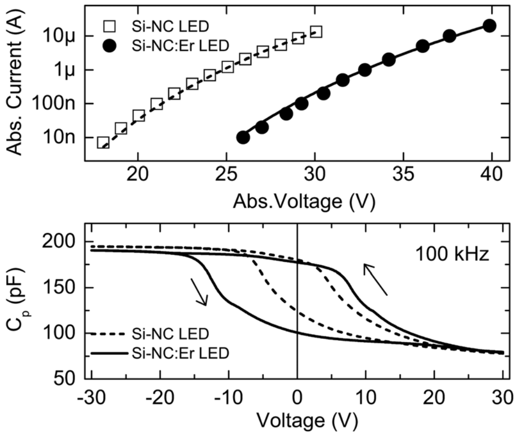

FIG. 2. (top) Forward current-voltage characteristics of Si-NC and Si-NC:Er LEDs. Symbols are experimental data values at which EL is observed, lines are fits to the Fowler-Nordheim tunneling law. (bottom) Capacitance-voltage characteristics of the Er-doped and undoped Si-NC LEDs. The signal frequency is 100 kHz. The arrows show bias scanning direction in the *C-V* measurements.

Figure 3 (top panel) shows the integrated spectral EL intensity of the Si-NC and Si-NC:Er LEDs as a function of injection DC current in the visible range and at wavelengths bracketing the 1.54 μm Er emission, respectively. For low injection currents, EL intensity at 1.54 μm increases linearly with the DC current. However, at high currents a sublinear growth with injected current is observed. On the contrary, the visible emission from Si-NCs increases almost linearly (with a slope of 0.91 ± 0.01 in the log-log coordinates) as a

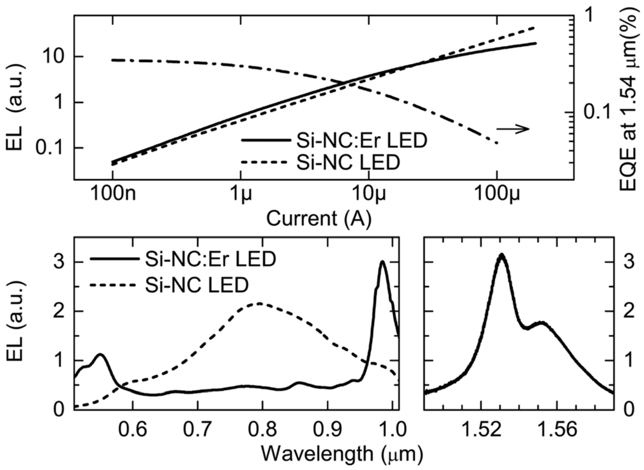

FIG. 3. Integrated EL spectral intensity with wavelengths bracketing 1.54 μm (left axis, solid line) and in the visible range (left axis, dot line) for Si-NC:Er LED and Si-NC LED, respectively, as a function of DC injected current. Please note that absolute values of the EL intensity in the visible and IR ranges are not to compare (the *y*-axes are not the same). The dash-dot line shows the corresponding EQE values at 1.54 μm (right axis). (bottom) EL spectra at the injected current of 2 μA. The spectra are normalized to the detection system response.

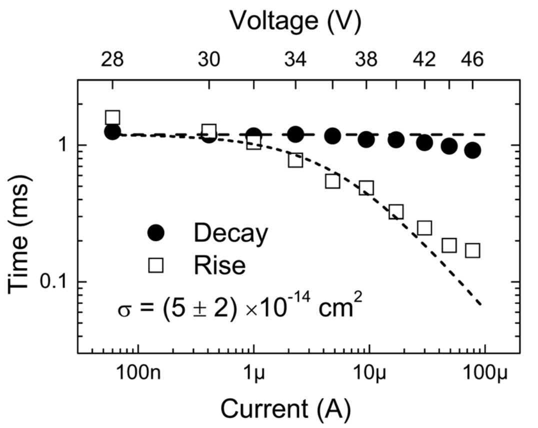

FIG. 4. Exponential decay and rise times of an integrated EL spectral intensity in IR as a function of LED driving voltage (top x-axis) and the corresponding current taken from the DC I-Vs in Fig. 2 (bottom x-axis). Measurement uncertainty is smaller than symbol sizes. The Er excitation cross-section value estimated from the data is $(5 \pm 2) \times 10^{-14}$ cm^2. The lines are guides to the eye with a constant value of the decay time of 1.2 ms and an Er excitation cross-section value of 5.9×10^{-14} cm^2.

function of the current. The saturation of the 1.54 μm emission may be attributed to both a limited amount of optically active Er ions and to the onset of nonradiative recombination processes.[11,16,23] The presence of the last is evidenced by the decrease of the luminescence decay time shown in Fig. 4, which we will discuss later.

Figure 3 also shows the EQE of Er-doped Si-NC LED emitting at 1.54 μm. It is noteworthy that these EQE values are among the best values reported so far for the Er-doped silicon LED (see for example Refs. 24 and 25). The EL spectra of the Si-NC LED and of the Si-NC:Er LED for a same injected current of 2 μA are shown in the bottom panel of the Fig. 3. The emission of the Si-NC LED is characterized by a broad peak centered at around 770 nm (see the middle picture of the low panel of Fig. 1), which originates from excitonic recombinations in the Si-NCs. The Si-NC:Er LED emission spectrum shows in addition to the broad Si-NC emission several sharp peaks at around 550, 660, 850, 980, and 1535 nm due to the excited Er states emission (presence of the peaks at 660 and 850 nm is more evident at higher currents). It has to be noted that the green emission at 550 nm (see the right picture of the low panel of Fig. 1) is not due to the Er up-conversion because the peak intensities of the various emission bands increase linearly as the injection current increases. The linear increase is observed in a broad range of currents up to 20 μA. At larger currents, we observed some signs of the cooperative up-conversion.[26] High driving voltages (Fig. 2) along with the presence of the multiple Er peaks indicate that Er emission is mainly due to direct impact excitation of Er ions and not to indirect Er excitation via energy transfer from Si-NCs. The energy transfer between Si-NCs and Er ions cannot be completely ruled out since the Si-NC emission peak is much weaker in the Si-NC:Er LED than in the undoped device.

Another argument for the interaction between Er and Si-NCs is the value of the excitation cross-section of Er. This can be estimated by measuring the exponential rise and decay time of EL.[4,11,23] The result is shown in Fig. 4. The excitation cross-section value extracted from the data is $(5 \pm 2) \times 10^{-14}$ cm^2. Note that the evaluation is based only on the rise and decay times for driving voltages larger than 30 V. For lower driving voltages, the 1.54-μm EL rise time exceeds 1.20 ± 0.02 ms, which is equal to the EL decay time. We also note that the EL decay time is similar to the measured 1.54-μm photoluminescence (PL) lifetime of 1.31 ± 0.05 ms. We measured an excitation cross-section value which is larger than the known value of direct impact excitation of Er in SiO$_2$, $(6 \pm 2) \times 10^{-15}$ cm^2,[27] and which is close to the indirect Er excitation cross-section value for Er coupled to Si-NCs.[4,25] It is noteworthy that the decrease in the decay lifetime only moderately accounts for the decrease in EQE shown in Fig. 3. Saturation of optically active Er concentration might account for the rest of this decrease.

In summary, the results of the DC excitation presented in this section suggest that electrical current is due to electron tunneling mediated by Si-NCs in the Si-NC LED and Er-related defects in the Si-NC:Er LED. They also show that Er is primarily excited by impact of high energy electrons. The impact of holes is believed to be small because of a negligible hole current due to the larger valence band offset of Si and Si-NCs than the conduction band offset.[28]

B. Bipolar pulsed excitation

Figure 5 shows the peak EL intensity at 770 nm and the spectrally integrated EL intensity bracketing 1.54 μm as a function of the driving frequency, f, for a bipolar pulsed excitation scheme. Here the LEDs are driven by varying the bias periodically and rapidly (within ~400 ns) from forward to reverse and from reverse to forward with a square waveform at a frequency f. At low driving frequencies, $f \ll 1$ kHz, the EL intensity at 1.54 μm (bottom panel in Fig. 5) decreases a little with the frequencies for high driving voltages and increases for low driving voltages, being much weaker for the low bias. As the driving frequency approaches 800 Hz, which corresponds to the inverse of Er emission lifetime, the

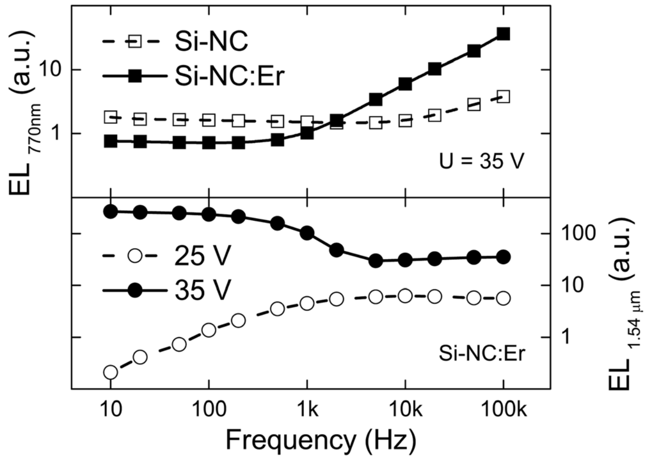

FIG. 5. (top panel) Peak EL intensity at 770 nm as a function of bipolar-pulse driving frequency with a fixed RMS voltage of 35 V for both Si-NC and Si-NC:Er LEDs. (Bottom panel) Integrated EL spectral intensity in a wavelength range bracketing 1.54 μm as a function of bipolar-pulse driving frequency at a fixed RMS voltage of 25 and 35 V for the Si-NC:Er LEDs. The meaning of the different symbols is stated in the figure legend.

EL intensity decreases (increases) for high (low) bias. In a frequency range $f \gg 1$ kHz, which we name a moderate frequency range, it changes only slightly for both the high and low bias. This behavior is accompanied by an increase of the peak EL intensity at 770 nm (Fig. 5, top panel; high bias). It should be noted that the onset frequency of this increase is around 800 Hz unlike the undoped Si-NC LED where the EL starts to significantly increase above 10 kHz. The EL decay lifetime of Si-NCs is around 5 μs (measured by both PL and EL), which corresponds to a frequency of 200 kHz. These high frequencies are not available with our instruments and, so that, the lifetime of Si-NCs does not limit the EL intensity in the studied frequency range.

The frequency dependence of the EL intensity is reflected in evident changes of the Si-NC:Er LED spectral characteristics, which are shown in Fig. 6 for high bias only. The multiple Er emission peaks weaken, including the emission at 1.54 μm (Fig. 5), and the peaks at 550, 660, and 850 nm disappear at the moderate frequencies. The Si-NC emission peak emerges. We attribute these changes to a change in the dominant excitation mechanism of Er ions: from electron impact to the energy transfer between Si-NCs and Er ions. Under the pulsed excitation scheme, sequential injection of electrons and holes into Si-NCs takes place at the bias transitions.[9] More efficient injection into Si-NCs at high injection frequencies (more bias transitions for a same time period) provides additional indirect Er excitation by means of the energy transfer at the bias transitions. This explains an increase of the Er emission at 1.54 μm with injection frequency at low voltages (there is no emission by impact), for example 25 V shown in Fig. 5. Note that optical excitation experiments show that only ~1% of the total Er population is coupled to the Si-NCs.[29] Therefore, if we assume that this holds true also for electrical excitation, it is this 1% of Er ions which shows an increased excitation due to a better energy transfer from the Si-NCs. If the injection frequency is smaller than the Er emission rate of about 800 Hz, both Si-NCs and Er are in relaxed states and follow the frequency. If the excitation frequency is higher than the Er emission rate (while still smaller than the Si-NC emission rate of 200 kHz), Er stays in an excited state and further excitation is limited by nonradiative processes. It should be noted that intensity of Er emission due to impact excitation decreases by a factor of 2 when the driving frequency increases from 10 Hz to 100 kHz. This follows from a measurement of Er emission intensity at 1.54 μm versus driving frequency of high-voltage forward bias pulsed excitation, which turns the LED on and off. This decrease however cannot account for the decrease in EL intensity shown in Fig. 5 (bottom panel, full symbols) which is due to the bipolar pulsed excitation.

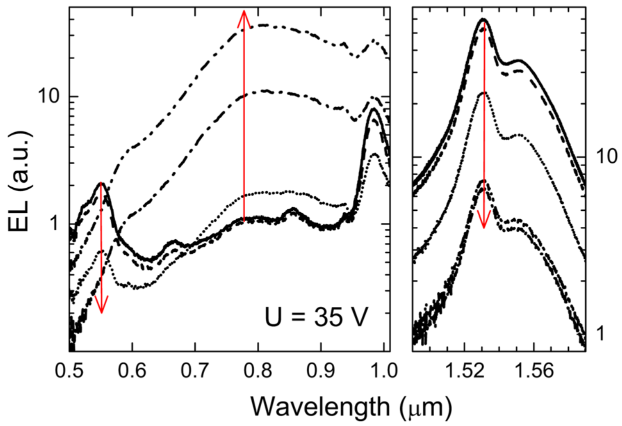

FIG. 6. The EL spectra at 10, 100, 1 k, 10 k, and 50 kHz for the Si-NC:Er LEDs shown in Fig. 5 for a fixed RMS voltage of 35 V. The ascending frequency order is indicated by the arrows.

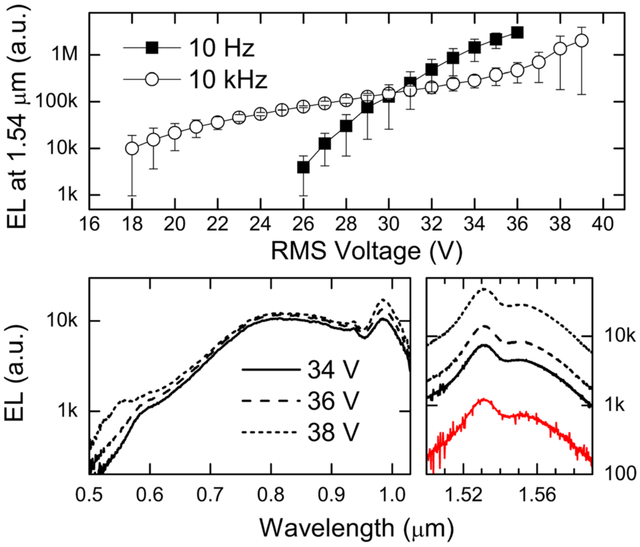

FIG. 7. EL intensity at 1.54 μm as a function of RMS voltage under bipolar pulsed electrical excitation for two driving frequencies 10 Hz (squares) and 10 kHz (circles). The low panels show EL spectra at 34, 36, and 38 V_{RMS} at 10 kHz. Notice an appearance of the Er emission band at 550 nm at 38 V. The lowest red line at the right – EL spectrum at 30 V_{RMS} at 10 Hz. No light emission was detected in the visible region at 30 V_{RMS} at 10 Hz.

The fact that the energy transfer between Si-NCs and Er-ions becomes a dominant Er excitation mechanism at the moderate frequency range is further supported by the voltage dependence of EL intensity at 1.54 μm shown in Fig. 7. The voltage dependence is stronger for low than for moderate injection frequencies. It is important that the EL signal in the moderate frequency range is observed at lower driving voltages than in DC or low frequency excitation, namely the onset of EL was measured at around 18 V_{RMS} (Fig. 7). Beyond this value, charge trapping in the oxide arrests EL. The energy transfer remains the main excitation mechanism of Er up to about 36 V_{RMS} at moderate frequencies. This is supported by the EL spectra shown in Fig. 7. There are no

TABLE I. Er excitation mechanisms. Low frequency stands for driving frequencies lower than the Er emission rate, moderate frequency — frequencies higher than the Er emission rate, but lower than the EL decay rate of Si-NCs.

	Low frequency, $f < \sim 1$ kHz	Moderate frequency, 1 kHz $\ll f <$ 200 kHz
Low voltages, U < 25 V	N/A	Transfer
Moderate voltages, 25 V < U < 36 V	Transfer and Impact	Transfer
High voltages, U > 36 V	Impact	Impact

Er-related peaks at wavelengths below 980 nm at low-to-moderate voltages, while an Er peak centered at around 550 nm is observed at 38 V_{RMS}. At high voltages, ca. 36 V_{RMS}, and moderate frequencies, the EL emission is dominated by impact. Table I summarizes the obtained results in a broad range of excitation frequencies and voltages in terms of a dominant excitation mechanism of Er-ions under electrical pumping.

IV. CONCLUSIONS

We have observed a change in the Er excitation mechanism under pulsed electrical injection and studied its dependence on the injection frequency and voltage pulse amplitude. We ascribe Er emission at high voltages (for both DC and pulsed injection) to the impact excitation by high energy electrons while Er emission is due to the nonradiative energy transfer from Si-NCs at low voltages. The Er emission at the low voltages becomes accessible only at moderate injection frequencies which are larger than the inverse of Er emission lifetime of a few milliseconds. This behavior is quite general since we observed similar trends (Table I) on a number of other Si-NC:Er LEDs with various structural parameters. For clarity, here we discussed a single kind of LED.

ACKNOWLEDGMENTS

This work was supported by EC through the project ICT-FP7-224312 HELIOS and by Italy-Spain integrated actions. D. N.-U. thanks the financial support of AGAUR through the Beatriu de Pinòs program. We acknowledge the contribution from Nicola Daldosso at an early stage of the work and Eveline Rigo for the photographs of the LEDs.

[1] O. Jambois, F. Gourbilleau, A. Kenyon, J. Montserrat, R. Rizk, and B. Garrido, Opt. Express **18**, 2230 (2010).

[2] J. D. B. Bradley and M. Pollnau, Laser Photonics Rev. **5**, 368 (2011).

[3] M. E. Castagna, S. Coffa, M. Monaco, L. Caristia, A. Messina, R. Mangano, and C. Bongiorno, Physica E (Amsterdam) **16**, 547 (2003).

[4] F. Iacona, D. Pacifici, A. Irrera, M. Miritello, G. Franzo, F. Priolo, D. Sanfilippo, G. Di Stefano, and P. G. Fallica, Appl. Phys. Lett. **81**, 3242 (2002).

[5] A. Muscara, M. E. Castagna, S. Leonardi, and S. Coffa, IEEE J. Quantum Electron. **47**, 1362 (2011).

[6] G. Franzo, V. Vinciguerra, and F. Priolo, Appl. Phys. A: Mater. Sci. Process. **69**, 3 (1999).

[7] I. Izeddin, D. Timmerman, T. Gregorkiewicz, A. S. Moskalenko, A. A. Prokofiev, I. N. Yassievich, and M. Fujii, Phys. Rev. B **78**, 035327 (2008).

[8] A. Pitanti, D. Navarro-Urrios, N. Prtljaga, N. Daldosso, F. Gourbilleau, R. Rizk, B. Garrido, and L. Pavesi, J. Appl. Phys. **108**, 053518 (2010).

[9] R. J. Walters, G. I. Bourianoff, and H. A. Atwater, Nature Mater. **4**, 143 (2005).

[10] M. Peralvarez, C. Garcia, M. Lopez, B. Garrido, J. Barreto, C. Dominguez, and J. A. Rodriguez, Appl. Phys. Lett. **89**, 051112 (2006).

[11] F. Priolo, C. D. Presti, G. Franzo, A. Irrera, I. Crupi, F. Iacona, G. Di Stefano, A. Piana, D. Sanfilippo, and P. G. Fallica, Phys. Rev. B **73**, 113302 (2006).

[12] G. M. Miller, R. M. Briggs, and H. A. Atwater, J. Appl. Phys. **108**, 063109 (2010).

[13] N. Prtljaga, D. Navarro-Urrios, A. Marconi, A. Anopchenko, J.-P. Colonna, F. Milesi, N. Daldosso, O. Jambois, B. Garrido, J.-M. Fedeli, and L. Pavesi, Opt. Mater. **33**, 1083 (2011).

[14] F. Lenz, A. Hryciw, R. DeCorby, and A. Meldrum, Appl. Phys. Lett. **95**, 091909 (2009).

[15] S. Cueff, C. Labbe, B. Dierre, F. Fabbri, T. Sekiguchi, X. Portier, and R. Rizk, J. Appl. Phys. **108**, 113504 (2010).

[16] J. M. Sun, W. Skorupa, T. Dekorsy, M. Helm, and A. N. Nazarov, Opt. Mater. **27**, 1050 (2005).

[17] O. Jambois, J. M. Ramirez, Y. Berencen, D. Navarro-Urrios, A. Anopchenko, A. Marconi, N. Prtljaga, A. Tengattini, P. Pellegrino, N. Daldosso, L. Pavesi, J.-P. Colonna, J.-M. Fedeli, and B. Garrido, J. Phys. D: Appl. Phys. **45**, 045103 (2012).

[18] O. Jambois, Y. Berencen, K. Hijazi, M. Wojdak, A. J. Kenyon, F. Gourbilleau, R. Rizk, and B. Garrido, J. Appl. Phys. **106**, 063526 (2009).

[19] L. Palmetshofer, Y. Suprun-Belevich, and M. Stepikhova, Nucl. Instrum. Methods Phys. Res. B **127**, 479 (1997).

[20] D. Konig, M. Rennau, and M. Henker, Solid-State Electron. **51**, 650 (2007).

[21] A. Nazarov, J. M. Sun, W. Skorupa, R. A. Yankov, I. N. Osiyuk, I. P. Tjagulskii, V. S. Lysenko, and T. Gebel, Appl. Phys. Lett. **86**, 151914 (2005).

[22] T. Z. Lu, M. Alexe, R. Scholz, V. Talalaev, R. J. Zhang, and M. Zacharias, J. Appl. Phys. **100**, 014310 (2006).

[23] B. Garrido, C. Garcia, S. Y. Seo, P. Pellegrino, D. Navarro-Urrios, N. Daldosso, L. Pavesi, F. Gourbilleau, and R. Rizk, Phys. Rev. B **76**, 245308 (2007).

[24] P. M. Fauchet, Silicon Photonics **94**, 177 (2004).

[25] N. Daldosso and L. Pavesi, Laser Photonics Rev. **3**, 508 (2009).

[26] J. M. Ramírez, O. Jambois, Y. Berencén, D. Navarro-Urrios, A. Anopchenko, A. Marconi, N. Prtljaga, N. Daldosso, L. Pavesi, J.-P. Colonna, J. M. Fedeli, and B. Garrido, "Polarization strategies to improve the emission of Si-based light sources emitting at 1.55 μm" Mater. Sci. Eng. B (to be published).

[27] S. Wang, A. Eckau, E. Neufeld, R. Carius, and C. Buchal, Appl. Phys. Lett. **71**, 2824 (1997).

[28] G. Seguini, S. Schamm-Chardon, P. Pellegrino, and M. Perego, Appl. Phys. Lett. **99**, 082107 (2011).

[29] N. Prtljaga, D. Navarro-Urrios, A. Tengattini, A. Marconi, A. Anopchenko, F. Ferrarese Lupi, O. Jambois, J. M. Ramirez, Y. Berencen, B. Garrido, F. Milesi, J.-P. Colonna, J.-M. Fedeli, and L. Pavesi (unpublished).

Materials Science and Engineering B 177 (2012) 734–738

Contents lists available at SciVerse ScienceDirect

Materials Science and Engineering B

journal homepage: www.elsevier.com/locate/mseb

Short communication

Polarization strategies to improve the emission of Si-based light sources emitting at 1.55 μm

J.M. Ramírez[a,*], O. Jambois[a], Y. Berencén[a], D. Navarro-Urrios[a], A. Anopchenko[b], A. Marconi[b], N. Prtljaga[b], N. Daldosso[d], L. Pavesi[b], J.-P. Colonna[c], J.-M. Fedeli[c], B. Garrido[a]

[a] Departament d'Electrònica, Universitat de Barcelona, Carrer Martí i Franquès 1, Barcelona 08028, Spain
[b] Nanoscience Laboratory, Department of Physics, University of Trento, Via Sommarive 14, Povo (Trento) 38123, Italy
[c] CEA, Léti, Minatec Campus 17 rue des Martyrs, 38054 Grenoble Cedex 9, France
[d] Dipartimento di Informatica, Università di Verona, Strada Le Grazie 15, 37134 Verona, Italy

ARTICLE INFO

Article history:
Received 12 July 2011
Received in revised form 14 October 2011
Accepted 5 December 2011
Available online 20 December 2011

Keywords:
Silicon nanocrystals (Si-ncs)
Erbium
Pulsed voltage
Electroluminescence

ABSTRACT

We present a electroluminescence (EL) study of the Si-rich silicon oxide (SRSO) LEDs with and without Er^{3+} ions under different polarization schemes: direct current (DC) and pulsed voltage (PV). The power efficiency of the devices and their main optical limitations are presented. We show that under PV polarization scheme, the devices achieve one order of magnitude superior performance in comparison with DC. Time-resolved measurements have shown that this enhancement is met only for active layers in which annealing temperature is high enough (>1000 °C) for silicon nanocrystal (Si-nc) formation. Modeling of the system with rate equations has been done and excitation cross-sections for both Si-nc and Er^{3+} ions have been extracted.

1. Introduction

Silicon based light sources have been widely investigated for their implementation in integrated photonic circuits [1–8]. Complementary metal–oxide-semiconductor (CMOS) compatibility would allow for cheap mass-fabrication and for electronic–photonic function integration in the same chip. In particular, the fabrication of an efficient electrically pumped source working in the near infrared would be of a great interest due to its applications in telecommunications [9]. With such an idea, Er^{3+} doped materials were fabricated and embedded in MOS devices to develop Si-based sources emitting at 1.54 μm [10,11]. It was demonstrated later that the inclusion of Si-ncs in Er^{3+} doped silica resulted in efficient room-temperature Er^{3+} luminescence under optical pumping [12–15]. The much larger effective absorption cross-section of Si-ncs with regard to Er^{3+} ions and the efficient coupling between them was an attractive perspective for the near future. Moreover, higher excitation cross-sections were measured in both species under electrical pumping [16,17], giving a room for improvement in these devices. However, the role of Si-ncs in Er^{3+} doped silica under electrical pumping is not fully resolved yet, as the excitation mechanisms and the physics involved are different from the optical pumping.

In order to shed light on this issue, Si-based light emitting devices (LEDs) with undoped Si-ncs (emitting in the visible) or doped with Er^{3+} ions (emitting in the near infrared) have been fabricated. The contribution of Si-ncs to the electro-optical properties and the influence of the annealing treatment for visible and infrared devices are reported, as well as the main excitation mechanisms involved in the electroluminescence. Moreover, PV studies have allowed us to investigate the EL response with the driving frequency, determining an optimized frequency of operation to maximize the EL of Si-ncs in more than one order of magnitude with respect to the electroluminescence under DC excitation.

2. Experimental

Three different MOS capacitors were fabricated on P-type silicon wafers doped at 1×10^{15} at/cm^3. The oxide was replaced by an optically active layer. A SRSO layer 50 nm thick was deposited by Low Pressure Chemical Vapor Deposition (LPCVD) with two different silicon excess (9% and 16%). Layers were annealed for 1 h at 900 °C (D1 and D3) or at 1100 °C (D2) to induce the phase separation of the SRSO in Si and SiO_2. An Er^{3+} implantation was performed in one sample (D3), with a fluence of 1×10^{15} at/cm^2 and 25 keV of energy. Er^{3+} ions were activated by a post implantation annealing performed at 800 °C for 6 h. The implantation profile and the Si

---

* Corresponding author. Tel.: +34 934039175.
E-mail address: jmramirez@el.ub.es (J.M. Ramírez).

0921-5107/$ – see front matter © 2011 Elsevier B.V. All rights reserved.
doi:10.1016/j.mseb.2011.12.023

Table 1
Fabrication parameters of the devices under study.

Device	Si (%)	Ann. temp. (1 h)	Er^{3+} implant. (25 keV)	Post-ann. temp. (6 h)
D1	9	900 °C	–	–
D2	16	1100 °C	–	–
D3	9	900 °C	10^{15} at/cm^2	800 °C (6 h)

excess were further confirmed by Secondary Ion Mass Spectroscopy (SIMS) and X-ray Photoelectron Spectroscopy (XPS). Details on the procedure and results can be found in Ref. [18]. Finally, a highly n-type doped (1×10^{20} at/cm^3) polysilicon layer 100 nm thick was deposited and used as a semitransparent gate electrode. The area of devices is 0.09 mm^2. The details of each of the three layers are resumed in Table 1.

EL measurements were performed at room temperature. LEDs were biased under forward condition, i.e. negative voltages over the gate, with a probe station (Cascade Microtech Summit 1100) driven either by a semiconductor device analyzer (Agilent B1500A) for DC measurements, or by a square pulse generator for pulsed excitation (Agilent 8114A).

EL was collected either with a photomultiplier tube (PMT) or with a cryogenically cooled charged coupled device (CCD), placed behind an Acton 2300i grating spectrometer for spectra recording. A digital oscilloscope was used for time resolved measurements. All the spectra were corrected from the spectral response.

3. Results

3.1. Power efficiency

The electro-optical characterization of the devices was done by polarizing them from low voltages until breakdown, collecting at the same time the leakage current through the gate and the emitted EL. High electric fields of around 10 MV/cm at the maximum were reached.

Fig. 1 shows the comparison of the power efficiency (η) between visible (a) and infrared (b) emitting LEDs as a function of the DC voltage (forward condition). It is defined as the ratio between the collected optical power and the applied input power:

$$\eta = \frac{\text{Opt. power}\ \ (w)}{\text{Elect. power}\ \ (w)} \times 100 \tag{1}$$

obtaining a maximum of $\eta_{D2} = 4 \times 10^{-4}\%$ in the visible range and $\eta_{D3} = 10^{-2}\%$ in the infrared. A decrease of the power efficiency takes place in both devices when the voltage is increased. Nonetheless, this latter fact can be controlled for visible LEDs (see Fig. 1a) by decreasing both the amount of Si excess in the matrix and the annealing temperature, achieving a wide range of voltages (from 17 V to 35 V) where the power efficiency remains almost constant, but at lower values. This suggests the existence of a compromise between the power efficiency and its non-dependence on the voltage in such systems.

The threshold voltage of electroluminescence (V_{TH}) can be extracted from the insets of Fig. 1a (16 V for D1 and 21 V for D2) and Fig. 1b (26 V for D3), where the EL has been represented as a function of the applied DC voltage in arbitrary units. For visible emitting LEDs, the threshold of the EL is directly correlated with the annealing temperature, as smaller V_{TH} are obtained when the annealed temperature is lower. However, no substantial difference was observed in devices with the same annealing treatment but different Si excess (9% and 16%). Regarding the Si-nc size, although TEM measurements were not accomplished in the samples annealed at 900 °C and at 1100 °C, similar EL spectral shapes centered at the same wavelength were obtained for devices D1 and D2, suggesting similar mean Si-nc diameters in both samples regardless of the applied annealing temperature (900 °C or 1100 °C). Moreover, the size of the Si-nc was roughly estimated considering the theoretical results of Delerue et al., where the emitted λ is correlated with the Si-nc diameter as follows [19]:

$$E = 1.12 + \frac{3.73}{d^{1.39}} \tag{2}$$

where E is the emission energy and d the diameter of the Si-nc. A mean value of (4.7 ± 0.3) nm was found for the sample annealed at 900 °C, and (4.5 ± 0.3) nm for the one annealed at 1100 °C. Although these results seem to be contradictory with the well establish belief that the Si-nc growth is expected to increase with the temperature, it is important to remark that at the lowest temperature, i.e. 900 °C, there is no significant crystallization of Si nanoparticles [20] and hence they grow as amorphous Si clusters. This assumption is reinforced when considering the quantum confinement of e-h pairs

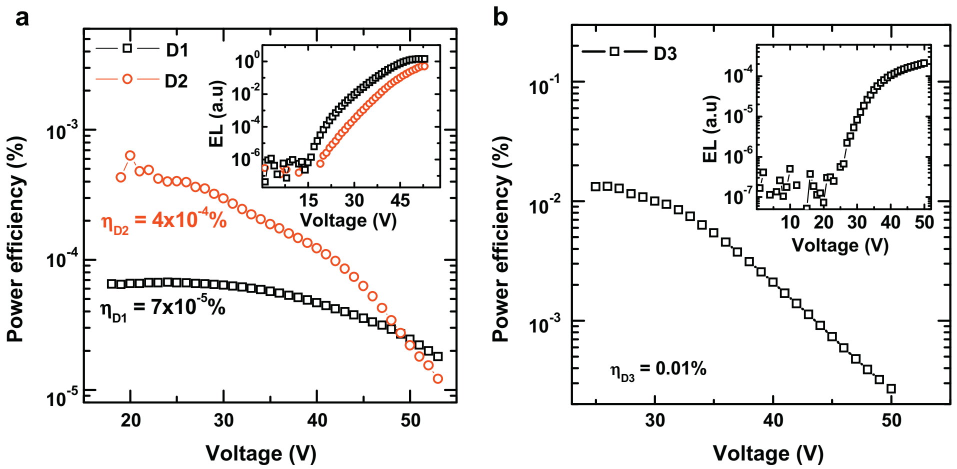

Fig. 1. Power efficiency as a function of the voltage for visible LEDs (a) annealed at 900 °C (black squares) or at 1100 °C (red circles) and for infrared LEDs (b) annealed at 900 °C with a post implantation annealing (black squares). The inset shows the EL in arbitrary units as a function of the voltage for both visible (inset a) and infrared LEDs (inset b). (For interpretation of the references to color in this figure legend, the reader is referred to the web version of this article.)

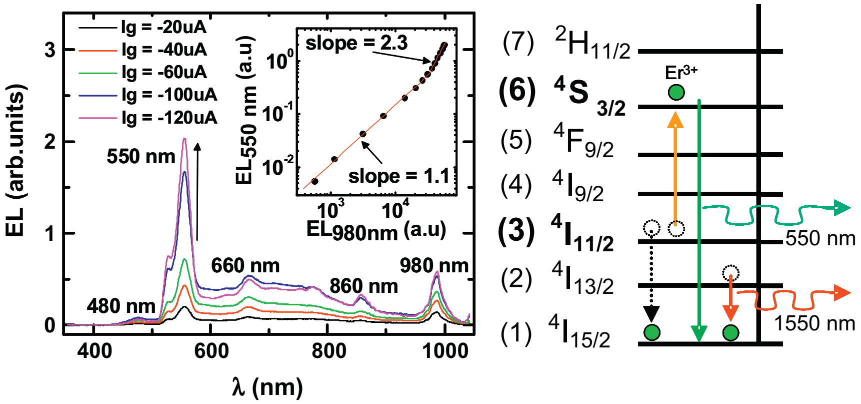

Fig. 2. (Left) visible EL transitions of erbium ions at different input currents. The inset shows the EL emission at 550 nm as a function of the EL at 980 nm. (Right) the diagram shows (i) an upconversion process where one excited Er^{3+} promotes another one in the same excited state $^4I_{11/2}$ (upwards arrow) to higher energy levels ($^4S_{3/2}$) with the following emission at 550 nm; (ii) Er^{3+} emission at 1550 nm from the first excited level ($^4I_{13/2}$) to the ground state ($^4I_{15/2}$).

inside these nanocomposites [21], since the comparison of the EL spectra for D1 and D2 under the same current density (10 mA/cm^2) provides higher EL intensity (5 times) in the sample annealed at 1100 °C.

In addition, the comparison between D1 (visible) and D3 (infrared) with an extra annealing treatment at 800 °C for 6 h shows a clear shift in the V_{TH} of about 10 V, suggesting that the erbium implantation and the post-implantation annealing treatment remarkably affect the EL(V) characteristics.

By other side, the saturation of the EL at high electric fields (above 8 MV/cm) in both devices is ascribed to a saturation of the number of excited luminescent centers and/or quenching of the additional excitation by the increasing amount of current. The quantification of the inverted fraction of excited luminescent centers was done for the infrared (D3), obtaining values around 20% for this sample, equally than Ref. [14].

3.2. *Limiting factors of Er^{3+} ions*

Focusing on infrared emitting LEDs (D3), we observed that one of the main limiting mechanisms involved in the emission of the first excited level of Er^{3+} when pumping at high current densities (above 100 mA/cm^2) was the cooperative up-conversion. The excitation of an Er^{3+} ion from one transition state to another one with higher energy as a consequence of the interaction with a neighboring erbium becomes critical at high fluxes [22]. This effect was experimentally proved in our devices by collecting the visible spectrum when the polarization current applied is increased, as can be observed in Fig. 2. At low input currents, the EL of every transition level increases linearly with respect to the other ones. However, at a certain current, the excited level $^4S_{3/2}$ becomes overpopulated by the $^4I_{11/2}$ level, enhancing the EL of the transition $^4S_{3/2} \rightarrow {}^4I_{15/2}$ and diminishing the decay times involved in the first excited transition. Therefore, a sudden slope change occurs when the EL at 550 nm ($^4S_{3/2} \rightarrow {}^4I_{15/2}$) is plotted as a function of the EL at 980 nm ($^4I_{11/2} \rightarrow {}^4I_{15/2}$), as observed in the inset of Fig. 2. Moreover, the emission at 1.55 μm saturates at these high fluxes, whereas the emission at 550 nm becomes quadratic with the current until the breakdown of the device.

On the other hand, the existence of a threshold voltage (26 V) to obtain simultaneously the infrared EL in addition with the visible EL peaks attributed to higher Er^{3+} transitions points out that carriers have energies ranged from 0.8 eV (EL at 1550 nm) to 2.5 eV (EL at 488 nm) from the very beginning of the EL [10]. Then, considering the EL spectra of the Er^{3+} doped SiO_2 free of Si-ncs [23] and taking into account that the energy transfer rates occurs at lower energy values [24], we ascribe the Er^{3+} excitation to the direct impact of hot carriers highly accelerated. This idea was further corroborated by studying the transport mechanisms prevailing inside layers with two well known models [25]; (i) Poole–Frenkel conduction of thermally activated carriers; (ii) Fowler–Nordheim tunneling of hot carriers through a triangular barrier height. Therefore, the fit of these models over the $I(V)$ curves of visible and infrared LEDs determined that at low-moderate voltages, in which the EL does not show up, the main transport occurs through trap assisted centers (Poole–Frenkel), whereas at high voltages the Fowler–Nordheim mechanism would be the responsible of the conduction, coinciding with the EL emission [26].

3.3. *Pulsed voltage excitation and time-resolved measurements*

In order to study the excitation and de-excitation properties involved in the EL, LEDs were polarized under a negative square pulsed voltage (from 0 to −30 V). The driving frequency was swept from 10 Hz to 1 MHz. Results for visible emitting LEDs (D1 and D2) are shown in Fig. 3a. Each point corresponds to an integrated EL spectrum. The comparison between the frequency evolution of the EL in D1 (black squares) and D2 (red circles) under a negative square pulse with the same voltage than the one applied in the DC EL (black dashed line and red dotted line) reveals a clear difference between them. Whereas the emission of the D1 does not show an improvement with regard to the DC value, the EL of D2 becomes increased above the DC value of about one order of magnitude at 20 kHz. Note that the inverse of this value coincides with the experimental lifetime obtained from Si-ncs (50 μs) [27]. This EL improvement was quantified by diminishing the input voltage in order to obtain comparable EL values with the ones provided by the DC polarization, determining a diminution of 5 V in the input AC voltage (from 0 to −25 V, blue triangles in Fig. 3a) with regard to the same EL in DC (at −30 V).

In addition, time-resolved measurements were carried out in D1 and D2 so as to understand the frequency evolution of the visible EL under PV excitation. Looking at the device D2, a transient EL overshoot is observed when the polarization is switched off (Fig. 3b). On the contrary, no EL overshoot arises when biasing D1 under the same polarization conditions. Therefore, the enhancement of the EL intensity under PV excitation observed in device D2 (Fig. 3a, red empty circles) is attributed to the sum of this EL overshoot with the DC value of the EL (shown in Fig. 3b). We associate the presence of the overshoot in sample D2 with the thermal treatment of the sample. If an adequate annealing temperature is performed, the crystallization of Si-ncs occurs and hence the created excitons

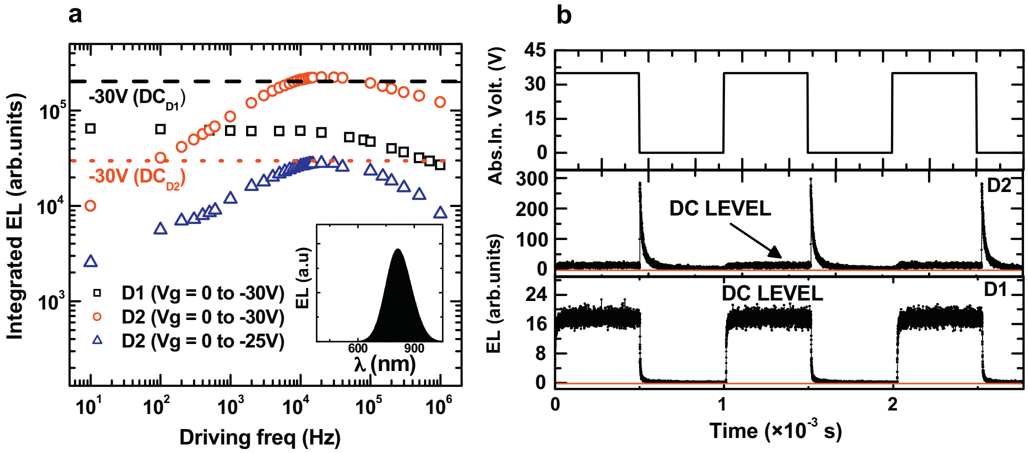

Fig. 3. (a) Integrated PV electroluminescence as a function of the driving frequency for visible LEDs (D1 and D2) with 30 V of peak-to-peak voltage (black squares and red circles). Blue triangles represents the EL(freq) of D2 for an input switch on voltage of −25 V. The EL in DC is also represented in both D1 and D2 by a black dashed line and a red dotted line. The inset of (a) shows a typical spectrum at a frequency of 10 kHz. (b) Time-resolved measurements for D1 (bottom panel) and D2 (middle panel) under the square voltage function from 0 to −35 V represented in the top panel in absolute units. The arbitrary units of the bottom and middle panel can be compared. (For interpretation of the references to color in this figure legend, the reader is referred to the web version of this article.)

remain inside the Si-ncs even after the voltage switch off. At this moment, the wave function overlap of each confined e-h pair is maximized and consequently the probability of radiative recombination is increased [28]. Furthermore no Auger processes due to injected hot carriers would be involved during the off voltage state [29], obtaining an EL enhancement of one order of magnitude compared to the DC level of the EL. On the contrary, applying an insufficient annealing temperature no Si crystallization takes place, providing a weak excitonic confinement inside them and stimulating the exciton migration out of the Si-nc. This hypothesis was further supported by comparing the lifetimes in samples D1 and D2 [30]. A difference of 10 times was detected between the sample D1 (∼3 μs) and sample D2 (∼30 μs). Thus, these results strengthen the importance of the annealing temperature in these LEDs.

For infrared LEDs (D3), no improvement of the EL at 1.55 μm was detected under AC compared with the DC excitation. The evolution of the integrated EL as a function of the driving frequency and time resolved measurements were similar than D1, without EL overshoot. However, in this case, the lack of improvement of the infrared signal cannot be related to the non-crystallization of Si-ncs, as we have shown that they act just as conduction centers for hot carriers and not as sensitizers. In our layers, Er^{3+} ions would be directly excited with hot electrons. This suggests that Auger processes above mentioned occurring in the Si-ncs are not affecting the Er^{3+} ions significantly.

From Fig. 3, the absorption cross-section was estimated in visible (D1) and infrared (D3) LEDs taking into account a nearly two level system, which has been used by many authors before [31,32]. Starting from the dynamic rate equation,

$$\frac{dN_2}{dt} = \sigma\frac{j}{e}(N_{\mathrm{total}} - N_2) - \frac{N_2}{\tau_{\mathrm{decay}}} \tag{3}$$

with

$$\frac{1}{\tau_{\mathrm{decay}}} = \frac{1}{\tau_{\mathrm{rad}}} + \frac{1}{\tau_{\mathrm{non\text{-}rad}}} \tag{4}$$

where σ is the effective absorption cross-section, j is the incident current density, e the single electron charge, τ_{decay} is the total lifetime (radiative (τ_{rad}) and non-radiative ($\tau_{\mathrm{non\text{-}rad}}$)), and N_{total} and N_2 the total implanted and the excited Er^{3+} ions in the first energy

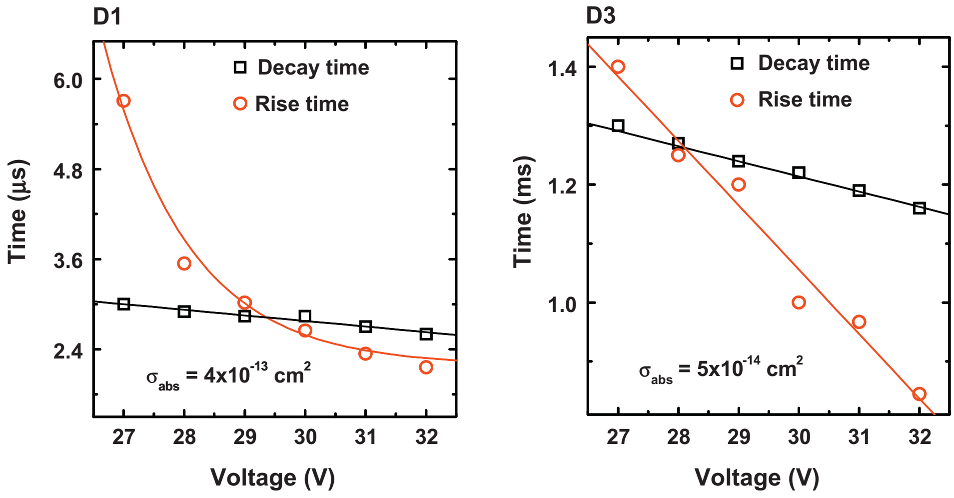

Fig. 4. Experimental decay and rise times as a function of the applied voltage for visible (a) and infrared (b) LEDs. Fitted lines are guides to the eye.

level, respectively. Also, knowing that EL $\propto N_2/\tau_{\text{decay}}$, the following relation can be obtained [31],

$$\frac{1}{\tau_{\text{rise}}} = \frac{1}{\tau_{\text{decay}}} + \frac{j}{e}\sigma \tag{5}$$

being σ the absorption cross-section of the luminescent centers. A single exponential was used to fit the decay in the Er^{3+} doped sample. For Si-ncs, a stretched exponential decay is typically reported in the literature [33],

$$\text{EL}(t) = \text{EL}_0 \exp\left[-\left(\frac{t}{\tau_{\text{decay}}}\right)^{\beta}\right] \quad \text{with} \quad \beta < 1 \tag{6}$$

Fig. 4 shows the decay lifetime (τ_{decay}, black squares) and the rise time (τ_{rise}, red circles) as a function of the applied voltage, under a negative square pulsed polarization at very low frequencies (10 Hz). Notice that both lifetimes decrease with the voltage bias, regardless of the emission range of the devices (visible or infrared emitting LEDs). Also, the rise time observed is higher than the decay time at low voltages (below 30 V), which has been ascribed to charge transport among Si-ncs, suggesting that the absorption cross-section cannot be calculated as a nearly two level system in this range (see Eq. (5)). Nonetheless, Eq. (5) has been used to estimate the absorption cross sections from 30 V and above, where $\tau_{\text{decay}} > \tau_{\text{rise}}$ obtaining a $\sigma_{\text{abs}} = 4 \times 10^{-13}$ cm^2 with a $\beta = 0.8$ for Si-ncs and $\sigma_{\text{abs}} = 5 \times 10^{-14}$ cm^2 for Er^{3+} ions. Therefore, the absorption cross-section of Si-ncs is 8 times higher than the one of erbium ions, in agreement with previous works [32], which have reported a difference of 5 times between them.

4. Conclusions

We have studied the EL properties of LPCVD SiO_x layers doped or not with Er^{3+} ions, under DC and pulsed polarization. Under DC excitation, we show that annealing temperature affects both power efficiency and its dependence with voltage. In addition, the annealing treatment has been demonstrated to be an important parameter to enhance the EL properties under pulsed polarization. In the visible, an increase of the EL-frequency characteristics is observed for the layers having well crystallized Si nanoclusters. This results in a well defined EL overshoot appearing when the pulsed voltage is in off state and attributed to the suppression of Auger effect in the Si-nc and to the e-h wave function overlap, allowing the radiative recombination of the remaining excitons. However, no EL improvement was observed for Er^{3+} doped layers. Moreover, the excitation of Er^{3+} ions has been ascribed to direct impact excitation.

Acknowledgements

This work is supported by HELIOS Project (FP7 224312) and ITO9ILB2F9 (Integrated Italia-Spain Action) Project.

References

[1] G. Franzò, A. Irrera, E.C. Moreira, M. Miritello, F. Iacona, D. Sanfilippo, G. Di Stefano, P.G. Fallica, F. Priolo, Appl. Phys. A 74 (2002) 1.
[2] L. Pavesi, L. Dal Negro, C. Mazzoleni, G. Franzò, F. Priolo, Nature 408 (2000) 440.
[3] A. Pérez-Rodríguez, O. González-Varona, B. Garrido, P. Pellegrino, J.R. Morante, J. Appl. Phys. 94 (2003) 254.
[4] M.V. Wolkin, J. Jorne, P.M. Fauchet, G. Allan, C. Delerue, Phys. Rev. Lett. 82 (1999) 197.
[5] K. Cho, N. Park, T. Kim, K. Kim, G. Sung, J. Shin, Appl. Phys. Lett. 86 (2005) 71909.
[6] L. Dal Negro, J. Yi, L. Kimerling, S. Hamel, A. Williamson, G. Galli, Appl. Phys. Lett. 88 (2006) 233109.
[7] O. Jambois, Y. Berencén, K. Hijazi, M. Wodjak, A.J. Kenyon, F. Gourbilleau, R. Rizk, B. Garrido, J. Appl. Phys. 106 (2009) 63526.
[8] Y. Berencén, J. Carreras, O. Jambois, J.M. Ramírez, J.A. Rodríguez, C. Domínguez, C.E. Hunt, B. Garrido, Opt. Express 19 (2011) A234.
[9] A. Polman, J. Appl. Phys. 82 (1997) 1.
[10] S. Coffa, G. Franzò, F. Priolo, A. Pacelli, A. Lacaita, Appl. Phys. Lett. 73 (1998) 93.
[11] G.T. Reed, A.K. Kewell, Mater. Sci. Eng. B 40 (1996) 207.
[12] M. Fujii, M. Yoshida, Y. Kanzawa, S. Hayashi, K. Yamamoto, Appl. Phys. Lett. 71 (1997) 1198.
[13] H.-S. Han, S.-y. Seo, J.H. Shin, Appl. Phys. Lett. 79 (2001) 4568.
[14] O. Jambois, F. Gourbilleau, A.J. Kenyon, J. Montserrat, R. Rizk, B. Garrido, Opt. Express 18 (2010) 3.
[15] D. Navarro-Urrios, A. Pitanti, N. Daldosso, F. Gourbilleau, R. Rizk, B. Garrido, L. Pavesi, Phys. Rev. B 79 (2009) 193312.
[16] A. Irrera, D. Pacifici, M. Miritello, G. Franzò, F. Priolo, F. Iacona, D. Sanfilippo, G. Di Stefano, P.G. Fallica, Appl. Phys. Lett. 81 (2002) 1866.
[17] M.E. Castagna, S. Coffa, M. Monaco, A. Muscara, L. Caristia, S. Lorenti, A. Messina, Mater. Sci. Eng. B 105 (2003) 83.
[18] N. Prtljaga, D. Navarro-Urrios, A. Marconi, A. Anopchenko, J.-P. Colonna, F. Milesi, N. Daldosso, O. Jambois, B. Garrido, J.M. Fedeli, L. Pavesi, Opt. Mater. 33 (2011) 1083.
[19] C. Delerue, G. Allan, M. Lannoo, Phys. Rev. B 48 (1993) 11024.
[20] F. Iacona, C. Bongiorno, C. Spinella, S. Boninelli, F. Priolo, J. Appl. Phys. 95 (2004) 3723.
[21] O. Jambois, H. Rinnert, X. Devaux, M. Vergnat, J. Appl. Phys. 100 (2006) 123504.
[22] R. Kapoor, C.S. Friend, A. Biswas, P.N. Prasad, Opt. Lett. 25 (2000) 5.
[23] Rare-Earth Implanted MOS Devices for Silicon Photonics, first ed., Springer Series in Materials Science, Springer, 2010.
[24] I. Izeddin, D. Timmerman, T. Gregorkiewicz, A.S. Moskalenko, A.A. Prokofiev, I.N. Yassievich, M. Fujii, Phys. Rev. B 78 (2008) 035327.
[25] X.D. Pi, O.H.Y. Zalloum, A.P. Knights, P. Mascher, P.J. Simpson, J. Phys. Condens. Matter 18 (2006) 9943–9950.
[26] O. Jambois, J.M. Ramírez, Y. Berencén, D. Navarro-Urrios, P. Pellegrino, A. Anopchenko, A. Marconi, N. Prtljaga, A. Tengattini, N. Daldosso, L. Pavesi, J.-P. Colonna, J.-M. Fedeli, B. Garrido, J. APD, in press.
[27] J. Valenta, N. Lalic, J. Linnros, Appl. Phys. Lett. 84 (2004) 9.
[28] C. Delerue, G. Allan, M. Lannoo, Phys. Rev. B 64 (2001) 193402.
[29] A. Irrera, F. Iacona, I. Crupi, C.D. Presti, G. Franzò, C. Bongiorno, D. Sanfilippo, G. Di Stefano, A. Piana, P.G. Fallica, A. Canino, F. Priolo, Nanotechnology 17 (2006) 1428–1436.
[30] S. Gardelis, A.G. Nassiopoulou, N. Vouroutzis, N. Frangis, J. Appl. Phys. 105 (2009) 113509.
[31] F. Priolo, G. Franzò, D. Pacifici, V. Vicinguerra, F. Iacona, A. Irrera, J. Appl. Phys. 89 (2001) 264.
[32] F. Iacona, D. Pacifici, A. Irrera, M. Miritello, G. Franzò, F. Priolo, D. Sanfilippo, G. Di Stefano, P.G. Fallica, Appl. Phys. Lett. 81 (2002) 3242.
[33] J. Linnros, N. Lalic, A. Galeckas, V. Grivickas, J. Appl. Phys. 86 (1999) 6128.

JOURNAL OF APPLIED PHYSICS **116**, 083103 (2014)

Role of silicon excess in Er-doped silicon-rich nitride light emitting devices at 1.54 μm

J. M. Ramírez,[1,a)] S. Cueff,[2] Y. Berencén,[1] C. Labbé,[3] and B. Garrido[1]
[1]*MIND-IN2UB, Department Electrònica, Universitat de Barcelona, Martí i Franquès 1, Barcelona 08028, Spain*
[2]*Institut des Nanotechnologies de Lyon, École Centrale de Lyon, Écully 69134, France*
[3]*Centre de Recherche sur les Ions, les Matériaux et la Photonique (CIMAP), UMR 6252 CNRS/CEA/Ensicaen/UCBN, Caen 14050, France*

(Received 23 July 2014; accepted 11 August 2014; published online 25 August 2014)

Erbium-doped silicon-rich nitride electroluminescent thin-films emitting at 1.54 μm have been fabricated and integrated within a metal-oxide-semiconductor structure. By gradually varying the stoichiometry of the silicon nitride, we uncover the role of silicon excess on the optoelectronic properties of devices. While the electrical transport is mainly enabled in all cases by Poole-Frenkel conduction, power efficiency and conductivity are strongly altered by the silicon excess content. Specifically, the increase in silicon excess remarkably enhances the conductivity and decreases the charge trapping; however, it also reduces the power efficiency. The main excitation mechanism of Er^{3+} ions embedded in silicon-rich nitrides is discussed. The optimum Si excess that balances power efficiency, conductivity, and charge trapping density is found to be close to 16%. © *2014 AIP Publishing LLC*. [http://dx.doi.org/10.1063/1.4893706]

I. INTRODUCTION

Silicon-based integrated photonics have garnered strong interest as a potential technology platform that is able to overcome the limitations of the microelectronics industry.[1] However, despite the large number of silicon-based photonic components already available, an efficient device emitting at 1.54 μm for on-chip light distribution has not been developed yet. Several attempts were accomplished using Er-doped silicon-rich oxides as active material, taking advantage from the superior optoelectronic performance provided by silicon nanoclusters (Si-ncs).[2] Also in that line, some research groups have suggested using silicon nitride as the primary element in a new CMOS-compatible photonic platform to develop not only passive photonic components but also active devices.[3,4] In fact, silicon nitride is potentially an ideal host for Er as its band gap enables good electrical injection while minimizing undesirable effects, such as two-photon absorption and energy back transfer.[5]

Nonetheless, despite the promising capabilities offered by Er-doped silicon-rich nitrides (Er-SRN), most research solely focuses on their optical properties. Only a few works are dedicated to study the optoelectronic properties of such materials.[5,6] As a consequence, the excitation mechanisms of luminescent centers and the correlation with the carrier transport inside Er-SRN films are still not well understood and are often subject of controversy among authors. Efficient Er sensitization from the SiN_x matrix has been proposed to explain the observed Er electroluminescence (EL) and the high excitation cross-section extracted ($\sim 10^{-15}\,cm^2$) under Poole-Frenkel conduction.[5,7] However, higher energy radiative transitions of Er with energy values up to 2.3 eV are often reported in erbium-doped nitrides.[5,8] Such visible Er emission lines are not characteristic features of an energy transfer process between Er and a silicon-based host.[9] Moreover, other works in which similar host matrices have been studied (such as silicon-rich oxides), suggested impact excitation of hot electrons as the main excitation mechanism of Er ions.[10] For all this, the study of the optoelectronic properties as well as the excitation mechanisms of Er^{3+} ions embedded in different silicon nitride hosts is interesting and deserves a thorough investigation.

With this motivation in mind, we show in this work that SRN films are suitable matrices to accommodate a large quantity of electrically excitable Er^{3+} ions and that the amount of Si excess plays a significant role in the conduction and emission characteristics. This study allows devising a material with optimized composition for maximizing electrical to optical conversion as well as device operation lifetime. For that, different Si excess contents were incorporated during the deposition and used to control the optoelectronic properties of our devices. In particular, the effect of the Si excess on the main transport mechanism, the charge trapping, and the electroluminescence efficiency is investigated, revealing a direct correlation between the charge trapping, the power efficiency, and the layer conductivity. Finally, such correspondence will be used to provide an optimum Si excess that yields the best optoelectronic performance of Er-SRN light emitting devices.

II. EXPERIMENTAL DETAILS

Er-SRN films were deposited on p-type silicon substrates ⟨100⟩ with boron doping of 1×10^{15} at./cm^3 by co-sputtering silicon and Er_2O_3 targets under an argon plasma flow rate of 10 sccm. A variable nitrogen gas flow rate (0.5 sccm, 0.75 sccm, 0.85 sccm, and 1 sccm) was introduced in

---

[a)] Author to whom correspondence should be addressed. Electronic mail: jmramirez@el.ub.edu Tel.: +34 93 4039176. Fax: +34 93 4021148.

the chamber for nitrogen incorporation. Substrate deposition temperature was set to 500 °C. All active layers have a nominal thickness of 50 nm. Later on, a highly n-doped polysilicon layer 100 nm-thick was deposited by low pressure chemical vapor deposition (LPCVD) and used as a semi-transparent electrode. Samples were subsequently annealed at 950 °C for 30 min in N_2 environment to passivate the top electrode and to activate Er^{3+} ions. The final Si excess was measured by X-ray photoelectron spectroscopy (XPS), obtaining four different values: 12%, 16%, 20%, and 40%. Time-of-flight secondary ion mass spectrometry (Tof-SIMS) was used to estimate the Er concentration, which was around of 5×10^{20} at/cm^3 for all samples.[11] The bottom contact was defined by covering the wafer backside with a thin aluminum layer. Finally, an aluminum box was deposited on top of the polysilicon electrode, along the device perimeter, to guarantee the voltage homogeneity in the upper electrode.[6] Electrical characterization was performed using a probe station connected to a semiconductor device analyzer (B1500A). EL was collected from a near-infrared objective and driven to a grating spectrometer coupled to an infrared photomultiplier tube detector (H10330–75). All experiments were performed at room temperature.

III. RESULTS AND DISCUSSION

The device cross-section and the polarization schema of devices are presented in Fig. 1. All samples were biased under accumulation regime, i.e., a negative voltage is applied to the top electrode with a voltage ramp of 0.1 V/s. Fig. 2(a) shows the current density-electric field (J-E) characteristic of Er-SRN films with different Si excess, being the current density (J) the ratio between the injected current and the device area and the electric field (E) the ratio between the applied voltage and the Er-SRN film thickness. Progressive (i.e., from zero to the maximum voltage before the device breakdown) and regressive (i.e., from maximum voltage to zero values) sweeps are displayed together for comparison. An increase in current density by several orders of magnitude and a diminution of the turn-on voltage can be observed when the Si content is increased. This is an expected trend as Si excess is known to introduce intra-band conductive states within the host either as a consequence of Si-ncs formation or due to the defect generation.[5] Also, notice that during the regressive sweep, at low electric fields, injected current density changes direction upon certain applied electric field. This effect can be observed in the inset of Fig. 2(a), where injected current density crosses the zero current condition and turns negative even for a positive electric field polarization (i.e., around 2.5 MV/cm in the inset of Fig. 2(a)). Such a phenomenon indicates that a gradual charge trapping takes place in the film during progressive sweep. This trapping produces an internal electric field that opposes the externally driven polarization until a certain value in the regressive sweep, where both become identical (zero current condition).[12] From this value on, the further decrease in the external electric field implies a net electric field in the opposite direction. The quantification of the maximum internal electric field (E_{int}) in each sample can be easily calculated from the zero current condition. Thus, a value of 2.5 MV/cm was found for the sample corresponding to a Si excess of 12%, 1.5 MV/cm for the one with 16%, 0.6 MV/cm for the one with 20% and 0.15 MV/cm for the sample with 40%. The trapped charge density (ρ_{trapped}) at zero current condition can be estimated[13]

$$\frac{E_{\mathrm{int}}}{t} = \frac{\rho_{trapped}}{C_{film}},$$

where C_{film} (~10–40 pF) is the dielectric capacitance of each device measured at low frequency condition (1 kHz) and t is

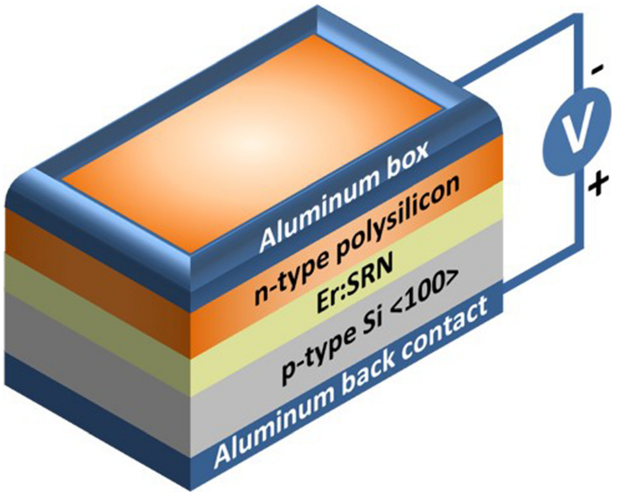

FIG. 1. Device cross-section and polarization schema of devices.

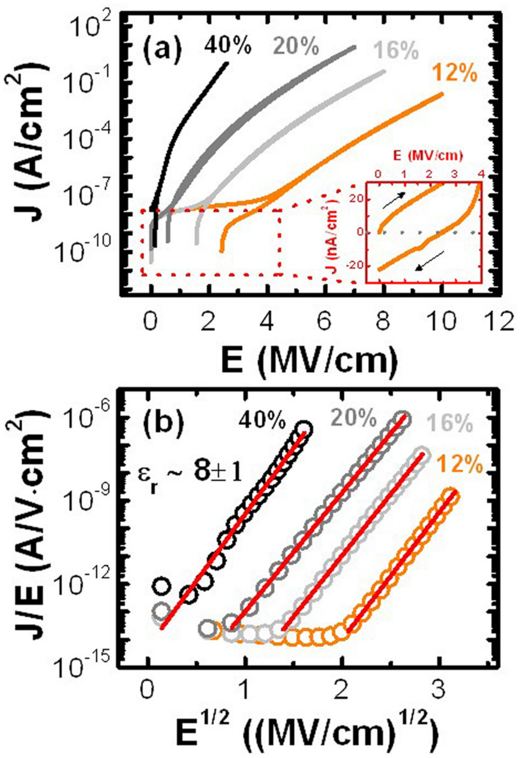

FIG. 2. (a) J(E) characteristic of films with different Si excess. Inset shows a magnified region of a linear (J-E) plot for sample with 12% of Si excess under low electric field polarization. (b) Poole-Frenkel representation of experimental J(E) curves.

the layer thickness. The calculated values of ρ_{trapped} for Si excess of 12%, 16%, 20%, and 40% are found to be 1.1 μC/cm^2, 0.15 μC/cm^2, 0.06 μC/cm^2, and 0.04 μC/cm^2, respectively. Notice that ρ_{trapped} systematically decreases with the Si incorporation. Although the increase in Si excess is often correlated with an increase in charge trapping probability,[14] it may also be instrumental for the charge trapping release via hopping between Si-ncs and/or neighboring intra-band states for a sufficiently high density of Si excess. Indeed, this is what we observe in our films for the studied Si excess range (from 12% up to 40%). Therefore, high Si excess is desirable from the electrical point of view as it promotes the charge transport via intra-band conductive states (conductivity enhancement) and also minimizes fixed charge located at trapping centers.

In order to understand the excitation mechanisms that lead to Er^{3+} emission, the current transport at high fields has been investigated. All samples have been shown to follow a Poole-Frenkel (P-F) trend in the form of[6]

$$J \propto E \exp\left(-\frac{E_A}{kT}\right)\exp\left(\frac{q}{kT}\left(\frac{qE}{\pi\varepsilon\varepsilon_0}\right)^{1/2}\right),$$

where E$_A$ is the average trap activation energy, kT is the thermal energy, q is the elementary charge, and ε_r and ε_0 are the relative and absolute permittivity, respectively. The relative permittivity value can be roughly estimated from the slope of the linear fit when plotting the experimental J(E) curve in a P-F representation, as in Fig. 2(b). The average ε_r in our samples is 8 ± 1. This value is reasonable as it lies between the relative permittivity of stoichiometric silicon nitride (∼7) and pure silicon (∼12).

The macroscopic nature of the measured current makes difficult to distinguish between different charge transport mechanisms occurring simultaneously. As a consequence, only the most relevant transport mechanism (in terms of current density) prevails when measuring J(E) curves (Fig. 2(a)). However, secondary mechanisms, such as hopping or hot carrier injection, cannot be completely discarded in our films. The dominance of thermally-assisted P-F conduction was further corroborated by measuring the J(E) characteristic at different temperatures up to 573 K (not shown). The average E$_A$ can be estimated if a mono-energetic trap distribution is considered. A mean value around 0.3 eV and 0.1 eV for E$_A$ was obtained under low and high voltage polarization, respectively, in agreement with a previous work where similar films with bulk-limited conduction were studied.[15] Therefore, current transport takes place mainly along electrically tunable conductive channels under the silicon nitride conduction band (for electrons) and valence band (for holes).

Fig. 3(a) depicts the optical power density at 1.54 μm as a function of the injected current density for all devices. A typical EL spectrum at 1.54 μm is shown in inset of Fig. 3(a). As can be observed, the incorporation of Si excess provides: (i) lower optical power density and (ii) an effective tuning of the current density onset for EL emission at 1.54 μm (J$_{\text{EL-Th}}$). In particular, a gradual shift of J$_{\text{EL-Th}}$ towards higher values takes place when the Si excess increases. This fact points out a detrimental effect of Si excess on the Er^{3+} excitation, producing a diminution of the generated photons per injected electron and therefore a decrease in the Er^{3+} excitation efficiency.

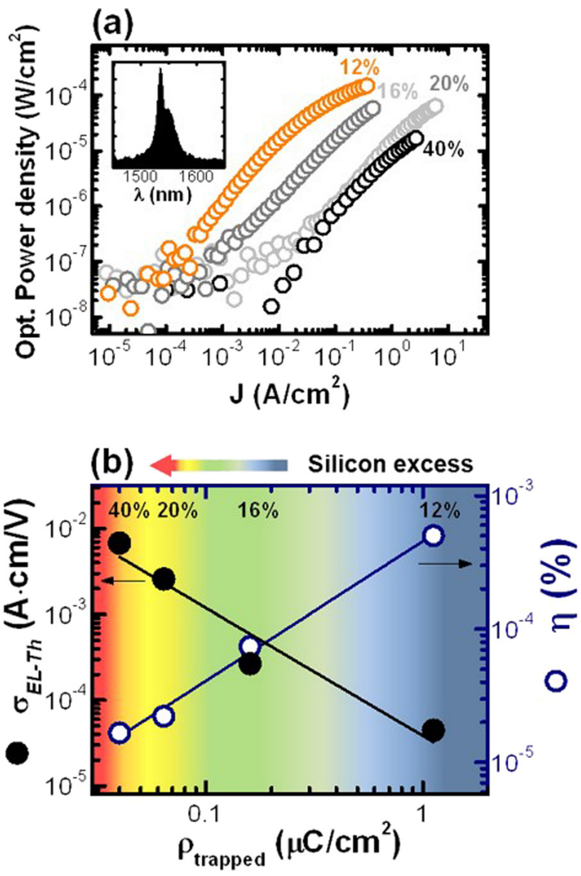

FIG. 3. (a) Total emitted optical power density of Er-SRN with different Si excess as a function of the injected current density. Inset shows an EL spectrum at 1.54 μm of device with 12% of Si excess taken at J = 0.02 A/cm^2. (b) Layer conductivity ($\sigma_{\text{EL-Th}}$, left axis) and power efficiency (η, right axis) of devices as a function of the trapped charge density (ρ_{trapped}). Values were taken at the EL onset. A color map background displays the evolution of the Si excess with the trapped charge density (from right to left).

Fig. 3(b) summarizes the optoelectronic properties of Er-SRN devices. The power efficiency of devices (η, defined as the ratio between the emitted optical power and the injected electrical power) and the conductivity of films ($\sigma_{\text{EL-Th}}$, which accounts for the ratio between current density and applied electric field) are plotted as a function of the trapped charge density at zero current condition. As can be observed, devices with higher ρ_{trapped} (low Si excess) also show higher power efficiency but lower conductivity. On the contrary, devices with low ρ_{trapped} (high Si excess) reveal good conductivity but low power efficiency.

Consequently, there is a strong trade-off between the power efficiency and the film conductivity for the studied range of Si excess. Such an opposite trend further confirms the formation of additional "non-radiative" intra-band conduction pathways formed by either defects or Si-ncs (or both) when the Si excess is increased. These intra-band conduction pathways provide an effective channel for the charge transport below the conduction band at the expense of EL efficiency. Furthermore, taking into account that low conductive films also require larger electric fields for a given current density (see Fig. 1(a)), one may point out the direct relation between the excitation efficiency and the applied electric field. This fact is of importance as the applied electric field is the one responsible for carrier acceleration in the dielectric conduction band and therefore suggests that the Er^{3+} excitation in SRN is mainly due to the direct impact excitation of hot carriers, similarly than in other RE-doped silicon oxides.[10,12] Thus, electrons in SRN would be thermally promoted to the conduction band by Poole-Frenkel ionization mainly, and accelerated by the action of the applied electric field until either they impact with an Er^{3+} ion (direct impact excitation) or they get trapped by another intra-band state. From this point on, they may either be thermally assisted to the conduction band for a subsequent Er^{3+} (or intra-band state) interaction again, or hop to the nearest available intra-band state without reaching the conduction band. For the latest, however, the excitation of an Er^{3+} ion is improbable. Therefore, a non-negligible number of electrically excitable Er^{3+} ions becomes effectively screened when the Si excess is incorporated. This interpretation explains: (i) the decrease in Er^{3+} excitation efficiency when increasing the Si excess (larger amount of intra-band states and scattering centers); (ii) the direct correlation between the power efficiency and the applied electric field; (iii) the fact that Er-doped silicon nitrides do not show an EL efficiency as high as Er-doped silicon oxides, as bulk-limited dielectric materials (i.e., silicon nitrides) present higher number of intra-band states (and hence higher trapping/de-trapping rate) compared with electrode-limited materials (i.e., silicon oxides).[16]

Another interesting feature that arises when inspecting Fig. 3(b) is the trapped charge density dependence of the device power efficiency. Interestingly, devices with higher trapped charge density also show an enhanced power efficiency performance. Bearing in mind that devices with higher trapped charge density will also be the first ones to reach the charge to breakdown limit,[12] we foresee larger instability and a diminution of the device operation lifetime in devices with higher power efficiency (and low conductivity) compared with the ones with lower efficiency performance (but higher conductivity). Thus, although the incorporation of Si excess in Er-SRN diminishes the overall EL efficiency, a small Si percentage may be used to further boost the conductivity and the reliability of devices, as well as to strongly diminish the EL onset voltage. Therefore, the crossing point in Fig. 3(b) indicates that the optimum balance between device conductivity and power efficiency is obtained when about 16% of Si excess is incorporated in the host matrix. This particular layer stoichiometry would provide an optimum optoelectronic performance of Er-SRN electroluminescent thin-films emitting at 1.54 μm.

IV. CONCLUSION

In conclusion, the role of Si excess in the optoelectronic properties of Er-SRN light emitting devices has been investigated, with silicon excess values ranging from 12% up to 40%. Poole-Frenkel conduction from thermally activated intra-band defects has been shown to be the main charge transport mechanism in all films. Electroluminescent films with low Si content have provided higher power efficiency at the expense of a much reduced layer conductivity and higher trapped charge density. On the contrary, high Si excess has shown to be instrumental to boost the film conductivity and the charge trapping release, although simultaneously displaying lower power efficiency performance. The evolution of the optoelectronic properties with the Si excess has allowed drawing conclusions on the main excitation mechanism of Er^{3+} ions, which has been found to be direct impact excitation. Finally, we provide an optimum Si excess of 16%, which balances both electrical and optical properties of Er-SRN thin-films emitting at 1.54 μm.

ACKNOWLEDGMENTS

This research is supported by the Spanish Ministry of Science and Innovation (TEC2012-38540-C02-01). J.M.R. acknowledges the financial support of Secretariat for Universities and Research of Generalitat de Catalunya through the program FI-DGR 2013. Authors acknowledge the Integrated Nano and Microelectronics Clean Room at IMB-CNM for sample fabrication through the ICTS access program (Project No. ICTS-NGG-235).

[1] A. J. Kenyon, Semicond. Sci. Technol. **20**, R65 (2005).

[2] O. Jambois, F. Gourbilleau, A. J. Kenyon, J. Montserrat, R. Rizk, and B. Garrido, Opt. Express **18**, 2230 (2010).

[3] D. J. Moss, R. Morandotti, A. L. Gaeta, and M. Lipson, Nat. Photonics **7**, 597 (2013).

[4] M. Cazzanelli, F. Bianco, E. Borga, G. Pucke, M. Ghulinyan, E. Degoli, E. Luppi, V. Véniard, S. Ossicini, D. Modotto, S. Wabnitz, R. Pierobon, and L. Pavesi, Nature Mater. **11**, 148 (2012).

[5] S. Yerci, R. Li, and L. Dal Negro, Appl. Phys. Lett. **97**, 081109 (2010).

[6] S. Cueff, J. M. Ramírez, J. A. Kurvits, Y. Berencén, R. Zia, B. Garrido, R. Rizk, and C. Labbé, Appl. Phys. Lett. **103**, 191109 (2013).

[7] Y. Yin, W. Xu, G. Ran, G. Qin, and B. Zhang, Funct. Mater. Lett. **4**(03), 255–259 (2011).

[8] Y. Berencén, J. M. Ramírez, and B. Garrido, in *Proceedings of the 2013 Spanish Conference on Electron Devices, CDE 2013* (IEEE Xplore, Valladolid, 2013), p. 245.

[9] S. Yerci, R. Li, S. O. Kucheyev, T. V. Buuren, S. N. Basu, and L. Dal Negro, IEEE J. Sel. Top. Quant. Electron. **16**(1), 114 (2010).

[10] A. Nazarov, J. M. Sun, W. Skorupa, R. A. Yankov, I. N. Osiyuk, I. P. Tjagulskii, V. S. Lysenko, and T. Gebel, Appl. Phys. Lett. **86**, 151914 (2005).

[11] S. Cueff, C. Labbé, L. Khomenkova, O. Jambois, P. Pellegrino, B. Garrido, C. Frilay, and R. Rizk, Mater. Sci. Eng. B **177**, 725 (2012).

[12] L. Rebhole and W. Skorupa, *Rare-Earth Implanted MOS Devices for Silicon Photonics*, Springer Series in Materials Science (Springer, 2010).

[13] S. M. Sze, *Physics of Semiconductor Devices*, 2nd ed. (Wiley, New York, 1981).

[14] E. Kapetanakis, P. Normand, D. Tsoukalas, K. Beltsios, J. Stoemenos, S. Zhang, and J. van den Berg, Appl. Phys. Lett. **77**, 3450 (2000).

[15] Y. Berencén, J. M. Ramírez, O. Jambois, C. Domínguez, J. A. Rodríguez, and B. Garrido, J. Appl. Phys. **112**, 033114 (2012).

[16] D. J. DiMaria and J. R. Abernathey, J. Appl. Phys. **60**, 1727 (1986).

APPLIED PHYSICS LETTERS **103**, 191109 (2013)

Electroluminescence efficiencies of erbium in silicon-based hosts

Sébastien Cueff,[1,2,a),b)] Joan Manel Ramírez,[3,a)] Jonathan A. Kurvits,[2,4] Yonder Berencén,[3]
Rashid Zia,[2,4] Blas Garrido,[3] Richard Rizk,[1] and Christophe Labbé[1,b)]
[1]*Centre de Recherche sur les Ions, les Matériaux et la Photonique (CIMAP),*
UMR 6252 CNRS/CEA/Ensicaen/UCBN, Caen 14050, France
[2]*School of Engineering, Brown University, Providence, Rhode Island 02912, USA*
[3]*MIND-IN2UB, Department Electrònica, Universitat de Barcelona, Martí i Franquès 1,*
Barcelona 08028, Spain
[4]*Department of Physics, Brown University, Providence, Rhode Island 02912, USA*

(Received 26 July 2013; accepted 17 October 2013; published online 6 November 2013)

We report on room-temperature 1.5 μm electroluminescence from trivalent erbium (Er^{3+}) ions embedded in three different CMOS-compatible silicon-based hosts: SiO_2, Si_3N_4, and SiN_x. We show that although the insertion of either nitrogen or excess silicon helps enhance electrical conduction and reduce the onset voltage for electroluminescence, it drastically decreases the external quantum efficiency of Er^{3+} ions from 2% in SiO_2 to 0.001% and 0.0004% in SiN_x and Si_3N_4, respectively. Furthermore, we present strong evidence that hot carrier injection is significantly more efficient than defect-assisted conduction for the electrical excitation of Er^{3+} ions. These results suggest strategies to optimize the engineering of on-chip electrically excited silicon-based nanophotonic light sources. *© 2013 AIP Publishing LLC*. [http://dx.doi.org/10.1063/1.4829142]

Research towards fabricating efficient electrically driven silicon-based light sources holds promise for the full integration of nanophotonics with microelectronics on a silicon chip.[1] To circumvent the intrinsically low photon emission probability in silicon, researchers have investigated methods to dope silicon-based host materials with more efficient light emitters.[2–4] For this purpose, Er^{3+} ions have attracted considerable interest because their near-infrared 1.5 μm emission coincides with the "C-band" of optical telecommunication.[5] In silicon though, Er^{3+} ions undergo significant thermal quenching due to non-radiative energy back-transfer to the host matrix.[3] Strategies to avoid such electronic back-transfer consist of using large bandgap silicon-based hosts such as SiO_2 or Si_3N_4. While these latter host materials were shown to be a good platform for Er^{3+} photoluminescence, their insulating properties impede carrier injection and transport for electrically-driven devices.

To address this electrical challenge, researchers have sought to embed Er^{3+} ions in engineered host materials that allow for efficient injection of carriers at low operating voltages. For example, recent studies investigated the influence of host composition on the electroluminescence (EL) properties of Er^{3+}:SiN_x (Ref. 6) and Er^{3+}:SiO_x (Refs. 7–9) as well as other oxide hosts such as Er^{3+}:TiO_2 (Ref. 10) and Er^{3+}:ZnO.[11,12] However, it can be difficult to interpret and resolve the conflicting results reported in the literature because of the disparities in electrical and optical properties between different hosts as well as the fabrication-dependent properties observed for similar materials.[13,14]

In this letter, we report on a systematic comparison of several figures of merit for Er^{3+} EL in different silicon-based CMOS-compatible hosts. To this end, we investigate the electrical and optical properties of Er-doped electroluminescent devices fabricated with three distinct hosts for the active layer: silicon dioxide (SiO_2), silicon nitride (Si_3N_4), and silicon-rich nitride (SiN_x). By using the same fabrication equipment, processing techniques, and device geometry (e.g., emitter layer thickness and area) for all samples, we seek to isolate the host material dependencies of the Er-doped active layers. While all devices display 1.5 μm emission under electrical injection, we show that their respective properties such as external quantum efficiency, electrical transport characteristics, and excitation cross-sections significantly differ, sometimes by orders of magnitude.

The Er-doped Si-based active layers were all deposited by the same confocal magnetron sputtering equipment at high substrate temperature (500 °C).[15] Near stoichiometric Er^{3+}:SiO_2 and Er^{3+}:Si_3N_4 were produced by cosputtering from Er_2O_3 and either SiO_2 or Si_3N_4 targets under a plasma of pure argon. Er^{3+}:SiN_x was grown using reactive sputtering by flowing 0.6 sccm of nitrogen and 10 sccm of argon inside the chamber during cosputtering of Si and Er_2O_3 targets. The resulting SiN_x host is silicon-rich with $x \approx 0.8$.[16] All active layers are 50 nm-thick and deposited on a p-type silicon substrate (1×10^{15} at./cm^3). The Er concentration, as measured by secondary ion mass spectrometry (SIMS), was typically found to be around $[Er] = 1 \times 10^{20}$ cm^{-3}. A heavily doped (1×10^{20} cm^{-3}) 100-nm thick n^+-polysilicon top electrode is subsequently deposited directly on top of the active layer by low pressure chemical vapor deposition (LPCVD). The devices are then post-annealed at 950 °C for 30 min under pure N_2. To form electrical contacts, aluminum and chromium were deposited on the top and bottom of the structure, respectively; the top aluminum contacts were patterned in the shape of isolated squares (200 μm by 200 μm) with empty square center (60 μm by 60 μm) to allow for efficient electrical excitation and light extraction (a sketch of the device is shown inset of Fig. 1(a)). All electro-optical

---

[a)] S. Cueff and J. M. Ramírez contributed equally to this work

[b)] Authors to whom correspondence should be addressed. Electronic addresses: sebastien_cueff@brown.edu and christophe.labbe@ensicaen.fr experiments were performed under forward bias (i.e., negative voltage applied to the polysilicon electrode) allowing higher current to flow through the active layer. A probe station and a semiconductor device analyzer were used to monitor I–V characteristics. The electroluminescence signal was collected from the top half of the device through the Si electrode by a microscope objective (NA: 0.4). For spectral analysis, the light was dispersed by a spectrograph and measured with a calibrated photomultiplier tube (PMT). Time-resolved measurements were carried out using a pulse generator, and EL decay traces were recorded with a digital GHz oscilloscope connected to the PMT.

Figure 1 displays both the current density and the EL signals of the three layers investigated as a function of the applied voltage (until reaching the electrical breakdown of the active layer). A typical EL spectrum is displayed in the inset of Fig. 1(b); the EL spectrum for all samples showed a similar line shape. One can readily observe a clear trend in the electrical properties when nitrogen is introduced and when Si-excess content is increased: as shown in Fig. 1(a), the threshold voltage is decreased, and the maximum current density is enhanced. Consequently, as shown in Fig. 1(b), the onset voltage for EL is strongly reduced, from ∼45 V to ∼7 V, when the composition of the host changes from SiO_2 to SiN_x. However, a collateral effect is that the maximum EL intensity is reduced by around one order of magnitude. At this stage, it is unclear whether it is due to the observed disparities in breakdown voltages or to intrinsic differences in the active layers' properties, and we therefore provide in the following a thorough investigation of the underlying physical mechanisms involved in this process.

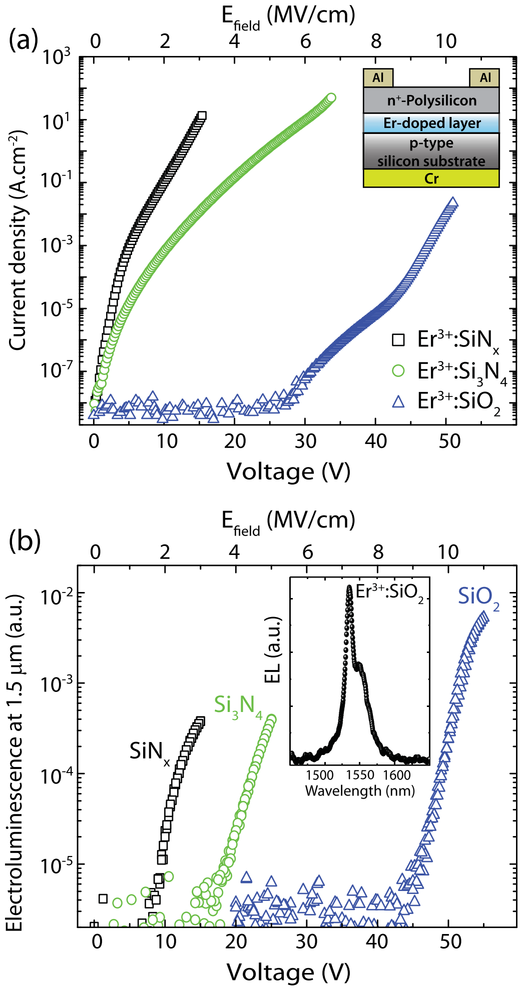

FIG. 1. (a) Current density as a function of the applied voltage for $Er^{3+}:SiN_x$, $Er^{3+}:Si_3N_4$, and $Er^{3+}:SiO_2$. Inset: scheme of the device's geometry. (b) Electroluminescence intensity at 1.5 μm for the same devices as a function of the applied voltage. Inset: typical EL spectrum obtained (only $Er^{3+}:SiO_2$ is displayed for clarity).

A typical figure of merit for electroluminescence efficacy is external quantum efficiency (EQE), which is given by the ratio between emitted photons and injected electrons. Using a calibrated PMT, the EQE values were obtained as a function of current density. As shown in Figure 2, the EQE of $Er^{3+}:SiO_2$ (2%) is three orders of magnitude higher than those of $Er^{3+}:SiN_x$ (10^{-3}%) and $Er^{3+}:Si_3N_4$ (4×10^{-4}%). Although all fabricated electroluminescent devices have identical device geometries, the material into which Er^{3+} ions are embedded alters the coupling to radiative modes through two effects: (i) changes in the local field around Er^{3+} and (ii) modification of the Fresnel coefficients at the interfaces.[17–20] These combined effects imply that increasing the host refractive index should enhance the power radiated to the upper half space of the structure and thus collected by our detection system (see supplementary material[21]). This trend is not observed in our measurements, in which the lowest refractive index ($n_{SiO2} = 1.5$) yields the highest EQE. Such a statement indicates that the differences in the measured EQE do not arise from optical effects caused by the change of refractive index but rather from different excitation efficiencies. Further insight is given hereafter through analysis of both electrical transport and excitation cross sections of the Er^{3+} ions.

Due to the dielectric and amorphous character of the active medium, the electrical transport of carriers in such insulating layers typically shows a non-Ohmic behavior. To describe the conduction properties, a whole range of models are available in the literature among which the most commonly reported are Fowler-Nordheim Tunneling[22] (FNT) and Poole-Frenkel (PF) thermionic emission.[23] As displayed in Figure 3, we find that the electrical transport in nitride-based layers is a bulk-limited process assisted by localized

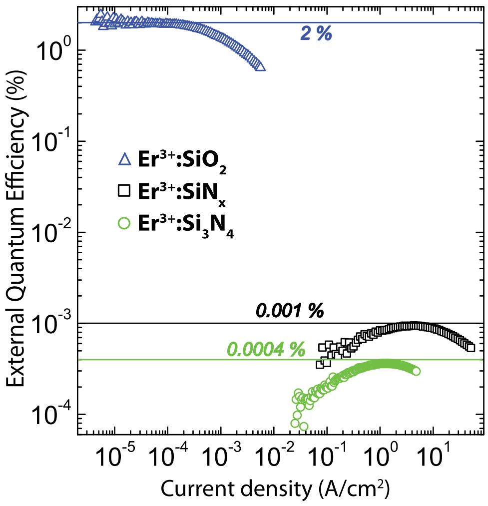

FIG. 2. EQE for the near-infrared emission (1.3 μm–1.6 μm) as a function of injected current for the three investigated light emitting devices.

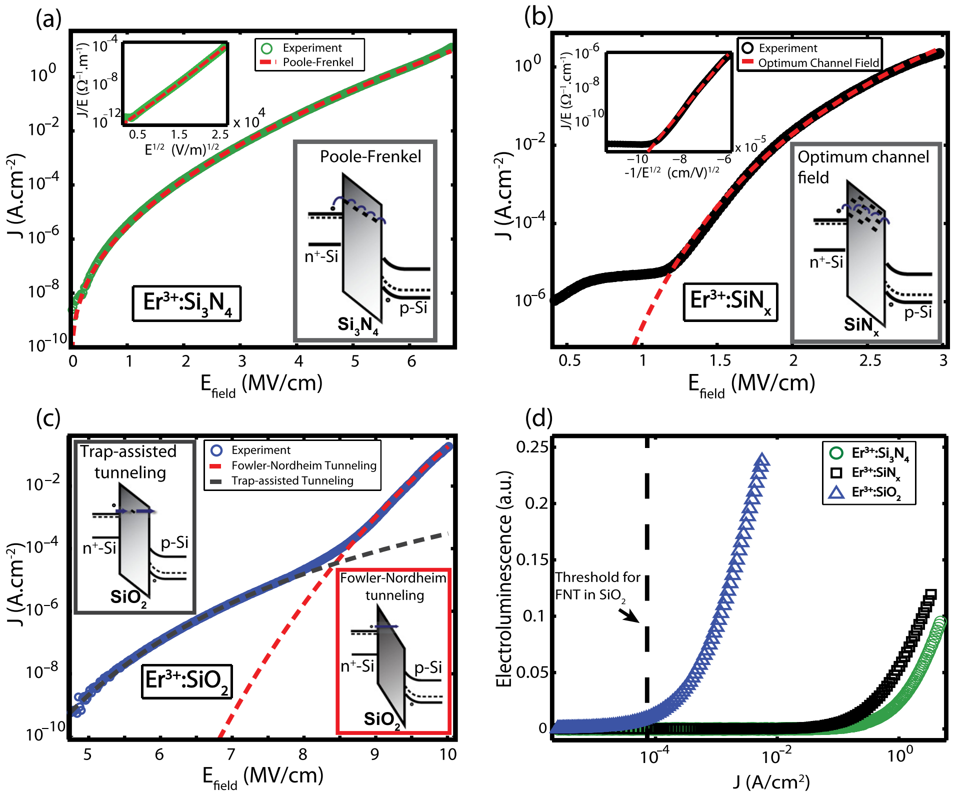

FIG. 3. Current density-electric field (J-E) characteristics response of (a) Er^{3+}:Si_3N_4, (b) Er^{3+}:SiN_x, and (c) Er^{3+}:SiO_2 together with fits from theoretical models. Insets: schematics highlighting the modeled conduction mechanisms. (d) Electroluminescence signal at 1.5 μm as a function of current density.

states in the bandgap, consistent with a previous study.[24] Specifically, the J-E curves are best described by PF conduction[25] and optimum-channel field emission[26,27] for Er^{3+}:Si_3N_4 and Er^{3+}:SiN_x, respectively (more information in the supplementary material[21]). On the other hand, the electrical transport in SiO_2 is first enabled by trap-assisted tunneling (from 5 to 8 MV/cm) and subsequently followed by hot carrier injection due to FNT mechanism at high fields (greater than 8 MV/cm). Interestingly in this latter case, the resulting EL signal starts to be significant only after reaching the FNT regime (see Fig. 3(d)). This suggests that the injection of hot electrons in the conduction band is a more efficient process for the excitation of Er^{3+} ions than trap-assisted conduction.

The excitation cross section of Er^{3+} ions is a key parameter to understand the efficiency of the excitation process under electrical pumping. Er^{3+} ions comprise numerous excited states that usually require a detailed set of rate equations to provide accurate modeling of the electronic transitions.[28] However, in the low pump regime, two reasonable assumptions can be made: (i) non-radiative relaxation from higher lying states is much faster than the long relaxation from $^4I_{13/2}$ level and (ii) there are no non-linear processes (e.g., excited state absorption or energy transfer between ions). At low current flux, we can therefore model the system under study as a quasi-two-level-system even if the excitation occurs at higher-lying states (see supplementary material[21]).[29] Therefore, in the steady-state regime, the electroluminescence intensity is described by $EL = \frac{\sigma\frac{J}{q}\tau}{\sigma\frac{J}{q}\tau+1}EL_{max}$.[30] By measuring separately the lifetime τ of our samples, the excitation cross-section σ can be extracted by fitting the measured EL signal as a function of the current flux (J/q). It is found that the σ values for Er^{3+}:Si_3N_4, Er^{3+}:SiN_x, and Er^{3+}:SiO_2 are 3×10^{-16} cm^2, 1×10^{-15} cm^2, and 3×10^{-14} cm^2, respectively (cf., Fig. 4). Similar values were already reported for Er^{3+}:SiN_x,[6] and the σ for Er^{3+}:SiO_2 is among the highest excitation cross-sections reported in the literature.[8,31] Comparable range of σ values can be obtained by investigating the dynamics of EL intensity of our samples (see supplementary material[21]).

To have an independent confirmation of the differences in excitation efficiency, we provide an evaluation of the number of excited Er^{3+} ions in each sample. One can roughly estimate a lower bound for the fraction of electrically excited Er^{3+} ions by using the following relation[7]: $\frac{N^*_{Er}}{[Er]} = A\frac{W_{opt}\tau}{h\upsilon S d}$, where A is a correction factor that takes into account both the total transmittance at 1.5 μm through the top polysilicon layer and the collection of the detection system (these combined effects reduce the detected power to 2% of the total emitted power for all investigated layers), W_{opt} is the detected optical power, τ the measured lifetime, $h\upsilon$ the energy of light emission, S the emitting area, and d the thickness of the active layer. While the fraction of excited Er^{3+} ions for SiN_x and Si_3N_4 are found to be 0.08% and 0.09%, respectively, it is significantly higher in SiO_2 for which it is estimated to be around 15%. Although potential clustering of erbium could limit the light emission in some cases,[32] such a phenomenon would affect all samples equally as the same fabrication process and thermal treatment were used for all devices. Furthermore, we can infer on the basis of lifetime evolution versus current flux that nonlinear effects such as energy transfer could occur at high flux in Si_3N_4 but neither in SiN_x nor in SiO_2 (see supplementary material[21]). This phenomenon is therefore not responsible for the large differences in efficiencies between nitride and oxide hosts.

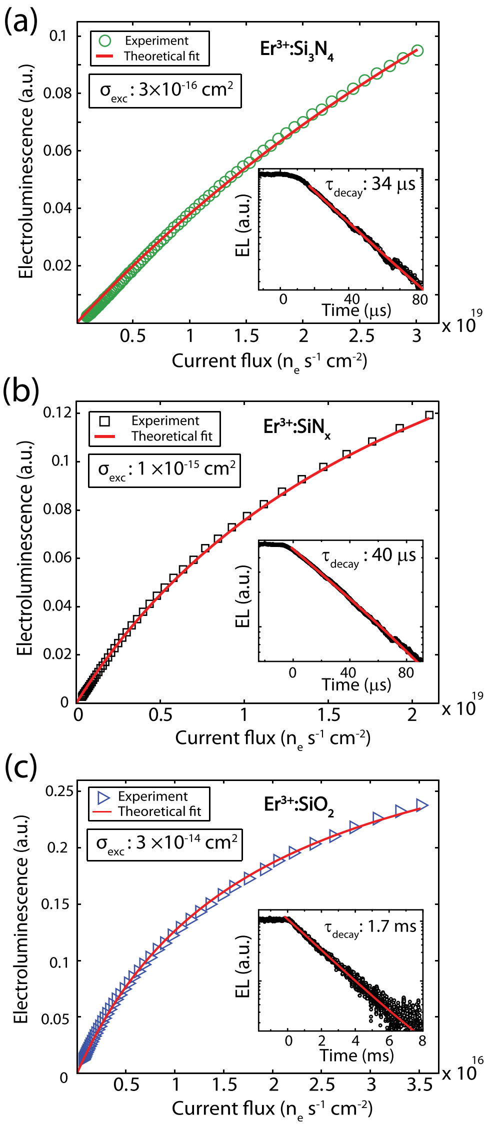

FIG. 4. Electroluminescence signal as a function of current flux for (a) Er^{3+}:Si_3N_4, (b) Er^{3+}:SiN_x, and (c) Er^{3+}:SiO_2 along with their corresponding theoretical fits to extract values of excitation cross-sections. Insets: measured lifetimes and fits.

Note that the low number of excited Er^{3+} ions in nitrogen-containing electroluminescent devices (Si_3N_4 and SiN_x) is correlated with the bulk-limited conduction mechanism in these materials. While this process allows for good conduction properties and low onset voltage for EL, it strongly reduces the excitation efficiency of Er^{3+} ions. In such a regime, the Er^{3+} excitation could occur via either energy transfer between traps and Er^{3+} ions[6,8,10–12] or impact excitation.[8] In the case of energy-transfer excitation, the donor-acceptor interaction is distance-dependent,[33] and the probability for such a process to occur is therefore low (Note that the fraction of excited Er^{3+} ions found here is comparable to the one for Er^{3+} ions sensitized by energy-transfer from Si nanoclusters.[33,34]) On the other hand, potential impact excitation of Er^{3+} would require the injection of hot electrons having energies higher than the first excited state of Er^{3+} (0.8 eV). As measured by DiMaria *et al.*, the number of injected hot electrons in nitride-based layers is almost four-orders of magnitude lower than in a similar SiO_2 layer because of electrical trapping.[35] Indeed, although FNT transport of carriers in SiO_2 yields a relatively low conductivity, it ensures the injection of a high number of hot carriers.[35,36] Besides, as shown by Fischetti *et al.*,[36] in the range of electric fields applied in the present study (8–10 MV/cm), the energy of hot electrons in SiO_2 is distributed over an average value of around 3 eV, i.e., more than enough to pump the Er^{3+} ions to the first excited state by impact excitation. The significantly higher number of injected hot electrons in SiO_2 compared to nitride-based layers provides a straightforward explanation of the large differences in excitation cross sections and in the number of excited Er^{3+} ions. Interestingly, these correlations between electrical transport and excitation efficiencies can be inferred from the Er^{3+}:SiO_2 sample alone because it demonstrates both types of conduction mechanisms. Indeed the abrupt increase in Er^{3+} EL as soon as the FNT regime starts (Fig. 3(d)) provides a direct and striking confirmation of the higher efficiency of the hot carrier injection as compared to defect-assisted conduction for the excitation of Er^{3+} ions.

In conclusion, we have demonstrated that although both electrical conduction and onset voltage for the electroluminescence of Er^{3+} are greatly enhanced in nitrogen-containing Si-based samples, their excitation efficiencies are well below that of Er^{3+}:SiO_2. These results suggest that defect-assisted transport of carriers is a much less efficient process than hot electron injection for the electrical excitation of Er^{3+}. Despite the large excitation cross sections and EQE values for EL in Er^{3+}:SiO_2 electroluminescent devices, their very high onset voltage remains largely incompatible with current CMOS technology. On the other hand, the extremely low onset voltage for EL in Er^{3+}:SiN_x appears very promising. Therefore, future studies should focus on electrical and material engineering to combine the advantages of both hosts to efficiently inject hot carriers at low voltages. In this framework, heterostructures composed of nanometer-thick multilayers appear to be a promising direction for investigation.[37]

The authors thank C. M. Dodson, M. Jiang, S. Karaveli, and D. Li for helpful discussions and C. Frilay for technical assistance. We acknowledge the Instituto de Microelectronica de Barcelona (IMB-CNM, CSIC) and especially J. Montserrat and C. Domínguez for the sample processing. Financial support was provided, in part, by the Air Force Office of Scientific Research (PECASE award no. FA-9550-10-1-0026) and by the National Science Foundation (CAREER award no. EECS-0846466). J.M.R. thanks the financial support of AGAUR through the program FI-DGR 2013.

[1] B. Jalali and S. Fathpour, J. Lightwave Technol. **24**, 4600 (2006).
[2] B. Zheng, J. Michel, F. Y. G. Ren, L. C. Kimerling, D. C. Jacobson, and J. M. Poate, Appl. Phys. Lett. **64**, 2842 (1994).
[3] A. J. Kenyon, Prog. Quantum Electron. **26**, 225 (2002).
[4] L. Pavesi, L. Dal Negro, C. Mazzoleni, G. Franzo, and F. Priolo, Nature **408**, 440 (2000).
[5] J. F. M. Digonnet, *Rare-Earth-Doped Fiber Lasers and Amplifiers, Revised and Expanded* (CRC Press, 2002), p. 71.
[6] S. Yerci, R. Li, and L. Dal Negro, Appl. Phys. Lett. **97**, 081109 (2010).
[7] O. Jambois, F. Gourbilleau, A. J. Kenyon, J. Montserrat, R. Rizk, and B. Garrido, Opt. Express **18**, 2230 (2010).
[8] J. M. Ramírez, F. Ferrarese Lupi, O. Jambois, Y. Berencén, D. Navarro-Urrios, A. Anopchenko, A. Marconi, N. Prtljaga, A. Tengattini, L. Pavesi,

J. P. Colonna, J. M. Fedeli, and B. Garrido, Nanotechnology **23**, 125203 (2012).

[9] S. Cueff, C. Labbé, O. Jambois, Y. Berencén, A. J. Kenyon, B. Garrido, and R. Rizk, Opt. Express **20**, 22490 (2012).

[10] Y. Yang, L. Jin, X. Y. Ma, and D. R. Yang, Appl. Phys. Lett. **100**, 031103 (2012).

[11] E. F. Pecora, T. I. Murphy, and L. D. Negro, Appl. Phys. Lett. **101**, 191115 (2012).

[12] Y. Yang, Y. Li, L. Xiang, X. Ma, and D. Yang, Appl. Phys. Lett. **102**, 181111 (2013).

[13] A. Nazarov, J. M. Sun, W. Skorupa, R. A. Yankov, I. N. Osiyuk, I. P. Tjagulskii, V. S. Lysenko, and T. Gebel, Appl. Phys. Lett. **86**, 151914 (2005).

[14] K. Sun, W. J. Xu, B. Zhang, L. P. You, G. Z. Ran, and G. G. Qin, Nanotechnology **19**, 105708 (2008).

[15] S. Cueff, C. Labbé, J. Cardin, J.-L. Doualan, L. Khomenkova, K. Hijazi, O. Jambois, B. Garrido, and R. Rizk, J. Appl. Phys. **108**, 064302 (2010); S. Cueff, C. Labbé, J. Cardin, and R. Rizk, IOP Conf. Ser.: Mater. Sci. Eng. **6**, 012021 (2009).

[16] S. Cueff, C. Labbé, L. Khomenkova, O. Jambois, P. Pellegrino, B. Garrido, C. Frilay, and R. Rizk, Mater. Sci. Eng. B **177**, 725 (2012).

[17] G. L. J. A. Rikken and Y. A. R. R. Kessener, Phys. Rev. Lett. **74**, 880 (1995).

[18] C. M. Dodson and R. Zia, Phys. Rev. B **86**, 125102 (2012).

[19] R. J. Glauber and M. Lewenstein, Phys. Rev. A **43**, 467 (1991).

[20] L. Zampedri, M. Mattarelli, M. Montagna, and R. R.Goncalves, Phys. Rev. B **75**, 073105 (2007).

[21] See supplementary material at http://dx.doi.org/10.1063/1.4829142 for calculation of power radiated, analysis of the electrical properties, and electroluminescence dynamics.

[22] R. H. Fowler and L. W. Nordheim, Proc. R. Soc. London, Ser. A **119**, 173 (1928).

[23] J. Frenkel, Tech. Phys. USSR **5**, 685 (1938); Phys. Rev. **54**, 647 (1938).

[24] Y. Berencén, J. M. Ramírez, and B. Garrido, in *Proceedings of the 2013 Spanish Conference on Electron Devices, CDE 2013* (IEEE Xplore, Valladolid, 2013).

[25] M. Ieda, G. Sawa, and S. Kato, J. Appl. Phys. **42**, 3737 (1971).

[26] M. Pollak and J. J. Hauser, Phys. Rev. Lett. **31**, 1304 (1973).

[27] M. Nardone, M. Simon, I. V. Karpov, and V. G. Karpov, J. Appl. Phys. **112**, 071101 (2012).

[28] D. Pacifici, G. Franzò, F. Priolo, F. Iacona, and L. Dal Negro, Phys. Rev. B **67**, 245301 (2003).

[29] A. J. Kenyon, M. Wojdak, I. Ahmad, W. H. Loh, and C. J. Oton, Phys. Rev. B **77**, 035318 (2008).

[30] S. Coffa, G. Franzó, and F. Priolo, Appl. Phys. Lett. **69**, 2077 (1996).

[31] F. Iacona, D. Pacifici, A. Irrera, M. Miritello, G. Franzò, F. Priolo, D. Sanfilippo, G. Di Stefano, and P. G. Fallica, Appl. Phys. Lett. **81**, 3242 (2002).

[32] N. Prtljaga, D. Navarro-Urrios, A. Tengattini, A. Anopchenko, J. M. Ramírez, J. M. Rebled, S. Estradé, J.-P. Colonna, J.-M. Fedeli, B. Garrido, and L. Pavesi, Opt. Mater. Express **2**, 1278 (2012).

[33] B. Garrido, C. García, S.-Y. Seo, P. Pellegrino, D. Navarro-Urrios, N. Daldosso, L. Pavesi, F. Gourbilleau, and R. Rizk, Phys. Rev. B **76**, 245308 (2007).

[34] M. Wojdak, M. Klik, M. Forcales, O. B. Gusev, T. Gregorkiewicz, D. Pacifici, G. Franzo, F. Priolo, and F. Iacona, Phys. Rev. B **69**, 233315 (2004).

[35] D. J. DiMaria and J. R. Abernathey, J. Appl. Phys. **60**, 1727 (1986).

[36] M. V. Fischetti, D. J. DiMaria, S. D. Brorson, T. N. Theis, and J. R. Kirtley, Phys. Rev. B **31**, 8124 (1985).

[37] H. Krzyżanowska, K. S. Ni, Y. Fu, and P. M. Fauchet, Mater. Sci. Eng. B **177**, 1547 (2012).

Supplementary Material:

Electroluminescence Efficiencies of Erbium in Silicon-Based Hosts

Sébastien Cueff [1,2,a),b)], Joan Manel Ramírez[3,a)], Jonathan A. Kurvits[2,4], Yonder Berencén[3],
Rashid Zia[2,4], Blas Garrido[3], Richard Rizk[1] and Christophe Labbé[1,b)]

[1] Centre de Recherche sur les Ions, les Matériaux et la Photonique (CIMAP), UMR 6252
CNRS/CEA/Ensicaen/UCBN, France
[2] School of Engineering, Brown University, Providence, RI 02912, USA.
[3] MIND-IN2UB, Department Electrònica, Universitat de Barcelona, Martí i Franquès 1, 08028,
Barcelona, Spain.
[4] Department of Physics, Brown University, Providence, RI 02912, USA

[a)] These authors contributed equally to this work

[b)] Corresponding authors: sebastien_cueff@brown.edu, christophe.labbe@ensicaen.fr

1. Influence of the refractive index on the power radiated

An emitter’s spontaneous emission rate is affected by the local field generated by the surrounding dielectric medium. So-called local field corrections only affect electric dipole (ED) transitions and not magnetic dipole (MD) transitions.[17] However, the emission rate of MD transitions scale with the density of states following a n^3 dependence (n being the refractive index of the host). MD transitions in trivalent erbium can represent more than 50% of the emission at 1.5 µm, and their contribution is therefore not negligible.[18] The total effective spontaneous emission rate as a function of the refractive index of the host can be written as follows: $\Gamma_{eff} = \Gamma_{ED}.n.f(n) + \Gamma_{MD}.n^3$ where Γ_{ED} (Γ_{MD}) is the ED (MD) transition rate, and $f(n) = (3n^2/(2n^2+1))^2$ is the local field correction factor following the so-called real cavity model.[17,19,20] Changing the host refractive index also modifies the Fresnel reflection and transmission coefficient at the different interfaces, which in turns modifies the field profile in the active layer and therefore alters the power radiated to the far field. Emission patterns were calculated according to the Green’s dyadic formalism for isotropic ED and MD emitters embedded in the layered structure shown in the inset of figure 1b.[38] This angular distribution was then integrated over the range of angles collected by our detection system to obtain the total power radiated as a function of host refractive index. This yields a straightforward qualitative result: when the host’s refractive index value is increased the power radiated to the upper half space of the structure is enhanced (see Figure S1).

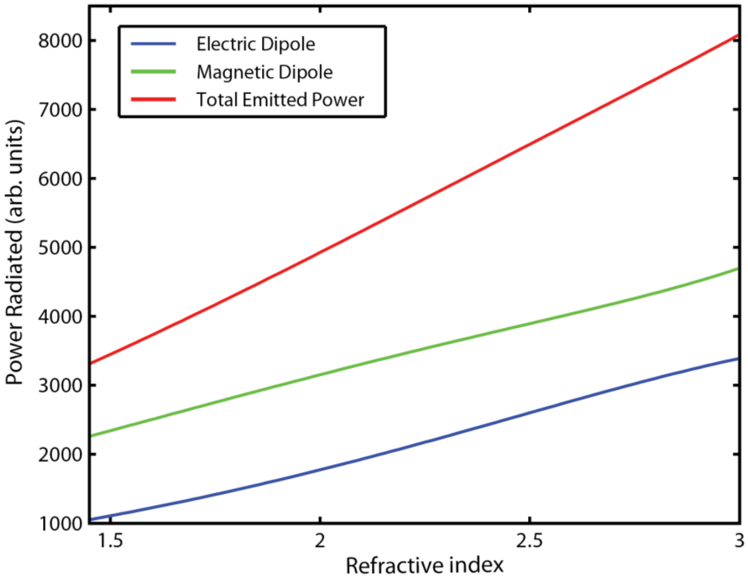

Figure S1: Power radiated at 1.5 µm by Er^{3+} ions on the upper half of the LEDs and collected by our detection system (NA=0.4) as a function of the refractive index of the Er^{3+} host material.

2. Electrical properties

Er^{3+}:Si_3N_4 is a prototypical example of the PF mechanism in which conduction is enabled by a thermally activated field-assisted carrier emission from coulombic traps to the extended states of the dielectric. We use a detailed model proposed by Ieda *et al.*[25] and described by: $J \propto E\,exp\left(\frac{1}{kT}\sqrt{\frac{q^3E}{\pi\epsilon_0\epsilon_r}}\right)$, with E the electric field, *k* the Boltzman's constant, *T* the temperature, ε_0 and ε_r respectively the absolute and relative permittivities. Using ε_r as a free fit parameter, a reasonable fit was obtained and allowed us to extract a value of 10.5 for ε_r (see Fig. 3a). This value is slightly higher than the expected ε_r for a stoichiometric Si_3N_4 (~7-9), which indicates the presence of a small silicon-excess in the active layer. The good agreement between fit and experiment demonstrates that conduction is exclusively enabled by the PF mechanism via localized states in the bandgap of Si_3N_4.

Concerning the Er^{3+}:SiN_x layer, it is well-known that amorphous SiN_x layers contain a high number of defects whose energies are either treated as distributed localized states or band tail states.[39,40] While PF and FNT models failed to accurately fit our experimental results, we found a qualitative agreement with the so-called 'optimum channel field emission' conduction model,[26,27] which is based on a mechanism where electrons follow the 'optimum pathways' among spatially close localized states. This model can be seen as an extension of the PF model with a distribution of trap energies instead of a single trap energy. It is expressed by the following relation: $\frac{J}{E} \propto \sigma_0\,exp\left(-\sqrt{\frac{A}{qE}}\right)$, where σ_0 is the conductivity and $A=8E_F\,\lambda/\alpha$, which is a function of the Fermi level (E_F), the localization radius (α) and a parameter λ that depends on the density of localized states, the temperature, the localization radius and the film thickness of the layer. As it is not the point of this study to extract the values of all these parameters but rather to gain insight into the conduction mechanism within the active layer, we chose to use σ_0 and *A* as fit parameters, to find a qualitative agreement between the J-E curves of Er^{3+}:SiN_x and the optimum channel field emission model (see Fig. 3b). The good qualitative agreement between experiment and theory suggests that electrical transport is mediated by defects states in SiN_x, in agreement with previous studies.[24]

For Er^{3+}:SiO_2, the conduction mechanism is not unique and comprises two main processes: from 5 MV/cm to 8 MV/cm, the current is slowly increasing while between 8 MV/cm to 10 MV/cm the current is rapidly increasing (Fig. 3c). The first process is found to be best described by the so-called trap-assisted tunneling (TAT) model in which traps whose energy lies in the insulator's bandgap provide relays for carriers to tunnel through the oxide from one electrode to the other.[41] Such a mechanism is described by $J \propto exp\left(-\frac{A\sqrt{\phi_t}(5\phi_t-3\phi_B)}{2}/E\right)$ where $A = \frac{4\sqrt{2qm_{ox}}}{3\hbar}$, Φ_t is the trap energy depth taken from the SiO_2

conduction band, Φ_B is the energy barrier between electrode and oxide, m_{ox} = 0.4 m_0 the effective mass of electrons in the active layer and E is the electric field.[41] For the fits, we set the energy barrier between Si and SiO_2 (Φ_B) to the commonly reported value of 3.2 eV.[8,42] Using Φ_t as the only free fit parameter, a good agreement is found between the model and the experiment for Φ_t = 2.5 eV, which is in accordance with a recent study[24] and indicates the presence of traps in the bandgap. The subsequent high-voltage conduction regime after 8 MV/cm is found to be best described by a Fowler-Nordheim Tunneling (FNT) conduction mechanism. To fit our experimental results, we used a detailed FNT model proposed by Forbes *et al.*[43] which is described by: $J = \tau_F^{-2} a\, \phi_B^{-1} E^2 exp\left(-\nu_F b \phi_B^{3/2}/E\right)$, with J the current density ($A.m^{-2}$), Φ_B the energy barrier (eV), and E the electric field ($V.m^{-1}$). τ_F and ν_F are dimensionless factors to account for the deviation from a perfectly triangular barrier between electrode and oxide. a and b are respectively called ‘first’ and ‘second’ Fowler-Nordheim constants. They are defined as: $a = q^3/8\pi h \approx 1.541 \times 10^{-6}$ A.eV.V^{-2}, and $b = 8\pi\sqrt{2m_{ox}}/3qh \approx 6.83 \times 10^{9}$ $eV^{-3/2}$.V.m^{-1}. We set m_{ox} = 0.4 m_0 and Φ_B = 3.2 eV and use τ_F and ν_F as free fit parameters. The values of these latter parameters, as extracted from fits, were found to be 0.044 and 1.625, respectively. For an unperturbed, perfectly triangular, energy barrier τ_F and ν_F should be both unity. The values found here for our devices demonstrate that there is a departure from a perfectly triangular energy barrier.

As displayed in Figure 3c, the entire J-E curve of $Er^{3+}:SiO_2$ can be accurately modeled by TAT conduction followed by a FNT mechanism at high fields. The good agreement with theory therefore indicates the succession of two different mechanisms to enable the transport of carriers in $Er^{3+}:SiO_2$: (i) at ‘medium’ electric fields, carriers tunnel from n^+-Si electrode to traps in SiO_2 band gap before reaching the p-Si substrate, (ii) at high electric fields, the band bending is strong enough for carriers to tunnel directly from the n^+-Si electrode to the conduction band of SiO_2.

3. Electroluminescence dynamics

As discussed in the main text, assuming a quasi-two-level-system, the following rate equation can give a satisfactory description of the system:

$$\frac{dN_{Er}^{*}}{dt} = \sigma \frac{J}{q}(N_{Er} - N_{Er}^{*}) - \frac{N_{Er}^{*}}{\tau} \qquad (1)$$

Where N_{Er} is the total number of excitable Er^{3+} ions among which $N_{Er}{}^{*}$ are actually in the excited state, σ is the excitation cross-section (cm^2), J/q is the current flux ($n_{electrons}s^{-1}cm^{-2}$) and τ is the lifetime (including radiative and non-radiative de-excitation) at 1.5 µm. Upon excitation of the system by a step pulse and assuming that $EL \propto N_{Er}^{*}/\tau_{rad}$, solving eq. 1 gives: [30]

$$EL(t) = \frac{\sigma \frac{J}{q}\tau}{\sigma \frac{J}{q}\tau + 1} EL_{max} \left\{1 - exp\left[-\left(\sigma \frac{J}{q} + \frac{1}{\tau}\right)t\right]\right\}, \qquad (2)$$

with $EL_{max} \propto {}^{N_{Er}}/_{\tau_{rad}}$. In order to extract values of σ, one can investigate the EL signal as a function of current flux (J/q) in the time domain at the turn-on and turn-off of the LED. The time-resolved EL is well described by the following relation: $1/\tau_{rise} = \sigma J/q + 1/\tau_{decay}$, where τ_{rise} and τ_{decay} are respectively the rise time (i.e. excitation time) and the decay time (including radiative and non-radiative de-excitation) at 1.5 µm. This relation holds for pump regime in which τ_{decay} stays constant. As can be seen in figure S2, this is true at each current flux for Er^{3+}:SiN_x and Er^{3+}:SiO_2 but it is correct only for low current flux for Er^{3+}:Si_3N_4.

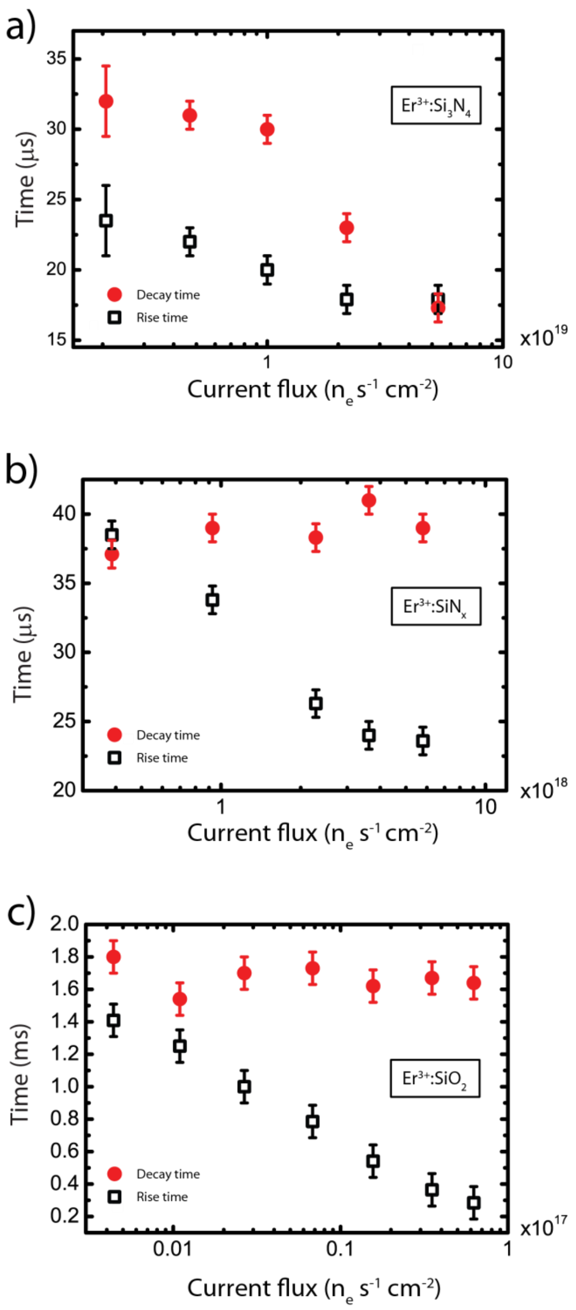

Figure S2: Decay time and rise time as a function of current flux for Er^{3+}-doped a) Si_3N_4, b) SiN_x and c) SiO_2. Decay times remain constant as a function of current fluxes except for the one of $Er^{3+}:Si_3N_4$ which is altered at high current flux, suggesting non-linear phenomenon.

This altered decay time at high current fluxes in Si_3N_4 can be explained by non-linear interactions such as cooperative upconversion or energy transfer between ions arising from the close proximity between ions due to high doping concentrations. On the other hand, the constant lifetime for the other two samples ($Er^{3+}:SiN_x$ and $Er^{3+}:SiO_2$) as a function of current flux ensures that no such effects are occurring in these latter samples.

From the plot of the excitation rate ($1/\tau_{rise}$) as a function of the current flux, we can extract the excitation cross-section σ of the system under consideration. To rule out any non-linear processes, only the linear parts are fit on the aforementioned plots. It is found that the excitation cross-sections σ for Er^{3+}:Si_3N_4, Er^{3+}:SiN_x and Er^{3+}:SiO_2 are respectively 8 (±2) $x10^{-16}$ cm^2, 3 (±2) $x10^{-15}$ cm^2 and 5 (±2) $x10^{-14}$ cm^2 (cf. fig. S3), which are comparable to the values extracted from steady-state measurements (fig. 4 in the main text).

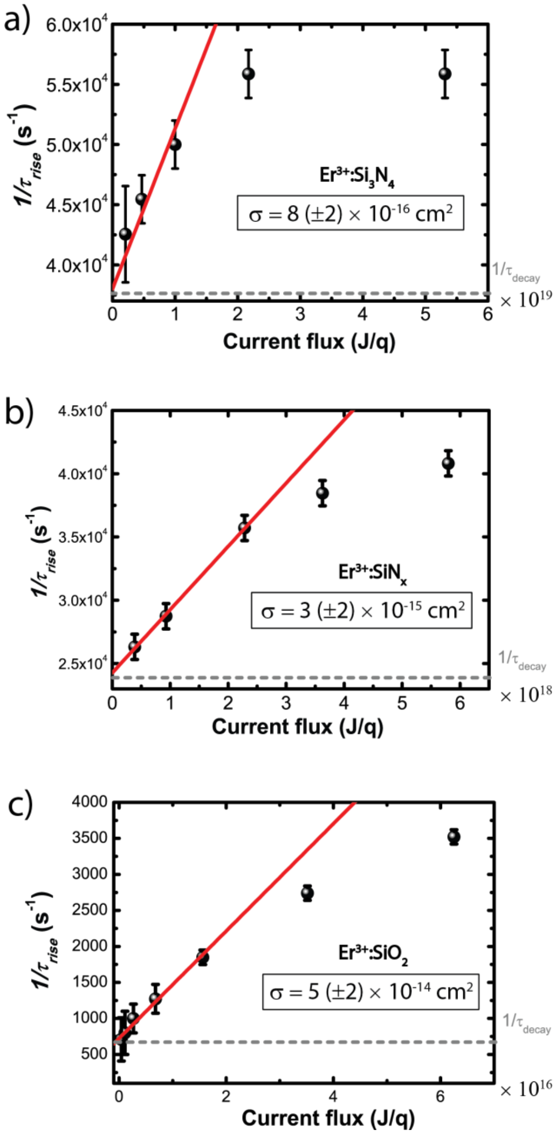

Figure S3: Inverse rise time as a function of current flux for Er^{3+}-doped a) Si_3N_4, b) SiN_x and c) SiO_2. Only the linear part (low pump regime) is fit to extract values of excitation cross-sections.

Supplementary references

[38] L. Novotny, & B. Hecht, Principles of Nano-Optics (Cambridge Univ. Press, Cambridge, 2006).

[39] M. Wang, M. Xie, L. Ferraioli, Z. Yuan, D. Li, D. Yang and L. Pavesi, J. Appl. Phys., **104**, 083504 (2008).

[40] S. Yerci, R. Li, S. O. Kucheyev, T. van Buuren, S. N. Basu, and L. D. Negro, IEEE J. Sel. Top. Quantum Electron. **16**, 114 (2010)

[41] M. P. Houng, Y. H. Wang, & W. J. Chang, J. Appl. Phys., **86**, 1488 (1999).

[42] A. Hadjadj, O. Simonetti, T. Maurel, G. Salace and C. Petit, Appl. Phys. Lett. **80**, 18 (2002)

[43] R. G. Forbes and J. H. B Deane. Proc. R. Soc. A **463,** 2907 (2007).

APPLIED PHYSICS LETTERS **103**, 081102 (2013)

Carrier transport and electroluminescence efficiency of erbium-doped silicon nanocrystal superlattices

J. M. Ramírez,[1,a)] Y. Berencén,[1] L. López-Conesa,[1] J. M. Rebled,[1,2] F. Peiró,[1] and B. Garrido[1]

[1]*MIND-IN2UB, Departament d'Electrònica, Universitat de Barcelona, Martí i Franquès 1, 08028 Barcelona, Spain*

[2]*Institut de Ciència dels Materials de Barcelona (ICMAB-CSIC), Campus de la UAB, 08193 Bellaterra, Spain*

(Received 12 June 2013; accepted 31 July 2013; published online 19 August 2013)

A detailed study of transport phenomena and electroluminescence of erbium-doped silicon-rich oxide/silicon oxide superlattices is presented. Extended states conduction is thermally activated from Poole-Frenkel traps located at silicon nanocrystals or its interface. These traps provide bulk limited conduction at low and medium electric fields. In contrast, under high electric fields, conduction is governed by trap-assisted tunneling of electrons from the electrode to the active layer conduction band. Superlattice electroluminescence efficiency at 1.5 μm and injected electron energy distribution in the conduction band are evaluated and compared to a silicon dioxide and a silicon-rich oxide single layer. This work sheds light on the implementation of alternative electroluminescent device architectures with strong emphasis in the hot electron engineering.

[http://dx.doi.org/10.1063/1.4818758]

Silicon-rich oxide/silicon dioxide (SRO/SiO_2) superlattices have attracted much attention within the silicon optoelectronics community due to the many benefits that are foreseen.[1] Intense research is being carried out toward its implementation in thin film photovoltaics as efficient absorbers or down-shifters in tandem solar cells.[2,3] Tight control of the silicon nanocrystal (Si-nc) size can be easily obtained by adjusting the inter-distance of the SiO_2 diffusion barrier, allowing for a self-organized array of size-controlled Si-ncs embedded in a SiO_2 matrix. Consequently, challenging approaches that comprise gradual absorption tunability across the superlattice structure can be anticipated.[4] SRO/SiO_2 superlattices have been used not only as active part in tandem solar cells but also as electroluminescent layers in light emitting devices, obtaining high electroluminescence (EL) power efficiency and turn-on voltage values as low as 1.7 V.[5] Also, an interesting scenario comes out when embedding Er^{3+} ions in SRO/SiO_2 superlattices because a narrow emission line at telecom wavelengths is obtained. Additionally, good control of the Er-Si-nc coupling distance could be provided if a proper SiO_2 barrier thickness is conceived.[6,7] Therefore, appealing perspectives can be envisioned for the electrical injection in Er-doped SRO/SiO_2 superlattices. In fact, a prior work already demonstrated the feasibility of these structures by implementing electroluminescent devices using the multilayer approach and a lateral carrier injection scheme.[8] However, not much attention was paid to the understanding of charge transport in such systems, neither to the evaluation of the main excitation mechanisms of Er^{3+} ions, which remains unclear nowadays.

In this work, a thorough analysis of the electroluminescence and the vertical charge transport of Er-doped SRO/SiO_2 superlattices is presented. We demonstrate that the comparison of the current transport and the EL characteristic in the superlattice structure with that of Er-doped SiO_2 and Er-doped SRO single layers yields comprehensive understanding of the charge transport phenomena as well as the identification of the excitation mechanism of Er^{3+} ions in the SRO/SiO_2 superlattice. Also, the evaluation of average kinetic energy of injected electrons in the superlattice conduction band is carried out.

The superlattice structure was formed by subsequent plasma enhanced chemical vapor deposition (PECVD) of 2 nm thick SiO_2 layers and 3 nm thick SRO with a nominal Si excess of 20% on top of a P-type Si substrate. The bilayer is repeated 6 times. The total nominal thickness of the superlattice is 30 nm with an average Si excess of 12%. Conventional annealing at 900 °C for 1 h was performed in order to induce Si phase separation. A single Er implantation with a dose of 1×10^{15} at/cm^2 at 20 keV was fulfilled, followed by a post-implantation annealing at 800 °C for 6 h in order to remove defects and to activate Er^{3+} ions. Highly N-type doped polycrystalline silicon (Polysilicon) 100 nm thick is used both as electrode and as a semitransparent optical window. Additionally, Er-doped SiO_2 and Er-doped SRO single layers were deposited with same fabrication parameters than the superlattice. Average Si excess of 12% was defined in the SRO layer. A semiconductor device analyzer was used to obtain the quasi-static current-voltage characteristic with a step of 40 mV/s. The visible EL spectra were recorded with a calibrated liquid nitrogen cooled charge coupled device detector placed behind a monochromator. An infrared calibrated photomultiplier was used to collect the EL signal at 1.54 μm.

Figure 1(a) shows the polarization and cross-section schemes of the device. The bright field transmission electron microscopy (TEM) image in Figure 1(b) confirms a well-defined superlattice structure. In addition, the silicon content in the Er-doped superlattice has been mapped by means of energy filtered TEM (EFTEM) using the Si plasmon peak (17 eV) signal in the Electron Energy Loss (EEL) spectrum (inset). It is worth noticing that the superlattice geometry was

---

a)Electronic mail: jmramirez@el.ub.edu

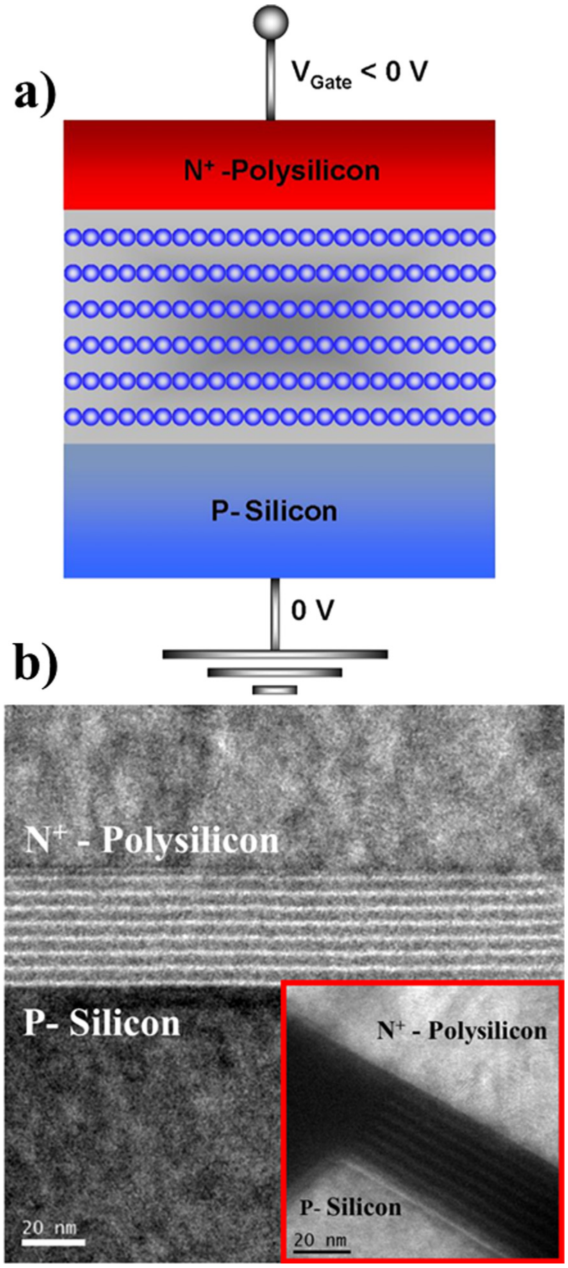

FIG. 1. (a) Device cross-section and polarization scheme of devices. The device structure is defined by a highly N-type doped polycrystalline silicon electrode (N^+-Polysilicon) on top, the Er-doped nanocrystal superlattice, and a P-type doped ($\sim 10^{17}\,\mathrm{cm}^{-3}$) monocrystalline silicon substrate (P-Silicon) at the bottom. (b) Bright field TEM image of the Er-doped superlattice. Darker layers correspond to the SRO (inset: EFTEM image using the 17 eV Si plasmon peak; bright contrast corresponds to SRO layers, substrate and top contact).

successfully preserved even after the Er implantation and the post annealing treatment, obtaining an abrupt SRO/SiO_2 interface and deposited thicknesses that are in agreement with the nominal parameters ((2.4 ± 0.3) nm for the SiO_2 layers and (3.0 ± 0.3) nm for the SRO layers). Remarkably, evident Er clusterization is only present in the single layers and not in the superlattice structure. In fact, an earlier work on similar layers with same Er implantation estimated that more than 50% of the total implanted Er would actually become clusterized, resulting in non-emitting Er-aggregates that were observed in TEM images.[9] In that case, however, a different fabrication technique (low-pressure chemical-vapor deposition) was used to deposit similar SRO/SiO_2 superlattices. Also, the superlattice structure was barely preserved, causing partial mixing of SRO and SiO_2 layers that may eventually facilitate Er diffusion within the matrix. Although detailed analysis of the Er aggregation in SRO/SiO_2 superlattices has not yet been accomplished, preliminary results point out that a well defined superlattice structure may effectively reduce undesired Er clusterization. Further structural and compositional properties of current Er-doped superlattices can be found in Ref. 10.

Figure 2 shows the current density (J) as a function of the electric field (E) (Figures 2(a)–2(c)) and the external quantum efficiency, EQE (Figure 2(d)), of the Er-doped SRO/SiO_2 superlattice (SRO/SiO_2), the Er-doped silicon dioxide (SiO_2) single layer, and the Er-doped SRO single layer. The EL onset is highlighted with filled dots in Figures 2(a)–2(c). The predominant transport mechanisms are plotted for each curve. In particular, the Er-doped superlattice presents two different conduction mechanisms that depend on the applied electric field. Poole-Frenkel emission (P-F) of thermally activated conduction between localized states in the gap assisted by the electric field predominates at low and medium fields (3–6 MV/cm).[11] The expression used for the fit reads as

$$J_{PF} \approx E \times \exp\left(-\frac{\left(\varphi_t - \sqrt{q^3E/(\pi\varepsilon)}\right)}{k_BT}\right), \tag{1}$$

where J is the current density, E is the applied electric field, ϕ_t is the trap energy taken from the bottom of the SiO_2 conduction band, q is the electron elementary charge, k_B is the Boltzmann constant, T is the temperature, and ε the material

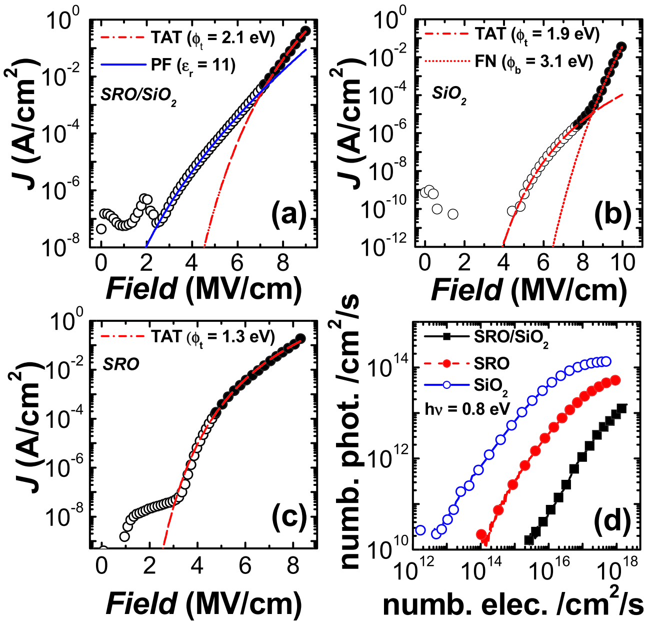

FIG. 2. J(E) characteristic and conduction mechanism fitting of the Er-doped SRO/SiO_2 superlattice (a), the Er-doped SiO_2, (b) and the Er-doped SRO single layer (c). Blue straight line represents the Poole-Frenkel conduction, dashed-dotted line the trap-assisted tunneling, and dotted line the Fowler-Nordheim conduction. Filled dots highlight the infrared EL at 1.5 μm for each layer. (d) Emitted photon flux as a function of the injected electron flux of the three layers under study.

permittivity (being $\varepsilon = \varepsilon_r \times \varepsilon_{r0}$ where ε_r and ε_0 are the relative and absolute permittivity, respectively).

A mean relative permittivity of $\varepsilon_r = 11$ was obtained from the P-F fit in the superlattice. Notice that this value lies closer to the relative permittivity of silicon ($\varepsilon_r = 12$) than to the one of silicon dioxide ($\varepsilon_r = 4$). A plausible explanation of this atypical deviation will be discussed later on. Moreover, an average monoenergetic activation energy of $E_a = 150$ meV was obtained from the Arrhenius plot of the J(E) characteristic. This value commensurates with previous works were similar layers were studied, also providing a diminution of the activation energy when the electric field is increased.[12] On the other hand, transport mechanism switching takes place from 7 MV/cm on yielding an electrode-limited current conduction instead of a bulk-limited one. Concretely, trap-assisted tunneling model yielded good fitting of the experimental J(E) curve, with a mean trap energy of $\phi_t = 2.1$ eV if a uniformly distributed trap concentration is assumed.[13] This implies that the tunneling event would be assisted by an interfacial trap, which is placed at 2.1 eV below the conduction band. For reasons of clarity and comprehensibility, from now on let us call "Si-nc traps" those defects related to Si-ncs ($\phi_t = 150$ meV) and "SiO_2 traps" the ones that belong to the silicon dioxide ($\phi_t \sim 2$ eV).

Similarly, the predominant transport mechanism found in the Er-doped SiO_2 layer (Figure 2(b)) was a trap-assisted tunneling at low and medium fields (from 4 MV/cm to 8 MV/cm, dashed dotted line) with a mean trap energy of 1.9 eV, and a Fowler-Nordheim tunneling at higher fields with a potential barrier height of 3.1 eV, in agreement with the one obtained by electrons at the electrode-SiO_2 interface (~3.2 eV).[11] The formulas used for the trap-assisted tunneling and the Fowler-Nordheim fits are, respectively,

$$J_{TAT} \approx \exp\left(-\frac{4\sqrt{2m^*}}{3\hbar q} \times \frac{\varphi_t^{3/2}}{E}\right), \tag{2}$$

$$J_{FN} \approx E^2 \times \exp\left(-\frac{4\sqrt{2m^*}}{3\hbar q} \times \frac{\varphi_b^{3/2}}{E}\right), \tag{3}$$

where m^* is the electron effective mass, $\hbar$ the reduced Planck constant, and ϕ_b the electrode-active layer barrier height at the interface.

It is worth to mention that the trap energy level for the trap-assisted tunneling ($\phi_t = 1.9$ eV) correlates well with the one obtained for the superlattice in the high field regime (2.1 eV). Therefore, trap-assisted tunneling at high fields suggests that only the very first nanometers of SiO_2 are relevant for the barrier transparency (the ones closer to the electrode-active layer interface, i.e., the first SiO_2 layer of the superlattice). Consequently, it seems reasonable to assume that the trap-assisted tunneling in both the superlattice and the SiO_2 is mediated by interfacial deep traps inherent to the SiO_2 and not by shallow states created *ad-hoc* when including Si-ncs. This is contrary to what is observed in the Poole-Frenkel regime at low and medium fields (see Figure 2(a)).

Then, the transport phenomena in the Erbium-doped Silicon nanocrystal superlattice can be summarized as follows: (i) at low and medium fields, where the PF mechanism predominates, monoenergetic trap-channel conduction situated at 150 meV below the conduction band would prevail, associated to Si-ncs extended states and/or surrounding defects at the Si-nc interface, and (ii) at high fields, where interfacial trap states situated at ~2 eV from the SiO_2 conduction band would be responsible for the trap-assisted tunneling.

On the contrary, only one single transport mechanism predominates in the single Er-doped Silicon-rich oxide layer (Figure 2(c)) from 4 MV/cm up to the device breakdown. In that case, a trap-assisted tunneling conduction with averaged trap energy of 1.3 eV was found. Notice that this trap energy lies between the one obtained for the superlattice at low and medium fields (Si-nc traps with $E_a = 150$ meV) and the one attributed to intrinsic defects in SiO_2 (located at 2.1 eV below the conduction band), suggesting that a combination of both Si-nc traps and interfacial SiO_2 traps may assist the tunneling process of electrons in this case. This hypothesis is well founded and seems reasonable for single layers since Si-ncs are not ordered and may be located closer to the electrode-active layer interface.

Figure 2(d) depicts the emitted photon flux at 1.54 μm (0.8 eV) as a function of the injected electron flux for each layer (EQE). It is clearly illustrated that the most efficient layer is the Er-doped SiO_2 (blue empty dots), followed by the Er-doped SRO (red filled dots) and finally the Er-doped superlattice (black squares). The emitted photon-injected electron flux quantification allows us to accurately determine the number of electrons needed to create one photon with energy of 0.8 eV. A photon/electron ratio of $1/(3 \times 10^2)$ was found for the SiO_2 layer, $1/(3 \times 10^3)$ for the SRO and $1/(1 \times 10^5)$ for the superlattice. In addition, a linear slope of the EQE was found over a wide range of injected electrons in all layers, denoting fixed photon-electron ratio. Nevertheless, slope diminution of the Er-doped SiO_2 EQE characteristic is observed under high electron injection, pointing out saturation of the electrically excitable Er fraction (the J(E) curve does not saturate at this point). A slight saturation is also seen in the Er-doped SRO layer, in opposition to the Er-doped superlattice where no emitted photon saturation was detected until the breakdown. This fact suggests that the excitation efficiency of injected electrons can be strongly modulated depending on the layer design.

Additionally, an interesting feature comes out when comparing the transport mechanism with the EL onset of the studied layers, because EL only shows up when a trap-assisted tunneling conduction dominates (see filled dots in Figures 2(a)–2(c)). In fact, this is a distinguishing mark that points out that direct impact excitation of injected carriers becomes the main excitation mechanism of Er^{3+} ions in all layers, rather than energy-transfer from Si-ncs to Er^{3+} ions.[14] In that situation, the Er excitation efficiency would strongly depend on the injected electrons in the conduction band, and in particular on; (i) the number of injected electrons, (ii) the average "time of flight" in the conduction band, and (iii) the average kinetic energy of injected electrons. This scenario also explains the high EQE found in the sample without Si-ncs, as SiO_2 provides superior features to the injected electrons in the conduction band, with average kinetic energy values of 3 eV, mean free paths of 3 nm, and lower scattering rates compared to SRO layers.[15] On the other hand, Si-ncs yield additional inelastic electron scattering in the conduction band, these Si-ncs being excited by direct impact excitation and leading to the often observed EL signal of Si-ncs in Er-doped SRO layers.[14] In addition, the probability of excitation of Er^{3+} ions diminishes if hopping transport between neighboring Si-ncs takes place, as electrons can travel across the active layer without facing the SiO_2 conduction band.[16] Noteworthy, this latter effect cannot be completely discarded on the basis that local charge transport of single events is far beyond our detection capabilities.

In order to further investigate the transport mechanisms and the origin of Er excitation in the Er-doped silicon nanocrystal superlattice, we measured and quantified the emitted photon flux in the visible range of the spectra. It turns out that the visible Er spectrum is a useful tool that yields an approximate fingerprint of the average kinetic energy of injected electrons in the conduction band. Results are summarized in Figure 3(a). EL spectra of all layers were obtained from the visible EL onset. The maximum injected electron flux was maintained sufficiently low in order to avoid up-conversion mechanisms, which may lead to false interpretation of the results. Interestingly, none of the Er emission lines were detected in the Er-doped superlattice, being only observable the broad emission of Si-ncs centered at 1.4 eV (see the top spectrum in Figure 3(a)). On the contrary, sharp emission lines clearly showed up for Er-doped SiO_2 and Er-doped SRO layers along the detected spectrum (middle and bottom spectra in Figure 3(a)), all of them well correlated with the higher energy levels of Er^{3+} ions.[17]

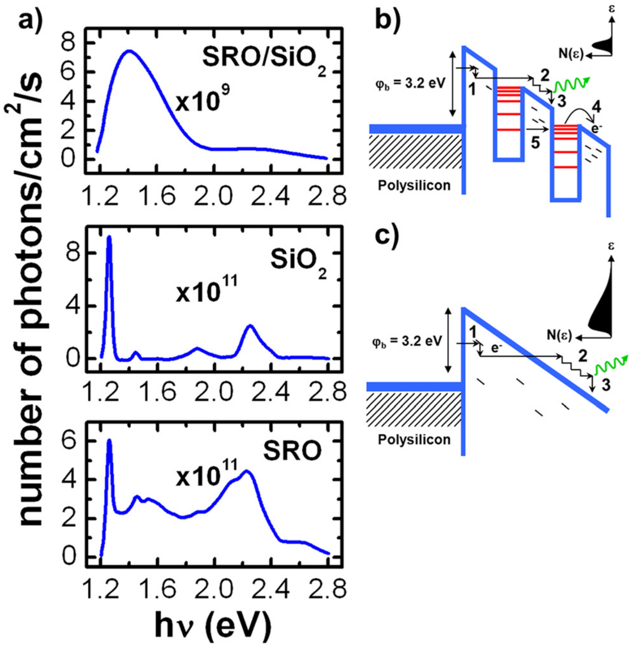

FIG. 3. (a) Visible EL spectra of the Er-doped superlattice (top), the Er-doped SiO_2 single layer (middle), and the Er-doped SRO single layer (bottom), taken by injecting constant electron flux of $2 \cdot 10^{16}$ electrons/cm^2/s. ((b) and (c)) Energy band diagrams of the Er-doped superlattice and the Er-doped SiO_2, respectively. Number 1 refers to a trap-assisted tunneling event, 2 depicts inelastic scattering, 3 is direct impact excitation, 4 is a Poole-Frenkel process, and 5 corresponds to a hopping event between neighbor nanocrystals.

Additionally, no change in the line-shape of the spectra for the studied injected electron flux range was detected, hence maintaining the same intensity ratio between different Er lines. Moreover, the integrated optical power density of Er-doped single layers (SiO_2 and SRO) is much higher (about two orders of magnitude) than the one obtained from the Er-doped superlattice, similar to the previously observed infrared EL (see Figure 2(d)).

Thus, assuming direct impact as the main excitation mechanism for Er^{3+} ions in all the studied samples, we demonstrate that the high EL efficiency in single layers is correlated with a hotter electron distribution.[18] Consequently, the superlattice would necessarily present an average energy value of injected electrons lower than 1.26 eV, as no related Er^{3+} emission is observed in the visible spectra (see Figure 3(a), top). Then, the origin of the broad EL observed in the superlattice cannot be attributed to a direct impact excitation of Si-ncs but to a different mechanism able to sustain the excitonic nature of the emission. A suitable possibility is the P-F ionization of the Si-nc itself (or its surrounding media), allowing for the efficient electron trapping and the exciton creation with a hole from the Si valence band. Besides, although the former study of the transport mechanisms at high field has shown potential barrier heights that are in better agreement with electron injection from the electrode to the active layer conduction band rather than hole injection from the substrate to the active layer valence band,[15] we can not discard also small contribution of holes being injected in the superlattice, and eventually forming electron-hole pairs inside Si-ncs. In fact, this kind of bipolar injection was already reported in the literature where Er-undoped SRO/SiO_2 superlattices were studied.[5] In the same line, it is worth to mention that although an infrared EL boosting of Er^{3+} ions by means of an energy transfer process mediated by Si-ncs (antenna effect) cannot be completely avoided, we believe that it is not relevant under high field d.c. polarization given that direct impact excitation is known to excite a much larger Er population.[14]

Charge transport and EL excitation mechanisms are summarized in Figures 3(b) and 3(c). Trap-assisted tunneling (1), acoustic-phonon scattering events (2), direct impact excitation of optically active Er^{3+} ions (3), thermally activated conduction in Si-ncs (4), and electron hopping between Si-ncs (5) are depicted in the Er-doped superlattice (Figure 3(b)) and the Er-doped SiO_2 (Figure 3(c)), respectively. A qualitative profile of electron kinetic energy distribution is sketched in the N(ε) diagram in Figures 3(b) and 3(c), showing a high energy tail distribution (above 2.2 eV) solely in the Er-doped SiO_2 layer. Although the origin of the energy tail suppression of injected electrons in the superlattice would need a profound analysis that lies out of the scope of this paper, a plausible explanation would be an increase of the scattering ratio and a diminution of the average mean free path of injected electrons as a consequence of the superlattice geometry. Then, acoustic-phonon runaway in the superlattice would become unlikely on the basis that low kinetic energy values were measured.[18]

Thus, the implementation of SRO/SiO_2 superlattices in structures that require an electron injection scheme would provide much larger operation device lifetimes since typical degradation processes such as trap creation or electron energy release at the active layer-substrate interface are unambiguously correlated with highly energetic electrons in the conduction band.[19] Moreover, additional layer architectures were accurate control of the average kinetic energy of injected electrons in the active layer conduction band are anticipated. On the basis of the present work, we propose the combination of a thin SiO_2 accelerator layer (5–10 nm) with a single electroluminescent layer (20 nm) composed by a silicon-rich oxide (or nitride) doped with erbium (or other rare earth ions) to provide superior electroluminescent performance.

In summary, the charge transport phenomena and the main Er excitation processes responsible for the infrared EL emission have been investigated in Er-doped SRO/SiO_2 superlattices. Poole-Frenkel conduction mediated by Si-ncs has provided for thermally activated conduction shallow paths at low and medium applied fields, whereas trap-assisted tunneling supported by SiO_2 defects has proved to lead the charge transport at high fields. Also, infrared EL has been ascribed to direct impact excitation of Er^{3+} ions by means of injected electrons in the superlattice conduction band. Furthermore, the absence of Er emission lines in the visible EL spectra of the Er-doped superlattice has allowed identifying less energetic electron injection distribution in the conduction band compared to single layers. Hot electron engineering (HEE) of the active layer stack is proposed by combining a thin SiO_2 accelerator with an electroluminescent layer to obtain efficient Silicon-based electroluminescent devices at 1.5 μm.

Authors wish to thank CEA LETI for the sample fabrication and Dr. J. M. Fedeli for the technical assistance. J. M. Ramírez thanks the financial support of AGAUR through the program FI-DGR 2013 and also D. Navarro-Urrios for fruitful discussions. J. M. Rebled thanks the CSIC for a JAE predoc grant. We acknowledge the Nanoscience Laboratory (University of Trento) and especially Professor L. Pavesi for his contribution in an early stage of the work. TEM facilities at the Scientific and Technological Centers of the University of Barcelona (CCiT-UB) and the FIB sample preparation in the Plataforma de Nanotecnologia-PCB are also acknowledged.

[1] C. W. Jiang and M. A. Green, J. Appl. Phys. **99**, 114902 (2006).

[2] X. J. Hao, A. P. Podhorodecki, Y. S. Shen, G. Zatryb, J. Misiewicz, and M. A. Green, Nanotechnology **20**, 485703 (2009).

[3] F. Sgrignuoli, G. Paternoster, A. Marconi, P. Ingenhoven, A. Anopchenko, G. Pucker, and L. Pavesi, J. Appl. Phys. **111**, 034303 (2012).

[4] S. Gutsch, J. Laube, A. M. Hartel, D. Hiller, N. Zakharov, P. Werner, and M. Zacharias, J. Appl. Phys. **113**, 133703 (2013).

[5] A. Marconi, A. Anopchenko, M. Wang, G. Pucker, P. Bellutti, and L. Pavesi, Appl. Phys. Lett. **94**, 221110 (2009).

[6] G. Franzò, E. Napolitani, P. Cardile, S. Boninelli, A. Marino, and F. Priolo, Semicond. Sci. Technol. **26**, 055002 (2011).

[7] V. Y. Timoshenko, M. G. Lisachenko, B. V. Kamenev, O. A. Shalygina, P. K. Kashkarov, J. Heitmann, M. Schmidt, and M. Zacharias, Appl. Phys. Lett. **84**, 2512 (2004).

[8] H. Kryzanowska, K. S. Ni, Y. Fu, and P. M. Fauchet, Mater. Sci. Eng. B **177**, 1547 (2012).

[9] N. Prtljaga, D. Navarro-Urrios, A. Tengattini, A. Anopchenko, J. M. Ramírez, J. M. Rebled, S. Estradé, J. P. Colonna, J. M. Fedeli, B. Garrido, and L. Pavesi, Opt. Mat. Express **2**, 1278 (2012).

[10] A. Eljarrat, L. López-Conesa, Y. Berencén, J. M. Ramírez, B. Garrido, S. Estradé, and F. Peiró, "Structural and compositional properties of Er-doped silicon nanocluster/oxide for multilayered photonic devices studied by STEM-EELS," Nanoscale (submitted).

[11] O. Jambois, J. M. Ramírez, Y. Berencén, D. Navarro-Urrios, A. Anopchenko, A. Marconi, N. Prtljaga, A. Tengattini, P. Pellegrino, N. Daldosso, L. Pavesi, J. P. Colonna, J. M. Fedeli, and B. Garrido, J. Phys. D: Appl. Phys. **45**, 045103 (2012).

[12] Y. Berencén, J. M. Ramírez, O. Jambois, C. Domínguez, J. A. Rodríguez, and B. Garrido, J. Appl. Phys. **112**, 033114 (2012).

[13] W. J. Chang, M. P. Houng, and Y. H. Wang, J. Appl. Phys. **90**, 5171 (2001).

[14] J. M. Ramírez, F. Ferrarese Lupi, O. Jambois, Y. Berencén, D. Navarro-Urrios, A. Anopchenko, A. Marconi, N. Prtljaga, A. Tengattini, L. Pavesi, J. P. Colonna, J. M. Fedeli, and B. Garrido, Nanotechnology **23**, 125203 (2012).

[15] D. J. DiMaria, T. N. Theis, J. R. Kirtley, F. L. Pesavento, D. W. Dong, and S. D. Brorson, J. Appl. Phys. **57**, 1214 (1985).

[16] K. C. Kao, *Dielectric Phenomena in Solids* (Elsevier Academic Press, California, 2004).

[17] J. M. Ramírez, O. Jambois, Y. Berencén, D. Navarro-Urrios, A. Anopchenko, A. Marconi, N. Prtljaga, N. Daldosso, L. Pavesi, J. P. Colonna, J. M. Fedeli, and B. Garrido, Mater. Sci. Eng. B **177**, 734 (2012).

[18] D. Arnold, E. Cartier, and D. J. DiMaría, Phys. Rev. B **49**, 10278 (1994).

[19] D. A. Buchanan and D. J. DiMaria, J. Appl. Phys. **67**, 7439 (1990).

CHAPTER 3

3. Electrically Pumped Er-Doped Light Emitting Si Slot Waveguides for On-Chip Optical Routing at 1.54 μm

This section is entirely devoted to the development and characterization of electrically pumped light emitting Er-doped Si slot waveguides. After the insight provided on the main optoelectronic properties of vertically emitting Er-doped MIS devices with different Si-based hosts, it would also be interesting to explore the most important features of these active layers when embedded in a new optoelectronic device that yields in-plane light emission. The successful implementation of this new design would enable the on-chip light distribution in fully integrable silicon photonic platforms with no need of external coupling by a bulky laser source.

The chapter is divided in four main parts, as follows: (i) a brief outlook on the advantages of this configuration and some prior interesting works available in the literature; (ii) a review of the most important theoretical points to take into account when designing these structures; (iii) a detailed reasoning of the main design considerations carried out, as well as the mask layout description and main fabrication steps; and finally (iv) the optoelectronic characterization of slot waveguides. A summary of the main points and conclusions extracted is detailed at the end of this chapter.

3.1. The horizontal optoelectronic approach

From a technological point of view, the study of Si-based vertically emitting devices based on MIS structures (like the ones studied in the previous chapter) is very convenient. They can be fabricated using standalone and well-validated CMOS technology, with almost the same processing steps than the ones required for the fabrication of CMOS capacitors. This fact has a positive impact on the final device performance since high reproducibility and good optoelectronic properties are generally found during wafer testing. Nevertheless, being one of the final aims of Er-doped Si-based devices the on-chip optical routing in integrated photonic chips for datacom purposes, a horizontal configuration with in-plane light emission is needed. In fact, despite many works have reported on the optoelectronic properties of Er-doped Si-based vertically emitting devices [1-4], there are only few publications that propose an integrated optical link consisting in a light emitting device coupled to a waveguide.

The first attempt to accomplish such milestone came from the Cornell Nanophotonics Group in 2009 [5]. In that work, a slot waveguide with a polycrystalline silicon top cladding was proposed to enable electrical injection in a thin dielectric material. Such novel design responded to a number of strong requirements imposed by electrically pumped light emitting devices based on MOS structures: (i) an optical cavity with high quality factor (Q) to procure light amplification, (ii) a thin dielectric layer to ease carrier injection, and (iii) a low loss design in which the optical mode is mostly confined in the dielectric layer. In spite of the fact that slot waveguide ring resonators were proposed as good candidates for electrically driven tunneling devices such as electrically pumped Si-based light sources, only a passive device characterization was performed in ref. 5.

Shortly after, other research groups reported on similar slot waveguide device architectures for integrated photonics. Among them, special attention should be paid to some outstanding publications that account for the integration of the light emitter with a guiding system. For instance, Atwater Research Group in Caltech suggested a pulsed excitation scheme in waveguide-confined Er-SiO_x layers containing Si-ncs [6]. In their work, the rate equations were modelled and the optimum conditions for optical gain were proposed. In particular, they found a simulated modal gain of 0.9 dB/cm for a 10 nm thick Er-SiO_x layer operating under pulsed excitation, and extrapolated to a maximum modal gain of 2 dB/cm by increasing the layer thickness up to 50 nm. Also, they stated the impossibility of obtaining optical gain under continuous electrical pumping since carrier absorption is expected to produce high losses in the light emitting waveguide. Nevertheless, they made some debatable considerations such as the fact that only energy transfer governs Er^{3+} emission under electrical pumping. As a result, rate equations were solved using Si-ncs dynamical parameters uniquely.

Another interesting contribution was reported by Jayatilleka and co-workers, led by Prof. J. A. Kenyon [7]. They presented a novel electrically pumped silicon waveguide approach combining a MIS structure with a rib waveguide. An Er-doped SiO_x was proposed as active layer. Finite difference time domain (FDTD) simulations demonstrated that a high percentage of emitted light by the MOS-like structure was coupled into the rib waveguide (up to 75%).

Also, researchers from the semiconductor materials division at the Helmholtz Zentrum Dresden Rossendorf, in Germany, reported theoretical simulations of Si_3N_4/SiO_2 waveguides designed to maximize coupled light emission from a Si-based LED in butt-coupling configuration. A confinement factor of 74% and a coupling efficiency of 66% was reported [8].

As seen, the development of electrically driven integrated optical links remains interesting for the silicon photonics community. However, all of the above presented works are based on theoretical simulations and not on experimental characterization. To the best of my knowledge, only few attempts to fabricate the Si-based light emitting device integrated with the passive waveguide have been realized [9, 10]. Ideally, in these works the light emission from a Si light emitting device with an embedded SiO_x layer is coupled to a Si_3N_4 waveguide and finally detected by a p-n diode (see figure 1 (b)). In practice however, only ref. 10 reported a successful functionality of the Si photonic chip after complex analysis of its optoelectronic performance. Since transmitted wavelength was far from the one used in telecom (650 nm instead of 1.54 μm), they suggested using their photonic chips as compact sensors once Si_3N_4 waveguides are functionalized. Despite this breakthrough, authors did not perform any design optimization of the light emitter, neither on the effective coupling with the waveguide. As a consequence, only a small percentage of emitted light was transmitted towards the Si detector.

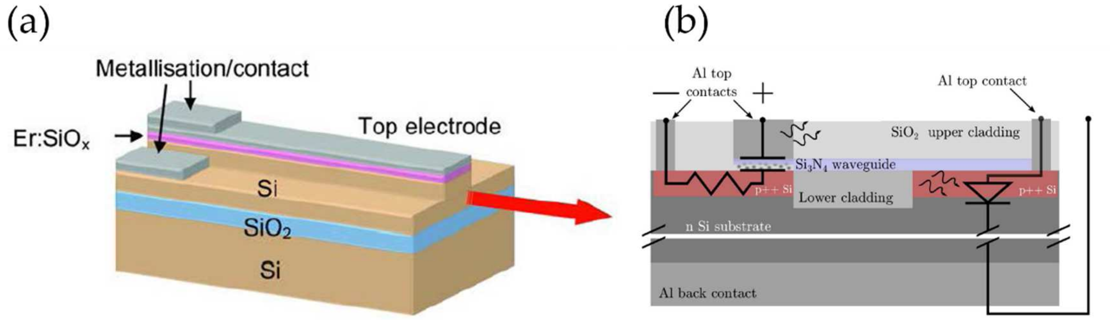

Figure 3.1. (a) Scheme of the proposed in-plane light emitting device, with the MIS structure coupled on top of a RIB waveguide (extracted from ref. 7). (b) Integrated photonic chip with (from left to right); (i) the light emitting MIS device emitting at 650 nm, (ii) the coupled Si_3N_4 waveguide and (iii) the Si photodetector (extracted from ref. 10).

Apart from the evident technological challenge of the proposed integrated systems, these contributions represent a nice piece of work and also a starting point for future Si-based complex integrated systems. Nevertheless, an electrically pumped Er-doped Si-based light emitter in waveguide configuration has not yet been fabricated. In the following, I will detail the work done in that direction, and the main results extracted from the optoelectronic characterization of the first electrically pumped Er-doped Si-based optical link for on-chip optical routing at 1.54 μm.

3.2. Theoretical framework

Slot waveguides were demonstrated in 2004 [11]. In that work, authors reported on good mode confinement in a low-index thin-film when embedded between two high-index slabs (claddings), taking advantage of the electric field discontinuity at the interfaces to enhance light confinement. Assuming Maxwell's equations, the electric displacement vector $\vec{D}$ should satisfy the continuity condition at the interface, i.e.:

$$\vec{D}_{slot} = \vec{D}_{slab} \Rightarrow \varepsilon_{slot} \cdot \vec{E}_{slot} = \varepsilon_{slab} \cdot \vec{E}_{slab} \Rightarrow n^2_{slot} \cdot \vec{E}_{slot} = n^2_{slab} \cdot \vec{E}_{slab} \tag{3.1}$$

Now, we can separate the electric field at the interface in two perpendicular components, one horizontal and one transversal to the interface:

$$n^2_{slot} \cdot \vec{E}_{//slot} = n^2_{slab} \cdot \vec{E}_{//slab} \tag{3.2}$$

$$n^2_{slot} \cdot \vec{E}_{\perp slot} = n^2_{slab} \cdot \vec{E}_{\perp slab} \tag{3.3}$$

Whereas the horizontal component does not require any field discontinuity to satisfy equation 3.2, a completely different situation is needed for the transversal case. Being $n^2_{slot} << n^2_{slab}$, the transversal electric field vector must compensate to satisfy equation 3.3, i.e. $\vec{E}_{\perp slot} >> \vec{E}_{\perp slab}$.

Therefore, only the amplitude of the transversal component of the electric field will be enhanced inside the slot material. In this case, the electric field distribution of the TM mode is governed by the following equation:

$$E_{\perp} \propto cosh(\gamma_{slot} x) \qquad for\ |x| < |t_{slot}|/2 \tag{3.4}$$

Where γ_{slot} is the field decay coefficient in the slot material, t_{slot} is the thickness of the slot and x is the distance taken from the middle of the slot material, i.e. $x = 0$ at $t = |t_{slot}|/2$. Figure 3.2 shows a scheme of the slot waveguide with the evanescent field superimposed.

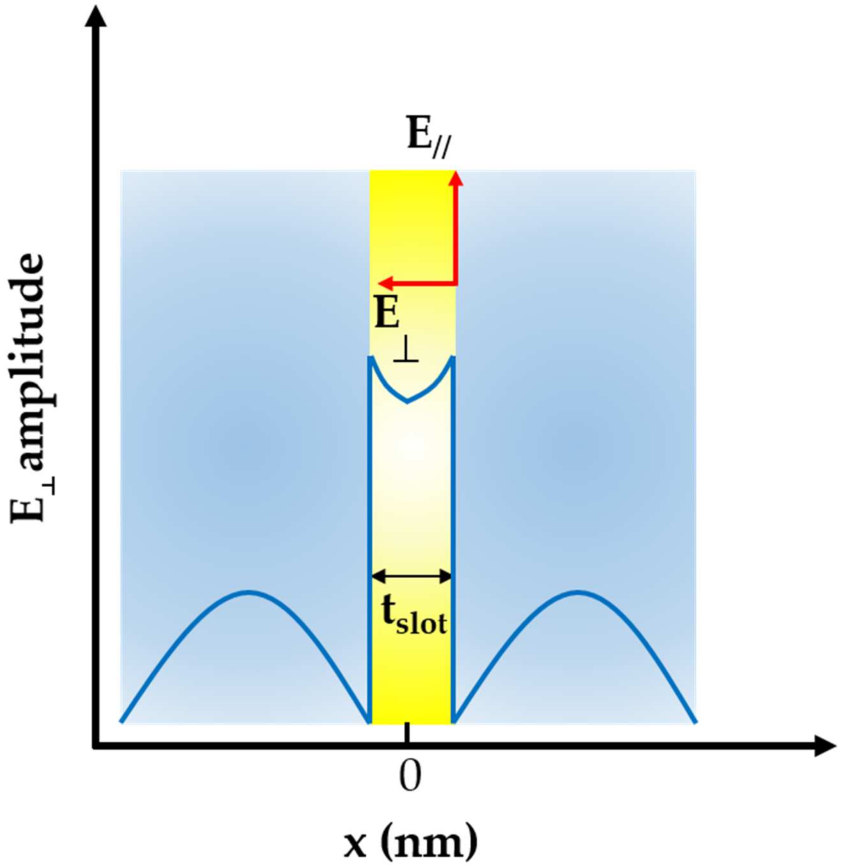

Figure 3.2. Transverse magnetic field profile of a slot waveguide.

Two different slot configurations are typically reported depending on the slot orientation: horizontal or vertical. The horizontal configuration provides transversal magnetic (TM) mode confinement (modal field oriented perpendicular to the substrate plane), whereas in the vertical configuration the transversal electric (TE) mode is enhanced (parallel to the substrate plane). Despite both configurations are well suited for the development of electrically pumped slot waveguides, the horizontal configuration has only been considered in this chapter. Bearing in mind that the fabrication process is normally performed in a standard CMOS line facility that uses a planar technology, the horizontal approach offers a series of technological advantages compared to the vertical configuration. Moreover, side wall roughness losses are minimized in the horizontal slot waveguide. On the counterpart, horizontal slot waveguides are more sensitive to bending loss and lateral leakage.

The waveguide geometry is also an important factor when designing slot waveguides at telecom wavelengths. A monomodal transmission of the fundamental mode (m = 0) with a high field confinement factor is desired. This parameter quantifies the fraction of optical power confined in the waveguide with respect to the total transmitted power, and can be calculated with the following formula:

$$\Gamma_{CF} = \frac{n_{slot} \iint\limits_{D_{slot}} |E(x,y)|^2 dxdy}{c\mu_0 \iint\limits_{D_{total}} Re\{E(x,y) \times H^*(x,y)\} \cdot \boldsymbol{e}_z dxdy} \tag{3.5}$$

Where D_{slot} and D_{total} are the dimensions of the slot and the entire waveguide, respectively, c is the speed of light in vacuum, μ_0 is the permeability of free space, $E(x,y)$ and $H(x,y)$ denote the vectorial electric and magnetic mode profiles and $\boldsymbol{e}_z$ is the unit vector in the direction of propagation. In slot waveguides, this fraction is normally lower compared to planar waveguides, between 30-40%.

One of the most important characteristics that verify the efficiency of a particular set of waveguides as on-chip optical transmission channels is the quantification of propagation losses. The benchmark for acceptable propagation losses in a passive waveguide is of the order of 1 dB/cm. They are defined as:

$$P_{out}(L) = CP_{in}e^{-\alpha L} \tag{3.6}$$

Where P_{out} is the collected optical power, P_{in} the incident optical power, C is the coupling factor, α is the propagation loss coefficient and L the transmitted distance.

Propagation losses originate from four main sources: volume scattering, surface scattering, absorption and radiation.

Volume scattering. Strongly depends on the distribution of scattering centres in the propagating layer. Is typically modelled using a λ^{-3} dependence (λ^{-1} in some cases) [12].

Interface scattering. Although there are many models available in the literature that estimate the interface scattering, a simple approximation could be performed with the following formula [13]:

$$\alpha_s = \frac{\cos^3\theta}{2\sin\theta}\left(\frac{4\pi n_1\left(\sigma_u^2+\sigma_l^2\right)^{\frac{1}{2}}}{\lambda_0}\right)^2\left(\frac{1}{t_{slot}+\frac{1}{k_{yu}}+\frac{1}{k_{yl}}}\right) \tag{3.7}$$

Being σ_u the root mean square (rms) roughness for the upper waveguide interface, σ_l the rms for the lower waveguide interface, and k_{yu} the decay constant of the upper and lower cladding, respectively.

Absorption. There are mainly two types of absorption: the band edge absorption and the free carrier absorption [14]. The first one becomes predominant when operating at wavelengths that have energy values close to the bandgap of the material in which the light is being transmitted. For wavelengths with energies well below such bandgap, the main absorption losses are dominated by free carriers uniquely. In that case, absorption losses read as:

$$\Delta\alpha = \frac{e^3\lambda_0^2}{4\pi^2c^3\varepsilon_0 n}\left(\frac{N_e}{\mu_e(m_e^*)^2}+\frac{N_h}{\mu_h(m_h^*)^2}\right) \tag{3.8}$$

Where N_e is the free electron concentration, N_h is the free hole concentration, m^*_e and m^*_h are the effective mass of electron and holes respectively, μ_e is the electron mobility, and μ_h is the hole mobility.

Radiation losses in optical waveguides. Although this term is normally negligible, it may be important in some cases in which abrupt curvature of waveguides or fast optical rates are required.

As introduced before, our main purpose is to develop optically active slot waveguides electrically driven. As a consequence, Er^{3+} ions will be introduced in the slot region. The host for Er^{3+} ions was chosen according to the main results extracted from Er-doped MIS devices (see previous chapter). Being SiO_2 the best host for Er^{3+} ions, two sets of waveguides with different slot materials were fabricated: an Er-implanted high temperature sotoichiometric oxide (HTO) and an Er-implanted SiO_x deposited by LPCVD. Top and bottom waveguide claddings will also function as injecting electrodes to allow for charge injection in the waveguide. These two additional elements will surely modify the intrinsic propagation losses of slot waveguides. Actually, a correct device design is critical to guarantee the optimum device performance. Therefore, a careful evaluation of the materials to be used and the optimum waveguide geometry have to be considered first. The next part will detail the main design singularities of our slot waveguides, as well as the processing steps needed to fabricate such structures.

3.3. Device design, mask layout and fabrication

- **Device design**

The waveguide design was subjected to several constraints: (i) a slot thickness of about 50 nm or lower to allow for the electrical injection, (ii) a monomodal confinement with low propagation losses at 1.54 μm, (iii) a structure able to inject electrons in the slot layer and (iv) a compact design compatible with the materials normally used in a standard CMOS line. In particular, the third point was especially challenging since electron injection requires a nearly metallic layer which is known to induce large propagation losses, hence being in controversy with the second point. In fact, this is a major aspect when designing electrically driven slot waveguides. Assuming that the 30-40% of the signal will be confined inside the slot active region where Er^{3+} ions are located, the remaining 60-70% will be transmitted through the cladding injectors. Moreover, being the waveguides fabricated on a standard SOI wafer with a buried oxide 220 nm thick, the bottom cladding will be formed using monocrystalline silicon, whereas polysilicon will be deposited to operate as a top cladding.

Despite the fact that polysilicon is known to be a lossy material for optical transmission due to the large number of interfaces present in adjacent polysilicon grains, it was the most favorable option from the electrical viewpoint since it has high electron mobility and good electrical properties. Thus, in order to reduce propagation losses due to large mode overlap with the polysilicon and with heavily doped regions, an asymmetric winged cross-section was defined in the waveguide, with a pedestal-like shape in the lower monocrystalline cladding and highly doped electrode wings. Such asymmetric configuration 'pushes' the optical mode down and minimizes the overlap with the polysilicon. In addition, the highly doped winged regions are far away from the confinement region and therefore carrier absorption is minimized. A similar strategy was tackled for the doping of the lower Si cladding. In order to minimize propagation losses by carrier absorption, a doping gradient profile was performed. Hence, a top-down doping gradient profile was engineered in the monocrystalline silicon pedestal, from a moderate doping of 10^{17} at./cm^3 close to the slot interface to a value of 10^{19} at./cm^3 at the interface with the buried oxide. Waveguide cross-section and film mode matching (FMM) simulations of the spatially confined optical mode can be observed in figure 3.3.

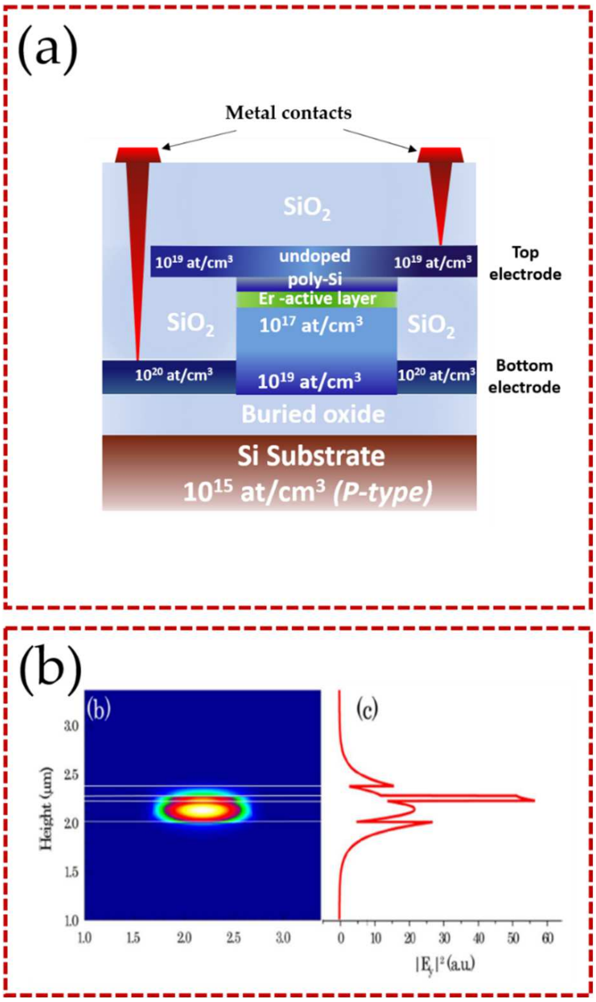

Figure 3.3. (a) Waveguide cross-section with doped regions (dark blue) and undoped or lightly doped regions (light blue). The active slot region is marked in green. The non-uniform doping in the low Si cladding is depicted by a degraded dark-to-light blue tonality. Image extracted from *paper XI*. (b) Optical mode simulations of the slot waveguide using an FMM solver (FIMWAVE, Photon Design). Simulations have been done by Nikola Prtljaga. Figure extracted from *paper X*.

Paper X further insights on the main device design and optical simulations of slot waveguides. Optical FMM simulations of the structure are presented in that work. A slot confinement factor of $\Gamma = 0.42$ was reported (significantly higher than in narrower slot waveguides [5]), $\Gamma = 0.1$ in the undoped polysilicon top cladding and only a value of $\Gamma < 0.01$ in the heavily doped electrode wings. Remarkably, the low influence of the top polysilicon cladding on the propagated optical mode relaxes error tolerances of the polysilicon deposition. Therefore, an optimum polysilicon thickness for electrical injection was chosen. It is worth mentioning that the confinement factor was obtained in a wide range of slot thicknesses (from 0 to 100 nm) and refractive index values (from 1.45 to 1.95) to analyze the influence of the parameter deviation from the nominal values. Also, optimization of the waveguide width was performed. In that case, since only monomodal propagation of the fundamental TM mode is desired, the waveguide width should be narrow enough to deplete higher propagation modes but maintaining the active material volume as large as possible to obtain measurable signals at the device output. Based on these considerations, a maximum waveguide width of 1 µm was obtained.

- **Mask layout**

The mask layout was designed bearing in mind the above requirements. Three different waveguide widths were defined: 300 nm, 500 nm and 1 µm. Although, as already stated, wider waveguides are preferred due to a larger material volume fraction, thinner waveguides were also intentionally designed to study the evolution of the EL signal with the waveguide width. Also, different waveguide lengths were designed to quantify propagation losses by means of the cutback technique: 1 mm, 1.5 mm, 2 mm, 2.5 mm and 3 mm. therefore, 15 different slot waveguides were defined in each dye. The slot waveguide can be divided in two main parts (see figure 3.4): the active region, where injecting electrodes and metal contacts are defined to excite Er^{3+} ions located in the slot, and the passive region, with a tapered passive slot waveguide (with no Er^{3+} implantation nor metal contacts) that departs from the same device cross-section and slowly widens up to 12 µm. A grating coupler with a period of 0.8 µm and a groove depth of 150 nm is attached to allow for on-chip light extraction with an angle of 25° from the normal.[12] Finally, an antireflecting shaped waveguide is defined at the waveguide end to avoid undesired backscattering.

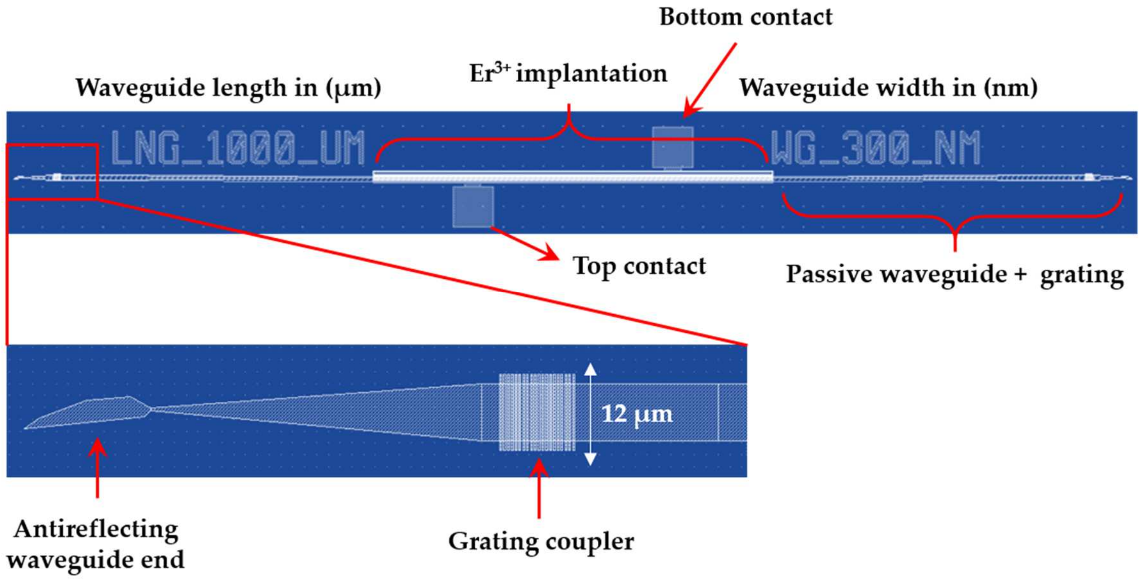

Figure 3.4. Mask layout of a single slot waveguide. Zoom-in region at the end of the waveguide, displaying the grating coupler and the antireflecting waveguide end.

---

[12] *It should be noted that the design of the grating couplers was not carried out in this work since the technological partner provided an already optimized design operating at 1.54 µm.*

Apart from the electrically driven slot waveguides, additional test waveguides were included in the mask layout to determine the electrical behavior of the top and bottom electrodes. Such new devices present identical geometrical parameters than slot waveguides, but with both metal contacts placed on either the top or the bottom electrode to measure the conductivity. Five different lengths were designed: 500 nm, 750 nm, 1 μm, 1.25 μm and 1.5 μm. As no optical signal is to be transmitted through these waveguides, the passive optical elements were not drawn in this case (passive waveguide and grating). A device cross-section is shown in figure 3.4.

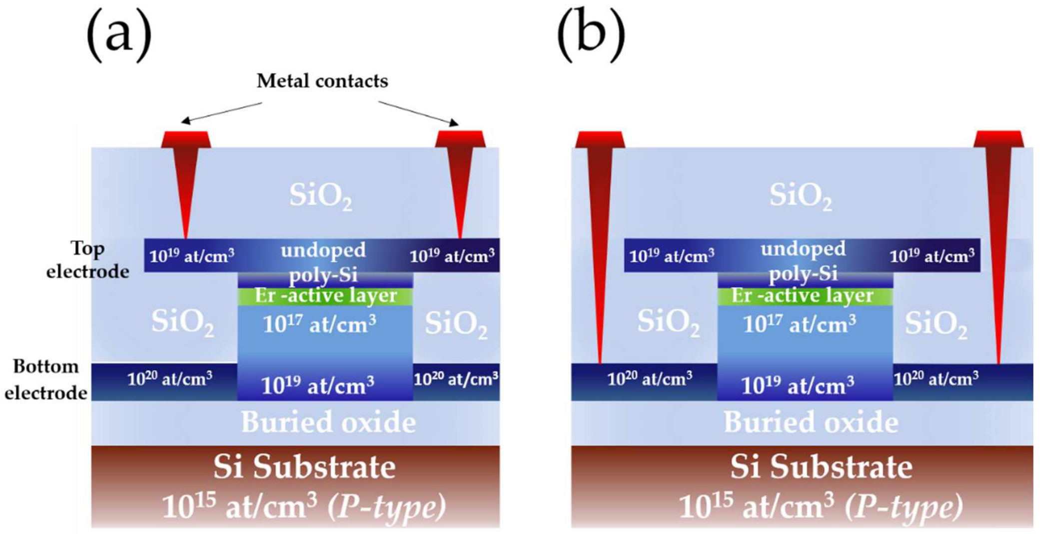

Figure 3.4. Device cross-section of (a) top contact test waveguides and (b) bottom contact test waveguides.

Hence, the final mask layout of a single wafer die is:

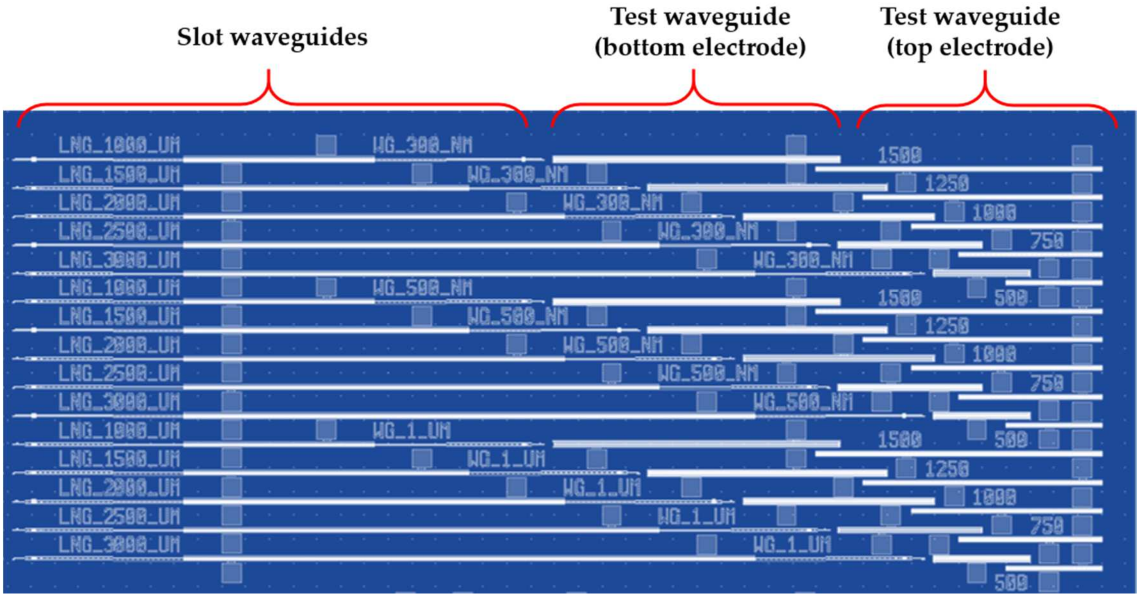

Figure 3.5. Wafer die containing slot waveguides (left part) and bottom (centre) and top (right) electrode test waveguides.

- **Device fabrication**

Once the mask layout is designed, the fabrication process takes place at the foundry. Samples were fabricated at CEA LETI (Grenoble) using a 200 nm CMOS line. The process flow is described in *paper XI*. There are, mainly, two major points that will be recalled since they deserve especial attention: the active layer deposition and the non-uniform doping in the lowest Si cladding.

The slot active material is a fundamental part for the light generation and consequently an efficient layer should be embedded. In that case, and bearing in mind that the host matrix should also be CMOS compatible with a low index refractive index to allow for light confinement in the slot (Simulations provided good results in a range between 1.45 and 1.95), a high quality thermal oxide (HTO) was finally chosen, followed by an Er-implantation dose of 10^{15} at./cm^2 at 20 keV (see *papers X* and *XI* for further details). This material can be easily grown in a CMOS line and presents a favorable local environment for Er^{3+} ions. In addition, it is among the most efficient silicon-based host for Er^{3+} excitation under electrical pumping (see previous chapter). On the counter part, the device lifetime will be reduced by the rapid increase of permanent charge trapping in the matrix due to new generated defects by hot electron injection. In order to mitigate such effect and release part of the trapped charge density out of the slot material, an additional run of slot waveguides was fabricated, but replacing the Er-doped HTO slot layer by an Er-doped Si-nc/SiO_2 multilayer. In that case, a substoichiometric LPCVD technique was used to obtain the slot material. A multilayer deposition sequence of 2 nm of SiO_2 and 3 nm of SiO_x was performed up to a final active layer of 50 nm. Gas flow rates were adjusted to obtain a Si excess of 20% in each SiO_x sub-layer, alternated with stoichiometric SiO_2 sub-layers. An average Si excess of 12% was measured in the slot layer. Same Er implantation than in the HTO active layer was performed in this case.

Concerning the non-uniform doping in the lowest Si cladding, a technologically challenging method was used. In particular, the doping gradient profile was achieved by thermal diffusion of the heavily doped electrode wings at the bottom. This step supposed a critical point in the fabrication of slot waveguides, since it is very difficult to perform such a steep doping profile from 10^{19} at/cm^3 to 10^{17} at/cm^3 in only 220 nm by thermal diffusion (see figure 3.3).

Fabricated devices underwent a first inspection by means of SEM characterization, displaying accurate features in accordance with the mask layout. Figure 3.6 (a) shows a set of electrically driven waveguides of different lengths. As it can be observed, the shortest one (at the top of the image) shows two metal contacts to enable the electrical injection in the slot region (a zoom-in region of a single metal contact is observed in figure 3 (b)). The output grating and the antireflecting waveguide end are observed in figures 3 (c) and 3 (d), showing size features in accordance with the preliminary design.

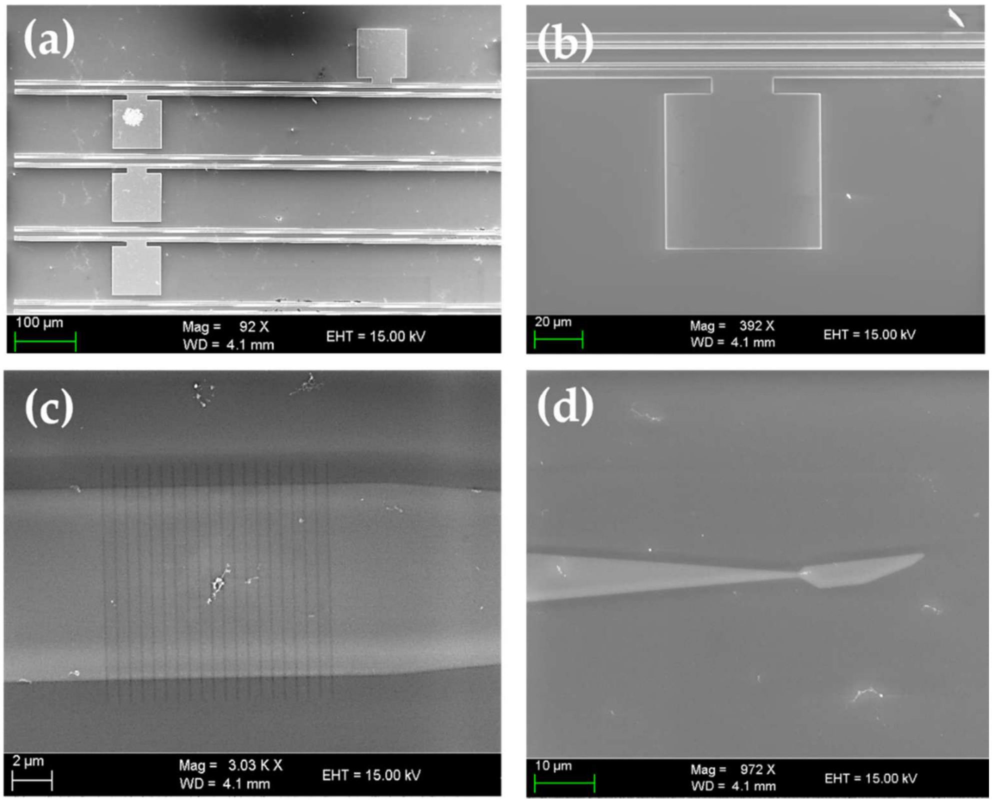

Figure 3.6. (a) Field of electrically driven slot waveguides. (b) Magnified top view of the top electrode contact. (c) Output grating coupler. (d) Antireflecting shaped waveguide.

The waveguide cross-section was also observed. For that, a set of waveguides was cleaved and placed at the SEM with a sample holder in a 90° orientation. Results are shown in figure 3.7. Electrode layer thicknesses are in agreement with nominal values. Similarly, the Si pedestal that provides asymmetry to the waveguide is well defined below the slot active region, with an average thickness of 220 nm.

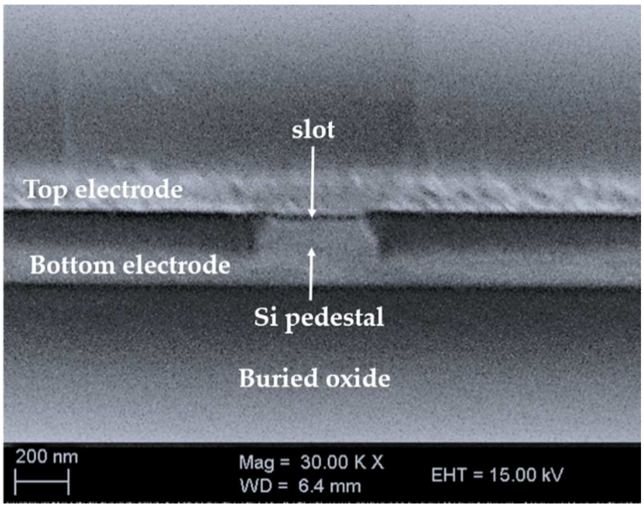

Figure 3.7. SEM image of the slot waveguide cross-section.

Finally, a TEM characterization was carried out in both Er-implanted slot layers to investigate their morphological structure.[13] Whereas the Er-doped HTO layer showed an expected morphology in concordance with previous layers (see previous chapter, figure 2.14) and a layer thickness of about 50 nm, a rather different trend was observed in the Si-nc/SiO_2 multilayer. Despite the fact that an abrupt compositional transition was observed at the substrate-active layer interface (figure 3.8 (a)), EFTEM images filtering by the Si plasmon peak (17 eV, figure 3.8 (b)) and the SiO_2 plasmon peak (23 eV, figure 3.8 (c)) denoted randomly distributed Si-ncs in the slot active layer. Therefore, the multilayer deposition performed during the fabrication process was not preserved at the end of the process. Such morphological anomaly may be originated by different causes: (i) an aggressive thermal treatment, (ii) the Er-implantation, (iii) a non-optimized deposition process. The first hypothesis could be easily discarded by comparing annealed and not annealed multilayers. Unfortunately, not annealed samples were not provided by the foundry. Despite this drawback, such hypothesis seems not logical from our viewpoint since similar multilayers with same annealing budget were successfully fabricated in the same facility. The same applies for the second hypothesis, in which Er-implantation is suggested as a possible cause of the multilayer mixing. If that would be the case, the morphology of multilayered samples fabricated by other techniques (such as PECVD) would have been mixed accordingly. Instead, a well-defined multilayer structure was obtained after an equivalent annealing treatment and Er-implantation (see *paper IX*). Therefore, the only suitable explanation for the multilayer mixing is a non-optimized fabrication technique. In fact, despite multilayer fabrication of PECVD samples had previously been carried out at CEA-LETI, the LPCVD multilayer deposition was firstly tested in our devices, and therefore it was not yet optimized. In spite of this unexpected deviation from the ideal morphology, the characterization of the Er-implanted SiO_x layer as a single bulk active layer and its comparison with the Er-implanted HTO is still interesting.

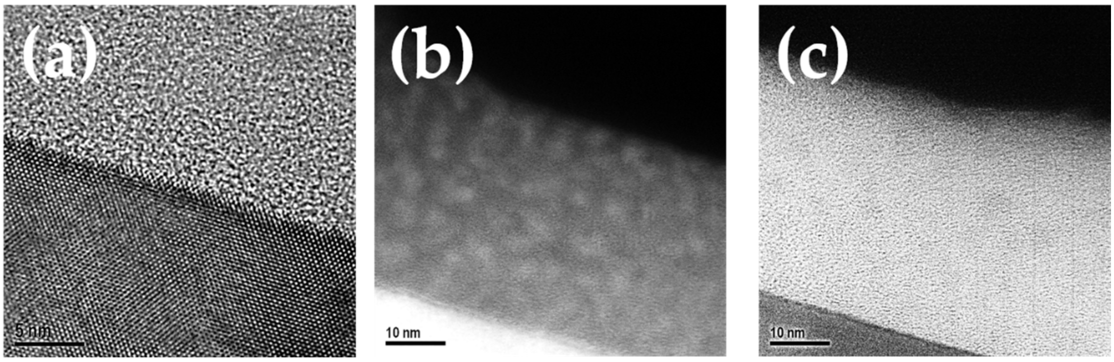

Figure 3.8. (a) TEM image of the Er-SiO_x layer showing a well-defined interface with the substrate. EFTEM image of the same layer fitering by the Si plasmon peak at 17 eV (b) and the SiO_2 plasmon peak at 23 eV (c).

---

[13] *Samples were prepared by Focus Ion Beam.*

As it has been shown, the race towards the development of an on-chip optical link is an arduous task with multiple challenges. In this section, the main technological steps and issues have been discussed starting from the device design, the definition of the mask layout and finally the device fabrication with the subsequent morphological characterization.

In the next section I will detail the main optoelectronic characterization performed on Er-doped Si slot waveguides and the main conclusions extracted from this analysis.

3.4. Optoelectronic characterization of slot waveguides

The optoelectronic characterization of Er-doped slot waveguides can be divided in two main parts: the passive characterization, in which no electrical signal is applied over devices, and the active characterization, where slot waveguides are polarized accordingly to enable carrier injection inside the active layer.

3.4.1. Passive characterization

The first step to characterize our slot waveguides is to study their passive optical performance. Key parameters such as propagation losses, coupling losses, grating transmittance or the optimized angle of collection are of high importance to evaluate the quality of waveguiding photonic elements.

- **Grating couplers**

Two experiments were performed to characterize grating couplers. Firstly, an evaluation of the best incident/collection angle was performed. As only a single output coupler is needed, slot waveguides were cleaved between one grating coupler and the waveguide electrodes (see figure 3.4). The input laser was fiber coupled and mounted on a high precision rotation stage. Then the fiber tip was located perpendicular over the grating coupler, and the angle sequentially changed from 0° to 45°, while collecting the output signal from the waveguide facet. In order to guarantee optical mode transmission through the slot region and not through other adjacent layers such as buried oxides, claddings or even the polysilicon electrode, output signal was firstly collected with an infrared Charge-Coupled Device (CCD). As the spatial location of the propagated mode roughly coincided with the spatial position of the slot, we could verify good mode confinement and transmission through the region of interest. Once light propagation was validated, the infrared CCD was replaced by an infrared PhotoMultiplier Tube (PMT) to collect the intensity of the propagated mode. Moreover, in order to proof that only TM mode was being transmitted through the slot waveguide, a rotating polarizer was placed at the cleaved waveguide output with an optimized angle for TM mode, and rotated 90° while measuring the output signal. As no light was detected in the PMT in this configuration, we can guarantee that only TM mode propagates through slot waveguides.

Once the optimum coupling angle was obtained, a second measurement was carried out. This time, the laser wavelength was slowly swept from 1500 nm to 1600 nm, while collecting the output mode intensity at each step. Such experiment provided the spectral transmittance of the grating coupler in the range of interest, around the emission of the first excited transition of Er^{3+} ions.

Main results of the grating coupler characterization are reported in *paper X*. An optimum incident angle of 25° is shown, and a transmittance spectrum with a maximum at around of 1535 nm can be observed.

- **Propagation and coupling losses**

As already discussed previously, the propagation loss coefficient (α, in cm^{-1}) allows devising the efficiency of a waveguiding system. Nevertheless, the ability of an optical channel to guide light efficiently is conditioned not only by the fraction of light transmitted through the waveguide, but also by the coupling efficiency between the light source and the waveguide (coupling loss factor, $\alpha_{coupling}$). Therefore, total insertion losses (IL) in our slot waveguides will be defined by:

$$IL(dB) = 10\,log\left(\frac{P_{out}}{P_{in}}\right) = \alpha_{prop} \cdot L \cdot log(e) + 10\,log(C) = \alpha_{prop} \cdot L + \alpha_{coupling} \qquad (3.9)$$

Notice that α_{prop} can be provided either in cm^{-1} (as in equation 3.6) or in dB/cm (as in the above equation). Similarly, $\alpha_{coupling}$ is normally displayed in dB.

Thus, the cut-back technique directly provides both parameters. An average propagation loss of 40±5 dB/cm and a coupling loss of 20±5 dB was measured in both Er-doped SiO_2 (and SiO_x) slot waveguides. Figure 3.9 shows a representative linear fit of the measured insertion losses as a function of the waveguide length for a propagated wavelength of 1530 nm. Similarly than for output couplers, the cut-back technique was performed over a wide range of propagated wavelengths: from 1500 nm to 1600 nm. This time, however, no remarkable loss variation was observed for different wavelengths, suggesting that propagation losses are not dominated by Er^{3+} absorption [14]. Moreover, similar propagation losses were obtained in both waveguides, in spite of the fact that Si-ncs are known to introduce additional losses in waveguides [15]. These values further confirmed the existence of a dominant absorption loss which is independent from the slot material.

Paper X provides a comprehensive explanation of the unexpectedly high propagation losses measured in both waveguides. They are attributed to processing defects associated with the chemical polishing (CMP) of devices. As a consequence, part of the propagation mode would be overlapped with heavily doped electrode wings, inducing high carrier absorption. In addition, the increasing doping gradient at the bottom Si pedestal where part of the optical mode is propagated may have not been successfully performed, hence also being heavily doped below the slot region.

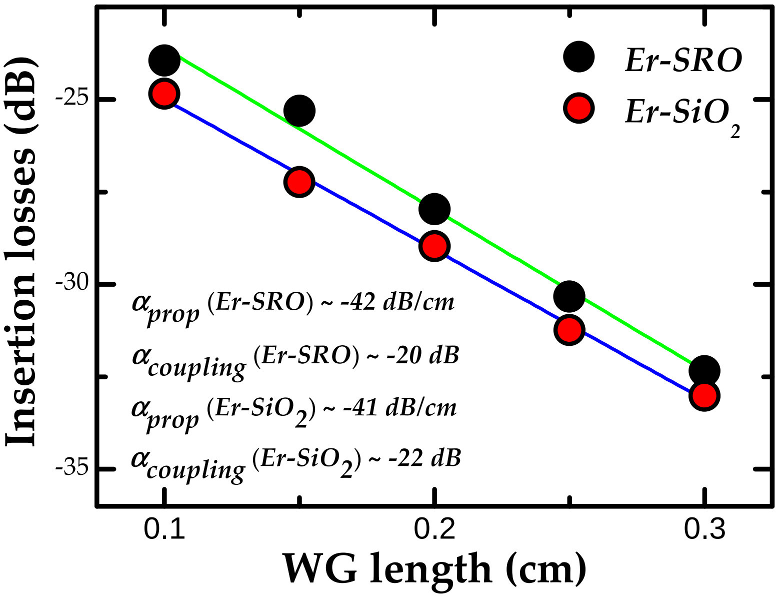

Figure 3.9. Total insertion losses (coupling losses + propagation losses) as a function of the waveguide length for an electrically pumped Si slot waveguide containing an Er-doped SiO_2 slot (red dots) or an Er-doped SiO_x slot (black dots). The linear fit of each data set is shown in blue and green, respectively.

Despite the passive characterization of Er-doped slot waveguides revealed some issues in the fabrication process that yielded high propagation losses in the structure, the slot waveguides showed good mode confinement in the slot and efficient light extraction by means of the output couplers. Moreover, the direct comparison with other active photonic elements previously reported in the literature (mainly Si modulators) denoted similar propagation losses, especially in MOS-based devices with polycrystalline silicon electrodes [16].

3.4.2. Active characterization

This section details the main optoelectronic characterization carried out in Er-doped slot waveguides.

- **Electrode characterization**

Top and bottom electrodes were first characterized using the above described test waveguides (see figure 3.4). In particular, the I-V characteristic and the electrode resistivity will be evaluated. For that, we will measure the I-V curve of all test waveguides.

In order to characterize the bottom electrode, devices were swept from *0* to *1 V* while measuring the injected current. The I-V characteristic presented a nearly ohmic behavior with a constant resistivity. The electrode resistivity can be correlated with the electrode resistance, the area of electron injection and the device length by equation 3.10:

$$RS = \rho L \tag{3.10}$$

Therefore, a linear trend should be observed when plotting the R·S product as a function of the device length. Figure 3.10 (a) depicts this figure of merit. A value of $\rho \sim 4\ m\Omega\cdot cm$ was obtained from the linear data fit. Notice that this value is very close to the one commonly reported in boron-doped silicon for a concentration of 10^{19} cm^{-3} ($\rho \sim 9\ m\Omega\cdot cm$) [17]. Despite the fact that a doping gradient was desired at the the bottom Si pedestal, electrical measurements rather suggest a homogeneous doping of the bottom electrode since very low resistivity values were obtained. This fact further confirms our hypothesis on the measured propagation losses since high carrier absorption takes place at the bottom Si pedestal.

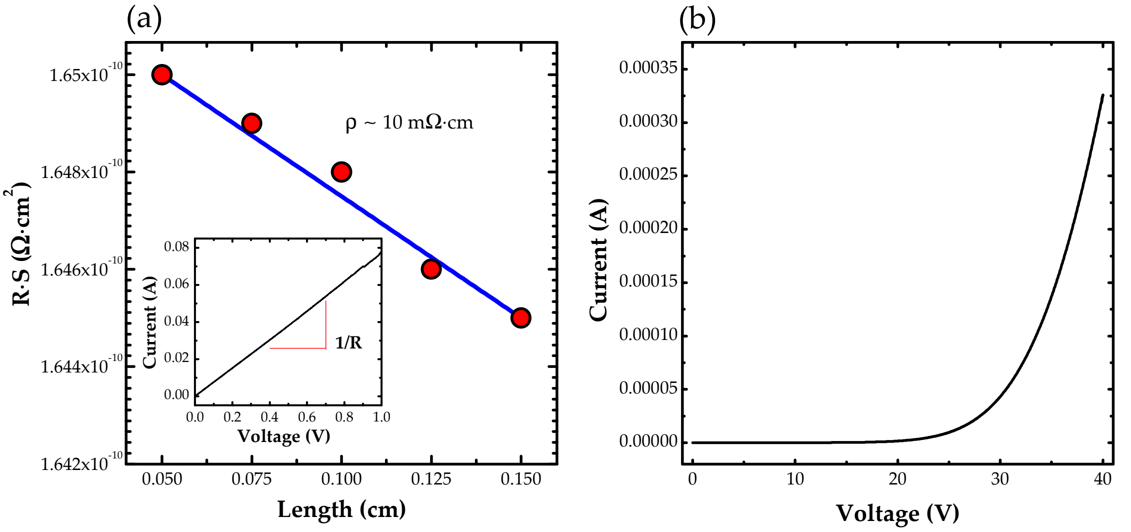

Figure 3.10. (a) R·S product of the bottom electrode as a function of the device length. The resistivity of the material is obtained from the slope of the fit directly (blue line), according to equation 3.10. Inset shows the I-V characteristic of a single electrode. (b) I-V characteristic of the top electrode.

Similarly, the top polysilicon electrode was characterized. This time, however, a rectifying behavior was obtained. High resistivity was measured in comparison with the bottom electrode. As a consequence, a voltage sweep from 0 to 40 V was performed in this case. The I-V curve is shown in figure 3.10 (b). Such trend indicates that the electrode resistivity varies with the voltage. This fact is in good agreement with the typical electrical response of a non-doped polysilicon layer [18]. *Paper XI* further insights on the electrical properties of the top polysilicon electrode, displaying the variation of the resistivity with the injected current density for both test waveguides (Er:Si-ncs and Er:SiO_2). In addition, a compact modeling of the electrical injection was carried out, suggesting a charge transport mechanism mainly governed by thermionic emission of electrons over the polysilicon grain boundaries. A mean potential barrier height of $\varphi_b \sim$ 0.4 eV and a grain size of $\langle a \rangle \sim$ 15 nm were extracted, in agreement with the accepted values. Moreover, a TEM characterization was performed to determine the average polysilicon grain size and thus validate the modeling of the electrical characteristic. Figure 3.11 shows a set of images taken in diffracting condition. As seen, polysilicon grain sizes expand from 10 nm up to 50 nm approximately, in accordance with the value extracted from the fitting of the I-V curve.

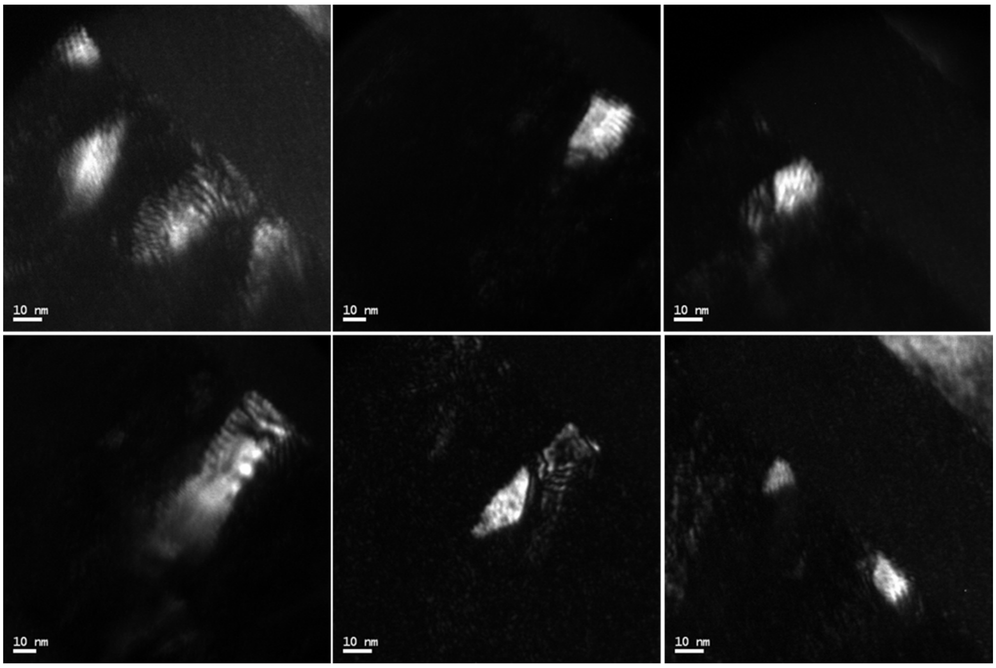

Figure 3.11. Dark field TEM images of the polysilicon electrode showing the corresponding grains in diffracting conditions. Grain size varies from 10 nm to 50 nm.

The study of the main electrical features of bottom and top electrodes by means of test waveguides has allowed identifying inherent peculiarities of the injecting electrodes. Some of them, such as the heavily doped Si pedestal, have been attributed to a non-optimized (and complex) fabrication process. Others, such as the top polysilicon electrode, have been accurately developed according to the preliminary design (with a non-doped region), and consequently have been characterized to further understand the electrode injection in the slot.

Next part will provide details on the electron injection and main transport in Er-doped Si-ncs (and SiO_2) Si slot waveguides.

- **Charge transport in the slot active layer**

Similarly than in the previous section, we will depart from the I-V characteristic to investigate the main transport mechanisms that govern charge flow in the slot. For that, slot waveguides were biased under a DC voltage sweep from 0 V up to close the device breakdown (~ 50-55 V).[14] *Paper XI* details the main results of this study. Mainly, the study is in good agreement with previously studied Er-doped MIS devices. Therefore, FNT of

---

[14] *It is worth to remark that all the voltages (or electric fields) displayed in paper XI are absolute values. The reader should recall that a negative voltage is applied over the top electrode to bias the slot waveguides, hence operating as the previously studied MIS light emitting devices.*

hot electrons injected from the top polysilicon electrode (chapter 2, section 2.1) was identified as the dominant charge transport mechanism over a range of ~ 6-11 MV·cm^{-1} (~ 25-50 V). In addition, higher effective barrier height was measured for the Er:SiO$_2$ slot compared to the Er:Si-ncs (1.9 eV versus 1.1 eV). Although this number is lower than what is normally expected from an Er-doped SiO$_2$ (or a SiO$_x$) with similar morphology (~ 3 eV and ~ 2 eV, respectively) (see previous chapter), it is reasonable assuming that charge injection in the slot is preceded by the transport mechanism that takes place in the top polysilicon electrode, i.e. the thermionic emission. Therefore, injected electrons in the slot already have a non-null energy value when they reach the electrode-active layer interface, as they previously had to overcome the potential barriers of the polysilicon grain boundaries. Such concatenated charge transport phenomena dominates the stationary injection ratio in the slot waveguides.

Another useful technique that is often performed when studying optoelectronic devices is the constant current stress (CCS) [19]. This measurement provides additional useful information about the charge trapping dynamics upon constant current injection. Thus, a current density of 0.05 A/cm^2 was defined in both slot waveguides, and the voltage monitored as a function of time. As seen in figure 3.12 (a), devices increased the driving voltage over time, suggesting that progressive negative charge trapping was taking place in both active layers. Bearing in mind that FNT is mainly dominated by electrons injected from the top polysilicon electrode by the action of a negative applied voltage, some of these charges will get trapped inside the dielectric slot layer. As a consequence, a screening effect is produced, reducing the overall injected current density in the dielectric layer. Nevertheless, as the current density was previously set at a fixed value, an increase of the applied voltage is carried out by the driving software in order to guarantee the same injection current density. This effect will inevitably end with the device breakdown once the applied voltage surpasses the breakdown limit. Interestingly, the effect of Si-ncs is clearly observed in this case, since lower charge trapping occurs in the Er-doped Si-ncs slot waveguide. After a stress cycle of 150 seconds, the Er:Si-ncs slot waveguide increases the driving voltage around of ΔV ~ 2 V, whereas the Er:SiO$_2$ slot waveguide has an approximate voltage drift of ΔV ~ 4 V. Moreover, a linear fit of the V-t characteristic allows devising the voltage drift per second (assuming a linear voltage increase), being 0.004 V/sec for the Er:Si-ncs slot waveguide and three times higher for the Er:SiO$_2$ slot waveguide, i.e. 0.012 V/sec. This ratio can be converted to number of trapped electrons per second by using the following relation:

$$|\Delta V| \approx \left|\frac{Q}{C_i}\right| \approx \left|\frac{\# e^- \cdot e}{C_i}\right| \qquad (3.11)$$

Where $\#e^-$ is the number of trapped electrons, e is the elementary charge and C_i is the slot layer capacitance, which can be directly extracted from C-V measurements at low frequency [1]. A similar value of C_i was obtained in both waveguides, in the order of pF (see figure 3.12). Thus, the number of trapped electrons per second in each device:

$$\left.\frac{\# e^-}{sec}\right|_{Er:Si-ncs} \approx \left|\frac{C_i \cdot \Delta V}{e}\right| \approx \left|\frac{11.2 \cdot 10^{-12} \cdot 0.004}{1.6 \cdot 10^{-19}}\right| \approx 28 \cdot 10^4 \, {}^{e^-}\!\!/_{sec} \tag{3.12}$$

$$\left.\frac{\# e^-}{sec}\right|_{Er:Si-ncs} \approx \left|\frac{C_i \cdot \Delta V}{e}\right| \approx \left|\frac{11.2 \cdot 10^{-12} \cdot 0.012}{1.6 \cdot 10^{-19}}\right| \approx 84 \cdot 10^4 \, {}^{e^-}\!\!/_{sec} \tag{3.13}$$

Another important parameter to inspect is the time-to-breakdown (t_{BD}). Equally than for the charge trapping rate, an estimation can be carried out from the experimental slope obtained in figure 3.12 (a). Assuming a maximum breakdown voltage of $|V_{BD}| \sim 50$ V in both cases, t_{BD} will be calculated departing from an initial driving voltage ($|V_{ini}|$) of 41 V for the Er:SiO$_2$ slot waveguide and 37.5 V for the Er:Si-ncs slot waveguide (roughly coinciding with the beginning of the linear regime in figure 3.12 (a)):

$$t_{BD}(Er : SiO_2) \approx \frac{|V_{BD} - V_{ini}|}{0.012 \, {}^{V}\!/_{sec}} \approx 750\, sec \tag{3.14}$$

$$t_{BD}(Er : Si - ncs) \approx \frac{|V_{BD} - V_{ini}|}{0.004 \, {}^{V}\!/_{sec}} \approx 3125\, sec \tag{3.15}$$

Thus, the Er:SiO$_2$ device will reach the breakdown limit after ~ 750 seconds (~ 12.5 minutes) for this particular current density, whereas the Er:Si-ncs slot waveguide will last ~ 3125 seconds (~ 52 minutes).

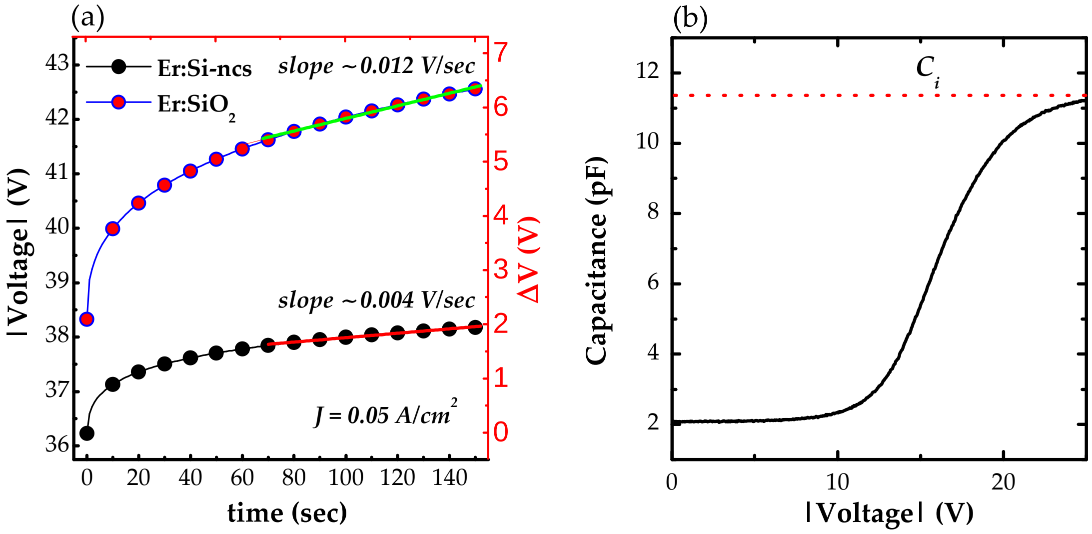

Figure 3.12. (a) V-t characteristic of electrically pumped Si slot waveguides containing either a stoichiometric Er-doped SiO$_2$ slot layer (black dots) or an Er-doped SiO$_2$ layer containing Si-ncs (red dots). (b) C-V curve measured at 1 kHz. The approximate value of C_i is marked with a red dotted line.

Summarizing, the most relevant electrical features of Er-doped slot waveguides have been revisited. Electrode injectors have been studied, and their main deviations from the theoretical behavior discussed. Also, the main charge transport mechanism in the active layer has been identified, finding some singularities that have been correlated with the particular morphology of the top polysilicon electrode. Finally, a singular charge trapping characterization has been accomplished over the V-t characteristic when devices are driven at a constant current density.

Next part will focus on the EL emission and on the electrical-to-optical conversion of slot waveguides.

- **EL and output power quantification under DC polarization**

Er-doped slot waveguides showed an EL feature at 1.54 μm upon external polarization. Injected electrons excited Er^{3+} ions via direct impact excitation. *Papers XI* and *XII* summarize the most relevant points of this study. Mainly, an EL threshold voltage of V_{th} ~ 25-30 V (6~ 7 MV/cm) was observed in both waveguides. This value is in well agreement with the hot electron injection by FNT in oxide materials, since at least 5 MV/cm are needed to efficiently inject electrons in the SiO_2 conduction band. An infrared EL spectrum similar to the one obtained in Er-doped MIS devices was measured from the output coupler, validating the Er^{3+} excitation in slot waveguides. Nevertheless, an additional test was required to demonstrate that generated EL signal was guided through the passive photonic circuit and out-coupled to the measurement unit. Being the collection system a Mitutoyo objective with NA = 0.4 placed on top of the output coupler and considering that the top polysilicon electrode is semitransparent for the transmitted wavelength, one may doubt on the origin of the detected light. In spite of the fact that the output coupler is far away from the edge of the polysilicon electrode (800 μm), the large area of detection (the objective field of view is 1 mm in diameter) may induce to question if whether the emission comes from a guided EL through the passive circuit or from the scattered light that escapes from the top electrode. Thus, the emitted EL spectrum was collected from either the top of the waveguide or from the output coupler. Results revealed a clear difference in the spectrum due to a different transmittance between the polysilicon and the output coupler (compare figure 2.26 in the previous chapter and figure 7 of *paper X*). Such divergences in the spectrum line shape clearly demonstrate that collected EL signal from the output coupler comes from a successful mode confinement and guidance through the passive circuit and not from the scattered EL that escapes from the top polysilicon electrode.

Once the origin of the collected EL at the output coupler is verified, an interesting figure of merit can be drawn when representing the total emitted optical power as a function of the injected current density (see *paper XI*). A maximum output power of tens of $\mu W/cm^2$ was measured in both waveguides. Remarkably, an unprecedented trend was disclosed. In particular, the optical power experienced a super-linear increase with the injected current density. Such fact is not typical from Er-doped MIS devices, where a sub-linear (or linear) behavior is normally reported. Moreover, bearing in mind that a super-linear behavior in the EL-J characteristic is normally observed when operating under amplified stimulated emission (ASE) conditions, one could think of a similar physical effect in our slot waveguides. However, the same trend was detected when placing the objective on top of the polysilicon electrode, pointing out that such behavior cannot be due to an optical amplification of the guided optical mode. Instead, it is believed to be caused by an inhomogeneous carrier injection in the active layer as a consequence of the non-doped polysilicon electrode. This particular behavior of the EL-J characteristic is highly reproducible in all slot waveguides, regardless of the waveguide length or width. *Paper XIII* shows complimentary EL-I measurements in various waveguides lengths, obtaining a super-linear slope in all cases.

Noteworthy, a similar optical power intensity was obtained from either top of the waveguide or the output coupler (i.e. tens of μW/cm^2). Such fact can be used to roughly estimate the percentage of guided optical power into the passive waveguide with respect to the totally generated optical power inside the active layer. In previous chapters I already provided a comprehensive development to calculate the fraction of emitted optical power into free space with respect to the totally generated optical power (defined as P_{opt}, see section 2.5), obtaining that around of 6% of the generated power was able to be transmitted through the polycrystalline silicon electrode. Similarly, this number can be applied in the present case, since the top waveguide electrode is very similar to the one used for uncoated Er-doped MIS devices. Moreover, as both collected optical power values are very similar in the slot waveguide (i.e. the top and guided optical power), it is reasonable to assume that only the 6% of the total generated power in the Er-doped slot waveguide has been successfully guided through the passive waveguide and collected by the measurement unit at the output coupler.

Another interesting result came up when studying the total emitted optical power as a function of both the waveguide width and length. Similarly than in the previous case, a super-linear evolution of the optical power was revealed in the first case comparing three different widths: 300 nm, 500 nm and 1 μm. This time, though, such super-linearity was not ascribed to the polysilicon electrode but to a different mode confinement in the slot layer. Being the width of 1 μm the optimum one for monomodal mode confinement at 1.54 μm, the further reduction in width will negatively influence the mode confinement, decreasing the collected power at the output coupler. With regard to the dependence of the output power as a function of the waveguide length, no remarkable differences were found. Therefore, all waveguides, regardless of their length, showed a very similar output power intensity. This fact can be explained by assuming the high propagation losses that the EL signal has to go through under bias polarization. Considering that passive propagation losses are already 40 dB/cm, an extra source of losses dominated by carrier absorption is triggered when the driving voltage is on. These losses would efficiently absorb part of the propagating EL mode in its way towards the passive circuit, decreasing the transmitted optical power at the end of the photonic chip. Last figure of *papers XI, XII* and *XIII* describes this situation making use of an electrical pump-and-probe configuration, and provides a first quantification of carrier absorption losses (further details on electrical pump-and-probe measurements will be provided in the next section). A maximum carrier absorption loss of 60 dB/cm was reported. Therefore, this value should be added to passive propagation losses, obtaining a maximum signal attenuation of 100 dB/cm when the driving voltage is on. In other words, photons generated at the opposite edge of a 1 mm long Er-doped slot waveguide will propagate through the entire waveguide before being collected and consequently will experience a loss factor of 10 dB. This means that only the 10% of the total generated emission coming from the opposite side will not be absorbed. Because of this, longer waveguides will only show marginal improvement on the emitted optical power since most of the generated light will be absorbed before reaching the output coupler.

Thus, a maximum emitted power of tens of pW can be transmitted into the passive optical circuitry. Although this number is still low, it is not far from the minimum optical power needed by an integrated photodiode. For instance, K. K. Mehta and co-workers reported outstanding sensing properties in polycrystalline silicon ring resonator photodiodes entirely fabricated in a CMOS line [20]. In this case, propagated light was confined in the intrinsic region of a p+/p/i/n/n+ diode. Dark currents as low as 50 pA were presented, with quantum efficiency (QE) values of 20%, calculated with the following formula:

$$QE = \frac{I(\lambda)}{P_{in}} \frac{h\upsilon}{e} \tag{3.16}$$

Where $I(\lambda)$ is the maximum photocurrent around the resonance and P_{in} is the input coupled power.

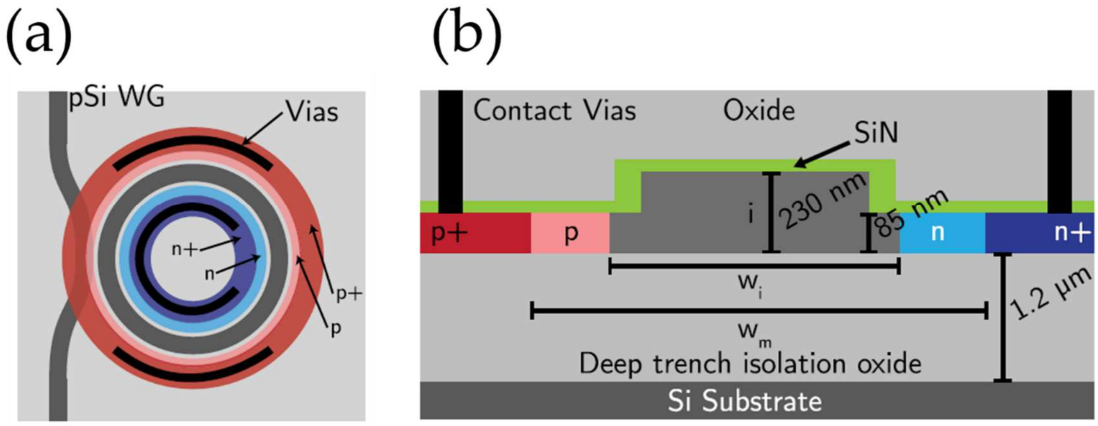

Figure 3.13. Top (a) and cross-section (b) schemes of a ring-resonator based photodetector. Images were extracted from ref. 20.

Therefore, assuming an eventual integration between our Er-doped slot waveguides and the above described Si photodetector, a guided optical power of 20 pW at 1.54 μm would be launched towards the photodetector. Thus, a value of I(λ) = 5 pA would be obtained using equation 3.16. This number, although being below the minimum current required to obtain a measurable signal in the photodiode (I(λ) > 50 pA), it is promising taking into account the room for improvement of our slot waveguides, especially concerning propagation losses and the presumably low fraction of collected optical power with respect to the totally generated optical power in the active layer. In addition, one has to bear in mind that the above described slot waveguides present two opposed output ports and therefore the optical power of the guided mode is split in two different modes, each one transmitted in an opposed direction. In spite of the fact that this configuration may be advantageous in some particular cases (for instance, in waveguide division multiplexing systems), for other applications it is not desired. Two suitable solutions can be engineered to solve this drawback: (i) the implementation of a mirror-like facet at one side of the waveguide, or (ii) the convergence of the passive optical circuitry in one single bus waveguide. The first option seems unlikely if propagation losses are not drastically reduced first, since reflected photons at the waveguide facet would have been guided through a much longer optical path (as long as twice the waveguide length in the worst case scenario). Therefore, the implementation of this new design is conditioned by an effective reduction of the propagation losses. However, this task may be tedious since several aspects must be addressed first, starting from the optimization of the device design, a more accurate fabrication process or an optimum active layer deposition.

Another alternative that only requires marginal design modification of the passive optical circuit is to joint both waveguide output ports together into one single bus waveguide. In this case however, special care should be taken with bending losses.

- **Electrical pump-and-probe measurements under pulsed voltage polarization**

Finally, an electrical pump-and-probe characterization was carried out to further insight into the optoelectronic properties of slot waveguides. Two different configurations were tackled: (i) a time-resolved approach and (ii) a locked-in amplifier technique to sort out the signal enhancement of the system.

The time-resolved configuration has allowed obtaining interesting features of slot waveguides. The experimental set-up used for this batch of measurements can be revisited in *paper XII*. Er-doped slot waveguides were electrically driven by a pulsed polarization with $|V_{on}| > |V_{th}|$ and $|V_{off}| = 0$ V while simultaneously collecting the guided EL signal at the maximum Er^{3+} emission (1528 nm in this case). Remarkably, a sharp EL overshoot was observed at the voltage switch off, correlated with the fast suppression of carrier absorption in slot waveguides. Upon DC voltage excitation, Er-doped slot waveguides present two competing mechanisms: the Er^{3+} EL and the carrier absorption. As a consequence, an EL signal modulated by CA losses is collected at the output. Nevertheless, since injected carriers recombine much faster than the Er^{3+} decay time (at least two orders of magnitude), there is a narrow time frame after the voltage switch off in which no injected carriers are present in the structure while a significant percentage of Er^{3+} ions is still in the excited state. Therefore, the EL emission from these ions would not be affected by carrier absorption losses, displaying an enhanced EL intensity. This effect was observed in the two Er-doped slot waveguides under study (Er:SiO_2 and Er:Si-ncs) for all waveguide lengths and widths. Also, the EL overshoot was only observed in the guided EL emission and not in the scattered EL collected from the top of the waveguide. Whereas CA in the guided EL takes place along the entire waveguide length (1 mm at least), the scattered EL is only affected by CA during few tens of nanometers at most (the active layer thickness and the polysilicon thickness). Noteworthy, I shall remark the differences between this effect and the one observed in time-resolved EL measurements of Si-ncs under pulsed polarization (see figure 3.22 in chapter 3). Whereas the Si-ncs EL overshoot was mainly dominated by auger quenching phenomena inside Si-ncs containing e-h pairs, the Er^{3+} EL overshoot here observed is rather caused by a carrier absorption process in which emitted radiation is rapidly absorbed by free electrons in the active layer conduction band.

In addition, the influence of Si-ncs was clearly evidenced in Er:Si-ncs slot waveguides, as they presented a less pronounced EL overshoot as a consequence of the enhanced charge trapping inside Si-ncs. In fact a first order quantification of the EL overshoot was performed, obtaining an EL enhancement of 25% for the Er:SiO_2 slot waveguide (15% for the Er:Si-ncs slot waveguide) with regard to the EL value under DC polarization. Therefore, it seems reasonable to assume that net optical gain at 1.54 μm, if any, must take place during this narrow time window in which carriers are suppressed but Er^{3+} ions are still excited. As a consequence, a study of the EL overshoot signal as a function of the injected current density was carried out. If optical gain dominates the EL overshoot, higher slope in the EL-J characteristic should be observed compared to the one obtained from the DC EL value. Nevertheless, no such effect was observed, obtaining similar trends for both the EL overshoot and the DC EL (slopes of ~ 2.6 and ~ 2.7 were measured, respectively). *Papers XI, XII* and *XIII* provide further details on the time-resolved characterization of Er-doped slot waveguides under pulsed voltage polarization.

Subsequently, a small CW probe signal at ~ 1.53 μm was introduced in slot waveguides driven by a pulsed polarization to further certify the absence of optical amplification. For that, a power comparable to the one provided by the EL signal was defined to avoid strong modification of level population. Results are summarized in *paper XII*. Mainly, a time-resolved feature with the probe signal superimposed to the EL emission was observed. Again, no evident optical amplification of the probe signal was measured.

Moreover, an alternative experiment was performed combining lock-in amplifier techniques with time-resolved measurements. This time, however, the probe signal was modulated at a different frequency value than the voltage source (200 kHz for the probe and 10 Hz for the pulsed polarization). Thus, a lock-in amplifier was used to lock the probe signal while measuring its temporal variation at the driving frequency of the voltage polarization (10 Hz). This configuration allows a complete filtering of the EL signal directly. A maximum probe transmittance of -60 dB/cm was obtained when V_{on} = |45 V|. However, no optical gain was detected irrespective of the amplitude of the polarization voltage in a wide range of wavelengths (from 1515 nm to 1540 nm). Also, a thermal effect was identified as a consequence of the high driving voltage applied on devices. In particular, a clear saturation of the modulation depth was observed for driving voltages of |25| V and beyond. Such value roughly coincides with the onset of FNT, suggesting that both mechanisms are well-correlated.

An illustrative example of the measured time-resolved probe signal transmittance in this new set-up configuration is shown in figure 3.14. In addition the expected probe signal shape that would have been observed if an optical amplification regime had been triggered at the voltage switch off is also drawn for comparison. Thus, a sharp signal overshoot is expected in the probe transmittance when the voltage is switched off. The observation of such feature would unambiguously validate the existence of a transitory optical amplification of the probe signal in absence of CA losses.

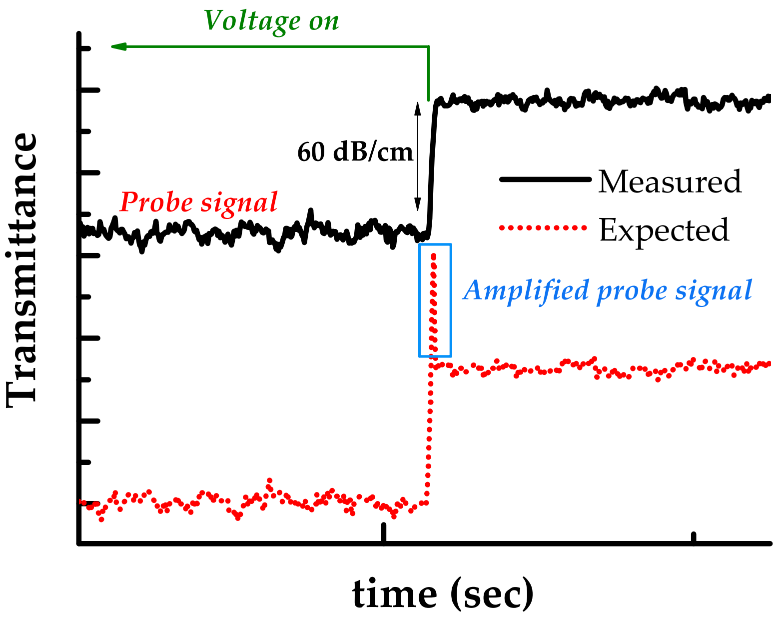

Figure 3.14. Comparison between the measured time-resolved probe signal transmittance at 1.53 μm (black solid line) and the expected (ideal) temporal behavior of a probe signal transmittance with an Er-doped gain media. The amplified transitory probe signal is highlighted by a blue circle.

Despite the lack of optical amplification in slot waveguides, they still show other interesting characteristics such as the fact that high modulation depths can be obtained, up to 75%. In addition, wide modulation bandwidth has been demonstrated (> 25 nm) and also a competitive DC power consumption of about 120 μW, which makes them attractive for other applications such as integrated modulators. *Paper XII* (last page, before conclusions) provides a comprehensive description of the main advantages of these devices and compare their optoelectronic performance with the one of several outstanding works in the literature. Finally, some hints to improve the current optoelectronic performance of Er-doped slot waveguides are described.

In view of the good modulation properties displayed, a coupled system of two concatenated slot waveguides could be engineered to develop a modulated light emission signal. Interestingly, both devices (the light emitter and the modulator) could be simultaneously fabricated in a mainstream CMOS line with marginal variation of the processing steps between them (only the light emitting device needs an Er implantation). Slot waveguides would be electrically isolated from each other to enable different driving polarizations, then both coupled to a functionalized optical link to build a photonic sensor chip. An integrated photodetector could be designed at the end of the photonic circuit. Figure 3.15 shows a scheme of the integrated system together with the working principle of devices. Several advantages are envisaged with this design, such as the fact that no external coupling from a bulky laser source is required, or the competitive low cost-per-chip provided due to their compatibility with the CMOS technology. Again, this design is subjected to a considerable improvement of the EL optical power, since transmitted emission would travel along a relatively long distance (as much as twice the length of a single slot waveguide).

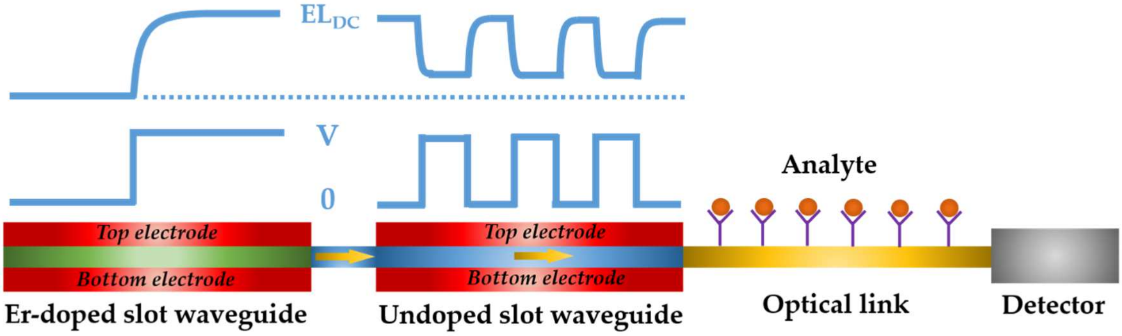

Figure 3.15. Top schematic view of the proposed integrated optical sensor chip using Er-doped and undoped slot waveguides. The polarization scheme of each device is illustrated along with the expected amplitude line shape of the guided EL signal.

3.5. Summary and outlook

The development and characterization of an integrated photonic circuit composed by a passive bus waveguide coupled to an Er-doped light emitting slot waveguide operating at 1.54 μm has been accomplished. A winged asymmetric waveguide cross-section was carefully designed to fulfill the optical and electrical constraints of the system. Two different Er-implanted oxide layers (an HTO and a SiO_x layer) have been deposited in the slot and used as active layers. The most important closing remarks of this work are:

- ✓ The fabrication process was successfully carried out in spite of the fact that several technological challenges were tackled. Good TM mode confinement was obtained from cleaved slot waveguides.
- ✓ Output couplers showed an optimum coupling angle of 25°, and a spectral transmittance with a maximum around of 1535 nm.
- ✓ High propagation losses of about ~ 40 dB/cm and coupling losses of ~ 20 dB were measured in both waveguides, suggesting that Si-ncs have a marginal contribution on the propagation losses.
- ✓ Despite that a gradient doping profile was desired at the bottom waveguide cladding (Si pedestal), most probably a uniform doping was finally obtained since an ohmic-like I-V characteristic with a constant resistivity of 4 mΩ·cm was measured at the bottom electrode.
- ✓ The lightly doped top waveguide cladding (top injecting polysilicon electrode) presented an expected charge transport mechanism dominated by thermionic emission that influences carrier injection into the active slot material.
- ✓ The electrical characterization of Er-doped Si slot waveguides denoted a charge transport in the active layer governed by FNT. The potential barrier height for injection was substantially reduced by the effect of Si-ncs and also by the preceding thermionic emission in the polysilicon electrode, as expected.
- ✓ The Er-doped slot waveguide containing Si-ncs presented lower charge trapping over time than the device free of Si-ncs, around of 4 times lower.
- ✓ A maximum output coupled power of tens of $\mu W/cm^2$ was measured in all waveguides regardless of the waveguide length, and also a super-linear trend in the EL-J characteristic, attributed to an inhomogeneous carrier injection from the top polysilicon electrode (top cladding).
- ✓ A rough estimation of the percentage of the out-coupled emission was done, obtaining that only the 6% of the totally generated radiation is successfully guided and extracted.

- ✓ Time-resolved measurements of the guided EL signal allowed identifying an interesting EL overshoot at the voltage switch off in all Er-doped waveguides, attributed to a much faster suppression of carrier absorption losses than the Er^{3+} radiative de-excitation.

- ✓ An electrical pump-and-probe in time-resolved configuration was performed by filtering out the contribution of the EL emission. The probe signal enhancement was tested at different voltages and current density values, obtaining no optical amplification and a strong transmittance attenuation up to -60 dB/cm.

- ✓ Er-doped slot waveguides showed a modulation depth of 75% and a DC power consumption of 120 μW which makes them suitable devices as integrated modulators.

3.6. List of references

[1] Rebohle, L., & Skorupa, W. (2010). *Rare-earth implanted MOS devices for silicon photonics: microstructural, electrical and optoelectronic properties* (Vol. 142). Springer Science & Business Media.

[2] Iacona, F., Irrera, A., Franzo, G., Pacifici, D., Crupi, I., Miritello, M., ... & Priolo, F. (2006). “Silicon-based light-emitting devices: properties and applications of crystalline, amorphous and Er-doped nanoclusters.” *Selected Topics in Quantum Electronics, IEEE Journal of, 12*(6), 1596-1606.

[3] Ramírez, J. M., Lupi, F. F., Jambois, O., Navarro-Urrios, D., Anopchenko, A., Marconi, A., Prtljaga, N., ... & Garrido, B. (2012). “Erbium emission in MOS light emitting devices: from energy transfer to direct impact excitation.” *Nanotechnology,23*(12), 125203.

[4] Coffa, S., Franzo, G., & Priolo, F. (1998). “Light emission from Er-doped Si: materials properties, mechanisms, and device performance.” *MRS bulletin,23*(04), 25-32.

[5] Preston, K., & Lipson, M. (2009). “Slot waveguides with polycrystalline silicon for electrical injection.” *Optics express*, *17*(3), 1527-1534.

[6] Miller, G. M., Briggs, R. M., & Atwater, H. A. (2010). “Achieving optical gain in waveguide-confined nanocluster-sensitized erbium by pulsed excitation.” *Journal of Applied Physics*, *108*(6), 063109.

[7] Jayatilleka, H., Nasrollahy-Shiraz, A., & Kenyon, A. J. (2011). “Electrically pumped silicon waveguide light sources.” *Optics express*, *19*(24), 24569-24576.

[8] Germer, S., Cherkouk, C., Rebohle, L., Helm, M., & Skorupa, W. (2013, May). “Si-based light emitter in an integrated photonic circuit for smart biosensor applications.” In *SPIE Microtechnologies* (pp. 876710-876710). International Society for Optics and Photonics.

[9] Juvert Sández, J. (2014). “Development and optimization of silicon based light sources for integration into a sensor platform.” Ph.D dissertation.

[10] González Fernández, A. A. (2014). “Studies and integration of Silicon-based light emitting systems.” Ph.D dissertation.

[11] Almeida, V. R., Xu, Q., Barrios, C. A., & Lipson, M. (2004). “Guiding and confining light in void nanostructure.” *Optics letters*, *29*(11), 1209-1211.

[12] Kerker, M. (2013). *The Scattering of Light and Other Electromagnetic Radiation: Physical Chemistry: A Series of Monographs*. Academic press.

[13] Chuang, S. L. (1995). *Physics of optoelectronic devices.* John Wiley & Sons.

[14] Navarro-Urrios, D., Lupi, F. F., Prtljaga, N., Pitanti, A., Jambois, O., Ramírez, J. M., ... & Pavesi, L. (2011). “Copropagating pump and probe experiments on Si-

nc in SiO_2 rib waveguides doped with Er: The optical role of non-emitting ions." *Applied Physics Letters*, *99*(23), 231114.

[15] Daldosso, N., Melchiorri, M., Pavesi, L., Pucker, G., Gourbilleau, F., Chausserie, S., ... & Dufour, C. (2006). "Optical losses and absorption cross-section of silicon nanocrystals." *Journal of Luminescence*, *121*(2), 344-348.

[16] Liu, A., Jones, R., Liao, L., Samara-Rubio, D., Rubin, D., Cohen, O., ... & Paniccia, M. (2004). "A high-speed silicon optical modulator based on a metal–oxide–semiconductor capacitor." *Nature*, *427*(6975), 615-618.

[17] http://www.cleanroom.byu.edu/ResistivityCal.phtml.

[18] Rai-Choudhury, P., & Hower, P. L. (1973). "Growth and characterization of polycrystalline silicon." *Journal of The Electrochemical Society*, *120*(12), 1761-1766.

[19] Tomita, T., Utsunomiya, H., Sakura, T., Kamakura, Y., & Taniguchi, K. (1999). "A new soft breakdown model for thin thermal SiO_2 films under constant current stress." *Electron Devices, IEEE Transactions on*, *46*(1), 159-164.

[20] Mehta, K. K., Orcutt, J. S., Shainline, J. M., Tehar-Zahav, O., Sternberg, Z., Meade, R., ... & Ram, R. J. (2014). "Polycrystalline silicon ring resonator photodiodes in a bulk complementary metal-oxide-semiconductor process." *Optics letters*, *39*(4), 1061-1064.

JOURNAL OF LIGHTWAVE TECHNOLOGY, VOL. 31, NO. 3, FEBRUARY 1, 2013

Toward a 1.54 μm Electrically Driven Erbium-Doped Silicon Slot Waveguide and Optical Amplifier

A. Tengattini, D. Gandolfi, N. Prtljaga, A. Anopchenko, J. M. Ramírez, F. Ferrarese Lupi, Y. Berencén, D. Navarro-Urrios, P. Rivallin, K. Surana, B. Garrido, J.-M. Fedeli, and L. Pavesi

***Abstract*—In this paper, we report on the first attempt to design, fabricate, and test an on-chip optical amplifier which works at 1540 nm and can be electrically driven. It is based on an asymmetric silicon slot waveguide which embeds the active material. This is based on erbium-doped silicon rich silicon oxide. We describe the horizontal asymmetric slot waveguide design which allows us to get a high field confinement in a nanometer thick active layer. In addition, we detail the complex process needed to fabricate the structure. The waveguides have been characterized both electrically as well as optically. Electroluminescence can be excited by hot carrier injection, due to impact excitation of the Er ions. Propagation losses have been measured and high values have been found due to processing defects. Pump and probe measurements show a voltage dependent strong attenuation of the probe signal due to free carrier accumulation and absorption in the slot waveguide region. At the maximum electrical pumping level, electroluminescence signal is in the range of tens of μW/cm^2 and the overall loss of the device is only -6 dB. Despite not demonstrating optical amplification, this study shines some light on the path to achieve an all-silicon electrically driven optical amplifier.**

***Index Terms*—Electroluminescence (EL), erbium, horizontal slot waveguide, silicon photonics.**

I. INTRODUCTION

ERBIUM (Er^{3+})-doped silicon-rich-oxide (SRO) films offer a promising material platform for the development of compact waveguide amplifiers and lasers [1], [2]. A particular advantage of this approach with respect to Er^{3+} in glass is given by the possibility of electrical excitation of Er^{3+} [3]. In order to have an efficient electrical injection, very thin films are required [4], [5]. In addition, multilayered SRO structures allow for bipolar direct tunneling [6]. Slot waveguides, where light confinement happens in a thin low refractive index layer sandwiched by two thick high refractive index material, emerge as a natural choice [7]–[9]. The slot geometry allows also for a straightforward electrical contact definition [4], [5], [10].

In this paper, we will present the design, the modeling, the fabrication, and the characterization of slot waveguides for electrically pumped waveguide amplifiers based on erbium-doped material. These have been fabricated in a standard complementary metal–oxide semiconductor (CMOS) fab line.

II. DESIGN AND SIMULATION

There are two possible slot orientations that could be considered for the realization of a slot waveguide-based amplifier: vertical and horizontal [4], [11]. In the vertical configuration, significant optical losses may be induced by slot wall roughness [4], [12]. Although significant progresses have been made recently [13], [14], multilayered material deposition on side walls remains a rather challenging task even by the conformal growth [12]. On the contrary, horizontal slot Er^{3+}-doped SRO structures, which might also consist of alternating layers of SRO and SiO$_2$ [15], are easier to deposit and process [17]. Therefore, in this study, we opt for a horizontal slot configuration. Clearly, field enhancement effects due to the slot waveguide geometry are observed for transverse magnetic TM polarization only.

While very precise control of device dimensions can be achieved by using electron beam lithography [12], optical lithography is preferred for industrial applications and mass production. Unfortunately, electrically driven devices have a very complex design, involving multiple lithographic patterning steps [16]. Thus, special attention has to be paid in order to relax optical alignment constrains between different mask levels.

Another relevant issue is the choice of the slot wall material. Monocrystalline silicon has superior electrical and optical properties but it cannot be grown in a CMOS process. It is only available as a substrate or device layer in silicon-on-insulator (SOI) wafers. Consequently, the top slot cladding or even the whole slot waveguide has to be deposited. Polycrystalline silicon (polysilicon) or amorphous silicon can be used [5], [17], polysilicon being better suited for electrically injection devices due to a better electrical mobility [5]. This motivates our choice of a polycrystalline silicon top cladding.

Low optical losses in polysilicon can be achieved by long high temperature annealing in the presence of hydrogen [5]. However, this may be impractical as it may interfere with optimum thermal budget for Er^{3+}-doped SRO films and causes

---

Manuscript received August 22, 2012; revised November 26, 2012; accepted November 26, 2012. Date of publication November 30, 2012; date of current version December 31, 2012. This work was supported by the European Commission, through the Project ICTFP7-224312 HELIOS and by Italy–Spain integrated actions.

A. Tengattini, D. Gandolfi, N. Prtljaga, A. Anopchenko, and L. Pavesi are with the Nanoscience Laboratory, Department of Physics, University of Trento, 38123 Povo, Italy (e-mail: tengattini@science.unitn.it; d.gandolfi@science.unitn.it; nikolap@science.unitn.it; anopchenko@science.unitn.it; pavesi@science.unitn.it).

J. M. Ramírez, F. Ferrarese Lupi, Y. Berencén, and B. Garrido are with the Departament d'Electronica, Universitat de Barcelona, 08028 Barcelona, Spain (e-mail: jmramirez@el.ub.es; fferrarese@el.ub.es; yberencen@el.ub.es; bgarrido@el.ub.edu).

D. Navarro-Urrios was with the Departament d'Electronica, Universitat de Barcelona, 08028 Barcelona, Spain. He is now with the Catalan Institute of Nanotechnology, 08193 Bellaterra, Spain (e-mail: danielnavarrourrios@gmail.com).

P. Rivallin, K. Surana, and J.-M. Fedeli are with the CEA Grenoble, 38054 Grenoble Cedex, France (e-mail: pierre.mur@cea.fr; kavita.surana@cea.fr; jean-marc.fedeli@cea.fr).

Color versions of one or more of the figures in this paper are available online at http://ieeexplore.ieee.org.

Digital Object Identifier 10.1109/JLT.2012.2231050

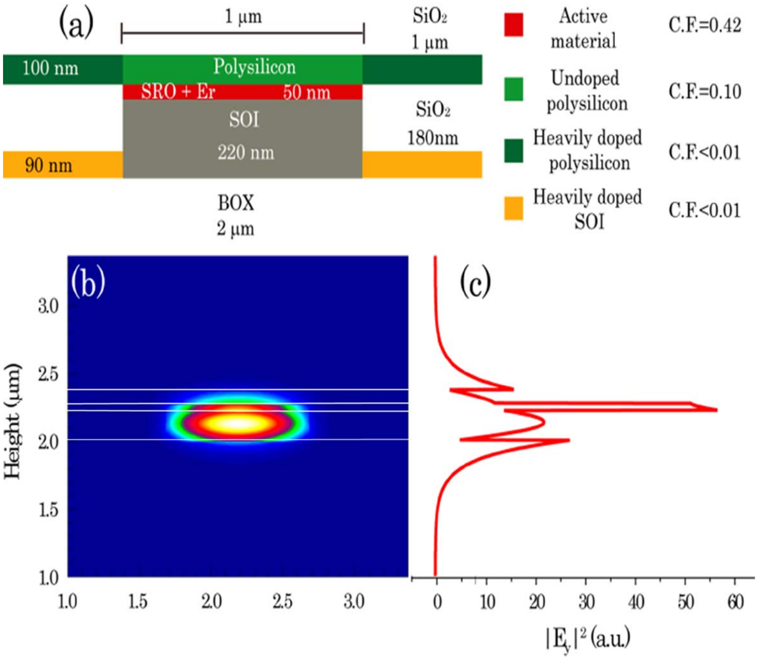

Fig. 1. (a) Schematic of the asymmetric slot waveguide for electrical injection. C.F. stands for confinement factor which gives the fraction of the optical electric field in the indicated area. (b) Intensity profile of the fundamental TM mode. (c) Vertical electric field profile of the fundamental optical TM mode.

dopant out-diffusion. Therefore, to reduce the optical losses, it is more convenient to minimize the fraction of the light guided in the polycrystalline part, while still maintaining a high fraction of field in the slot region. This can be achieved by an asymmetric geometry of the slot waveguide [see Fig. 1(a)]. The asymmetric geometry still allows for a large field fraction in the slot region while minimizing the field in the polysilicon top cladding layer [see Fig. 1(b) and (c)].

The slab character of the polycrystalline silicon top cladding allows for extremely easy lithographic patterning of electrodes since the top polysilicon width does not influence critically the optical waveguiding in the TM polarization.

The structure optimization (layer thicknesses) has been performed with a commercially available fully vectorial mode solver based on the film mode matching method (FIMWAVE, Photon Design). The whole structure is defined on commercially available SOI wafer with a 220 nm thick silicon layer on the top of a buried oxide (BOX) (2 μm thick). The active material thickness in the slot was fixed to 50 nm, an optimum value for a slot waveguide amplifier [18], [20] and a maximum value for which efficient electrical injection in multilayer samples has been demonstrated [3], [19]. Previous reports indicate a maximum Er modal gain of 2 dB/cm in a slot waveguide with 50 nm thick active material [20].

The waveguide width of 1 μm has been chosen in order to increase the active material volume. For this width, the fundamental TM mode displays high confinement in the slot region [see Fig. 1(a)], while the higher order modes exhibits high radiative losses and, practically, do not contribute to light propagation.

The thicknesses of the top cladding and bottom electrodes, which form side slabs named wings in the following, have been chosen in order to maintain good electrical conductivity while still inhibiting the mode leaking towards the wings [see Fig. 1(a) and (b)]. Moreover, as the optical field does not penetrate in wings, doping can be increased providing with good electrical contacts. Additionally, the slot parameters chosen for the fabrication are quite robust with respect to fabrication-induced variations, including the changes of active material thickness or refractive index (different silicon excess, thermal treatments; see Fig. 2).

III. EXPERIMENTAL DETAILS

A. Waveguides Processing

The waveguides have been fabricated on SOI wafers in a 200 mm CMOS pilot line of the CEA, Lèti. The schematics of the typical process flow are reported in Fig. 3. Commercially available SOI wafers with 220 nm of lightly doped p-type Silicon (Si) layer on a 2 μm thick BOX were used for device manufacturing. The device layer was implanted with boron to form a concentration gradient, with high concentration near the BOX and light doping in the proximity of the surface (10^{17}/cm^3).

The active layer with a thickness of 50 nm was grown on Si [see Fig. 3(a)]. It consists either of stoichiometric or non-stoichiometric (silicon rich) oxide. Stoichiometric silicon oxide was an high temperature oxide and was used as a reference sample. SRO was deposited by low-pressure chemical vapor deposition (LPCVD) in a multilayer sequence. A layer of 2 nm of silicon dioxide and a layer of 3 nm of SRO, with a nominal silicon content excess of 20%, were repeated ten times. The gases used are N_2O and silane, only the ratio changes for the SiO_2 and the SRO layers. For the SRO step, the time is 16 min and 30 s, with a ratio between the N_2O and the SiH_4 equal to 200/40 sccm, while for the oxide step, the time is 26 min and the ratio between the gases 960/40 sccm.

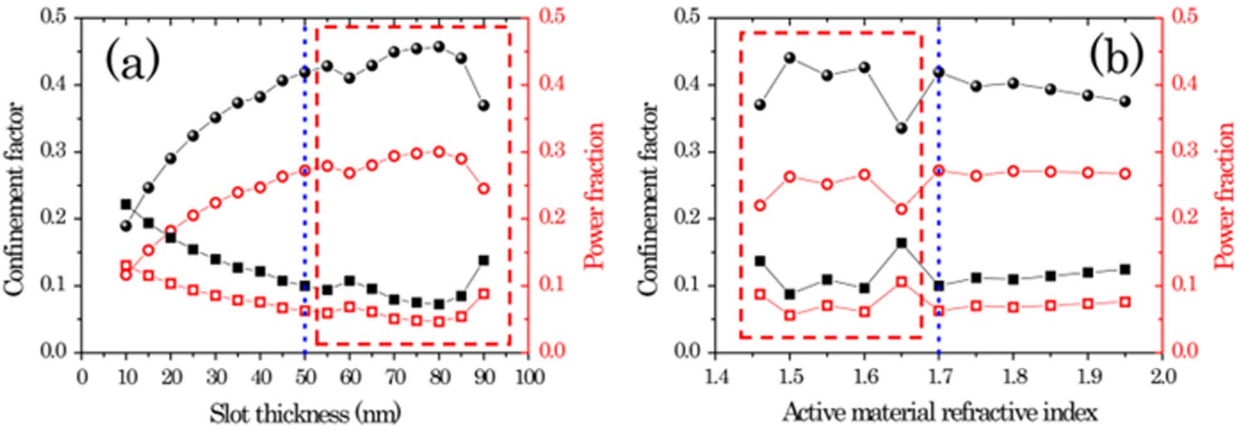

Fig. 2. Confinement factor (black full symbols) and power fraction (red empty symbols) of the fundamental TM mode in the slot region (circles) and polysilicon top cladding (squares) as a function of (a) active material thickness and (b) active material refractive index. Vertical blue-dotted line indicates nominal parameters. Red-dashed square indicates the range of parameters for which fundamental TM mode experiences additional radiative losses due to "leaking" toward the waveguides "wings."

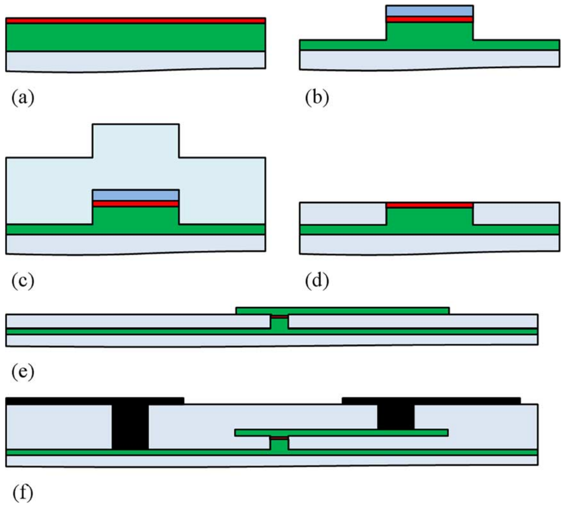

Fig. 3. Schematic overview of the processing steps for the realization of the Er^{3+}-doped electrically driven asymmetric horizontal slot waveguide. (a) Deposition on the lightly boron-doped SOI wafer (light blue—BOX, green—silicon layer) of the active layer (red—Er^{3+}-doped SRO or silica). (b) Waveguide definition by a partial 90 nm etch of the silicon layer on the BOX (the blue layer is a mask layer); (c) Bottom electrode in the wings are implanted with boron, while the mask layer protects the waveguide core; the whole structure is then covered with an oxide. (d) Excess silica and hard mask (blue) are removed in a CMP step. (e) Top polycrystalline silicon cladding is deposited and defined yielding the slot waveguide; (f) Vias openings and metal deposition define the metal contacts (black), for electrical injection in the slot waveguide.

A measured overall silicon content excess in the stack of 8.7% was determined *ex situ* by the X-ray photoelectron spectroscopy. The active layers were then annealed at 900 °C for 1 h. This thermal treatment promotes the phase separation and the silicon nanocluster formation in SRO active layer. TEM analysis shows a loss of layering in the annealed film. Erbium was finally introduced by ion implantation with a dose of $10^{15}/\text{cm}^2$ and energy of 20 keV. A peak Er^{3+} concentration of $\approx 3.5 \times 10^{20}/\text{cm}^3$ in the center of the active layer was determined by the secondary ion mass spectrometry. Erbium clustering was also observed. Additional details on the active layer morphology are reported in [21].

The waveguide has been defined by etching 90 nm of the silicon layer on the BOX [see Fig. 3(b)]. The waveguide formation is followed by boron implantation into the areas outside the slot region ("wings") and silicon dioxide deposition [see Fig. 3(c)]. The postimplantation annealing is performed at 800 °C for 6 h in order to activate both the Er^{3+} ions and the boron implant. Afterward, the hard mask on the top of the waveguide surface is removed in a chemical–mechanical polishing/planarization (CMP) steps [see Fig. 3(d)]. An undoped top polycrystalline silicon layer 116 nm thick is deposited by LPCVD at 620 °C [see Fig. 3(e)]. The top polysilicon layer is doped outside the slot area (wings) with phosphorus to an electron concentration of $10^{19}/\text{cm}^3$. A CMOS compatible Ti/TiN/AlCu metal stack is used for contacts [see Fig. 3(f)].

Fig. 4(a) shows the layout of the fabricated waveguides. The real thickness of the active layer is ≈40 nm. To couple the light in and out, the waveguides are ended with an adiabatic taper and a grating coupler. SEM images of cross section of the fabricated waveguide show that the initial design is reproduced in the fabrication [cf., Figs. 4(b) and 1(a)].

In the following, the waveguides containing the layer with the Er^{3+} ions in silica will be labeled as $Er{:}SiO_2$, while the ones with the silicon nanocrystals will be labeled as Er:Si-NCs.

B. Measurement Setup

The realized structures have been experimentally characterized, both electrically and optically. The whole setup has been built on a commercial probe station (Suss MicroTec PM8), where both optical and electrical probes have been used. The optical probes have been realized by using single-mode tapered fibers facing the gratings with the optimized input angle (spot diameter of 2.5 ± 0.3 μm at a working distance of 14 ± 2 μm). A photograph of the probes during a measurement is shown in Fig. 5.

The electrical analysis has been performed using a semiconductor device analyzer (Agilent B1500A). The connections to the device are achieved via triaxial cables, terminated with a sharp probe tip contacts. Optical characterization has been done using two different infrared tunable lasers (NetTest Tunics BT

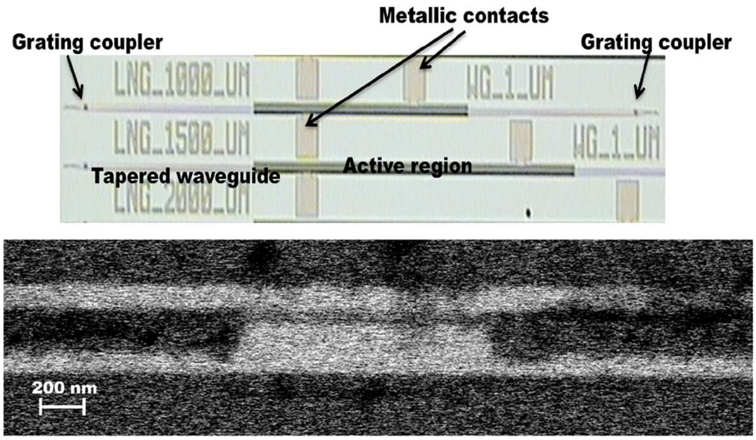

Fig. 4. (a) Top view optical image of the waveguides. Note that Er was implanted only in the region covered by the metal line (label active region). (b) SEM image of the fabricated waveguide cross-section. Dark and light regions correspond to silicon oxide and silicon, respectively.

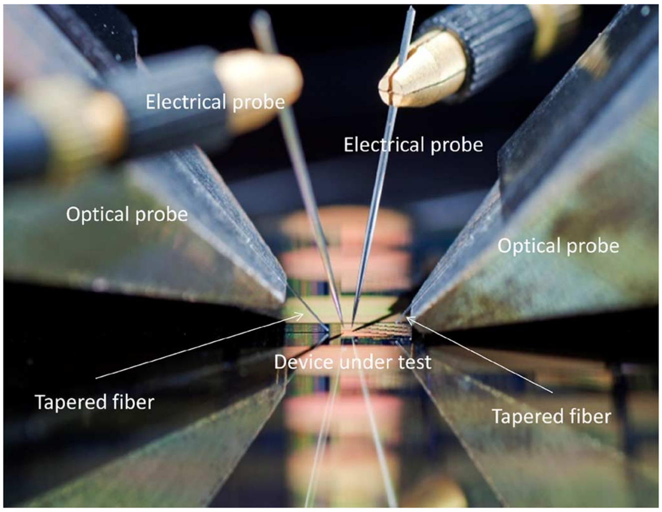

Fig. 5. Details of the experimental setup. The photograph shows a zoom on the measurement region, with the two probes for the electrical contacts and the two infrared tapered fibers for the optical signals.

or Santec TSL-210F). The transmitted signal is analyzed with an optical spectrum analyzer (OSA Anritsu MS9710B).

To measure electroluminescence (EL), a photon counting module (IdQuantique Id201) is used. As a vision system for alignment purposes, an infrared camera mounted on a microscope has been used.

IV. EXPERIMENTAL RESULTS AND DISCUSSION

A. *I–V Characteristics*

Current–voltage (*I–V*) characteristics show a rectifying behavior with a larger conductivity in the Er:Si-NCs waveguides. In forward bias, the silicon nanoclusters enhance the electrical conductivity, leading to higher currents for the same voltage bias (see Fig. 6). On the other hand, these high currents lead to a low breakdown voltage. In fact, while for the Er:Si-NCs waveguides the maximum voltage is around 40 V, for the Er:SiO_2 devices higher voltage (up to 48 V) can be applied without breaking the device. Similar behaviors have been already observed in light-emitting diodes with the same active material [22], [23].

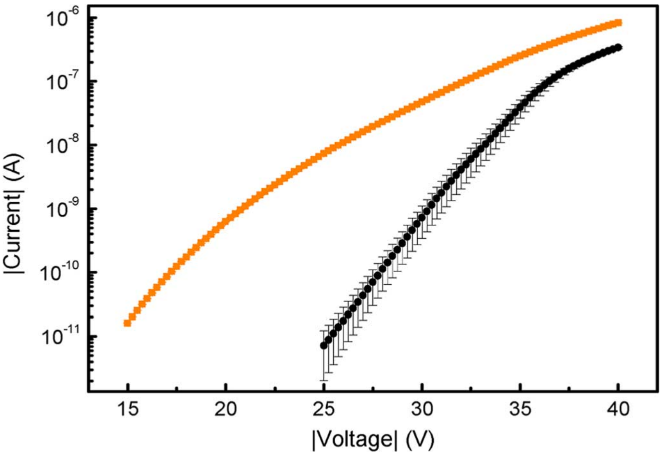

Fig. 6. *I–V* characteristics. The black and the orange lines stand for the Er:SiO_2 and the Er:Si-NCs waveguides, respectively.

The tunneling current in these waveguides obeys the Fowler–Nordheim law at high injection levels, like the ones shown in Fig. 6 [24]. Therefore, energetic unipolar injection is achieved which eventually yields impact excitation of the Er ions.

B. *Grating Couplers*

First, we characterized the input gratings. This study has been performed by using only one grating and collecting the light directly from the output facet of a cleaved waveguide. The gratings were designed to couple in only TM light which is the one where the field enhancement in the slot region is achieved. The grating coupler pitch and depth are 810 and $\approx$166 nm, respectively. Indeed only the TM polarized light was transmitted and no light could be detected when the polarization was rotated by 90°. Then, a laser light was scanned in the region between 1500 and 1600 nm and the incident angle is varied to look for optimum coupling efficiency. Fig. 7(a) shows the transmitted intensity at a fixed wavelength of 1540 nm as a function of the incident angle (with respect to the normal). The optimum coupling angle is 25° at which a coupling efficiency of $-(24 \pm 2)$ dB is achieved. Scanning the signal wavelength at this angle the

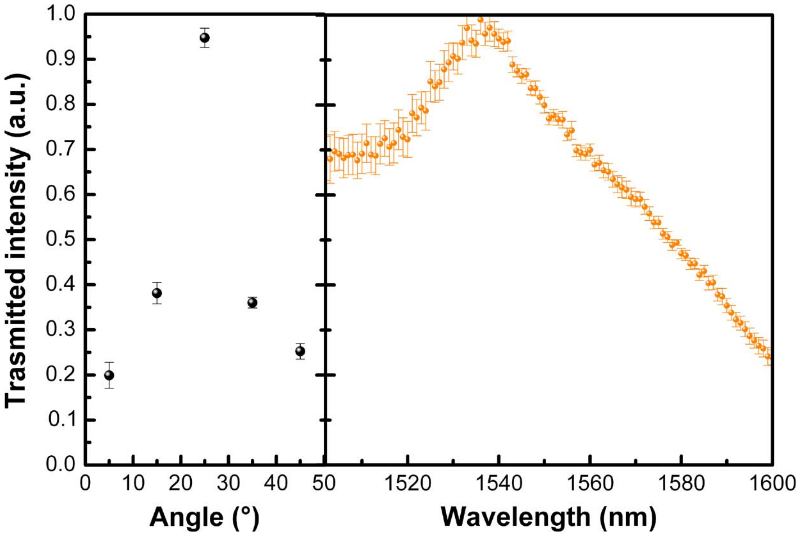

Fig. 7. Transmitted intensity in a 1 mm long waveguide (a) as a function of the incident angle and (b) as a function of the wavelength.

transmission spectrum reported in Fig. 7(b) is obtained. It has to be reported that changing the coupling angle the peak of the transmitted spectrum shifts as expected [25].

C. Propagation Losses

Propagation losses have been evaluated by using waveguides with different lengths (1–3 mm). The propagation losses are (40 ± 5) dB/cm in the region between 1500 and 1600 nm for both waveguide types. No wavelength dependence is observed. Therefore, the Er absorption losses—estimated to 3 dB/cm at 1540 nm [26]—are masked by scattering losses due to processing defects, mainly associated to the CMP process. This is inferred since a significant variation of the propagation losses from die to die on the same wafer has been observed, with fluctuations in excess of ±20 dB. The random variations in the waveguide thickness due to the imprecise CMP could lead to mode leaking toward the heavily doped wings and, consequently, to combined effect of radiative and free carrier absorption (FCA) losses. This explanation is confirmed by a simple estimation with the values of the FCA in silicon reported in the literature [27]. It is moreover worth mentioning that the scattering/absorption losses in polysilicon top cladding are probably contributing as well, despite the asymmetrical design of the slot waveguides.

D. Electroluminescence

An electro-optical characterization has been performed by monitoring the EL as a function of the applied biasing voltage.

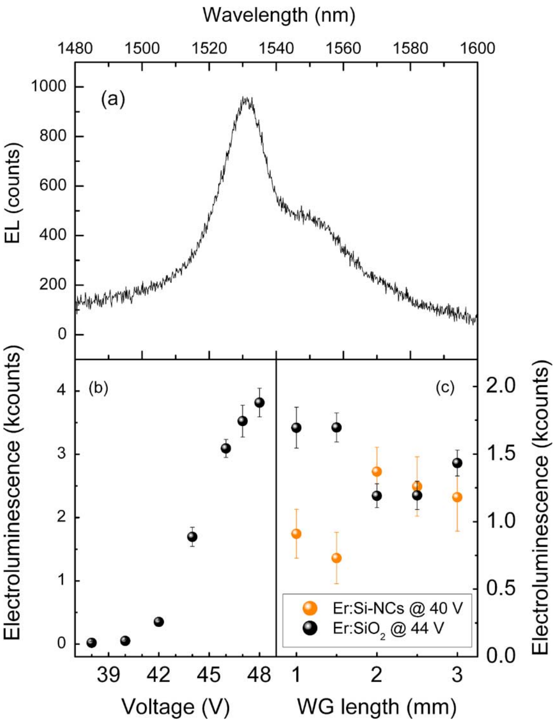

Fig. 8. (a) EL spectra for a voltage of 44 V, collected from the top of the Er:SiO$_2$ waveguide. (b) EL signal as a function of the applied voltage for the 1 mm long Er:SiO$_2$ waveguide. Signal is collected at the grating output. (c) EL as a function of the waveguide length for the two different devices at a fixed applied voltage of 40 and 44 V, respectively. Signal is collected at the grating output.

Stronger EL is observed in the devices without the nanoclusters than in the device with the silicon nanoclusters for the same applied voltage. In Fig. 8(a), the EL spectrum when the emission is collected by placing a fiber directly on top of the waveguide is reported. This EL spectrum evidences that we excite the Er ions by impact excitation caused by hot carrier injection. Fig. 8(b) reports the EL collected by a tapered fiber from the output grating as a function of the applied voltage for the Er:SiO$_2$ waveguides. This shows that light is guided in the active part of the device and emitted from the grating. The voltage range, where the EL signal can be detected, is very small [only 10 V—see Fig. 8(b)] and peaked at high voltages. The optical power density collected is in the range of tens of μW/cm^2, which increases linearly with the electric field applied and superlinearly with the injected current [24]. The optical conversion efficiency, defined as the ratio between the output optical power and the forced electrical power, is equal to 10^{-4}%. Interestingly, the light intensity does not depend appreciably on the waveguide length. Fig. 8(c) shows this dependence for both the Er:SiNCs and the Er:SiO$_2$ waveguides at a fixed applied voltage, respectively, of 40 and

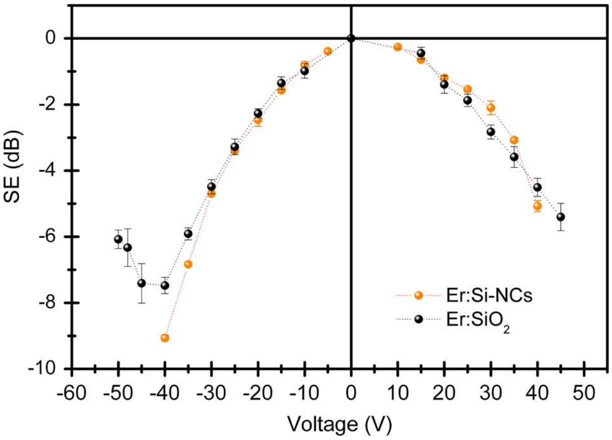

Fig. 9. SE as a function of the applied voltage for the two different waveguides, 1 mm long, at a fixed probing wavelength of 1550 nm.

44 V. These data indicate that the collected emission is coming from a region close to the grating independently on the waveguide length due to the high propagation losses.

E. Pump–Probe Experiment

Finally, we test the transmission of a probe signal as a function of the applied voltage. This experiment could give insights on the suitability of this approach for an on-chip optical amplifier. Fig. 9 shows the ratio between the transmitted signal at an applied bias U versus the transmitted signal for $U = 0$ V—this quantity is usually named signal enhancement (SE). The reported data are for a signal wavelength of 1550 nm and for the Er:Si-NCs waveguides. We observed that the SE decreases for increased bias voltage. No dependence on the signal wavelength is observed too. We attribute this effect to charge accumulation in the Si-NC [28] or defects in the oxide and to the FCA phenomenon, caused by the injected current in the silicon slot waveguide. The losses are higher in forward bias (negative voltage applied to the gate) than in the reverse one, because the injected electron current is higher, too. Very interestingly, in the Er:SiO$_2$ waveguides, the behavior of the SE is not monotonic, but at higher injection rate, in the forward polarization regime, it starts to increase. This absorption bleaching is observed for voltages lower than -40 V (forward bias), and only for the TM polarization of the input light. The reasons of this interesting behavior are under further investigations. The main point is that the overall loss of the device, at the maximum electrical pumping level, is only -6 dB. We do observe a loss reduction of 2 dB with respect to the optical losses at the lower levels of electrical pumping. However, the magnitude of this enhancement is larger than the maximum estimated enhancement value calculated from the emission cross section of Er^{3+} in this active material and the Er^{3+} concentration. This fact weakens the idea of optical gain and suggests the idea of absorption bleaching, which can be due to various factors (change in electrical transport across device, heating, etc.) influencing the optical losses in the studied devices under high electrical pumping. In fact, the optical losses increase, due to the injected current, because of absorption of the injected charges, accumulation of carriers in the interfaces, and the refractive index change due to the injected carriers. Assuming that the accumulated charges change only the refractive index, for our doping concentration, a change of the refractive index of the order of $\Delta n = 0.01$ is expected [29]. Due to this change, we estimate a maximum increase of the propagation losses of 10 dB/cm, due to the higher overlap of the optical mode with lossy regions of the waveguide. Thus, it can be concluded that the refractive index change is probably of secondary importance with respect to the optical losses induced by FCA and accumulation.

V. CONCLUSION

Electrically driven erbium-doped slot waveguides, having erbium ions and silicon nanoclusters in the active region, have been designed and fabricated. We do observe guided EL caused by emission from electrically excited erbium ions. Unfortunately, due to the high propagation and FCA losses, no optical amplification has been observed. A necessary condition to develop silicon-based optical amplifiers which exploit Er as active material is to improve significantly the process to reduce the propagation losses. In this paper, we have reported a first attempt in this direction.

ACKNOWLEDGMENT

The authors would like to thank A. Marconi and O. Jambois for the contribution at an early stage of this work and E. Rigo for the photograph of the experimental setup.

REFERENCES

[1] D. Liang and J. E. Bowers, "Recent progress in lasers on silicon," *Nature Photon.*, vol. 4, no. 8, pp. 511–517, Jul. 2010.
[2] J. D. B. Bradley and M. Pollnau, "Erbium-doped integrated waveguide amplifiers and lasers," *Laser Photon. Rev.*, vol. 5, no. 3, pp. 368–403, May 2011.
[3] O. Jambois, F. Gourbilleau, A. J. Kenyon, J. Montserrat, R. Rizk, and B. Garrido, "Towards population inversion of electrically pumped Er ions sensitized by Si nanoclusters," *Opt. Exp.*, vol. 18, no. 3, pp. 2230–2235, Feb. 2010.
[4] C. A. Barrios and M. Lipson, "Electrically driven silicon resonant light emitting device based on slot-waveguide," *Opt. Exp.*, vol. 13, no. 25, pp. 10092–10101, Dec. 2005.
[5] K. Preston and M. Lipson, "Slot waveguides with polycrystalline silicon for electrical injection," *Opt. Exp.*, vol. 17, no. 3, pp. 1527–1534, Feb. 2009.
[6] A. Marconi, A. Anopchenko, M. Wang, G. Pucker, P. Bellutti, and L. Pavesi, "High power efficiency in Si-nc/SiO$_2$ multilayer light emitting devices by bipolar direct tunneling," *Appl. Phys. Lett.*, vol. 94, pp. 221110-1–221110-3, 2009.
[7] V. R. Almeida, Q. Xu, C. A. Barrios, and M. Lipson, "Guiding and confining light in void nanostructure," *Opt. Lett.*, vol. 29, no. 11, pp. 1209–1211, Jun. 2004.
[8] Q. Xu, V. R. Almeida, R. R. Panepucci, and M. Lipson, "Experimental demonstration of guiding and confining light in nanometer-size low-refractive-index material," *Opt. Lett.*, vol. 29, no. 14, pp. 1626–1628, Jul. 2004.
[9] Y. C. Jun, R. M. Briggs, H. A. Atwater, and M. L. Brongersma, "Broadband enhancement of light emission in silicon slot waveguides," *Opt. Exp.*, vol. 17, no. 9, pp. 7479–7490, 2009.
[10] P. Muellner, N. Finger, and R. Hainberger, "Lateral leakage in symmetric SOI rib-type slot waveguides," *Opt. Exp.*, vol. 16, no. 1, pp. 287–294, 2008.
[11] P. Sanchis and A. Martinez, "Design of silicon-based slot waveguide configurations for optimum nonlinear performance," *J. Lightw. Technol.*, vol. 25, no. 5, pp. 1298–1305, May 2007.

[12] E. Jordana, J.-M. Fedeli, P. Lyan, J. P. Colonna, P. E. Gautier, N. Daldosso, L. Pavesi, Y. Lebour, P. Pellegrino, B. Garrido, J. Blasco, F. Cuesta-Soto, and P. Sanchis, "Deep-UV lithography fabrication of slot waveguides and sandwiched waveguides for nonlinear applications," in *Proc. 4th IEEE Int. Conf. Group IV Photon.*, 2007, no. 1, pp. 1–3.

[13] R. Ding, T. Baehr-Jones, W.-J. Kim, B. Boyko, R. Bojko, A. Spott, A. Pomerene, C. Hill, W. Reinhardt, and M. Hochberg, "Low-loss asymmetric strip-loaded slot waveguides in silicon-on-insulator," *Appl. Phys. Lett.*, vol. 98, no. 23, pp. 233303-1–233303-3, 2011.

[14] A. Spott, T. Baehr-Jones, R. Ding, Y. Liu, R. Bojko, T. O'Malley, A. Pomerene, C. Hill, W. Reinhardt, and M. Hochberg, "Photolithographically fabricated low-loss asymmetric silicon slot waveguides," *Opt. Exp.*, vol. 19, no. 11, pp. 10950–10958, May 2011.

[15] A. Anopchenko, A. Marconi, E. Moser, S. Prezioso, M. Wang, L. Pavesi, G. Pucker, and P. Bellutti, "Low-voltage onset of electroluminescence in nanocrystalline-Si/SiO_2 multilayers," *J. Appl. Phys.*, vol. 106, no. 3, pp. 033104-1–033104-8, 2009.

[16] T. N. Theis, "The future of interconnection technology," *IBM J. Res. Devel.*, vol. 44, no. 3, pp. 379–390, May 2000.

[17] R. Guider, N. Daldosso, A. Pitanti, E. Jordana, J.-M. Fedeli, and L. Pavesi, "NanoSi low loss horizontal slot waveguides coupled to high Q ring resonators," *Opt. Exp.*, vol. 17, no. 23, pp. 20762–20770, Nov. 2009.

[18] J. T. Robinson, K. Preston, O. Painter, and M. Lipson, "First-principle derivation of gain in high-index-contrast waveguides," *Opt. Exp.*, vol. 16, no. 21, pp. 16659–16669, Oct. 2008.

[19] A. Anopchenko, A. Marconi, M. Wang, G. Pucker, P. Bellutti, and L. Pavesi, "Graded-size Si quantum dot ensembles for efficient light-emitting diodes," *Appl. Phys. Lett.*, vol. 99, no. 18, pp. 181108-1–181108-3, 2011.

[20] G. M. Miller, R. M. Briggs, and H. A. Atwater, "Achieving optical gain in waveguide-confined nanocluster-sensitized erbium by pulsed excitation," *J. Appl. Phys.*, vol. 108, pp. 063109-1–063109-5, 2010.

[21] N. Prtljaga, D. Navarro-Urrios, A. Tengattini, A. Anopchenko, J. M. Ramírez, J. M. Rebled, S. Estradé, J.-P. Colonna, J.-M. Fedeli, B. Garrido, and L. Pavesi, "Limit to the erbium ions emission in silicon rich oxide films by erbium ion clustering," *Opt. Mater. Exp.*, vol. 2, pp. 1278–1285, 2012.

[22] A. Tengattini, A. Marconi, A. Anopchenko, N. Prtljaga, J. M. Ramírez, O. Jambois, Y. Berencén, D. Navarro-Urrios, B. Garrido, F. Milesi, J. Colonna, J.-M. Fedeli, and L. Pavesi, "1.54 μm Er doped light emitting devices: The role of the silicon content," in *Proc. IEEE Int. Conf. Group IV Photon.*, 2011, pp. 77–79.

[23] J. M. Ramírez, F. Ferrarese Lupi, O. Jambois, Y. Berencén, D. Navarro-Urrios, A. Anopchenko, A. Marconi, N. Prtljaga, A. Tengattini, L. Pavesi, J. P. Colonna, J. M. Fedeli, and B. Garrido, "Erbium emission in MOS light emitting devices: From energy transfer to direct impact excitation," *Nanotechnology*, vol. 23, p. 125203, 2012.

[24] J. M. Ramírez, F. F. Lupi, O. Jambois, Y. Berencén, D. Navarro-Urrios, A. Anopchenko, N. Prtljaga, A. Tengattini, L. Pavesi, J. P. Colonna, P. Rivallin, J. M. Fedeli, and B. Garrido, "Er-doped light emitting slot waveguides monolithically integrated in a silicon photonic chip," *Nanotechnology*, 2012, submitted for publication.

[25] D. Taillaert, F. Van Laere, M. Ayre, W. Bogaerts, D. Van Thourhout, P. Bientsman, and R. Baets, "Grating couplers for coupling between optical fibers and nanophotonic waveguides," *Japn. J. Appl. Phys.*, vol. 45, no. 8A, pp. 6071–6077, 2006.

[26] D. Navarro-Urrios, F. Ferrarese Lupi, N. Prtljaga, A. Pitanti, O. Jambois, J. M. Ramírez, Y. Berencén, N. Daldosso, B. Garrido, and L. Pavesi, "Copropagating pump and probe experiments on Si-nc in SiO_2 rib waveguides doped with Er: The optical role of non-emitting ions," *Appl. Phys. Lett.*, vol. 99, pp. 231114-1–231114-3, 2011.

[27] D. K. Schroder, R. N. Thomas, and J. C. Swartz, "Free carrier absorption in silicon," *IEEE Trans. Electron Devices*, vol. ED-25, no. 2, pp. 254–261, Feb. 1978.

[28] D. Navarro-Urrios, A. Pitanti, N. Daldosso, F. Gourbilleau, R. Rizk, G. Pucker, and L. Pavesi, "Quantification of the carrier absorption losses in Si-nanocrystal rich rib waveguides at 1.54 μm," *Appl. Phys. Lett.*, vol. 92, pp. 051101-1–051101-3, 2008.

[29] R. A. Soref and B. R. Bennett, "Electro optical effects in silicon," *IEEE J. Quantum Electron.*, vol. QE-23, no. 1, pp. 123–129, Jan. 1987.

Author biographies not included by author request due to space constraints.

IOP PUBLISHING NANOTECHNOLOGY

Nanotechnology **24** (2013) 115202 (8pp) doi:10.1088/0957-4484/24/11/115202

Er-doped light emitting slot waveguides monolithically integrated in a silicon photonic chip

J M Ramírez[1], F Ferrarese Lupi[1], Y Berencén[1], A Anopchenko[2], J P Colonna[3], O Jambois[1], J M Fedeli[3], L Pavesi[2], N Prtljaga[2], P Rivallin[3], A Tengattini[2], D Navarro-Urrios[4] and B Garrido[1]

[1] MIND-IN2UB, Departament d'Electrònica, Universitat de Barcelona, Martí i Franquès 1, E-08028 Barcelona, Spain
[2] Nanoscience Laboratory, Department of Physics, University of Trento, Via Sommarive 14, Povo I-38123, Italy
[3] CEA, Léti, Minatec campus 17 rue des Martyrs, F-38054 Grenoble cedex 9, France
[4] Catalan Institute of Nanotechnology (CIN2-CSIC), Campus UAB, edifice CM3, E-08193 Bellaterra, Spain

E-mail: jmramirez@el.ub.es

Received 3 July 2012, in final form 25 January 2013
Published 28 February 2013
Online at stacks.iop.org/Nano/24/115202

Abstract
An integrated erbium-based light emitting diode has been realized in a waveguide configuration allowing 1.54 μm light signal routing in silicon photonic circuits. This injection device is based on an asymmetric horizontal slot waveguide where the active slot material is Er^{3+} in SiO_2 or Er^{3+} in Si-rich oxide. The active horizontal slot waveguide allows optical confinement, guiding and lateral extraction of the light for on-chip distribution. Light is then coupled through a taper section to a passive Si waveguide terminated by a grating which extracts (or inserts) the light signal for measuring purposes. We measured an optical power density in the range of tens of $\mu W/cm^2$ which follows a super-linear dependence on injected current density. When the device is biased at high current density, upon a voltage pulse (pump signal), free-carrier and space charge absorption losses become large, attenuating a probe signal by more than 60 dB/cm and thus behaving conceptually as an electro-optical modulator. The integrated device reported here is the first example, still to be optimized, of a fundamental block to realize an integrated silicon photonic circuit with monolithic integration of the light emitter.

(Some figures may appear in colour only in the online journal)

1. Introduction

One of the open challenges in silicon photonics is a monolithically integrated light source [1]. Up to date, from the standalone device point of view, the most successful approach is based on heavily doped strained germanium on silicon. Indeed, an injection laser emitting around 1.5 μm based on this material has been recently demonstrated [2]. However, the feasibility of its integration into silicon technology has yet to be demonstrated owing to the narrow process margins in its fabrication. On the other hand, and as an alternative to high refractive index Ge, it is appealing to exploit silicon oxide since it has a very high refractive index contrast with silicon, is a good host for optically active rare earth ions (e.g., Er^{3+}) [3], and is a matrix where Si nanoclusters (Si-ncs) can be easily formed (then obtaining the silicon-rich oxide, SRO). The last point is instrumental for optically pumped devices which increase and spectrally broaden the effective Er^{3+} excitation cross-section through the Si-ncs sensitization process [4, 5]. For electrically pumped devices SRO is also beneficial as a controlled injector. The gate electrode/SRO energy band offset can be easily adjusted depending on the silicon excess precipitation (the higher the silicon excess precipitation of the SRO, the lower the energy barrier). Furthermore, the density of silicon precipitates and related defects modulate the conductivity of the SRO (and thus the average energy distribution of the conducting electrons), which in turn translates into an Er impact ionization efficiency [6–8]. Moreover, an enhancement of the Er^{3+} emission in doped Si-ncs is expected due to the Purcell effect [9, 10]. Er^{3+}-doped active waveguides are easy to fabricate by using the concept of a slot waveguide [11], where optical confinement inside a thin slot layer of low refractive index material is achieved. Low propagation losses can be achieved even in slot waveguide structures designed for electrical injection [12]. Thus silicon slot waveguides provide a MOS (metal–oxide–semiconductor) capacitor type of injecting structure while at the same time maintaining light confinement and propagation along the slot. This makes possible lateral light extraction for on-chip distribution, in contrast with standard MOSLED (metal–oxide–semiconductor light emitting diode), where light emission is vertical [13, 14].

In this work we demonstrate a light emitting diode working at 1.54 μm integrated within a slot waveguide and coupled to a passive waveguide through a tapered region. The light emission can be directly modulated by the electrode voltage signal and distributed on-chip. Although yet to be demonstrated, should the slot material have net gain due to Er^{3+} inversion, optical feedback in the slot waveguide section through a Fabry–Perot or a micro-ring resonator would allow laser emission at 1.54 μm in an integrated functional configuration.

2. Device performance

Figure 1 shows the realized device, where an active waveguide is coupled to a passive waveguide that ends in a surface grating for light signal extraction. The devices were fabricated in a CMOS (complementary MOS) line on a p-type silicon on insulator (SOI) wafer with a 220 nm thick silicon device layer and 2 μm buried oxide (BOX). The active waveguide geometry is based on an asymmetric slot waveguide, where a thin 40 nm slot layer is sandwiched between two silicon-doped layers to permit electrical injection in the slot. The waveguide width is 1 μm. The design has been optimized by using a fully vectorial mode solver based on the film mode matching (FMM) method. Optimization yields an asymmetric geometry to enhance the optical confinement of the transverse magnetic (TM) polarized mode in the slot region. In this way, the mode overlap with the top polysilicon electrode is minimized, which, in turn, decreases the absorption losses. The bottom electrode of the waveguide has been produced by means of a boron implantation with a dose of 5×10^{12} at. cm^{-2} at 25 keV of energy. Two different materials have been used in the slot layer: Er^{3+}-doped SiO_2 (high temperature oxide) and Er^{3+}-doped SRO. The SRO has been deposited by low-pressure chemical vapour deposition (LPCVD) with a silicon excess of 11.5%, then annealed at 900 °C for 1 h in a N_2 atmosphere in order to promote the phase separation and nanocluster precipitation (step I in figure 2). Er^{3+} doping was obtained by ion implantation to get an Er concentration peak of 5×10^{20} at. cm^{-3}. For the sake of clarity, the waveguide containing the Er^{3+} and Si-ncs will be labelled as Er:Si-ncs, while the other one is labelled as $Er:SiO_2$. Subsequently, undoped polysilicon 100 nm thick and high-temperature oxide 180 nm thick were deposited on top of the layers (figure 2, step II). The lower slab in the waveguide (Si pedestal) and the bottom electrode wings were then formed through partial silicon etch at the sides of the waveguide structure, starting from the top polysilicon, the active layer and finally the bottom polysilicon down to 90 nm (thickness of the bottom electrode).

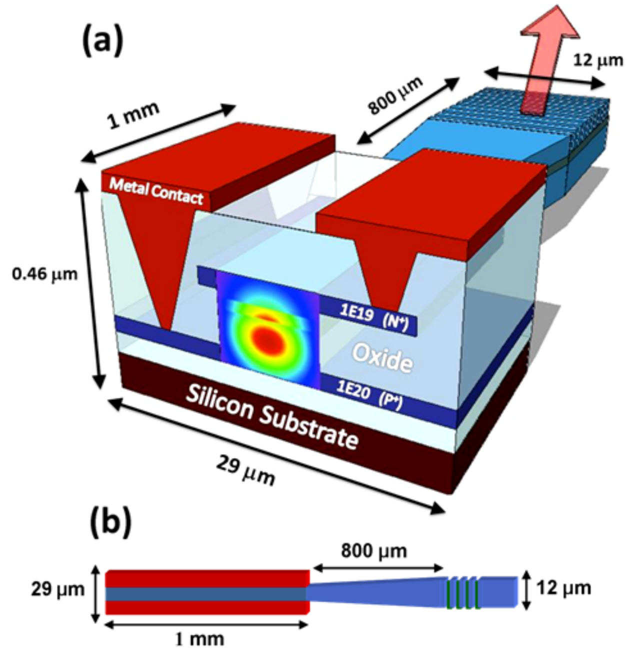

Figure 1. (a) 3D schematics of the integrated photonic device. On the cross-section of the active slot waveguide (40 nm of slot) we have reported the simulated profile of the fundamental TM mode. The blue region refers to silicon, light blue to silicon oxide and red to metals. (b) Top view of the integrated system with the active slot waveguide (left), the slot taper (centre) and the passive Si waveguide with the output coupler (right).

The 220 nm thick Si pedestal has graded p-type doping in order to reduce the free-carrier density in the optical mode region. The gradient in the doping was achieved by several boron implantations which yielded a doping of $\sim10^{17}$ at. cm^{-3} in the region under the active slot layer. This value gradually increases to $\sim10^{19}$ at. cm^{-3} in the region far from the active slot layer and becomes $\sim10^{20}$ at. cm^{-3} in the 90 nm thick bottom electrode. Notice that this step becomes crucial for proper device operation. For this purpose the implantation dose and energy values were first simulated in order to adjust a proper lateral diffusion (in the x direction) of the implanted ions, taking advantage of the isotropic condition in the monocrystalline silicon (figure 2, step III). A cross-section view of the simulated boron concentration and

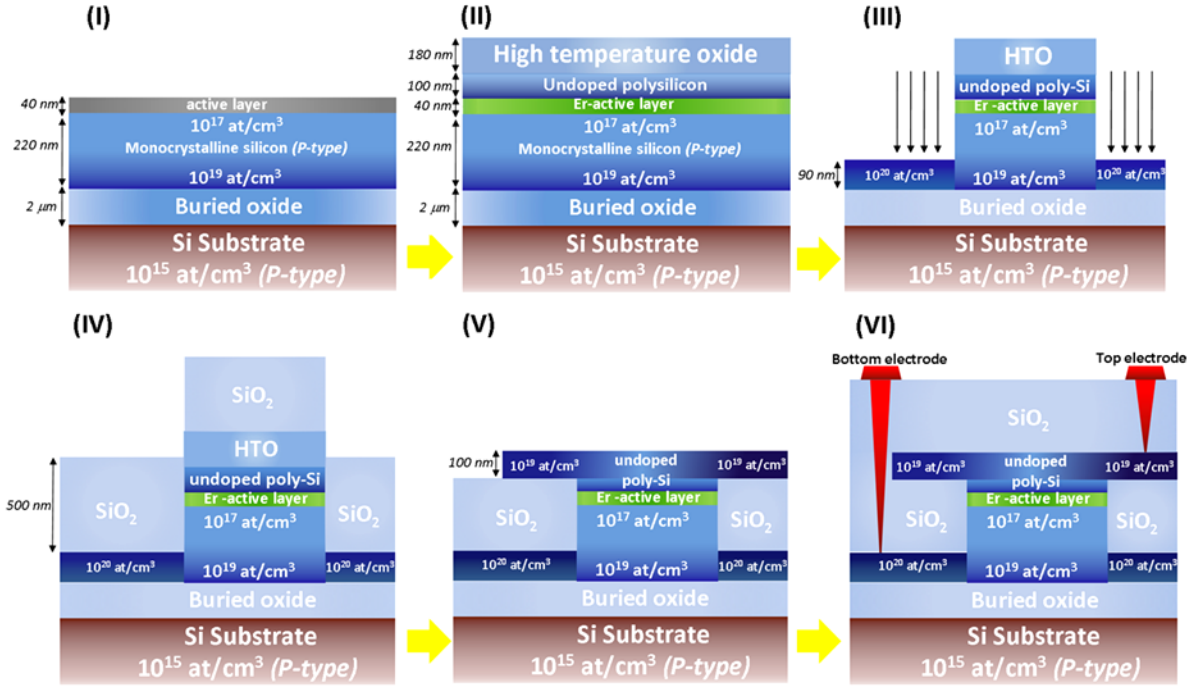

Figure 2. Process flow of the slot waveguides.

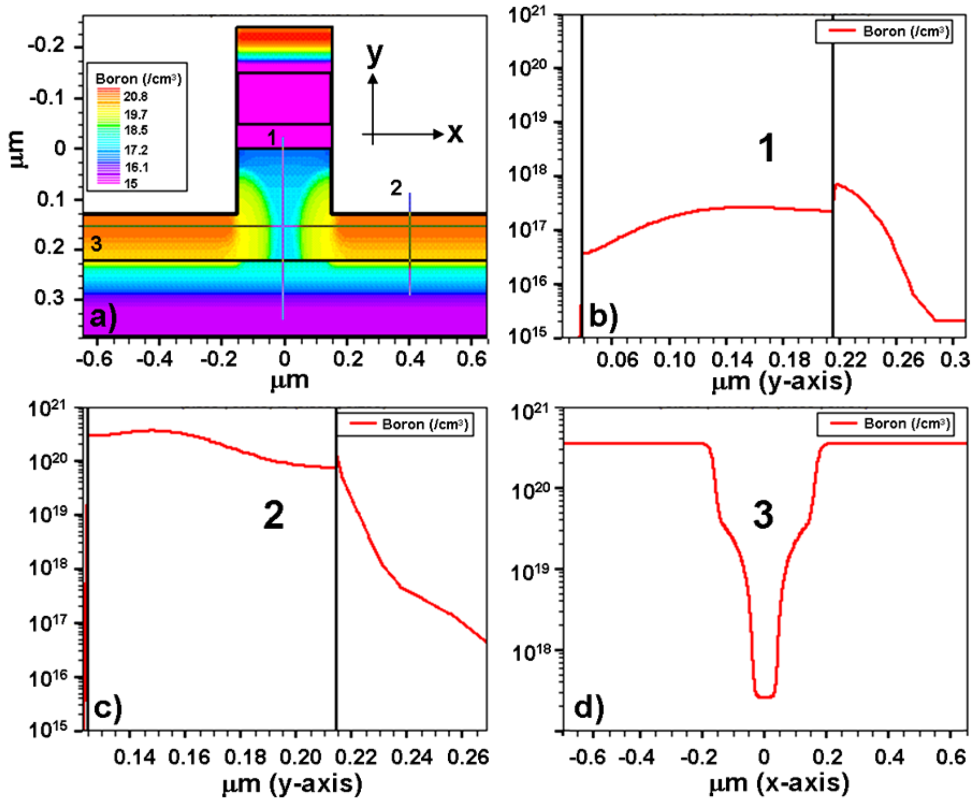

Figure 3. (a) Total boron concentration inside the waveguide. A coloured legend and a coordinate system (*x*–*y*) with labelled straight lines (1, 2 and 3) have been defined to show the doping gradient (at. cm^{-3}) and the concentration profile in three different sections, i.e. the Si pedestal (b, line 1), the bottom electrode wing (c, line 2) and along the bottom electrode cross-section (d, line 3).

three different profiles (two in the *y* axis and one across the *x* axis) are shown in figure 3 to illustrate the doping. Profile 1 (figure 3(b)) accounts for the graded doping in the Si pedestal (lower asymmetric slab), with a minimum (maximum) boron concentration of 3×10^{16} at. cm^{-3} (10^{18} at. cm^{-3}). It is worth noticing that the top doping values were defined lower than the ones reported for the final device because of the expected lateral diffusion (in the *x* direction) of electrode dopants when submitted to the thermal treatment, hence increasing the total doping in the Si pedestal. Profiles 2 and 3 (figures 3(c) and (d)) show the boron doping concentration for the bottom electrode wing in the *y* axis and *x* axis directions, respectively (a maximum of 3.5×10^{20} at. cm^{-3} is expected in both cases). Then, Er^{3+} activation and matrix damage recovery were performed on both layers through a post-annealing treatment at 800 °C for 6 h.

Afterwards, a 500 nm thick SiO_2 was deposited on the top polysilicon and used as a spacer (figure 2, step IV), followed by a chemical polishing of the surface, reducing the upper polysilicon thickness from 100 nm down to 20 nm. The 100 nm thick top silicon layer is formed by polycrystalline silicon deposition at 620 °C without intentional doping. Only the side regions (wings) are doped by a phosphorus implantation, obtaining a maximum doping concentration of $\sim 10^{19}$ at. cm^{-3} (figure 2, step V). The dopants of both electrodes were activated by a fast annealing at 950 °C for 60 s. The highly doped electrodes are finally contacted by the metallization, for which TiN and AlCu alloys have been used (figure 2, step VI). It is worth noticing that the top polysilicon layer is almost transparent for the vertically emitted photons at 1.54 μm by Er^{3+} ions. The final active device size is: 1 mm (length) × 29 μm (width) × 0.46 μm (height). Passive propagation losses in these devices at 1.54 μm were ~4 dB, which is high but commensurate with the length of the slot section (1 mm). A passive slot waveguide-based taper was also fabricated to optimize the coupling between the active device and the passive waveguide. The taper tip is 1 μm wide at the beginning (equal to the active section) and it extends for 800 μm with a final width of 12 μm matching the width of passive section. The same steps were used in the process flow for the taper and passive waveguide fabrication, except for the doping and the Er^{3+} implantation. Finally, the light extraction was carried out through an output coupler. The grating coupler was fabricated after the taper-passive waveguide system, by engraving trenches in the passive waveguide down to the monocrystalline silicon. Such a structure is 16 μm long and 12 μm wide, with a grating period of 0.8 μm, a grating groove depth of 150 nm and a collection angle tilted 25° from the normal. Notice that the passive device geometry (slot taper and output coupler) was designed in accordance with the technological constraints (i.e. they were adjusted to ease alignment tolerances).

The electric polarization of the active waveguides was performed using a semiconductor device analyser (Agilent B1500 equipped with high-resolution measurement units) and a Cascade Microtech SUMMIT probe station with Faraday and optical shielding, attoguard and triaxial cabling, adapted in order to perform both optical and electrical characterization. The emitted light was collected with an infrared objective and then coupled to a grating spectrometer interfaced with a calibrated photomultiplier. Placing the objective on top of the active waveguide allows recording of the scattered light fraction emitted vertically by the waveguide, while placing the objective on the grating allows measurement of the guided light fraction along the waveguide. This guided light is then channelled into the passive waveguide and out-coupled through the grating. By using the grating as an input port and a cleaved facet of the active waveguide as the output port, it is possible to perform transmission experiments (pump and probe measurements) where electrical excitation of the waveguide acts as a pump signal, the probe signal being provided by an external laser coupled into the waveguide (see figure 4). For this purpose the waveguide was driven with a pulse generator (square pulsed voltage at 10 Hz) while the probe signal was provided by an infrared laser at 1528 nm, externally modulated at 200 kHz using an arbitrary waveform generator. The transmitted signal was measured by using a lock-in amplifier synchronized with the probe to filter out the electroluminescence (EL). Finally the signals were monitored with a digital oscilloscope with a temporal resolution of 0.5 μs.

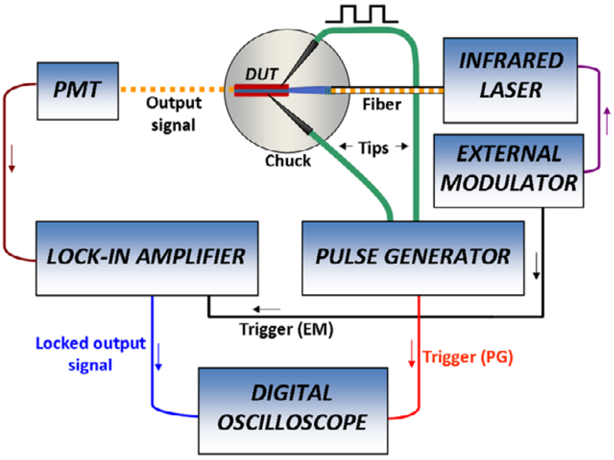

Figure 4. Electrical pump and probe setup.

3. Results and discussion

Figure 5(a) shows the $I(V)$ characteristics under forward bias of the active slot waveguides for the two slot materials studied (Er^{3+} in SiO_2 and Er^{3+} in SRO). Forward bias means here that a DC negative voltage was applied to the n-type doped top electrode. This particular configuration yields electron injection at the top electrode and hole accumulation at the lower interface. We will not give details on inversion (reverse bias) characteristics here as the currents involved are orders of magnitude lower (rectification) and thus light emission is very poor. As demonstrated in earlier test capacitors of a similar type driven into accumulation [8, 15], hole transport through the slot can be ruled out due to the large energy offsets between the valence bands of silicon and those of SiO_2 or SRO, which are in the range 4.0–4.7 eV. Instead, the band offset for electrons is in the range 1.6–3.1 eV (depending on silicon excess precipitation). Nevertheless, one expects a certain degree of hole injection and trapping at the lower interface (seen as displacement current), as previously demonstrated in pulse programming of Si-ncs memories [16]. The devices were biased up to device

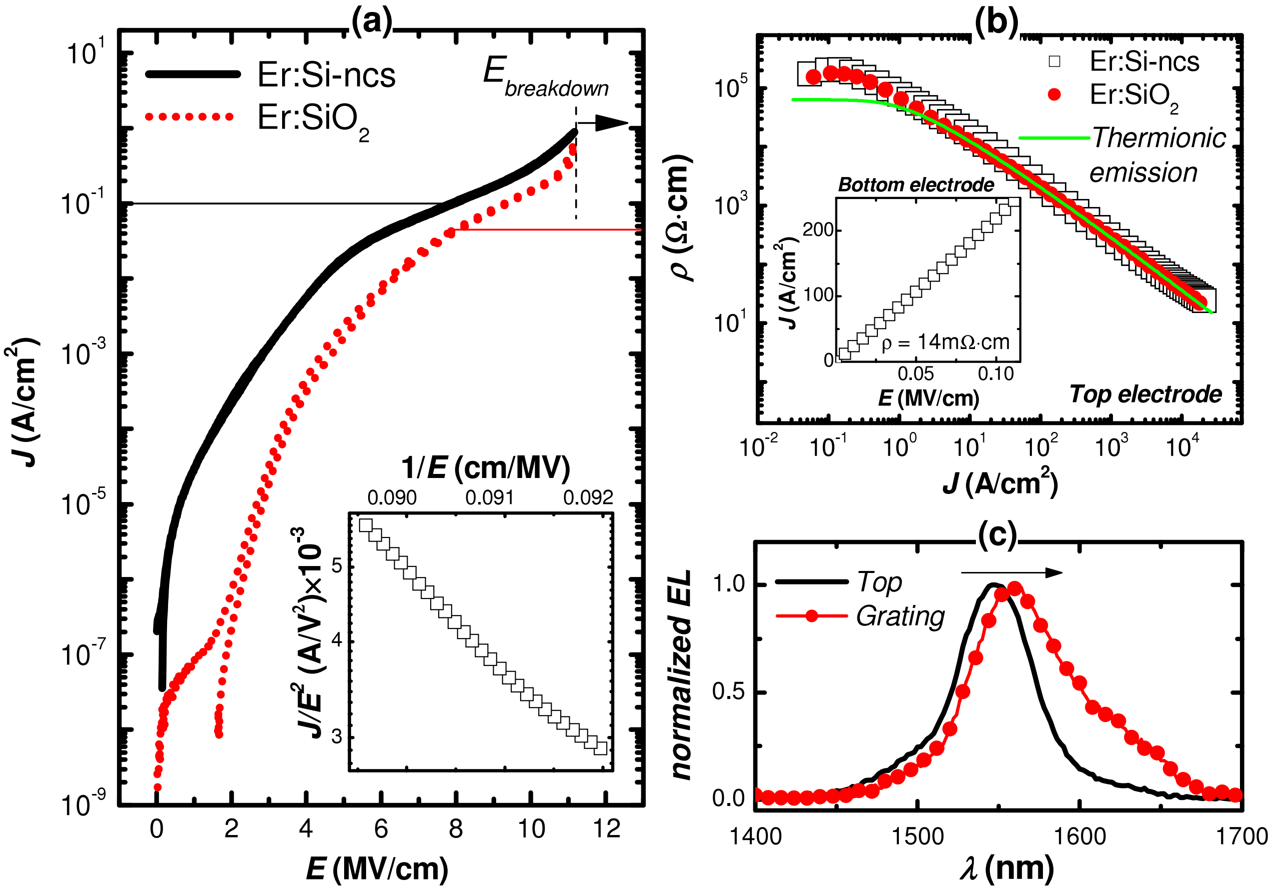

Figure 5. (a) Current density versus applied electric field $J(E)$ characteristics for the Er:Si-ncs device (solid line) and the Er:SiO$_2$ device (dotted line) up to device breakdown. Horizontal lines mark the onset of electroluminescence for the two devices. Inset, the Fowler–Nordheim plot for the Er:SiO$_2$ device. (b) Resistivity values of the top electrode for the Er:Si-ncs device (empty squares) and the Er:SiO$_2$ device (filled dots) as a function of the injected current density. The line shows the curve fitting using the thermionic emission model. Inset, $J(E)$ characteristic for the bottom electrode. (c) Comparison between the emitted EL spectrum collected from the active waveguide surface (straight line) and from the output grating coupler (dotted line).

breakdown, which was usually between 11 and 12 MV cm^{-1}, a value that is compatible with a high-quality silica layer grown on silicon [17]. The voltage sweeping step was fixed at 50 mV s^{-1}, which is small enough for achieving quasi-static $I(V)$ curves by allowing trap charging/discharging quasi-equilibrium at each step (as seen from the pulsed polarization dynamics of the system). The horizontal lines in figure 5(a) represent the current density threshold for EL emission (red for the Er:SiO$_2$ device and black for the Er:Si-ncs device). Specifically, the threshold field for light emission was around 6.5 MV cm^{-1} for both samples and threshold currents were 64 mA cm^{-2} and 26 mA cm^{-2} for the Er:Si-ncs and the Er:SiO$_2$ devices, respectively. These values of threshold field correlate with the onset for the electrode-limited Fowler–Nordheim tunnelling current, which starts to dominate at around 6 MV cm^{-1}. We can consider this threshold as a profound modification of the transport properties of electrons through the layer: (i) for voltages below this threshold, the current is bulk limited and proceeds by hopping between trap states (either tunnel or Poole–Frenkel type, as deduced from fittings not shown) for which carriers remain cold and do not gain enough energy to excite Er^{3+} ions and (ii) for voltages above this threshold, the electrons are injected into the conduction band of SiO$_2$ or SRO and are accelerated by the strong electric field up to average final energies in the range 3.0–4.5 eV for fields in the range 6–11 MV cm^{-1}, as shown by DiMaria *et al* from Monte Carlo simulations [17]. Accelerated electrons thus have enough energy to impact and excite Er^{3+} ions to the first excited (0.8 eV–1550 nm) or even to upper excited levels (1.27 eV–980 nm, 1.46 eV–850 nm, . . .). The EL spectroscopy of the upper levels of Er^{3+} (up to 2.54 eV–488 nm emission) can be observed in the emission spectra of MOSLED capacitors of similar type to the waveguides reported here [18]. As stated before, above the EL threshold, the $I(V)$ characteristics are well within the Fowler–Nordheim tunnelling dependence (see inset of figure 4(a)). Thus, for a given electric field E, the tunnelling current density J through the active layers is [8, 19]:

$$J = \frac{q^3E^2}{8\pi h\phi_b}\exp\left(-\frac{4\sqrt{2m^*_{\mathrm{ox}}\,(\phi_b)^3}}{3\hbar qE}\right) \tag{1}$$

where q is the elementary charge, $\hbar$ is the reduced Planck's constant, ϕ_b is the potential barrier height at the electrode-active layer interface and $m^*_{\mathrm{ox}} = 0.5\ m_{\mathrm{e}}$ is the effective mass of the injected electrons [20, 21]. The curve fitting yields an effective barrier height of 1.9 ± 0.4 eV (1.1 ± 0.3 eV) for the Er:SiO$_2$ (Er:Si-ncs) layer. These values are considerably lower than the ones reported in [8] for Er:SiO$_2$ (Er:Si-ncs) MOSLEDs, which we believe it is due to the presence of the lightly doped top polysilicon in the slot waveguide region, as we will demonstrate in the following. The injected current in the active layer is in fact preceded by the conduction mechanisms taking place within the lightly doped (high resistivity) upper polysilicon layer. These mechanisms were further validated by measuring additional test devices, where two metal stripes were contacted to the two side-wings of the top electrode. Results showed a current density dependent resistivity—from $10^5\ \Omega \cdot$ cm (at 1 MV cm^{-1}) to 15 $\Omega \cdot$ cm (at 11.5 MV cm^{-1}), as seen in figure 5(b). Therefore the dominant conduction mechanism through the lightly doped polysilicon is thermionic emission over the potential barriers at the grain boundaries (grain boundary carrier trapping mechanism) [22]. In this case, the expression for the current density (J) is:

$$J = 2A^*T^2 \exp\left(\frac{q\varphi_b}{kT}\right) \sinh\left(\frac{qV}{2kT} \cdot \frac{\langle a\rangle}{L}\right) \qquad (2)$$

where A^* is Richardson's constant, φ_b is the potential barrier height at the grain boundary, kT is the thermal energy, L is the length of the polysilicon layer, $\langle a\rangle$ is the mean grain size and V the total applied voltage. From this equation, the resistivity can be obtained as:

$$\rho = \frac{V}{LJ} = \frac{V}{2A^*LT^2} \frac{\exp\left(\frac{q\varphi_b}{kT}\right)}{\sinh\left(\frac{qV}{2kT} \cdot \frac{\langle a\rangle}{L}\right)}. \qquad (3)$$

A good fit to the data is obtained with a potential barrier height of 0.43 ± 0.05 eV and a mean grain size of 15 ± 2 nm (green line in figure 5(b)). Note that these values agree with previous reports on similar material [23, 24]. In contrast, the bottom electrode showed an Ohmic behaviour (see inset of figure 5(b)) with a resistivity of 14 m$\Omega \cdot$ cm. As a result, the low barrier height ϕ_b found at the electrode-active layer interface can be explained by assuming that injected electrons already face the electrode-active layer interface with energies above the conduction band (warm electrons) as a consequence of the thermionic transport and acceleration due to the voltage drop within the lightly doped polysilicon electrode [25].

Figure 5(c) shows the normalized Er^{3+} spectra collected either at the active waveguide surface (straight line) or at the output grating coupler (dotted line) for a bias of 10 MV cm^{-1}. The typical Er^{3+} emission spectrum is observed. Er^{3+} are excited mainly by impact excitation of highly energetic carriers after acceleration in the SiO$_2$ or SRO [8]. Note a shift of about 10 nm and a different line shape between the two spectra. Since this shift and line shape difference are not observed when EL is collected from a cleaved facet of the active waveguide, they are thought to be due to the filtering action of the output grating due to some unavoidable random errors in its fabrication [26].

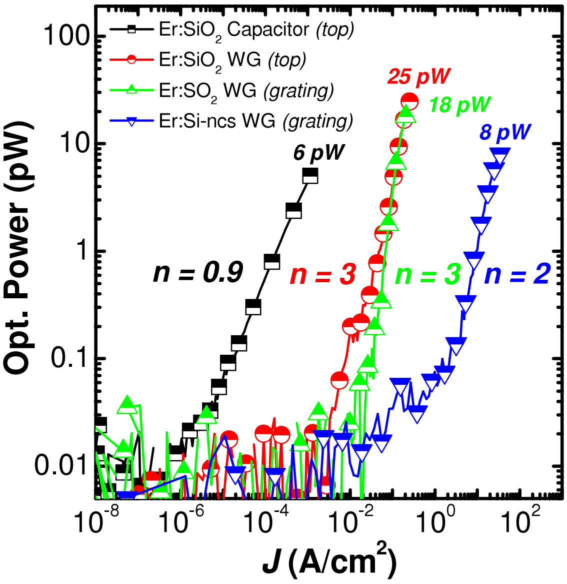

Figure 6. Optical power as a function of the injected current density for both waveguide devices (circles correspond to vertical EL collected from the waveguide of the Er:SiO$_2$ device, while the triangles correspond to the EL recorded from the grating either of the Er:SiO$_2$ or of the Er:Si-ncs devices) and for an Er^{3+}-doped SiO$_2$ capacitor (squares) used as a control device. The devices were biased from 0 V to −46 V (close to voltage breakdown). Let us note that to facilitate the comparison the emitted optical power of the capacitor has been scaled by 10 to reduce its effective area to the active waveguide area (10^{-5} cm^{-2}). This scaling is based on the linear relation we found between the emitted optical power and the area of similar MOS devices.

Figure 6 reports the emitted optical power versus the injected current density for the two devices studied here as well as for a capacitor MOSLED control device used as reference. The control device consists of a highly n-type doped (10^{20} at. cm^{-3}) top polysilicon gate electrode (100 nm thick) with a surface of 10^{-4} cm^2, a 40 nm thick Er^{3+}-doped SiO$_2$ active layer with the same characteristic as the slot layer in the Er:SiO$_2$ device, and a bottom p-type Si substrate [8]. As can be observed in figure 6, the control device (capacitor) has the lowest EL threshold current density (5×10^{-6} A cm^{-2}). This value is four orders of magnitude lower than those for the waveguide devices ($\sim 10^{-2}$ A cm^{-2}). On the other hand, the emitted optical powers are of the same order of magnitude (but slightly higher for the slot waveguides). This fact suggests a lower external quantum efficiency (η_{ext}) for the waveguide devices than for the control capacitor. The low η_{ext} may be due to a low extraction efficiency and/or a low internal quantum efficiency (η_{int}). A low η_{int} might be due to the resistive polysilicon injectors, where a significant voltage drop occurs, which in turn decreases the electric field strength for impact excitation of Er^{3+} ions. In addition, the maximum emitted power collected at the waveguide surface (half-filled circles in figure 6) and at the grating (half-filled triangles in figure 6) are similar. This suggests that a good coupling efficiency between the active and the passive waveguide is achieved and that most of the coupled light exits from the grating. The Er:Si-ncs waveguide device has lower η_{ext} than the Er:SiO$_2$ waveguide device (see the

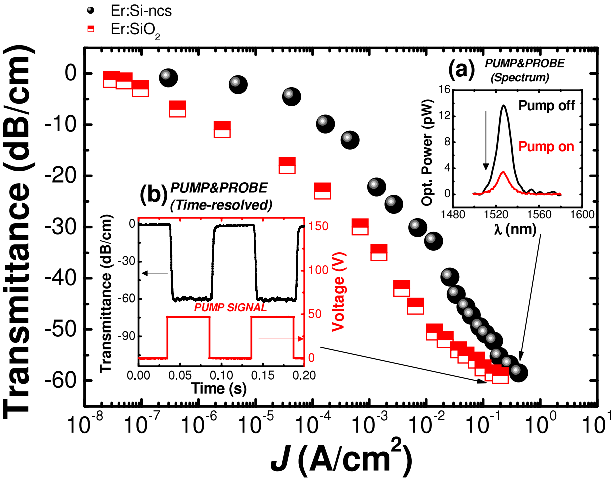

Figure 7. Free-carrier absorption (in dB cm^{-1}) of the waveguide device at 1528 nm as a function of the injected current density *J*. Inset (a), the attenuation of the probe spectrum when the bias is switched on. Inset (b), the modulated voltage and the transmitted signal as a function of time for the highest current density used.

inverted half-filled triangles in figure 6). This is expected since the electron energy distribution is anticipated to be colder for SRO than for SiO$_2$. Si-ncs act as trapping centres (and thus as pathways for cold electron hopping conduction) but also as scattering centres for energetic electrons in the conduction band. Additional reasons rely on the fact that a significant fraction of Er^{3+} in Si-ncs can be non-radiative due to additional defects in the material or an insufficient oxidation state of Er due to the presence of Si–Si bonds [27]. Remarkably, the light emission (EL) versus current density (J) characteristics shows a power law dependence with an 'n' exponent:

$$EL \propto J^n \tag{4}$$

with $n = 0.9$ for the capacitor [15], $n = 2$ for the Er:Si-ncs device and $n = 3$ for the Er:SiO$_2$ device. The super-linear $EL(J)$ dependence of the emission in the waveguides was further validated by measuring many other devices with 2 and 3 mm long active waveguides in the photonic chip, finding no correlation between the super-linear behaviour (higher 'n' exponents) and the waveguide length. Additional experiments on the lifetime of Er^{3+} emission show that the lifetime drops for high voltage and high current injection. Nevertheless, we discard stimulated emission to explaining super-linearity since we did not observe any line narrowing in the emission spectra when J is increased. Furthermore, the super-linearity can also be observed in the $EL(J)$ collected at the waveguide surface (vertical emission) were the cavity amplification effect is completely ruled out (data reported as half-filled circles for the Er:SiO$_2$ waveguide in figure 6). To suggest an explanation of the origin of the super-linearity we note that the main electrical difference between the capacitor and the waveguide devices is the electrical characteristic of the top electrode. In the capacitor it behaves as Ohmic contact (resistivity of 4 m$\Omega \cdot$ cm) while in the waveguide devices it is a thermionic injector. Therefore, it is reasonable to assume that the upper electrode is not equipotential in all of its area. For low J, most of the electron injection occurs near the wings of the silicon top electrode due to the high polysilicon resistivity. At high J, i.e. high electric fields, the injection spreads over the whole active layer since the polysilicon resistivity drops. This increases the effective excited active layer volume, which explains the $EL(J)$ nonlinearity. As an alternative explanation, one may adopt that the most energetic hot electrons can excite multiple Er^{3+} ions, but, again, if this was the case, super-linearity should also be observed for capacitors. Since the effective barrier height is larger for Er:SiO$_2$ than for Er:Si-ncs, we expect the EL to grow faster for the former.

Finally, in order to evaluate the additional absorption losses of the waveguides due to injected carriers, we performed transmission measurements of a probe laser signal at 1.54 μm with electrical pumping of the waveguide (electrical pump and optical probe configuration). The inset (a) of figure 7 shows that the transmitted spectrum of the probe signal attenuates significantly when the bias is switched on. The analysis of the time dependence of the probe transmitted signal (inset (b) of figure 7) revealed a time response of few microseconds, which can be directly related to the free-carrier lifetime. The probe transmittance decreases significantly when the injected current density is increased (figure 7). Consequently, we conclude that additional absorption at high current is due to carrier absorption, either trapped carriers (which generate space charge in the SiO$_2$ and SRO) or free conducting carriers. A maximum probe transmittance attenuation of -60 dB cm^{-1} (at 0.5 A cm^{-2}) is observed for both waveguide devices. Note that the Er:SiO$_2$ device shows higher carrier absorption than the Er:Si-ncs device. This difference can be explained by the fact that the sample containing Si-ncs is more conductive and space charge is expected to be less prominent. To further corroborate this hypothesis, notice that current–voltage characteristics reveal a wider shift between progressive and regressive I–V scans for the Er:SiO$_2$ device than for the Er:Si-ncs device (see figure 5(a) at low applied bias). This hysteresis width is directly related to the trapped charge density. This behaviour can be translated directly into an electro-optical modulator concept with a 60 dB cm^{-1} of attenuation difference of the probe beam between 'on' and 'off' states. This electro-optical modulator could then be engineered together with the light emitting source. In these non-optimized devices, the measured carrier absorption time response was in the range of few μs (equal to our setup resolution) suggesting device operation frequencies of at least hundreds of kHz.

4. Conclusions

In summary, Er^{3+}-doped Si-based light emitting slot waveguides were designed, fabricated and characterized. Two different compositions of the active layer were compared: an Er^{3+}-doped SiO$_2$ layer and an Er^{3+} and Si-ncs codoped SiO$_2$ layer. It was demonstrated that Si-ncs are useful to get a better injection into the active device layer. On the other hand, the Er^{3+}-doped silica active layer yields higher efficiency since more hot carriers can be injected in an active material, leading to more efficient Er^{3+} impact excitation.

It is worth noting that the waveguide device ensures the propagation of emitted radiation. This allows an interface with a similar passive waveguide and emitted signal collection through a surface grating structure. This is also a first example of a monolithically integrated infrared source that can be used in silicon photonics. Moreover, this work clarifies the route towards further device optimization. In fact, most of the limitations are associated with the device electrodes. In addition, a novel use of the free-carrier absorption which results from the injection of free carriers into slot waveguides is suggested: an integrated modulator with a high extinction ratio or an integrated variable-optical attenuator. Finally, here is reported a first attempt at a monolithic integrated optoelectronic chip where the source, the waveguide and the output couplers are simultaneously fabricated within the same CMOS compatible process.

Acknowledgments

This work was supported by the Spanish Ministry of Science through the project LASSI (TEC2009-08359), by the EC through the project ICT-FP7-224312 HELIOS and by Italy–Spain integrated actions. D N-U is grateful for the financial support of AGAUR through the Beatriu de Pinòs program.

References

[1] Pavesi L, Dal Negro L, Mazzoleni C, Franzò G and Priolo F 2000 *Nature* **408** 440–4

[2] Camacho-Aguilera R E, Cai Y, Patel N, Bessette J T, Romagnoli M, Kimerling L C and Michel J 2012 *Opt. Express* **20** 11316–20

[3] Adler D L, Jacobson D C, Eaglesham D J, Marcus M A, Benton J L, Poate J M and Citrin P H 1992 *Appl. Phys. Lett.* **61** 2181–3

[4] Fuji M, Yoshida M, Kanzawa Y, Hayashi S and Yamamoto K 1997 *Appl. Phys. Lett.* **71** 1198–200

[5] Izzedin I, Timmerman D, Gregorkiewicz T, Moskalenko A S, Prokofiev A A, Yassievich N and Fujii M 2008 *Phys. Rev.* B **78** 035327

[6] DiMaria D J and Dong D W 1980 *J. Appl. Phys.* **51** 2722–35

[7] Jambois O *et al* 2012 *J. Phys. D: Appl. Phys.* **45** 045103

[8] Ramírez J M *et al* 2012 *Nanotechnology* **23** 125203

[9] Jayatilleka H, Nasrollahy-Shiraz A and Kenyon A J 2011 *Opt. Express* **19** 24569–76

[10] Creatore C, Andreani L C, Miritello M, Lo Savio R and Priolo F 2009 *Appl. Phys. Lett.* **94** 103112

[11] Almeida V R, Xu Q, Barrios C A and Lipson M 2004 *Opt. Lett.* **29** 1209–11

[12] Preston K and Lipson M 2009 *Opt. Express* **17** 1527–34

[13] Walters R J, Bourianoff G I and Atwater H A 2005 *Nature Mater.* **4** 143–6

[14] Sun J M, Skorupa W, Dekorsky T, Helm M, Rebohle L and Gebel T 2005 *J. Appl. Phys.* **97** 123513

[15] Anopchenko A *et al* 2012 *J. Appl. Phys.* **111** 063102

[16] Garrido B, Cheylan S, González-Varona O, Pérez-Rodríguez A and Morante J R 2003 *Appl. Phys. Lett.* **82** 4818–20

[17] Arnold D, Cartier E and DiMaria D J 1994 *Phys. Rev.* B **49** 10278

[18] Ramírez J M *et al* 2012 *Mater. Sci. Eng.* B **177** 734

[19] Fowler R H and Nordheim L 1928 *Proc. R. Soc.* A **119** 181

[20] Hadjadj A, Simonetti O, Maurel T, Salace G and Petit C 2002 *Appl. Phys. Lett.* **80** 3335

[21] DiMaria D J, Kirtley J R, Pakulis E J, Dong D W, Kuan T S, Pesavento F L, Theis T N and Cutro J A 1984 *J. Appl. Phys.* **56** 401

[22] Lee J Y M and Cheng C 1982 *J. Appl. Phys.* **53** 490

[23] Joshi D P and Bhatt D P 1990 *IEEE Trans. Electron Devices.* **37** 237

[24] Säynätjoki A, Riikonen J and Lipsanen H J 2003 *Mater. Sci.: Mater. Electron.* **14** 417

[25] Umemoto Y, Schaff W J, Park H and Eastman L F 1993 *Appl. Phys. Lett.* **62** 1964

[26] Roelkens G, Van Thourhout D and Baets R 2006 *Opt. Express* **14** 11622–30

[27] Priolo F, Presti C D, Franzò G, Irrera A, Crupi I, Iacona F, Di Stefano G, Piana A, Sanfilippo D and Fallica P G 2006 *Phys. Rev.* B **73** 113302

Electrical pump & probe and injected carrier losses quantification in Er doped Si slot waveguides

J. M. Ramírez,[1,*] Y. Berencén,[1] F. Ferrarese Lupi,[1] D. Navarro-Urrios,[4] A. Anopchenko,[2] A. Tengattini,[2] N. Prtljaga,[2] L. Pavesi,[2] P. Rivallin,[3] J. M. Fedeli,[3] and B. Garrido[1]

[1]MIND-IN2UB, Departament d'Electrònica, Universitat de Barcelona, Martí i Franquès 1, Barcelona 08028, Spain
[2]Nanoscience Laboratory, Department of Physics, University of Trento, Via Sommarive 14, Povo 38123, Italy
[3]CEA, Léti, Minatec campus 17 rue des Martyrs, Grenoble 38054, France
[4]Catalan Institute of Nanotechnology (CIN2-CSIC), Campus UAB, edifice CM3, Bellaterra 08193, Spain
[*]jmramirez@el.ub.es

Abstract: Electrically driven Er^{3+} doped Si slot waveguides emitting at 1530 nm are demonstrated. Two different Er^{3+} doped active layers were fabricated in the slot region: a pure SiO_2 and a Si-rich oxide. Pulsed polarization driving of the waveguides was used to characterize the time response of the electroluminescence (EL) and of the signal probe transmission in 1 mm long waveguides. Injected carrier absorption losses modulate the EL signal and, since the carrier lifetime is much smaller than that of Er^{3+} ions, a sharp EL peak was observed when the polarization was switched off. A time-resolved electrical pump & probe measurement in combination with lock-in amplifier techniques allowed to quantify the injected carrier absorption losses. We found an extinction ratio of 6 dB, passive propagation losses of about 4 dB/mm, and a spectral bandwidth > 25 nm at an effective d.c. power consumption of 120 μW. All these performances suggest the usage of these devices as electro-optical modulators.

OCIS codes: (130.0250) Optoelectronics; (160.5690) Rare-earth-doped materials.

References and links

1. B. Jalali and S. Fathpour, "Silicon Photonics," J. Lightwave Technol. **24**(12), 4600–4615 (2006).
2. R. Soref, "The Past, Present, and Future of Silicon Photonics," IEEE J. Sel. Top. Quantum Electron. **12**(6), 1678–1687 (2006).
3. M. Lipson, "Guiding, modulating, and emitting light on silicon-challenges and opportunities," J. Lightwave Technol. **23**(12), 4222–4238 (2005).
4. J. D. B. Bradley and M. Pollnau, "Erbium-doped integrated waveguide amplifiers and lasers," Laser Photon. Rev. **5**(3), 368–403 (2011).
5. J. Cardenas, C. B. Poitras, J. T. Robinson, K. Preston, L. Chen, and M. Lipson, "Low loss etchless Silicon photonic waveguides," Opt. Express **17**(6), 4752–4757 (2009).
6. Y. A. Vlasov, M. O'Boyle, H. F. Hamann, and S. J. McNab, "Active control of slow light on a chip with photonic crystal waveguides," Nature **438**(7064), 65–69 (2005).
7. V. R. Almeida, Q. F. Xu, C. A. Barrios, and M. Lipson, "Guiding and confining Light in void nanostructure," Opt. Lett. **29**(11), 1209–1211 (2004).
8. M. Galli, D. Gerace, A. Politi, M. Liscidini, M. Patrini, L. C. Andreani, A. Canino, M. Miritello, R. Lo Salvio, A. Irrera, and F. Priolo, "Direct evidence of light confinement and emission enhancement in active silicon-on-insulator slot waveguides," Appl. Phys. Lett. **89**, 241114 (2006).
9. K. Preston and M. Lipson, "Slot waveguides with polycrystalline silicon for electrical injection," Opt. Express **17**(3), 1527–1534 (2009).
10. H. Jayatilleka, A. Nasrollahy-Shiraz, and A. J. Kenyon, "Electrically pumped silicon waveguide light sources," Opt. Express **19**(24), 24569–24576 (2011).
11. J. M. Ramírez, F. Ferrarese Lupi, Y. Berencén, A. Anopchenko, J. P. Colonna, O. Jambois, J. M. Fedeli, L. Pavesi, N. Prtljaga, P. Rivallin, A. Tengattini, D. Navarro-Urrios, and B. Garrido, "Er-doped light emitting slot waveguides monolithically integrated in a silicon photonic chip," Nanotechnology (to be published).

#175955 - $15.00 USD Received 11 Sep 2012; revised 30 Oct 2012; accepted 1 Nov 2012; published 12 Dec 2012

12. D. Navarro-Urrios, A. Pitanti, N. Daldosso, F. Gourbilleau, R. Rizk, G. Pucker, and L. Pavesi, “Quantification of the carrier absorption losses in Si-nanocrystal rich rib waveguides at 1.54 μm,” Appl. Phys. Lett. **92**, 051101 (2008).
13. T. Creazzo, B. Redding, E. Marchena, S. Shi, and D. W. Prather, “Free-carrier absorption modulation in silicon nanocrystal slot waveguides,” Opt. Lett. **35**(21), 3691–3693 (2010).
14. G. M. Miller, R. M. Briggs, and H. A. Atwater, “Achieving optical gain in waveguide-confined nanocluster-sensitized erbium by pulsed excitation,” J. Appl. Phys. **108**, 063109 (2010).
15. R. Sun, P. Dong, N. N. Feng, C. Y. Hong, J. Michel, M. Lipson, and L. Kimerling, “Horizontal single and multiple slot waveguides: optical transmission at $\lambda = 1550$ nm,” Opt. Express **15**(26), 17967–17972 (2007).
16. D. J. DiMaria and D. W. Dong, “High current injection into SiO_2 from Si rich SiO_2 films and experimental applications,” J. Appl. Phys. **51**(5), 2722–2735 (1980).
17. J. M. Ramírez, F. Ferrarese Lupi, O. Jambois, Y. Berencén, D. Navarro-Urrios, A. Anopchenko, A. Marconi, N. Prtljaga, A. Tengattini, L. Pavesi, J. P. Colonna, J. M. Fedeli and B. Garrido, “Erbium emission in MOS light emitting devices: from energy transfer to direct impact excitation,” Nanotechnology **23**, 125203 (2012).
18. F. Iacona, D. Pacifici, A. Irrera, M. Miritello, G. Franzò, and F. Priolo, “Electroluminescence at 1.54 μm in Er-doped Si nanocluster-based devices,” Appl. Phys. Lett. **81**, 3242 (2002).
19. A. C. Turner-Foster, M. A. Foster, J. S. Levy, C. B. Poitras, R. Salem, A. L. Gaeta, and M. Lipson, “Ultrashort free-carrier lifetime in low-loss silicon nanowaveguides,” Opt. Express **18**(4), 3582–3591 (2010).
20. J. Liu, M. Beals, A. Pomerene, S. Bernardis, R. Sun, J. Cheng, L. C. Kimerling, and J. Michel, “Waveguide-integrated, ultralow-energy GeSi electro-absorption modulators,” Nat. Photonics **2**(7), 433–437 (2008).
21. S. Y. Seo, J. Lee, Jung H. E. S. Shin, B. Kang, and S. Bae, “The thermo-optic effect of Si nanocrystals in silicon-rich silicon oxide thin films,” Appl. Phys. Lett. **85**, 2526 (2004).
22. R. C. Zaccuri, G. Coppola, and M. Iodice, “Thermo-electro-optical analysis of an integrated waveguide-vanishing-based optical modulator,” J. Opt. A: Pure Appl. Opt. **8**(7), S567–S573 (2006).
23. W. M. Green, M. J. Rooks, L. Sekaric, and Y. A. Vlasov, “Ultra-compact, low RF power, 10 Gb/s silicon Mach-Zehnder modulator,” Opt. Express **15**(25), 17106–17113 (2007).
24. L. Chen, K. Preston, S. Manipatruni, and M. Lipson, “Integrated GHz silicon photonic interconnect with micrometer-scale modulators and detectors,” Opt. Express **17**(17), 15248–15256 (2009).
25. L. Liao, D. Samara-Rubio, M. Morse, A. Liu, D. Hodge, D. Rubin, U. D. Keil, and T. Franck, “High speed silicon Mach-Zehnder modulator,” Opt. Express **13**(8), 3129–3135 (2005).
26. G. T. Reed, G. Mashanovich, F. Y. Gardes, and D. J. Thomson, “Silicon optical modulators,” Nat. Photonics **4**(8), 518–526 (2010).
27. A. Liu, R. Jones, L. Liao, D. Samara-Rubio, D. Rubin, O. Cohen, R. Nicolaescu, and M. Paniccia, “A high-speed silicon optical modulator based on a metal-oxide-semiconductor capacitor,” Nature **427**(6975), 615–618 (2004).
28. A. Anopchenko, A. Marconi, E. Moser, S. Prezioso, M. Wang, L. Pavesi, G. Pucker, and P. Bellutti, “Low-voltage onset of electroluminescence in nanocrystalline-Si/SiO2 multilayers,” J. Appl. Phys. **106**, 033104 (2009).

1. Introduction

On-chip integration of photonic devices using CMOS manufacturing tools has become an appealing perspective in the last years [1, 2]. Many encouraging work has heralded silicon photonics as a suitable platform to develop photonic integrated circuits (PIC) that can compete within the aggressive performance and cost demands of short scale telecommunications market [3]. Of particular interest are Er^{3+} doped light emitting devices due to their potentiality as a signal source or amplifier for the C-band at 1.53 μm [4]. Silicon photonics technology has already established platforms in which are possible to integrate low-loss waveguides, electro-optical modulators, switching devices, multiplexers and even detectors [3, 5, 6]. However, all of them lessen if considering architectures suitable for electrical injection and light confinement simultaneously, as the required electrical contacts and the thin film configuration may compromise the effective confinement of the structure. Recently, the slot waveguide configuration was proposed as an alternative geometry able to solve these drawbacks, yielding good mode confinement in a very thin layer with low refractive index [7]. To this end, several work investigated on the optical and electrical properties of slot waveguides, showing promising characteristics for their implementation as functional building blocks [8, 9]. Active slot waveguides where light can be generated and simultaneously coupled to the rest of the photonic circuit were successfully designed [10] and fabricated [11] recently. Er^{3+} doped Si-rich oxide (SRO) was used as a slot layer to yield good injection efficiency and high electroluminescence (EL) performance. Also, much attention has been paid to carrier absorption (CA) losses at 1.53 μm in Si-nanocrystal (Si-ncs) waveguides by means of optical pumping [12], determining an accurate characterization of the optical losses even in slot waveguides [13]. Still, the possible performance of this

#175955 - $15.00 USD Received 11 Sep 2012; revised 30 Oct 2012; accepted 1 Nov 2012; published 12 Dec 2012

geometry in an electrical pump & probe scenario have only been modeled [14], but never studied experimentally.

In this work we report the optoelectronic characteristics and the results of an electrical pump & probe study of Er^{3+} doped Si-based light emitting slot waveguides. Two different active slot waveguides were studied. An Er^{3+} doped oxide (SiO_2) layer was compared with an Er^{3+} doped SiO_2 containing Si-ncs. Such measurements were performed in order to quantify the injected CA losses inside the structure and to investigate on the signal enhancement of the probe signal at 1.53 μm. Finally a plausible modulation scheme in a 1 mm long waveguide is proposed, using the fast dynamics of accumulated carriers at the slot-Si interface in order to modulate the optical signal at competitive frequencies. We obtain an extinction ratio of 6 dB, a spectral bandwidth > 25 nm and a maximum operating power ~120 μW.

2. Device design and setup performance

The Si slot waveguide structure, whose cross section is shown in Fig. 1, was fabricated on silicon on insulator (SOI) wafer. It consists of a thin Er^{3+} doped active layer (SiO_2 or SRO) 40 nm thick, embedded between two Si slabs (horizontal configuration). The preferred deposition techniques for the active layer were low-pressure chemical vapor deposition (LPCVD) for the SRO (with a nominal Si excess of 11.5%) or high temperature oxidization for the SiO_2. The crystalline silicon of the SOI wafer was used as a bottom slab, while the top slab was obtained by a polycrystalline silicon layer which is 100 nm thick and is used both as slab for the waveguide and as an electrode for current injection. N-type doping with a maximum of 10^{19} at./cm^3 was defined at the sides of the polysilicon, remaining the central part undoped. Similarly, using a self alignment method with the specific annealing of the structure, a graded p-type doping profile was defined for the bottom crystalline silicon with an increasing doping concentration that starts near the active layer (10^{17} at./cm^3) down to the bottom electrode with a nominal value of 10^{19} at./cm^3 (see the device cross-section on top of Fig. 1). The bottom electrode (90 nm thick) was 10^{20} at./cm^3 p-type doped. Deep ultraviolet (DUV) lithography was used to define 1 μm wide (x-axis) and 1 mm long waveguides (in z-direction). The structure is cladded by a stoichiometric high temperature oxide (HTO). Finally, vias were etched down to the doped part of the waveguides and Al metal electrodes were formed (see ref. [11]). An optical mode confinement factor of 40% was calculated, defined as the ratio of the optical power in the slot and the total optical power [15].

The total footprint of the active structure is 29 μm wide (along the x-direction), 0.46 μm thick (y-axis) and 1mm long (z-axis). Figure 1 (top panel) shows the waveguide cross-section. The active waveguide is coupled from both facets to a passive slot Si waveguide by means of a slot taper. The latter structure presents an initial width of 1 μm (x-axis), which matches the width of the active waveguide, a length of 800 μm (z-axis) and a final width of 12 μm (passive Si waveguide width). The waveguide cross-section is the same for both taper and active region, except for the top and bottom electrodes, the p-type graded implantation in the lower slab and the Er^{3+} implantation. Figure 1 (bottom panel) shows a top schematic view of the active waveguide-taper-passive waveguide system.

#175955 - $15.00 USD Received 11 Sep 2012; revised 30 Oct 2012; accepted 1 Nov 2012; published 12 Dec 2012

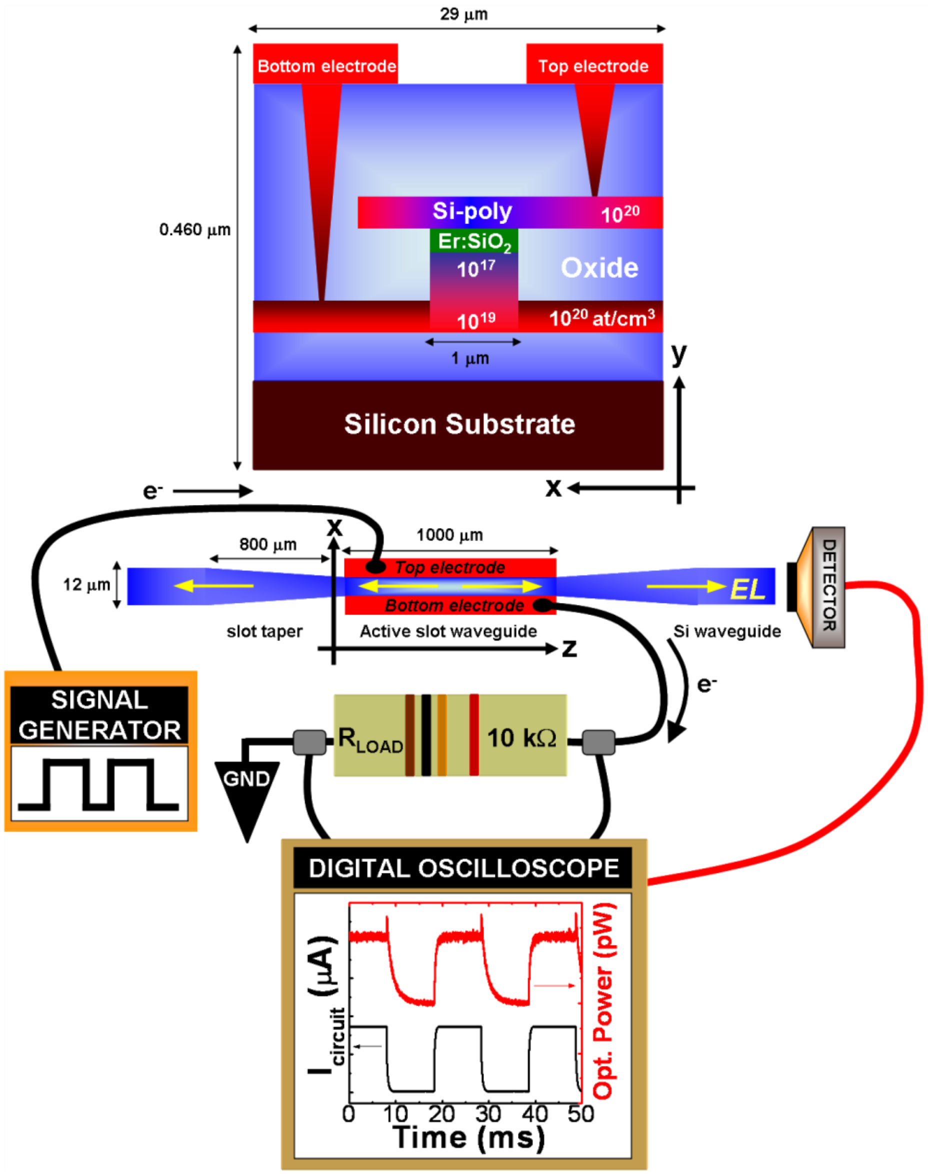

Fig. 1. Slot waveguide cross-section (top panel) and top schematic view (bottom panel) of the integrated system with the experimental configuration used for the measurements. A coordinate system (crossed arrows) is shown to facilitate a spatial view of the waveguides.

The waveguides are excited by a square wave pulse produced by a signal generator (Agilent 8114A), which is directly linked to the top electrode of the waveguide. A load resistance (10 kΩ) is connected in series with the bottom electrode and used to monitor the injected current (see Fig. 1, bottom panel). Simultaneously, the output EL emission at 1528 nm is collected from the waveguide facet by a PMT detector (H10330-25) interfaced with a monochromator with a spectral resolution of 0.1 nm. Both the injected current in the waveguide and the generated EL are monitored through a digital oscilloscope (Agilent DSO 8064A).

Electrical pump & probe measurements were also performed by coupling an infrared laser-diode with a maximum power at 1528 nm (Thorlabs FPL 1009P) in the slot waveguides by means of an output coupler (see ref. [11] for further details). An infrared camera

#175955 - $15.00 USD Received 11 Sep 2012; revised 30 Oct 2012; accepted 1 Nov 2012; published 12 Dec 2012

(Hamamatsu c2741) was used to monitor the guided mode at the output of the waveguide and ensure its good confinement. A pin-hole was also placed before the detection stage to solely select the guided light. Once the probe alignment and detection is optimized, the electric pump is switched on (square wave pulse), and the output signal is recorded.

3. Experimental results

J(V) curves were obtained under negative voltages (accumulation) up to the device breakdown (between −47 V and −48 V) with a quasi-static step voltage of 10 mV/s. Figure 2(a) shows the data, including the range of voltages (from −25 V up to the breakdown) where one single transport mechanism can be identified (Fowler-Nordheim, FN injection). A decrease of the tunneling barrier height was observed when the Si-ncs are embedded, facilitating the electrical injection (higher currents are obtained for the Er:Si-ncs layer) and improving the reliability and device lifetime [16]. Under FN injection, infrared EL was emitted, indicating that the main excitation mechanism is direct impact excitation of the Er ions via the hot carriers injected in the active layer. The characteristic Er emission spectra were observed for the two waveguides (see Fig. 2(b)). Bearing in mind that the spectral resolution of our setup is 0.1 nm, the evolution of the EL spectrum was studied as a function of the applied voltage amplitude revealing no modification of the spectra with increasing voltage, nor any spectral narrowing effects.

A time-resolved characterization of the EL and of the injected current was performed. An example is shown within the digital oscilloscope of Fig. 1 (bottom panel). A clear EL overshoot is observed when the pump voltage is switched off (top signal), which is not correlated with the injected current since no overshoot is observed on the bottom signal.

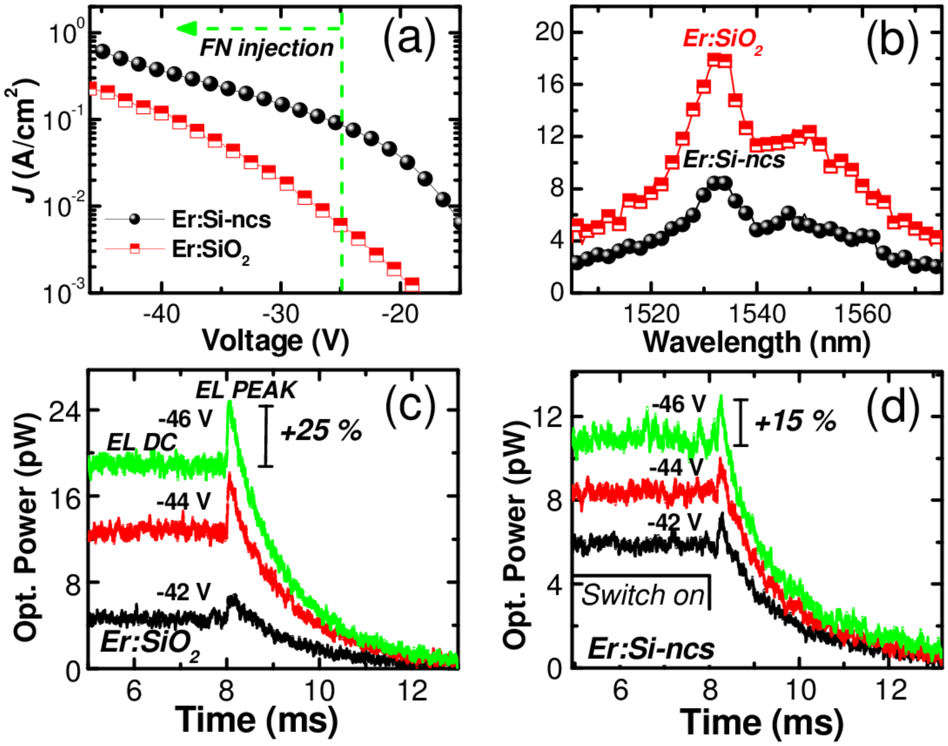

Fig. 2. (a) *J(V)* characteristics of the waveguides under accumulation. (b) EL spectra of both layers obtained under a square wave pulse (V_{pp} = −44 V). (c and d) Time-resolved EL measurements at 1528 nm of the Er:SiO$_2$ (c) and the Er:Si-ncs (d) slot waveguides as a function of the voltage polarization in the top electrode.

#175955 - $15.00 USD Received 11 Sep 2012; revised 30 Oct 2012; accepted 1 Nov 2012; published 12 Dec 2012

Notice that this feature is not typical for Er^{3+} doped capacitors [17]. Moreover, such an EL peak can be observed in both active waveguides for a voltage range where EL signal is present, until the device breakdown (see Fig. 2(c) and Fig. 2(d)). For comparison, time-resolved EL was also collected from the top of the waveguide (the EL passing through the top polysilicon electrode), but no EL overshoot was observed at any voltage (not shown). From now on, the EL obtained under a constant pump voltage has been labeled as EL_{DC} and the EL overshoot as EL_{PEAK}. Defining the EL relative increase (Δ_{EL}) as:

$$\Delta_{EL}\left(\%\right)=\frac{EL_{PEAK}-EL_{DC}}{EL_{DC}}\cdot 100 \tag{1}$$

A value of 25% (15%) is obtained for the $Er{:}SiO_2$ (Er:Si-ncs) waveguide. In order to further investigate the origin and evolution of this peak, both EL_{DC} and EL_{PEAK} values were studied as a function of the injected current in several waveguides. For that, the pump voltage polarization was swept from –41 V to –46 V (from EL onset upwards) with a step voltage of 0.5 V. A superlinear increase of EL_{DC} and EL_{PEAK} as a function of the injected current is reported in Fig. 3(a). A power law fit yields exponent of 2.62 ± 0.08 for the EL_{PEAK} and 2.71 ± 0.07 for the EL_{DC} for an $Er{:}SiO_2$ waveguide; lower exponents of 2 (in average) are observed for the Er:Si-ncs waveguide (not shown). In addition, almost identical superlinear slope was identified in the $EL_{DC}(J)$ characteristic collected from the top of the waveguide. The lightly doped top polysilicon is thought to be the origin of superlinearity since is the only difference (in terms of cross-section) between our waveguides and light emitting MOS capacitors [17]. A plausible explanation would be that at low voltages the distributed electric field along the top polysilicon is not equipotential because of the non-doped central region. Therefore, the Er^{3+} excitation would take place at the side of the top polysilicon where the top electrode is contacted (see Fig. 1). Increasing the applied voltage would spread the electric field across the top polysilicon, also expanding the effective excitation active area. The exponent difference shown between $Er{:}SiO_2$ and Er:Si-ncs waveguides is attributed to a higher barrier height for the former that provides better hot carrier acceleration (then a faster growth of the EL). Therefore, neither the EL_{DC} nor the EL_{peak} are related to an amplifying process inside the waveguides (amplified spontaneous emission, ASE). Furthermore, additional measurements in waveguides with different lengths (1.5 mm, 2 mm, 2.5 mm and 3 mm), showed no dependence between the EL and the waveguide length; the same optical power and similar exponents were obtained in all the waveguides. This behavior was attributed to the on-chip propagation losses which account to 40 dB/cm and prevent photons generated at a distance longer than 1 mm to reach the waveguide facet. Additionally, an EL saturation at high current injection is observed in Fig. 3(a), suggesting either a saturation of the excitable Er^{3+} fraction or the onset of device breakdown (i. e. appearance of additional current pathways that do not contribute to the Er^{3+} excitation). The analysis of the rise (τ_{rise}) and decay (τ_{decay}) times yields single exponential decays (Fig. 3(b)). The following functions were used to extract the characteristic times from the experimental data:

$$EL_{off}(t)=EL_{peak}\cdot e^{-\frac{t}{\tau_{decay}}} \tag{2}$$

$$EL_{on}(t)=EL_{DC}\left\{1-e^{-\frac{t}{\tau_{rise}}}\right\} \tag{3}$$

A decay time of 1.7 ms which is independent on the injected current was obtained for the $Er{:}SiO_2$ waveguide (1.2 ms for the Er:Si-ncs). On the contrary, a strong injected current dependence was observed for the rise time in both waveguides which varies from 1.6 ms (small injected currents) to 0.18 ms (large injected current). From these values and assuming a simple two level model, an injection excitation cross-section σ of the Er^{3+} ions of $\sim 1\times 10^{-14}$ cm^2 was found. Notice that this value fits with the one reported for Er^{3+} doped silicon

#175955 - $15.00 USD Received 11 Sep 2012; revised 30 Oct 2012; accepted 1 Nov 2012; published 12 Dec 2012

dioxides [18]. An upper injection CA lifetime of 10 μs was also measured, equal to our time circuit constant (τ_{RC} ~*10 μs*). Nevertheless, lower CA lifetimes (in the order of few ns) are expected in our devices for an optimized experimental setup (with lower τ_{RC}) [19].

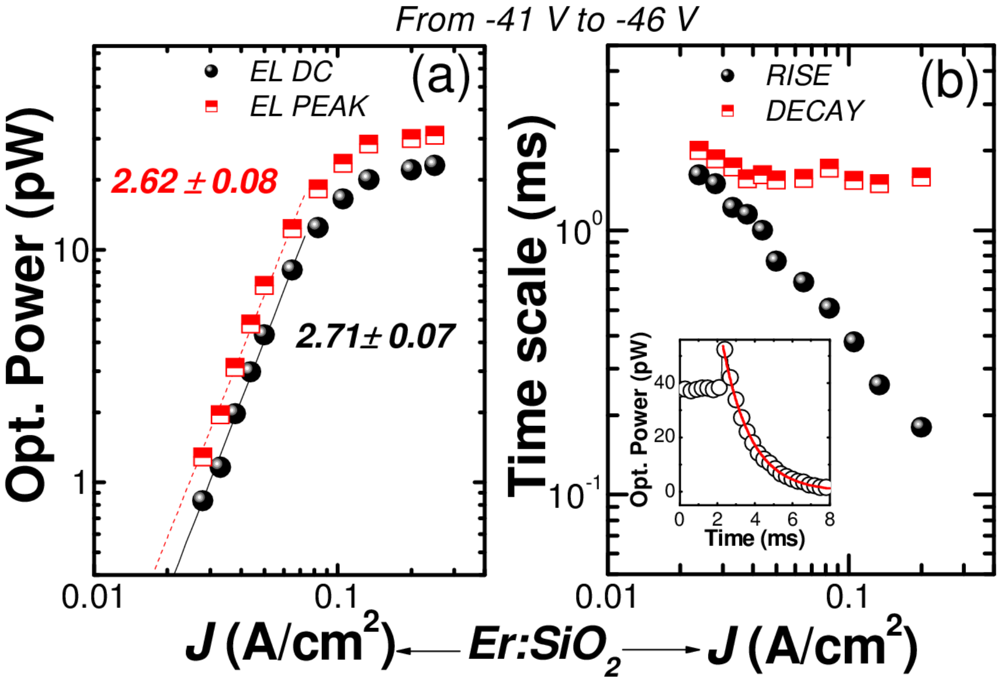

Fig. 3. (a) Intensity of the DC and peak EL value as a function of the injected current density for the two waveguides studied. (b) Decay (half filled squares) and rise (circles) times as a function of the injected current. The inset shows an example of a decay fit of the experimental data. This figure shows a representative measurement in an Er:SiO$_2$ waveguide.

Disregarding stimulated emission, the sharp EL_{PEAK} can be explained by taking into account two independent mechanisms: The excited Er recombination dynamics and the CA dynamics. When the pump voltage is switched on, additional optical losses (superimposed to the propagation losses, α_{prop}) are generated due to the injected carriers (CA losses). When the pump is turned off, the injected carriers recombine. Carrier recombination reduces the waveguide losses to α_{prop}, and since the Er^{3+} lifetime is long, an increase of the EL signal is observed. This explains the EL_{PEAK}. The difference in the EL_{PEAK} value in the two waveguides suggests carrier trapping within the active waveguide due to the Si-ncs.

Further insight comes from time-resolved electrical pump & probe measurements. A continuous probe signal at 1528 nm was coupled to the waveguide with a power comparable to the EL signal. This is done in order to work on the low signal gain regime, where the probe signal does not modify the population of the levels. Then, a square voltage signal (0 to negative value) with a frequency of 50 Hz is used as a pump source. The different panels of Fig. 4 show the evolution of the EL (I_{EL}, black curves at the bottom) and of the transmitted probe signals ($I_{p\&p}$, red curves on top) for different pump voltages within a voltage interval where I_{EL} is detectable. For clarity, it has been identified the time window in which only the probe signal is propagating and the pump is switched off (indicated by *p-off*), and also the one in which the pump is activated (*p-on*). It is clear that, within the *p-on* region, $I_{p\&p}$ gets strongly attenuated with respect to the *p-off* region and reaches the I_{EL} level for pump voltages of −44 V (and above). In particular, in the *p-off* region at −42 V, a small overshoot contribution in $I_{p\&p}$ is observed during the first milliseconds. This contribution becomes a sharp peak for higher pump voltages. However, it essentially reproduces the temporal behavior observed in the I_{EL} dynamics (black line) already discussed. Thus, $I_{p\&p}$ can be explained in terms of CA losses, which dramatically quench the probe signal when carrier injection occurs.

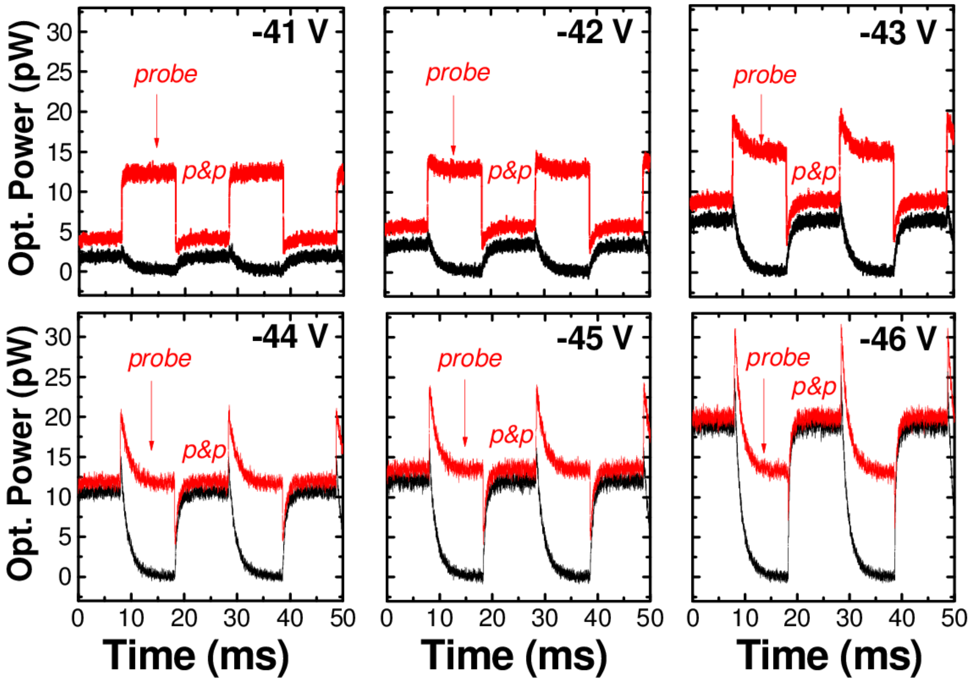

Fig. 4. Electrical pump & probe measurements of an Er:SiO_2 waveguide at 1528 nm (top red line) under square wave electrical bias. Each panel refers to different square wave amplitude. The EL has been also measured for each voltage polarization (black line at the bottom).

To isolate the temporal behavior of the probe transmittance from the EL contribution, the following equation has been applied:

$$Transmittance = \frac{10}{L}\log\left(\frac{I_{p\&p} - I_{EL}}{I_{probe}}\right) \qquad (4)$$

where L is the waveguide length and I_{probe} is the asymptotic value of $I_{p\&p}$ during the p-off phase. The transmittance is illustrated on Fig. 5 for the case of the highest voltage amplitude (–46 V).

#175955 - $15.00 USD Received 11 Sep 2012; revised 30 Oct 2012; accepted 1 Nov 2012; published 12 Dec 2012

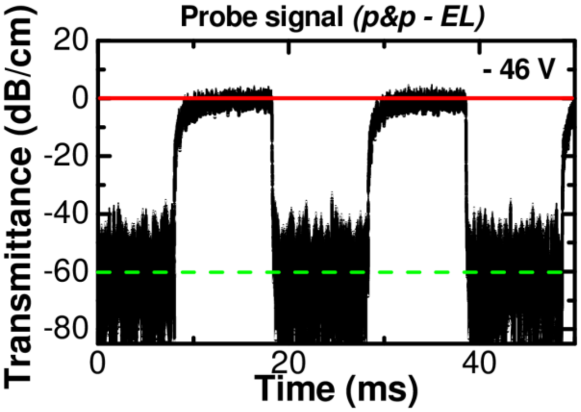

Fig. 5. Transmittance at 1528 nm in the Er:SiO$_2$ waveguide for a square wave bias of −46 V. This figure was obtained by subtracting the EL signal to the pump & probe measurements of the panel in the right-bottom side of the Fig. 4. The green dashed line marks the average transmittance when the voltage source is on.

It is clearly revealed that no signal enhancement is present (the threshold is marked with a horizontal red line) even within the p-off region, where the injected CA losses are suppressed and the peaks on I_{EL} and $I_{p\&p}$ were evident. During the pumping time, the average injected CA losses can be as high as 60 dB/cm (see the green dashed line in Fig. 5). It is also worth noticing that a slow recovery of the probe signal can be identified when the pump is switched off. Other authors have already observed this phenomenon under optical pumping, and attributed it to a thermal contribution when high pump fluxes are applied [12]. In our devices, the slow recovery time is observed starting at −25 V. This evidences that the waveguides are subjected to a high thermal budget under electrical polarization.

Finally, an additional pump & probe approach was carried out by modulating simultaneously the probe signal (200 kHz) and the voltage source (10 Hz). In that case, a lock-in technique in combination with a time-resolved configuration was used. The lock-in amplifier locked on the probe beam transmission, and its output signal monitored by the oscilloscope which was triggered by the voltage source. This way the modulation depth caused by the injected CA losses was carefully monitored, since the EL is filtered out by the lock-in. The square wave voltage amplitude was changed from 0 to −45 V, with a step voltage of 2.5 V. Results are shown in Fig. 6, where the time-resolved transmittance of a probe beam at 1528 nm (Fig. 6(a)) and the spectral transmittance (Fig. 6(b)) are characterized under different amplitude voltages. The probe signal is strongly attenuated under injection, and becomes more evident as the square wave voltage increases. Notice that no spectral dependence of the attenuation (Fig. 6(b)) is observed at any voltage for probe beam wavelengths from 1515 nm to 1540 nm, i.e. over a 25 nm interval.

#175955 - $15.00 USD Received 11 Sep 2012; revised 30 Oct 2012; accepted 1 Nov 2012; published 12 Dec 2012

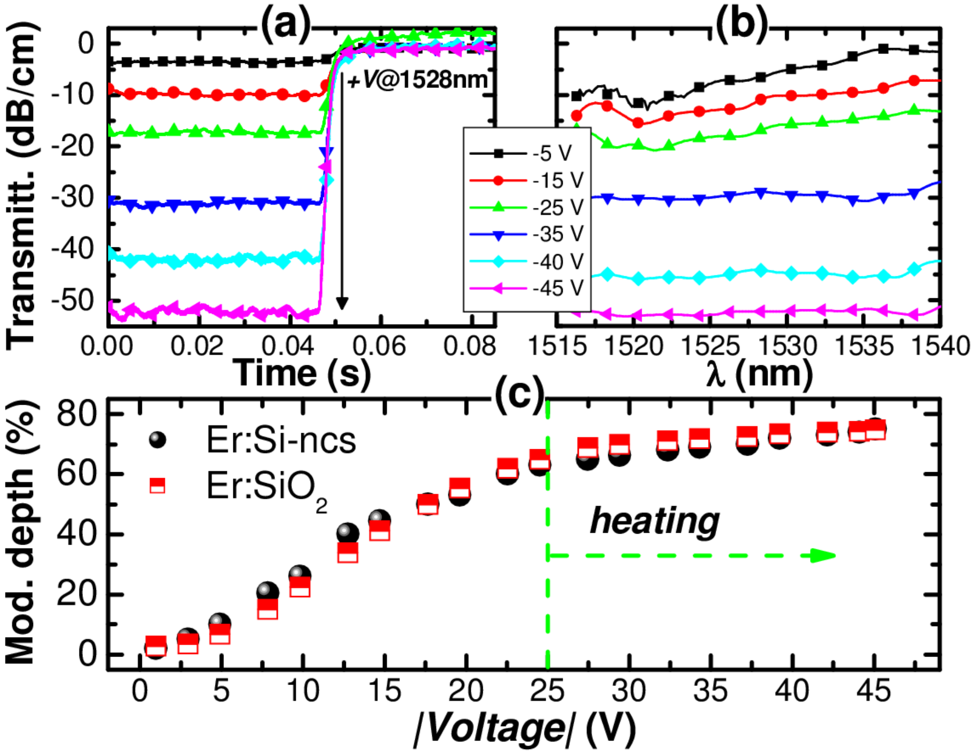

Fig. 6. (a) Time-resolved probe intensity transmittance at 1528 nm and (b) spectral transmittance for different voltages (given in the legend) and for the Er:SiO$_2$ waveguide. (c) Modulation depth as a function of the applied voltage for the two waveguides. The green dashed line indicates the threshold where heating effects start to be sizable.

Figure 6(c) shows the voltage dependence of the modulation depth (η) of the transmission beam. This represents the contribution of the injected CA as a function of the applied voltage for the two waveguides under study. The following equation was used [20]:

$$\eta(\%) = [1 - \exp(-\Delta\alpha(V)L)] \cdot 100 \tag{5}$$

where $\Delta\alpha(V)$ is the loss variation due to the applied bias. A linear trend is obtained for applied voltages < 25 V, then triggering a regime in which the modulation depth tends to saturate (from 25 V and above). Notice that this voltage coincides with the FN injection onset. Also, considerable heating of the waveguide is expected under these medium-high pump voltages (see the slow recovery time of the probe signal in Fig. 5). Heating affects the refractive index and, hence, promotes the optical mode delocalization which, in turn, induces the saturation of the modulation depth [21, 22]. On the contrary, a rather different condition prevails for voltages below the tunnel injection threshold (25 V). In that case, negligible CA contribution due to the injected current across the slot layer is predicted (the current being ~*nA*). Carriers are mainly accumulated at the slot interface when the polarization is switched on. Therefore, the heating is reduced while modulation can be achieved. A maximum modulation depth of 75% is observed in both waveguides, which corresponds to an absolute extinction ratio of 6 dB in our 1 mm long waveguides. Notice that the inclusion of Si-ncs does not improve the modulation capabilities of our waveguides.

Since this value is comparable with that of d.c. based pn junction silicon modulators [23, 24], it is interesting to analyze our 1 mm long waveguides as potential candidates as integrated electro-optical modulators. Measured propagation losses are almost 4 dB, a value which is lower than the ones of Mach-Zehnder (MZ) optical modulators [25]. The length is 1 mm which is also shorter than the one of MZ modulators and yields a lower footprint in the

#175955 - $15.00 USD Received 11 Sep 2012; revised 30 Oct 2012; accepted 1 Nov 2012; published 12 Dec 2012

photonic chip. In addition, although the voltage needed for a 6 dB modulation is quite high (~40 V) and introduces some heating, the current remains very low (~3 μA), providing d.c. operational power of 120 μW which is a competitive value for silicon modulators [26]. The spectral bandwidth (minimum of 25 nm, see Fig. 6(b)) is wider and the thermal stability is better with respect to ring resonator or MZ based modulators, which rely on the interferometry. Though not demonstrated here, a modulation speed > 1 GHz is foreseen by using the accumulation of carriers at the interface as considered in previous work [27]. Then, assuming a modulation speed of 1GHz, the estimated energy per bit would be around of 120 fJ·bit^{-1} similar to that of the most efficient modulators [24]. Therefore, all the presented characteristics can be used to develop a robust electro-optical modulator with the slot layer entirely formed by a SiO_2 only (with no Er implantation neither Si-ncs). Also, an active waveguide modulator can be anticipated if using Er-doped SiO_2 waveguides. In that case, monomodal EL at 1.53 μm would be generated in the waveguide and directly modulated avoiding the on-chip coupling of an external laser (the light source and the modulator would be integrated within a single silicon photonic chip). A remarkable improvement of the optoelectronic characteristics is expected in slot waveguide modulators when optimization of the top electrode is performed. A more accurate doping distribution and a multilayer structure of SiO_2 and silicon-rich oxide (SRO) in the slot can be also engineered to reduce the onset voltage required for the modulation [28].

4. Conclusions

An injection voltage dependent study of Er^{3+} doped slot waveguides have been performed to quantify the injected carrier induced losses. The Er^{3+} electroluminescence has been characterized at 1.53 μm for two different active materials (Er^{3+} doped SiO_2 or Si-rich oxide) in the slot region of the waveguides. In time-resolved experiments, we obtain a sharp EL peak when the voltage is switched off due to the different lifetimes of excited Er^{3+} ions and of the generated carriers. An electrical pump & probe measurement has allowed us to determine the injected carrier losses in 1 mm long waveguides, obtaining an extinction ratio in d.c. modulation of 6 dB with an operation power consumption of 120 μW and a spectral bandwidth > 25 nm. Further improvements in terms of power consumption can be considered if the top electrode, the active slot layer and the doping distribution are optimized.

Acknowledgments

This work was supported by the Spanish Ministry of Science through the project LASSI (TEC2009-08359), and by the EC through the project ICT-FP7-224312 HELIOS and by Italy-Spain integrated actions. The authors thank Alessandro Marconi and Olivier Jambois for contributions at an early stage of this work.

#175955 - $15.00 USD Received 11 Sep 2012; revised 30 Oct 2012; accepted 1 Nov 2012; published 12 Dec 2012

Electrically pumped Er-doped light emitting slot waveguides for on-chip optical routing at 1.54 μm

J. M. Ramírez*[a], Y. Berencén[a], D. Navarro-Urrios[b], F. Ferrarese Lupi[c], A. Anopchenko[d], N. Prtljaga[d], P. Rivallin[e], A. Tengattini[d], J. P. Colonna[e], J. M. Fedeli[e], L. Pavesi[d], and B. Garrido[a]
[a]MIND-IN2UB, Departament d'Electrònica, Universitat de Barcelona, Martí i Franquès 1, 08028 Barcelona, Spain.
[b]Catalan Institute of Nanotechnology (CIN2-CSIC), Campus UAB, edifice CM3, Bellaterra 08193, Spain
[c]Laboratorio MDM, IMM-CNR, Via C. Olivetti 2, 20864 Agrate Brianza (MB), Italy
[d]Nanoscience Laboratory, Department of Physics, University of Trento, Via Sommarive 14, Povo 38123, Italy.
[e]CEA, Léti, Minatec campus 17 rue des Martyrs, 38054 Grenoble cedex 9, France.

ABSTRACT

Optoelectronic properties of Er^{3+}-doped slot waveguides electrically driven are presented. The active waveguides have been coupled to a Si photonic circuit for the on-chip distribution of the electroluminescence (EL) signal at 1.54 μm. The Si photonic circuit was composed by an adiabatic taper, a bus waveguide and a grating coupler for vertical light extraction. The EL intensity at 1.54 μm was detected and successfully guided throughout the Si photonic circuit. Different waveguide lengths were studied, finding no dependence between the waveguide length and the EL signal due to the high propagation losses measured. In addition, carrier injection losses have been observed and quantified by means of time-resolved measurements, obtaining variable optical attenuation of the probe signal as a function of the applied voltage in the waveguide electrodes. An electro-optical modulator could be envisaged if taking advantage of the carrier recombination time, as it is much faster than the Er emission lifetime.

Keywords: Erbium, electroluminescence, silicon photonics, slot waveguide, silicon modulators, silicon nanocrystals.

1. INTRODUCTION

Rare earth (RE) light emitting devices are elements of interest in the Silicon Photonics research because they provide electroluminescent (EL) signals at convenient wavelengths. They are employed either to fabricate visible or infrared light emitting devices [1, 2]. Among the large number of rare earth ions used to produce visible light emission, we may cite cerium (Ce^{3+}) due to its blue emission around of 440 nm, europium (Eu^{3+}) with an emission line at 620 nm, gadolinium (Gd^{3+}) that emits at 316 nm or terbium (Tb^{3+}) emitting around of 555 nm. On the contrary, ytterbium (Yb^{3+}) and erbium (Er^{3+}) are mostly developed for infrared applications, with emission lines at 975 nm and 1550 nm, respectively. In particular, Er^{3+} is the most investigated RE ion in Silicon Photonics because of its infrared emission that matches the minimum of absorption of silica, providing an ideal scenario to develop high efficient optical communications working in the third telecom window. This advantage has been already exploited by the well known erbium-doped fiber amplifiers (EDFAs) which have become key elements in the large-scale telecommunications [3]. Later on came its miniaturized counterpart, the erbium-doped waveguide amplifiers (EDWAs), intended for compact and cost-effective on-chip communications [4]. Nevertheless, all of the mentioned devices need to be optically pumped by bulky monochromatic light sources like LASERs (Light Amplification of Stimulated Emission of Radiation), which strongly limit their applications as compact and portable systems because of the critical alignment required between the LASER and the optical amplifier. In order to solve this drawback, several research groups are working toward the development of integrated Er-doped light emitters able to intrinsically generate optical signals at 1.54 μm under the excitation of an electric field (electroluminescent light sources) [5, 6]. Some attempts have been done in that direction, providing a major insight on the optoelectronic properties of Er-doped devices fully fabricated with the complementary

Integrated Photonics: Materials, Devices, and Applications II, edited by Jean-Marc Fédéli, Laurent Vivien, Meint K. Smit,
Proc. of SPIE Vol. 8767, 87670I · © 2013 SPIE · CCC code: 0277-786X/13/$18 · doi: 10.1117/12.2017250

metal-oxide-semiconductor (CMOS) technology. However, most of these devices are based on capacitor-like structures and yield vertical emission only, being difficult the on-chip light propagation.

Enabling light generation and propagation in the very same device can become a rough task as several factors should be considered in order to succeed. Starting from the electrical point of view, there is a must for using thin films (few tens of nanometers) as electroluminescent layers to provide good current injection for Er excitation. On the other hand, light guiding at 1.54 μm in very thin layers can be only achieved by using the slot waveguide geometry, where the light is confined in the material with the lowest refractive index [7]. Also, a careful design should be implemented in order to reduce the confined light fraction in the electrodes due to the high propagation losses induced in such structures (a highly doped polysilicon, normally), since high doped electrodes are needed to guarantee ohmic injection. Although these requirements strongly limit the range of materials to be used, SiO_2 as active layer turns out to be a good material for this purpose as it presents a lower refractive index with respect to silicon ($n = 1.5$ for SiO_2, $n = 3.5$ for Si), is a good host for Er^{3+} ions, and can be easily fabricated and controlled with the CMOS technology. Additionally, its electrical properties can be modified embedding silicon nanocrystals (Si-ncs) which enhance the charge transport through the layer [8].

Therefore, the present work is devoted to the development of electroluminescent slot waveguides based on Er^{3+}-doped SiO_2 layers with Si-ncs. The slot waveguide has been simultaneously fabricated with the passive photonic circuit that consists in an adiabatic taper, a bus waveguide and a grating coupler for vertical light extraction (to ease the wafer testing). Different waveguide geometries have been analyzed, varying the waveguide width and length subsequently. Results show good EL properties at 1.54 μm but no dependence with the waveguide length due to the high propagation losses measured. Largest EL signal is obtained from the widest slot geometry (1 μm), suggesting that light confinement at 1.54 μm is better suited in such structure. Carrier injection losses are observed in all devices, showing probe signal attenuation of tens of dB/cm.

2. RESULTS AND DISCUSSION

2.1 Device design

Light emitting devices (LEDs) have been fabricated in slot waveguide configuration in a standard CMOS line. They consist in a slot layer 40 nm thick embedded between two slab layers that are also used as injection electrodes. The bottom p-type electrode has been formed by doping the monocrystalline silicon layer of the SOI wafer (10^{20} at/cm^3), whereas the top one is a highly doped polysilicon layer 100 nm thick (10^{20} at/cm^3, n-type). Looking at the device geometry, several considerations were taken into account in order to preserve propagation losses as low as possible. First of all, asymmetric slot structure was defined, being the lower slab-electrode thicker than the top one. This approach reduces the light confinement in the top polysilicon slab, which is known to be a lossy material for light propagation. In addition, a doping gradient was performed on the lower slab in order to minimize the free-carrier absorption. Similarly, inhomogeneous n-type doping was applied in the top polysilicon layer, remaining the central part undoped. Concerning the slot material, two different active layers are here tested: A deposited silicon-rich oxide (SRO) and a high thermal oxide (HTO), both with an Er^{3+} implantation of about $5 \cdot 10^{20}$ at/cm^3. Optimized adiabatic tapers, passive bus waveguides and gratings were also included in the final mask so as to form the final Si photonic chip. Further details on fabrication steps and deposition parameters of the entire photonic chip can be found in ref. 9 and 10.

Five waveguide lengths were studied (1 mm, 1.5 mm, 2 mm, 2.5 mm and 3 mm), as well as three different waveguide widths (1 μm, 500 nm and 300 nm). Figure 1 shows a schematic view of the photonic chip.

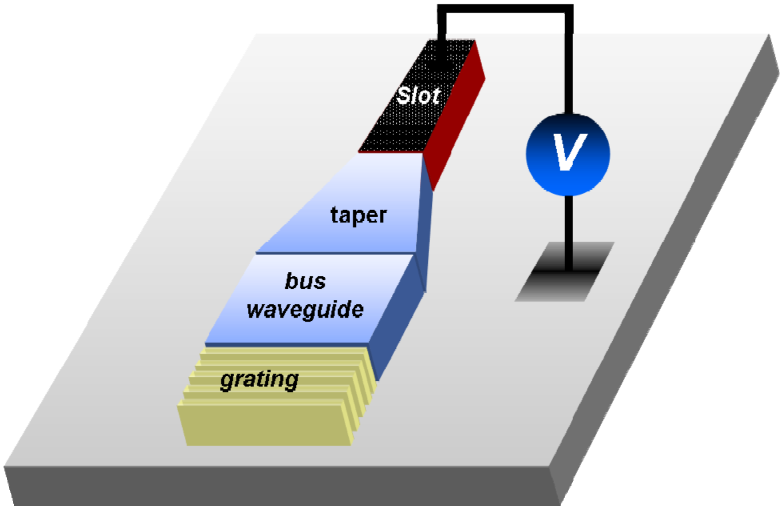

Figure 1. Schematic view of the photonic chip, with the active slot waveguide and the passive circuit formed by the adiabatic taper, the bus waveguide and the grating coupler.

Passive propagation losses were measured by using the cut-back technique (with the voltage switched off), obtaining similar propagation losses in both slot materials (40 dB/cm in average). Notice that the high propagation losses are a direct consequence of the slow group velocity (v_g) found in the slot waveguides ($v_g = c/ 4$).

2.2 Optoelectronic characteristics

Current-voltage (I(V)) characteristic of slot waveguides was obtained in forward polarization (i.e. negative voltages at the top electrode) until the device breakdown. Also, EL at 1.54 µm was collected from the grating coupler using an infrared photomultiplier detector. Figure 2 compares the experimental results (in absolute values) of the Er^{3+}-doped SRO (sample A1) with the Er^{3+}-doped SiO_2 waveguide (A0) for the 1 µm width slot waveguide and three different lengths (1 mm, 2 mm and 3 mm). Looking at the I(V) characteristic (insets in Figure 2), we observe that sample containing Si-ncs (A1) presents higher conductivity than sample without Si-ncs (A0) at a fixed voltage. That is somehow expected since Si-ncs are commonly used to enhance the transport properties of some dielectric materials (Si_3N_4 or SiO_2, for example) either by trap assisted tunneling (TAT) or by thermal assisted mechanisms (e.g. Poole-Frenkel conduction) [8, 11]. In our case, experimental I(V) curves better fit with the Fowler-Nordheim tunneling conduction in both samples, suggesting a TAT conduction electrode-limited [9] rather than a bulk-limited mechanism [12]. When looking at the EL(I) characteristic however, higher external quantum efficiency (EQE) is observed in sample without Si-ncs (A0). Nevertheless, this feature is not surprising if taking into account that the Er^{3+} excitation is mainly governed by direct impact of hot carriers in the conduction band [13]. Embedding Si-ncs enhances the carrier transport via TAT but also diminishes the average energy of the injected hot carriers in the conduction band. Consequently, they excite a smaller number of Er^{3+} ions in one single tunneling event, hence lowering the EQE.

Another interesting characteristic of our active slot waveguides is the superlinear exponent in the EL(I) curve (see slopes in Figure 2) that can be observed either from the grating coupler (guided EL) or from the top of the waveguide and through the top polysilicon electrode (scattered EL). It is worth noticing that this trend is not observed in Er^{3+}-doped capacitors since the EL signal is proportional to the injected current with a linear exponent (slope ~ 1) [14]. Furthermore, the superlinear exponent is very reproducible in samples A1 and A0 indistinctively, being the ones obtained from sample A0 (Figures 2d, 2e and 2f) slightly higher in most cases (compare Figure 2b and 2e, for example). At this point, we should point out that although the super linearity seems to decrease for longer waveguides (compare Figure 2a and 2c), we would rather prefer not to make any assertion since there is a relatively large dispersion along the wafer for that particular value (but superlinear in all cases), obtaining an average slope from all the tested devices of ~2 for sample A1 and ~3 for A0 (each panel in Figure 2 only shows experimental curves of one particular device).

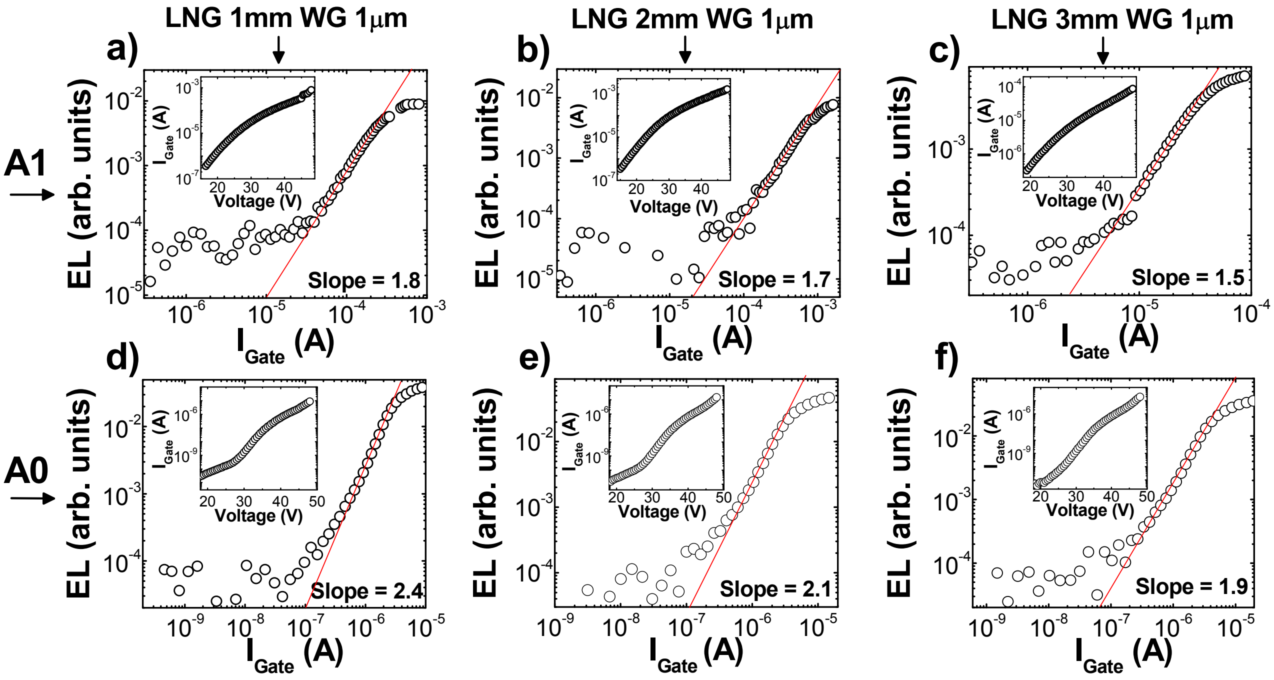

Figure 2. EL(I) curves at 1.54 μm of the Er^{3+}-doped slot waveguide containing Si-ncs (A1) for three different lengths (panels a, b and c, the length symbolized as LNG). Inset at each panel shows the corresponding I(V) curve. Panels d, e and f depicts the same feature for the Er^{3+}-doped slot waveguide without Si-ncs (A0). All the displayed measurements correspond to the widest waveguides (1 μm, symbolized as WG), although similar results were obtained for thinner waveguides (500 nm and 300 nm).

Although the physical origin of this super linearity is not clear and need further investigation, we discard amplified stimulated emission (ASE) as very similar exponents were also found in the scattered EL collected through the top polysilicon electrode, where there is no light confinement. As a tentative explanation, we suggest an effect of the non-uniformly doped top electrode that may produce an inhomogeneous carrier injection in the active layer [9].

Additionally, time-resolved EL was performed in slot waveguides, obtaining a typical Erbium EL decay time of 1.7 ms and a rise time that varies from 1.6 ms at low carrier flux to 0.18 ms at high flux values. Both decay and rise times were well-fitted to a single exponential function. Moreover, an interesting EL overshoot is observed only when collecting the EL from the grating (guided EL). A comparison between the top scattered EL (empty circles) and the guided EL (empty squares) can be observed in Figure 3. Similar decay and rise times were also obtained either from the top or from the grating. Focusing on the EL overshoot, a rise time of at least 10 μs was detected, equal to our setup resolution. Therefore, we attribute the origin of this peak to an effect of the injected carrier losses in the slot waveguide. Applying a voltage on top of the polysilicon electrode stimulates the current injection across the active slot layer, which produces EL at 1.54 μm via direct impact excitation but also induces an additional source of losses due to injected carriers in the region where light is being confined. Consequently, two different mechanisms are competing, giving rise to an averaged EL value (see the EL value at 0.002 s in Figure 3). Then, switching off the polarization allows the recombination of injected carriers which are faster than the mean radiative emission time of Er^{3+} ions (around of 1 ms), hence removing one mechanism from the slot and causing the EL signal to suddenly increase with a rise time that coincides with the typical recombination time of injected carriers (see the EL overshoot of the grating EL) [15].

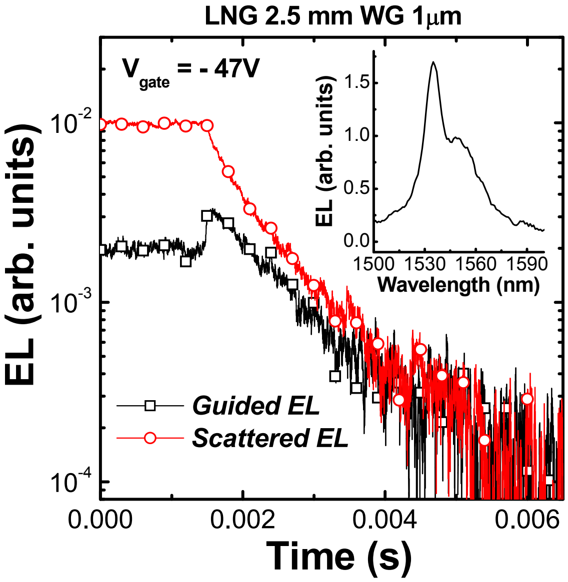

Figure 3. Time-resolved EL measurements at 1.54 μm collected from the grating (guided EL, empty squares) or from the top of the waveguide (scattered EL, empty circles). This measurement corresponds to a particular waveguide with a length of 2.5 mm (LNG) and a width of 1 μm (WG). Inset shows a typical EL spectrum of the Er^{3+} emission.

Further insight into the optoelectronic properties comes from the comparison of the time-resolved guided EL between different waveguide widths but with the same length (Figure 4). In that case, the guided EL signal scales with the waveguide width (Figure 4a) and the EL overshoot is preserved. This is somehow expected since wider waveguides also implies larger areas of active material. Nevertheless, non-linear ratio was found between the guided EL and the waveguide width (Figure 4b), contrary to what is expected for LED (the EL scales linearly with the area of devices). In addition, the top scattered EL was also studied as a function of the waveguide width obtaining a linear correlation between them (not shown). Although the non-linearity in the EL(WG) curve might be ascribed to an amplification process in waveguides, we suggest that it can be mostly due to a better confinement in wider waveguides rather than an amplifying phenomena. Simulations using Film Mode Matching (FMM) solvers and the non-dependence of the guided EL with the waveguide length (for one single width) further supported this hypothesis.

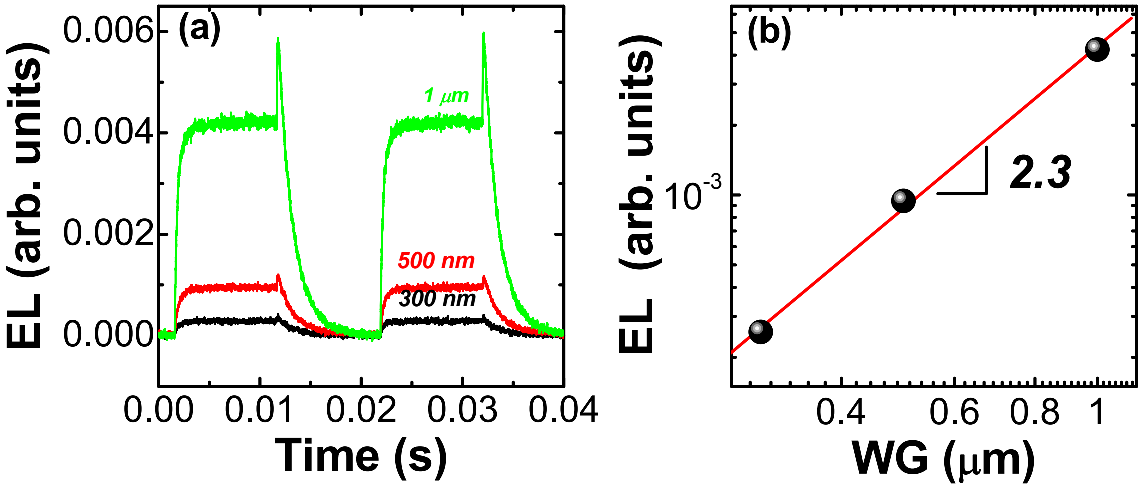

Figure 4. (a) Time-resolved EL signal for one single waveguide length (1 mm) but three different waveguide widths (300 nm, 500 nm and 1 μm). (b) Ratio between the guided EL signal and the waveguide width.

Finally, carrier injection losses in the waveguide have been quantified by using an external LASER signal at 1.53 μm. A continuous probe was coupled from the grating coupler, being the output signal directly collected from the waveguide facet. It is worth noticing that the probe signal intensity has been settled much higher than the EL signal in order to minimize the contribution of the EL in the output signal. Then, a time-resolved measurement was launched while sequentially switching on and off different voltages in the waveguide. This situation is depicted in Figure 5, where the time-resolved optical transmittance of the probe signal is shown under different polarization voltages. Carrier injection losses at each voltage have been quantified in terms of dB/cm, ranging from 0 dB/cm (when the voltage is off) to -52 dB/cm at 45 V. A maximum attenuation of -60 dB/cm was achieved at 48 V, very close to the device breakdown condition. Also, thermal effects start being sizable at 25 V (and above), causing longer recovery times of the probe signal when the voltage is off [15].

Therefore, we propose using these slot waveguides as potential integrated electroluminescent modulators for specific applications where ultrafast data rates are not needed, but the compactness of the system (biosensing applications, for example). Although not demonstrated here, data rates of at least hundreds of KHz are envisaged looking at the carrier recombination times (10 μs at least), which are much faster than the Er lifetime.

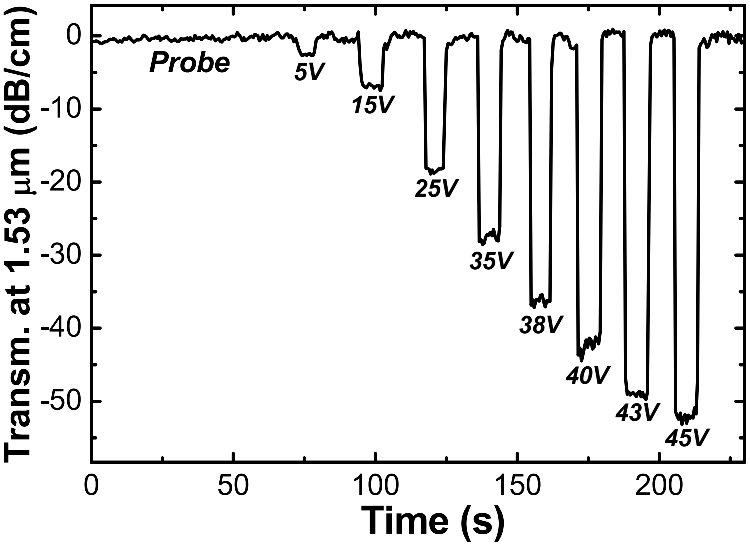

Figure 5: Time-resolved Optical transmittance of the probe signal under different polarization voltages.

3. CONCLUSIONS

The optoelectronic properties of Er^{3+}-doped slot waveguides and its integration in a Si photonics circuitry have been studied and demonstrated, respectively. An interesting super linear exponent in the EL(I) characteristic has been found in all the studied devices, which was thought to be due to the inhomogeneous carrier injection in the active slot layer. An indirect observation of additional carrier losses when the voltage is switched on has been performed by means of time-resolved measurements of the guided EL signal. Also, a non-linear ratio between the EL and the waveguide width has been observed, obtaining larger EL values for the widest slot waveguide due to a better light confinement. Finally, the injected carrier losses have been quantified in dB/cm by using a continuous probe signal at 1.53 μm and performing time-resolved optical transmittance measurements in waveguides, showing variable probe attenuation as a function of the applied voltage until values up to -60 dB/cm.

REFERENCES

[1] Prucnal, S., Sun, J. M., Skorupa, W. and Helm, M. "Switchable two-color electroluminescence based on a Si metal-oxide-semiconductor structure doped with Eu," Appl. Phys Lett. 90(18), 181121 (2007).

[2] Palm, J., Gan, F., Zheng, B., Michel, J. and Kimerling, L.C. "Electroluminescence of erbium-doped silicon," Phys. Rev. B 54(24), 17603-17615 (1996).

[3] Giles, C. R. and Desurvire, E. "Modeling erbium-doped fiber amplifiers," J. Lightw. Technol. 9(2), 271-283 (1991).

[4] Kik, P.G. and Polman, A. "Erbium doped optical-waveguide amplifiers on silicon," MRS bulletin 23(4), 48-54 (1998).

[5] Polman, A. "Erbium implanted thin film photonic materials," J. Appl. Phys. 82(1) 1-39 (1997).

[6] Yerci, S., Li, R. and Dal Negro, L. "Electroluminescence from Er-doped Si-rich silicon nitride light emitting diodes," Appl. Phys. Lett. 97(8), 081109 (2010).

[7] Barrios, C. A. and Lipson, M. "Electrically driven silicon resonant light emitting device based on slot-waveguide," Opt. Express 13(25), 10092-10101 (2005).

[8] DiMaria, D. J. and Dong, D. W. "High current injection into SiO_2 from Si rich SiO_2 films and experimental applications," J. Appl. Phys 51(5), 2722-2735 (1980).

[9] Ramírez, J. M., Ferrarese Lupi, F., Berencén, Y., Anopchenko, A., Colonna, J. P., Jambois, O., Fedeli, J. M., Pavesi, L., Prtljaga, N., Rivallin, P., Tengattini, A., Navarro-Urrios, D. and Garrido, B., "Er-doped light emitting slot waveguides monolithically integrated in a silicon photonic chip," Nanotechnology 24, 115202 (2013).

[10] Tengattini, A., Gandolfi, D., Prtljaga, N., Anopchenko, A., Ramírez, J. M., Ferrarese Lupi, F., Berencén, Y., Navarro-Urrios, D., Rivallin, P., Surana, K., Garrido, B., Fedeli, J. M. and Pavesi, L., "Toward a 1.54 μm Electrically Driven Erbium-Doped Silicon Slot Waveguide and Optical Amplifier," J. Lightw. Technol. 31(3), 391-397 (2013).

[11] Dal Negro, L., Yi, J. H., Michel, J., Kimerling, L. C., Hamel, S. Williamson, A. And Galli, G. "Light-emitting silicon nanocrystals and photonic structures in silicon nitride," IEEE J. Sel. Top. Quant. Elec. 16(1), 114-123 (2010).

[12] Berencén Y., Ramírez J. M., Jambois O., Domínguez C., Rodríguez J. A. and Garrido B. "Correlation between charge transport and electroluminescence properties of Si-rich oxide/nitride/oxide-based light emitting capacitors," J. Appl. Phys. 112, 033114 (2012).

[13] Ramírez, J. M., Ferrarese Lupi, F., Jambois, O., Berencén, Y., Navarro-Urrios, D., Anopchenko, A., Marconi, A., Prtljaga, N., Tengattini, A., Pavesi, L., Colonna, J. P., Fedeli, J. M. and Garrido, B. "Erbium emission in MOS light emitting devices: from energy transfer to direct impact excitation," Nanotechnology 23, 125203 (2012).

[14] Anopchenko, A., Tengattini, A., Marconi, A., Prtljaga, N., Ramírez, J. M., Jambois, O., Berencén, Y., Navarro-Urrios, D., Garrido, B., Milesi, F., Colonna, J. P., Fedeli, J. M. and Pavesi, L. "Bipolar pulsed excitation of erbium-doped nanosilicon light emitting diodes," J. Appl. Phys. 111, 063102 (2012).

[15] Ramírez, J. M., Berencén, Y., Ferrarese Lupi, F., Navarro-Urrios, D., Anopchenko, A., Tengattini, A., Prtljaga, N., Pavesi, L., Rivallin, P., Fedeli, J. M. and Garrido, B. "Electrical pump & probe and injected carrier losses quantification in Er doped Si slot waveguides," Opt. Express 20(27), 28808-28818 (2013).

CHAPTER **4**

4. Structural and Luminescence Properties of Cerium and Terbium Doped Silicon Oxides and Oxynitrides Fabricated by ECR-PECVD

Among the lanthanides available in the periodic table, Ce and Tb elements are of particular interest to develop Si-based light sources as they present intense narrow emission lines in the visible spectrum range when ionized in the 3+ state. These emissions are located around 450 nm (blue emission) and 550 nm (green emission) for Ce and Tb, respectively. Such unique optical properties make them potential candidates for the implementation of compact low-cost solutions in different arenas such as solid state lighting (SSL) or high-resolution microdisplays [1, 2]. RE-doping of Silicon-based materials can be performed in a CMOS line, providing several advantages such as the usage of a mature and reliable technology that allows mass fabrication or the possibility to implement in a single process the electronic drivers along with the optical functionality. Another point in favour is the ease with which a specific colour emission can be obtained during the fabrication process, just by choosing a different RE dopant. Furthermore, they provide high versatility of implementation since different Ce- and Tb-doped Si-based light emitting sources can be conveniently mixed with Eu-doped light sources to obtain a three-colour-based RGB system [1]. White light emission is also feasible if an adequate balance of the emission intensity of the three components is performed. Indeed, several device architectures can be tackled in this case, since RE co-doping of Ce^{3+}, Tb^{3+} and Eu^{3+} ions can be implemented in a single layer to provide a uniform white emission, or conveniently separated in individual layers, each one with a single RE-doping, to form a multilayer device structure.

This chapter describes the investigation conducted in luminescent Ce- and Tb-doped thin-film oxides and oxynitrides fabricated by ECR-PECVD. Despite that most of my previous effort was dedicated to study Er-doped Si-based devices, I also had the invaluable opportunity to gain further insight on the fabrication, the structural and the optoelectronic characterization of other RE-doped luminescent materials at the final stage of my PhD. Indeed, it could be well understood as a progression of the prior research into alternative RE-doped materials with complex host matrices. For that, and taking advantage of the extended know-how within the Centre for Emerging Device Technologies (CEDT) at McMaster University (Canada) in thin film deposition, a promising novel road map to explore and develop RE-doped light emitting materials with applications in the visible range of the electromagnetic spectrum was developed.

Indeed, this part of the work can be considered as a continuation of a previous investigation on Ce- and Tb-doped SiO_x thin films carried out by P. R. J. Wilson during his P. h. D. studies at McMaster University [3]. In his dissertation, he reported on the strong bright luminescence originated from $Ce_2Si_2O_7$ silicates in Oxygen-Rich Silicon Oxide films (ORSO). Such Ce-doped nanocrystallites were formed after high temperature annealing at 1200°C, and showed a PL intensity of about one order of magnitude higher compared to similar samples free of Ce-doped crystallites. Moreover, he suggested that an energy transfer process from Ce-doped nanocrystallites to Tb^{3+} ions arised in co-doped samples, yielding a green PL emission which was even higher than the one provided from Ce-doped nanocrystallites. The main argument in favour of this energy exchange between $Ce_2Si_2O_7$ silicates and Tb^{3+} ions is the fact that even for a very small amount of Tb doping, below 0.1%, the observed green emission is remarkably stronger than for a Ce-free Tb-doped SiO_x with a much higher Tb doping (between 1-5%).

In view of the preceding investigation on such topic, I was intrigued by the wide range of possibilities that Ce- and Tb-doped SiO_x thin films offered, and therefore I tried to provide a further insight on this issue. Mainly, and taking into account the advantages offered by SiN_x layers over SiO_x layer from the electrical and optical point of view (see previous chapters), I focussed on the effect of the nitrogen incorporation in Ce- and Tb-doped SiO_x thin films. For that, a gradual oxygen-by-nitrogen substitution was carried out in samples, sweeping the layer composition from SiO_2 to SiO_xN_y. Also, the effect of annealing treatment on the layer morphology, the optical constants and their PL properties was studied. I shall mention that unlike in the work conducted by P. R. J. Wilson, in which the investigation of Ce_2O_7 silicates in ORSO films took up most of his efforts, it was not my intention to reproduce such results in my films due to a number of reasons:

(i) Unfeasible high Ce-doping of about 10-11% was required to obtain large amounts of Ce_2O_7 silicates inside layers. Noteworthy, subsequent attempts to obtain large fractions of Ce_2O_7 silicates demonstrated bad reproducibility of results with significantly lower Ce concentration than expected due to the fact that the deposition system used is not suited for very high RE incorporation (5% at most).

(ii) The high annealing temperature required to obtain such silicates are in the upper limit of the CMOS compatibility. Although, theoretically, an annealing temperature of 1200°C could be accomplished in a CMOS foundry, the majority of the available equipment to carry out this task (for instance, a tubular furnace) often presents several parts made of quartz silica (or derivates), which have a similar melting point and thus it becomes impractical for the development of Silicon-based light emitting devices. Therefore, the fabrication of the samples described here after was performed away from these extreme conditions, i.e. with low RE-doping (1%) and at annealing temperatures slightly below the upper limit for CMOS compatibility (1180°C at most).

As for the research framework within which this work is conducted, it has been carried out within the Spanish project LEOMIS and allowed the electro-photonics Lab at Barcelona to complement the knowledge acquired during years of intense investigation on the design, structural, morphological and optoelectronic characterization of Si-based light emitting devices. One of the main purposes of this work is to study the influence of the host matrix on the luminescent properties of Ce^{3+} and Tb^{3+} ions using CMOS compatible materials such as SiO_x or SiO_xN_y thin films.

A complete description of the sample batch and the fabrication methodology used to develop Ce- and Tb-doped SiO_x and SiO_xN_y is provided in the following. Also, the structural, morphological and optical characterization carried out in single layers containing one singular dopant (either Ce^{3+} or Tb^{3+}) is described, and the main conclusions highlighted. Later on, the sample co-doping is tackled and compared with the multilayer approach in which different RE-doped layers containing a single dopant are stacked. Moreover, the optoelectronic properties of these samples will be tested. Finally, an amorphous sub-nanometre Tb-doped SiO_xN_y/SiO_2 superlattice is proposed to overcome some of the drawbacks encountered in the development of Si-based light emitting devices. A summary of the most relevant points and conclusions derived from this work are detailed at the end of this chapter.

4.1. Sample batch description and fabrication methodology

Since one of the main purposes of this study is to investigate the influence of the host matrix composition on the luminescent properties of Ce^{3+} and Tb^{3+} ions, a series of samples with different stoichiometry were fabricated. Previous chapters have shown that both Er-doped SiO_x and SiN_x offer different advantages that complement each other. As a consequence, a bilayer design composed of an accelerator SiO_2 layer and an electroluminescent Er-doped SiN_x layer was proposed to boost the overall performance of devices. However, an alternative approach can be tackled by merging both materials during the deposition process, providing a ternary compound formed by silicon, oxygen and nitrogen, i.e. a SiO_xN_y. Such a new host for RE ions is expected to yield superior optical performance while retaining good electrical properties. From the optical viewpoint, RE ions would benefit from an oxygen-coordinated local environment and higher solubility. As for the electrical performance, a bandgap shrinkage would take place upon incorporation of nitrogen into SiO_2, improving charge injection. Moreover, previous chapters have shown larger charge-to-breakdown in nitride-based layers compared to silicon oxides. Surprisingly, and despite the above presented advantages, RE-doped SiO_xN_y thin films have not yet been extensively studied by the silicon photonics community. There are only few reported works, most of them being focussed on the PL properties uniquely [4-6]. On the contrary, a large number of publications on RE-doped SiO_x and SiN_x are available in the literature [7-9]. Such off-stoichiometric layers belong to two sides of the scalene triangle shown in figure 1, where the refractive index of amorphous silicon (a-Si), silicon dioxide (SiO_2) and silicon nitride (Si_3N_4) has been represented as a function of the layer stoichiometry. As can be observed, there is another side of the triangle that corresponds to the ternary SiO_xN_y matrix with different stoichiometric values. Precisely, this side of the scalene triangle is the one of interest in this work.

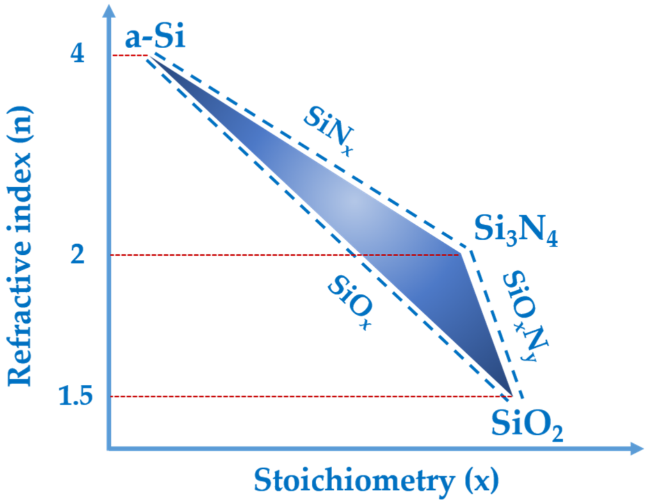

Figure 4.1. Relation between the refractive index of a-Si, Si_3N_4 and SiO_2 and the layer stoichiometry. The refractive index corresponds to a wavelength of 633 nm.

In order to obtain a consistent variation of the layer composition in the desired direction of the triangle of figure 4.1, a gradual substitution of oxygen by nitrogen was performed in a SiO_2 layer fabricated in an ECR-PECVD system. Thus, in an ideal case scenario, the layer stoichiometry will sweep from SiO_2 to Si_3N_4 just by adjusting the precursor gas flow rates in the deposition chamber. In that regard, I shall note that I departed from an optimized SiO_2 recipe provided by the CEDT at McMaster University. In particular, a diluted mixture of 30% of silane (SiH_4) in argon with a gas flow rate of 2.5 Standard Cubic Centimetre per Minute (sccm) and an O_2/Ar mixture (10%) flowing at 25 sccm was used for the fabrication of the SiO_2 layer. Then, the gradual substitution of oxygen by nitrogen in the layer composition was carried out by reducing the O_2/Ar gas flow rate by 5 sccm every time, while incorporating the same amount of N_2/Ar gas flow rate in the deposition chamber (also diluted at 10%). This particular methodology provided six different samples, all of them with a different composition. Table 4.1 describes the complete set of fabricated samples with the most relevant fabrication parameters highlighted.

Samples were deposited in a custom-designed ECR-PECVD system. This equipment deserves special attention since it provides a series of advantages compared to other deposition techniques. A comprehensive description of the ECR-PECVD system used at McMaster University can be found in *paper XIV* and also in ref. 10. The most important points in favour of this particular equipment are:

(i) Low substrate damage by highly ionized particles. In that case, the resonance glow discharge responsible for the plasma generation takes place inside an adjacent chamber, far away from the substrate. As a consequence, only low energetic ionized particles (20-30 eV) collide with the substrate.

(ii) Better control of layer stoichiometry. The fact that the plasma is remotely generated in an adjacent chamber allows having better control of the timing of the deposition.

(iii) In-situ RE doping. Probably the most important factor. A couple of RE-showerhead towers placed in front of the substrate allow for continuous in-situ RE doping. A metal-organic RE precursor located inside a container equipped with a heating jacket sublimates the RE material, which is transported and directed towards the substrate by means of an Ar transmission line. Such soft doping procedure provides a homogeneous RE incorporation in deposited samples without any additional damage, in contrast with ion implantation.

Sample description along with the most relevant deposition parameters are shown in table 4.1:

Sample	**SiH4/Ar**		**N2/Ar**		**O2/Ar**		**Ce/Ar**		**Tb/Ar**	
	Rate (sccm)	**Pressure (mTorr)**	**Rate (sccm)**	**Pressure (mTorr)**	**Rate (sccm)**	**Pressure (mTorr)**	**Rate (sccm)**	**Pressure (mTorr)**	**Rate (sccm)**	**Pressure (mTorr)**
SiO_xN_y_1	2.5	0.3	0	0.3	25	2.95	-	-	-	-
SiO_xN_y_2	2.5	0.3	5	0.9	20	2.95	-	-	-	-
SiO_xN_y_3	2.5	0.3	10	1.45	15	2.95	-	-	-	-
SiO_xN_y_4	2.5	0.3	15	1.95	10	2.95	-	-	-	-
SiO_xN_y_5	2.5	0.3	20	2.4	5	2.95	-	-	-	-
SiO_xN_y_6	2.5	0.3	25	2.9	0	2.9	-	-	-	-
$Tb:SiO_xN_y$_1	2.5	0.3	0	0.3	25	2.9	-	-	5	3.4
$Tb:SiO_xN_y$_2	2.5	0.3	5	0.9	20	2.95	-	-	5	3.45
$Tb:SiO_xN_y$_3	2.5	0.3	10	1.45	15	3	-	-	5	3.5
$Tb:SiO_xN_y$_4	2.5	0.3	15	1.95	10	2.95	-	-	5	3.45
$Tb:SiO_xN_y$_5	2.5	0.3	20	2.35	5	2.95	-	-	5	3.45
$Tb:SiO_xN_y$_6	2.5	0.3	25	2.9	0	2.9	-	-	5	3.45
$Ce:SiO_xN_y$_1	2.5	0.3	0	0.3	25	2.95	5	3.45	-	-
$Ce:SiO_xN_y$_2	2.5	0.3	5	0.85	20	3	5	3.5	-	-
$Ce:SiO_xN_y$_3	2.5	0.3	10	1.45	15	3	5	3.5	-	-
$Ce:SiO_xN_y$_4	2.5	0.3	15	1.95	10	2.9	5	3.5	-	-
$Ce:SiO_xN_y$_5	2.5	0.3	20	2.4	5	2.95	5	3.45	-	-
$Ce:SiO_xN_y$_6	2.5	0.3	25	2.9	0	2.95	5	3.45	-	-

Table 4.1. Description of the sample batch. Gas flow rates and partial gas pressures are shown in sccm and Torr units.

Samples were deposited on highly n-type doped two-inches single-side polished Si wafers with a resistivity lower than 0.005 Ω·cm.[15] Specific heating of certain components in the deposition system was performed. Starting from the rotating substrate stage, a temperature of 350°C was defined in the controller. This value corresponds to a substrate temperature of ~ 120°C. Similarly, RE transmission lines and showerhead towers were heated to 225°C, slightly above the temperature defined for the RE heating cell to avoid RE solidification in the transmission line (180°C for Tb deposition and 215°C for Ce). Once the temperature of each component is defined, the following deposition methodology is carried out: departing from an initial gas pressure of $4.3 \cdot 10^{-4}$ Torr in the deposition chamber, the diluted precursor silane mixture is first introduced into the deposition chamber with a gas flow rate of 2.5 sccm. As explained in *paper XIV*, it is worth noting that the silane precursor gas is directly introduced into the deposition chamber and not into the ECR chamber to avoid Si deposition on their surrounding walls. Thus, only Ar, O_2 and N_2 are let in the ECR chamber. A shutter placed in front of the sample stage minimizes Si deposition on the substrate during this part of the process. Then the gas pressure in the deposition chamber is measured (0.3 mTorr for a 2.5 sccm, see table 4.1). Later on, the desired gas mixture is introduced in the ECR chamber (either O_2/Ar or N_2/Ar), and the microwave plasma power is activated, ensuring a maximum output power difference of 500 W between the forward and reflected signal by means of a power detector. Then, generated plasma in the ECR chamber flows into the deposition chamber through a dispersion ring with gas inlets evenly distributed at its perimeter, and reacts with the already present silane gas. The gas pressure in the deposition chamber is measured again, and noted.

Finally, the same process is repeated one more time if a third reactive gas is needed, with the subsequent gas pressure measurement. Notice that the chamber gas pressure shown in table 4.1 increases when an additional gas mixture is introduced. Once all reactive gases are introduced, the RE argon transmission line is activated to perform the in-situ RE doping. Again, this process further increases the final gas pressure in the chamber. Finally, the shutter opens and the deposition process takes place on the heated substrate. Layer deposition was carried out during 60 minutes. This time provides a layer thickness of ~ 60-100 nm depending on the desired stoichiometry (the system was previously calibrated by measuring the layer thickness as a function of the deposition time). It is worth noting that previous homogeneity tests performed by former members of the CEDT at McMaster University established a negligible deposition inhomogeneity of 1% in a three-inch wafer [3].

After sample deposition, wafers were conveniently diced using a dicing saw (see figure 4.2 (a)). The individual die dimensions are ½ inch × ½ inch (1.27 cm × 1.27 cm). Thus, nine dies per wafer with equivalent layer composition were obtained (see figure 4.2(b)). Such fact allowed us to study the influence of the annealing temperature on the luminescent properties of a particular layer stoichiometry. Therefore, a different annealing temperature was defined for each die: 500°C, 600°C, 700°C, 800°C, 900°C,

---

[15] *Si wafers were cleaned in diluted HF (10%) prior to the deposition to remove the native oxide.*

1000°C, 1100°C, 1180°C and an as-deposited (AD) die. All samples were annealed in an N_2 atmosphere for 60 minutes.

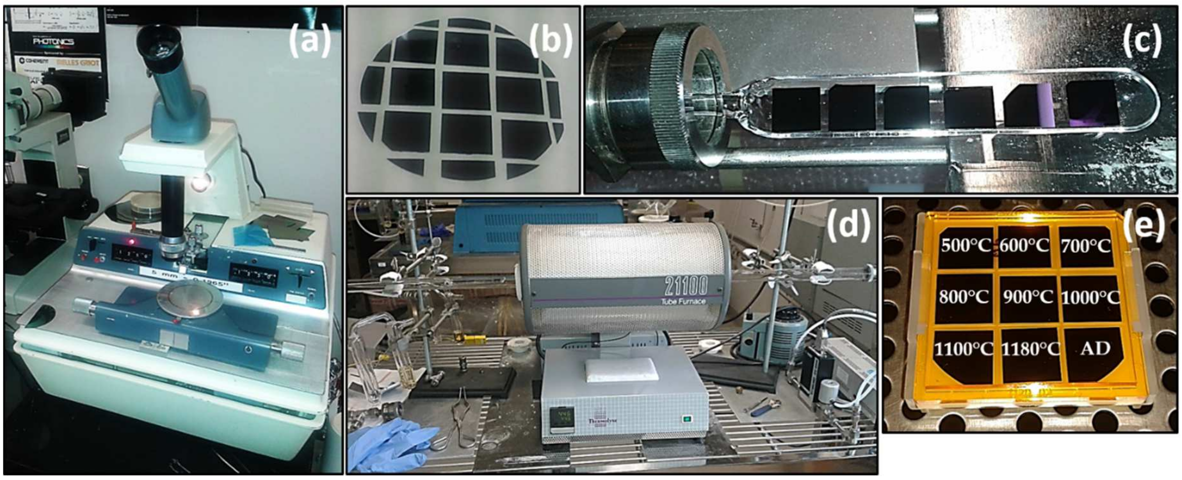

Figure 4.2. (a) Dicing saw used to die wafers. (b) A deposited wafer just after the dicing. (c) Annealing boat with different wafer dies. (d) Quartz tube furnace system used to anneal samples. (e) Storage box with different sample dies, each one annealed at a different temperature.

This procedure allows obtaining 18 different layer compositions (table 4.1) and 9 different annealing temperatures, which leads to 162 different samples that should be analysed. Therefore, a characterization methodology was followed to study such a huge number of samples. Firstly, Variable Angle Spectroscopic Ellipsometry (VASE) measurements were performed to determine the layer thickness, the refractive index and the extinction coefficient. Then, Rutherford Backscattering Spectrometry (RBS) was conducted to resolve the layer stoichiometry of samples. Finally, the luminescence of samples was assessed under photon excitation (PL measurements). Also, a TEM characterization was accomplished for specific samples to further insight on the sample morphology. The next sections provide a detailed analysis of the most relevant results and conclusions extracted from this study.

4.2. Variable Angle Spectroscopic Ellipsometry (VASE)

The optical properties and film thickness of the deposited samples were determined by ellipsometry using a J. A. Woollam M-2000U UV-Vis ellipsometer with near-infrared extension. A linearly polarized light beam is sent towards the sample, and reflected back at the surface. Then, the reflected light is collected by a detector, which measures the polarization change of the light beam by means of two parameters: Ψ (the ratio of incident and reflected light beam amplitudes) and Δ (the phase difference induced by reflection). A brief explanation of the fundamental principle is provided in the following:

First consider the Snell's law for reflection and refraction at the interface between two isotropic non-absorbing media with different refractive index (n) and phase velocity (v):

$$n_1 \cdot sin(\phi_1) = n_2 \cdot sin(\phi_2) \tag{4.1}$$

Now, assume the two polarization vectors $\vec{E_p}$ (parallel) and $\vec{E_s}$ (senkrecht, i.e. perpendicular) both of which are perpendicular to the direction of light propagation (see figure 4.3). Thus, according to Fresnel reflection coefficients r_{12}^p and r_{12}^s, the ratio of amplitude of outgoing to incoming light beams is determined by:

$$r_{12}^p = \frac{n_2 \cdot cos(\phi_1) - n_1 \cdot cos(\phi_2)}{n_2 \cdot cos(\phi_1) + n_1 \cdot cos(\phi_2)} \tag{4.2}$$

$$r_{12}^s = \frac{n_1 \cdot cos(\phi_1) - n_2 \cdot cos(\phi_2)}{n_1 \cdot cos(\phi_1) + n_2 \cdot cos(\phi_2)} \tag{4.3}$$

Then, the reflectance of a single interface can be obtained:

$$R^p = \left| r_{12}^p \right|^2 \tag{4.4}$$

$$R^s = \left| r_{12}^s \right|^2 \tag{4.5}$$

However, the above described equations are not valid for absorbing thin films with multiple interferences. In that case, a different formulation applies, assuming that r^s and r^p are both complex numbers, the total reflectance can be obtained:

$$r_{total}^p = \frac{r_{12}^p + r_{13}^p \cdot exp(-j2\beta)}{1 + r_{12}^p \cdot r_{13}^p \cdot exp(-j2\beta)} \tag{4.6}$$

$$r_{total}^s = \frac{r_{12}^p + r_{23}^p \cdot exp(-j2\beta)}{1 + r_{12}^p \cdot r_{23}^p \cdot exp(-j2\beta)} \tag{4.7}$$

Where $\beta = 2\pi\left(\frac{d}{\lambda}\right) \cdot n_2 \cdot cos(\phi_2)$ is the phase change from top to bottom of the film and n_3, ϕ_3 correspond to the Snell parameters of the substrate (see figure 4.3). Therefore, being δ_1 and δ_2 the phase of the incident and reflected light beam, respectively, the phase difference induced by reflection is determined:

$$\Delta = \delta_1 - \delta_2 \tag{4.8}$$

Similarly, the ratio of amplitudes is given by:

$$tan(\Psi) = \frac{\left| r_{total}^p \right|}{\left| r_{total}^s \right|} \tag{4.9}$$

Finally, both equations can be combined in the form:

$$tan(\Psi) \cdot exp(j\Delta) = \frac{r_{total}^p}{r_{total}^s} \tag{4.10}$$

Which provides the two physical magnitudes measured by ellipsometry, Ψ and Δ. Further insight into the fundamental basis of ellipsometry can be found elsewhere [11].

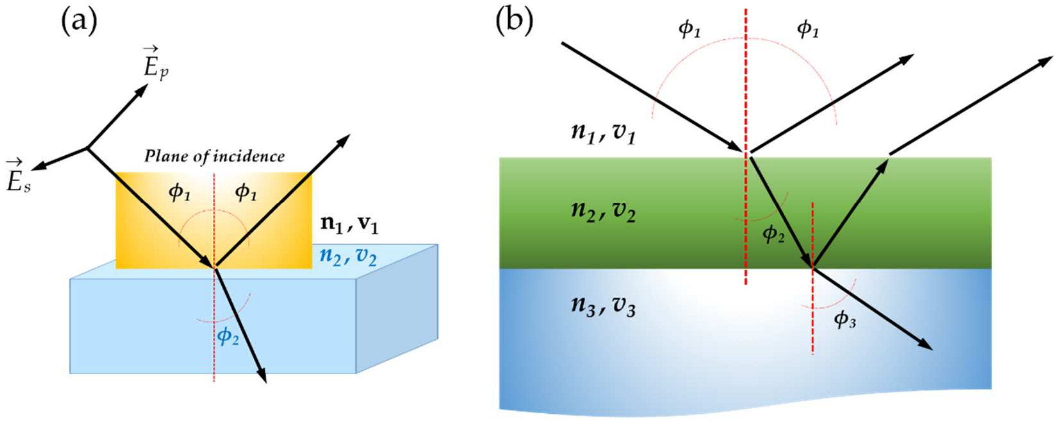

Figure 4.3. Description of the angles of incidence, refraction and reflection for a single interference (a) and for multiple interferences (b).

The modelling of experimental data was performed using the CompleteEASE™ software package [11]. There is a huge number of models available in the literature, depending on the nature of our films. First of all, one has to consider the morphology of the substrate, since different modelling is required for transparent or absorbing substrates. Backside substrate reflections may also be considered in some cases. For instance, a single-side polished Si substrate is preferred to a double-side polished one as reflected light beams are minimized due to the roughness-induced scattering at the backside of the substrate. In that regard, and despite the fact that the software is able to model light beam depolarization due to backside reflections, a more complex modelling is required and consequently only single-side polished Si substrates were considered in this work. In that line, also important is the light absorbance of the measured film. Non-absorbing thin films can be modelled using a simple Cauchy model in which the extinction coefficient is zero and hence only two variables need to be determined: the layer thickness and the refractive index. The Cauchy dispersion relation is given by:

$$n(\lambda) = A_n + {B_n}/{\lambda^2} + {C_n}/{\lambda^4} \tag{4.11}$$

With A_n being the amplitude related parameter of the refractive index and B_n, C_n the constants that provide the curvature of the index versus wavelength. Such relation, despite not considering light absorption in the film, becomes a useful tool and a good starting point to provide a first approximation of modelled variables, especially in thin oxide films where the absorption is expected to be low for the studied wavelength window (from 250 nm to 1680 nm). Moreover, an initial layer thickness can also be roughly estimated from previous calibration of the deposition system (around of 60-80 nm). Therefore, only the wavelength-dependent refractive index is unknown.

Once the refractive index is obtained, a second modelling iteration using the previously extracted parameters from Cauchy dispersion relation was carried out, this time considering film absorption. In this case, a complex index of refraction ($\tilde{n}$) is defined:

$$\tilde{n} = n + ik \tag{4.12}$$

Where *n* is the real part of the refractive index and *k* is the absorption loss when the electromagnetic wave propagates through the material (extinction coefficient). Thus, a B-spline model was used to obtain both parameters. Contrary to the previous model, B-spline assumes an absorption loss, hence modelling the experimental measurements with a basis spline through evenly spaced points. Basis spline curves are then smoothly interpolated between control points. This model however, despite providing a first approximation of *k* values as a function of wavelength, should also be carefully inspected since it is based on a flexible mathematical approach and not on a physical phenomenological model, and consequently meaningless values and expressions could be obtained in some cases.

Finally, a third iteration was performed using a Kramers-Kronig consistent model. As a consequence, a general oscillator (gen-osc) was used to parametrize previously obtained n(λ) and k(λ) parameters from the B-spline model. The gen-osc layer uses a combination of various oscillator line shapes to match the optical constants, providing physical consistency to the model. A single Tauc-Lorentz oscillator was considered in this case, although a large number of oscillators are available (such as Gaussian, Drude or Cody-Lorentz). Once experimental curves went through all the process, a last evaluation is performed using the ‘parameter uniqueness’ of the software package. Such option verifies the model uniqueness of a particular parameter for a given interval of values. Then, the software displays the Mean Square Error (MSE) between experimental and modelled data for the entire range of chosen values, displaying an absolute minimum based on an iteration procedure of a least square fitting for the value that better adjusts the experimental data.

In order to further clarify the above guidelines that lead to an appropriate modelling of the samples under study, figure 4.4 displays an illustrative example using sample SiO_xN_y_6. Experimental Ψ (red line) and Δ (green line) values for an incidence angle of 55° are represented together with the modelled curve assuming a Cauchy dispersion relation (dashed black line) and a Tauc-Lorentz oscillator (straight blue line). As seen, a more accurate fitting is obtained with the oscillator model.

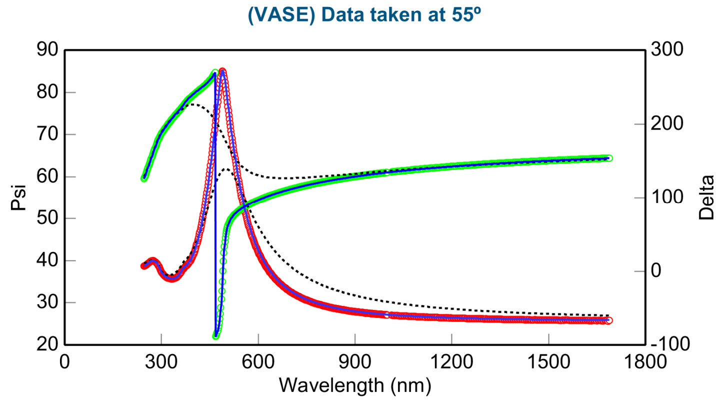

Figure 4.4. Measured Ψ (red line) and Δ (green line) parameters as a function of the incident wavelength for an incident angle of 55°). Dashed black and straight blue lines represent the data modelling using a Cauchy dispersion relation and a single Tauc-Lorentz oscillator model, respectively.

Such fitting of experimental parameters is simultaneously performed over 5 different incident angles (55°, 60°, 65°, 70° and 75°) to provide a more accurate adjustment. After this, the optical constants are extracted. An example is depicted in figure 4.5. As shown, *n* and *k* parameters extracted from the Cauchy modeling showed significant deviation from the ones obtained with the Tauc-Lorentz model, evidencing the strong dependance of the model chosen on the extracted optical constants.

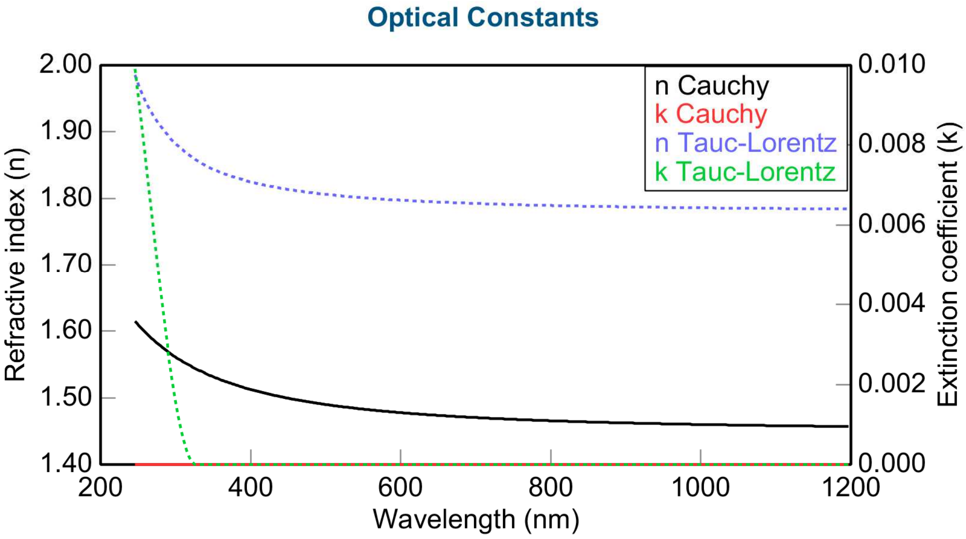

Figure 4.5. Comparison between the extracted optical constants (n and k) from sample SiOxNy_6 using a Cauchy dispersion relation (black and red straight lines) or a Tauc-Lorentz oscillator model (blue and green dashed lines).

Figure 4.6 shows the wavelength dependence of the modelled optical parameters extracted from non-annealed undoped SiO_xN_y samples, i.e. from SiO_xN_y_1 to SiO_xN_y_6 (see table 4.1). It is worth noting that samples SiO_xN_y_1 (N_2/Ar = 0 sccm), SiO_xN_y_2 (N_2/Ar = 5 sccm) and SiO_xN_y_3 (N_2/Ar = 10 sccm), both present similar optical constants, with *n ~ 1.5* at 633 nm and *k ~ 0* for the entire range of studied wavelength values. Therefore, we can anticipate an analogous layer composition between them, which in turn is expected to be very close to the one of SiO_2 since a similar n value is typically reported [12]. It is worth noting that, in this case, a Cauchy dispersion relation was used instead of a Kramers-Kronig model due to the fact that no light absorption was measured for the studied range of wavelengths (from 250 nm to 1650 nm). As a consequence, consistent parametrization of the optical constants could not be performed. Nevertheless, a fairly good fit can be obtained when using the Cauchy dispersion relation to model experimental data extracted from non-absorbing films.

On the contrary, samples SiO_xN_y_4 (N_2/Ar = 15 sccm), SiO_xN_y_5 (N_2/Ar = 20 sccm) and SiO_xN_y_6 (N_2/Ar = 25 sccm) display unique optical constants that denote a different layer stoichiometry. Consistent increase of *n* and *k* is shown for higher gas flow rates, up to a value of *n ~ 1.8* at 633 nm and *k ~ 0.01* at 250 nm. Since the real part of the refractive index is slightly below the one typically reported for a silicon nitride, we may outline that layer composition of sample SiO_xN_y_6 does not match with the one of a silicon nitride but to a silicon oxynitride, despite that oxygen was not intentionally introduced in the chamber for this sample (see table 4.1).[16] Another hint that denotes a substantial change of the layer stoichiometry for samples SiO_xN_y_4, SiO_xN_y_5 and SiO_xN_y_6 is the diminution of the energy band absorption edge when the nitrogen gas flow rate is increased. Such effect provides a characteristic wavelength red-shift of the absorption onset in the k-λ plot, as seen in figure 4.6 (b). Moreover, the material's effective bandgap can be roughly estimated by converting the wavelength absorption edge to energy. If doing so, a value of $E_g \sim 4.3\ eV$ was obtained for SiO_xN_y_4, $E_g \sim 4.1\ eV$ for SiO_xN_y_5 and $E_g \sim 3.8\ eV$ for SiO_xN_y_6.

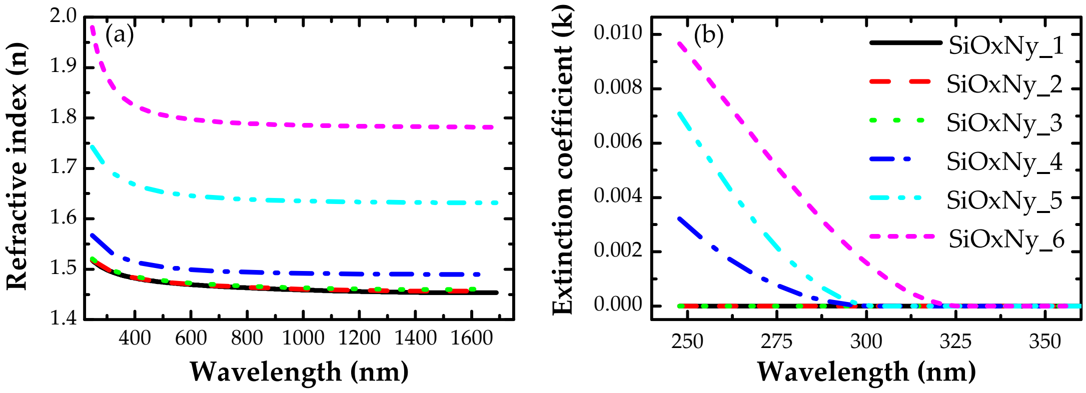

Figure 4.6. Real (a) and imaginary (b) parts of the refractive index as a function of the incident wavelength for non-annealed undoped SiOxNy layers.

In view of the above presented results, we can differentiate between two main groups of samples: **Silicon oxides** (i.e. samples SiO_xN_y_1, SiO_xN_y_2 and SiO_xN_y_3) and **silicon oxynitrides** (SiO_xN_y_4, SiO_xN_y_5 and SiO_xN_y_6). Similarly, Ce- and Tb-doped samples were also studied by means of ellipsometry. As anticipated, a nearly identical evolution of the optical parameters as a function of the incident wavelength was obtained, since the low RE doping of ~ 1% is not expected to drastically modify the optical constants of deposited samples. In this case however, another variable was introduced: The annealing temperature. The evolution of the optical constants and the layer thickness as a function of the annealing temperature has been investigated. A summary of the most important features extracted from VASE measurements on Ce- and Tb-doped samples is shown in figures 4.7 and 4.8. Starting with figure 4.7, Panels at the left (a, c and e) show the layer thickness (*t*) and the real (*n*) and imaginary (*k*) components of the complex refractive index (taken at 633 nm and 250 nm, respectively) of different Tb-doped samples with different annealing temperatures (see legend) as a function of the nitrogen gas pressure relative to the total gas pressure in the deposition chamber. Similarly, right panels (b, d and f) depict the evolution of the very same parameters (i.e. *t*, *n* and *k*) as a function of the annealing temperature for samples with the same layer stoichiometry (i.e. the same nitrogen gas pressure ratio).

---

[16] *Further details on the exact layer composition can be reviewed in papers XIV and XV and also in the next section, together with a comprehensive discussion of the origin of such undesired oxygen contamination.*

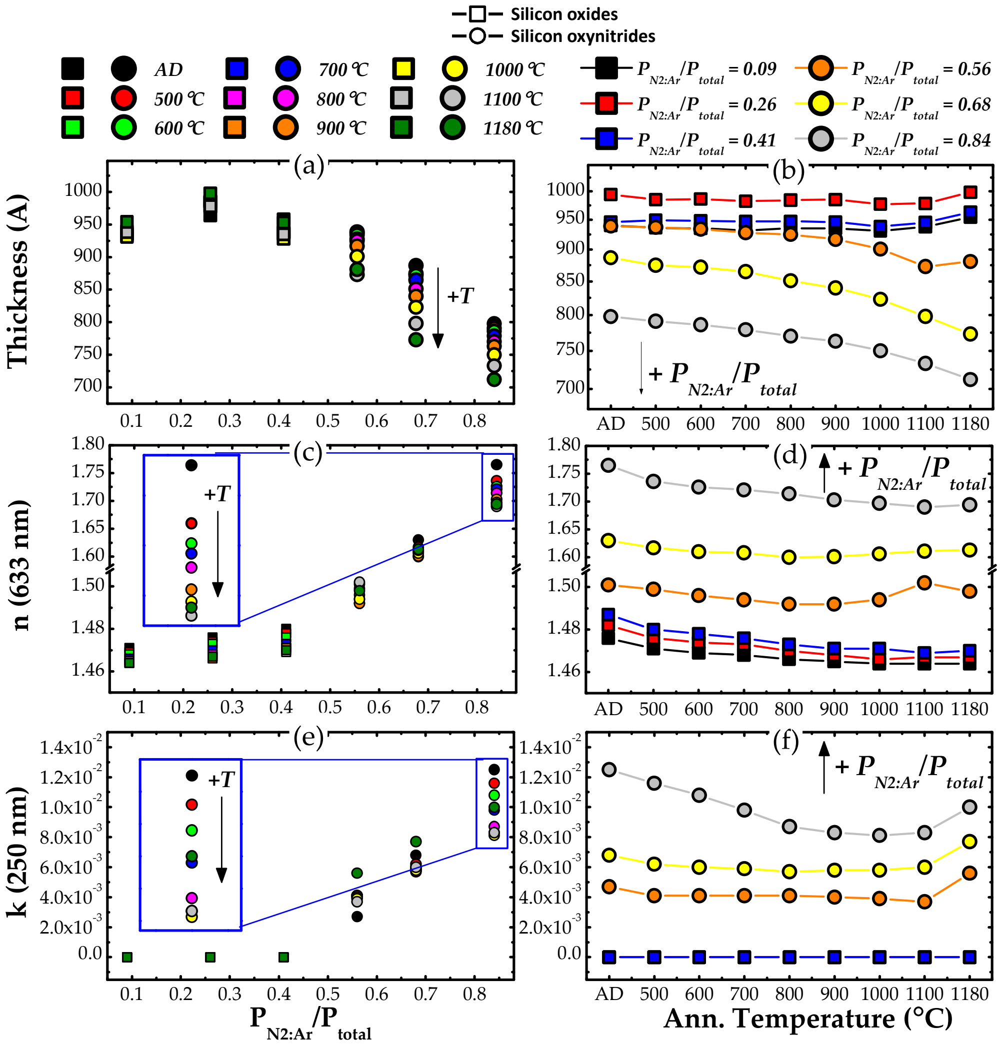

Figure 4.7. Evolution of film thickness (t) and real (n) and imaginary (k) parts of the complex refractive index as a function of the relative N_2:Ar gas pressure in the chamber (left panels (a), (c) and (e)) and the annealing temperature (right panels (b), (d) and (f)) of Tb-doped silicon oxides (squares) and Tb-doped oxynitrides (circles).

Several conclusions can be extracted from this study. First of all, silicon oxides (coloured squares) do not seem to drastically change any of the analysed parameters neither when increasing the nitrogen gas pressure ratio in the chamber (left panels) nor when annealing at higher temperatures (right panels), pointing to a very similar layer composition between them as in undoped samples. Thus, an average layer thickness of t ~ 95-100 nm is obtained. Remarkably, no light absorption was measured in the range of studied wavelengths (from 250 nm to 1650 nm), with n ~ 1.5 at 633 nm (a Cauchy dispersion relation was used, equally than for undoped samples). On the contrary, remarkable differences are observed in silicon oxynitrides (coloured dots) when an oxygen by nitrogen substitution takes place in the film composition, providing a consistent shrinkage of the layer thickness (panel (a) in figure 4.7) and an increase of the real and imaginary parts of the complex refractive index (panels (c) and (e), respectively). Similarly, the increase of the annealing temperature further shrinks the layer thickness of silicon oxynitrides (panel (b) in figure 4.7) and slightly reduces n and k (panels (d) and (f)). In that regard, it is interesting to note that the extinction coefficient seems to invert the decreasing tendency for high annealing temperatures (when Ann. Temp. > 1100°C)). The decrease in the measured film thickness when sweeping the layer stoichiometry from a SiO_2 to a SiO_xN_y can be attributed to the fact that silicon oxynitrides have higher layer density with respect to silicon oxides ($2.8\ g\cdot cm^{-3}$ versus $2.6\ g\cdot cm^{-3}$). As a consequence, the film becomes compacted when replacing oxygen by nitrogen in the composition. With regard to the increase of the extinction coefficient for the highest annealing temperature, I may speculate on the fact that in that case layer composition may be affected by deep morphological changes, leading to different phases in the sample due to, for instance, a partial clusterization of RE dopants similarly to Er-doped thin films (see chapter 2, *paper III*), increasing the absorption loss in the film. Moreover, a gradual decrease of the absorption band edge was observed in Tb-doped silicon oxynitrides, with similar values to the ones obtained in figure 4.6 (b).

An analogous study was carried out in Ce-doped oxides and oxynitrides. Likewise, figure 4.8 summarises the behaviour of the main optical parameters and the film thickness as a function of the nitrogen gas pressure ratio relative to the total pressure in the chamber (left panels) and the annealing temperature (right panels).

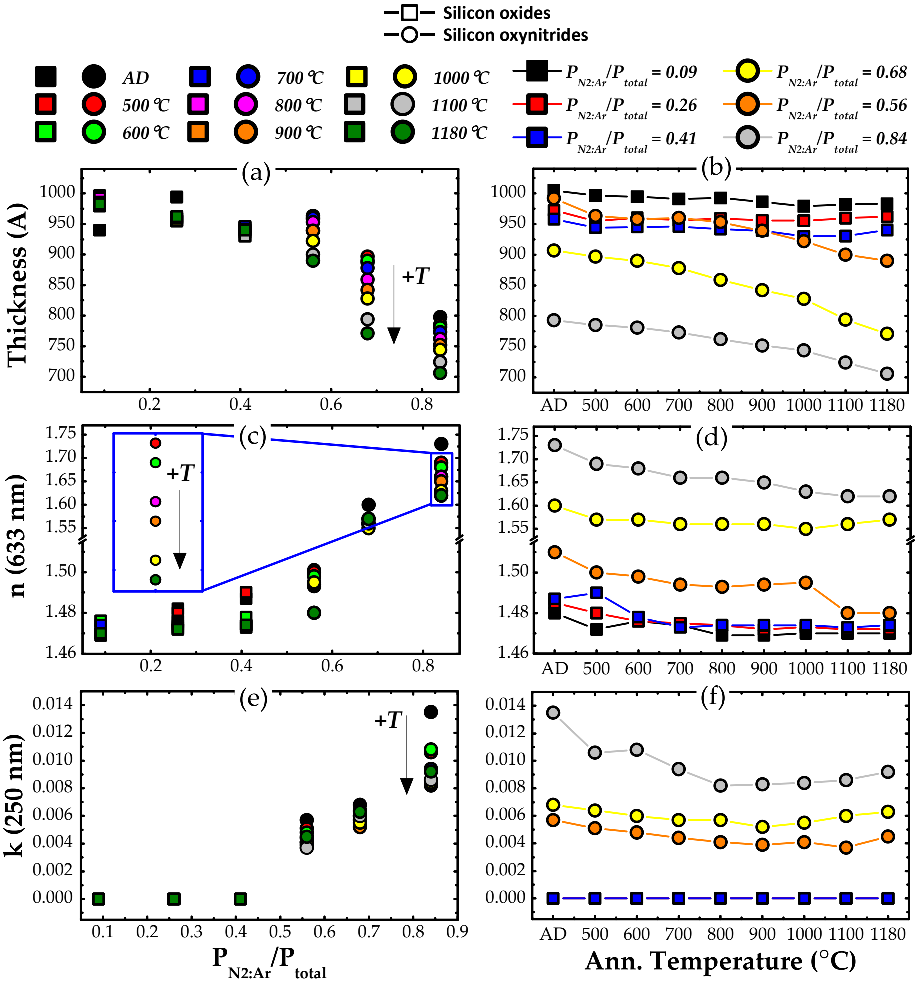

Figure 4.8. Evolution of film thickness (t) and real (n) and imaginary (k) parts of the complex refractive index as a function of the relative N_2:Ar gas pressure in the chamber (left panels (a), (c) and (e)) and the annealing temperature (right panels (b), (d) and (f)) of Ce-doped silicon oxides (squares) and Tb-doped oxynitrides (circles).

A similar trend was obtained for Ce-doped films, with highly transparent Ce-doped oxides (*k ~ 0*) and a slight increase of film absorption in Ce-doped oxynitrides for high annealing temperatures (see panel (f) in figure 4.8). Consistent film thickness shrinkage is also observed in Ce-doped oxynitrides, obtaining a mean film thickness that varies from 100 nm down to 70 nm. Also the same absorption band edge than for undoped and Tb-doped samples was obtained.

Therefore, comparing the main features from Ce- and Tb-doped oxides and oxynitrides with the ones obtained from undoped as-deposited samples, we can assure that RE-doping does not remarkably modify the thickness, uniformity and optical constants of the films. In addition, RE-doped and undoped silicon oxides have an effective energy bandgap higher than 5 eV and are expected to be nearly stoichiometric since a refractive index of n ~ 1.5 has been measured, similar to SiO_2. On the contrary, RE-doped oxynitrides have shown measurable absorption losses upon excitation with UV light, obtaining a consistent decrease of the effective bandgap when the nitrogen gas flow rate is increased, being lower than 5 eV in all cases. Such results provide consistent evidences of the successful incorporation of nitrogen in the SiO_2 matrix. Nevertheless, additional characterization is needed to obtain an accurate estimation of the layer composition. Next part will provide further insight on this subject by using RBS technique.

4.3. Rutherford Backscattering Spectrometry (RBS)

The RBS technique is a useful non-destructive analytical tool that allows quantifying the composition of a given sample. It is based on the elastic collision that occurs when a highly energetic (in the order of MeV) charged ion beam ($^4He^+$ in this case) is directed towards a sample, producing a backscattering of incident ions with the nuclei of the elements that compose the target. Thus, the energy of scattered ions can be measured by placing a detector in the plane of collision, hence allowing the identification of the target nuclei. The energy loss ratio between incident ($E_{incident}$) and reflected ($E_{reflected}$) beams is commonly called kinematic factor:

$$\frac{E_{reflected}}{E_{incident}} = k = \left(\frac{M_1 \cos(\theta_s) + \sqrt{M_2^2 - M_1^2 \left(\sin(\theta_s)^2\right)}}{M_1 + M_2} \right)^2 \tag{4.13}$$

Where M_1 and M_2 are the masses of the incident and targeted nuclei respectively, and θ_s is the scattered angle. Similarly, the energy gain ratio (E_{target}) of the targeted nuclei is defined by:

$$\frac{E_{target}}{E_{incident}} = 1 - \frac{E_{reflected}}{E_{incident}} \tag{4.14}$$

Such relations, combined with the well-known scattering cross-section of each element, permit one to determine the layer composition of the target. Hence, this process is mainly dominated by elastic nuclei-nuclei interactions. Nevertheless, for the range of incident ion beam energies, $^4He^+$ ions also lose energy through collisions mainly with the electrons of the targeted sample. Notice that whereas energy loss phenomena due to nuclei collisions (nuclear stopping) is dominant at low energies (< 100 keV), it becomes negligible at higher energies (MeV), hence being electronic stopping the main source of energy loss. These collisions, although they are not sufficient to significantly deviate the trajectory of incident ions nor to produce measurable backscattering, they are strong enough to cause a gradual diminution of the incident ion energy as the penetration depth increases. This effect is commonly referred as stopping power, and may be conveniently used to obtain an approximate depth profile of a particular element for analysed depths lower than the physical limit (~ 2 μm for $^4He^+$ ions). Also, this phenomenon can be used to obtain the layer thickness provided that the sample density is known. The most important advantages of RBS analysis are: (i) it is a non-destructive technique; (ii) quantifies layer composition with no need of a reference sample; (iii) has a good depth resolution of the order of several nanometers and (iv) has a good sensitivity to heavy elements, being able to precisely determine parts-per-million. It is worth noting that RBS does not provide useful information about the chemical bonding of elements and thus complimentary techniques such as X-ray Photoelectron Spectroscopy (XPS) are required to provide a further insight on this issue. Two different scattering geometries are available: the IBM geometry (incident beam, exit beam and surface normal of the sample are in the same plane) and the Cornell geometry (the sample is rotated, hence being the incident beam, the exit beam and the rotation axis in one plane). In general, Cornell geometry is more accurate since good mass and depth resolution are obtained simultaneously. Further details on RBS analysis can be found elsewhere [13].

RBS measurements in our samples were carried out in the Tandetron Accelerator Laboratory at Western University (Canada), under the supervision of Dr. Lyudmila Goncharova. A Cornell geometry was used, with the samples tilted at an angle of $\theta = 5°$ and a dose of 4 μC with an energy of 1.8 MeV for $^4He^+$ ions. In addition, samples were randomly rotated to further minimize substrate channelling. A reference Sb-doped Si sample with known Sb doping concentration was first measured and modelled to guarantee the proper functioning of the experimental setup. The RBS spectra were fit using the SIMNRA simulation software [14]. This software accounts for multiple large and small angle scattering events and also for geometrical scattering. In addition, simulations are based on Ziegler data [15], in which the stopping powers are calculated assuming Bragg's assumption with an ion-target interaction that is independent from the environment.

Figure 4.9 shows a practical example of RBS data processing of a Tb-doped SiO_2 sample. As seen, good fitting of experimental data is provided, obtaining a quantification of the layer composition. Concretely, an atomic concentration of $1.9 \cdot 10^{17}$ at/cm^2 was measured for Si, $3 \cdot 10^{17}$ at/cm^2 for O and $5 \cdot 10^{15}$ at/cm^2 for Tb. These values confirm our previous hypothesis on the stoichiometry of silicon oxides (see previous section), since the obtained atomic concentration is very close to the one of SiO_2. As expected, Tb shows the highest reflected energy ($E_{reflected}$ ~ 1600 keV) since presents the highest atomic number. Moreover, the measured signal does not show a delta-like signal at a certain energy but rather a broad peak that denotes a uniform Tb doping in the sample. Similarly, an oxygen-related broad peak superimposed to a background is located at 630 keV. Precisely, the background corresponds to the RBS signal of the Si substrate, and extends from low energies up to ~ 1050 keV. This effect puts forward the importance of the substrate in RBS analysis. In particular, this technique is suitable for targeted materials composed of 'heavy' elements that have been deposited on 'light' substrates with lower atomic numbers. By doing so, we avoid undesired signal overlap (as the one that takes place between the silicon substrate and the oxygen peak in figure 4.9) and improve the resolution of the analysis. In our case however, and despite the existing overlap between the two elements, a good estimate of the oxygen atomic concentration was obtained since the oxygen peak was well-resolved above the Si substrate in all cases.

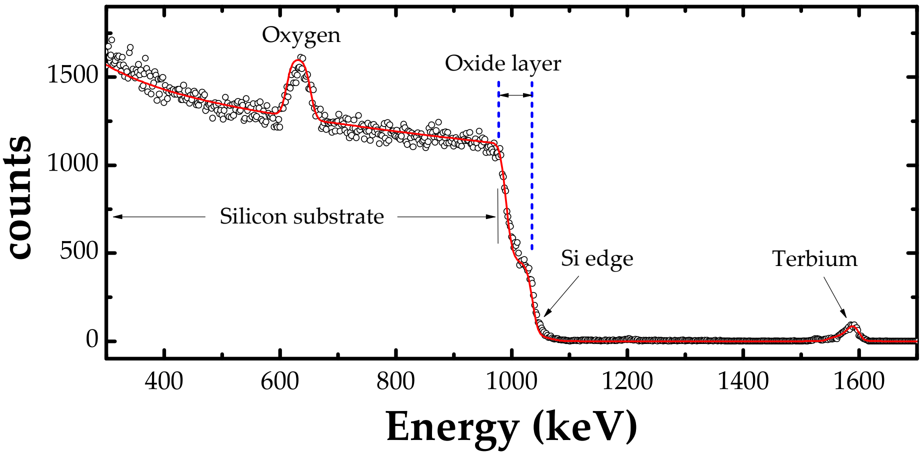

Figure 4.9: RBS data of sample Tb:SiO$_x$N$_y$_1 (empty circles) with the simulated spectrum superimposed (red line). Each peak corresponds to a different element.

Noticeably, a two-step decay of the Si signal is also observed around the Si edge (see figure 4.9). The origin of such feature can be explained as a transition in the Si signal. Starting from the backscattered signal where the Si edge is located (~ 1050 keV) and going towards lower reflected energies, incident ions first collide with the Si nuclei of the SiO$_2$ layer, and then with the ones of the Si substrate. Thus, since the Si substrate has a higher number of Si nuclei than the deposited layer, higher number of counts is detected (see the intensity difference in the y-scale axis). In addition, the energy loss produced by electronic interaction when incident ions pass through the deposited layer is clearly observed (delimited by the blue dashed lines).

Interestingly, a more accurate fitting of the experimental RBS data can be performed. For that, a multilayer approach should be considered. Basically, the sample under study is sliced into several sub-layers, each one taken as an individual film with unique and independent parameters. Then, the in-depth atomic concentration of deposited film can be better resolved. An example is shown in figure 4.10 for a Ce-doped sample, where only the Ce peak has been simulated for convenience. As can be observed, the uniform division of the deposited film in four different sub-layers allowed an accurate modelling of the Ce peak (each sub-layer has a thickness $t = t_{total}/4$ in this case). Finer simulations can be carried out by further slicing the film under study.

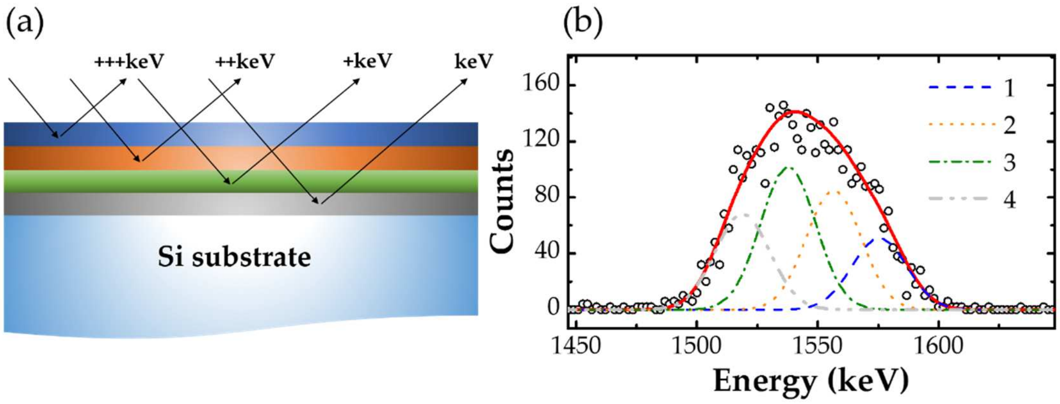

Figure 4.10. Fine simulation of the Ce-related RBS signal of sample Ce:SiO_xN_y_6 considering four independent sub-layers.

The RBS spectra of as-deposited Ce- and Tb-doped samples are shown in figure 4.11. Similar features were obtained regardless of the RE doping. Notice that whereas silicon oxides only display a single broad peak (associated with oxygen) that overlaps with the substrate background, a second signal (corresponding to nitrogen) superimposed to the background and located at lower energies is observed for silicon oxynitrides (more evident in samples RE:SiO_xN_y_5 and SiO_xN_y_6). Again, this fact reinforces our previous conjecture on the layer stoichiometry based on ellipsometry measurements. A fairly constant RE incorporation of $N_{RE} \sim (3\pm1)\times10^{20}\ at/cm^3$ was identified in all samples, regardless of the RE dopant. *Paper XIV* provides a comprehensive description of the layer composition by means of RBS analysis for Tb-doped samples, whose values are summarised in table 4.2 (very similar values were obtained for Ce-doped samples).

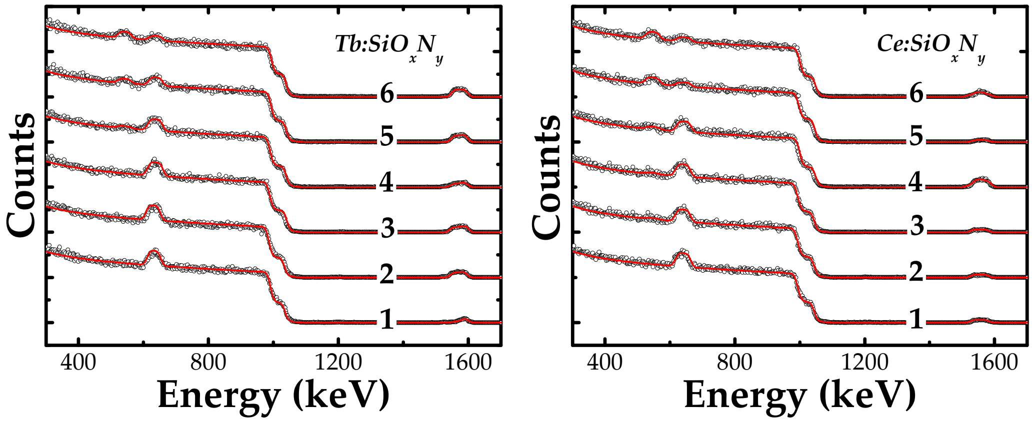

Figure 4.11. Experimental RBS data (empty circles) and simulated spectra (red line) of Tb-doped SiO_xN_y samples (left) and Ce-doped SiO_xN_y samples (right). Spectra have been arbitrarily shifted for clarity.

Sample	Si	N	O
	(at/cm^3)	(at/cm^3)	(at/cm^3)
RE:SiO$_x$N$_y$_1	2.1×10^{22} (30%)	-- (0%)	5×10^{22} (70%)
RE:SiO$_x$N$_y$_2	2.1×10^{22} (30%)	-- (0%)	5×10^{22} (70%)
RE:SiO$_x$N$_y$_3	2.2×10^{22} (33%)	-- (0%)	4.5×10^{22} (67%)
RE:SiO$_x$N$_y$_4	2.2×10^{22} (33%)	9×10^{21} (12%)	5×10^{22} (55%)
RE:SiO$_x$N$_y$_5	2.2×10^{22} (33%)	1.9×10^{22} (27%)	2.8×10^{22} (40%)
RE:SiO$_x$N$_y$_6	2.3×10^{22} (35%)	2.8×10^{22} (42%)	1.5×10^{22} (22%)

Table 4.2. Atomic concentration (in absolute numbers and in percentage) of Si, N and O of as-deposited samples, regardless of the RE dopant.

An interesting comparison between Ce- and Tb-related RBS signals is presented in figure 4.12. Samples Tb:SiO$_x$N$_y$_3 and Ce_SiO$_x$N$_y$_3 are compared for convenience, since they provide a representative example of the entire range of studied samples. Simulations of experimental data were carried out by splitting films in several sub-layers, as described in figure 4.10. Interestingly, despite having atomic numbers which are close in the periodic table (Z = 58 for Ce and Z= 65 for Tb), clear differences are observed in both RBS peaks, shifting the Ce signal towards lower energy values (~ 20 keV), as expected from equation 4.13. The Ce doping profile shows the most common situation in our samples, in which RE ions are homogeneously distributed in depth, displaying a flat plateau for a range of energies (from 1530 keV to 1570 keV in figure 4.12). In some cases however, a non-uniform RE distribution is observed (see the Tb peak), with a slightly higher concentration towards the surface of the film. In spite of this deviation, a similar optoelectronic response is expected in all samples.

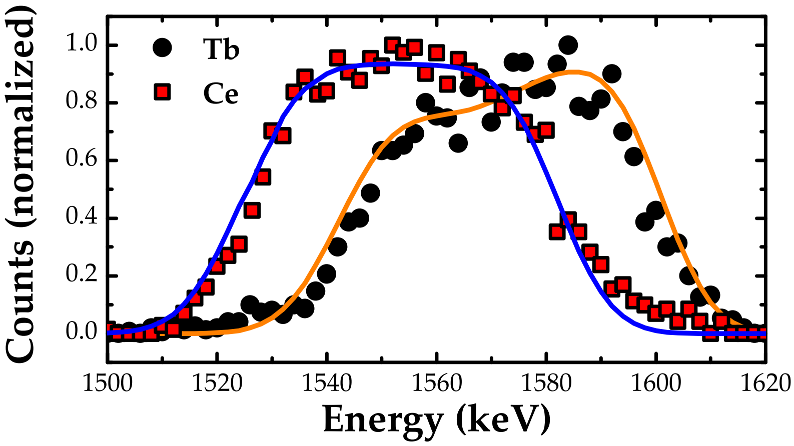

Figure 4.12. Comparison between the normalized Tb peak of sample Tb:SiOxNy_3 (black circles) with the one associated with Ce, obtained from sample Ce:SiOxNy_3 (red squares). Simulated curves are also shown.

Finally, let us add a few words about the influence of the annealing temperature on the distribution of RE ions inside layers. Despite not being measured for this particular set of samples, strong deviation of the RE in-depth profile from as-deposited samples is not expected for a wide range of temperatures due to the low diffusivity of RE ions in silicon oxides (or oxynitrides). At most, some RE clustering could be expected when annealing at high temperatures (from 1000°C on) based on previously reported results on RE-doped oxides available in the literature [16-18], which in fact coincide with the previous study carried out in this dissertation on Er-doped oxides (see chapter 2). Furthermore, an additional indirect evidence of the morphological changes that take place under high thermal budget is the observation of an enhancement of the absorption loss coefficient (see figure 4.7). In fact, we shall recall a previous work from the CEDT research group and the Institute of Physics (Wroclaw University of Technology, Poland) in which the authors detailed the evolution of the RBS spectra as a function of the annealing temperature in similar Tb-doped SiO_x films[17], obtaining an almost equivalent Tb in-depth profile and evincing Tb clusterization for samples annealed at 1200°C [16].

4.4. Luminescence properties of Ce- and Tb-doped silicon oxides and oxynitrides

The investigation conducted on the luminescence properties of Ce- and Tb-doped silicon oxides and oxynitrides will be detailed in this section. Prior to that, however, a brief introduction to the main optical properties and atomic structure of each RE ion is mandatory. Particularly, Ce^{3+} ions deserve especial attention since they have some peculiarities with respect to other RE ions such as the fact that the transitions responsible for the emission are not parity forbidden [19]. As a consequence, the radiative $5d^1$-to-$4f^1$ transition have short luminescence lifetimes of about few nanoseconds [20], contrary to the ones observed for Er^{3+} or Tb^{3+} ions in which luminescence decay times around of 1 ms are generally measured [21]. Moreover, these transitions are strongly dependent on the local environment, in contrast to other RE ions in which luminescence is governed by intra-4f transitions, which are known to be almost host independent. Thus, the degree of covalent bonding plays an important role in the final optical performance of Ce-doped samples. Bearing in mind these considerations, an interesting scenario is envisaged for the samples studied in this chapter since Ce^{3+} ions were embedded in different host matrices.

On the other hand, Tb^{3+} ions emit through the intraband 4f transition, similar to Er^{3+} ions, and therefore they only interact weakly with the environment. As a consequence, narrow spectral lines and long lifetimes are commonly obtained. The emission is mainly governed by parity forbidden electric dipole f-f transitions, which become probable in presence of an asymmetric host. Figure 4.14 illustrates the diagram of energy states for Ce^{3+} and Tb^{3+} ions, with the most probable transitions highlighted.

---

[17] *The samples of this work where fabricated at the same facility and following a very similar methodology than the ones described in this chapter.*

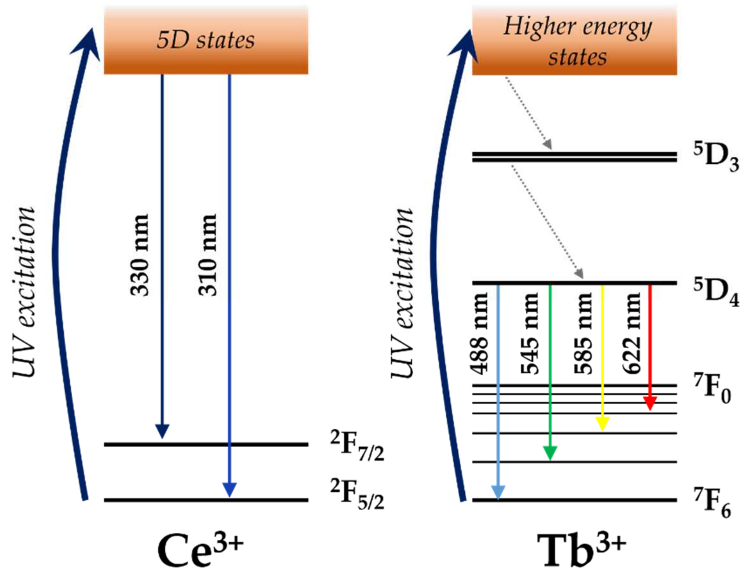

Figure 4.14. Ce^{3+} and Tb^{3+} radiative transitions.

PL emission from samples was obtained by exciting them with a CW external lasing source at 325 nm (He-Cd laser). Intense blue and green luminescence was observed in daylight conditions in Ce- and Tb-doped samples, respectively (see figure 4.15). Noticeably, the light emission was even observed in non-annealed samples. In fact, *paper XIV* reports on this aspect, and suggests the implementation of these layers in other platforms with more restricted annealing conditions. For instance in flexible electronics, where substrates are typically made of polyimide, Polyether Ether Ketone (PEEK) or transparent conductive polyester films, all of them with remarkably lower melting points than Si (300-400°C).

Ce-doped samples display two different features: a broad PL peak centred at 425 nm, and a weaker emission at 545 nm not related to any other radiative recombination in Ce^{3+} excited states (see figure 4.15). Whereas, Tb-doped host matrices present a PL spectrum peaking at 545 nm, with weaker emission lines located at 488 nm, 585 nm and 622 nm, all of them belonging to different Tb^{3+} excited states (see figure 4.14). In fact, the wavelength at which the second peak is observed in Ce-doped samples coincides with the position of the highest Tb^{3+} emission. Indeed, one may also recognize the other Tb^{3+} emission lines overlapping the broad emission for some spectra of Ce:SiO_xN_y samples (for instance, see the Ce^{3+} PL spectrum at the left side of figure 4.15). Therefore, we conclude that this emission originates from a cross-contamination of Tb in the deposition chamber while fabricating Ce-doped samples. I may note that the source of contamination was not clearly identified at the time of this writing. A similar Tb^{3+}-related residual luminescence was found in non-doped SiO_xN_y samples after a thorough cleaning of RE transmission lines, showerhead towers and the deposition chamber, and with the heating cells valves carefully closed while depositing samples. Moreover, Tb contamination due to effective desorption of residual material at the walls of the annealing tube was discarded since a different quartz tube was used to anneal each group of samples, either Ce- or Tb-doped samples. In spite of this drawback, the residual

Tb^{3+} emission is much lower than the one originating from Ce^{3+} ions, and therefore it will be intentionally overlooked in Ce-doped SiO_xN_y samples from now on.

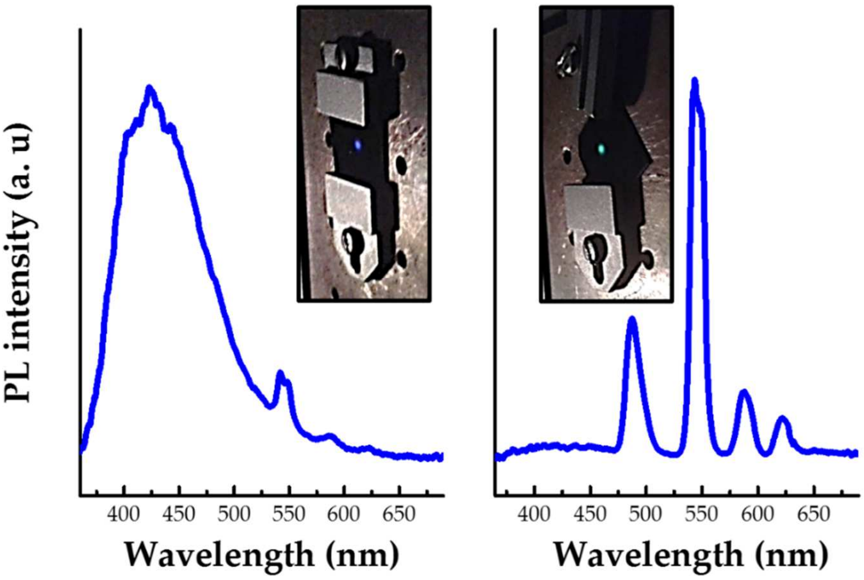

Figure 4.15. Ce^{3+} (left) and Tb^{3+} PL spectra under 325 nm laser excitation. Insets show the corresponding bluish and greenish emission from as-deposited Ce-doped (left) or Tb-doped (right) SiO_xN_y layers, respectively.

Prior to further detailing the luminescence properties of these samples, it is of uttermost importance to unravel the origin of the broad blue emission in Ce-SiO_xN_y samples. Unlike Tb-doped SiO_xN_y layers that show a light emission pattern that can be unambiguously identified with Tb^{3+} radiative relaxation from excited states, the broad bluish emission from Ce-doped samples may create some controversy since other luminescence species (such as Si-ncs in Si_3N_4) with similar PL characteristics in the very same wavelength range have also been reported [22]. In addition, time-resolved measurements would not shed light on this issue since both emissions display decay times shorter than our setup resolution (few µs), hence preventing the identification of the luminescent centre. A plausible method to unambiguously identify the origin of the broad blue emission is by measuring the evolution of PL intensity as a function of the annealing temperature. Bearing in mind the inert environment in which the annealing treatment was performed and the fact that the annealing temperature stimulates matrix passivation with the subsequent reduction of intraband defects, an effective diminution of the PL intensity with the annealing temperature would be expected if such emission is truly dominated by intraband radiative recombination at localized defect sites. Far from being the case, a notable increase of the maximum PL intensity was measured for high annealing temperatures, as depicted in figure 4.16:

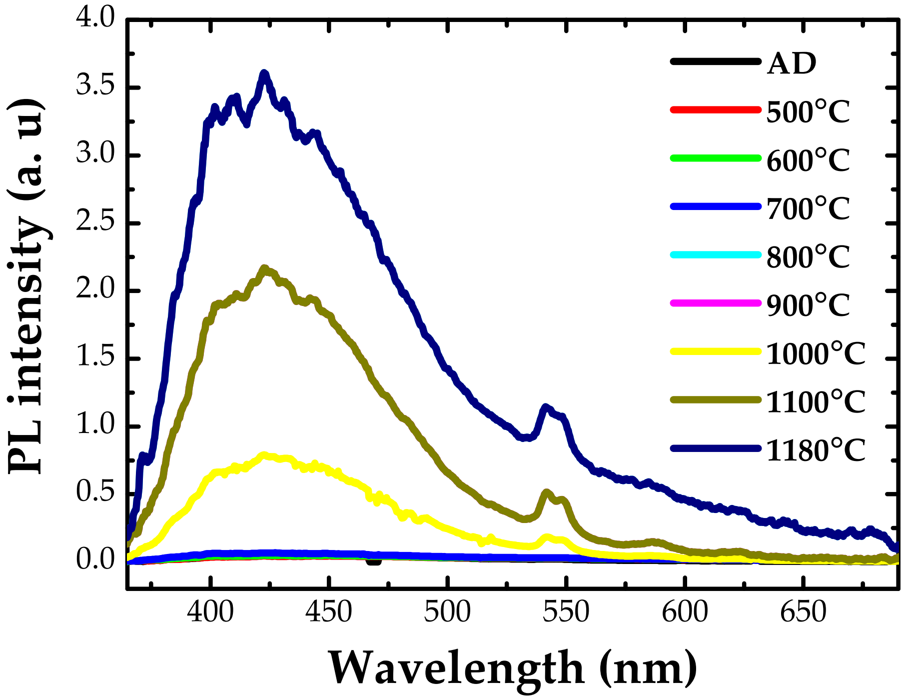

Figure 4.16. PL emission of Ce:SiO_xN_y_6 sample with different annealing temperatures.

Therefore, we can attribute the bluish emission to coordinated Ce^{3+} ions and not to intraband radiative recombination at localized defect sites in the host matrix. Other works have already reported similar results in Ce-doped oxides, ascribing the luminescence enhancement to a gradual formation of Ce silicates in the film [19]. To gain further insight on the effect of the annealing temperature on the luminescence properties of RE-doped layers, the PL intensity of all samples has been plotted as a function of the annealing temperature (see figure 4.17).[18] A considerable PL improvement is obtained in most of the samples when the annealing temperature is increased up to 900°C, over a factor of 35 in some cases. From this value on, RE-doped silicon oxides show a gradual decrease of the PL intensity, whereas a stable value or even a slight increase is seen in RE-doped silicon oxynitrides. It is worth to recall that since the UV absorption decreases with the annealing temperature except for the highest value at 1180°C (see the ellipsometry characterization, section 4.2), the fact that the PL-T feature shows an opposite trend up to 900°C in silicon oxides and 1100°C in silicon oxynitrides suggests that the latter ones provide a better local environment for RE ions, increasing the number of RE emitting centres.

---

[18] *The PL emission has been normalized by the layer thickness and by the corresponding collected light fraction of emitted power radiated as a function of layer refractive index, assuming a lambertian emission.*

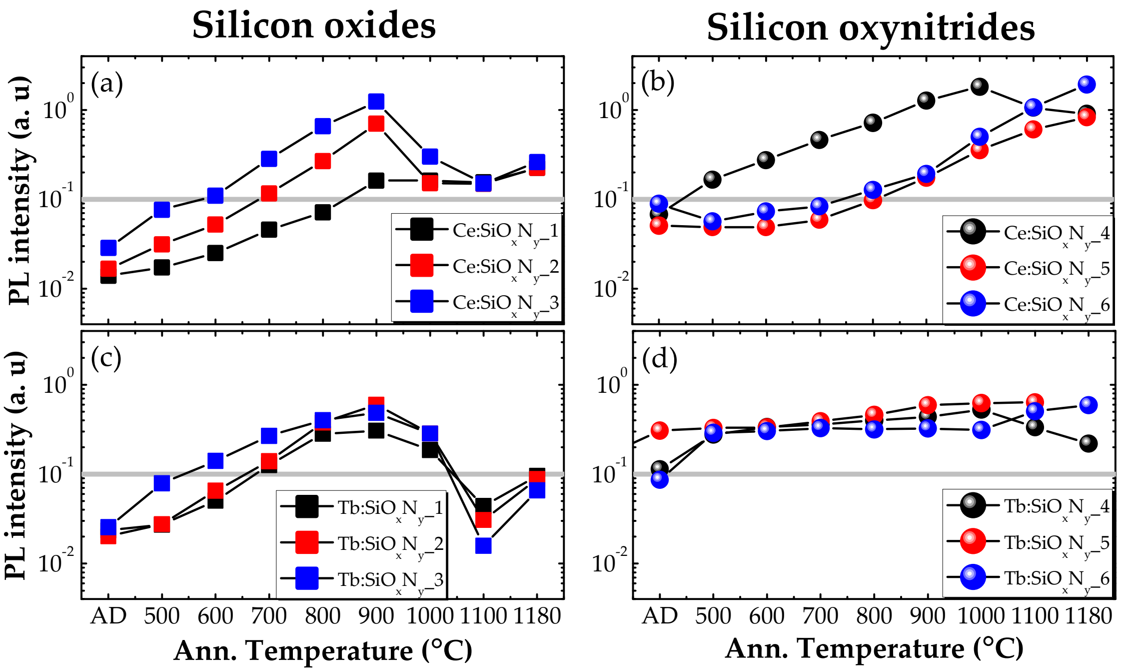

Figure 4.17. Effect of the annealing temperature on the PL intensity of Ce- and Tb-doped silicon oxides (panels (a) and (c)) and Ce- and Tb-doped oxynitrides (panels (b) and (d)).

Concerning the PL decrease for temperatures beyond 900°C in RE-doped silicon oxides, RE clustering seems to be the most plausible explanation, in accordance with previously studied Er-doped oxides and other authors [3, 16, 17, 19]. On the contrary, silicon oxynitrides show an ever increasing PL signal with increasing annealing temperatures, suggesting lower RE clustering due to a lower diffusion in the host matrix, equal to Er-doped silicon nitrides (see chapter 2, section 2.3).

Another remarkable feature of RE-doped silicon oxides is the sudden increase of the recorded PL signal for the sample annealed at the highest temperature, i.e. at 1180°C (see panels (a) and (c) of figure 4.17). This fact becomes more evident when inspecting the whole PL-T characteristic, since a decreasing trend is displayed for the annealing temperatures of 1000°C and 1100°C (attributed to RE clustering, as explained above). Therefore, the further increase of the annealing temperature up to 1180°C is expected to lessen the PL intensity even more, contrary to what is actually depicted in figure 4.17 (a) and 4.17(c). In fact, such improvement of the PL intensity under extreme annealing temperatures has been previously reported in similar layers, and attributed to the formation of RE-silicates [3, 19]. In our samples, despite the annealing treatment was intentionally limited to slightly lower temperatures than 1200°C to avoid the formation of RE silicates in the layer, VASE and PL measurements depicted a sudden change in the layer properties that point to a different layer morphology. Consequently, a thorough examination was fulfilled by TEM characterization in the pursuit of finding tiny RE crystallites. Indeed, the existence of such structures was verified in our layers at the substrate-active layer interface, as seen in figure 4.18. Lattice fringes can be observed along the interface, with an inter-atomic distance between 0.2-0.4 nm. It is worth mentioning that this distance does not correlate with any Si crystalline phase, hence discarding the presence of Si-ncs in the sample. Additional EFTEM characterization further confirmed the absence of Si-ncs. On the contrary, they are in good agreement with other works in which a similar inter-atomic distance was reported in Ce silicates [19]. Therefore, we ascribe these crystalline phases to RE silicates. Also, I shall remark that such structures were only found at the substrate-active layer interface but not in other parts of the samples, suggesting that the high periodicity of the Si substrate may induce the formation of RE silicates with crystalline phases. Instead, amorphous RE clustering was clearly seen at the rest of the sample, further supporting our previous argumentation on the decrease of PL intensity under high annealing temperature.

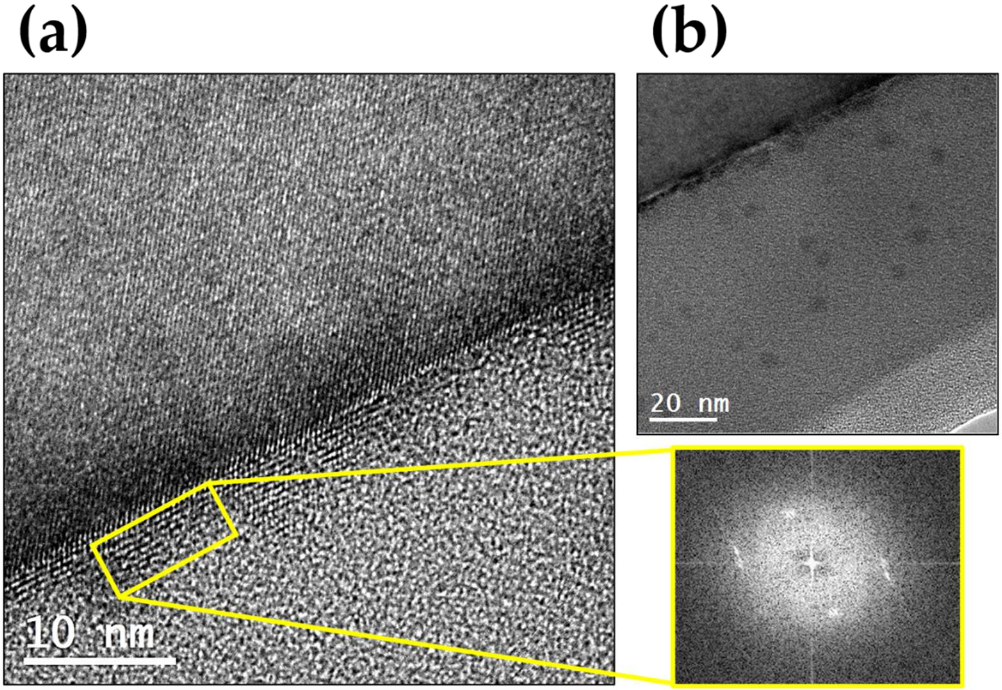

Figure 4.18. (a) HRTEM image of the sample Ce:SiO_xN_y_6 annealed at 1180°C, showing ordered lattice fringes at the substrate-active layer interface. A FFT on a localized region highlighted with the yellow box yielded the unambiguous identification of crystalline planes, whose mean inter-atomic distance varied from 0.2 nm to 0.4 nm. (b) TEM image of the very same sample. Homogeneously distributed dark spots correspond to amorphous RE clusters. The brighter layer at the bottom-right side of the image corresponds to a SiO_2 buffer layer intentionally deposited in this particular sample to prevent sample oxidation due to prolonged exposure to ambient conditions.

Additional conclusions can be drawn upon careful inspection of figure 4.17. First of all, we shall note a considerably larger PL emission of as-deposited RE-doped silicon oxynitrides compared to silicon oxides (a factor of 5 approximately). Even for annealed samples, the PL intensity is usually higher for silicon oxynitrides compared to silicon oxides upon identical annealing treatment. There are two plausible causes that may explain this fact: (i) the silicon oxynitride matrix provides a more favorable host environment for Ce- and Tb-doped samples than the silicon oxide, and therefore a larger number of emitting RE ions can be accommodated in the former; or (ii) the incident optical pumping can be absorbed by the silicon oxynitride host more efficiently, hence yielding a superior RE excitation via an energy transfer process. Assuming the previously presented reasoning on this very same issue when inspecting the layer morphology in Er-doped oxides and nitrides (see chapter 2, section 2.3), the first hypothesis seems to be the most logical since Ce^{3+} and Tb^{3+} ions are expected to behave in a similar manner to Er^{3+} ions. Thus, higher RE clustering is expected in silicon oxides compared to silicon oxynitrides. Nevertheless, the second conjecture is also suitable provided that silicon oxynitrides present lower bandgap and enhanced absorption in the UV range compared to silicon oxides (see figure 4.6 (b)). Additional measurements in which the PL intensity of both groups of samples is compared under resonant excitation condition could shed light on this issue. Unfortunately, even when pumping with energies lower than the bandgap of the host, we cannot guarantee some sort of energy transfer from the host matrix to RE ions mediated by resonant intraband defect sites. Ongoing investigations are being performed in our laboratory to address these open questions.

The spectral shape of Ce- or Tb-doped SiO_xN_y samples with different layer composition (from sample 1 to sample 6) was also inspected, showing no remarkable variation regardless of the stoichiometry of the host (see figure 4.19). I may note that although a similar PL spectral shape was anticipated for Tb^{3+}-doped layers, a rather different situation was expected for Ce^{3+} samples since their radiative emission takes place in outer 5d-to-4f transitions which may be influenced by changes in the local environment. In spite of this, we did not observe such trend in our samples, except for a couple of exceptional cases in which a small shift of few nanometers was observed in the PL spectrum. However, such slight variations were very rare in our samples and did not correlate with, for instance, the annealing treatment or the layer composition, as it would be expected for the current set of samples. Ongoing work is being done in that regard to further inspect the local environment of Ce^{3+} and Tb^{3+} ions in silicon oxides and oxynitrides.

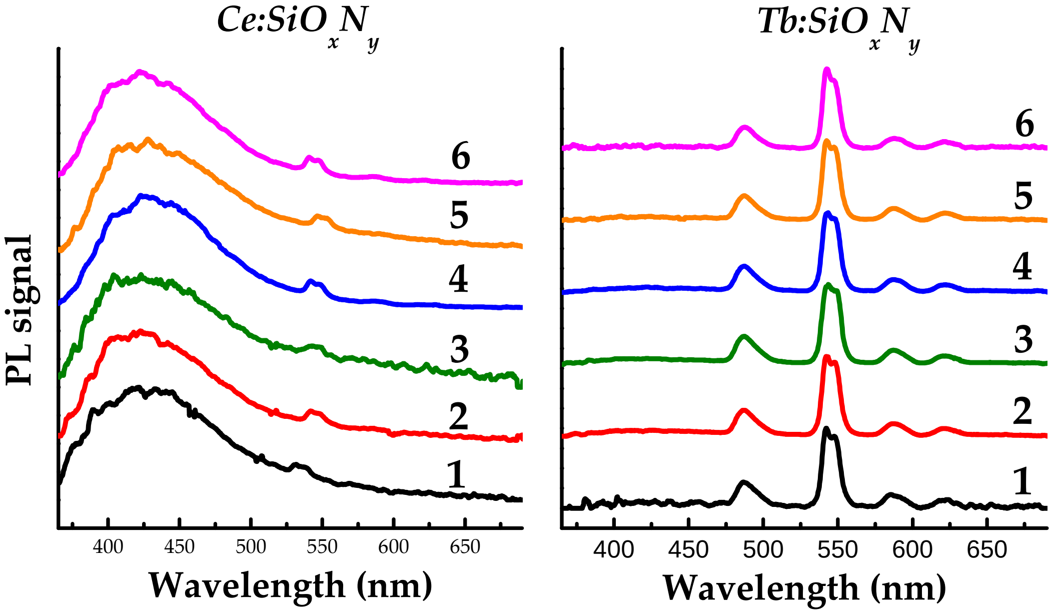

Figure 4.19. PL spectra of Ce-doped (left) and Tb-doped (right) SiO_xN_y samples. The spectra have been arbitrarily up-shifted.

Finally, a last figure of merit is presented in figure 4.20, with the maximum PL intensity of samples with different annealing temperatures plotted as a function of the real part of the refractive index (n). Since the annealing temperature does not markedly change the layer composition (and consequently nor the refractive index), the data belonging to a particular stoichiometry is disposed along narrow vertical stripes. Thus, the PL intensity of RE-doped silicon oxides (i.e. samples SiO_xN_y_1, SiO_xN_y_2 and SiO_xN_y_3) is placed at the left part of the x-axis scale, within the light blue stripe, since lower n values were measured. Similarly, the data for silicon oxynitrides (marked with a dashed box in the graph) is shown at gradually higher n values, in accordance with the oxygen by nitrogen substitution (see the light brown stripes). As already discussed, this figure clearly evidences the differences of the luminescence characteristics between RE-doped silicon oxides and silicon oxynitrides. Whereas the data belonging to RE-doped silicon oxides is widely spread along the y-axis scale, a much reduced range of values is shown for RE-doped silicon oxynitrides. Moreover, considerably higher PL intensity is obtained for the latter, pointing out that RE-doped silicon oxynitrides provide superior luminescence performance compared to RE-doped silicon oxides.

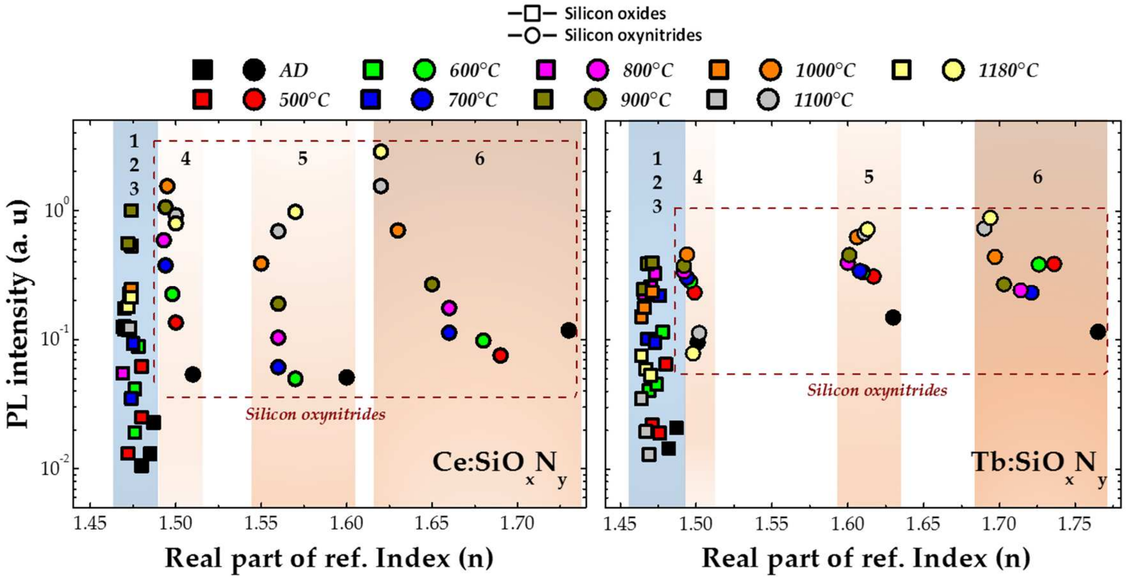

Figure 4.20. PL-n characteristic of Ce-doped (left) and Tb-doped (right) SiO_xN_y samples. Coloured squares (dots) correspond to the maximum PL intensity of silicon oxides (silicon oxynitrides) with different annealing temperatures. Dashed boxes highlight the data obtained from silicon oxynitrides.

Thus, the PL properties of Ce- or Tb-doped silicon oxides and oxynitrides have been explored in this section, displaying interesting features that mainly depend on the layer stoichiometry and the annealing temperature. Strong PL has been observed even for non-annealed samples, providing a solid starting point for the development of Si-based light sources and microdisplays. With this goal in mind, and based on the main results here extracted, the next sections will focus on the investigation of RE co-doped layers and multilayers to explore the versatility of our silicon oxides and oxynitride hosts in different layer architectures. Two main purposes will be tackled: (i) the layer co-doping and the sequential multilayer stack of different RE-doped layers; and (ii) a preliminary optoelectronic characterization of samples by means of electroluminescent test devices.

4.5. Layer co-doping and multilayer approach

As already introduced at the beginning of this chapter, one of the most important applications of luminescent RE-doped silicon oxides is the development of silicon-based light sources as basic optoelectronic building blocks for sensing and microdisplays. With this aim in mind, alternative layer approaches were investigated to provide the PL spectra with a much wider palette of colours by combining Ce^{3+} and Tb^{3+} ions in a single luminescent structure. Several requirements must be fulfilled in order to accomplish that purpose, since the active structure should comprise outstanding optical properties while retaining good electrical injection. Thus, bearing in mind the overall properties of silicon oxynitrides presented previously, we opted for the composition with lower oxygen content (sample SiO_xN_y_6 in table 4.1) to allocate RE ions in spite of the fact that lower power efficiency is expected in electrically driven devices (see chapter 2, section 2.6).

Once the host material is chosen, the most appropriate layer architecture should be implemented. For that, we may tackle two different architectures: a single co-doped layer or a sequential approach in which either Ce^{3+} or Tb^{3+} thin films are piled up to form a multilayer structure. It is worth noting that both systems present a series of advantages and disadvantages. With regard to the single layer co-doping, the main point in favour is the simplicity of the active building block and the good compactness of the film. On the other hand, we will deal with lower PL emission from each element as a consequence of a reduced RE solubility in the host (both RE ions share the same host matrix). Moreover, ion-ion interactions cannot be controlled, leading to potentially undesired situations in which one RE ion acts as a sensitizer for the other (as is the case for Ce^{3+} and Tb^{3+} ions), hence compromising the colour of the emission [20, 23]. This latter drawback can be easily avoided by stacking several active layers of different RE doping in a multilayer sequence. Moreover, the solubility limit in each layer is enhanced since only a single RE dopant is present in the host matrix. However, the multilayer approach entails other issues such as a high number of interfaces or a technologically challenging fabrication process.

Therefore, in order to evaluate the pros and cons of each layer architecture, 6 different samples were designed and fabricated. Figure 4.21 describes the geometry of each sample. The first five samples are co-doped with Ce^{3+} and Tb^{3+} ions, starting from a SiO_xN_y single layer 60 nm thick (sample I), a bilayer comprising a 30 nm thick Ce:SiO_xN_y and a 30 nm thick Tb:SiO_xN_y (sample II), and a series of different multilayers of 4 (sample III), 12 (sample IV) or 35 (sample V) RE-doped sub-layers with interleaved SiO_2 spacers 5 nm thick. Finally, a challenging Tb-doped sub-nanometre SiO_xN_y/SiO_2 superlattice was designed and fabricated to test the robustness of the fabrication process and to investigate the feasibility of implementation of these structures as electroluminescent layers (sample VI). It is worth mentioning that, if applicable, Ce-doped sub-layers were always placed above Tb-doped sub-layers to avoid photon reabsorption from Tb^{3+} ions in the upper hemisphere of the emission.

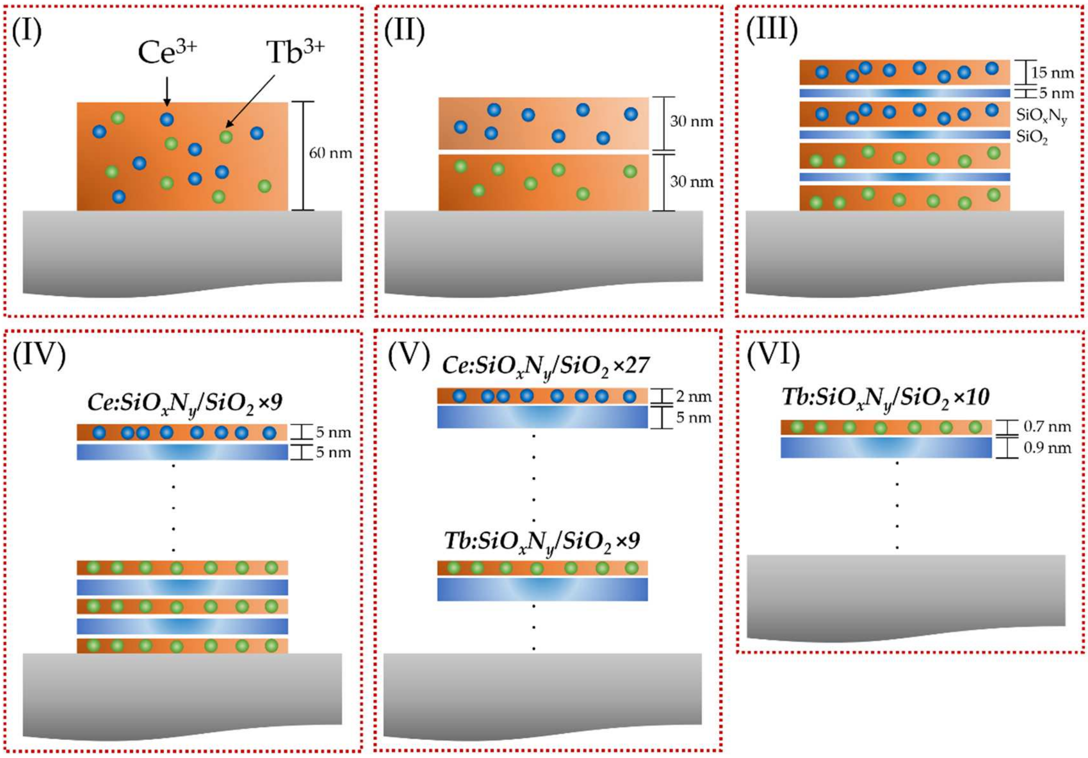

Figure 4.21. Description of the samples under study, being (I) a Ce and Tb co-doped SiO_xN_y single layer; (II) a bilayer composed by a Ce:SiOxNy and aTb:SiOxNy single layers; (III) a multilayer composed by 2 layers of Tb:SiOxNy and 2 layers or Ce:SiOxNy; (IV) a multilayer of 3 Tb:SiOxNy layers and 9 Ce:SiOxNy layers; (V) a multilayer composed by 9 layers of Tb:SiOxNy and 27 layers of Ce:SiOxNy; and finally (VI) a sub-nanometre Tb:SiOxNy superlattice structure. Each sub-layer of the multilayer is separated by a SiO_2 spacer of 5 nm, except for the superlattice, were a SiO_2 thickness of 0.9 nm was defined.

A first inspection of the multilayer structure was provided by TEM characterization. There were, mainly, three major points concerning the multilayer morphology that needed verification; (i) the correct positioning of the multilayer structure (although the CEDT at McMaster University has been working with RE doped single layers for many years, it was the first time that a multilayer approach like the one proposed in this dissertation was fabricated in their facility); (ii) the robustness of the multilayer over the annealing temperature (There is a considerable risk of multilayer intermixing for high annealing temperatures); and (iii) the formation of RE silicates in the layer when annealed at high temperatures. Indeed, based on the previous results shown in this section, small crystalline fractions are expected for the highest annealing temperature (1180°C), as a recovery of the PL intensity is observed as well as an enhancement of the extinction coefficient. In spite of this fact, however, large crystallites are discarded since the PL intensity is not well above the signal of lower annealing temperatures, as would be expected for a luminescent layer containing large fractions of Re silicates [3, 19]. Thus, in order to shed more light on these queries, two different layer architectures were characterized by TEM (design III and VI in figure 4.21), each one with a different annealing temperature (as-deposited and at 1180°C). Figure 4.22 shows the main results extracted from the layer design III. Figures on top, i.e. 4.22 (a), (b) and (c) correspond to the as-deposited sample, whereas figures 4.22 (d), (e) and (f) belong to the sample annealed at 1180°C. At a first glance, we can observe a well-defined multilayer structure in both samples (compare figures 4.22 (a) and (d)), with features in agreement with the nominal design, i.e. RE:SiO_xN_y sub-layers (12±1) nm thick with interleaved SiO_2 spacers of (5±1) nm thick. Noteworthy, the structure is preserved after the annealing treatment, with marginal layer intermixing, if any. Such statement can be corroborated by comparing the EFTEM images of the as-deposited sample (figures 4.22 (b) and (c)) with the ones from the sample annealed at 1180°C (figures 4.22 (e) and (f)), where the RE:SiO_xN_y sub-layer show a different brightness than the SiO_2 spacers in both cases.

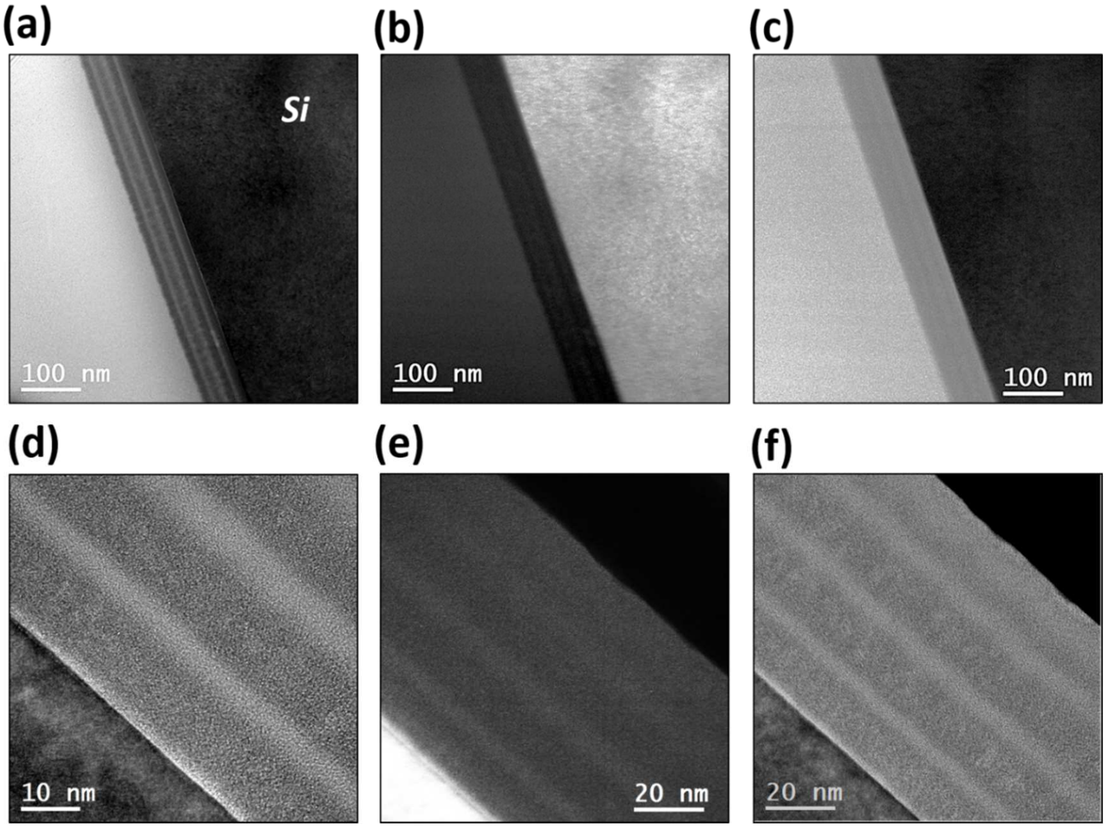

Figure 4.22. As-deposited multilayer structure III (see figure 4.21) showing (a) an HRTEM image, (b) an EFTEM image filtering by the Si plasmon peak (17 eV), and (c) an EFTEM image filtering by the SiO_2 plasmon peak (23 eV). (d), (e) and (f) correspond to the same multilayer design, but annealed at 1180°C, being (d) the HRTEM image, (e) the EFTEM image filtering by the Si plasmon peak, and (f) the EFTEM image filtering by the SiO_2 peak.

To further corroborate the robustness of our RE-doped multilayers, the superlattice structure (design VI) was also characterized after deposition and after a high temperature annealing treatment at 1180°C. In that case however, substantial differences were observed with respect to the previous multilayer design. Despite the initial deposition of a high quality superlattice structure, with abrupt interfaces, a layer thickness in agreement with the nominal values and with no evident waviness (see figure 4.23 (a)), the high thermal budget applied to the superlattice caused the partial destruction of the structure, as displayed in figure 4.23 (b). Indeed, only the first 8 deposited sub-layers were preserved, the rest being completely destroyed after the annealing treatment.

Moreover, an amorphous agglomeration of Tb:SiO_xN_y of about 20 nm is clearly observed at the top part of the superlattice. A FFT was performed over a single cluster to discard the formation of Tb silicates in the structure, revealing its amorphous nature (see the orange square box in figure 4.23 (b)).

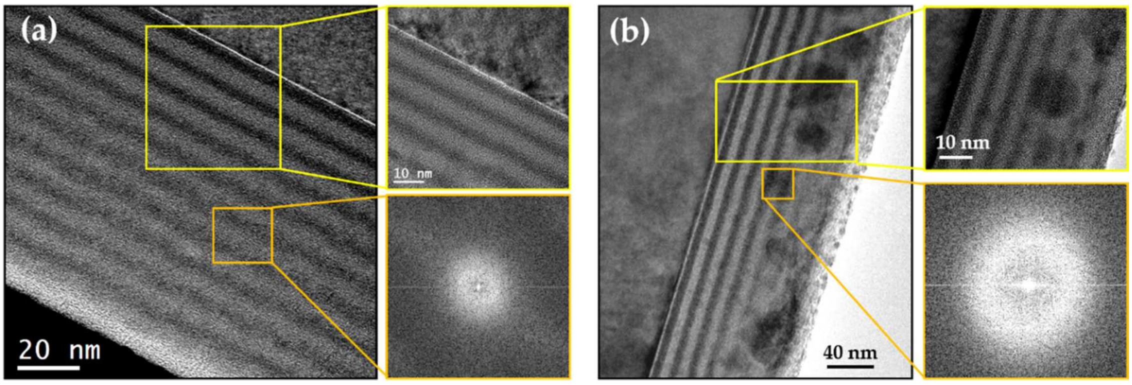

Figure 4.23. As-deposited Tb-doped SiO_xN_y/SiO_2 superlattice (a) and after an annealing treatment at 1180°C for 1 h (b). Yellow and orange square boxes depict a magnified region of the superlattice structure and the FFT of a localized zone of the superlattice, demonstrating the amorphous nature of the as-deposited superlattice and also of the dark spots corresponding to Tb:SiO_xN_y agglomerations in figure (b). EFTEM images were also performed, obtaining similar results than the ones shown in figure 4.22 (not shown).

Thereby, we succeeded in the fabrication of the multilayers and the superlattices, although the applied thermal budget for the latter was high enough to cause large layer intermixing. This fact could be explained by taking into account that the superlattice structure is made of much thinner sub-layers in comparison with the multilayer, hence being prone to mixing upon high thermal treatment. The same reasoning applies for the gradual increase of layer inter-mixing for subsequently deposited sub-layers, since the first ones lie on a smooth crystalline substrate, whereas the rest must settle over an increasingly rough amorphous material. In order to establish an upper limit for these structures, a new TEM analysis of a Tb-doped superlattice at a reduced annealing temperature of 1000°C was performed. A well-preserved superlattice structure was obtained, with no layer mixing nor amorphous agglomerations. The most important highlights from the TEM characterization carried out over such new set of Tb-doped superlattices can be reviewed in *paper XV*.

As for the rest of the multilayer designs, despite additional TEM characterization of these samples not being available, all of them are expected to maintain the sequential structure up to, at least 1000°C, equal to the Tb-doped superlattice. Also, despite single layer co-doping with different RE ions was already performed on this system previously [3], the simultaneous incorporation of two RE ions into the growing film through the showerhead towers adds an extra level of complexity to the fabrication process and therefore, it should be carefully inspected. Moreover, the deposition of several multilayers, each one with different RE doping, was not previously accomplished in this particular deposition system, and consequently further verification is also needed since the RE incorporation may not be efficient in very thin films of only few nanometers. Thus, an RBS characterization was conducted on samples to determine the RE percentage and the layer stoichiometry (see figure 4.24 (a)), revealing a layer composition in accordance with the one previously obtained for silicon oxynitrides (with a variable nitrogen content of 10-30%) and a RE incorporation that differs from 0.1% to 1% depending on the sample.[19] RBS data modeling of the RE peak at 1550 keV was also performed (figure 4.24 (b)), disclosing even Ce and Tb doping in samples I, II and III and higher Ce concentration in samples IV and V, as expected. It is worth mentioning that the limited resolution of the experiment did not allow us to observe the sudden RE signal drop expected when incident ions are backscattered by the nuclei of the SiO_2 spacers, providing the RBS signal with a periodic ripple that would match with the periodicity of the SiO_2 layers.

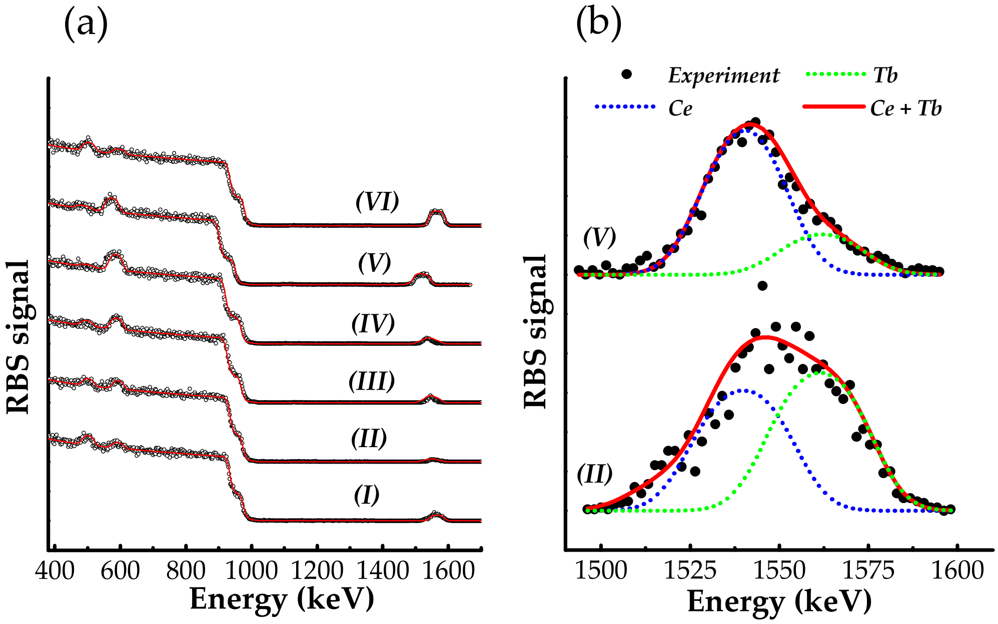

Figure 4.24. (a) Experimental RBS data of samples (open circles) and simulated energy profile using SIMNRA software. (b) Experimental RBS peak of the RE concentration (dots) of samples II and V with the simulation superimposed (red line). Dotted blue and green lines depict the simulated energy profiles of Ce and Tb, respectively.

PL measurements performed on samples allowed distinguishing particular features that strongly depend on the stack design. The characteristic PL spectrum of each sample is shown in figure 4.25. Additionally, the evolution of Ce^{3+} and Tb^{3+} emission features is plotted as a function of the annealing temperature in figure 4.26. Notice that Ce^{3+} radiative transitions are observed in all samples except for the Ce-undoped sample VI, where only the Tb^{3+} emission lines are seen, as expected. Interestingly, the Ce and Tb co-doped single layer displays a Ce^{3+} emission that is weaker than in samples II and III in spite of the fact that the same Ce content was measured in the RBS analysis. On the

---

[19] *Same RE doping was carried out in all the structures, and with identical fabrication parameters than for the previous set of samples (single layers, see table 4.1), i.e. with a heating cell temperature for Tb and Ce metal organic precursors of 180°C and 215°C respectively, being the RE transmission lines and the showerhead towers at 225°C.*

contrary, much higher Tb^{3+} emission was measured in sample I with respect to the rest of samples (see figure 4.26).

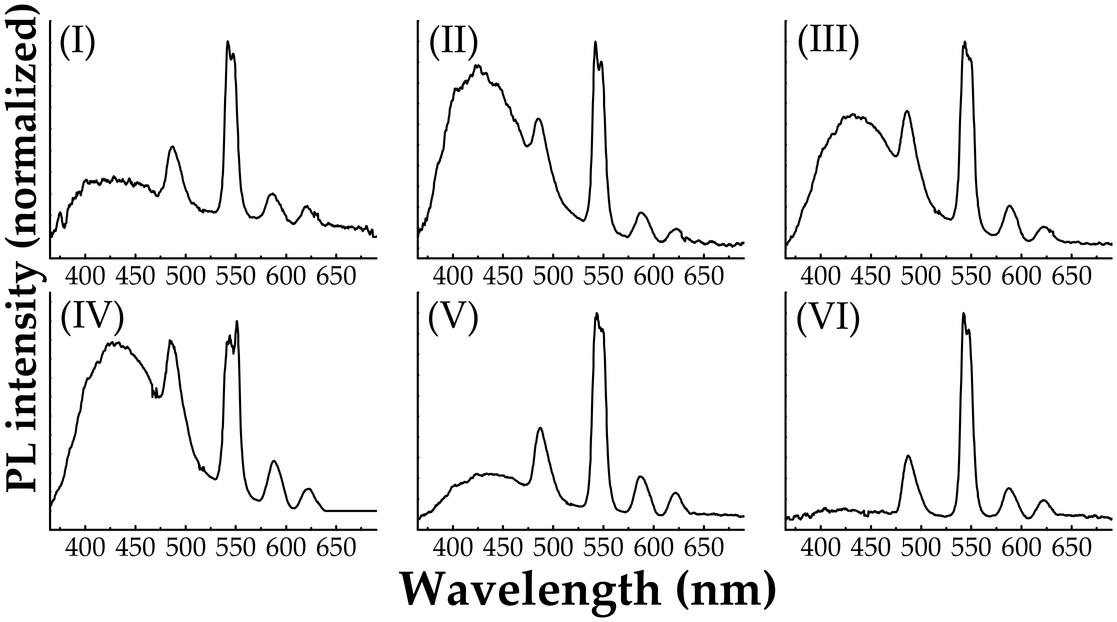

Figure 4.25. PL spectra taken upon 325 laser excitation on samples annealed at 1000°C.

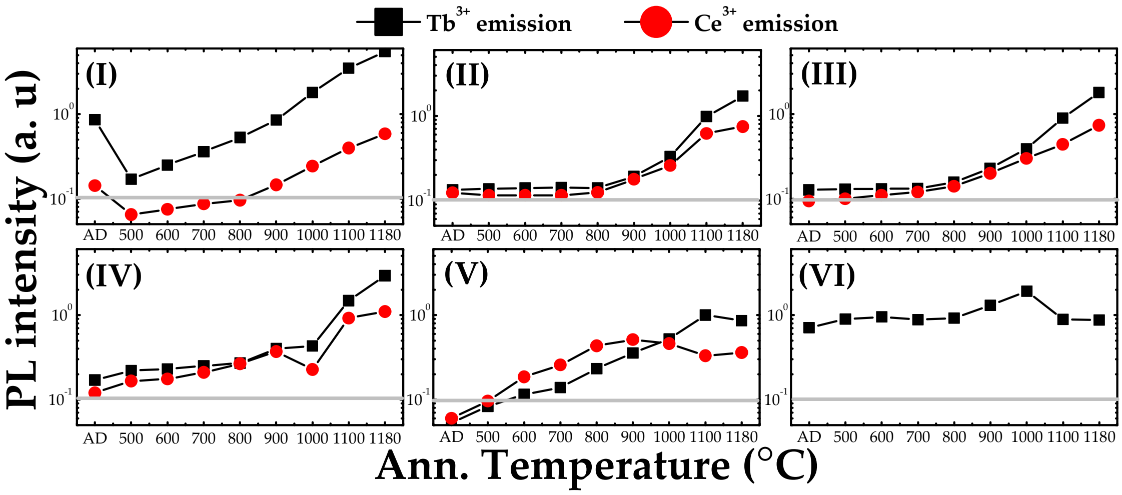

Figure 4.26. Maximum PL intensity of Tb^{3+} (squares) and Ce^{3+} (dots) emission as a function of the annealing temperature for the new set of samples. The y-axis scales are comparable.

As a matter of fact, these features suggests an energy transfer from Ce^{3+} ions to neighbouring Tb^{3+} ions, as proposed by other authors [22, 23]. Hence, such effect would be suppressed when RE dopants are placed away from each other, as in samples II and III. Nevertheless, the PL characteristic of samples IV and V revealed an unexpectedly high Tb^{3+} emission, in spite of the fact that Ce- and Tb-doped sub-layers are well separated by at least 5 nm in the worst case scenario. Indeed, much brighter Ce^{3+} emission was expected from these structures since a Ce concentration between 3 to 5 times higher than the one of Tb was measured by RBS analysis (see figure 4.24 (b)). Such behaviour could be taken as a hint of the non-negligible cross-contamination of Tb in Ce-doped sub-layers. As explained in previous sections, the RBS technique is not able to resolve RE concentrations lower than 0.1%. By that means, the presence of Tb was not identified in Ce-doped samples although a clear PL features was collected upon 325 nm laser excitation (see figure 4.16). Similarly, we may have overlooked Tb contamination in the Ce-doped sub-layers forming the multi-layered samples, and consequently the enhanced Tb^{3+} emission would be assisted by an energy transfer from Ce^{3+} ions placed in the vicinity. In spite of this unforeseen issue, bright Ce^{3+} and Tb^{3+} luminescence with different spectral line shapes was obtained in all samples. With regard to the influence of the annealing temperature on the PL intensity of samples, an increasing trend is generally measured for higher values for the two RE emissions, in agreement with silicon oxynitrides (see figure 4.26).

Therefore, and taking into account the large number of PL spectra obtained at this point from the entire set of analysed samples (single RE-doped layers, RE co-doped layers and multilayers), a preliminary colorimetric study could be accomplished to assess the suitability of these luminescent layers as unit pixel cells in full colour micro-displays. For that, the chromaticity coordinates of 8 different PL spectra were calculated based on the XYZ colour space created by the International Commission on Illumination (CIE) in 1931. As seen in figure 4.27, the XYZ coordinates of the studied spectra follow a gradual variation over an imaginary straight line that crosses the CIE diagram from blue to green. Indeed, this feature strongly resembles the one previously reported by P. R. J Wilson in his work on Ce- and Tb-doped silicon oxides, validating the suitability of RE-doped silicon oxynitrides as alternative bright luminescent layers with wide colour tunability. Moreover, an encouraging scenario is foreseen for the optoelectronic functionality based on the several advantages that silicon oxynitride thin films offer over silicon oxides.

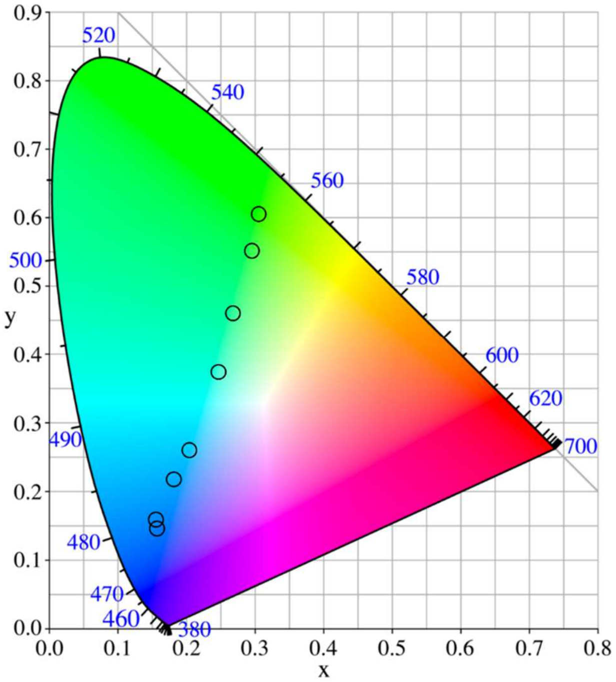

Figure 4.27. XYZ coordinates of 8 different Ce- and/or Tb-doped samples in the 1931 CIE chromaticity diagram.

In order to better illustrate this feature, figure 4.28 correlates the gradual tunability of the predominant colour of the emission extracted from the CIE chromaticity diagram with the PL spectrum of each sample. The dominant wavelength and the colour purity are also shown for comparison. As seen, the colour purity is higher at the ends of the coloured stripe, and decreases when approaching the centre, being minimum for the turquoise tonality.

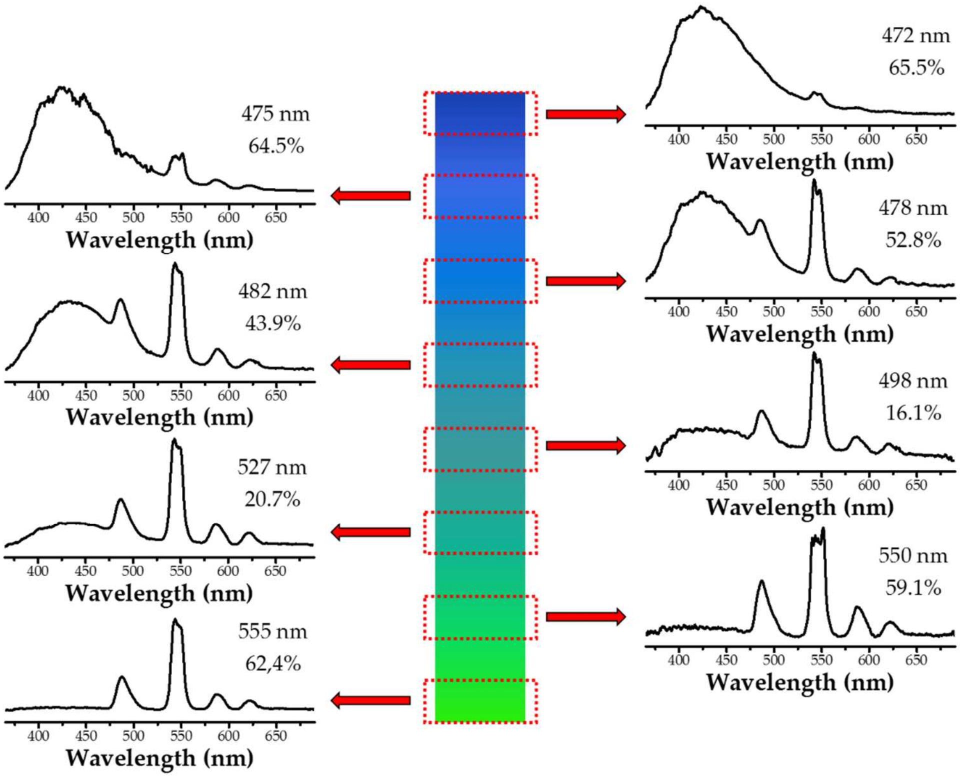

Figure 4.28. Correlation between the dominant colours obtained from the CIE diagram and the PL spectra of different samples. The dominant wavelength and the colour purity are also shown.

Finally, figure 4.29 shows the emission of three representative RE-doped samples with different dominant wavelengths taken with a smart phone camera in daylight conditions. Intense PL emission can be observed upon UV excitation at 325 nm, displaying either a cobalt blue emission (figure 4.29 (a)), a turquoise tonality (figure 4.29 (b)) or an emerald green luminescence (figure 4.29 (c)). Noteworthy, a similar emission easily observable by the naked eye was observed in all samples, regardless of the layer stoichiometry or the annealing temperature.

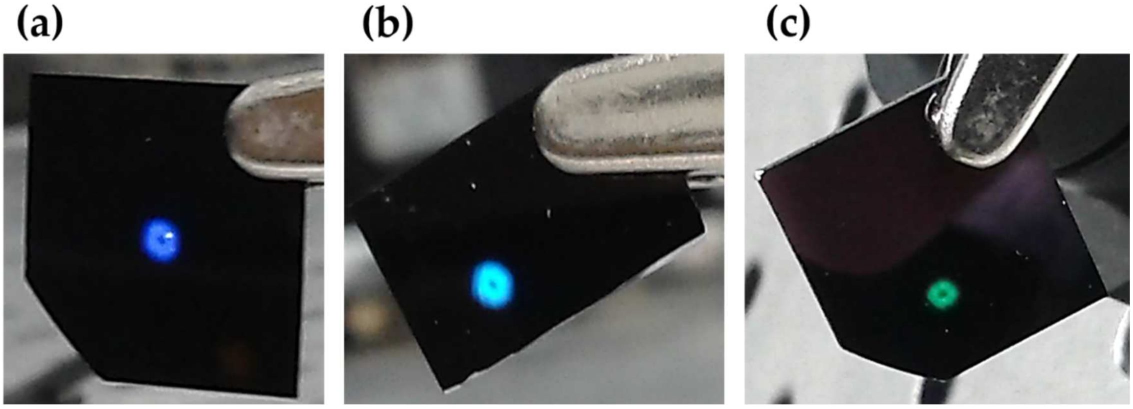

Figure 4.29. (a) Sample Ce:SiO$_x$N$_y$_6 (see table 4.1), (b) Ce- and Tb-doped SiO$_x$N$_y$ bilayer (sample II in figure 4.26), and (c) the Tb-doped SiO$_x$N$_y$/SiO$_2$ superlattice (sample VI in figure 4.26), all annealed at 1000°C. Images were taken with a smart phone camera of 5 Mega Pixels.

Thus, the appropriate mixing of Ce^{3+} and Tb^{3+} ions in different layer architectures has resulted in fascinating optical properties that could be exploited to develop new Si-based light sources with different applications. Efficient RE incorporation has been demonstrated in co-doped single layers and in thin multilayer structures, opening the road towards complex multilayer stacks with outstanding functionality. Strong PL emission has been observed in all samples, with a wide colour tunability ranging from deep blue to pistachio green depending on the morphology of the sample. Such encouraging features put forward the likeliness of implementing such structures as electroluminescent layers in electrically driven devices. With this aim in mind, the next section will be dedicated to the development of simple electroluminescent test devices containing the previously studied Ce- and/or Tb-doped thin films.

4.6. Preliminary optoelectronic characterization: Development of electroluminescence test devices

The fabrication of electroluminescent test devices in RE-doped oxide and oxynitride thin films became a challenging task for several reasons. Firstly, because the Electro-Photonics Lab at the University of Barcelona lacked of hands-on experience in fabrication and device processing. Secondly, we were limited to the equipment available in the cleanroom facility of the Faculty of Physics at the University of Barcelona. The object of such strong constraint was motivated by the several advantages that are foreseen, since the development of an in-house fabrication procedure would provide higher versatility of implementation and will save time (and of course money) compared to the standard processing available at the technological institutions. Therefore, in view of these requirements, a simple but effective method to fabricate electroluminescent test devices was tackled. In that regard, one of the most popular approaches commonly reported is to deposit a Transparent Conductive Oxide (TCO) dot such as Indium Tin Oxide (ITO) on top of the luminescent layer and cover the back side with aluminium. Nevertheless, despite being conceptually simple, this method requires a good command of the lithographic process to pattern the upper ITO electrode. An alternative strategy that does not require any knowledge of optical lithography is the shadow mask configuration. In that case, the sample to be patterned is introduced in the deposition chamber and covered by a metallic mask with tiny open sites that reproduce the desired electrode shape that should be patterned. By doing so, the evaporated material is only allowed to go through these perforated sites, promoting a selective deposition over the sample.

An EB-PVD system was used to fabricate the electrodes. This technique is especially suited for metals and TCOs, and is able to provide high quality films with excellent electronic and optical properties. Also, it offers a lower level of contamination with respect to thermal evaporation, since only the material is heated up to evaporation temperatures. See chapter 1 for a more detailed description of this deposition system.

A sketch of the EB-PVD system available in the cleanroom is shown in figure 4.30 (Pfeiffer classic 500). The driving gas turbine of the turbopump system is placed at the back of the chamber to pump the chamber down to operative pressures (10^{-5}-10^{-6} mbars). The sample is located at the upper side of the chamber, covered by the mask and mechanically attached to a rotational stage that can be heated up to 600-700°C by means of a halogen lamp. The electron beam gun is placed at the bottom of the chamber. A high voltage driven tungsten filament generates the electron beam, which is deflected by a number of magnets, and driven towards the targeted material placed in the crucible. Also, the system is equipped with a quartz crystal sensor and a mechanical shutter to control the deposition rate. Noticeably, the deposition system can be remotely controlled by a thin film deposition controller (SQC-300) that governs the e-beam gun at will in order to match the pre-set deposition conditions.

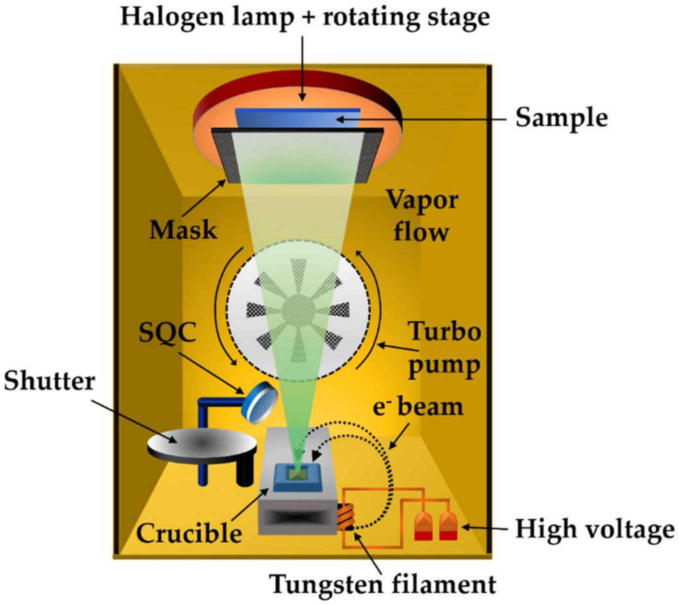

Figure 4.30. Schematic diagram of the electron beam evaporation system. The vacuum chamber contains: A tungsten filament driven by a high voltage power supply, a crucible containing the targeted material (ITO pellets in this case), a shutter, a quartz crystal sensor, a turbo pump system and a substrate holder composed by a rotating stage and a halogen lamp.

Prior to going into the details of the fabrication of the electrodes by the shadow mask approach, a preliminary study of the optical and electrical properties of the deposited materials was performed to validate the process. For that, a series of ITO and Al thin films with different fabrication parameters were deposited onto glass substrates to test their conductivity and transmittance of ITO over a wide range of wavelengths. In that regard, it is worth mentioning that the development of a good upper electrode was rather more challenging than for the back side electrode since we had to cope with two imperatives: a good layer conductivity and an elevated transmittance.

After several iterations, we found an optimum set of parameters for both materials. In particular, a deposition rate of 5Å/s and a layer thickness of 200 nm yielded good ohmic behaviour and a resistivity of ~ 10^{-8} Ω·m in Al when deposited at room temperature. On the contrary, a much lower deposition rate was required for ITO films, with 0.5-2Å/s being the rate that provided best results. Also, a temperature of 200°C was set in the halogen lamp, which corresponds to a real substrate temperature of 100°C in the sample. Let us add a few words about the ITO optimization. Although higher deposition rates could be accomplished for ITO deposition, it also normally requires an extra source of oxygen to compensate for the poor directivity of the evaporated oxygen extracted from the target (ITO pellets). In our case however, we were limited to low deposition rates since an oxygen gas flow source was not available at the time. Such low rates provided better layer stoichiometry in the deposited layer and diminished defect states due to oxygen vacancies, hence improving the transmittance significantly. Another important factor to take into account is the layer thickness. As already mentioned, the top ITO electrode should retain good electrical and optical properties. For that, one may think of reducing the ITO thickness as much as possible to increase the layer transparency. Nevertheless, ITO films experience a considerable increase of the layer resistivity for layer thicknesses comparable to the mean grain size (of about tens of nanometers), since the number of electrical paths that connect adjacent grains becomes strongly reduced [24]. Consequently, ITO films with a mean thickness of 200 nm were deposited, beyond the expected mean grain size (tens of nm). Figure 4.31 (a) outlines this particular situation.

Once the ITO layer is deposited, an annealing treatment is required to improve the layer crystallinity and remove defect sites. These latter ones are potential trapping centres of injected carriers, which reduces both the conductivity and the layer transmittance via partial electronic screening of incoming charges and enhanced photon absorption (or scattering) of incident light. Different annealing temperatures were investigated, all of them above 200°C, which is the lower limit for ITO crystallization, and lower than 700°C to mitigate potential changes in the morphology of RE-doped layers. An inert atmosphere of N_2 was used to anneal samples. An optimized annealing temperature of 500°C resulted in a layer conductivity of ~ 10^{-6} Ω·m and a transmittance of about 80-90% in the whole visible range (see figure 4.31 (b)). These values are in good agreement with the ones previously reported in other works, validating the fabrication process [24].

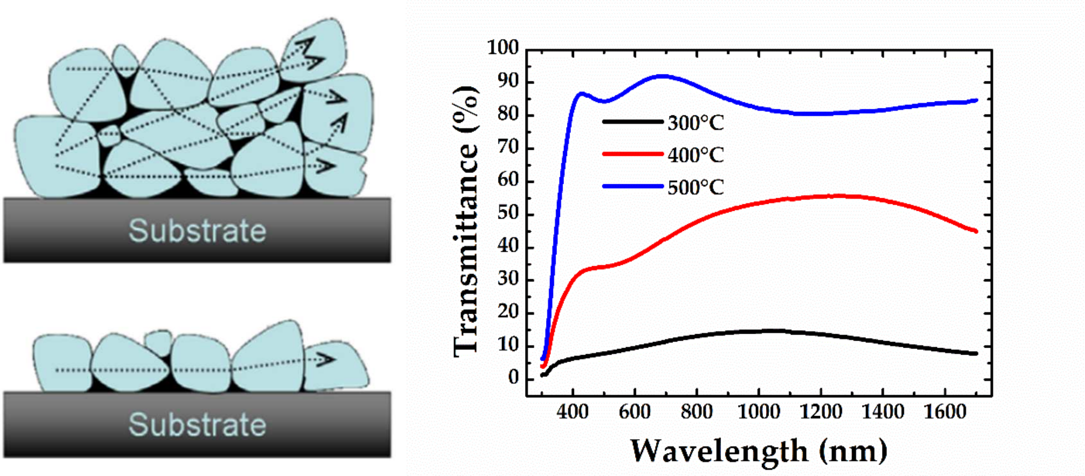

Figure 4.31. (a) Schematic comparison showing the available conductive pathways in an ITO layer with a thickness higher than the mean grain size (top draw) and comparable to the grain size (lower draw). This figure was extracted from [24]. (b) Transmittance spectra of an ITO layer 150 nm thick deposited onto a glass substrate, upon different annealing temperatures. Measurements were done by O. Blázquez.

The mask was also fabricated ad hoc. A simple mask layout was first defined, consisting of various circular dots of different radii ranging from 100 µm up to 1 mm, whose geometric arrangement in the mask can be observed in figure 4.32 (a). In order to obtain such tiny features with high precision, laser ablation was performed over a thin nickel sheet of 100 µm.[20] In spite of having a resolution of a few µm, the contour of the hollow dots in the nickel mask were not completely smooth when further inspecting the mask with an optical microscope, showing a non-uniform profile that becomes especially accentuated for the smaller features (see figures 4.32 (b) and (d)). Still, such drawback does not invalidate the first attempt to test the optoelectronic feature of RE-doped thin films since the line shape of the top electrode is not expected to critically affect the optoelectronic functionality of samples. Hence, once the quality of the materials was validated and the mask fabricated, the shadow mask approach was performed over selected RE-doped samples. Three different samples were chosen: A Tb-doped SiO_2 single layer ($Tb:SiO_xN_y\_1$ in table 4.1), a Ce-doped SiO_xN_y single layer ($Ce:SiO_xN_y\_6$) and the Tb-doped SiO_xN_y/SiO_2 superlattice (sample VI), all of them annealed at 1000°C for 1h in N_2. Figure 4.32 (c) shows a photograph of a single RE-doped sample with the ITO electrodes already patterned and annealed at 500°C for 1h in N_2 atmosphere.

---

[20] *The mask layout was provided by the Nanophotonics Technology Center (NTC) in Valencia, and the laser ablation was performed by the Spanish company Cipsacircuits, S. A.*

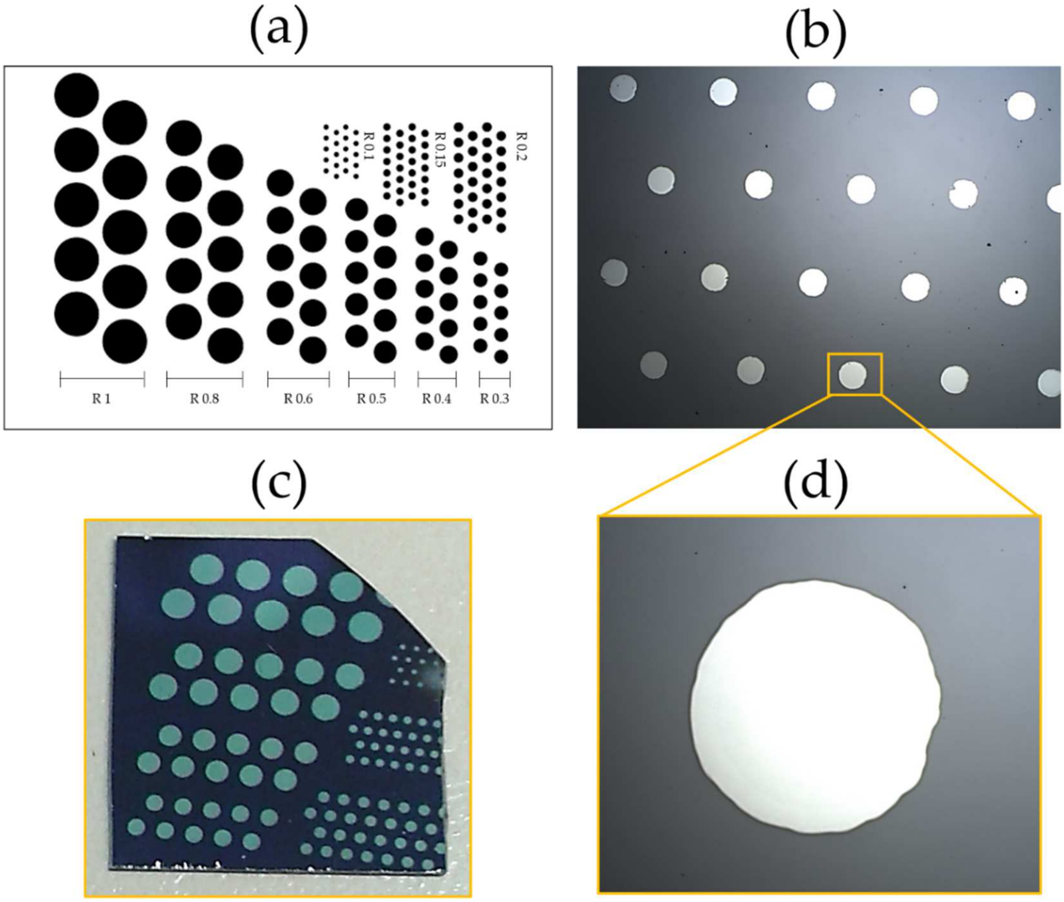

Figure 4.32. (a) Mask layout for the patterning of the upper ITO electrode. The radii of each dot is specified for completeness. (b) Top view of the perforated nickel mask showing the smaller dots of the mask layout (with R = 100 μm). (c) A RE-doped sample with the ITO electrodes patterned on top, after annealing at 500°C for 1h in N_2 ambient. (d) zoom-in region of a single hollow dot of the nickel mask. Images (b) and (d) were obtained with an optical microscope, and image (c) was taken with a smart phone camera of 5 Mega Pixels.

A further inspection of the ITO electrodes was carried out by means of a FE-scanning electron microscopy (SEM) analysis (Jeol JSM-7100F). A summary of the most relevant features is provided in figure 4.33. As seen, a fairly circular shape was obtained, with a well-defined contour and a good reproducibility among different dots. Moreover, the microstructure of the ITO electrodes was examined, showing a dense granular structure with a mean grain size of 100 nm. Remarkably, this value is slightly higher than the one typically reported in ITO films, i.e. between 30 and 60 nm [25]. An ongoing investigation of several ITO electrodes fabricated with different parameters is being done at the time of this writing to identify the origin of such discrepancies.

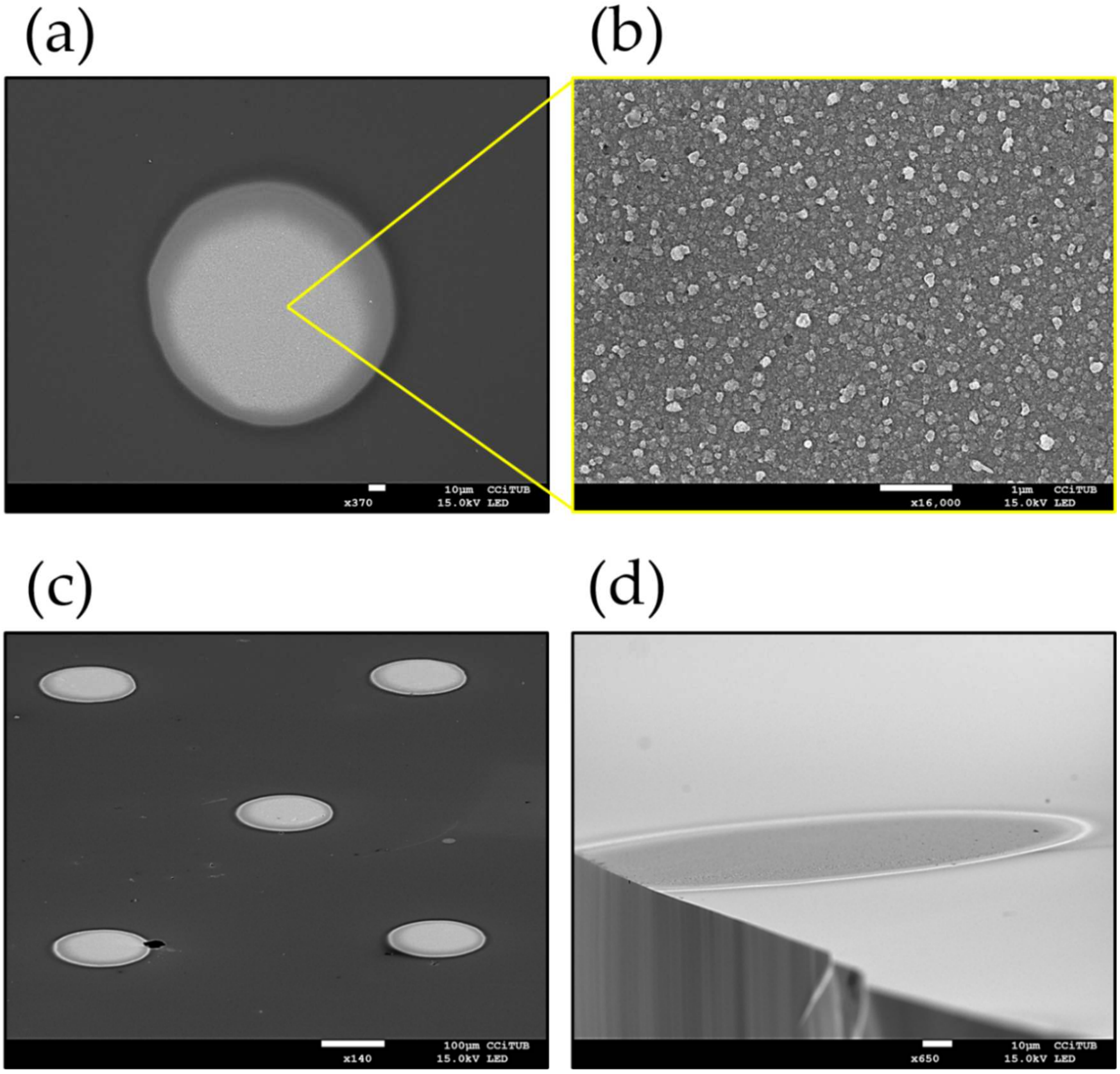

Figure 4.33. (a) Top view SEM image of a single ITO electrode. A magnified region is depicted in (b), showing the granular structure of ITO electrodes. (c) and (d) show tilted SEM images of a field of ITO electrodes and a partially cut single ITO electrode, respectively.

A preliminary optoelectronic characterization was accomplished over fabricated devices.[21] For that, a series of I-V sweeps from 0 V to negative voltages in forward and backward directions were performed, with a small voltage step of 50 mV/sec. Good carrier injection was obtained from all devices. Furthermore, silicon oxides displayed lower current density values than silicon oxynitrides, suggesting a different charge transport mechanism. In fact, the modelling of the experimental data with the PF and TAT compact equations (see chapter 2) evidenced that a bulk-limited charge transport governs the silicon oxynitrides whereas a current injection phenomena strongly modulated by the electrode-active layer barrier height and assisted by nearby localized defects is the most probable charge transport mechanism in silicon oxides. A representative example is shown in figure 4.34. The J-E characteristic is observed along with the modelled charge transport phenomena, showing different electric field onsets

---

[21] *The optoelectronic characterization of the Tb-doped SiO_xN_y/SiO_2 superlattice can be found in paper XV and will be summarized at the end of this chapter.*

for each mechanism, i.e. around of ~ 3 MV/cm for the PF conduction and ~ 6 MV/cm for the TAT model, in agreement with previously studied Er-doped oxides and nitrides (see chapter 2). Relative permittivity and potential barrier height values obtained in different devices with PF and FNT charge transport oscillated between ε_r ~ 8-13 and ϕ_b ~ 1-3eV respectively. Also, the hysteresis between forward and backward sweeps denotes the existence of a permanent charge trapping in the active layer that screens incoming charge injection. As a consequence, lower current density is measured in the backward sweep with regard to the forward condition for the same electric field polarization. Furthermore, it is worth mentioning that despite the fact that most of the analysed devices showed an electrical response in accordance with the one reported in figure 4.34, a large variability in the J-E curves was observed among them. As a consequence, experimental data was modelled using a wide range of parameters, as already shown for the relative permittivity and the potential barrier height. Such lack of reproducibility in the analysed devices (about 20 different devices were tested in each sample) impedes a thorough optoelectronic characterization and limits the accuracy of our conclusions. In spite of this drawback, a clear difference in the charge transport properties with a similar feature than the one displayed in figure 4.34 was observed in about the 60% of the studied devices in samples Tb_SiO_xN_y_1 (silicon oxide) and Ce_SiO_xN_y_6 (silicon oxynitride).

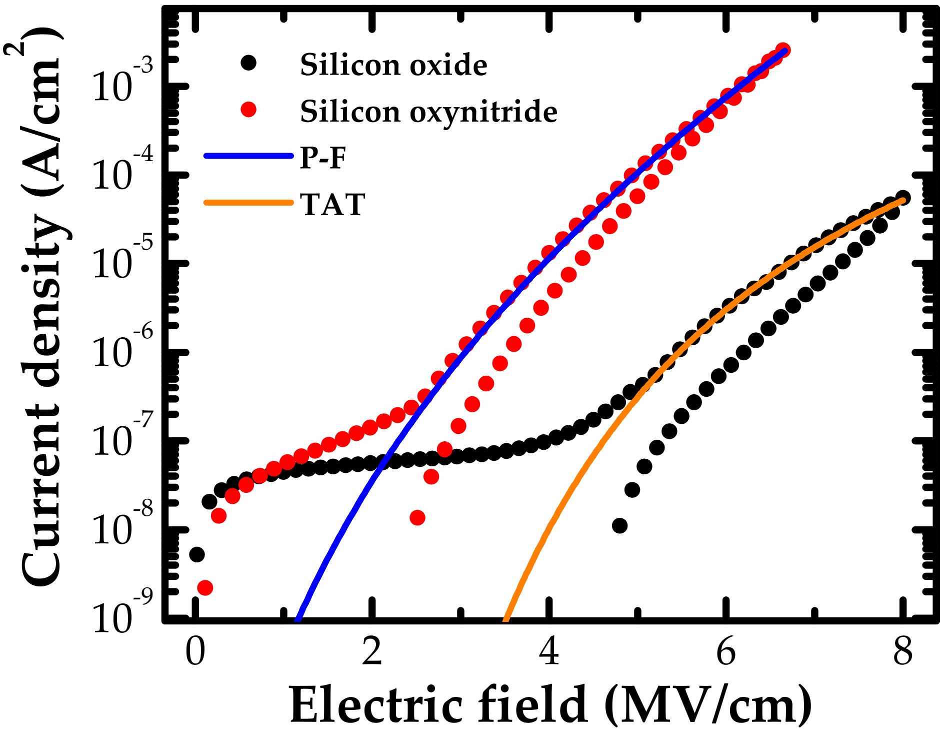

Figure 4.34. Comparison between the J-E characteristic in different electroluminescent test devices containing either a luminescent Tb-doped SiO_2 layer (black dots) or a Ce-doped SiO_xN_y layer (red dots). PF and TAT models are also displayed, showing a good agreement with experimental data.

Similarly, the EL spectra of both samples were measured upon continuous current excitation, obtaining the typical emission lines of Ce^{3+} and Tb^{3+} ions.[22] A representative EL feature of both samples is shown in figure 4.35. Broad Ce^{3+} emission can be observed in the Ce-doped silicon oxynitride, together with a smaller peak located at 550 nm and associated to Tb^{3+} emission due to residual contamination, in agreement with the PL characterization. On the other hand, the Tb-doped silicon oxide displayed a well-defined EL spectrum showing the most probable Tb^{3+} radiative transitions. In this case however, no other RE-related emission was collected, also in accordance with previously studied Tb-doped thin films. Various EL spectra taken at different current density values were also recorded, revealing a similar line shape regardless of the level of current injection. In addition, an estimation of the EQE of these devices was performed. It is worth to recall that this parameter is of major relevance to test the quality of electroluminescent devices since it defines the electrical-to-optical conversion under DC polarization (see chapter 2). Noteworthy, an EQE $< 10^{-3}\%$ was obtained in all cases. Such a value is lower than expected, especially for the Tb-doped SiO$_2$ layer taking into account that values as high as 1% were measured in Er-doped SiO$_2$ layers emitting at 1.54 μm (see chapter 2, section 2.5). There could be several origins of this poor performance in comparison with previously studied devices, the simple device processing adopted being the most probable as well as the lack of robustness of the deposited ITO electrodes that may not be suited for the high voltage stress conditions to which they are subjected.

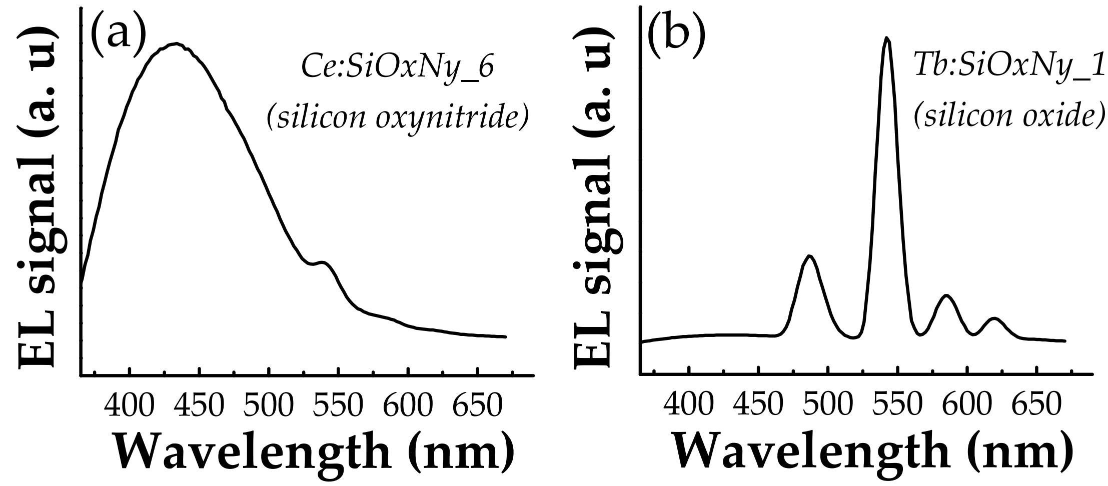

Figure 4.35. EL spectra of Ce:SiO$_x$N$_y$_6 (a) and Tb:SiO$_x$N$_y$_1 (b) devices taken upon high current density excitation of 10^{-3} A/cm^2 and $3\cdot10^{-5}$ A/cm^2, respectively.

In order to gain further insight on this issue, a reliability test in RE-doped single layers was carried out. For that, a constant current density above the EL threshold was forced over the ITO electrode while monitoring the V-t characteristic of devices. Surprisingly, all devices broke down after 30 minutes of continuous operation. Furthermore, such

---

[22] *It is worth to mention that since the EL spectra were collected with an equipment that has lower spectral resolution than the one used to obtain the PL spectra, the characteristic doublet of Tb*$^{3+}$ *emission at 550 nm cannot be resolved, although it is also expected.*

rupture gave rise to a sudden increase of the V-t characteristic up to the compliance limit. This effect is a conclusive feature and suggests that the electrode is no longer supplying the desired current injection ratio, hence forcing the driving source to rapidly raise the voltage to maintain the pre-set current density value, which would be no longer reached. A visual inspection of the top ITO electrode by means of an optical microscope further confirmed this hypothesis, as the topology of the electrode surface showed a network of burned pathways in broken devices. Also, such local damaging of the ITO electrode seemed to start around the contact location were the polarization tip is placed. A set of images of a single ITO electrode with the polarization tip placed at different locations is shown in figure 4.36 to demonstrate this effect. Starting from left to right, the first picture depicts the surface topology of an ITO electrode from sample Ce_SiO$_x$N$_y$_6 after 10 minutes of DC operation, with a pre-set current density of 10^{-3} A/cm^2. As seen, a homogeneous topology is observed. On the contrary, the second image shows a series of randomly distributed burned pathways around the tip for the same ITO electrode after 30 minutes of continuous polarization. Thus, the electrode surface becomes clearly damaged, and it can no longer supply the desired current injection ratio. In view of this result, we can verify that the poor reliability of analysed devices is caused by the early breakdown of the ITO electrode upon high voltage polarization. In addition, the fact that the burned region is placed at a close distance from the tip contact point suggests that, in spite of the high conductivity measured in ITO layers, the applied voltage is slightly higher in the vicinity of the contact point, hence being more prone to breakdown compared to the rest of the electrode. An additional measurement was performed to corroborate this hypothesis, this time changing the contact point of the polarization tip (see the third image from the left). Again, the region around the contact point became burned after several minutes of DC polarization. Finally, the same process was carried out in a different place of the ITO electrode, with a very similar outcome, as seen at the right of figure 4.36.

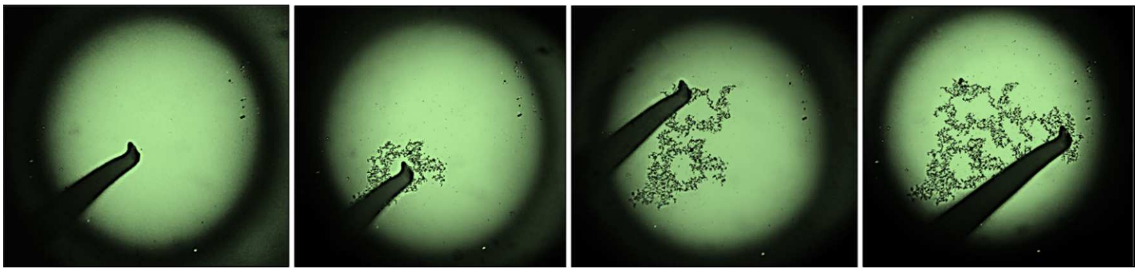

Figure 4.36. Top view of a single test device fabricated over a Ce-doped SiO$_x$N$_y$ layer annealed at 1000°C for 1h in N$_2$ (sample Ce_SiO$_x$N$_y$_6) upon constant current density of 10^{-3} A/cm^2. The green circular dot corresponds to the ITO electrode, being the black shadow superimposed the polarization tip. From left to right: (i) after 10 minutes of continuous operation; (ii) after 30 minutes of continuous operation; and after (iii) 15 minutes and (iV) 5 minutes of continuous operation and with a different contact point. The green colour displayed does not correspond to an EL emission, but to a combined effect of absorbed and backscattered wavelengths of the microscope backlight.

Therefore, the early device breakdown is mainly generated at the top ITO electrode. This drawback may explain the low EQE values measured and also the poor reproducibility and reliability of the analysed devices. In that regard, a fundamental point to take into account is the high voltage applied over the devices. Being the studied RE-doped samples of several tens of nanometers, a high voltage polarization is needed to obtain current density values above the threshold of emission. To give some numbers, a value of $|V_G|$= 40 V is required for a silicon oxide, and around of $|V_G|$= 30 V for a silicon oxynitride. Then, these values induce a high voltage stress over the device, leading to the early breakdown of the deposited ITO electrode.

Interestingly, it should be noted that a completely different behaviour was observed for those devices patterned onto the Tb-doped superlattice. In that case, much more stable optoelectronic characteristic was obtained, with good reproducibility and enhanced reliability. In addition, and contrary to what has been previously reported above for the RE-doped single layers, the early breakdown of the ITO electrode was rarely observed in the Tb-doped superlattice test devices, hence corroborating our conjectures. Our interpretation is well founded on the basis that Tb-doped superlattice devices require a much lower voltage operation since the superlattice is only 15 nm thick. As a consequence, a measurable EL signal is already obtained when applying a voltage as low as ~ 7 V. These voltages are about 5 times lower than for the RE-single layers, and therefore have a considerably smaller impact on the electrode. Because of this, a more accurate optoelectronic characteristic was obtained from Tb-doped superlattices. *Paper XV* provides a comprehensive description of these structures in terms of sample fabrication, layer composition, morphology and the optoelectronic characterization. For the latter, two remarkable features were disclosed; firstly a PF conduction that strongly resembles the one previously reported for Er-doped Si-ncs superlattices was obtained, suggesting that the large number of interfaces that electrons have to pass through causes the bulk-limited conduction. Secondly, the stable operation of devices offered the possibility to perform a sequential study of the EL spectrum for increasing current densities, obtaining a linear EL-J feature for the entire EL onset.

Another key point to assess the optoelectronic characteristic of Tb-doped superlattices is the measurement of the EQE. A value very similar to that previously obtained for RE-doped single layers was also obtained in this case (< 10^{-3}%). Nevertheless, we believe that such modest performance has a different origin in this case. Rather than attributing it to a deficient functionality of the top ITO electrode, the poor electrical-to-optical conversion is presumed to be caused by the inherently low hot electron injection ratio provided by the PF conduction, which governs the charge transport in Tb-doped superlattices. I may note that in high contrast with the RE-doped single layers, the optoelectronic characteristic of Tb-doped superlattices is thought to be limited by the active layer itself and not by the ITO electrode. Indeed, we may find an interesting trade-off between the electrical and optical performance of these devices. From one side, Tb-doped superlattices present interesting characteristics since they show measurable EL signal at voltages as low as 7 V, hence being potential candidates for the 'ultimate'[23] CMOS compatibility. On the other hand however, the bulk-limited conduction offers low RE excitation rates, resulting in a mediocre EQE value.

In summary, electroluminescent test devices have been fabricated onto RE-doped thin films to perform a simple optoelectronic characterization. Despite showing good current injection ratios and an EL spectrum in agreement with RE radiative transitions, additional issues such as the poor reproducibility and reliability of devices prevented us from a more accurate device characterization in RE-doped single layers. Only the Tb-doped superlattice showed robust optoelectronic features. The origin of such divergences between single layers and the superlattice has been attributed to the fact that much lower driving voltages are required in the latter. As a consequence, the top ITO electrode is subjected to lower stress voltages, offering stable operation for longer time. Better optoelectronic performance is foreseen in optimized ITO electrodes. Ongoing work on the ITO fabrication is being done to improve its overall performance by means of, for instance, reactive evaporation in an oxygen-rich plasma environment.

4.7. Final remarks

Ce- and Tb-doped silicon oxides and oxynitrides have been successfully fabricated in thin film configuration by means of an ECR-PECVD system equipped with in-situ RE doping capability. VASE measurements, RBS analysis and TEM characterization over different samples yielded devising the layer composition as well as the structural and morphological properties. Also, a thorough study of the luminescence properties was carried out upon UV light excitation. Finally, a preliminary optoelectronic characterization was accomplished in simple test devices to explore the suitability of these layers to function as Si-based light emitting devices. The most important closing remarks of this chapter are:

- ✓ Ce- and Tb-doped silicon oxynitrides with different layer stoichiometry were fabricated departing from a SiO_2 matrix. A gradual oxygen by nitrogen substitution was performed by controlling the income gas flow rate of precursor gases, sweeping from a RE: SiO_2 to a RE:SiO_xN_y matrix.
- ✓ Extracted optical constants (n and k) from VASE measurements yielded a different labelling of fabricated samples in two main groups: silicon oxides, with n ~ 1.5 and k ~ 0, and silicon oxynitrides, with increasing n and k values from n ~ 1.5 ($k \sim 4\times10^{-3}$) to n ~ 1.8 ($k \sim 1\times10^{-2}$).
- ✓ The evolution of the layer thickness and the optical constants was studied as a function of the annealing temperature, obtaining a diminution of all parameters (t, n and k) for higher annealing temperatures. A sudden leap of the extinction

---

[23] *In most cases, a device design is considered CMOS compatible if it fulfills the condition of being completely fabricated inside a standard CMOS facility. Nevertheless, for many authors it should also be compatible with the power supply values of a standard microelectronic chip, which are, at most, of few volts and tens of mA.*

coefficient was measured for the highest annealing temperature at 1180°C, and attributed to the formation of RE clusters.

- ✓ Strong PL emission observed by the naked eye in daylight conditions was obtained from all samples, regardless of the annealing temperature. Also, a different PL-T characteristic was obtained for RE-doped Silicon oxides and silicon oxynitrides, being the PL emission from the latter ones almost insensitive to the annealing temperature.
- ✓ A pronounced PL enhancement was measured for the highest annealing temperature in all samples, correlated with the partial formation of RE silicates at the interface with the Si substrate.
- ✓ The RE co-doping and the multilayer approach were investigated. Experimental RBS data performed over RE co-doped samples demonstrated an efficient and even RE incorporation. Similarly, the morphology of multi-layered samples was validated by TEM characterization, denoting a robust structure that becomes partially mixed only when annealing at very high temperatures (1180°C).
- ✓ The PL spectra of RE co-doped samples showed a wide colour tunability from cobalt blue to emerald green along a straight line of the CIE chromaticity diagram.
- ✓ EL test devices were patterned over three different RE-doped samples: A Tb-doped SiO_2 layer, a Ce-doped SiO_xN_y layer and a Tb-doped SiO_xN_y/SiO_2 superlattice. An in-house fabrication process was developed to deposit transparent ITO electrodes by means of a shadow mask approach in an electron beam evaporator.
- ✓ All samples presented good electrical injection, being the charge transport of silicon oxides limited by the electrode-active layer barrier height (TAT), while that of silicon oxynitrides mainly governed by bulk-limited conduction.
- ✓ Despite observing an EL spectrum in agreement with RE radiative transitions, poor device reliability was proven in single layers. Moreover, a simple inspection of the ITO surface topology confirmed a progressive degradation of the top electrode upon high voltage excitation.
- ✓ Remarkably, Tb-doped superlattices showed an outstanding optoelectronic performance compared to RE-doped single layers, with stable operation over several hours and good reproducibility. PF conduction was identified as the main charge transport mechanism. Also, a linear evolution of the EL-J characteristic was obtained, with an EL onset voltage as low as ~ 7V. Such value is significantly lower than in RE-doped single layers, of a factor of 5, and therefore is believed to be a decisive factor to explain the improved device lifetime of Tb-doped superlattices over RE-doped single layers.

4.8. List of references

[1] Rebohle, L., & Skorupa, W. (2010). *Rare-earth implanted MOS devices for silicon photonics: microstructural, electrical and optoelectronic properties* (Vol. 142). Springer Science & Business Media.

[2] Pavesi, L., & Turan, R. (Eds.). (2010). *Silicon nanocrystals: fundamentals, synthesis and applications*. John Wiley & Sons.

[3] Wilson, P. R. (2013). *Study of Luminescent Silicon-Rich Silicon Nitride and Cerium and Terbium Doped Silicon Oxide Thin Films*.

[4] Jeong, H., Lee, S., Yong Sung, G., & Shin, J. H. (2011). "Design and Fabrication of Tb-Doped Silicon Oxy-Nitride Microdisk for Biosensor Applications." *Photonics Technology Letters, IEEE*, *23*(2), 88-90.

[5] Dierre, B., Xie, R. J., Hirosaki, N., & Sekiguchi, T. (2007). "Blue emission of Ce^{3+} in lanthanide silicon oxynitride phosphors." *Journal of materials research, 22*(07), 1933-1941.

[6] Xie, R. J., & Hirosaki, N. (2007). "Silicon-based oxynitride and nitride phosphors for white LEDs—A review." *Science and Technology of Advanced Materials, 8*(7), 588-600.

[7] Kenyon, A. J., Chryssou, C. E., Pitt, C. W., Shimizu-Iwayama, T., Hole, D. E., Sharma, N., & Humphreys, C. J. (2002). "Luminescence from erbium-doped silicon nanocrystals in silica: Excitation mechanisms." *Journal of Applied Physics, 91*(1), 367-374.

[8] Kenyon, A. J. (2002). "Recent developments in rare-earth doped materials for optoelectronics." *Progress in Quantum Electronics, 26*(4), 225-284.

[9] Sun, J. M., Skorupa, W., Dekorsy, T., Helm, M., Rebohle, L., & Gebel, T. (2005). "Bright green electroluminescence from Tb^{3+} in silicon metal-oxide-semiconductor devices." *Journal of applied physics, 97*(12), 123513-123513.

[10] Dabkowski, R. P. (2012). *Installation of a New Electron Cyclotron Plasma Enhanced Chemical Vapour Deposition (ECR-PECVD) Reactor and a Preliminary Study of Thin Film Depositions.*

[11] Hale, J.,& Johs, B. (2009) "CompleteEASE™ Data Analysis Manual." Lincoln, Nebraska:J. A. Woollam Co., Inc., 2011.

[12] Malitson, I. H. (1965). "Interspecimen comparison of the refractive index of fused silica." *JOSA*, *55*(10), 1205-1208.

[13] Mayer, M. (2003, May). "Rutherford backscattering spectrometry (RBS)." In*Workshop on Nuclear Data of Science and Technology: Materials Analysis*.

[14] Mayer, M. (1997). "SIMNRA user's guide."

[15] Ziegler, J. F. (1977). *Helium: stopping powers and ranges in all elemental matter*(Vol. 4). pergamon.

[16] Podhorodecki, A., Zatryb, G., Misiewicz, J., Wojcik, J., Wilson, P. R. J., & Mascher, P. (2012). "Green light emission from terbium doped silicon rich silicon oxide films obtained by plasma enhanced chemical vapor deposition." *Nanotechnology*, *23*(47), 475707.

[17] De Graaf, D., Stelwagen, S. J., Hintzen, H. T., & de With, G. (2003). “Tb^{3+} luminescence as a tool to study clustering of lanthanide ions in oxynitride glasses.” *Journal of non-crystalline solids, 325*(1), 29-33.

[18] Sun, J. M., Prucnal, S., Skorupa, W., Dekorsy, T., Muchlich, A., Helm, M., ... & Gebel, T. (2006). “Electroluminescence properties of the Gd^{3+} ultraviolet luminescent centers in SiO$_2$ gate oxide layers.” *Journal of applied physics, 99*(10), 103102-103102.

[19] Li, J., Zalloum, O., Roschuk, T., Heng, C., Wojcik, J., & Mascher, P. (2009). “The formation of light emitting cerium silicates in cerium-doped silicon oxides.” *Applied Physics Letters, 94*(1), 011112.

[20] Pankratov, V., et al. "Mechanism for energy transfer processes between Ce^{3+} and Tb^{3+} in LaPO4: Ce, Tb nanocrystals by time-resolved luminescence spectroscopy." *physica status solidi (b) 247.9* (2010): 2252-2257.

[21] Seo, S. Y., & Shin, J. H. (2004). “Enhancement of the green, visible Tb^{3+} luminescence from Tb-doped silicon-rich silicon oxide by C co-doping.” *Applied physics letters, 84*(22), 4379-4381.

[22] Kim, B. H., Cho, C. H., Kim, T. W., Park, N. M., Sung, G. Y., & Park, S. J. (2005). “Photoluminescence of silicon quantum dots in silicon nitride grown by NH$_3$ and SiH$_4$.” *Applied Physics Letters*, *86*(9), 091908.

[23] Chonggeng, M. A., Sha Jiang, and Zhou Xianju. "Energy transfer from Ce^{3+} to Tb^{3+} and Eu^{3+} in zinc phosphate glasses." *Journal of Rare Earths 28.1* (2010): 40-42.

[24] Wan, N., Wang, T., Sun, H., Chen, G., Geng, L., Gan, X., ... & Chen, K. (2010). “Indium tin oxide thin films for silicon-based electro-luminescence devices prepared by electron beam evaporation method.” *Journal of Non-Crystalline Solids*, *356*(18), 911-916.

[25] Gulen, M., Yildirim, G., Bal, S., Varilci, A., Belenli, I., & Oz, M. (2013). “Role of annealing temperature on microstructural and electro-optical properties of ITO films produced by sputtering.” *Journal of Materials Science: Materials in Electronics*, *24*(2), 467-474.

On the photoluminescence of as-deposited Tb-doped silicon oxides and oxynitrides fabricated by ECR-PECVD

J. M. Ramírez[a], J. Wojcik[b], Y. Berencén[a], P. Mascher[b] and B.Garrido[a]

[a]Departament d'Electrònica, Universitat de Barcelona, Barcelona 08028, Spain
[b]Department of Engineering Physics and Centre for Emerging Device Technologies, McMaster University, Hamilton, Ontario L8S 4K1, Canada

ABSTRACT

In-situ doping of Tb^{3+} ions in silicon oxides and oxynitrides deposited by electron-cyclotron-resonance plasma enhanced chemical-vapour (ECR-PECVD) has been performed. Oxygen and nitrogen gas flow rates were changed to produce a gradual substitution of oxygen by nitrogen in the host matrix. Bright green luminescence from as-deposited layers is observed by the naked eye under daylight conditions. Tb-doped nitrogen-rich samples showed a considerable photoluminescence (PL) enhancement compared to Tb-doped silicon oxides. An optimum layer composition for efficient Tb^{3+} excitation under non-resonant optical pumping is obtained. The combination of a low temperature treatment with bright luminescence could be instrumental for the development of light emitting devices in other platforms with more restrictive temperature requirements.

Keywords: Electron-cyclotron-resonance plasma enhanced chemical vapour deposition, in-situ doping, terbium photoluminescence.

1. INTRODUCTION

Since the last two decades, rare-earth (RE) doped silicon-based luminescent materials have attracted significant attention due to their potential for implementation in several areas of our society [1]. For instance, they are believed to be key elements to overcome some of the current limitations encountered in the microelectronics industry. Having almost reached the physical limit in the ultra large scale integrated circuits, the aggressive and ever expanding market demand pushes toward the implementation of alternative technology platforms with superior performance while being energetically efficient and sustainable [2]. As a consequence, intense research has been done in that direction, providing competitive photonic building blocks which aim to replace most of the electronic on-chip components [3, 4]. Unfortunately, and despite the important breakthroughs accomplished by the silicon photonics community [5, 6, 7], the monolithic integration of an efficient, reliable, and electrically driven light source has not yet been achieved. Such elements would be instrumental not only for the implementation of photonic integrated circuits but also as a new asset for solid state lighting (SSL) based on silicon technology.

Nowadays, the majority of multicolour displays and light emitting diodes (LEDs) used in SSL are made of expensive III-V related compounds and therefore, they cannot be fully integrated with their electronic drivers in a CMOS line [8]. In addition, most of these light emitting devices use wavelength converting phosphor coatings in order to tune the emission from the active layer (usually blue or UV light), increasing the complexity of implementation and fabrication cost while diminishing the overall optical properties (deterioration of the colour rendition) [9]. Also, and despite being made from RE silicon-based materials such as silicon oxynitrides, current phosphor coatings present other drawbacks such as the very high temperatures needed for sintering or the impossibility of depositing uniform films with good planarity [8, 10]. Other device technologies such as organic approaches offer good efficacy and high performance, although they also present other related issues such as complex device design and packaging or low device operation lifetime [11]. Thus, RE-doped thin-film silicon light emitters offer a unique framework of possibilities to explore. In spite of being still far from commercial lighting devices in terms of luminous efficacy, they present better lumens per dollar ratio and simpler pixel cell as the wavelength converter can be avoided if an adequate RE mixing is performed in the active layer. For instance, a combination of Ce^{3+} ions (blue emission), Tb^{3+} ions (green emission) and Eu^{3+} ions (red emission) could be employed in one single device to develop monolithic white LEDs [12].

Therefore, the development of RE-doped luminescent thin films using mainstream CMOS technology with more relaxed thermal conditions is sound. In particular, silicon oxides have been largely studied in thin film configuration as they offer a good local environment for RE ions and consequently boost their optical properties. As a case in point, Er-doping in SiO_2 has been widely reported for silicon light emitting devices working at telecom wavelengths [13]. Similarly, Tb-doped SiO_2 has also been studied as a suitable active layer for the monolithic integration of green light emitting devices [14]. However, other CMOS compatible materials such as silicon nitrides and oxynitrides are not often studied in thin film configuration as potential candidates to allocate luminescent RE ions. In fact, silicon nitrides and oxynitrides present some advantages compared to silicon oxides. Among others, they have larger refractive index and a lower carrier injection barrier between the electrode and the active layer [15]. These unique conditions could lead to the implementation of high quality resonant devices operating at low voltages. Moreover, silicon nitride has proven to be an excellent platform for the realization of active devices with superior functionality [16]. Surprisingly, only few works are focussed on the luminescent properties of thin film RE-doped silicon nitride LEDs [17, 18].

Therefore, in this work we discuss the photoluminescence (PL) properties of as-deposited Tb-doped silicon oxides and oxynitrides fabricated by electron-cyclotron-resonance plasma enhanced chemical-vapour deposition (ECR-PECVD). In particular, bright green PL emission observable by the naked eye is obtained from as-deposited Tb^{3+}-doped samples. Luminescent films were successfully fabricated by in-situ Tb-doping and maintaining the same terbium and silicon content while gradually substituting oxygen by nitrogen in the matrix. The effect of the PL properties of the oxygen-nitrogen substitution was investigated. Moreover, the fact that samples presented strong PL intensity despite being heated up only during the deposition process to moderate temperatures (135 °C) opens the pathway towards its implementation in other platforms with more restrictive temperature requirements. Among other applications, they could be used as active layers in flexible photonics where the temperature of the process is often limited to 400 °C [19].

2. THE ECR-PECVD SYSTEM

Tb-doped films were deposited by means of an electron-cyclotron-resonance plasma enhanced chemical vapour deposition. This technique offers several advantages compared to the ‘conventional’ radio frequency (RF)-PECVD process often used for the development of luminescent thin films. The main difference between them relies on the fact that in RF-PECVD, the substrate is immersed in the plasma where the resonant glow discharge takes place. As a consequence, highly energetic ionized particles and other radicals may impact on the substrate and the growing film directly, causing damage and unwanted deposition of other elements. However, this situation no longer applies in an ECR-PECVD system, as the plasma is remotely generated far away from the substrate. Therefore, the substrate is only affected by low energetic ionized particles from the plasma arriving with energy values of 20-30 eV. In addition, a better control of the layer stoichiometry is achieved by remote plasma generation, as precursor gases can be introduced at different locations in the chamber (see figure 1). Nevertheless, the most interesting feature of the ECR-PECVD system used in this work is its possibility of combining a high quality CVD growth process with in-situ rare-earth doping by using a non-aggressive procedure. For that, a couple of RE-showerhead towers were designed and placed in front of the substrate at a distance that allows efficient adsorption of sublimated RE elements into the growing film. This method, sometimes referred as ‘soft layer doping’, provides excellent doping uniformity and larger RE incorporation compared to other techniques used for RE doping such as ion implantation [12]. In that case, although it is possible to obtain a flat dopant profile in ion implanted films by subsequent implantation of RE elements at different energy values, there is evident damage to the host matrix that cannot always be fully recovered with a post-implantation annealing treatment. Therefore, ECR-PECVD with RE doping capabilities offers a versatile and convenient platform to develop silicon-based thin films with superior optical properties.

A scheme of the ECR-PECVD setup is shown in figure 1. The system can be divided into two main parts: the ECR chamber and the deposition chamber. The ionized reactive species are generated in the ECR chamber by the impact of accelerated electrons in the precursor gases (plasma). Electrons responsible for the ionization of gases are driven by a microwave source (Astex HS-1000) that provides an incident power of 500 W at a frequency of 2.45 GHz. The electron cyclotron resonance is accomplished by a helical electromagnet that provides a magnetic field of 875 G. In order to prevent damage by reflection in the magnetron head and also to avoid power fluctuations during the deposition process, continuous monitoring of the reflected power was performed using a reflected power detector (Astex-CS-1000 circulator). The generated microwaves are introduced into the ECR chamber (10 cm long) through a quartz window. Precursor gas incorporation into the chamber is led by means of a dispersion ring with gas inlets evenly distributed at its perimeter. Oxygen and nitrogen precursor gases where both incorporated in a 10% diluted mixture of argon, i. e. 10% of O_2 (or N_2) in Ar, with a variable flow rate that ranges from 0 to 25 sccm depending upon the targeted layer composition. It is worth mentioning that the silicon precursor gas (SiH_4) was not incorporated in the ECR chamber directly in order to avoid deposition of silicon into the walls of the resonant chamber and the quartz window. A water cooling system was needed to address the considerable heating of the ECR chamber due to the poor axial confinement of the single magnet configuration.

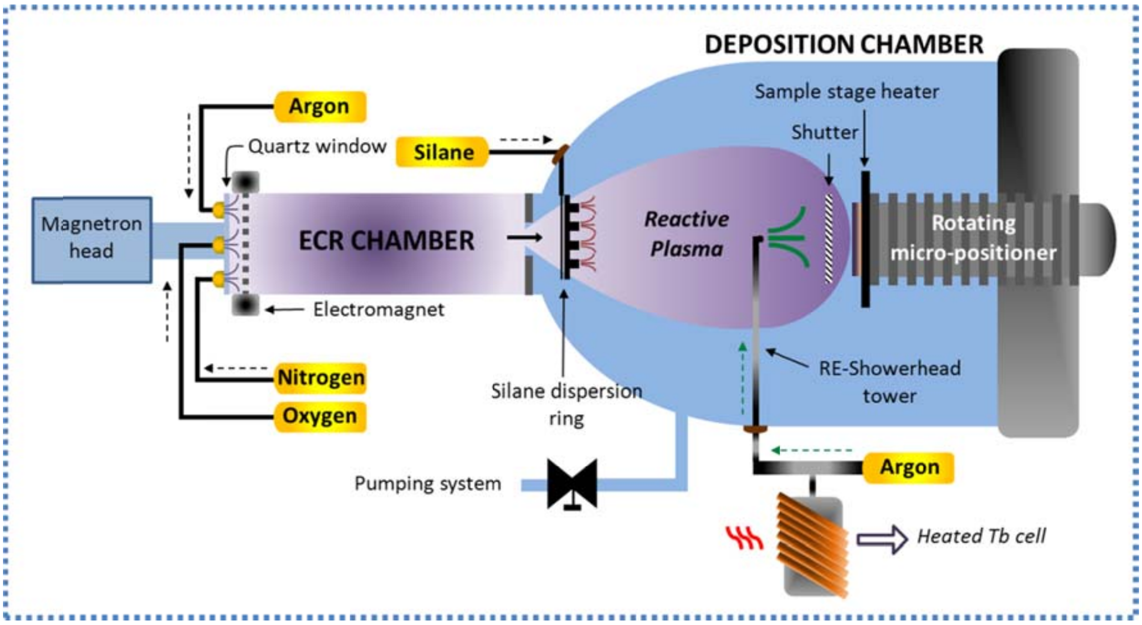

Figure 1: ECR-PECVD deposition system.

The deposition chamber includes the silane dispersion ring, a rotating sample stage heater where the sample is located and the rare-earth showerhead towers for the in-situ doping of thin films. Silicon was introduced through a 30% silane in argon flow of 2.5 sccm. This value was kept constant for the complete set of studied samples in this work. A turbo-molecular drag pump (Pfeiffer TMH 520) was used to obtain the optimum vacuum conditions for deposition, reaching base pressures of 1×10^{-9} Torr. A set of thermocouple and convection gauges are used to monitor the base pressure under low-medium vacuum values and a hot cathode ion gauge for high vacuum measurements. During deposition, however, and because the previously described gauges are gas sensitive, a capacitive manometer was used to measure realistic pressure values. The substrate is mounted onto a rotating sample stage at an angular velocity of 25 rpm and heated up to 135 °C (which corresponds to a temperature of 350 °C in the stage heater). The distance between the substrate and the silane dispersion ring is around of 10 cm. Finally, rare-earth doping is performed by means of a couple of showerhead towers allocated in front of the substrate, at a distance of 5 cm. A volatile metal organic rare-earth precursor (Tb[tmhd]$_3$ for the terbium doping) is contained in a canister that can be evenly heated by using and electrical heating jacket. After proper heating of the RE cell, the metal organic precursor sublimates in the heated canister and is transported towards the showerhead towers by an argon carrier gas with a constant flow rate of 5 sccm. The doping level is controlled by adjusting the cell temperature directly. It is worth mentioning that the transporting lines and showerhead towers are also heated in order to avoid re-solidification of the RE elements through cooling during transport towards the deposition chamber. A manually controlled shutter placed between the substrate and the showerhead towers effectively blocks the deposition process when necessary.

3. SAMPLE FABRICATION

A batch of six Tb-doped layers were fabricated, all of them with the same Tb concentration but different matrix stoichiometry. In order to study the effect of the substitution of oxygen by nitrogen in the PL properties of samples, a gradual increase of the N_2:Ar gas flow rate was defined, with a step of 5 sccm and a maximum value of 25 sccm. Similarly, the O_2:Ar gas flow was decreased to the same extent. The SiH_4:Ar gas flow was kept constant for all samples so as to maintain the same amount of silicon in all layers. The operating pressure for the entire batch of samples was around of 3.3 mTorr. Table 1 summarizes the fabrication parameters of the samples under study with the measured gas flow values and partial run pressures:

Table 1: Gas flow rates and partial gas pressures of precursor gases.

# sample	**SiH_4:Ar (sccm / mTorr)**	**O_2:Ar (sccm / mTorr)**	**N_2:Ar (sccm / mTorr)**
1	2.5 / 0.3	25 / 3	0 / ------
2	2.5 / 0.3	20 / 2.10	5 / 0.90
3	2.5 / 0.3	15 / 1.55	10 / 1.45
4	2.5 / 0.3	10 / 1.05	15 / 1.95
5	2.5 / 0.3	5 / 0.65	20 / 2.35
6	2.5 / 0.3	0 / ------	25 / 3

Tb-doping was accomplished by heating the Tb-cell to 180 °C and the rest of the circulating circuit (argon gas line and showerhead towers) to 225 °C. The argon carrier gas flow in the rare-earth lines was set to 5 sccm. Layers were grown on a low resistivity n-type Si substrate (< 0.05 Ω·cm) during 1 hour with a nominal deposition rate of 1.5 nm/minute, which results in a final layer thickness of about 90 nm. The layer composition was determined by Rutherford Backscattering Spectrometry (RBS) using a 2.0 MeV $_4He^+$ beam, an angle of incidence of 5° from normal, a scattering angle of 170°, a dose of 4 µC and using the random sample rotation mode to reduce channeling effects. Experimental measurements were simulated using the software package SIMNRA 6.04 [20]. A nearly constant Tb concentration of 3×10^{20} at/cm^3 was found in all samples (< 1% of Tb doping), and a variable oxygen concentration that ranges from 5×10^{22} at/cm^3 for an oxygen gas flow of 25 sccm (sample 1, table 1), to a value of 1.5×10^{22} at/cm^3 when the oxygen gas flow line is closed (sample 6, table 1). On the contrary, nitrogen incorporation was not evident until a N_2:Ar gas flow of 15 sccm was defined, obtaining a mean concentration of 9×10^{21} at/cm^3 (sample 4, table 1). From this point on, the nitrogen incorporation increases to a value of 1.9×10^{22} at/cm^3 (sample 5, table 1) and finally to a value of 2.8×10^{22} at/cm^3 for the highest nitrogen gas flow rate (sample 6, table 1). Concerning the silicon content, an almost constant value of 2.2×10^{22} at/cm^3 was measured in all samples.

In order to better illustrate the evolution of each sample with the reactive precursor gases, figure 2 depicts the sample composition (in percentage) as a function of the ratio between the N_2:Ar partial pressure ($P_{N2:Ar}$) and the total run pressure in the chamber (P_{total} , i.e. 3.3 mTorr). As can be observed, the oxygen percentage remains almost constant (70±3%) for the three lowest N_2:Ar gas flow rates previously defined (0, 5 , and 10 sccm), with approximately the same silicon content (~ 30±3%) and no evident nitrogen incorporation. As a consequence, from this point on samples 1, 2 and 3 will be labelled as 'silicon oxides'. On the contrary, samples 4, 5 and 6 present an interesting case of study. Despite having silicon content similar to silicon oxides (33±2%), they present a gradual oxygen-by-nitrogen substitution in the layer composition when increasing the nitrogen gas flow ratio (for flow rates of 15, 20, and 25 sccm, respectively). In fact, the oxygen percentage in sample 4 (55%) decreases to 40% in sample 5 and to 22% in sample 6, whereas the nitrogen content follows the opposite trend (12% in sample 4, 27% in sample 5 and 42% in sample 6). Therefore, samples 4, 5 and 6 will be labelled as ‘oxynitrides’ due to their evident nitrogen content.

Notice that samples get oxidized even when there is no O_2:Ar gas flow in the chamber (sample 6), in spite of the fact that good base pressure was measured before layer deposition. Such oxygen contamination was ascribed to the usage of a volatile metal organic RE precursor (Tb[tmhd]$_3$) that contains oxygen in its molecular formula ($C_{33}H_{60}O_6Tb$). Therefore, other volatile RE precursors should be used if oxygen-free silicon nitride layers are desired.

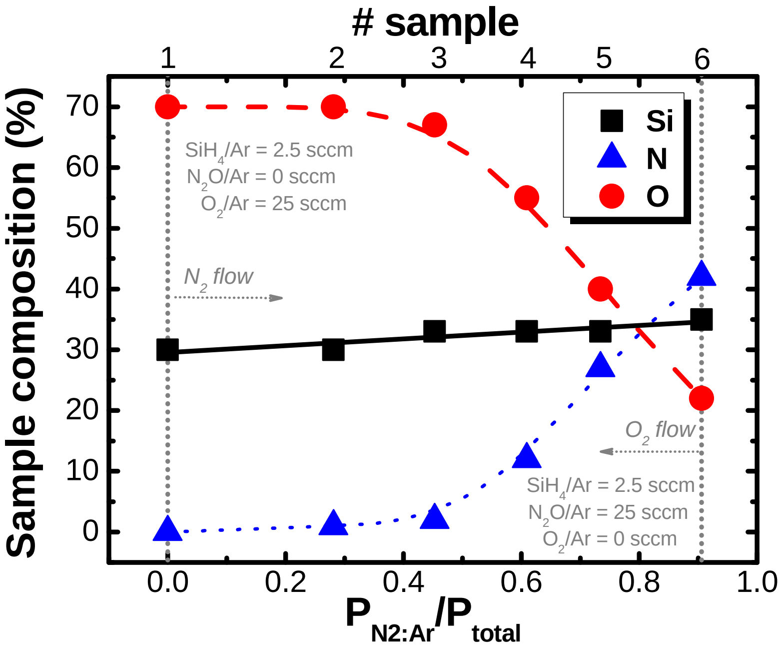

Figure 2: Sample composition (in percentage) of silicon (black squares), nitrogen (blue triangles) and oxygen (red dots) as a function of the ratio between the N_2:Ar partial gas pressure and the total run pressure inside the chamber (P_{total}). Vertical short dotted grey lines mark the zero point from which the gas flow rate is gradually increased (N_2:Ar on the left side and O_2:Ar on the right). Straight, dotted and dashed lines are guides to the eye.

4. PHOTOLUMINESCENCE

After deposition, the photoluminescence of samples was investigated. It is worth mentioning that samples did not undergo any post-deposition annealing treatment previous to PL characterization. Visible PL was obtained after excitation of samples with a 325 nm He-Cd laser excitation source. The PL was collected using a lens coupled to a fibre optic cable directed onto a visible charge-coupled device (CCD) spectrometer (Ocean Optics S2000). Bright green emission easily observable by the naked eye under daylight conditions was obtained from all samples suggesting that a large number of terbium ions are oxidized in the Tb^{3+} state [12]. A typical PL spectrum from excited samples is shown in figure 3(a). As seen, only the excited transitions corresponding to the $^5D_4$ state are visible, with a maximum PL intensity around of 545 nm, where the doublet is positioned. In addition, a broad PL emission band in the UV region is detected (400 nm-450 nm), attributed to radiative transitions of dangling bonds located within the band gap of the host matrix [21]. The comparison of the spectral line shape and relative peak intensity between samples did not show any remarkable change, indicating that the inclusion of nitrogen in the matrix does not significantly modify the local environment of Tb^{3+} ions. Nevertheless, the PL intensity strongly varies from sample to sample. In particular, silicon oxides provide noticeably lower PL emission than oxynitrides (almost one order of magnitude). Figure 3(b) shows this situation. Similarly to figure 2, the PL maximum intensity is plotted as a function of the ratio between the N_2:Ar partial pressure ($P_{N2:Ar}$) and the total operating pressure in the chamber (P_{total}). Interestingly, for a single Tb concentration (3×10^{15}

at/cm^2), the substitution of oxygen by nitrogen in the host matrix causes a remarkable PL enhancement of Tb^{3+} ions. Moreover, assuming that a poor resonant excitation of Tb^{3+} ions under 325 nm laser excitation takes place [14], the correlation of the PL enhancement with the high nitrogen content could be attributed to a substantial improvement of the non-resonant excitation of luminescent centers from the host matrix (energy transfer process). In addition, if we now focus solely on the oxynitrides, there seems to be an optimum layer composition for which the Tb^{3+} emission is maximized (see figure 3(b)) that corresponds to 33% silicon, 40% oxygen and 27% nitrogen. Thus, this layer composition provides bright green PL emission of Tb^{3+} ions without the need for additional annealing treatments.

Nevertheless, it is important to remark that these optimum element percentages were taken from non-annealed Tb-doped oxynitrides and therefore we cannot guarantee that there might not be deviations in terms of optimum layer composition when an appropriate annealing treatment is performed. Forthcoming investigations on these very same samples with different annealing treatments will shed light on this point.

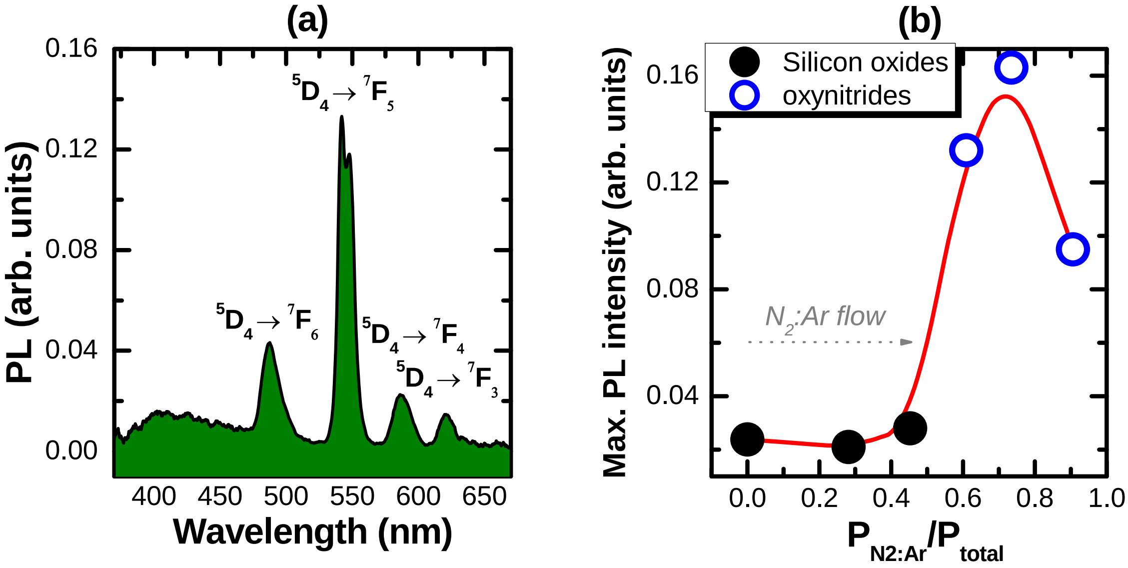

Figure 3: (a) Typical PL spectrum of a non-annealed Tb-doped oxide under laser excitation at 325 nm. (b) Evolution of the maximum PL intensity (taken at 545 nm) as a function of the ratio between the partial N_2:Ar gas pressure and the total run pressure in the chamber.

5. CONCLUSIONS

The PL properties of thin film Tb-doped silicon oxides and oxynitrides deposited by ECR-PECVD were investigated. The possibility of generating the reactive plasma in a remote location from the substrate and the in-situ rare-earth doping capability of this particular system allowed us to obtain high quality films with excellent Tb-doping uniformity. Moreover, bright green emission of Tb^{3+} ions easily observable by the naked eye was obtained without the need for post-deposition annealing treatment. Also, PL enhancement was achieved when replacing oxygen by nitrogen in the host matrix, yielding an optimum layer composition for efficient excitation of Tb^{3+} ions under optical pumping in as-deposited silicon oxynitrides.

ACKNOWLEDGEMENTS

The authors wish to thank O. Taggart for the sample fabrication and Dr. P. Wilson for fruitful discussions. This work was financially supported by the Spanish Ministry of Science and Innovation (Project No. TEC2012-38540-C02-01). J. M. R. acknowledges the financial support of Secretariat for Universities and Research of Generalitat de Catalunya through the program FI-DGR 2013 and the staff of the Centre for Emerging Device Technologies (CEDT) at McMaster for their generous support.

REFERENCES

[1] Kitai, A. [Luminescent Materials and Applications], Wiley, Chichester, U.K, (2008).

[2] Vivien, L. and Pavesi, L., [Handbook of Silicon Photonics], Taylor & Francis Group, LLC., Boca Raton, USA (2013).

[3] Jalali, B, and Fathpour, S., "Silicon photonics," Journal of Lightwave Technology, 24, 4600–4615, (2006).

[4] Liu, A., Jones, R., Liao, L., Samara-Rubio, D., Rubin, D., Cohen, O., Nicolaescu, R., and Paniccia, M., "A high-speed silicon optical modulator based on a metaloxide-semiconductor capacitor," Nature, 427, 615–618, (2004).

[5] Ramírez, J. M., Ferrarese-Lupi, F., Berencén, Y., Anopchenko, A., Colonna, J. P., Jambois, O., Fedeli, J. M., Pavesi, L., Prtljaga, N., Rivallin, P., Tengattini, A., Navarro-Urrios, D., and Garrido, B., "Er-doped light emitting slot waveguides monolithically integrated in a silicon photonic chip," Nanotechnology, 24, 115202, (2013).

[6] Thomson, D. J., Gardes, F. Y., Fedeli, J. M., Zlatanovic, S., Hu, Y. F., Kuo, B. P. P., Myslivets, E., Alic, N., Radic, S., Mashanovich, G. Z., and Reed, G. T., "50-Gb/s Silicon Optical Modulator," Opt. Express, 24(4), 234-236, (2012).

[7] Rong, H., Jones, R., Liu, A., Cohen, O., Hak, D., Fang, A., and Paniccia, M., "A continuous-wave Raman Silicon laser," Nature 433, 725-728, (2005).

[8] Ponce, F. A., Bour, D. P., "Nitride-based semiconductors for blue and green light-emitting devices," Nature, 386(6623), 351-359, (1997).

[9] George, N. C., Denault, K. A., Seshadri, R., "Phosphors for Solid-State White Lighting," Annual Review of Materials Research, 43, 481-501, (2013).

[10] Xie, R. J., Hirosaki, N., "Silicon-based oxynitride and nitride phosphors for white LEDs-A review," Sci. Technol. Adv. Mater. 8, 588-600 (2007).

[11] D'Andrade B. W., Forrest, S. R., "White Organic Light-Emitting Devices for Solid –State Lighting," Adv. Mater., 16(18), 1585-1595, (2004).

[12] Rebohle, L., Skorupa, W., [Rare-Earth Implanted MOS devices for Silicon Photonics], Springer-Verlag Berlin Heidelberg, (2010).

[13] Miritello, M., Lo Salvio, R., Iacona, F., Franzo, G., Irrera, A., Piro, A. M., Bongiorno, C., Priolo, F., "Efficient luminescence and energy transfer in erbium silicate thin films," Adv. Mater., 19(12), 1582-1588, (2007).

[14] Sun, J. M., Skorupa, W., Dekorsy, T., Helm, M., Rebohle, L., Gebel, T., "Bright green electroluminescence from Tb^{3+} in silicon metal-oxide-semiconductor devices," J. Appl. Phys. 97, 123513 (2005).

[15] Makarova, M., Sih, V., Warga, J., Li, R., Dal Negro, L., Vuckovic, J., "Enhanced light emission in photonic crystal nanocavities with Erbium-doped silicon nanocrystals," Appl. Phys. Lett. 92, 161107 (2008).

[16] Moss, D. J., Morandotti, R., Gaeta, A. L., and Lipson, M., "New CMOS-compatible platforms based on silicon nitride and Hydex for nonlinear optics," Nature Phot. 7, 597-607 (2013).

[17] Yerci, S., Li, R., and Dal Negro, "Electroluminescence from Er-doped Si-rich silicon nitride light emitting diodes," L., Appl. Phys. Lett. 97, 081109 (2010).

[18] Berencén, Y., Wutzler, R., Rebohle, L., Hiller, D., Ramírez, J. M., Rodríguez, J. A., Skorupa, W., Garrido, B., "Intense green-yellow electroluminescence from Tb^+-implanted silicon-rich silicon nitride/oxide light emitting devices," Appl. Phys. Lett. 103, 111102, (2013).

[19] McAlpine, M. C., Friedman, R. S., Jin, S., Lin, K., Wang, W. U., Lieber, C. M., "High-Performance Nanowire Electronics and Photonics on Glass and Plastic Substrates," Nano Lett. 3(11), 1531-1535, (2003).

[20] Rauhala, E., Barradas, N. P., Fazinic, S., Mayer, M., Szilágyi, E., Thompson, M., "Status of ion beam data analysis and simulation software" Nucl. Instr. And Meth. In Phys. Res. B, vol 244, pp. 436-456, Nov 2005.

[21] Bommali, R. K., Singh, S. P., Rai, S., Mishra, P., Sekhar, B. R., Prakash, G. V., Srivastava, P., "Excitation dependent photoluminescence study of Si-rich a-SiNx:H thin films," J. Appl. Phys., 112, 123518, (2012).

IOP Publishing Nanotechnology

Nanotechnology **26** (2015) 085203 (7pp) doi:10.1088/0957-4484/26/8/085203

Amorphous sub-nanometre Tb-doped SiO_xN_y/SiO_2 superlattices for optoelectronics

Joan Manel Ramírez[1], Jacek Wojcik[2], Yonder Berencén[1], Alícia Ruiz-Caridad[1], Sònia Estradé[1], Francesca Peiró[1], Peter Mascher[2] and Blas Garrido[1]

[1] MIND-IN2UB, Departament d'Electrònica, Universitat de Barcelona, Martí i Franquès 1, E-08028 Barcelona, Spain
[2] Department of Engineering Physics and Centre for Emerging Device Technologies, McMaster University,1280 Main St. W, Hamilton, Ontario L8S4L7, Canada

E-mail: jmramirez@el.ub.edu

Received 21 November 2014, revised 20 January 2015
Accepted for publication 21 January 2015
Published 6 February 2015

Abstract

Amorphous sub-nanometre Tb-doped SiO_xN_y/SiO_2 superlattices were fabricated by means of alternating deposition of 0.7 nm thick Tb-doped SiO_xN_y layers and of 0.9 nm thick SiO_2 barrier layers in an electron-cyclotron-resonance plasma enhanced chemical vapour deposition system with *in situ* Tb-doping capability. High resolution transmission electron microscopy images showed a well-preserved superlattice morphology after annealing at a high temperature of 1000 °C. In addition, transparent indium tin oxide (ITO) electrodes were deposited by electron beam evaporation using a shadow mask approach to allow for the optoelectronic characterization of superlattices. Tb^{3+} luminescent spectral features were obtained using three different excitation sources: UV laser excitation (photoluminescence (PL)), under a bias voltage (electroluminescence (EL)) and under a highly energetic electron beam (cathodoluminescence (CL)). All techniques displayed Tb^{3+} inner transitions belonging to $^5D_4$ levels except for the CL spectrum, in which $^5D_3$ transition levels were also observed. Two competing mechanisms were proposed to explain the spectral differences observed between PL (or EL) and CL excitation: the population rate of the $^5D_3$ state and the non-radiative relaxation rate of the $^5D_3$–$^5D_4$ transition due to a resonant OH-mode. Moreover, the large number of interfaces (trapping sites) that electrons have to get through was identified as the main reason for observing a bulk-limited charge transport mechanism governed by Poole–Frenkel conduction in the *J*–*V* characteristic. Finally, a linear EL–*J* dependence was measured, with independent spectral shape and an EL onset voltage as low as 6.7 V. These amorphous sub-nanometre superlattices are meant to provide low-cost solutions in different areas including sensing, photovoltaics or photonics.

Keywords: silicon-based light sources, amorphous superlattice, charge transport, Tb luminescence

(Some figures may appear in colour only in the online journal)

1. Introduction

Integrated optoelectronics and photonics are expected to provide high performance and environmentally sustainable high-tech solutions to the current limitations of the Si microelectronics industry. Taking advantage of the mainstream microelectronics CMOS technology, researchers are pushing towards the implementation of new photonic building blocks to overcome contemporary technological issues such as the interconnect bottleneck or the need for higher transfer data rates in telecom. Outstanding performance of photonic systems depends on the more than moore integration approach of optical, optoelectronic, photovoltaic and sensing functions in complex multi-functional lab-on-a-chip circuits [1]. Remarkable progress has been made in that direction, providing a route map towards advanced Si-based photonic platforms with promising features in all those mentioned arenas [2–5]. Key fundamental active building blocks of these Si-based photonic platforms are efficient light emitters, light detectors and light sensors. A multipurpose device basic building block suitable for large area, printed or transparent optoelectronics is the amorphous superlattice which is providing refractive index contrast between the sub-layers, electron transport in miniband states, quantum confinement, and can be engineered for light emission and/or detection. For example, making efficient light emitters out of silicon is a challenging milestone that has triggered the attention of the silicon photonics community since many years ago [6]. Several strategies have been adopted to further boost Si emission. Among others, single nano-emitters such as silicon nanocrystals (Si-ncs) or rare-earth (RE) ions have been widely used [7, 8].

RE-doped Si-based light emitters are particularly interesting when embedded in wide band gap materials such as SiO_2 because they provide intense narrow spectral emission while avoiding two-photon absorption or energy back transfer [9]. Er-doped oxides and sub-oxides are probably the most studied materials for this purpose, as they show intense light emission at 1.55 μm which make them suitable for on-chip telecom applications [8]. On the other hand, terbium shows the most promising features in the visible part of the spectrum. With a narrow greenish spectrum and an external quantum efficiency as high as 16%, Tb-doped silicon-based light emitters are bound to become valuable assets for several low-cost applications such as high resolution microdisplays or lab-on-a-chip biosensing, among others [10, 11].

Still, RE-doped oxides show several issues not yet resolved such as the trade-off between efficient carrier injection and device reliability or the degradation of light emission yield due to RE clustering during the annealing treatment [8, 12]. Therefore, it is interesting to inspect alternative approaches for RE ions embedded in silicon oxides to yield the optimum luminescence performance. Taking advantage of the good luminescence properties displayed by Tb-doped silicon nitrides [11, 13], a suitable strategy is to incorporate nitrogen in the host silicon oxide to enhance Tb^{3+} luminescence as well as to diminish the band gap for electrical injection. In addition, since RE diffusion is slower in silicon nitrides compared to silicon oxides, less Tb clustering is expected in SiO_xN_y layers [1]. Moreover, a superlattice approach in which SiO_2 barrier layers are alternated with Tb-doped SiO_xN_y layers can be engineered to further block Tb inter-diffusion. A similar approach has already been reported for SiO_x and SiN_x matrices in order to provide a well-ordered Si-nc array and tight control of the Si-nc size, as well as to reduce the electroluminescence (EL) onset voltage [14–16]. For the present study however, and despite of using individual Tb^{3+} ions instead of Si-ncs as luminescent centres, good control of Tb placement inside the matrix is also desired to avoid highly localized Tb concentrations that might lead to undesired Tb clustering. Furthermore, homogeneous distribution of Tb^{3+} ions in the host matrix favours the electrical-to-optical conversion because one maximizes Tb emission via multiple Tb excitation by a single injected electron. We strongly believe that demonstrating sub-nanometre control over the superlattice period allows for placing the doping atoms in its more favourable environment for excitation of luminescence and opens new routes to the engineering materials with targeted optical and electrical properties.

Therefore, in this work we present an amorphous sub-nanometre Tb-doped SiO_xN_y/SiO_2 superlattice (Tb–SiO_xN_y/SiO_2 a-SL) fabricated by electron-cyclotron-resonance plasma enhanced chemical vapour deposition (ECR-PECVD). The superlattice is composed of alternating 0.7 nm thick Tb-doped SiO_xN_y layers and SiO_2 barrier layers with a mean thickness of 0.9 nm. The thinness of SiO_2 layers provides an enhanced barrier transparency that easies the carrier injection at low onset voltage into the Tb-doped regions of the superlattice. The deposition of transparent indium tin oxide (ITO) electrodes by a shadow mask approach allowed us to perform optoelectronic characterization of the amorphous sub-nanometre Tb-doped SiO_xN_y/SiO_2 superlattice. Characteristic sharp spectral features of Tb^{3+} luminescence are identified under UV laser excitation as well as under electrical injection. The suitability to fabricate amorphous sub-nanometre structures by ECR-PECVD with good optoelectronic and morphological properties is validated. Among other low-cost applications, our Tb–SiO_xN_y/SiO_2 a-SL might be of importance for the development of photonic integrated circuits in which compact and high performance Si-based light emitting devices fully compatible with the CMOS technology are required.

2. Materials and methods

Tb–SiO_xN_y/SiO_2 a-SLs were grown on ⟨100⟩ highly N-type double side polished Si substrates by ECR-PECVD. Diluted SiH_4 (30% in Ar), O_2 (10% in Ar) and N_2 (10% in Ar) precursor gases were used to fabricate SiO_xN_y layers. A gas flow rate of 2.5 sccm was fixed for SiH_4/Ar, 5 sccm for O_2/Ar and 25 sccm for N_2/Ar, resulting in an average deposition rate of 0.2 Å s^{-1} and a run pressure of 3×10^{-3} Torr. Microwave power was set at 500 W. *In situ* Tb doping of SiO_xN_y layers was performed by heating a diffusion cell that contains a β-diketonate organic compound, tris (2,2,6,6-tetramethyl-3,5-heptanedionato)-Tb(III) (Tb(tmhd)3). A temperature of 215 °C was established to sublimate the organic compound. An argon carrier gas flow of 5 sccm was used to transport sublimated material towards the substrate. Pipelines and shower head towers were also heated to 225 °C to avoid Tb deposition in the distribution line. A nominal thickness of 0.7 nm was targeted for each Tb-doped SiO_xN_y layer. With regards to the SiO_2 barrier layers, only SiH_4/Ar (2.5 sccm) and O_2/Ar (25 sccm) lines were opened. A nominal thickness of 0.9 nm was defined for the SiO_2 barrier layer. It is worth

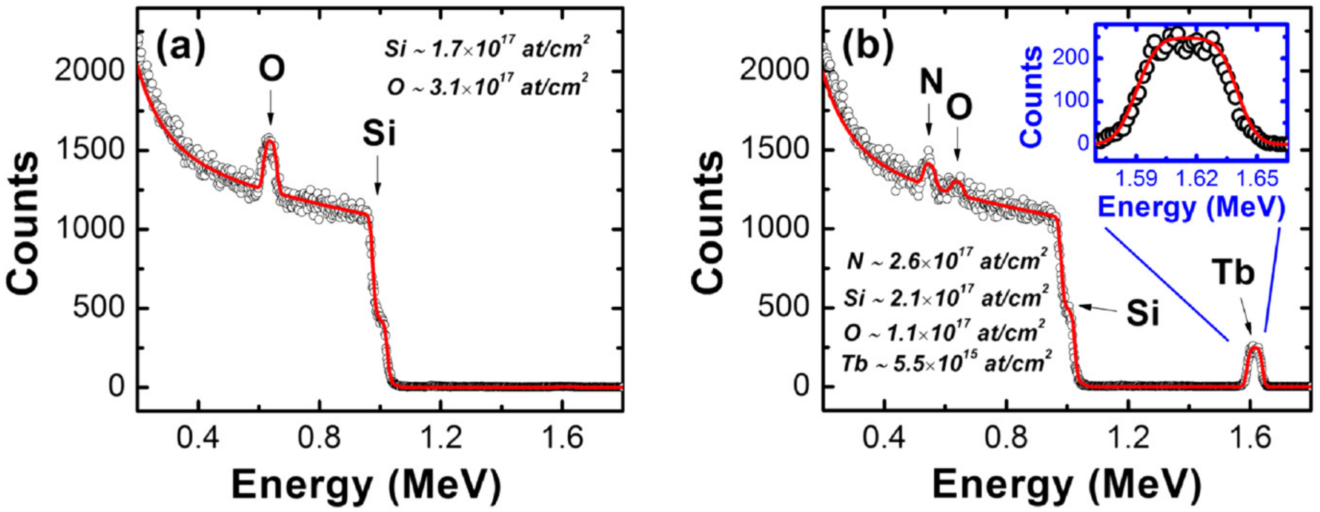

Figure 1. Experimental RBS data (hollow circles) with the simulated curve (red line) for the SiO_2 single layer (a) and the Tb-doped SiO_xN_y single layer (b). Inset shows a zoomed-in region of the RBS Tb peak.

noting that the Tb heating cell, distribution lines and Ar carrier gas lines were closed during this process to avoid undesired Tb incorporation in SiO_2 barrier layers. The final superlattice stack is composed of 10 Tb-doped SiO_xN_y layers with 9 alternating SiO_2 barrier layers, corresponding to a total thickness of 15 nm. The substrate was heated to a temperature of 120 °C, and rotated at 20 rpm to guarantee large area uniformity of the deposited layers (within a circular diameter of 4 inches). After deposition, an annealing treatment at 1000 °C for 1 h in an N_2 environment was performed to activate Tb^{3+} ions and to passivate the superlattice.

Transparent conductive electrodes were deposited on Tb–SiO_xN_y/SiO_2 a-SLs by Electron Beam Physical Vapour Deposition (EB-PVD) of commercial ITO pellets (90% In_2O_3, 10% SnO_2). A shadow mask approach was used to pattern the ITO electrodes. For that, precise perforation of small holes with radii of 100 μm was performed onto a 1 μm thick nickel layer by means of laser ablation. Then, the nickel mask was attached on the sample and mechanically fixed to the evaporation stage. The substrate stage was rotated at 10 rpm and heated to 100 °C. A base pressure of 8×10^{-7} Torr was obtained prior to deposition. ITO was deposited at a rate of 1 Å s^{-1}, with a final thickness of 150 nm and a deposition pressure of 5×10^{-6} Torr. No additional oxygen gas flow line was used. A post-deposition annealing treatment at 700 °C for 1 h in N_2 ambient was performed to improve electrode transparency. An average ITO transmittance of 90% in a range from 400 nm to 900 nm and a resistivity of about $7 \times 10^{-3}\ \Omega \cdot$cm were measured. Finally, a 200 nm thick aluminium back contact was deposited at a rate of 3 Å s^{-1} with no intentional substrate heating.

Rutherford backscattering spectrometry (RBS) measurements were performed in the Tandetron Accelerator Laboratory at Western University in London, ON (Canada), using 1.8 MeV $^4He^+$ ions in a Cornell geometry with a dose of 4 μC. Samples were oriented towards the beam at an angle of 5° to minimize substrate channelling. The superlattice cross-section was investigated by high-resolution transmission electron microscopy (HRTEM) using a JEOL 2010F TEM operating at 200 KeV. Samples were prepared by mechanical polishing and Ar^+ ion milling. Photoluminescence (PL) properties of samples were analysed using a 325 nm HeCd laser excitation source. The PL was collected with a lens coupled to a fibre-optic cable connected to a charge-coupled device spectrometer (Ocean Optics S2000). Cathodoluminescence (CL) experiments were performed on a FE–scanning electron microscopy (SEM) Jeol JSM-7100F equipped with a high resolution spectrometer (Gatan-MonoCL4) using an electron beam of 20 KeV and a maximum current of 36 nA. CL spectra were collected in monochromator mode with wavelengths ranging from 300 nm to 900 nm and an objective working distance of 1.2 cm. A probe station (Cascade Microtech Summit 110) coupled to a grating spectrometer (Acton 2300i) and a cryogenically cooled charge coupled device (PI spec-10-100B/LN) was used to obtain the *J–V* characteristic and the EL spectra of devices. A near field Mitutoyo objective was placed on top of the ITO electrodes to collect EL signal. Bias polarization was applied by means of semiconductor device analyzer (Agilent B1500A) connected to the probe station. All electro-optical experiments were carried out at room temperature.

3. Results and discussion

In order to obtain an accurate layer composition of each deposited sub-layer in the superlattice structure, two 50 nm thick single control layers (a SiO_2 and a Tb-doped SiO_xN_y layer) were first deposited under the same conditions as the layers composing the superlattice stack and measured by means of RBS. Notice that direct measurement of the RBS signal on the amorphous Tb-doped superlattice stack was avoided due to the expected layer mixing during sample decapping while obtaining the RBS data. Such layer mixing may induce an erroneous interpretation of layer components when performing the RBS data analysis. Experimental RBS

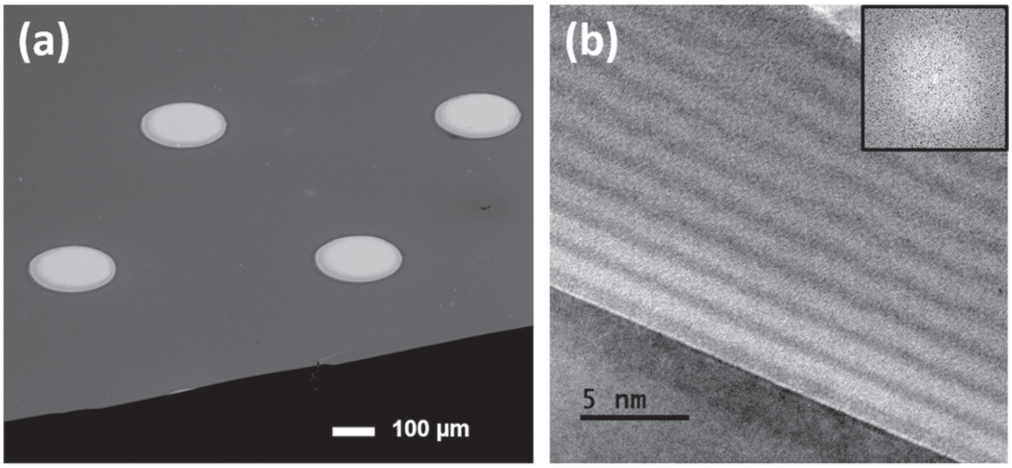

Figure 2. (a) Tilted SEM image of a field of ITO electrodes deposited using the shadow mask approach. (b) HRTEM image of the amorphous sub-nanometre Tb-doped superlattice cross-section and corresponding FFT (inset).

data of the SiO_2 layer (figure 1(a)) and the Tb-doped SiO_xN_ylayer (figure 1(b)) were fitted using the SIMNRA simulation data software [17]. This modelling of scattered elements allows determining the atomic concentration (excluding hydrogen) as a function of depth. An atomic concentration of 1.7×10^{17} at. cm^{-2} (Si) and 3.1×10^{17} at. cm^{-2} (O) was obtained for the SiO_2 layer, which corresponds to a concentration of 35% of silicon in the layer. Although this number is slightly higher than the one obtained from a stoichiometric SiO_2 layer (33.3% of Si), we do not expect this small Si excess of 1.7% to be critical to the morphology of the superlattice stack. Similarly, the RBS data from the Tb-doped SiO_xN_y layer displayed a Si content of 2.1×10^{17} at. cm^{-2} (~36% of the total atomic concentration) as well as oxygen and nitrogen peaks with atomic concentrations of 1.1×10^{17} at. cm^{-2} (~19%) and 2.6×10^{17} at. cm^{-2} (~44%), respectively. Moreover, an additional peak located at higher scattering energies (~1.6 MeV) denotes the presence of Tb in the layer. Interestingly, the Tb peak shows a flat plateau for energy values from 1.6 MeV to 1.63 MeV (see inset of figure 1(b)), denoting a uniform Tb concentration distribution throughout the SiO_xN_y layer. An atomic concentration of 5.5×10^{15} at. cm^{-2} of Tb was obtained, which corresponds to a value of ~1% of Tb doping in the SiO_xN_y layer.

Figure 2(a) shows a tilted SEM image of the field of ITO electrodes deposited on the Tb-doped superlattice with radii of 100 μm. The smooth contours and the good reproducibility displayed among electrodes validate the shadow mask approach as an efficient tool to fabricate electroluminescent test devices. HRTEM imaging was also performed on the Tb–SiO_xN_y/SiO_2 a-SL to determine its morphology and microstructure. Results are presented in figure 2(b), showing the Tb-doped superlattice cross-section with abrupt interfaces and no apparent waviness. Noticeably, the superlattice morphology is well preserved even after two different annealing treatments (first at 1000 °C and then at 700 °C), denoting the robustness of the process. The measured layer thickness is 0.70 ± 0.05 nm for the Tb-doped SiO_xN_y layer and 0.90 ± 0.05 nm for the SiO_2 barrier layer, in good agreement with the nominally defined layer thickness for each layer. Interestingly, no Tb clustering was observed in the superlattice. The absence of Tb agglomeration in the superlattice was rather unexpected since a previous work with lower Tb doping (0.1%) and a similar host matrix reported large Tb clustering at the layer interface [18]. In that work, Tb clustering was observed in silicon-rich oxide (SiO_x, being $x < 2$) layers with different layer stoichiometry after annealing at 1200 °C. Also, efficient reduction of Tb agglomeration was observed when increasing the number of Si-ncs. In our case, however, in spite of using lower annealing temperature, the absence of Tb clustering in the superlattice cannot be attributed to a Si-nc related effect since crystalline parts were not observed in the superlattice stack. To further corroborate this fact, a fast fourier transform (FFT) from the HRTEM image in figure 2(b) was obtained, showing no crystalline contribution (see inset of figure 2(b)). Therefore, the absence of Tb clustering should be attributed either to a different layer composition (a-SiO_xN_y instead of a-SiO_x) or due to different layer morphology (i.e. a superlattice instead of a single layer). An additional HRTEM study on Tb-doped SiO_xN_y and Tb-doped SiO_2 single layers with same fabrication parameters allowed us to discard the layer morphology, since small Tb clusters were only observed in the Tb-doped SiO_2 but not in the SiO_xN_y single layer. This argument is supported by previous reports on SiN_x thin films with similar Tb doping (1.4%), in which no presence of Tb clustering was detected [11, 19]. This fact is of major importance from the optical viewpoint since RE clustering is known to effectively quench the ion luminescence as a consequence of a different oxidation state [12]. Besides, and in spite of losing their luminescence properties, RE clusters still preserve their absorption properties and, therefore, negatively impact the excitation processes and their efficiencies [20].

Figure 3(a) illustrates the luminescence spectrum of the Tb–SiO_xN_y/SiO_2 a-SL under different excitation sources. The PL spectrum (bottom black line), CL spectrum (middle red line) and EL spectrum (upper blue line) are displayed together

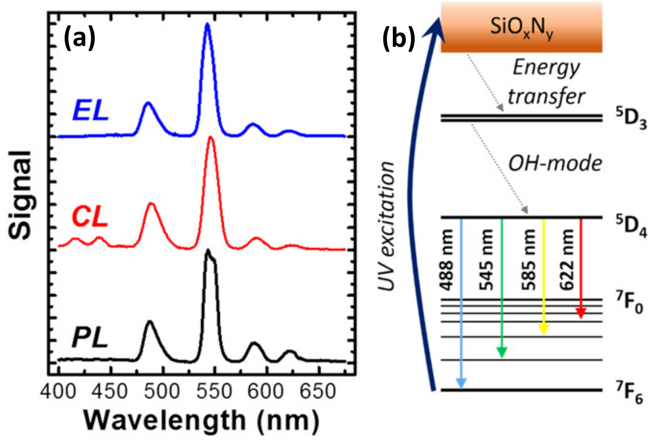

Figure 3. (a) Luminescence spectra of the Tb–SiO$_x$N$_y$/SiO$_2$ a-SL obtained under different excitation sources: UV laser excitation (bottom black line, PL spectrum), electron beam excitation (middle red line, CL spectrum), and finally an injected current density of 1.3×10^{-3} A cm^{-2} (upper blue line, EL spectrum). (b) PL excitation mechanism of Tb^{3+} energy levels with the non-radiative energy migration phenomena displayed.

for comparison. All spectra show common features, with typical Tb^{3+} related peaks that correspond to the deep-lying f state transitions, ^{5}D$_4$–^{7}F$_6$ (located at 488 nm), ^{5}D$_4$–^{7}F$_5$ (around of 545 nm), ^{5}D$_4$–^{7}F$_4$ (at 585 nm) and ^{5}D$_4$–^{7}F$_3$ (at 622 nm), as depicted in figure 3(b). Broad spectral peaks are observed in all cases, denoting a non-uniform local environment for the Tb^{3+} ions [21]. In addition, the differences in resolution among the different collection systems used yielded the observation of the Stark peak splitting of the ^{5}D$_4$–^{7}F$_5$ transition in the PL spectrum uniquely (see the PL peak at 550 nm in figure 3), although it is also expected in the emission band at 550 nm of the EL and CL spectra [22]. It is worth remarking that the CL spectrum shows inner Tb levels belonging to ^{5}D$_3$–^{7}F$_j$ transitions that are not observed in PL or EL measurements (^{5}D$_3$–^{7}F$_5$ transition emitting at 410 nm and ^{5}D$_3$–^{7}F$_4$ transition emitting at 430 nm, respectively). Such difference is probably due to a combination of two competing mechanisms: the population rate of the ^{5}D$_3$ level and the non-radiative relaxation rate of the ^{5}D$_3$–^{5}D$_4$ transition due to a resonant OH- mode [23]. Under PL and EL excitation, in spite of the fact that some Tb^{3+} ions can be excited up to the ^{5}D$_3$ transition, the probability of emission of this level becomes strongly quenched by the presence of a non-radiative relaxation due to a resonant OH-mode (see figure 3(b)). As a consequence, radiative emission from ^{5}D$_3$–^{7}F$_j$ transitions will only be observed if the number of Tb^{3+} ions located in the ^{5}D$_3$ level compensates the non-radiative relaxation of OH-modes. This condition would be fulfilled under a highly energetic electron beam, where an excitation energy of 20 KeV is provided to incident electrons (CL measurements). Under this condition, much higher lying Tb^{3+} states can be populated, leading to a higher population of the ^{5}D$_3$ state probably due to the de-excitation cascade of upper levels. In that case, the non-radiative relaxation phenomena would not be able to supress the emission from ^{5}D$_3$–^{7}F$_j$ transitions completely.

Concerning the excitation mechanisms that lead to the emission of Tb^{3+} ions, we shall differentiate between photon excitation (PL spectrum in figure 3(a)) and electron excitation (EL and CL spectra in figure 3(a)). Whereas direct impact of hot electrons is expected to mainly govern the Tb^{3+} excitation under electrical pumping [8, 11], the excitation of Tb^{3+} ions under optical pumping is believed to be mediated by an energy transfer process from the host matrix. The main reason supporting this argument lies on the fact that no Tb^{3+} resonant levels are found at the pumping energy at which the sample is irradiated (3.81 eV). As a consequence, an energy transfer process is likely to dominate the PL emission of the Tb–SiO$_x$N$_y$ a-SL. In fact, Jeong, *et al* already suggested that Tb^{3+} excitation in silicon oxynitride host matrices was mainly dominated by efficient carrier-mediated excitation of Tb^{3+}-related states [24].

Another interesting feature that arises from the direct observation of measured spectra in figure 3(a) is the absence of the broad base emission that is commonly observed either as a consequence of a radiative recombination in the Si-ncs or due to a band–tail radiative recombination between localized states associated with Si–N bonds [18, 25]. For the former one, the absence of Si-nc emission is further supported by HRTEM images in which no presence of Si-ncs was observed in the superlattice stack (see figure 2(b)). As for the absence of band–tail intra-band radiative recombination, we can speculate on the fact that such emission may actually occur in our superlattice, although in that case it is presumed to become completely screened by a much brighter Tb^{3+} emission and therefore it is not relevant from the luminescent viewpoint.

The electro-optical properties of electroluminescent test devices are disclosed in figure 4. Devices were biased applying a negative voltage on the ITO electrodes. Such configuration allows efficient electron flow from the ITO electrode towards the Al back contact. Furthermore, using a highly N-type doped Si substrate minimizes hole injection and transport from the Al back contact which is known to be one of the major causes of the early device breakdown [8]. The *J–V* characteristic of the amorphous Tb-doped superlattice was obtained using a double ramp sweep from 0 V to 10 V (close to the device breakdown voltage), with a voltage step of 0.1 V s^{-1}. Figure 4(a) shows the experimental *J–V* curve along with the EL onset of devices (filled dots) and a modelling of the ideal Poole–Frenkel (P–F) transport model superimposed for comparison [26]. As can be observed, good agreement with the experimental data is obtained from 2.5 V on, suggesting a thermally activated electron transport between intra-band localized states enhanced by the electric field. Hence, a bulk-limited mechanism mainly governs the charge transport in the Tb–SiO$_x$N$_y$/SiO$_2$ a-SL. Although this fact may be in direct contradiction to the previously suggested direct impact excitation of Tb^{3+} ions by hot electrons, we shall remark that the dominance of bulk-limited conduction does not exclude the existence of a small but not negligible hot electron percentage able to excite Tb^{3+} ions [27].

At this point, we shall mention the similarity of this result with previous work in our group, in which Er-doped silicon-

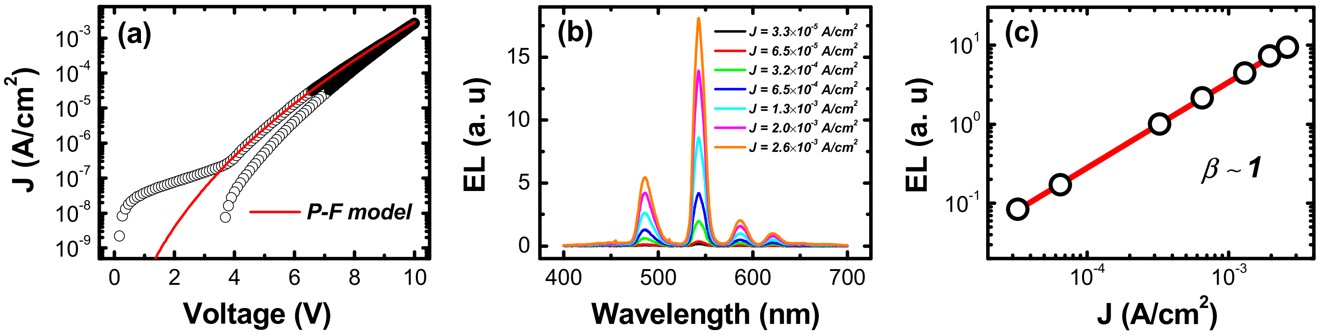

Figure 4. (a) J–V characteristic of the Tb–SiO$_x$N$_y$/SiO$_2$ a-SL with results of a Poole–Frenkel model calculation superimposed. Filled dots depict the EL onset of devices. (b) EL spectra taken under different injected current density values. (c) EL–J representation of the EL spectra shown in (b). Each point stands for the maximum EL value taken at 545 nm as a function of the injected current density (J). The linear fit displays a slope $\beta \sim 1$, which denotes a linear dependence between EL and J.

rich oxide/silicon dioxide superlattice structures were studied [28]. Despite the evident differences in superlattice composition between both superlattices (the SRO layers of the Er-doped superlattice contained a high density of Si-ncs) P–F charge transport was also determined to be effective over a wide range of electric fields. Nevertheless, Er-doped SRO/SiO$_2$ superlattices also showed a trap-assisted tunnelling mechanism under high electric fields which has not been identified in the Tb–SiO$_x$N$_y$/SiO$_2$ a-SL, most probably due to the fact that the latter ones have a lower breakdown voltage. In particular, the Er-doped SRO/SiO$_2$ superlattice surpasses the soft-to-hard breakdown transition around of 8.5 MV cm (~30 V, with the superlattice stack thickness, $t \approx 35$ nm), whereas the Tb-doped SiO$_x$N$_y$/SiO$_2$ superlattice reaches hard breakdown at 7 MV cm^{-1} (~10.5 V, with $t \approx 15$ nm). The fact that both superlattices present a bulk-limited conduction in a very similar range of electric fields in spite of having different superlattice composition suggests a general limitation of carrier injection that may be attributed to the large number of interfaces that electrons have to get through.

An applied voltage of ~6.7 V (4.5 MV cm^{-1}) and a current density of ~3×10^{-5} A cm^{-2} were identified as the experimental threshold values that yield a measurable EL signal. The EL spectrum of the amorphous sub-nanometre Tb-doped superlattice was collected under different current density injection values, obtaining a similar line shape (see figure 4(b)) and a linear dependence of the EL signal with the injected current density along the entire EL onset (figure 4(c)). Such characteristics are typical features of an excitation mechanism of Tb^{3+} ions mainly governed by direct impact excitation [8]. Nevertheless, we cannot completely discard the existence of a simultaneous energy transfer mechanism between the superlattice host matrix (presumably SiO$_x$N$_y$) and Tb^{3+} ions as well. The reason lies on the fact that hot electrons in the conduction band with high energy are needed to excite the most energetic ^{5}D$_4$–^{7}F$_6$ transition emitting at 480 nm (at least 2.6 eV). Although electrons in the conduction band of SiO$_2$ and Si$_3$N$_4$ single layers are known to have an average energy of 3 eV with a high energy tail able to excite Tb transitions [29], the relevance of these hot electrons in a-SLs is questionable since high scattering rates (and therefore low numbers of hot electrons) are expected [28]. Additional studies are required to provide a more detailed picture of the origin of the Tb^{3+} excitation in Tb–SiO$_x$N$_y$/SiO$_2$ a-SLs under electrical pumping.

4. Conclusions

In summary, amorphous sub-nanometre Tb-doped SiO$_x$N$_y$/SiO$_2$ superlattices were fabricated by means of ECR–PECVD. TEM images showed well-defined superlattice interfaces with no waviness and sub-nanometre dimensions per layer. HRTEM analysis showed an amorphous superlattice with no presence of crystalline phases in the structure. No Tb clustering was observed in the superlattice, attributed to a slower Tb diffusion in the SiO$_x$N$_y$ host matrix with respect to SiO$_2$. A shadow mask approach was adopted on the superlattice stack to fabricate transparent ITO electrodes to be used as electron suppliers for the optoelectronic characterization. The Tb^{3+} luminescence under three different excitation sources was compared, obtaining similar spectral features of ^{5}D$_4$ levels of Tb^{3+} under UV laser excitation at 325 nm (PL) and under a bias voltage (EL). Whereas, inner energy transitions belonging to ^{5}D$_3$ levels of Tb^{3+} were measured in samples excited with a highly energetic electron beam in CL measurements. The origin of these discrepancies in the spectra have been attributed to the presence of two competing mechanisms: the population rate of the ^{5}D$_3$ level and the non-radiative relaxation rate of the ^{5}D$_3$–^{5}D$_4$ transition due to a resonant OH- mode. Besides, the J–V curve of Tb-doped superlattices was measured, displaying a bulk-limited charge transport dominated by P–F conduction. The large number of interfaces that injected electrons have to get through has been identified as the most likely reason leading to the bulk-limited transport in our superlattices. In addition, the EL–J characteristic displayed a linear behaviour and a similar spectrum line shape up to the device breakdown, around 10.5 V. A relatively low EL onset voltage of 6.7 V was obtained, well below the reasonable 10 V limit required from a Si-based light source to be suitable for integration in a CMOS technology platform.

Acknowledgments

This research is supported by the Spanish Ministry of Science and Innovation (TEC2012-38540-C02-01). JMR acknowledges the financial support of Secretariat for Universities and Research of Generalitat de Catalunya through the program FI-DGR 2013 and also to Dr L Goncharova (Western University) for valuable help in the interpretation of RBS results. In Canada, this work was supported through a Discovery Grant of the Natural Sciences and Engineering Research Council (NSERC). TEM characterization was carried out in the Science and Technical Centers (CCiT) of the University of Barcelona with financial support of MAT2010-16407 and CSD2009-00013 Spanish research projects.

References

[1] Lockwood D J and Pavesi L (ed) 2011 *Silicon Photonics: II.* (Berlin: Springer)
[2] Boyraz O and Jalali B 2004 *Opt. Express* **12** 5269–73
[3] Reed G T, Mashanovich G, Gardes F Y and Thomson D J 2010 *Nat. Photonics* **4** 518–26
[4] Moss D J, Morandotti R, Gaeta A L and Lipson M 2013 *Nat. Photonics* **7** 597–607
[5] Rickman A 2014 *Nat. Photonics* **8** 579–82
[6] Hirschman K D, Tsybeskov L, Duttagupta S P and Fauchet P M 1996 *Nature* **384** 338–41
[7] Mangolini L J 2013 *Vac. Sci. Technol.* B **31** 020801
[8] Rebohle L and Skorupa W 2010 Rare-Earth implanted MOS devices for silicon photonics (*Springer Series in Materials Science*) (Berlin: Springer)
[9] Yerci S, Li R and Dal Negro L 2010 *Appl. Phys. Lett.* **97** 081109
[10] Sun J M, Skorupa W, Dekorsy T, Helm M, Rebohle L and Gebel T 2005 *J. Appl. Phys.* **97** 123513
[11] Berencén Y, Wutzler R, Rebohle L, Hiller D, Ramírez J M, Rodríguez J A, Skorupa W and Garrido B 2013 *Appl. Phys. Lett.* **103** 111102
[12] Prtljaga N *et al* 2012 *Opt. Mater. Express* **2** 1278–85
[13] Yuan Z, Li D, Wang M, Chen P, Gong D, Wang L and Yang D 2006 *J. Appl. Phys.* **100** 083106
[14] Creazzo T, Redding B, Marchena E, Murakowski J and Prather D W 2010 *J. Lumin.* **130** 631
[15] Zelenina A *et al* 2014 *J. Appl. Phys.* **115** 244304
[16] Marconi A, Anopchenko A, Wang M, Pucker G, Bellutti P and Pavesi L 2009 *Appl. Phys. Lett.* **94** 221110
[17] Mayer M 1997 *SIMNRA User's Guide, Report* IPP 9/113, Max-Planck-Institut für Plasma Physikz, Garching, Germany
[18] Podhorodecki A, Zatryb G, Misiewicz J, Wojcik J, Wilson P R J and Mascher P 2012 *Nanotechnology* **23** 475707
[19] Yuan Z, Li D, Wang M, Gong D, Cheng P, Chen P and Yang D 2008 *Mater. Sci. Eng.* B **146** 126–30
[20] Navarro-Urrios D, Ferrarese-Lupi F, Prtljaga N, Pitanti A, Jambois O, Ramírez J M, Berencén Y, Daldosso N, Garrido B and Pavesi L 2011 *Appl. Phys. Lett.* **99** 231114
[21] Yoshihara M, Sekiya A, Morita T, Ishii K, Shimoto S and Sakai S 1997 *J. Phys. D: Appl. Phys.* **30** 1908
[22] Podhorodecki A, Golacki L W, Zatryb G, Misiewicz J, Wang J, Jadwisienczak W, Fedus K, Wojcik J, Wilson P R J and Mascher P 2014 *J. Appl. Phys.* **115** 143510
[23] Romero V H, De La Rosa E, López-Luke T, Salas P and Angeles-Chavez C 2010 *J. Phys. D: Appl. Phys.* **43** 465105
[24] Jeong H, Seo S Y and Shin J H 2006 *Appl. Phys. Lett.* **88** 161910
[25] Kato H, Masuzawa A, Noma T, Seol K S and Ohki Y 2001 *J. Phys.: Condens. Matter* **13** 6541
[26] Pai D M 1975 *J. Appl. Phys.* **46** 5122
[27] Ramírez J M, Cueff S, Berencén Y, Labbé C and Garrido B 2014 *J. Appl. Phys.* **116** 083103
[28] Ramírez J M, Berencén Y, López-Conesa L, Rebled J M, Peiró F and Garrido B 2013 *Appl. Phys. Lett.* **103** 081102
[29] DiMaria D J and Abernathey J R 1986 *J. Appl. Phys.* **60** 1727

CHAPTER 5

---

5. Conclusions and future perspectives

5.1. Conclusions

A thorough investigation on the design, fabrication, morphology and the optoelectronic operation of RE-doped Si-based light emitting devices has been accomplished in this dissertation. The work carried out during my PhD can be divided in two main sections:

In the first part, a wide overview on Er-doped MIS structures emitting at 1.54 μm has been provided, from the fundamental physics of charge transport and EL phenomena to advanced device design, fabrication and characterization of novel EL structures for on-chip optical routing. Likewise, this part can be further divided in (i) vertically emitting Er-doped MIS devices and (ii) electrically pumped Er-doped waveguides designed to function in a coupled horizontal approach.

Focusing on Er-doped MIS devices, a simple structure composed by a semitransparent top electrode (polycrystalline silicon) and an Er-doped thin film of either a SiO_2 or a Si_3N_4 containing a variable dose of Si excess, both deposited over a p-type doped Si substrate, has allowed us to perform an exhaustive analysis of the optoelectronic properties of active layers. The most remarkable conclusions extracted from this study are:

(i) The charge transport mechanism in thin oxide films is strongly dependent on the density of intraband defects. Thus, a silicon dioxide layer or a sub-oxide (SiO_x) with low defect density has shown a charge transport mechanism mainly modulated by the electrode-active layer potential barrier height, i.e. a FNT or a TAT, whereas a silicon nitride or a silicon rich-nitride (SiN_x), which are known to be highly defective matrices, would present a bulk limited conduction (PF conduction). In that line, the incorporation of a Si excess has proved to be a highly effective tool to boost the electrical properties of layers by means of coherent introduction of additional defect sites. As a consequence, nitride-based thin films showing PF conduction enhance their conductivity significantly. For silicon oxides however, the incorporation of Si excess may affect not only the layer conductivity, but also the charge transport mechanism, being able to switch from an electrode-limited conduction for a low Si excess (FNT or TAT), to a bulk-limited conduction for high Si incorporation (~ 16% for the samples here studied).

Apart from the Si excess, the annealing treatment was also found to be a critical parameter that has a direct impact on the charge transport, especially in silicon oxides.

(ii) A novel analytical approach adapted from the one previously reported by Mikhaelashvili *et al.* has been developed to model charge transport phenomena. This new method is particularly efficient when two different transport mechanisms are concatenated during the J-E sweep.

(iii) Annealed Er-implanted silicon oxides have shown large Er clustering along a well-defined line below the film surface in agreement with the simulated ion stopping depth of implanted ions. On the contrary, smaller Er clustering has been observed in Er-doped samples deposited by co-sputtering of Er_2O_3 and SiO_2 targets, being the Er agglomerates homogeneously distributed, hence suggesting a uniform Er doping in the active layer. On the other hand, no evident Er clustering has been observed in Er-doped Si_3N_4 layers fabricated by co-sputtering and with the same Er dose than the other samples, pointing out that the nitrogen incorporation gives rise to significant enhancement of the RE solubility in thin oxides. Consequently, higher number of Er^{3+} ions suitable to emit is expected, increasing the total emitted optical power.

(iv) The origin of Er^{3+} excitation under electrical pumping has been disclosed in samples containing Si-ncs. It has been shown that either direct impact excitation of hot electrons injected over the conduction band or energy transfer from Si-ncs to Er^{3+} ions governs the EL emission of Er^{3+} ions. Different driving polarizations have been applied to trigger one mechanism or another. Thus, efficient switching between energy transfer and direct impact excitation has been demonstrated just by defining a particular driving scheme over devices.

(v) Excited state absorption of Er^{3+} ions has been identified as one of the major limitations of the EL emission at 1.54 μm under high current injection regime. In spite of this drawback, a first order calculation of the total number of emitting Er^{3+} ions has been performed, obtaining a value as high as 15% in an optimized run of co-sputtered devices. More recently, values as high as 50% of inverted Er^{3+} ions have been reported in a jointly work with the Institute of Ion Beam Physics and Materials Research in Desden [1].

(vi) The role of Si excess and the excitation efficiency of Er^{3+} ions in various Si hosts has been investigated, picturing a consistent trade-off between the power efficiency, the conductivity and the charge trapping density. Hence, devices with higher power efficiency presented lower conductivity and lacked of long device lifetimes since high charge trapping density was measured. On the contrary, high conductive devices showed stable device operation for several hours and reduced charge trapping density, although modest values of power efficiency were also reported. Therefore, in terms of efficiency, SiO_2 is the best Si-based host to allocate Er^{3+} ions, providing superior EL features compared to other matrices like stoichiometric silicon nitrides or silicon-rich oxides/nitrides. Thus, electrode-limited charge transport is the most efficient mechanism to excite luminescent centres inside a dielectric matrix.

(vii) Alternative layer morphologies have been successfully explored. In particular, the role of the accelerator and the injector layer on the electroluminescence of RE-doped silicon oxide (or nitride) thin films has been discussed. An improvement of more than one order of magnitude in the EL efficiency of a Tb-doped SiN_x layer has been demonstrated by attaching a thin SiO_2 layer of 30 nm. The origin of such enhancement has been attributed to a considerable increase of the number of injected hot electrons into the active layer. In view of these promising results, an Er-doped Si-ncs superlattice structure has been designed to restore the mean energy of injected electrons while passing through the active layer, hence boosting the EL emission at 1.54 µm. Unfortunately, such effect has never been observed in our devices. Instead, bulk-limited conduction (and therefore low hot electron injection ratio) and modest EL efficiency have been measured. The large number of interfaces that electrons have to pass through in their way towards the anode has been identified as the most probable cause of such low excitation efficiency. Finally, the implementation of a SiO_x layer with a high Si percentage (16%) operating as an efficient electron injector has been studied in light emitting field-effect transistors (LEFETs), obtaining enhanced electron injection only under low current injection regime.

Also, important conclusions have been drawn for the horizontal optoelectronic approach. A novel Er-doped Si slot waveguide electrically driven has been presented, with a device cross-section that resembles the one of vertically emitting Er-doped MIS devices, i.e. with a top polycrystalline silicon electrode, an Er-doped SiO_2 electroluminescent layer and a lightly doped Si substrate. This time however, the structures were fabricated over SOI wafers to provide strong light confinement in the slot. The most important points of this work are:

(viii) In view of the several technological challenges that entangled the fabrication of electrically pumped Er-doped slot waveguides in a CMOS facility, it is noteworthy to highlight that fabricated devices have provided, in general terms, a good overall optoelectronic feature. Therefore, efficient charge injection inside the active layers has been validated upon high voltage polarization, as well as a good optical TM mode confinement inside the slot region. Similarly, output couplers have been successfully tested, showing an optimum coupling angle of 25° and a maximum spectral transmittance around of 1.54 µm.

(ix) The passive characterization over two different Er-doped slot waveguides containing (or not) Si-ncs has allowed devising high propagation losses of ~ 40 dB/cm, and coupling losses of about 20 dB in both structures. The fact that very similar propagation losses have been measured regardless of Si-ncs suggests that light propagation is mostly restricted by geometrical factors and not by light absorption and/or scattering in Si-ncs.

(x) A particular electrical characterization conducted over top and bottom electrodes of Er-doped slot waveguides has allowed us to verify their suitability as charge injectors in the active layer. Whereas an ohmic-like conduction has been identified at the bottom electrode, a thermionic emission of injected charges over the polysilicon grain boundaries has been demonstrated to govern the charge transport in the top polysilicon electrode. The origin of such particular behavior is well-sustained taking into account that a non-uniform doping was intentionally performed over the central part of the top polysilicon electrode to reduce light absorption of the propagated mode. The modelling of experimental J-E curves has provided grain boundary barrier heights (~ 0.4 eV) and average grain sizes (~ 15 nm) in agreement with the literature and with the mean grain size measured in TEM images taken in diffracting conditions (between 10-50 nm).

(xi) The study on the electrical properties of Er-doped slot waveguides has denoted a charge transport mechanism in the active layers mainly governed by FNT. Unexpectedly low barrier heights have been extracted from the fit, attributed to the fact that charge transport into the active layer is modulated by the preceding thermionic emission at the polysilicon electrode. Accordingly, the Er-doped silicon oxide containing Si-ncs (Er:SiO_x layer) has presented a reduced barrier height compared to the active layer free of Si-ncs (Er:SiO_2 layer). In addition, Si-ncs has demonstrated to be instrumental elements to efficiently drain trapped charge in the active layer, as remarkably lower charge trapping has been measured in the Er:SiO_x layer. These results are in good agreement with vertically emitting Er-doped MIS devices.

(xii) The correct optoelectronic operation of Er-doped slot waveguides has been validated by comparing the infrared EL spectrum from Er^{3+} ions collected from two different locations of the Er-doped slot waveguide: the top of the polysilicon electrode (vertical emission, as in MIS devices) and from the grating coupler. Distinct spectral line shape has denoted dissonant origins of the collected signal, with a scattered and guided EL spectra unambiguously modulated by the polysilicon and output coupler transmittances, respectively. A maximum out-coupled emitted power density of tens of $\mu W/cm^2$ has been estimated in Er-doped slot waveguides. Despite different waveguide lengths have been characterized ranging from 1 mm up to 3 mm, similar output power values have been measured in all devices, suggesting that out-coupled optical power is mainly generated in a region of 1 mm at most from the edge of the waveguide. Also, a simple calculation has been carried out to quantify the approximate percentage of out-coupled optical power in comparison with the totally generated emission inside the active layer, obtaining that only the 6% of generated light is successfully propagated through the active device structure. This value, although still low, denotes that there is room for improvement in these devices.

(xiii) The EL-J characteristic of Er-doped slot waveguides have shown an unexpected super-linear trend in all devices regardless of the waveguide length. The origin of this particular feature has not been attributed to an amplification effect of Er^{3+} emission but to a non-uniform charge injection as a consequence of the non-homogeneous doping performed over the top polysilicon electrode.

(xiv) A thorough electrical pump-and-probe characterization in time-resolved configuration has been carried out over Er-doped slot waveguides for the first time to further insight on the dynamical properties of devices. A sharp overshoot of the guided EL signal at 1.54 μm has been observed under unipolar pulsed excitation at the voltage switch off. The origin of such unique feature of Er-doped slot waveguides (it was not observed in vertically emitting Er-doped MIS devices) has been attributed to the suppression of one of the two competing mechanisms of the EL signal under DC polarization. Therefore, being the EL normally governed by the trade-off between the Er^{3+} radiative de-excitation rate and the extra loss produced by carrier absorption losses due to the uninterrupted charge injection into the active layer, much higher EL signal is expected upon fast suppression of the latter effect. Thus, based on the fact that injected carriers are swept out from the active layer much faster than the Er^{3+} radiative de-excitation rate (~100 ns versus ~1 ms), there would be a small slot of time after the voltage switch off in which carrier absorption losses would be completely suppressed while being Er^{3+} ions still in the excited state. It is worth to remark that despite this interesting feature is also expected to occur in vertically emitting Er-doped MIS devices as the ones studied in the second chapter of this dissertation, a much lower carrier absorption loss is expected since generated photons in the active layer only have to travel through tens of nanometers, at most, before being emitted into free space. On the contrary, generated photons in Er-doped slot waveguides are guided through much longer distances (from 1 to few mm) before exiting through the output coupler, hence maximizing the interaction of the propagated mode with injected carriers.

(xv) A probe signal has been used to assess the optical gain of Er-doped slot waveguides in pump-and-probe configuration, showing no optical amplification and a transmittance attenuation that scales with the applied voltage up to a value of -60 dB/cm. Precisely, such strong voltage-dependent attenuation hase provided a modulation depth of 75% and a DC power consumption of 120 μW. These numbers are not far from the ones typically reported for integrated optical modulators and therefore suggests the suitability of this particular design to function as optical modulators. An integrated system composed by an Er-doped slot waveguide working as integrated light source and coupled to an undoped slot waveguide serving as optical modulator has been proposed.

Concerning the second block of this dissertation, additional RE ions such as Ce^{3+} and Tb^{3+} have been explored to provide light emission in other regions of the electromagnetic spectrum. In particular, these RE ions are of interest since they present an intense blue and green emission, respectively. Indeed, sintered RE-doped oxynitride powders are already widely used as down-converting phosphors for lighting applications. Nevertheless, the implementation of the very same materials in thin-film configuration using a CMOS facility and more restricting thermal budgets in accordance with the CMOS requirements has not yet been studied. Thus, the main purpose of this part of the work has been to investigate the structural and luminescence properties of Ce- and Tb-doped thin films fabricated using CMOS compatible tools and with a layer composition that varies from a silicon oxide to a silicon oxynitride. The effect of the annealing temperature on the morphology and luminescence of samples has also been studied. Finally, a preliminary optoelectronic characterization has been accomplished in electroluminescent test devices containing transparent conductive electrodes made of ITO and deposited by means of the shadow mask approach. The main conclusions drawn are:

(xvi) A successful variation of the layer stoichiometry has been accomplished by a gradual oxygen-by-nitrogen element substitution in the host matrix. Thus, we have departed from a ~ SiO_2 (30% of Si, 70% of O) and ended with a SiO_xN_y layer of around 70-90 nm thick with a maximum nitrogen concentration percentage of 42% (being Si the 35% and O the 22%). An in-situ RE doping of either Ce or Tb (or both simultaneously) has been performed, obtaining uniform RE distribution along the entire thickness of the deposited sample. The layer composition has been verified by means of RBS analyses over different samples. Similarly, VASE measurements have provided useful information about the layer thickness and the optical constants n and k, obtaining two well-differentiated groups depending on the value of k: silicon oxides, with n ~ 1.5 and k ~ 0, and silicon oxynitrides, with increasing n values from ~ 1.5 to ~ 1.9 and k > 0.

(xvii) The evolution of the layer thickness, the optical constants and the PL intensity of fabricated samples have been studied as a function of the annealing temperature from as-deposited samples up to 1180°C. The annealing treatment has always been carried out for 1h in a N_2 atmosphere. Worth noting, the PL intensity obtained under UV excitation is easily observable by the naked eye in daylight conditions, regardless of the annealing treatment. In general, n, t and k values have shown a gradual diminution with the increase of the annealing temperature, whereas the PL intensity has showed a positive increase up to, at least, 900°C for silicon oxides and up to 1180°C for silicon oxynitrides. Remarkably, the highest annealing temperature has provoked a sudden leap in the extinction coefficient k and also in the PL intensity (especially for silicon oxides). Such enhancement of the k and PL intensity values has been attributed to a non-negligible modification of the sample morphology. From one side, RE clustering occurs, hence contributing to light absorption but not to light emission. On the other hand, partial crystallization of RE agglomerations in RE silicates has been demonstrated, explaining the improvement of the PL intensity for such high annealing temperatures.

(xviii) RE co-doping of Ce^{3+} and Tb^{3+} ions in a single silicon oxynitride layer has been tackled. Efficient and homogeneous RE incorporation of both ions has been demonstrated. Similarly than for RE-doped single layers, the progression of the PL intensity as a function of the annealing temperature has been studied and compared to a bilayer in which each RE ion has been placed at a different sub-layer, and also to a series of multilayer stacks where either Ce-doped or Tb-doped silicon oxynitride sub-layers are sequentially deposited, each one separated by a SiO_2 spacer. In order to reveal the ultimate limit of the deposition system, a sub-nanometre SiO_xN_y/SiO_2 superlattice with selective Tb-doping only in the silicon oxynitride sub-layers has been designed and fabricated. The quality of this sequential approach has been validated by TEM characterization, obtaining a mean layer thickness of 0.7 nm and 0.9 nm for the Tb-doped SiO_xN_y luminescent sub-layer and the SiO_2 spacer respectively, also denoting a well-defined multilayer with sharp interfaces and negligible waviness. Also, partial destruction of the multilayer structure has been obtained only for the highest annealing temperature at 1180°C. Therefore, the multilayer stack is well-preserved for lower annealing temperatures such as 1000°C, even for the superlattice structure.

(xix) In view of the wide colour tunability of the PL emission from RE-doped single and multilayer samples, sweeping from cobalt blue to emerald green, a simple electroluminescent device was fabricated over luminescent thin films to test the optoelectronic operation. For that, tiny ITO dots with radii of a few hundreds of μm were fabricated to function as top electrodes. Similarly, an Al layer was deposited at the back of the sample to work as a back electrode. Three different samples have been investigated: a Ce-doped SiO_xN_y single layer, a Tb-doped SiO_2 single layer and the Tb-doped SiO_xN_y/SiO_2 superlattice, all of them annealed at 1000°C. Good carrier injection has been obtained in all devices, denoting different charge transport mechanisms in single layers, being the silicon oxynitride limited by the bulk (PF conduction) and the silicon oxide by the electrode (TAT). As for the EL signal, despite the recorded EL spectrum has showed sharp features in agreement with the different RE radiative transitions, poor device reliability and bad reproducibility from one device to another has been measured in both single layers. Moreover, a simple topologic inspection of the ITO surface has allowed us to unambiguously attribute the modest performance of fabricated devices to a progressive degradation of the top electrode upon high voltage excitation.

(xx) On the contrary, an outstanding optoelectronic performance has been displayed for the Tb-doped SiO_xN_y/SiO_2 superlattice compared to RE-doped single layers, with stable device operation over several hours and good device reproducibility. Charge injection has been found to be governed by PF conduction. Also, a linear evolution of the EL-J characteristic has been measured, in agreement with previously studied Er-doped MIS devices. Noticeably, the fact that the Tb-doped superlattice is only 15 nm thick in total has positively influenced on the reliability of devices. Having established the EL onset in ~ 7 V and the device breakdown around of 10 V, the top ITO electrode is subjected to a remarkably lower voltage compared to the electrodes deposited over RE-doped single layers. Such voltage difference is believed to be a decisive factor to explain the outstanding operation of Tb-doped superlattices over RE-doped single layers.

Thus, several conclusions on RE-doped Si-based light emitting devices have been drawn over the course of my Ph.D. The thorough investigation carried out during this time has allowed me to disclose different phenomena occurring in these devices. Also, I gained valuable experience in different research systems and tools, and developed a well-funded theoretical background on Si-based luminescent materials and optoelectronic devices. More importantly, I had the opportunity to develop a meticulous methodology in a scientific environment, also leading me to the acquisition of not less important transversal skills such as the group work, the critical self-analysis, or the tenacity and self-belief of your own ideas.

5.2. Future Perspectives

Finally, I would like to end this dissertation giving some hints about different interesting strategies that, from my humble viewpoint, could be tackled to continue the work here presented. Mainly, I provide 6 different proposals:

(i) Integrated design of concatenated Si-based light emitting devices.

Up to now, the vast majority of Si-based light emitting devices focuses on a single optoelectronic element fabricated over a Si wafer. This particular design was taken from the standard MOS capacitor directly, in which the oxide layer was replaced by the active layer. Thus, charge injection yielded a measurable EL signal when exciting luminescent centres, i.e. RE ions or Si-ncs. This approach has been widely spread over many silicon photonic research groups by a number of reasons: (i) initially, it was believed that the EL emission of Si-based light emitting devices was mainly governed by the electron-hole bipolar injection rate into Si-ncs in either a direct manner (EL emission from Si-ncs) or indirectly (emission of RE ions through effective energy transfer from Si-ncs). Therefore, a highly n-type doped polysilicon electrode and a p-type Si substrate would guarantee such phenomena. Nevertheless, after the thorough study of the origin of the EL emission in both Si-ncs and RE ions, we are in a position to certify that excitation takes place mostly through direct impact excitation of hot electrons over the conduction band. As a consequence, we can get rid of the MOS structure provided that efficient hot electron injection takes place in the active layer.

Another strong limitation of Si-based light emitting devices containing homogeneously distributed luminescent centres in a dielectric matrix is the total emitted optical power. There are, mainly, two different strategies to increase the optical power: increase the layer thickness of the active layer, hence increasing the number of luminescent centres, or to fabricated large area devices. Thick dielectric layers will necessary require huge driving voltages, since the applied voltage scales with the layer thickness (approximately one volt per nanometre in a SiO_2). Also, for the particular case of electrode-limited conduction, the increase of the layer thickness will gradually switch the charge transport to a bulk-limited mechanism, hence reducing the electrical-to-optical conversion. Because of these drawbacks, modest optical power density is recorded most times. On the other hand, large area devices have proven to be not reliable since the voltage cannot be homogeneously distributed along the electrode surface, hence inducing localized heating currents that rapidly degrade the optoelectronic performance of the device.

Furthermore, as already discussed in this dissertation, the ultimate integration of Si-based light emitting device would necessitate from a horizontal emitting approach. Therefore, although Er-doped slot waveguides fulfil this requirement, the emitted optical power is still low for on-chip applications.

To my viewpoint, the only suitable strategy that would fulfil all the above restrictions is to design concatenated series of Si-based light emitting devices. However, the design and fabrication of this concatenated structure may be an arduous task and therefore it should be carefully tackled. A simple design that would not require critical technological steps would be the one shown in figure 5.1. It consists of three Si-based light emitters disposed in a row and emitting horizontally to the plane of the substrate, equally than for Er-doped slot waveguides. The peculiarity of this design consists in placing each device in a vertical configuration instead of the typical horizontal configuration accomplished when fabricating planar devices, so that each electrode is placed at both sides of the active layer (not on top and at the bottom, as in a vertically emitting MIS device). In order to do so, an ITO grating-like structure has to be fabricated first on a SiO_2 buffer layer. Afterwards, the active material is deposited to fill in the ITO structure. Therefore, after CMP process to polish the surface, Al contact stripes should be defined on top of each ITO ridge. Finally, a simple electrical circuitry would be needed to polarize the structure accordingly, with a series of interleaved resistances working as voltage dividers. Thus, the polarized structure would inject charge from the ITO ridges into active layers simultaneously, increasing the total emitted optical power. I shall remark that for this particular design, since the ITO is deposited before the active layer, the annealing temperature required to activate RE ions in the active layer is limited by the one at which the optoelectronic properties of ITO electrode are optimum. Thus, bearing in mind the low temperature requirements of Re-doped SiO_xN_y layers (see chapter 4), it could be interesting to fill in the grating-like ITO voids with a host material based on a silicon oxynitride.

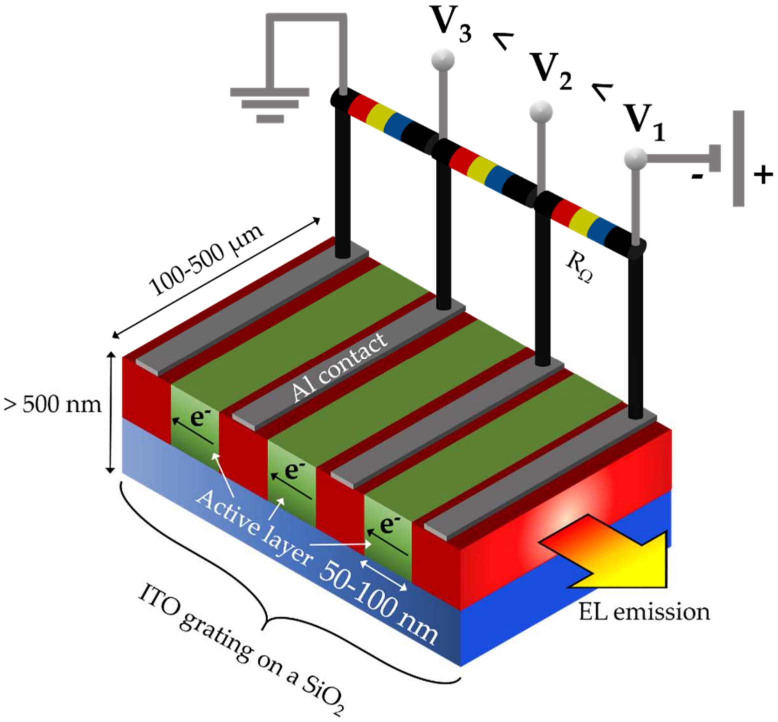

Figure 5.1. Proposed design showing three concatenated Si-based light emitting devices emitting in a horizontal plane to the substrate simultaneously. Depicted dimensions are only a suggestion.

(ii) Er-doped Si slot waveguides with an active layer composed by a SiO_2 accelerator and an Er-doped Si_3N_4 electroluminescent layer.

This proposal consists in the integration of the bilayer structure composed by a SiO_2 accelerator and an Er-doped Si_3N_4 electroluminescent layer in electrically pumped slot waveguides to improve the overall performance of the previously described waveguides containing a single Er-doped SiO_2 (or SiO_x) layer uniquely. Moreover, an alternative process flow could be performed to ease the fabrication process. Figure 5.2 describes the main steps required to fabricate this new batch of Er-doped SiO_2/Si_3N_4 slot waveguides. It is worth noting that this time a uniform doping is suggested for the top polysilicon electrode since a small overlap is expected for the propagated TM mode. Also, the lower Si cladding would be a non-doped monocrystalline silicon layer instead of a p-type doped Si with a steep doping gradient. Despite being advantageous from the optical viewpoint, it would modify the electrical performance of devices. In practice however, the intrinsic Si layer is only expected to increase the driving voltage required for the efficient charge injection. The most important advantages foreseen for this new design in comparison with the previous structure are: (i) an easier fabrication process, (ii) a better optical confinement, since the Si_3N_4 layer has higher index of refraction than SiO_2, (iii) faster device operation, and (iv) stable device operation, as this structure minimizes damaging due to charge trapping density and hot impact ionization at the cathode.

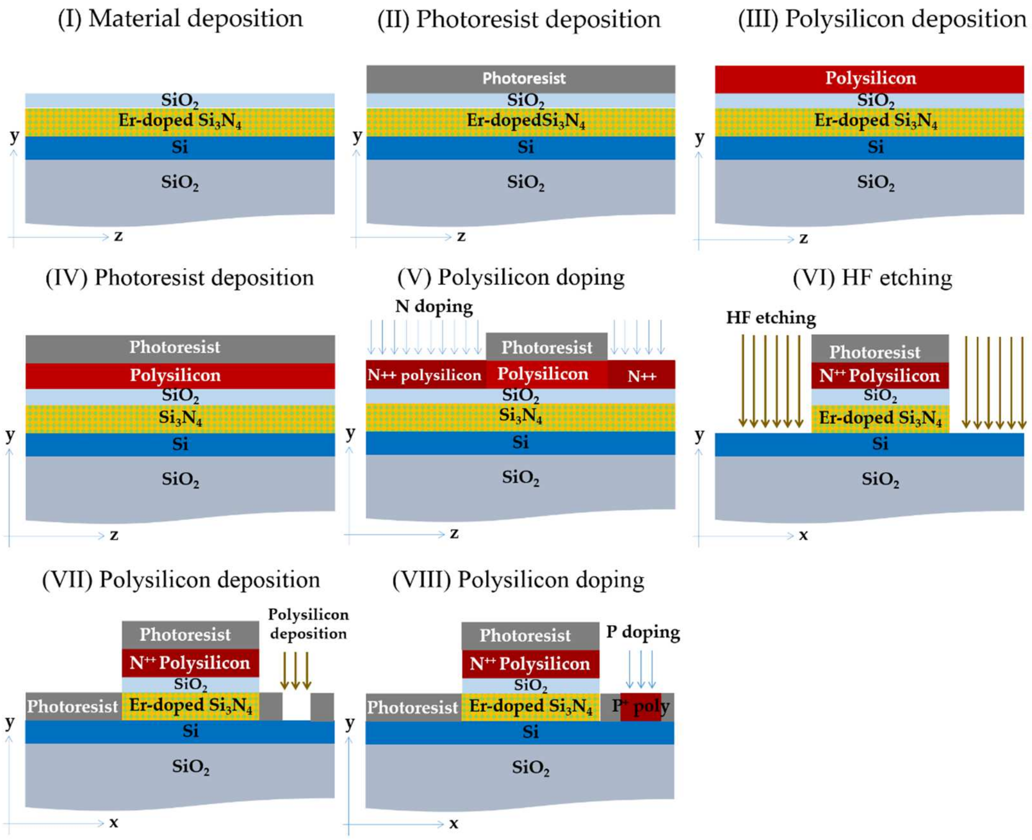

Figure 5.2. Summary of the main process flow steps required to fabricate Er-doped SiO_2/Si_3N_4 slot waveguides.

(iii) Development of Eu-doped silicon oxides and oxynitrides.

This is a natural step forward towards the implementation of a monolithically integrated white light source. After the stimulating results obtained from Ce- and Tb-doped silicon oxides and oxynitrides with bright and colour-tuneable luminescence, a red emitting thin film with similar optical properties is required to accomplish this breakthrough. Eu^{3+} ions are good candidates since they show intense red emission around of 611 nm when embedded in the appropriated host. Therefore, it would be interesting to disclose the luminescence properties of Eu-doped silicon oxides and oxynitrides, similarly than for the previously studied Ce- and Tb-doped thin films. Figure 5.3 shows the proposed device cross-section, with a multilayer stack composed by three SiO_xN_y layers of different RE doping, ie. Eu, Tb and Ce, and interleaved SiO_2 spacers to induce hot electron injection into the active layer. The specific ordering of each active layer with the Eu-doped thin film at the bottom, followed by the Tb-doped SiO_xN_y layer and finally the Ce-doped SiO_xN_y has been intentionally chosen to avoid photon reabsorption at superior levels.

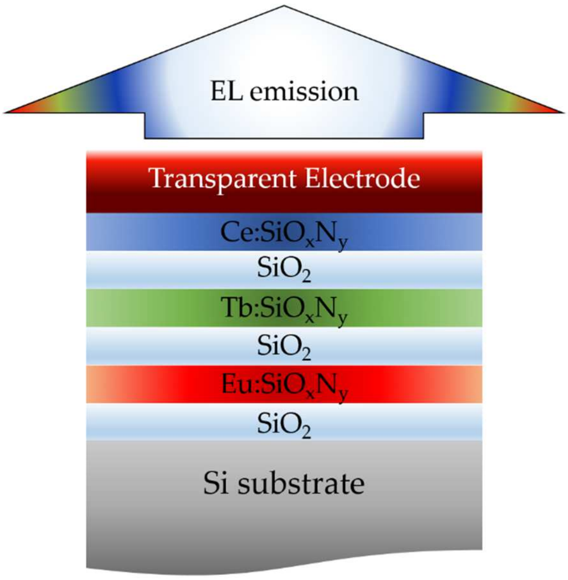

Figure 5.3. Device cross-section showing a multilayer stack of sequentially deposited RE-doped SiOxNy layers of different RE doping with interleaved SiO$_2$ spacers.

(iv) ITO deposition in an oxygen-rich plasma atmosphere and electrical isolation of electroluminescent test devices by selective HF etching.

Despite the ITO electrodes developed in this dissertation allowed us to perform a preliminary optoelectronic characterization of luminescent samples, several issues were identified, attributed to the modest quality of deposited materials. Despite several iterations with different fabrication parameters were performed prior to the final patterning of ITO electrodes onto luminescent layers, I suggest further investigation to optimize the process. For instance, at the time of this writing the annealing environment was limited to either N$_2$ or air. Although slightly better performance was obtained in N$_2$, it could also be interesting to inspect other annealing environments such as forming gas. However, to my opinion the most important assay on the ITO fabrication should be carried out while depositing the material, since good optoelectronic properties are generally reported when using an extra source of oxygen during the evaporation of ITO targets. Currently, a set of reactive plasmas is being installed in the EB-PVD system, and therefore high quality ITO electrodes are expected in the short term.

Another interesting approach that could be tackled to improve the performance of electroluminescence test devices is to accomplish the electrical isolation of devices. Normally, this task is carried out by the buried oxide spacer (BOX) for electrical devices fabricated in a CMOS facility. In our case however, we cannot make use of BOX to isolate devices since we use a shadow mask approach to pattern the top ITO electrodes. As a consequence current crowding may occur, diminishing the overall optoelectronic properties and reducing the device operation lifetime. A simple method is here proposed to avoid this undesired effect. Taking advantage from the very low etching rate that HF has on ITO in comparison with either SiO_2 or SiO_xN_y, a complete immersion in an HF solution after the ITO patterning would completely etch the non-patterned regions of the active layer down to the Si substrate.[24] Figure 5.4 illustrates the selective etching process.

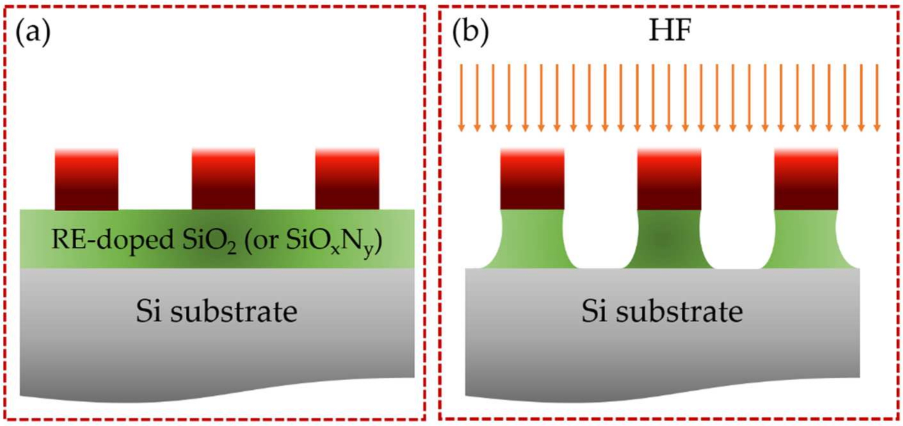

Figure 5.4. (a) Cross-section of the active layer (a RE-doped SiO_2 or SiO_xN_y thin film) with patterned ITO electrodes on top using the shadow mask approach. (b) HF selective etching of the un-patterned regions of the active layer, with the ITO electrodes working as mask protectors.

(v) Fabrication of electrically pumped light emitting disk resonators with different RE ions.

Another fascinating approach that could be tackled with RE-doped SiO_xN_y layers is the fabrication of electrically pumped light emitting disk resonators with different RE dopants. An example is depicted in figure 5.5, with three different electrically driven disk resonators containing either Ce^{3+} ions (bluish resonator at the left), Tb^{3+} ions (resonator at the centre) or Eu^{3+} ions (right side), each one coupled to a bus waveguide. The expected EL spectra is also displayed, with PL resonances superimposed to the PL emission of each RE ion. The main advantage of this system over passive resonators is the fact that the probe signal is generated in the chip directly, hence avoiding the laborious task of coupling light from a bulky external laser. Potential applications such as biosensing or multiple on-chip data processing are foreseen for this integrated photonic chip. Notice that, in order to succeed with the former proposed application, the ITO electrode should be smaller in diameter than the disk resonator so that generated EL mode is not fully covered by the ITO electrode and therefore interacts with its surrounding media. Another important point of discussion with this novel approach is the correct choice of the passive guiding material. Being the emissions from Ce^{3+}, Tb^{3+} and Eu^{3+} in the visible range, wide bandgap materials should be used to avoid absorption of propagated light. Consequently, Si is discarded since provides efficient absorption up to wavelengths of 1.1 μm. On the contrary, Si_3N_4 would be a good candidate, as it has a wide bandgap of about 5 eV, hence being transparent for the proposed wavelengths of

---

[24] *I shall acknowledge the members of the Valencia Nanophotonics Technology Center (NTC) at the Polytechnic University of Valencia, for their valuable contribution on this matter.*

emission, and displays excellent guiding properties. In fact, as already highlighted in the introduction of this dissertation, Si_3N_4 is becoming a trending material to implement CMOS photonic platforms [2, 3]. Therefore, the development of novel resonant Si-based light emitting devices with different operation wavelengths could be a captivating field to explore in the foreseeable future.

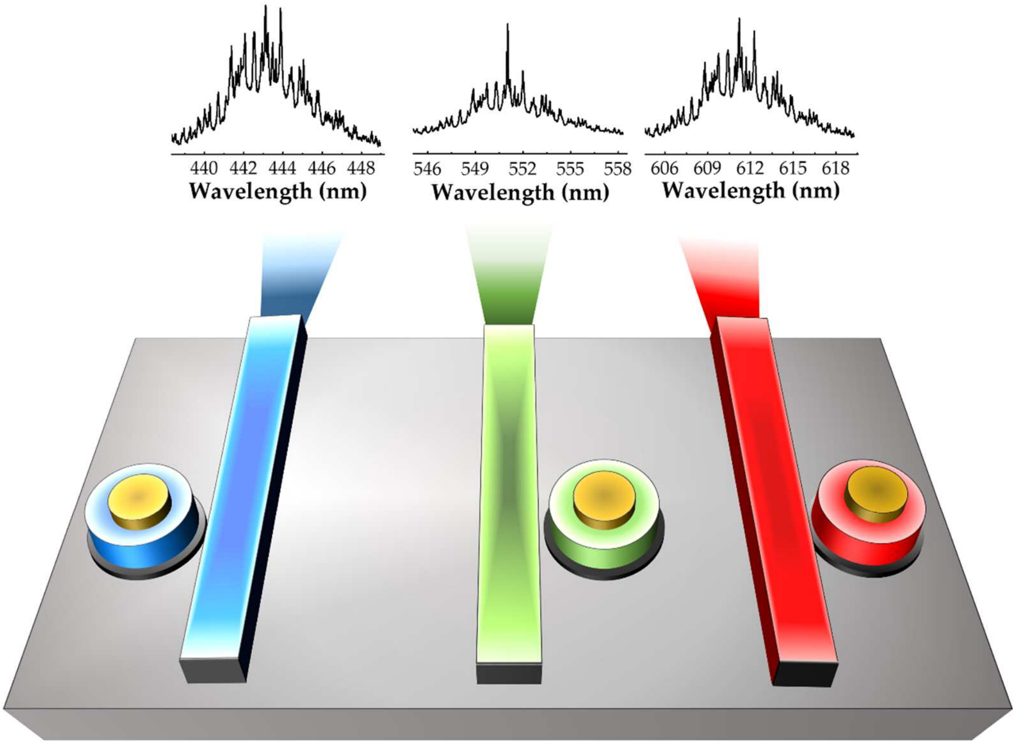

Figure 5.5. Proposed photonic chip containing RE-doped SiO_xN_y ring resonators electrically driven (see the top ITO electrode) coupled to passive bus waveguides for the on-chip routing and detection. The expected EL spectra taken around the maximum of emission of each RE ion is also displayed.

(vi) Exploring light emitting nanostructured materials with high conductivity and transparency: Ultimate integration of the active layer, the electrode and the outcoupling layer into a single assembly.

Finally, I would like to introduce an appealing ongoing work that is currently being carried out in the Electro-Photonics Lab in Barcelona. Having explored the luminescent properties of different luminescent centres embedded in dielectric hosts for years, recently we are looking into other host materials to allocate the luminescent centres. In particular, transparent conductive oxides triggered our attention due to the many benefits that they offer over other materials. By other side, we are also interested in boosting the outcoupling efficiency of the generated optical power inside the active layer. As previously described in chapter 2, the fraction of emitted optical power into free space is very low even with the deposition of an antireflecting coating (ARC). Therefore, other authors have investigated alternative strategies such as the growth of nanostructured transparent materials to function as transparent conductive electrodes with superior outcoupling efficiency [4]. Based on this interesting approach, we are pushing one step further towards the development of an electroluminescent and nanostructured transparent conductive electrode. In order to accomplish that aim, our proposal requires efficient RE doping of ITO NWs. Being the Eu-doping of ITO thin films successfully accomplished [5], in which bright red emission attributed to radiative de-excitation of Eu^{3+} transition lines was measured, an interesting scenario opens up with ITO NWs since they show considerable larger area of emission with respect to ITO thin films. Another crucial work that inspired this new research line in Barcelona is the one presented by J. Gao and co-workers [6]. In their paper, bright UV emission centred at 430 nm from RE-undoped ITO NWs was reported.

In our case, ITO NWs under different fabrication conditions have been successfully grown in the EB-PVD system of the Faculty of Physics. A complete structural, morphological and optical characterization of ITO NWs is currently being conducted to elucidate the most important features of these interesting nanostructures. Despite such study was still on at the time of this writing, I found some interesting phenomena that deserve mentioning. Firstly, I shall add a few words on the growth process. Instead of growing as individual entities, a tree-like structure with high density of branches was found to dominate the NW growth. Despite these structures are not novel as previously reported works already identified ITO NWs with high branching (also called nanowhiskers), they did not present such a high density network like the one of our nanostructures. The top-left image in figure 5.6 corroborates this fact, since a high density and homogeneous growth is observed over a region of 10^{-4} cm^2. Moreover, for this particular case, ITO NWs grew around a localized impurity unintentionally deposited over the substrate, forming a unique structure that strongly resembles to a sea urchin. Another particular characteristic of ITO NWs with high branching is the crystallographic orientation of the growth direction. Hence, since ITO is a cubic structure, adjacent NW branching would grow oriented in accordance with the crystallographic planes of the main branch. As a consequence, structures like the ones shown in the left-middle side of figure 5.6 are obtained. It is worth noting that these structures bear a likeness to a fir-tree forest. An SEM image of an isolated ITO NW is also displayed in the left-bottom side of Figure 5.6 to better illustrate the cubic branching orientation.

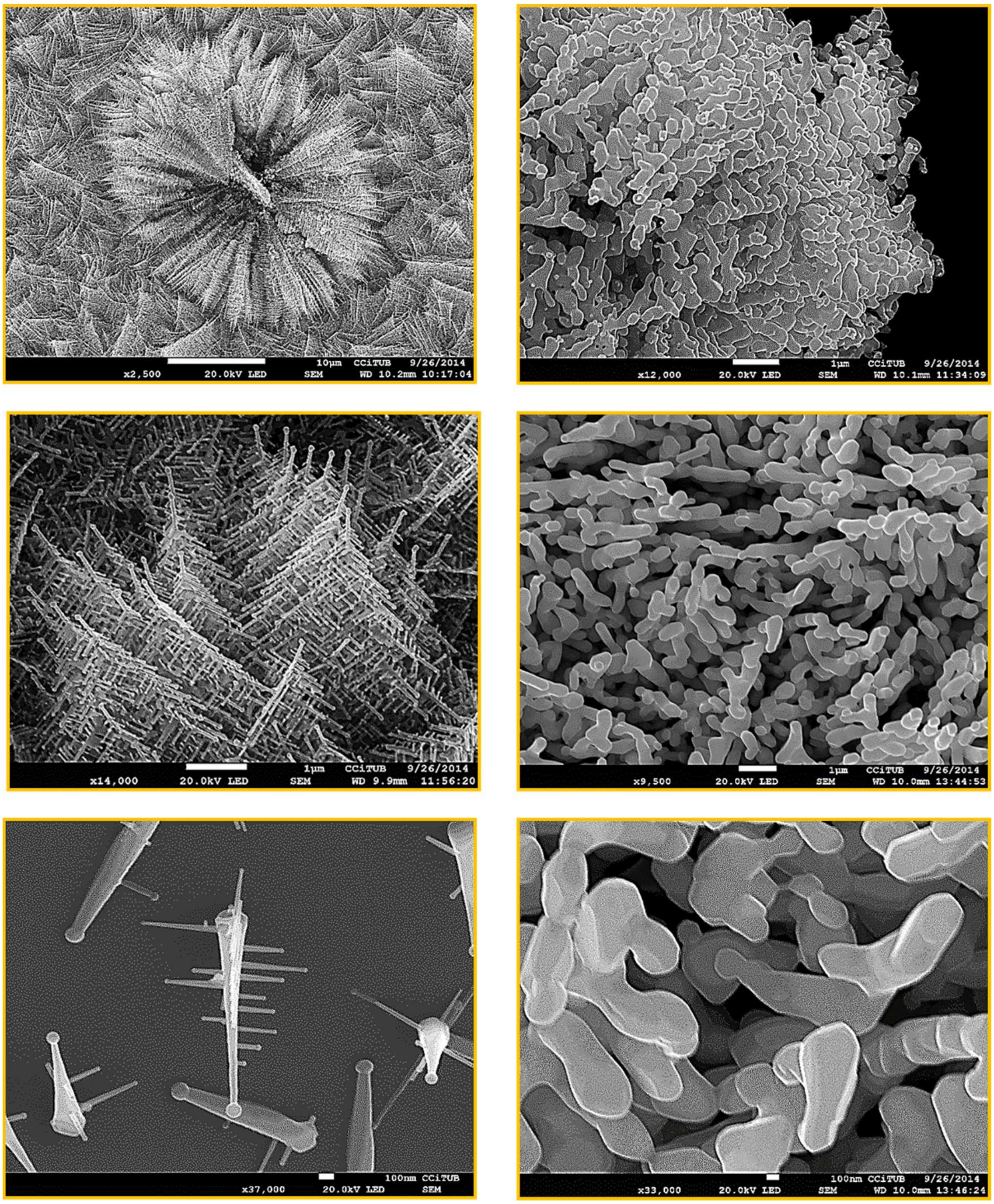

Figure 5.6. SEM images of fabricated ITO nanowhiskers (left side) and ITO nanocorals (right side). The magnification is sequentially increased from top-to-down in both cases.

Finally, a last highlight of ITO NWs is shown at the right side of figure 5.6. Upon high thermal annealing at 1200°C for 1h in N_2 atmosphere, the ITO nanowhiskers partially melted giving rise to new ITO nanostructures that strongly resemble a dense coralline structure. Although further investigation is needed to provide a more accurate picture of the overall performance of ITO nanocorals, preliminary PL measurements under UV laser excitation showed a PL intensity of about one order of magnitude higher than the one measured in ITO nanowhiskers annealed at much lower temperatures (700°C). The origin of this considerable enhancement of the luminescence signal remains unknown at present.

Hence, although more work needs to be done to disclose the properties of ITO NWs, we believe that it is a good starting point towards the development of electroluminescent transparent conductive oxides with outstanding performance.

5.3. List of references

[1] Rebohle, L., Berencén, Y., Wutzler, R., Braun, M., Hiller, D., Ramírez, J. M., ... & Skorupa, W. (2014). "The electroluminescence mechanism of Er^{3+} in different silicon oxide and silicon nitride environments." *Journal of Applied Physics,116*(12), 123104.

[2] Moss, D. J., Morandotti, R., Gaeta, A. L., & Lipson, M. (2013). "New CMOS-compatible platforms based on silicon nitride and Hydex for nonlinear optics." *Nature Photonics*, *7*(8), 597-607.

[3] Romero-García, S., Merget, F., Zhong, F., Finkelstein, H., & Witzens, J. (2013). "Silicon nitride CMOS-compatible platform for integrated photonics applications at visible wavelengths." *Optics express*, *21*(12), 14036-14046.

[4] O'Dwyer, C., Szachowicz, M., Visimberga, G., Lavayen, V., Newcomb, S. B., & Torres, C. S. (2009). "Bottom-up growth of fully transparent contact layers of indium tin oxide nanowires for light-emitting devices." *Nature nanotechnology,4*(4), 239-244.

[5] Ting, C. C., Tsai, C. H., Chien, Y. C., & Yu, C. T. (2012). "Enhanced Red Light Photoluminescence of the Europium and Yttrium Co-Doped ITO Powders." *Journal of the Electrochemical Society*, *159*(4), H400-H406.

[6] Gao, J., Chen, R., Li, D. H., Jiang, L., Ye, J. C., Ma, X. C., ... & Wu, T. (2011). "UV light emitting transparent conducting tin-doped indium oxide (ITO) nanowires." *Nanotechnology*, *22*(19), 195706.

Appendix A

A. Resum en Català

Durant els últims anys, l'interès que han proferit els dispositius luminescents basats en silici dopats amb terres rares ha anat augmentant de forma considerable per bona part de la comunitat investigadora que es dedica a la fotònica del silici. Un dels motius que incentiven aquesta investigació rau en els múltiples avantatges que es preveuen en cas d'aconseguir una eventual integració monolítica de les funcions electròniques i òptiques en un procés madur, estandarditzat i de fabricació en massa com és la tecnologia CMOS. Així doncs, problemes actuals de la microelectrònica com l'anomenat coll d'ampolla de les interconnexions (interconnect bottleneck en anglès) podrien ser solucionats mitjançant interconnexions òptiques de gran capacitat (superiors a 1 GB/seg.). També en altres àrees del coneixement tals com les telecomunicacions, el sensat mitjançant dispositius avançats, la metrologia òptica d'alta precisió o les tecnologies de la llum. De la mateixa manera, s'espera una important reducció de la despesa energètica mitjançant la convergència de la fotònica i l'electrònica en un sol chip, obtenint així dispositius més eficients que requereixen d'una menor demanda energètica.

En aquest context, la incorporació de diminuts centres luminescents com els nano-cristalls de silici o les terres rares a dins dels òxids de porta dels dispositius MOS ha estat proposat com una alternativa de baix cost per obtenir dispositius luminescents i fabricats de forma íntegra amb la tecnologia CMOS. Malgrat que el silici és un material amb una baixa eficiència lumínica degut a que té una banda d'energia indirecta, la nano-estructuració del mateix produeix un augment considerable de la luminescència mitjançant la de-localització de les funcions d'ona de l'electró a la banda de conducció i el forat a la banda de valència com a conseqüència del confinament quàntic. Així doncs, la luminescència d'aquestes nano-estructures és maximitzada, oferint un rang d'emissió que varia des del visible (al voltant del vermell, sobre els 610 nanòmetres) fins a l'infraroig proper (uns 850-900 nanòmetres), segons les dimensions dels nano-cristalls de silici. A més a més, els nano-cristalls de silici han demostrat propietats interesants com a sensibilitzadors d'altres espècies luminescents tals com les terres rares, oferint una bona absorció en l'ultraviolat i una major luminescència de la terra rara a la qual s'està sensibilitzant. Referent a l'activitat òptica de les terres rares, és important destacar que necessiten estar en un estat ionitzat per poder emetre fotons. L'emissió es produeix principalment per una des-excitació espontània d'un ió de terra rara excitat, emetent un fotó amb energia igual a la diferència entre l'estat excitat i el fonamental per al ió en qüestió. Així doncs, els ions de terres rares produeixen una luminescència espectral força estreta en concordança amb els diferents nivells energètics excitats, essent aquests característics segons l'element ionitzat. Es pot aconseguir un ample ventall d'emissions des de l'ultraviolat fins a l'infraroig proper.

Així doncs, i tenint en compte les interesants propietats descrites a l'anterior paràgraf, aquesta tesi presenta el treball dut a terme en la implementació de dispositius luminescents basats en silici i dopats amb terres rares per al desenvolupament de nous pilars optoelectrònics fonamentals compatibles amb la fotònica del silici. Aquest treball abasta des dels aspectes més fonamentals tals com l'estructura, la morfologia de les capes actives que contenen nano-cristalls de silici i/o ions de terres rares o l'estudi de l'origen de l'electroluminescència dels dispositius quan són polaritzats per diferents voltatges alterns, fins al desenvolupament de nous dispositius avançats basats en silici. En aquest cas, l'estudi portat a terme s'acompanya d'una descripció detallada del disseny de cada dispositiu, el disseny de la màscara de procés elaborada especialment per a la fabricació dels dispositius en cas que sigui necessari, així com el procés de fabricació dels mateixos i una caracterització optoelectrònica detallada amb les pertinents conclusions al final de cada capítol. També, al final d'aquesta tesi es proposen nous dissenys i arquitectures de dispositiu que pretén establir un mapa de ruta per millorar els dispositius estudiats en aquest tesi, i que està basat en l'experiència adquirida durant els quatre anys d'investigació en dispositius electroluminescents basats en silici.

Aquesta tesi està dividida en dos grans blocs: un primer bloc dedicat a l'estudi i desenvolupament de dispositius electroluminescents basats en silici i dopats amb erbi, amb una emissió al voltant de 1.54 μm amb aplicacions en telecomunicacions integrades de curta distancia, i una altra part focalitzada en l'estudi de les propietats estructurals i les propietats de capes fines luminescents d'òxids i oxinitrurs de silici dopats amb ions de ceri i terbi amb diferents composicions. Aquestes capes poden tenir aplicacions com a materials actius en sensors òptics o per la fabricació de micro-monitors (micro-displays en anglès) emetent en els tres colors primaris.

En la primera part de la tesi es detallen les propietats optoelectròniques de capacitats de tipus metall-aïllant-semiconductor (MIS, acrònim de l'anglès) amb un dopatge de ions d'erbi en l'òxid de porta, format bé per un òxid de silici o un nitrur de silici amb un excés de silici variable. En particular, es presenta un estudi acurat de la dependència de les propietats morfològiques de la matriu, els tractaments tèrmics o l'excés de silici sobre els fenòmens de transport de càrrega en capacitats MIS dopades amb erbi. En aquest context, s'ha identificat un mecanisme de transport de càrrega limitat per la capa dielèctrica quan el recuit tèrmic no aconsegueix eliminar la major part dels defectes intersticials de la matriu. Per altra banda, el mecanisme és limitat per la capacitat d'injectar càrrega de l'elèctrode quan el tractament tèrmic profereix un bon passivament de la matriu, eliminant la major part de defectes en la capa. De forma similar, però amb una incidència menor, s’ha detectat un canvi del mecanisme de transport variant únicament l’excés de silici en òxids de silici. Així doncs, el mecanisme principal de transport de càrrega passa de ser limitat per l’elèctrode (per un excés de silici petit) a ser limitat per la capa (excés de silici gran) quan es passa un cert llindar (al voltant del 16% de silici en excés). Per altra banda, s’ha investigat l’origen de l’excitació de l’erbi mitjançant l’estudi de l’electroluminescència de dispositius MIS sota diferents polaritzacions polsades. Així doncs, per a voltatges alts i freqüències baixes l’excitació ve dominada per l’impacte directe d’electrons calents a la banda de conducció, mentre que un procés de transferència d’energia entre els nano-cristalls de silici i l’erbi predomina per a voltatges baixos i freqüències altes per a una polarització bipolar simètrica. Sota condicions d’injecció de corrent extremes, s’observen fenòmens no lineals tals com l’absorció d’estats excitats que limiten la potència òptica dels dispositius. No obstant aquests comportaments apareixen sota condicions molt extremes on els dispositius estan a punt d’assolir la ruptura irreversible. L’estudi d’eficiència de l’electroluminescència estableix que els òxids de silici estequiomètrics (és a dir, sense excés de silici) que presenten mecanismes de transport limitats per l’elèctrode són els més eficients per a l’excitació de l’erbi, oferint majors potències òptiques respecte els nitrurs de silici o les capes amb més excés de silici que mostren una conducció de càrrega limitada per la capa dielèctrica. Aquest fet concorda amb la teoria dels electrons calents, que estableix que els mecanismes de transport limitats per l’elèctrode tenen un major nombre d’electrons calents respecte als limitats per la capa, i per tant una major probabilitat d’excitar els ions d’erbi. En contrapartida però, s’observa un temps de vida d’operació més curt en els dispositius més eficients. Aquest fet s’origina degut a que els electrons calents, tot i que exciten més ions d’erbi per segon, tenen molt poca selectivitat, i per tant també exciten altres impureses a dintre de la capa que fan que es deteriori més ràpid.

Per tal de millorar aquestes deficiències trobades en els dispositius MIS dopats amb erbi, aquesta tesi també planteja altres dissenys que permetin millorar l’eficiència de l’electroluminescència i mantenir un temps llarg d’operació dels dispositius. Una possible solució que es proposa és dissenyar una bicapa formada per un òxid de silici i un nitrur de silici dopat amb erbi. Aquesta nova configuració permet una gran injecció d’electrons calents des de la capa d’òxid de silici (accelerador) cap a la capa de nitrur de silici dopat amb erbi (fòsfor). Així doncs, es podria dir que aquest disseny és l’anàleg en configuració integrada del tub de rajos catòdics, ja que es basa en el mateix concepte (una primera fase d’acceleració d’electrons, i una segona etapa on impacten sobre el fòsfor per generar la imatge). En base als bons resultats obtinguts de l’estudi d’aquestes capes, es pot anar un pas més enllà i dissenyar dispositius en configuració de super-xarxa en els quals els electrons són contínuament accelerats a dintre de la capa mitjançant un seguit de capes fines d’óxid de silici intercalades amb capes de nitrur de silici dopades amb erbi de forma equiespaiada entre l'ànode i el càtode del dispositiu. En aquesta nova arquitectura, els electrons serien accelerats, perdrien energia amb el fòsfor de nitrur de silici degut a l'impacte amb les espècies luminescents (erbi en aquest cas), i serien accelerats novament per una segona capa d' òxid de silici, repetint així el cicle una i altra vegada fins a arribar al càtode del dispositiu. No obstant, a la pràctica, la caracterització d'aquestes super-xarxes dopades amb erbi ha resultat ser menys efectiva en quant a l'excitació de l'erbi es refereix. La raó principal d'aquesta inesperada resposta rau en el gran nombre de defectes intersticials presents a les interfícies de la super-xarxa. Com a conseqüència, el transport no és limitat per l'elèctrode com s'esperaria, sinó per la capacitat d'admetre càrrega de la capa, disminuint així el nombre d'electrons calents que viatgen per la capa i per tant reduint l'eficiència d'excitació de l'erbi. Un altre disseny de bicapa que s'inspecciona en aquesta tesi és l'injector d'electrons basat en una capa no estequiomètrica d'òxid de silici amb un excés de silici del 16%. La caracterització d'aquesta capa ha permès demostrar la seva eficiència per corrents d'injecció baixos, obtenint una millor excitació de l'erbi. En contrapartida la seva funcionalitat en règims d'alta injecció queda anul·lada i per tant l'eficiència de l'electroluminescència dels dispositius s'equipara al d'una capa simple d'òxid de silici dopat amb erbi.

Per una altra banda, aquesta tesi presenta un nou dispositiu de tipus MIS dopat amb erbi. Degut a que la integració monolítica de fonts de llum basades en silici també requereix d'un acoblament amb la resta del circuit fotònic, un nou disseny que combina un dispositiu MIS i una guia de tipus escletxa (slot waveguide en anglès) és proposat com a estructura capaç de generar llum de forma intrínseca a dintre de la capa (excitació de l'erbi mitjançant la injecció d'electrons calents) i al mateix temps confinar-la a dintre del dispositiu, així com transmetre-la i acoblar-la a la part passiva del xip fotònic. Així doncs, s'ha dissenyat una guia d'ona electroluminescent de tipus escletxa on la capa activa està formada bé per un òxid de silici estequiomètric, bé per un sub-òxid amb un excés de silici, essent ambdós capes dopades amb erbi. Aquest dispositiu s'acobla a una guia d'ona passiva i a una graella d'extracció de la llum (output grating coupler en anglès). L'estudi de les seves propietats optoelectròniques mostra un bon confinament del mode transversal magnètic (TM) a dins de la capa, així com una injecció eficient de corrent elèctrica en la capa. Les pèrdues de propagació són de uns 40 dB/cm, i les d'acoblament mitjançant la graella d'extracció de llum de uns 20 dB/cm. L'estudi dels mecanismes de transport a dins de la guia d'ona dopada amb erbi mostra una reducció de la barrera d'injecció que ve modulada per el mecanisme de transport que té lloc a la capa no dopada de policristall de silici. El sistema és capaç d'extreure una senyal d'electroluminescència de desenes de $\mu W/cm^2$, mesurats amb un detector situat a sobre de la graella d'extracció de llum. Aquest valor, tot i que encara és baix per a futures aplicacions, marca el primer pas cap a la integració en un sol procés de fonts de llum electroluminescents basades en silici i acoblades amb la seva circuiteria passiva. A més a més, es fa un anàlisi detallat de les propietats optoelectròniques per mitjà d'un esquema de tipus bombeig-i-prova (pump and probe en anglès) acoblant una senyal òptica de referència sobre les guies d'ona electroluminescents, obtenint una atenuació màxima de la senyal òptica de -60 dB/cm en condicions extremes de polarització, i una modulació efectiva del 75%. A més a més, s'ha descartat una eventual amplificació òptica de la senyal de referència després de passar per la guia d'ona electroluminescent. Finalment, es proposa un sistema acoblat més complex en el que es concatenen dues guies d'ona de forma seqüencial, una amb dopatge d'erbi i l'altra sense dopatge. Aquest nou esquema permetria la generació de llum amb una guia i la seva modulació amb l'altra, oferint un sistema complex format per una font de silici electroluminescent i in modulador, fabricats de forma simultània en un procés estandarditzat CMOS.

Respecte al segon bloc d'aquesta tesi, es detalla l'estudi realitzat en capes fines basades en òxids de silici i oxinitrurs de silici dopats amb ions de ceri i/o terbi, fabricats per dipòsit químic de vapor en un sistema equipat amb un generador de plasma per ressonància electrònica de ciclotró (ECR-PECVD en anglès). En una primera part, es presenta l'estudi realitzat sobre capes simples que contenen o bé ions trivalents de ceri (Ce^{3+}) o de terbi (Tb^{3+}), i una composició variable de la matriu en la que es parteix d'un òxid de silici estequiomètric i es va disminuint la concentració d'oxigen en favor del nitrogen, fins a obtenir un oxinitrur de silici. Cal remarcar que es fa una explicació detallada del mètode de fabricació portat a terme per a produir aquest tipus de variació gradual de la composició. A més a més, cada composició ha estat dividida en diverses mostres, i cada una d'elles recuita a diferents temperatures per tal de veure les variacions estructurals, morfològiques i luminescents degut al tractament tèrmic efectuat. Les tècniques de caracterització utilitzades en aquesta part de la tesi són fonamentalment l'el·lipsometria espectroscòpica d'angle variable (VASE en anglès), l'espectrometria de retro dispersió de Rutherford (RBS en anglès), la microscòpia electrònica de transmissió (TEM en anglès) i mesures espectroscòpiques de fotoluminescència sota una excitació de làser ultraviolat. Els resultats obtinguts mostren una emissió més intensa en les mostres recuites a la temperatura més alta d'aquest estudi (1180°C) i també una major absorció en l'ultraviolat degut a la formació de petits silicats cristal·lins de terra rara. A més a més, l'estudi de fotoluminescència confirma que els oxinitrurs de silici són les matrius més apropiades per allotjar terres rares degut a que presenten una intensitat de fotoluminescència que és molt poc sensible als recuits de temperatura, obtenint així una senyal majoritàriament estable i constant per a qualsevol temperatura de recuit en el rang estudiat. Per al contrari, els òxids de silici dopats amb terres rares presenten una major variabilitat de la senyal de fotoluminescència en funció de la temperatura de recuit escollida. No obstant, totes les mostres estudiades presenten una fotoluminescència degut a l'excitació de les terres rares molt intensa que es pot observar a simple vista amb la llum encesa, independentment del tractament tèrmic efectuat (inclòs mostres no recuites prèviament). A més a més, s'ha estudiat el dopatge simultani de dues terres rares alhora en una capa d 'oxinitrur de silici, així com una arquitectura de capa més complexa basada en superposició de diverses capes, cada una d'elles amb un dopatge de terra rara diferent i separades per capes d'òxid de silici (arquitectura de multicapa). La validació del mètode de fabricació de les multicapes ha estat duta a terme mitjançant la caracterització per TEM, garantint així l'estructura de multicapa amb interfícies ben definides. També cal destacar que l'estructura multicapa es conserva després del tractament tèrmic fins a temperatures de recuit de 1000°C. Apart de les estructures multicapa, també es presenta una estructura complexa de tipus super-xarxa en la que capes sub-nanomètriques d'òxid de silici s'intercalen entre capes d'oxinitrur de silici dopades amb Tb^{3+} (també nanomètriques). De forma similar, l'estudi de fotoluminescència en multicapes mostra una emissió intensa de les terres rares, i una sintonització de color que va des del blau cobalt característic dels ions de Ce^{3+} fins al verd maragda dels ions de Tb^{3+}. Aquest fet es corrobora mitjançant el diagrama cromàtic CIE, que mostra la variació de color en coordenades xyz al llarg d'una línia recta que va des de tonalitats blaves fins al verd maragda. Un cop estudiades les propietats estructurals, morfològiques i luminescents de les multicapes. Seguidament, es detalla l'estudi preliminar de les propietats optoelectròniques que s'ha dut a terme en algunes d'aquestes capes dopades amb terres rares. Per això ha sigut necessari dipositar elèctrodes transparents i conductors sobre les capes, així com un elèctrode posterior fet d'alumini. Això ha sigut possible gràcies a un sistema d'evaporació per feix d'electrons (electron beam evaporation, EBE en anglès) disponible a la sala blanca de la facultat de física. A més a més, el gravat dels elèctrodes transparents s'ha dut a terme mitjançant una tècnica de màscara d'ombra (shadow mask en anglès). Una primera inspecció dels mecanismes de transport en aquestes capes mostra una conducció limitada per l'elèctrode en els òxids de silici, mentre que els oxinitrurs de silici mostren una conducció per trampes limitada per la capacitat d'acceptar càrrega de la capa i no per la capacitat d'injecció dels elèctrodes. També es mostren els espectres d'electroluminescència obtinguts, demostrant així que les terres rares són excitades de forma adient degut a la càrrega injectada. No obstant, els dispositius de capa simple mostren poca fiabilitat, assolint la ruptura del dispositiu molt abans de l'esperat. Aquest fet ha estat atribuït als alts voltatges necessaris per injectar càrrega a la capa. En contrapartida, la super-xarxa sub-nanomètrica dopada amb Tb^{3+} mostra una millor fiabilitat dels dispositius, essent aquests operatius durant diverses hores ininterrompudament. En aquest cas però, un voltatge de només 7 V és suficient per produir la senyal d'electroluminescència. Finalment, es proposa un mapa de ruta alternatiu per expandir el coneixement adquirit en aquesta tesi sobre els dispositius electroluminescents basats en silici i dopats amb terres rares.

B. Awards: EMRS Best Poster Award 2013

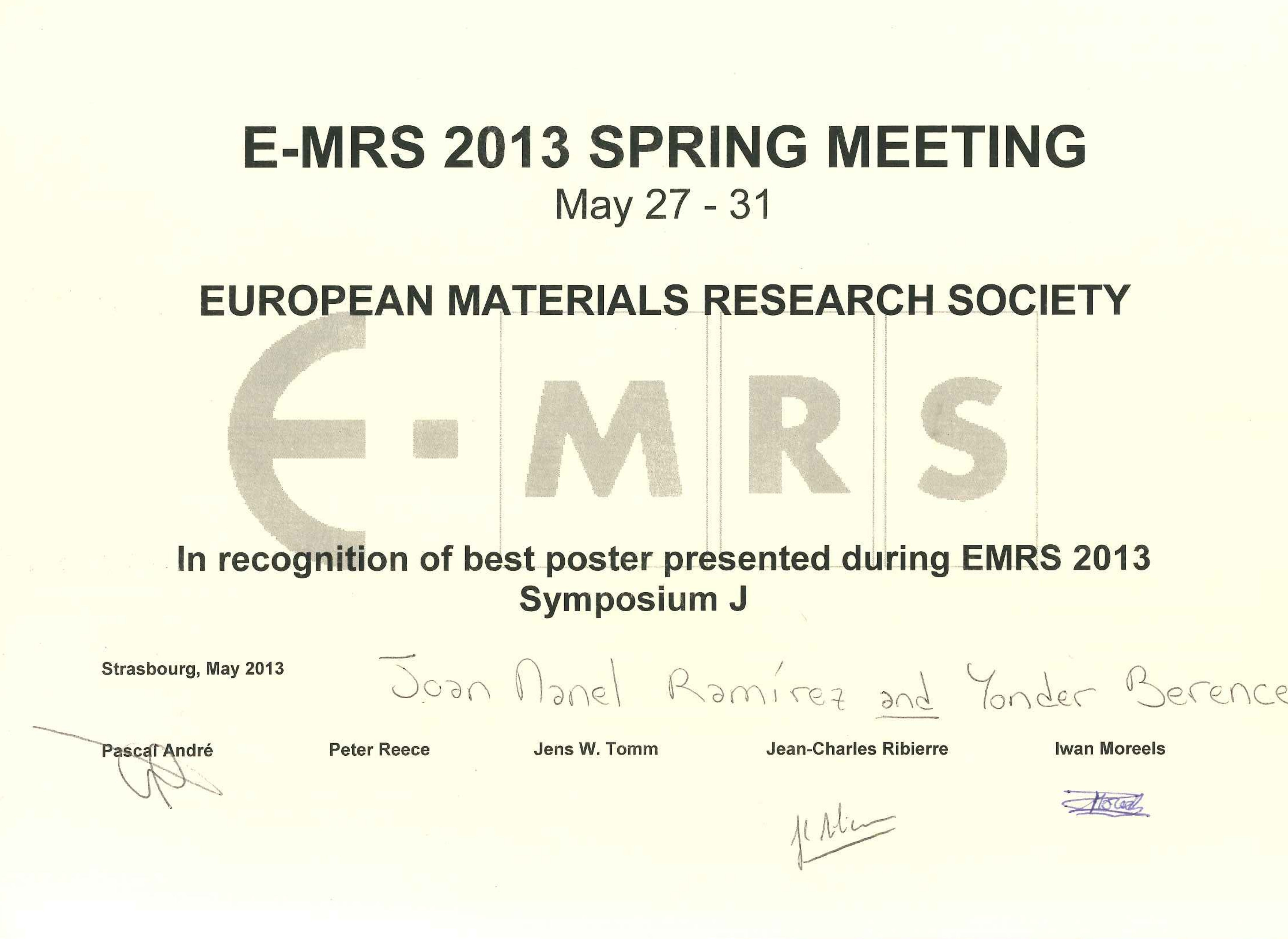

E-MRS 2013 SPRING MEETING

May 27 - 31

EUROPEAN MATERIALS RESEARCH SOCIETY

In recognition of best poster presented during EMRS 2013
Symposium J

Strasbourg, May 2013

Joan Manel Ramírez and Yonder Berencen

Pascal André	Peter Reece	Jens W. Tomm	Jean-Charles Ribierre	Iwan Moreels

SPIE. PHOTONICS EUROPE

Best Student Paper Award

Presented to

JOAN MANEL RAMÍREZ

Univ. of Barcelona, Spain

Silicon Photonics and Photonic Integrated Circuits Conference 9133-10:
On the photoluminescence of as-deposited Tb-doped silicon oxides and oxynitrides fabricated by ECR-PECVD

Presented by

Laurent Vivien
Seppo Honkanen
Lorenzo Pavesi
Stefano Pelli
2014 Conference Chairs

SPIE.